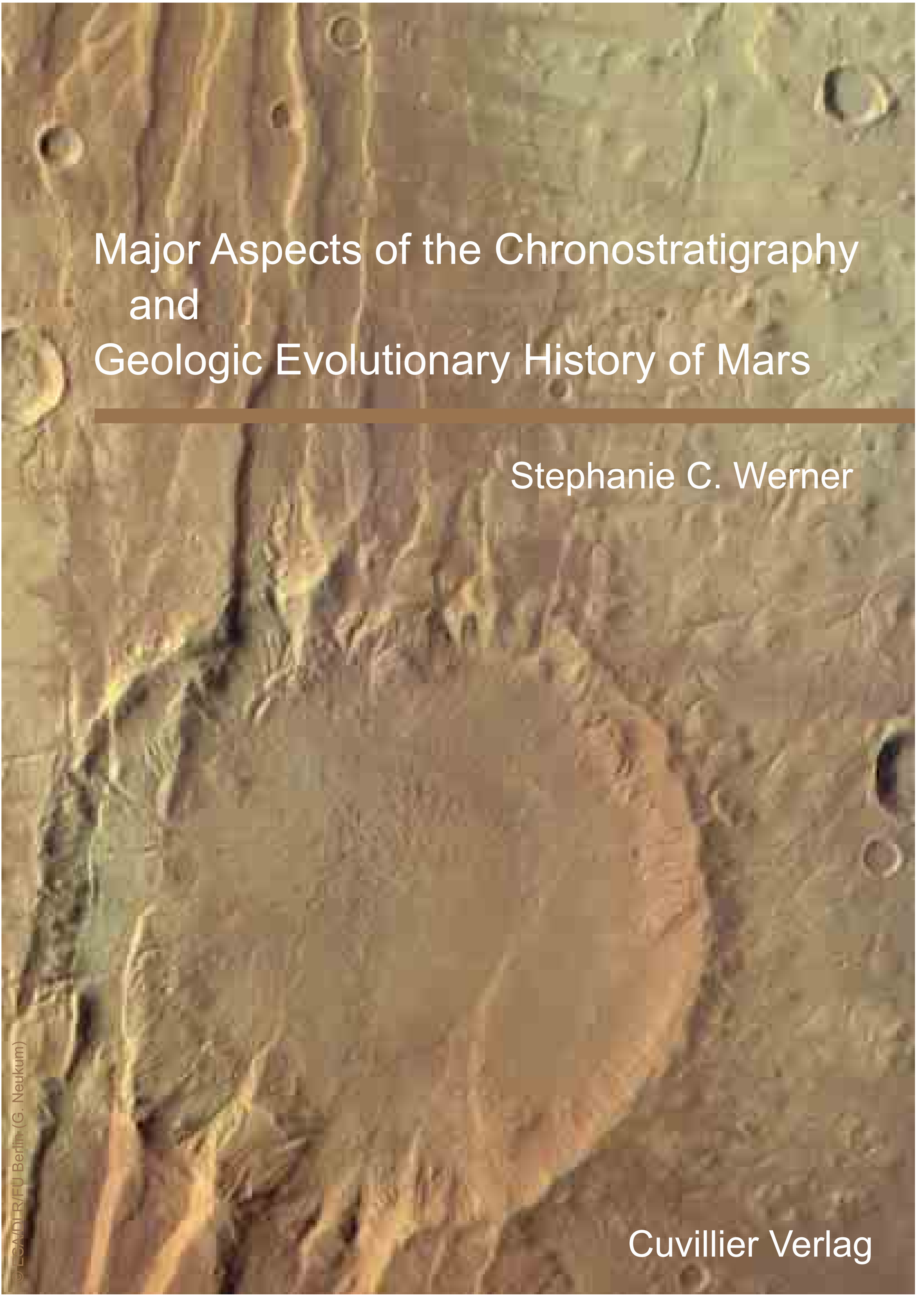

Major Aspects of the Chronostratigraphy and Geologic Evolutionary History of Mars

Stephanie C. Werner

Cuvillier Verlag

Major Aspects of the Chronostratigraphy

and

Geologic Evolutionary History of Mars

Dissertation zur Erlangung des Grades
eines Doktors der Naturwissenschaften

vorgelegt
von
Dipl.–Geophys. Stephanie C. Werner
aus
Würzburg

am Fachbereich Geowissenschaften
der Freien Universität Berlin
Berlin, 2005

Bibliografische Information Der Deutschen Bibliothek
Die Deutsche Bibliothek verzeichnet diese Publikation in der Deutschen Nationalbibliografie; detaillierte bibliografische Daten sind im Internet über http://dnb.ddb.de abrufbar.
1. Aufl. - Göttingen : Cuvillier, 2006
Zugl.: Berlin, Univ., Diss., 2005
ISBN 3-86537-774-2

Referent: Prof. Dr. G. Neukum
Korreferent: Prof. Dr. P. Janle
Tag der Disputation: 16.12.2005

Nonnenstieg 8, 37075 Göttingen
Telefon: 0551-54724-0
Telefax: 0551-54724-21
www.cuvillier.de

1. Auflage, 2006
Gedruckt auf säurefreiem Papier

ISBN 3-86537-774-2

Preface and Acknowledgement

This work has been performed within the scope of the German Research Foundation's Priority Program *Mars and the Terrestrial Planets* (Schwerpunktprogramm *Mars und die terrestrischen Planeten* der Deutschen Forschungsgemeinschaft, DFG SPP 1115) as part of the project *Chronostratigraphy of Mars* at the Freie Universität Berlin, Institute of Geological Sciences.

For understanding the evolution of planets, other than Earth, remote sensing data are essential. Here, imagery acquired during many missions to Mars were used. The American missions Viking, Mars Global Surveyor, Mars Odyssey, and especially the European mission Mars Express allowed these investigations. The author appreciates the outstanding work of experiment and instrument teams, especially those of the High Resolution Stereo Camera (HRSC) onboard Mars Express.

First and foremost I would like to gratefully acknowledge the enthusiastic supervision by Prof. Dr. Gerhard Neukum. Without the numerous scientific discussions with him, his provision of resources and from time to time offering direction, this thesis would not have been possible.

I would like to thank Prof. Dr. Peter Janle who initially opened my mind to planetary science, introduced me to a number of scientific problems and has been accompanying my scientific life as a friendly mentor, and who also kindly agreed to reviewing this thesis.

Within the project "Chronostratigraphy of Mars" I have had the opportunity to more closly work with two persons I have admired since I started understanding a little more about planets. Both influenced my thinking in a most fruitful way and some aspects of this thesis would not have been discussed without their inspiration. I thank Prof. Dr. Boris A. Ivanov and Prof. Dr. Alexander T. Basilevsky for their friendship and scientific advice. They also taught me kindness and cordiality always to be part of scientific collaboration.

Ursula Wolf not only provided technical support, patiently counting countless (innumerable) craters, but also listened and advised me in calmness and not to forget the aim of this work. Thank you very much!

This work also benefited from enthusiastic discussion within the HRSC Science Team and fruitful collaborations with Prof. Dr. Ronald Greeley, Dr. David Williams, Prof. Dr. James Head, III., Prof. Dr. Harald Hiesinger, Prof. Dr. John Murray, Prof. Dr. Bernhard Foing, Dr. Tanja Zegers, Prof. Dr. Peter Kronberg, Dr. Kenneth Tanaka. To share my results with my international colleagues I appreciate the permission to write in English, and thank Andrew Thorpe, Prof. Dr. Trond Torsvik, and Prof Dr. Gerhard Neukum for "polishing" the English.

The members of the planetology groups at the Freie Universität Berlin and DLR-Berlin, with whom I could not only discuss science but who also made life enjoyable should not be forgotten: Stephan van Gasselt, Roland Wagner, Ernst Hauber, Harald Hoffmann, Wilhelm Zuschneid. Many interesting scientific discussion started having a cup of coffee with Dr. Ljuba Moroz, Dr. Anders Erikson and Kerstin Seller, Dr.–Ing. Olaf Lotter, Dr. Jörg Ebbing and Melanie Mesli, Dr. Jörg Knollenberg, Dr. Susanne Wölz and many others.

My parents Barbara and Priv.–Doz. Dr. Peter–Christian Werner, who always supported me to do it my way, I thank them with all my heart. And last but not least my thanks go to Prof. Dr. Trond H. Torsvik, who is backing all my enthusiasm in life and science.

1. Abstract

This thesis was conducted in the framework of the German Research Foundation's priority program *Mars and the Terrestrial Planets* as part of the project *Chronostratigraphy of Mars*.

All global stratigraphic and geologic systems for Mars have been based on remote sensing data gathered during the Mariner 9 and Viking mission (Tanaka, 1986; Tanaka *et al.*, 1992a), culminating in three 1:15M–scale geologic maps by Scott and Tanaka (1986); Greeley and Guest (1987); Tanaka and Scott (1987). Generally, most of the surface–forming processes were placed in the early phase of the Martian evolution. Chrono–stratigraphic schemes for Mars are derived from imagery and crater frequencies observed during Mariner 9 and Viking missions, and however, led to a wide range of chronologic systems with no clear consensus on the absolute ages (Hartmann, 1973b; Soderblom *et al.*, 1974; Neukum and Wise, 1976; Hartmann *et al.*, 1981; Neukum and Hiller, 1981; Neukum, 1983; Strom *et al.*, 1992). Missions launched in the late 1990ies, such as Mars Global Surveyor and Mars Odyssey revealed very young volcanic surfaces, correlating in age with Martian meteorite crystallization ages (Hartmann, 1999a). Additionally, global topography (Smith *et al.*, 1999a,b, Mars Orbiter Laser Altimeter) and gravity data (Zuber *et al.*, 2000) as well as the discovery of strong remnant magnetization of the older Martian crust (Acuña *et al.*, 1999), implied a more continual and diverse evolution than previously thought.

Age determination techniques were initially developed for lunar applications during the late 1960s and early 1970s when automated and manned missions to the moon allowed for sample return of rock material. Radiometric rock ages (absolute ages) and correlation of these ages with crater size frequencies (relative ages) measured in units surrounding the landing sites, build standards for calibrating crater frequencies on the moon and other solid surface–bodies on a global scale.

The technique applied in this study has been developed and outlined by Neukum *et al.* (1975) for the moon and later other planets in general (Neukum, 1983). The methodical bases have been transferred to Mars (Neukum and Wise, 1976; Neukum and Hiller, 1981; Neukum, 1983; Neukum and Ivanov, 1994, and other solid–surface planetary bodies) and are the most reliable tools to define global age relations. Key is the single source of the inner solar system projectile population (asteroid belt,), was proven firmly (e.g. Neukum and Ivanov, 1994). However, the absolute chronology and absolute ages of different Martian stratigraphic units were known only crudely then due to the uncertainties primarily in the Martian impactor flux. In 2001, different approaches by Hartmann, Neukum and Ivanov to apply the underlying cratering chronology model and the lunar crater production function for the Martian case were successfully unified (Neukum *et al.*, 2001; Hartmann and Neukum, 2001; Ivanov, 2001). Nevertheless, due to limited coverage and resolution of the previously available imagery, it was not possible to measure the Martian calibration crater production function over a wide–enough crater size range. Now, imagery newly gathered by the High Resolution Stereo Camera (HRSC) experiment onboard ESA–Mars Express mission could be used. The experiment is capable to cover large areas at resolutions of up to 11 meter per pixel. The study presented here, was benefiting from the proprietary use of the HRSC imagery in the group of the Principal Investigator G. Neukum.

One major aim of this thesis was to improve and/or verify the existing chronostratigraphic system of Mars. The second major goal was to understand globally the geologic evolutionary history of Mars focusing on the volcanic and fluvial processes, determining consistent absolute ages and studying the sequence of events through time. This implies the photogeologic analysis of all available types of Martian imagery in order to cover the diversity of Martian landforms in time and space.

In order to unravel the evolutionary history of Mars, this study was notably concerned with testing the theoretically transferred lunar crater production function for the Martian case. As an outcome of this study the proposed Martian crater production function was proven over the entire (50 meters to 500 kilometers) crater diameter–size range by measurements and the time–independence of the Martian crater production function was confirmed. This was not possible earlier on the basis of the available imaging data . This result confirms that all craters have formed by a single projectile source from the asteroid belt. Any deviation (visible in kinks) from the confirmed Martian standard crater production function indicate resurfacing events. In such cases the method of age determination has been improved, and a procedure to derive the resurfacing age with high accuracy has been developed.

An additional topic has been to understand the contribution or "contamination" due to secondary cratering (craters generated by the ejecta of a "primary" crater). Constructing theoretical secondary crater size–frequency distributions and comparison with observed crater size–frequency distributions show that most models on secondary cratering ignore the time–dependence of the contributing number of secondary craters: An older surface would have a larger secondary contribution, because more abundant and larger primary craters must have contributed. Such a contribution which should also change the ratio of small–to–large crater frequencies is not observed. All measurements obtained in this and in other (similar) investigations, the data of which have been used in this thesis, have been performed in a crater–diameter range where at most 10% secondaries are contributing.

After proving the standard Martian crater production function, the applicability of the transferred cratering chronology model was tested. The formation ages of the large impact basins (diameters larger than 250 kilometers) on Mars have been determined and it is argued that these basins were formed no later than 3.9 Ga ago (1 Ga = 1^9 years = 1 billion of years). This result is in agreement with the situation on the moon and the general idea of a flux decay after the heavy bombardment period, the tail end of planetary formation. Hereby, the cratering chronology model has been affirmed once again. Independently, large volcanic surface units show crater frequencies and absolute ages derived from such measurements that are in very good agreement with crystallization ages of basaltic Martian meteorites. This support the applicability of the chronology model.

Applying these findings, the evolutionary history of Mars was studied in detail: Type areas of the Martian epochs (Noachian, Hesperian and Amazonian) such as Noachis Terra, Hesperia Planum, northern lowland regions, Amazonis and Elysium Planitia, have been examined. Of special interest were volcanic, fluvial and possible glacial processes. Therefore, the frequencies of craters superimposing geologic units in the northern hemisphere occupying lowlands and outflow channels were measured, as well as the dichotomy boundary separating the lowlands and highlands, following the new mapping approach by Tanaka *et al.* (2003); Tanaka *et al.* (2005) based on MOLA topography data. We aimedat understanding the role of water during the Martian geologic evolution.

Relics of episodic fluvial activity is observed as valley network systems in the highland regions (Carr, 1986). The spatial and temporal coincidence of these fluvial landforms and crustal remnant magnetization indicates that any precipitation potentially occurred in the presence of a dynamo–induced magnetic field. Despite the low gravitation of Mars a magnetic dipole–field kept the Martian atmosphere stable and possibly permitted a water cycle during the early Martian history (until latest 3.7

Ga ago). If a Martian ocean existed in the northern lowlands, it ceased before 3.7 Ga ago. While possible surface run–off manifested in the valley networks occurred until about 3.7 Ga, the latest forceful fluvial surface modification occurred during the formation of large outflow channels until 3.5 Ga ago. The latter, though, appears to have been triggered by volcanic activity in the vicinity of the largest volcanic province, the Tharsis rise. Similar correlations have been observed at a few highland volcanoes, e.g. Hadriaca Patera. The younger fluvial erosion is closely related to volcanic activity and occurred in episodes over the last 2 billion years. Extensive measurements at almost all volcanic constructs and in many volcanic plains allowed for the interpretation of the evolutionary history of Martian volcanic constructs. An interplay of volcanic processes with ancient and more recent fluvial and glacial activity is confirmed by our study. Globally, the volcanic activity started very early in the Martian evolution, major volcanic plains formed until about 3.7 Ga ago, e.g. Hesperia Planum. Most of the volcanoes show activity at least until 3.5 Ga ago. They achieved their present dimensions already at that time. Later volcanic resurfacing could not erase larger older impact craters and indicates that later volcanic activity was weaker than during the construct–forming period. Another major finding is that the volcanic activity on Mars continued until very recently (e.g. 2 Ma at the flanks of Olympus Mons, (Neukum *et al.*, 2004)), and is more wide–spread than believed earlier. The crystallization ages of basaltic Martian meteorites (about 180 Ma, 450 Ma and 1.3 Ga) confirm this finding. The enigmatic Medusae Fossae formation could be dated for the first time indicating that explosive volcanic eruption occurred even as recently as 1.6 Ga ago.

This thesis provides the first coherent view of the geological evolution of Mars, focusing on impact cratering, volcanic, fluvial and glacial processes. In addition to tectonics and aeolian dust distribution, such processes play a significant role in sculpting the Martian landscape. Notably the volcanic and related tectonic activity sheds lights on the internal dynamics and thermal evolution of planets.

By understanding the evolutionary history of Martian volcanic constructs, the formation time of large impact basins, as well as the evolution of the northern lowlands and the dichotomy boundary, essential time–markers have been gathered in this work. The global geological evolution of Mars is derived from ages determined in this work. As indicated by the Martian meteorite ALH84001, Martian crust had solidified around 4.5 Ga ago, but the oldest southern highland units reveal surface ages of only about 4.2 Ga.

The crustal dichotomy formed early during the crustal formation, but at least before the formation of the oldest impact basins Hellas and Isidis. The morphologically defined dichotomy between heavily cratered southern highlands and smooth northern lowland plains formed later. The basement of the northern lowland appears to be about 3.8 Ga old and was covered by two types of deposits later. Emplacement was partly due to fluvial activity during the outflow channel formation and ended about 3.5 Ga ago. Volcanic deposits emplaced through volcanic activity at the two volcanic centers Elysium and Tharsis contributed as well. Global volcanic activity is observed until about 3.7 Ga ago (volcanic plains formation in the highlands) and later activity focused on the volcanic vents in the Tharsis and Elysium region. Major volcanic activity over the last 3 billions of years is restricted to the large shield volcanoes in these two volcanic provinces and their vicinities. Fluvial landforms that formed later than 3.5 Ga (melting of subsurface ice) were triggered by volcanic activity.

This study revealed that the youngest epoch, the Amazonian, is reflected in a variety of landforms, and includes an absolute time span of three–quarters of the geological record of Mars. The crater size–frequency distributions measured in the northern lowlands reveal strong resurfacing events and a non–uniformity in age. This implys that the Amazonian–Hesperian

time–stratigraphic boundaries have to be revisited. In most of our investigations, based on high–resolution imagery (HRSC, THEMIS, and MOC–NA), large volcanic units have been formed later than 500 Ma ago. In addition, most surface morphologies associated to ice or subsurface ice (glacial and periglacial), such as lobated debris aprons, lineated valley fill, or possible rock glaciers, appear to be relics of the most recent "ice ages" on Mars. All landforms related to such processes have formed during the most recent eighth of the Martian geologic history. Based on these results, a revision of the boundary key units that would best represent those youngest Amazonian epochs in high–resolution imagery. A new subdivision of the last three billion of years Martian geologic history (considered Amazonian) should be considered.

Providing that the time–frame outlined in this study is correct, the timing for the thermodynamical evolution of Mars can be assessed. The apparent absence of plate tectonics on Mars and the presence of huge volumes of strongly magnetized crustal materials, requiring the presence of a strong dynamo field in ancient times, makes Mars an interesting planet to compare with the Earth or thermodynamical models for other terrestrial inner Solar System bodies.

2. Kurzfassung

Diese Arbeit ist im Rahmen des DFG–Schwerpunktprogramms *Mars und die terrestrischen Planeten* mit der Ausrichtung *Chronostratigraphie des Mars* durchgeführt worden.

Die globalen stratigraphischen und geologischen Systeme für den Mars basieren auf Fernerkundungsdaten der Mariner 9 sowie der Vikingmission (Tanaka, 1986; Tanaka *et al.*, 1992a). Diese geologischen Untersuchungen sind in drei geologischen Karten mit einem 1:15M–Maßstab von Scott and Tanaka (1986); Greeley and Guest (1987); Tanaka and Scott (1987) zusammengefasst worden. Üblicherweise wurden die meisten oberflächenformenden Vorgänge in die frühe Phase der Marsentwicklung gelegt. Chrono–stratigraphische Schemata für den Mars wurden aus Bildmaterial und Kraterhäufigkeiten abgeleitet, die während der Mariner 9 sowie der Vikingmission aufgenommen wurden. Diese führten aber zu eine Vielzahl von chronologischen Systemen, denen der klare Konsens in den absoluten Altern fehlte (Hartmann, 1973b; Soderblom *et al.*, 1974; Neukum and Wise, 1976; Hartmann *et al.*, 1981; Neukum and Hiller, 1981; Neukum, 1983; Strom *et al.*, 1992). Missionen, gestartet in den späten 1990ern wie Mars Global Surveyor und Mars Odyssey, gaben sehr junge vulkanische Oberflächen preis, deren Alter den Kristallisationsaltern von einigen Marsmeteoriten entsprachen (Hartmann, 1999a). Außerdem deuteten globale Topographie– (Smith *et al.*, 1999a,b, Mars Orbiter Laser Altimeter) und Schweredaten (Zuber *et al.*, 2000) sowie die Entdeckung einer starken remanenten Magnetisierung der älteren Marskruste (Acuña *et al.*, 1999) eine weiter andauernde und mannigfaltigere Entwicklungsgeschichte an als zuvor gedacht.

Die Methoden der Altersbestimmung wurden in den späten 1960igern und frühen 1970igern entwickelt, als automatisierte und bemannte Missionen zum Mond die Gesteinsprobennahme, deren radiometrische Altersbestimmung (absolute Alter) und eine Korrelation dieser Alter mit Kraterhäufigkeiten (relative Alter) in der Landestellenumgebung erlaubten und Standards zur Kalibration von Kraterhäufigkeiten für den gesamten Mond und auch auf anderen Planeten setzten. Die Techniken, die in dieser Studie angewandt werden, entwickelten Neukum *et al.* (1975) für den Mond und stellten sie detailliert für den Mond und andere Planeten dar (Neukum, 1983). Diese methodischen Grundlagen können auf dem Mars (und anderen festen planetaren Körpern) gleichermaßen angewandt werden (Neukum and Wise, 1976; Neukum and Hiller, 1981; Neukum, 1983; Neukum and Ivanov, 1994) und haben sich als zuverlässiges Hilfsmittel erwiesen, um globale Altersabhängigkeiten zu bestimmen. 2001 wurde der erfolgreiche Versuch unternommen, die zugrunde liegende Einschlagschronologie und lunare Kraterproduktionsverteilung vom Mond auf den Mars zu übertragen (Neukum *et al.*, 2001; Hartmann and Neukum, 2001; Ivanov, 2001). Hierbei wurden verschiedene Ansätze zusammengeführt. Allerdings war es wegen der begrenzten Abdeckung und Bildauflösung der Vikingdaten nicht möglich, die Kraterproduktionsverteilung des Mars durchgehend zu bestimmen. Mit den neuen Bilddaten, die durch das High Resolution Stereo Camera (HRSC) Experiment an Bord der ESA–MarsExpress–Mission gesammelt werden, kann diese Lücke überwunden werden. Dieses Experiment erlaubt Aufnahmen, die große Flächen mit bis zu 11 Meter pro Bildpunkt auflösen. Diese Studie profitierte unter anderem von der privilegierten Nutzung des HRSC Bildmaterials.

Ein Ziel dieser Arbeit ist es, das existierende chronostratigraphische System für den Mars zu verbesseren und/oder zu bestätigen. Ein weiteres Ziel ist es, die globale Entwicklungsgeschichte des Mars zu verstehen, wobei der Schwerpunkt auf die altersmäßige Erfassung der vulkanischen und fluviatilen Prozesse gelegt wurde. Dies impliziert eine photogeologische Analyse der für den Mars verfügbaren Bilddaten, um die vielfältigen Landschaftsformen des Mars in zeitlicher und räumlicher Verteilung soweit wie möglich einzuordnen.

Um die Entwicklungsgeschichte des Mars zu enträtseln, beschäftigt sich ein beträchtlicher Teil dieser Studie mit der Bestätigung der auf den Mars übertragenen theoretischen lunaren Kraterproduktionsverteilung und der Zuverlässigkeit des übertragenen Chronologiemodells. Innerhalb dieser Studie war es erstmals möglich, die für den Mars vorgeschlagene Kraterproduktionsverteilung über den gesamten Kraterdurchmesserbereich (von 50 Meter bis 500 Kilometer) zu belegen. Dies wurde erst durch die neuen Aufnahmen des HRSC–Experimentes an Bord des MarsExpress–Satelliten durchgängig möglich. Abweichungen von der bestätigten Mars–Standard–Kraterproduktionsverteilung deuten auf oberflächenverändernde Prozesse hin, die sich in einem Abknicken in der Verteilungskurve äußern. Für solche Fälle ist hier die Methode der Altersbestimmung verbessert und eine Prozedur entwickelt worden, die eine Alterseinordnung der Oberflächenüberprägung gestattet.

Ein weiterer Gegenstand dieser Studie ist, den Beitrag von bzw. die "Kontamination" durch Sekundärkrater zu untersuchen. Hierfür wurden theoretische Sekundärkraterverteilungen konstruiert und mit beobachteten Kratergrößenhäufigkeitsverteilungen verglichen. Es zeigt sich, dass die meisten Modelle zur Sekundärkratergenerierung die Zeitabhängigkeit dieses Prozesses ignorieren. Diesen Modellen folgend, wiese eine ältere Oberfläche einen höheren Sekundärkrateranteil auf, da eine höhere Anzahl größerer Primärkrater Sekundärkrater zur Kraterverteilung beiträgt. Dies wird nicht beobachtet. Alle in dieser oder vergleichbaren Studien durchgeführten Messungen sind außerdem in einem Kraterdurchmesserbereich vorgenommen worden für den höchstens von einem 10–prozentigen Anteil an Sekundärkratern ausgegangen werden muss.

Neben dem Nachweis der Mars–Standard–Kraterproduktionsverteilung ist auch die Anwendbarkeit der übertragenen Einschlagschronologie getestet worden. Hierfür sind die Entstehungsalter der großen Einschlagsbecken (mit Durchmessern über 250 Kilometern) auf dem Mars bestimmt worden. Keines der Becken ist jünger als etwa 3,9 Ga (1 Ga = 10^9 Jahre = 1 Milliarde Jahre) alt. Dies stimmt mit der Situation auf dem Mond überein und auch mit der allgemeinen Annahme, dass der Fluss insbesondere der größten Projektile nach dem Ende des schweren Bombardement (heavy bombardment) als "Schwanzende" der Planetenentstehung abklingt und bekräftigt das Einschlagschronologiemodell. Weitläufige Gebiete, die durch Vulkanismus entstanden sind, zeigen Kraterhäufigkeiten und daraus abgeleitete absolute Oberflächenalter, die gut mit Kristallisationsaltern von basaltischen Marsmeteoriten übereinstimmen und somit die Anwendbarkeit des Chronologiemodells unterstreichen.

Nutzt man diese Befunde, kann die Entwicklungsgeschichte des Mars detailliert untersucht werden: In den Typregionen der geologischen Epochen des Mars (Noachium, Hesperium und Amazonium), wie z. B. Noachis Terra, Hesperia Planum, den nördlichen Tiefländern, Amazonis und Elysium Planitia, ist erneut gemessen worden. Von besonderem Interesse sind vulkanische, fluviatile und mögliche glaziale Prozesse. Kraterhäufigkeiten sind für geologische Einheiten bestimmt worden, die insbesondere in den die nördlichen Hemisphäre einnehmenden Tiefländern und Ausflusstälern, sowie an der Dichotomiegrenze zwischen Hoch– und Tiefland liegen. Ziel war es, die Rolle des Wasser in der frühen Phase der Marsentwicklung besser zu verstehen. Episodische fluviatile Aktivität wird in Form von Talnetzwerken beobachtet, die man vorrangig in den alten Hochlandregionen findet. Die räumliche und zeitliche Koinzidenz von solchen fluviatilen Landschaftsräumen und krustaler remanenter Magnetisierung deutet darauf hin, dass eventuelle Niederschläge während eines vorhandenen dynamoinduzierten Magnetfeldes auftraten. Trotz der geringen Gravitation des Mars kann eine Atmosphäre stabil gehalten werden, wenn ein Magnetfeld vorhanden ist, und erlaubt einen möglichen Wasserkreislauf in der Frühphase der Marsentwicklung (bis vor etwa 3,7 Ga). Falls der Mars jemals einen Ozean in der nördlichen Tiefebene besessen hat, ist dieser spätestens vor etwa 3,7 Ga verschwunden. Während möglicher Oberflächenabfluss von Wasser – manifestiert in den Talnetzwerken – nur bis etwa vor 3,7 Ga auftrat, zeigt sich die letzte deutliche Oberflächenmodifikation durch fluviatile Aktivität in der Bildung der Ausflusstäler bis vor etwa 3,5 Ga. Letztere sind allerdings vermutlich durch vulkanische Aktivität im Einflussgebiet der größten Vulkanprovinz, der Tharsisaufwölbung, entstanden. Ähnliche Wechselwirkungen kann man auch an einigen Hochlandvulkanen, wie z.B. Hadriaca Patera, finden. Jüngere fluviatile Erosion ist eng mit vulkanischer Aktivität verknüpft, und ist episodisch auftretend über die letzten 2 Milliarden Jahre zu beobachten. Umfangreiche Messungen an den meisten Vulkanen und vielen vulkanischen Ebenen erlauben es die Entwicklungsgeschichte der Marsvulkane sehr genau zu interpretieren und bestätigen ein Wechselspiel zwischen vulkanischen Prozessen und früher als auch rezenterer fluviatiler und glazialer Aktivität. Global startete der Marsvulkanismus in der Frühphase der Marsentwicklung. Die meisten Vulkanebenen sind bis vor 3,7 Ga entstanden, z.B. Hesperia Planum. Die meisten Vulkane zeigen Aktivitätsphasen bis vor etwa 3,5 Ga und erreichen bis dahin ihre endgültige Größe. Folgende vulkanische Oberflächenüberprägung konnte die alten großen Krater nicht auslöschen. Hieraus ist eine Abschwächung der vulkanischen Aktivität nach der Aufbauphase abzuleiten. Ein weiterer wichtiger Befund ist, dass die vulkanische Aktivität auf dem Mars bis in jüngste Zeit anhält (z. B. 2 Ma an den Flanken des Olympus Mons), und der junge Vulkanismus großflächiger ist als zuvor angenommen. Die Kristallisationsalter der basaltischen Marsmeteoriten (etwa 180 Ma, 450 Ma und 1,3 Ga) stützen diese Befunde. Erstmalig konnte die Medusae Fossae Formation datiert werden, dies deutet darauf hin, dass explosiver Vulkanismus noch etwa vor 1,6 Ga aufgetreten sein könnte.

Diese Dissertation bietet erstmals eine kohärente Darstellung der Entwicklungsgeschichte des Mars, mit den Schwerpunkten Einschlagskraterentstehung, vulkanischen und fluviatilen (bzw. glazialen) Prozessen. Neben Tektonik und äolischer Staubverteilung, sind dies die bedeutendsten oberflächenformenden Prozesse auf dem Mars. Besonders die vulkanische und damit verbundene tektonische Aktivität spiegeln die innere Dynamik und thermische Entwicklung eines Planeten an der Oberfläche wider. Aus der Entwicklungsgeschichte der Marsvulkane, der Entstehungszeit der großen Einschlagsbecken und der Entwicklung der nördlichen Tiefebenen und der Dichotomiegrenze sind in dieser Dissertation die wesentlichen Zeitmarken bestimmt worden, um eine globale Entwicklungsgeschichte für den Mars aus diesen Altern abzuleiten. Das Kristallisationsalter des Marsmeteoriten ALH84001 belegt, dass sich die Marskruste vor etwa 4,5 Ga verfestigt hat, allerdings liegen die höchsten Alter der Hochlandgebiete, die mit der Kraterzählmethode bestimmt wurden, nur bei etwa 4,2 Ga. Die krustale Dichotomie hat sich vermutlich schon mit der Krustenentstehung ausgebildet, muss aber spätestens während der Entstehung der ältesten sichtbaren Einschlagsbecken Hellas und Isidis bestanden haben. Die morphologisch sichtbare Dichotomiegrenze, definiert als Grenze zwischen stark bekratertem Hochland und ebenem Tiefland, hat sich erst später gebildet. Das vermutliche Grundgestein der nördlichen Tiefebene erscheint mindestens 3,8 Ga alt und ist von zwei Materialtypen überlagert. Die Ablagerungen wurden zum Teil durch fluviatile Aktivität während der Ausflusstälerentstehung bis vor etwa 3,5 Ga und zum Teil vulkanisch aus den beiden Vulkanzentren Tharsis und Elysium in die Tiefebene eingetragen. Die fluviatilen Landschaftsformen, die sich später als vor 3,5 Ga formten, sind durch vulkanische Aktivität (Aufschmelzen von Eis im Untergrund) verursacht worden.

Diese Studie zeigte, dass während der jüngsten Epoche, dem Amazonium, vielfältige Landschaftsformen hervorgebracht wurden, sie aber in der geologischen Einordnung des Mars drei Viertel der absoluten Zeitspanne einnimmt. Die in der nördlichen Tiefebene gemessenen Kratergrößenhäufigkeitsverteilungen zeigen deutlich oberflächenüberprägende Ereignisse und eine Uneinheitlichkeit im Alter. Das heißt, eine Überprüfung der zeitstratigraphischen Grenze zwischen dem Hesperium und Amazonium ist nötig. Die meisten meiner Untersuchungen, basierend auf hochaufgelösten Bilddaten (HRSC, THEMIS und MOC), zeigen, dass große Gebiete von vulkanischen Einheiten eingenommen werden, die vor weniger als 500 Ma geformt wurden. Außerdem sind viele Oberflächenformen (glazial und periglazial), wie z. B. Schuttschürzen (lobated debris aprons), linienhafte Talverfüllungen (lineated valley fill) oder Blockgletscher, entstanden. Diese sind möglicherweise Relikte aus Eiszeiten aus dem jüngsten Achtel der Marsgeschichte. Hieraus ergibt sich die Notwendigkeit einer Revision der jüngsten Epoche der Marszeitalter. Hochaufgelöste Bilddaten würden eine neue Unterteilung der letzten drei Milliarden Jahre (z.Z. durchgehend Amazonium) erlauben.

Vorausgesetzt, dass der in dieser Studie gesetzte Zeitrahmen stimmt, kann man auch die zeitliche Abfolge der thermodynamischen Entwicklung vom Mars besser einschätzen. Die offensichtliche Abwesenheit von Plattentektonik und das Vorhandensein großer Volumen stark magnetisierten, krustalen Materials, das eines starken Dynamofeldes in der Frühphase der Marsentwicklung bedurfte, machen den Mars zu einem interessanten Planeten im Vergleich zur thermodynamischen Entwicklung der Erde und anderer terrestrischer Körper im inneren Sonnensystem.

Contents

3. Introduction and Motivation

Open Scientific Issues: The current understanding of Mars's geologic history in terms of sequence of events is mainly based on crater size–frequency measurements carried out on high resolution Viking imagery. Prerequisite to the interpretation of crater size–frequency data obtained in various geologic units of different ages is (1) the determination of the shape of the Martian crater production function, implying the primary source of projectiles which impacted the Martian surface, and (2) the application of a reliable cratering chronology model. It has been shown that asteroids from the main belt provided the primary source of impactors on the terrestrial planets in the inner solar system, as inferred from the complex shape of both the crater production function measured on these bodies and the asteroidal size distribution (Neukum, 1983; Neukum and Ivanov, 1994; Neukum *et al.*, 2001; Ivanov *et al.*, 1999; Ivanov, 2001; Werner *et al.*, 2002). For understanding the geologic evolution of a terrestrial planetary body it is necessary to place the different geological processes involved in shaping the planetary surface into a chronological sequence of events. At a regional or local scale, a relative stratigraphy can be derived by analyzing superposition relations and differences in the state of degradation between different geomorphological surface units. Global stratigraphic schemes for planetary bodies are based on the most common resurfacing process: the impacts of planetesimals which remain as crater or crater–related features on planetary surfaces. Through this random cratering process, the counting of the accumulated number of impact craters on planetary surfaces offers a valuable procedure in understanding the chronostratigraphy of a certain object.

Mars has a very diverse impact cratering record in terms of crater morphology, modification and crater frequency. Following the argumentation by Hartmann and Neukum (2001): Various stratigraphic units have been mapped on Mars and their relative ages have been determined by a combination of superposition relations and crater frequencies (Neukum and Hiller, 1981; Tanaka, 1986; Scott and Tanaka, 1986; Greeley and Guest, 1987; Tanaka and Scott, 1987). In principle, absolute ages can be estimated through impact crater frequencies, as it has been shown for the moon. However, the absolute chronology and absolute ages of different Martian stratigraphic units have been known only crudely due to the uncertainties primarily in the Martian impact flux. One approach to extract the crater production function from the geologically distorted record is to transfer the well known and measured production function of the moon to Martian impact conditions considering impact rate and scaling laws (Neukum and Wise, 1976; Neukum *et al.*, 2001; Hartmann and Neukum, 2001; Ivanov, 2001). Until now, due to limited coverage and resolution of the available imagery, it was not possible to measure the Martian crater production function over a wide–enough crater size range. A model for understanding the flux in Martian surroundings has been described by Wetherill (1967, 1979) and has been developed further with respect to dynamical relationships between planet–crossing and main–belt asteroids by Greenberg and Nolan (1989, 1993). Viking and Mariner 9 data analysis, however, led to a wide range of chronologic systems with no clear consensus on the absolute ages (Hartmann, 1973b; Soderblom *et al.*, 1974; Neukum and Wise, 1976; Hartmann *et al.*, 1981; Neukum and Hiller, 1981; Neukum, 1983; Strom *et al.*, 1992).

The most important step, the latest approach by Neukum *et al.* (2001); Hartmann and Neukum (2001); Ivanov (2001) who unified the two competing chronology models (Hartmann, 1973b, 1978; Hartmann *et al.*, 1981; Neukum and Hiller, 1981; Neukum, 1983) and evaluating the two differing styles of crater production functions which appear to agree over most of the diameter range.

Outlined already by Hartmann and Neukum (2001), the earliest Mariner data from 1965 to 1971, revealed heavily cratered terrain where the largest craters (D > 64 km) had crater frequencies similar to those in the lunar highlands, which indicated ages of 3800 to 4500 Ma (Leighton *et al.*, 1965). In the same region smaller craters (250 m <D<16 km) have lower numbers than in the lunar highlands and a wide range of degradation states suggesting losses of smaller craters by erosion and deposition (Öpik, 1965, 1966). This paucity is probably primarily the result of obliteration of craters by erosion and deposition by aeolian, fluvial, glacial and volcanic processes. It is still debated which of these processes is the most important. Although steady rates of obliteration are not applicable, changes in atmosphere thickness (Sagan *et al.*, 1973; Pollack *et al.*, 1987) or increased volcanism (Greeley and Spudis, 1981) or the abundance of permafrost associated with creep deformation (Squyres and Carr, 1986) as well as sporadic glacial erosion are reasonable. Mars Global Surveyor (MGS) added a new twist to understanding the youngest volcanic units by means of higher–resolution images down to 1.5 m/pxl. Crater statistics indicate for restricted areas, e.g. Elysium Planitia, ages less than 100 Ma or even 10 Ma (Hartmann and Berman, 2000). Furthermore, massive layering and mobility of dust and fine material is confirmed by Malin (1998) from MGS images. Investigations of the radiometric crystallization ages of Martian meteorites (SNC) appear to represent mafic igneous intrusions 1300 Ma ago (Nakhlites, Chassigny) and basaltic Shergottites indicate basaltic lava flows about 165 to 475 Ma ago (Nyquist *et al.*, 2001). ALHA 84001 with a crystallization age of 4500 Ma, probably samples the primordial crust of Mars. These meteorites indicate not only the young volcanic activity but also show evidence of liquid water due to alteration products (Shih *et al.*, 1998; Swindle *et al.*, 2000; Sawyer *et al.*, 2000; Bridges and Grady, 2000).

Motivation: One aim of this thesis is to improve and/or verify the existing chronostratigraphic system of Mars. The second goal is to globally understand the geologic evolutionary history of Mars focusing on the volcanic and fluvial processes, giving consistent absolute ages. This implies the photogeologic analysis of all available types of Martian imagery in order to cover all crater diameter ranges to verify the shape of the Martian crater production function. Having been operational at Mars since early 2004, the High Resolution Stereo Camera (HRSC) experiment onboard the European spacecraft MarsExpress introduced the opportunity to gather large image coverage at high resolution (12.5 m/pxl), and allowed measuring crater distributions on various geologic units of different ages. Complemented by data sets collected during the Viking, Mars Global Surveyor, and Mars Odyssey missions at different crater size ranges, the HRSC imagery allows us to determine the "real" shape of the Martian crater production function, not measurable on the previous imagery until now, and to confirm the stability of the crater–generating projectile population for the Martian case. The study also includes detailed investigation of the resurfacing history of the investigated areas and to examine erosion and crater obliteration processes. In parallel, the theoretical treatment, in cases where resurfacing may have occurred, has been developed further and the contribution of background secondary cratering has been investigated in detail to achieve a confident crater size–frequency/age relation.

Structure of the thesis: Firstly, the state of the art regarding the chronostratigraphy, the cratering chronology and the geologic history of Mars is described. Aspects of impact cratering on Mars are outlined in detail (Part I).

In Part II, age dating techniques are introduced. Improved methods for determining absolute ages in cases where resurfacing occurs and the relevance of background secondary cratering are quantified. Finally, the shape of the Martian crater production function for the entire measurable crater diameter range (10 meters to 500 kilometers) is given, based on measurements performed in this thesis. The confirmation and stability in time of the Martian crater production function is essential for the chronostratigraphical investigation.

Applying the knowledge summarized in Part I and II, the Martian stratigraphy is re-assessed (Part III): The determination of the Martian basin formation ages together with the correlation of Martian meteorite crystallization ages and large volcanic units supports the credibility of the Martian cratering chronology model, as it has been transferred from the moon to Mars by Hartmann and Neukum (2001). Detailed investigations of the evolution of the Northern Lowlands, the dichotomy boundary and related fluvial activity (modifying regionally the dichotomy boundary) as well as the global volcanic evolutionary history (in time and space) and the interplay of various processes (volcanic, fluvial, glacial, tectonic and aeolian) have led to a solid data base to finally derive the evolutionary history of Mars with respect to the individual processes.

These resulting global evolutionary aspects are summarized in Part IV, in comparison with previous interpretations of the global chronostratigraphic scheme as it was developed in the post–Mariner and post–Viking era.

With the data gathered in the context of this thesis, an attempt has been made to describe the internal and surface evolution of Mars throughout its whole history.

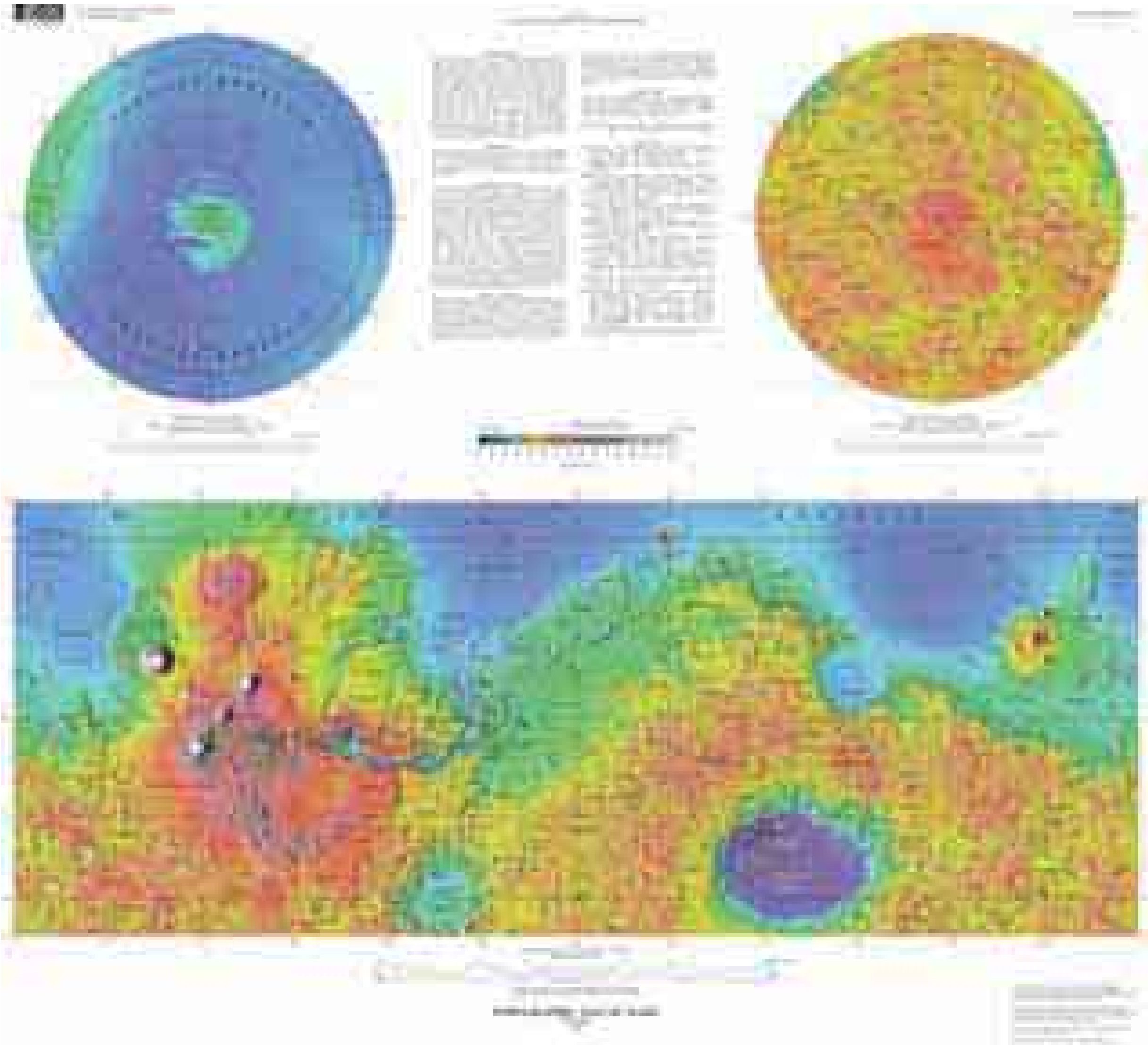

Figure 3.1.: The topographic map of Mars, prepared by the U.S. Geological Survey, based on Mars Orbiter Laser Altimeter data, shall give an overview of locations and general surface features as they are discussed in this thesis.

Part I.

Introduction to the Background Theory and Open Scientific Issues

4. The Base of Our Knowledge – The Moon, Earth and Venus

The Moon, our closest neighbour, is the best studied extraterrestrial object in our solar system. Moreover, the target of the first space missions culminating in manned landing and sample–return during the American Apollo and Russian Luna Programs (1969–1976). Therefore, the Moon is the only planetary body, apart from Earth, where we can relate rock samples as well as their composition and age, more or less confidently to specific geomorphologic units. Furthermore, based on isotope ratios and chemical composition, the differentiation of the Moon ended long ago, and based on its small size the Moon is considered to be no longer geologically active. The two dominant geological processes that have sculpted the lunar surface are impact cratering and mare volcanism. Volcanism as a surface shaping process has ended but impact cratering is still ongoing and is a process relevant to this thesis. The Moon has preserved much of its surficial magmatic and cratering record for most of its life span. Lunar surface interpretation allows us to look back into the early phase of planetary evolution, while on Earth, plate tectonics and resurfacing processes driven by large–scale mantle convection, change the visible surface and have erased most of its impact record. The current impact crater distribution on Earth (Fig. 4.1) is basically controlled as on any other extraterrestrial solid–surface body by its surface or crustal age.

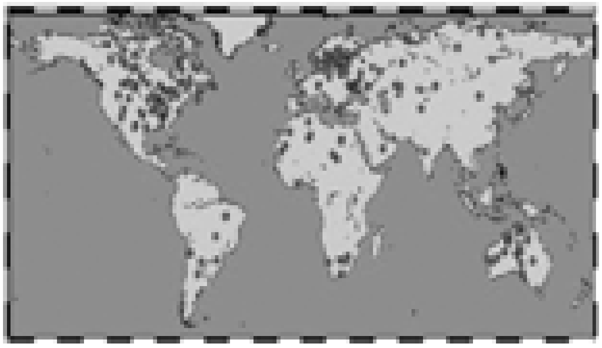

Figure 4.1.: Impact crater Distribution on Earth: Due to plate tectonics and erosional processes the impact crater population on Earth has been strongly modified. Especially oceanic crust is widely unaffected by craters due to its young age (less than 175 Ma). (Source: Earth Impact Database at the PASSC, University of New Brunswick, Canada)

The Earth

The densely cratered units are correlated with the cratons (based on crater counts, their mean age is ~ 400 Ma, (Neukum, 1983), while the crystallization ages of the rock could vary). The lack of craters in the oceanic crust is due to two reasons: (1) In general, oceanic crust is very young (on average 62 Ma; maximum age is ~ 175 Ma) and almost no craters are expected (Koulouris *et al.*, 1999). (2) Small impactors (less than $1 - 2$ km in diameter) do not affect the ocean floor because the motion of such projectiles is already decelerated when they reach a depth of about 1.5 km (Shuvalov, 2003) while the average depth of the ocean is about 5 km. Only a single impact event in deep water is known and there no crater is present: Eltanin in the Bellingshausen Sea (Gersonde *et al.*, 1997). Crater records on land of the smaller–size range (< 5 km) can be either erased by geological processes, e. g. erosion, or later exhumed after being buried under a protecting cover. Hence their frequency might not represent the real surface age (e.g. in Fennoscandia). Both processes have to be considered when crater size–frequency distributions are measured on planetary surfaces which are geologically more active than the Moon.

Venus

An additional factor on terrestrial crater size–frequency distributions is the shielding effect of the atmosphere, which on Venus is even stronger than on Earth (Ivanov *et al.*, 1992; McKinnon *et al.*, 1997). On Venus projectiles producing craters of diameters less than approximately 1 km are disrupted and possibly hit the surface as a swarm of fragments creating impact crater clusters, if they reach the surface at all. On the other hand, the recognition of craters on Earth's surface is highly biased by the accessibility of the area and the research activity within a specific region.

The Earth can be used as an analogue, but has its clearly limitations when exploring the past, although the well-dated rock record is of tremendous value. Therefore, the Moon has become, based on its cratering record, a time–stratigraphic calibration reference for the Earth–Moon system and the entire inner Solar System. A combination of interpreting ground–based and orbiter–based multispectral imagery and in–situ data promote the Moon (apart from the Earth) to be a valuable test case and calibrator for many methods based on remote sensing data.

4.1. Geologic Evolution of the Moon

The formation and evolution of the Moon is part of the evolution of the planetary system. Even in modern times, hypotheses of the origin of the Moon include capture from an independent solar orbit, rapid co–accretion or fission from the Earth. A variant of the fission hypothesis is that the Moon accreted rapidly from ejecta of a massive (proto–mars sized) impact on the Earth after its core had formed (Hartmann and Davis, 1975; Cameron and Ward, 1976; Cameron, 1986). These later alternatives are based on the commonly accepted idea that the Moon accreted from material similar to the Earth, as clearly shown by oxygen isotopes (Clayton and Mayeda, 1975; Hartmann *et al.*, 1986; Halliday, 2000). It is required that the Moon initially was in a completely or partially molten state (Canup and Agnor, 2000). Tidal interaction between the Earth and the Moon led to a quite stable orbital configuration of the satellite having a spin period equal to its orbital period, but slowing down the Earth with the Moon receding from the Earth (opposite to the Mars – Phobos situation, where the satellite is believed to move towards the main body (Yoder, 1995)). Due to the synchronous rotation of the Moon only half of the lunar surface is visible from Earth (near–side). The Moon, lacking an atmosphere, allows us even with the naked eye to identify bright and dark regions: the Face of the Moon. The near–side of the Moon is characterized by extensive darkish almost flat lava plains (Maria), mountain chains and brighter heavily cratered highland plateaus (Fig. 4.2).

The brighter plateaus are of anorthositic composition, and the primordial crust originated in the very beginning of the lunar geological history about 4.6 to 4.5 Ga ago (Halliday, 2000). This composition suggests fractional crystallization and differentiation from a global magma ocean (Taylor, 1982). The second stage of the evolution of lunar highland crust was its modification during a period from 4.4 to 3.9 Ga through the crystallization of mafic and ultramafic plutonic rocks (Shearer and Papike, 1999; James, 1980). Because the Moon, as all terrestrial planets, experienced a period of heavy bombardment (until 3.9 Ga ago), all of these early periods of magmatism, crust formation, and lunar mantle evolution are not preserved. The early upper lunar crust is perforated by impact craters of diverse sizes, covered by their polymict ejecta, and fractured and brecciated to depths of up to 20 km (megaregolith, Hartmann, 1973a). Mare basaltic magmatism followed the heavy bombardment period and basin formation, and occurred between 3.9 and 2 Ga ago. In small areas the gradual decay of volcanic activity even went on until 1 Ga ago, (e. g. Nyquist and Shih, 1992, and based on crater counts: Schaber (1973), or Hiesinger *et al.* (2002)).

Whereas impact cratering is a spatially random process, the maria are far from uniformly distributed. Images from the Moon's farside (Fig. 4.2) clearly show that more than 90% of the surface area of the lunar basaltic lava flows are located on the Earth–facing hemisphere,

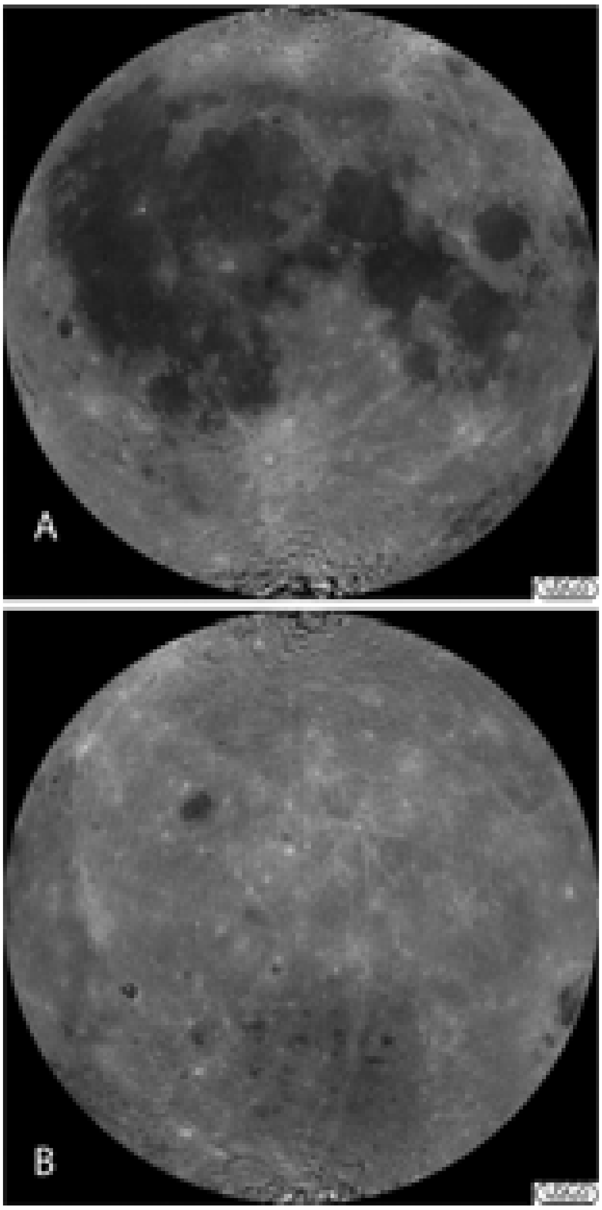

Figure 4.2.: Global Albedo Map of the Moon: These mosaics were processed by the U.S. Geological Survey, Flagstaff, Arizona, from images taken at a wavelength of 750 nm by Clementine (resolution: 5 km/pixel). In (A) the Earth–facing (near–side) of the Moon is shown, and in (B) the far–side.

and which is over 17 % of the total lunar surface (Head, 1975).

4.2. The Chronostratigraphy of the Moon

For planetary bodies, including the Moon, the stratigraphic system is based on photogeological mapping. In the case of the Moon, the lunar mapping and stratigraphic analysis was first derived from Earth–based telescopic photography and later updated from Lunar Orbiter and Apollo imagery. The boundaries of the lunar epochs are characterized by the formation of several large impact basins and a few younger craters. This was established by Shoemaker and Hackman (1962), using principles outlined by Gilbert (1893) and subsequently desribed comprehensively by Wilhelms (1987). The time–stratigraphic units are named (Fig. 4.3):

- Copernican System (the youngest)
- Erastosthenian System
- Upper Imbrian Series
- Lower Imbrian Series (nowadays, the Upper and Lower Imbrian Series are combined to the Imbrian System)
- Nectarian System
- Pre-Nectarian System (the oldest)

When investigating planetary geology and their sequences, local and regional interpretation are based on the principle of superposition, i.e. younger units overlie, cut, or overlap older ones. It is obvious that older units could accumulate more impact craters than younger surfaces, a principle that is used to understand relative surface ages (Öpik, 1960). As a standard method, crater frequencies are used to understand sequential processes when superposition relationships are lacking (e. g. Öpik, 1960; Shoemaker *et al.*, 1962; Baldwin, 1963, 1964; Hartmann, 1965, 1966; Soderblom, 1970; Neukum *et al.*, 1975; Neukum, 1983). The lunar stratigraphic system has been related to crater size–frequency schemes, so that geological units could be classified globally. In this

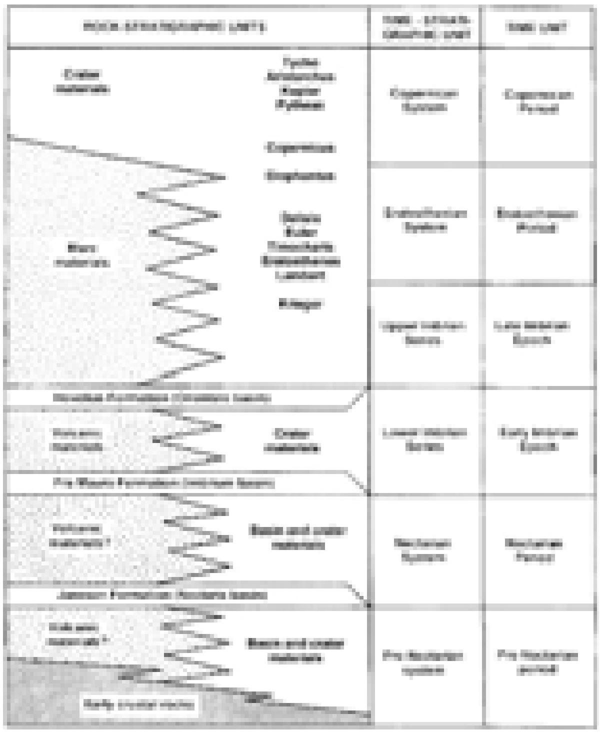

Figure 4.3.: The Lunar Stratigraphic Units (Wilhelms, 1987).

sense, craters are treated as a fossil Earth analogue for remote dating of planetary surfaces (McGill, 1977).

The first attempts to count craters on the Moon were based on telescopic photos. The diameter distribution for crater diameters larger than 1-2 km (see review by Hartmann, 2004) was recognized to be fitted in double logarithmic scale by a linear approach similar to the asteroid diameter distribution power laws:

$$\log N \;=\; k\,\log D^{b}, \tag{4.1}$$

where N can be understood as cumulative number of craters, D is the diameter and $b \sim -2$ for lunar craters. Nevertheless, Hartmann has consistently used log–incremental plots where N is the incremental number of craters in diameter bins of constant $\delta log D$. Mathematically, plotting cumulative or incremantal crater frequencies of craters larger than D result in identical slope steepnesses. A more comprehensive study gives a least–squares fit slope of -1.8 for lunar craters in this branch (Basaltic Volcanism Study Project, Hartmann *et al.*, 1981). Traditionally, this branch (i.e. larger than 1–2 km) is called *primary*, connoting that the craters originated from cosmic projectiles impacting with high speed.

To improve the method of determining surface ages by crater frequency measurements, and to better understand crater formation, the lunar craters have been investigated in detail by their morphology and size–frequency distributions. Lunar maria are smooth, homogeneous, and with clearly defined surface units, on which for most crater–size ranges representative distributions can be measured (i.e. no saturation limit has been reached). Crater counts on lunar maria are used to derive analytical descriptions of the *crater production function.* Partly based on astronomical observations, Shoemaker (1977); Hartmann and Wood (1971); Baldwin (1971); Hartmann *et al.* (1981); Chapman and Haefner (1967) favoured power–law dependences to delineate the crater distributions. For the smaller–size range, from about 1 km down to about 250 m (visible in lunar maria), $b = -3.82$ is a representative slope for this branch (Hartmann *et al.*, 1981). This second branch was suspected to be due to secondary craters produced by ejecta from lunar primary craters (Shoemaker, 1965).

One of the best power–law approaches advocated by W. K. Hartmann, describes the crater production function by a piece–wise three–segment power law:

$$\begin{aligned}
\log N &= -2.616 - 3.82\,\log D, \\
\text{for} \quad & D < 1.41\,\text{km} \\
\log N &= -2.920 - 1.80\,\log D, \\
\text{for} \quad & 1.41\,\text{km} < \text{D} < 64\,\text{km} \\
\log N &= -2.198 - 2.20\,\log D, \\
\text{for} \quad & D > 64\,\text{km}
\end{aligned} \tag{4.2}$$

This crater production function is a result of averaging individual crater counts in different mare areas.

Neukum *et al.* (1975, followed up by Neukum and König (1976); König (1977)) undertook a

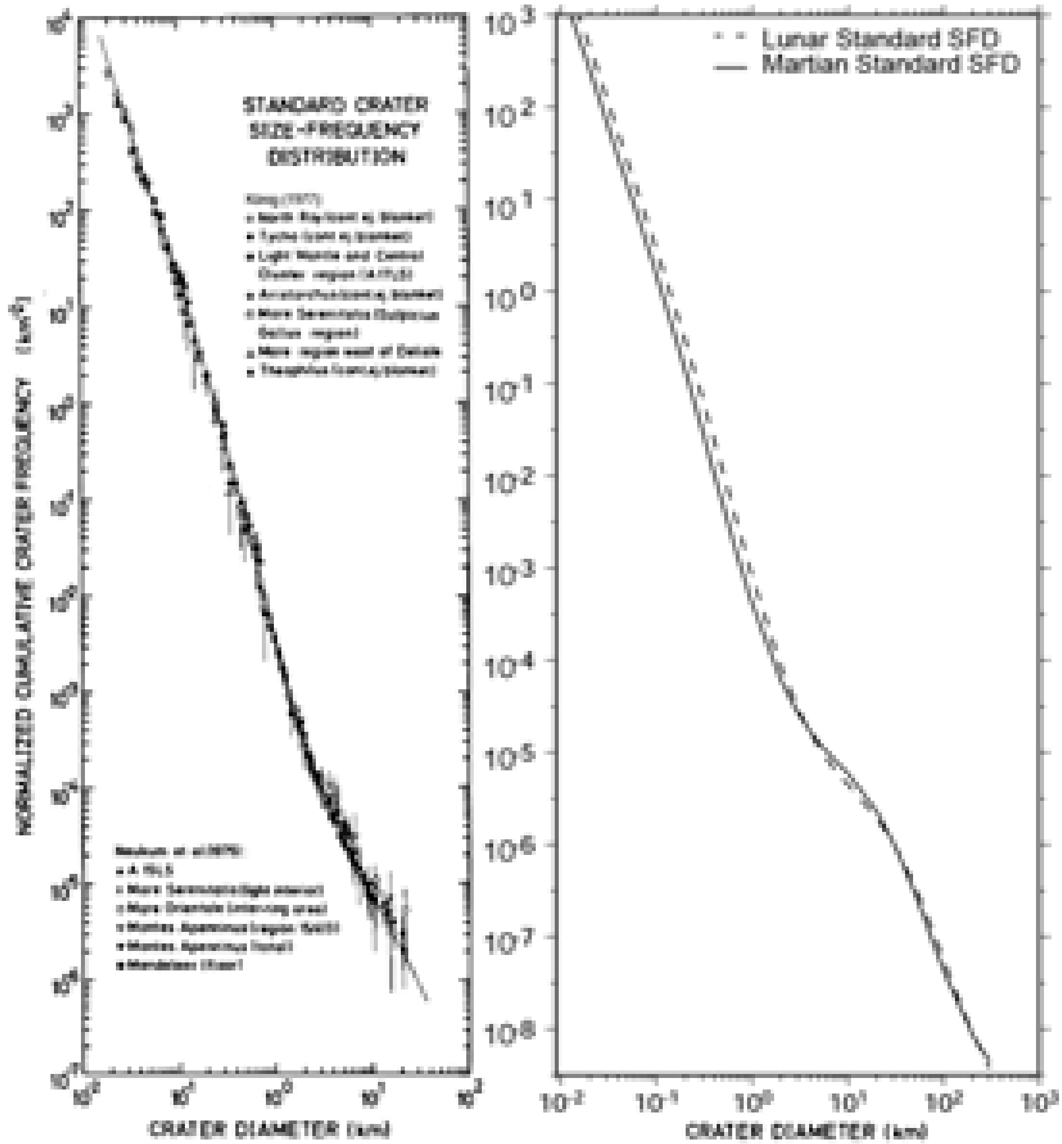

Figure 4.4.: The lunar crater production function from Neukum *et al.* (1975) and refined by Ivanov *et al.* (1999, 2001). The polynomial expression of eleventh order is given in equation 4.3.

detailed analysis of the distribution measuring lunar crater populations on geologically homogeneous areas of various age, and over a wide diameter range. They did not follow the concept of multiple power–law segments and fitted the following polynomial function:

$$\log N = \sum_{j=0}^{11} a_j \, [\log D]^j, \qquad (4.3)$$

which is somewhat s–shaped (Fig. 4.4). This crater production function is applicable to craters on the Moon, on other planets such as Mars with appropriate scaling considerations, and on asteroids (Neukum, 1983), which will be discussed later.

Neukum *et al.* (1975); Neukum (1983); Neukum and Ivanov (1994) were able to show that the shape of the crater size–frequency distribution is stable and approximatly invariant through time. Neukum and Ivanov (1994) proved the steep branch among sub-kilometer asteroidal craters as well as in the asteroid belt, and in the near-Earth orbit population (Werner *et al.*, 2002). Henceforth, they disproved the Shoemaker-era idea, that the steep branch on the Moon (or Mars) is associated with secondary ejecta from lunar (and Martian) primary craters. Hartmann (1999b, and others) pointed out that the steep branch found in the asteroid belt is presumably due to secondary "ejecta" from craters on asteroids, except that the fragments do not fall back onto the target asteroids but rather float in the belt and hit other asteroids, i.e. a collisionally evolved projectile distribution (e.g. Hartmann and Hartmann, 1968; Wetherill, 1967, 1979).

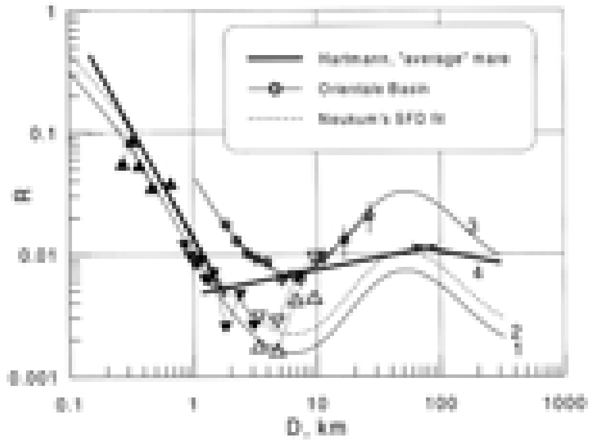

Figure 4.5.: Comparison between the two standard crater production function derived by Hartmann and Neukum in the R–representation. (filled triangles: crater counts at the Apollo 17 landing site by Neukum (1983) open triangles: counts by Hartmann *et al.* (1981)), 1, 2, 3: crater production function by Neukum, 4 crater production function by Hartmann.

Over the past few years, the lunar crater production function has been slightly refined (Ivanov *et al.*, 1999, 2001) by remeasuring the larger–crater part in the Orientale basin, and discussed in comparison with the Hartmann approach (Neukum *et al.*, 2001). While Hartmann's crater production function is based on averaged measurements in lunar maria, Neukum's crater production function is based on a number of measurements covering the full crater–size range. Comparing both approaches in R–plot form (differential size frequencies divided by D^{-3}) they fit observational data quite well. A maximum discrepancy to Hartmann's approach of a factor of 3 is observed in the diameter bins around $D = 6$ km (Neukum *et al.*, 2001). As demonstrated in Figure 4.5, the crater production function by Neukum fits observations slightly better.

Figure 4.6.: The Apollo and Luna landing–sites.

Ground–truth data in terms of absolute ages is, besides Earth, available only for the Earth's moon, and was gained when the first rock samples from the Moon were returned to Earth (Fig. 4.6). These were collected by astronauts at six Apollo landing sites. In addition, robotic sample returns came from Luna landings. Sampling locations, regional geology, and the absolute ages of lunar rocks are known and therefore the absolute age of geological units. The first absolute ages could be more or less confidently related to crater size frequency measurements. Approximately 20 lunar meteorites generally support the distinction between highland

Lunar Chronostratigraphy

System	Boundary structure	Radiometric Age [*Ga*]	Crater Frequency N(1) [km^{-2}]	Absolute Crater Retention Age [*Ga*]⋆
Copernican				
	Crater Copernicus	0.85	$1.3\ 10^{-3}$	1.5
Erastosthenian				
	Crater Erastosthenes		$3.0\ 10^{-3}$	3.2
Upper Imbrian				
	Orientale basin			3.7
Lower Imbrian				
	Imbrium basin	3.9	$3.5\ 10^{-2}$	3.9
Nectarian				
	Nectaris basin	4.1	$1.2\ 10^{-1}$	4.1
Pre-Nectarian				
	Highlands	4.4	$3.6\ 10^{-1}$	4.3

⋆ Ga, Giga anni (Latin: billion of years)

Table 4.1.: Epochs, cumulative crater frequencies N(1) (N: number of craters equal to and larger than 1 km in diameter per square kilometer), and absolute ages: The link to absolute ages are based on rock ages determined for the returned samples collected at the Apollo and Luna landing sites, see Fig. 4.6 (from Neukum, 1983).

and mare terrain, but cannot be ascribed to specific surface units (Grossman, 2000). Stöffler and Ryder (2001) provide an extensive review of all absolute rock ages and their reliability. They pointed out that the geologic and stratigraphic interpretation of isotope ages of lunar rock is not always straightforward because none of the rock samples was collected from bedrock units.

Cumulative crater size–frequency distributions measured for major rock–stratigraphic and time–stratigraphic units of the Moon's history are listed in Fig. 4.3.

Combining these cumulative crater frequencies as a function of lunar surface ages, a calibration curve allows for deriving a cratering rate in the Earth–Moon system as a function of time. This *cratering chronology model* is given here as expressed analytically by Neukum (1983) for crater size–frequency distributions, and related surface ages (Table 4.1):

$$N(\geq 1\text{km}) = 5.44 \cdot 10^{-14}[\exp(6.93\text{T}) - 1] + 8.38 \cdot 10^{-4}T \tag{4.4}$$

where N is the number of craters equal to and larger than 1 km in diameter per square kilometer in an area and T is the crater accumulation time (crater retention age) in Ga (Giga anni (Latin: billion of years)). This function is illustrated in Figure 4.7. Many other chronology models for the lunar cratering rate and the absolute retention ages (see Neukum, 1983; Wilhelms, 1987), based on similar sets of ages, have been published. All curves have in common that the cratering rate during the last 3 Ga was relatively constant within a factor of 2. Before this time, the cratering projectile flux was rapidly, exponentially decaying in time. This early period, in which 95% of the lunar craters were formed, is referred to as the *late heavy bombardment*.

The flux difference between the first half billion years and the following 3 to 4 billion years is observed on the surface of those planets and moons that lack the obliteration effect of geologic activity. The discrepancy in crater frequencies between heavily cratered terrains and less cratered plains units appears to be a 3.9 Ga marker horizon throughout the inner solar system (Wetherill, 1975). It was believed, that this projectile flux might be the remnant of the planetary formation period and asteroids

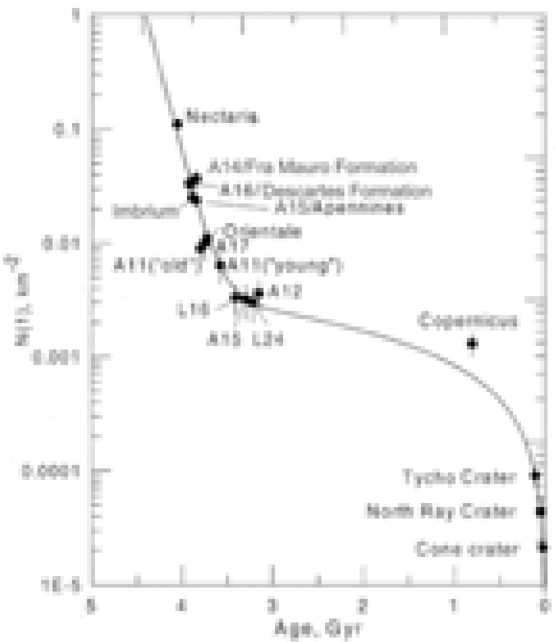

Figure 4.7.: The lunar chronology model with the referring ages and crater size frequencies of the landings sites (see also Fig. 4.6 and Table 4.1).

left over from this period (further discussion in Chapter 5.2).

Cratering rates, absolute surface ages, and a chronology model for the Moon allow us to establish an absolute lunar stratigraphy and to provide a standard reference curve for stratigraphic time that is applicable to other planetary bodies. This will be discussed in the following chapters with special focus on Mars.

5. The Adaptation from the Moon to Mars

In order to gain an understanding of the geologic evolution of a terrestrial planet, it is vital to place the different geological processes involved in shaping the planetary surface into chronological order. At regional or local scales, a relative stratigraphy can be derived by analyzing superposition relations and differences in the state of degradation between different geomorphological surface units. Global stratigraphic schemes for planetary bodies are based on the most common resurfacing process: the impacts of planetesimals that form crater or crater-related features on planetary surfaces. Through this random cratering process, counting of the accumulated number of impact craters offers a valuable procedure in understanding the chronostratigraphy. Absolute ages of cratered surfaces of solid surface bodies are derived by extrapolation from the impact flux for the Moon. Apart from Earth, the Moon is the only planetary body for which we have both a detailed stratigraphic history and rock samples that can be related to specific geologic or morphologic units. Therefore, the Moon has become a reference system for Mars (and other planetary bodies).

5.1. The Reference System, Moon: Cratering Record

The determination of relative and absolute ages of planetary surfaces is based on the random process of projectiles hitting planetary bodies and leaving scars, mainly as surface impact crater structures. The cratering record shows the bombardment integrated through the entire geological lifetime of a certain body. The record also reveals the geological history of a specific surface unit due to spacial variations of the crater frequencies and temporal variations of the crater-forming projectile flux. Prerequisites to the interpretation of crater size-frequency data for various geologic units of different ages include:

1. the determination of the shape of the crater–production function, implying the primary source of projectiles that impacted the planetary surface, and
2. the application of a cratering–chronology models.

The characteristics of the lunar crater size–frequency distribution and the derivation of the lunar chronology model has been described in Chapter 4. During the last decades, the investigation of the "true" Martian crater size-frequency distribution has been the focus of many studies and here the "state of the art" for Mars will be introduced.

5.2. The Reference System, Moon: Impactor Flux

It has been shown that asteroids from the main belt provided the primary source of impactors on the terrestrial planets in the inner solar system. This is inferred from the complex shape of both the crater production functions of these bodies, and the asteroid size distribution (Neukum, 1983; Neukum and Ivanov, 1994; Neukum *et al.*, 2001; Ivanov *et al.*, 1999, 2001; Ivanov, 2001; Werner *et al.*, 2002).

The lunar production function is the best studied among terrestrial planetary surfaces, based on an enormous amount of image data at all resolutions. The lunar production function is described as a polynomial function of 11^{th} degree (Neukum, 1983), and has recently been refined for the larger crater diameter range based on new counts in the Orientale basin region (Ivanov *et al.*, 1999, 2001). Since the same projectile population impacted inner solar system bodies (bodies derived from the asteroid belt, Ivanov *et al.*, 2001), the lunar production function can be scaled to impact conditions on these bodies, taking into account parameters such as impact velocity and angle of the projectile, surface gravity, atmospheric effects as well as density and rheologic properties of the target surfaces. A Martian production function polynomial, updated from older versions (Neukum and Wise, 1976; Neukum and Hiller, 1981; Neukum, 1983), has recently been constructed from the refined lunar production function, based on an estimation of crater scaling parameters (Ivanov, 2001).

In order to derive a cratering chronology model for Mars, cratering rates must be estimated from observations of planet-crossing asteroids.

5.3. The Mars–Moon Cratering Rate Ratio

Ivanov (2001) described a method to adapt the lunar production function and chronology model to Mars. In order to do this, he investigated the nature of crater–forming projectiles, the impact rate differences and the scaling laws for the crater formation.

From his discussion of possible projectile sources, it is clear that the best candidates are asteroids which developed from the main belt asteroids (having almost circular orbits around the sun between Mars and Jupiter) to so–called planet–crossing asteroids with orbits of higher eccentricity (compared to main belt asteroids). These asteroids or asteroidal fragments left their former orbits by injection to resonance phase space and/or close encounters with terrestrial planets. Both situations change the orbital parameters and force the body to higher eccentricities. The specific dynamic regime determines the fate of a certain body, which include ejection from the solar system, impact into a planet or for most the "solar sink", that is impacting into the sun (for review: Morbidelli, 1999).

Today, the population of planet-crossing asteroids in the larger size–range is well known, and observational effects are debiased by various approaches. Thus, it supplies us with a representative set of orbital parameters that are used to compare impact rates on Mars and the Moon. Based on this, impact probabilities and velocities were calculated (for details see Ivanov, 2001). Due to Martian orbit characteristics (eccentricity variation in the range of about 0.01 to 0.1 within a period of 2 Ma; Ward, 1992) the number of impactors are variable within a factor of 20 (Ivanov, 2001). Therefore, Mars and Moon impact rates are compared as time averages. The average impact rate for Mars is two times higher than the Moon for asteroids of the same size (Hartmann and Neukum, 2001). To compare the crater size–frequency distributions of the Moon and Mars, modern crater scaling laws for calculating the crater diameter ratio between Mars and the Moon are used (Schmidt and Housen, 1987).

These laws are based on the idea of describing the transient crater diameter with respect to the projectile diameter, impact velocity, impact angle (the efficiency of cratering), the target as well as projectile densities and gravity acceleration of the target body. For smaller craters the crater formation is dominated by composition (strength of the target rock) while for larger craters the crater growth is more influenced by the target gravity acceleration. Schmidt and Housen (1987); Neukum and Ivanov (1994); Ivanov (2001) included the transition diameter between the strength and gravity regime to be able to transfer the lunar crater size–frequency distribution to other planets. The final crater diameter is a result of gravitationally driven collapse of the transient cavity. This diameter depends again on the target material strength and gravity. Here an empirical rule (Pike, 1980b) is used, where the critical diameter varies inversely proportional to the surface gravity. This short overview reflects the guidelines to transfer the well–known lunar crater size–frequency distribution to any other terrestrial body (Schmidt

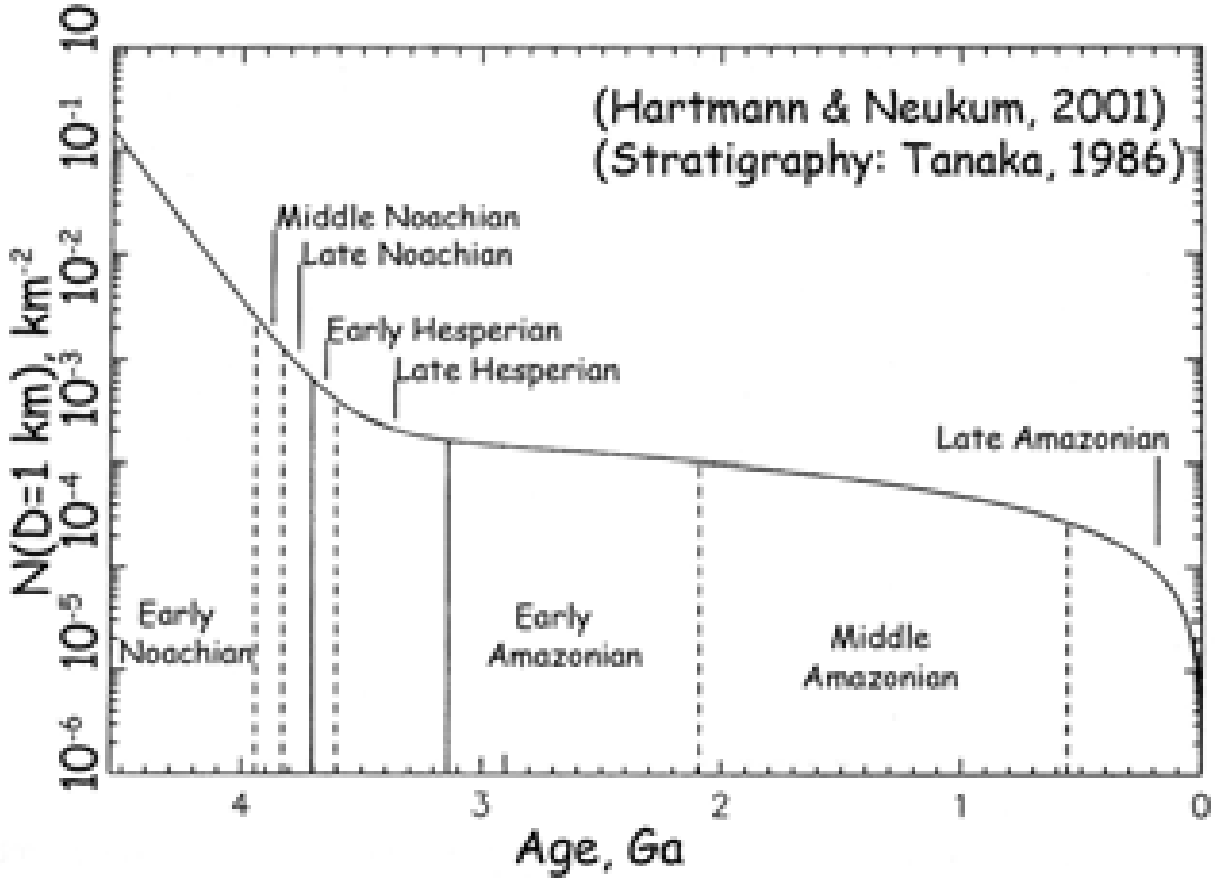

Figure 5.1.: Martian impact cratering chronology curve, showing the chronologic periods and epochs after the time-stratigraphic system of Tanaka (1986), with redefinition of the Lower (Early) Amazonian base crater frequency by Hartmann and Neukum (2001).

and Housen, 1987; Neukum and Ivanov, 1994; Ivanov, 2001).

Ivanov (2001) has performed the latest Moon–to–Mars re–calculation of their crater size–frequency distribution and shown that, due to different average impact velocities and surface gravity, the average crater on Mars is 1.5 times smaller than on the Moon for projectiles of the same diameter. Comparing the lunar and Martian crater size–frequency distributions, the cratering rate of Mars versus the Moon varies within a factor of 0.6 to 1.2, depending on the steepness of the production function curve [See Figure 4.4 B).

Neukum (1983); Neukum *et al.* (2001); Hartmann (1999b) and others agree that the projectile flux in the inner solar system is similar. Therefore, the Martian impact cratering chronology can also be described by a lunar–like bombardment, with an exponentially declining flux during a heavy bombardment period and a more or less constant flux from 3 to 3.3 billion years ago until present. The cumulative frequency for 1–km craters, dependent on exposure time T in billion years, can be described by the chronology curve of Neukum (1983) (see Chapter 4.2), and updated by Ivanov (2001):

$$N(1\mathrm{km}) = 3.22 \cdot 10^{-14}[\exp(6.93\mathrm{T}) - 1] + 4.875 \cdot 10^{-4} T \quad (5.1)$$

A graph of this equation is given in figure 5.1. Earlier attempts by Hartmann (1973);

Soderblom *et al.* (1974); Neukum and Wise (1976); Hartmann *et al.* (1981); Neukum and Hiller (1981); Strom *et al.* (1992) represent similar approaches, but they had no reliable cratering rates to transfer the chronology from the Moon to Mars. At that time, the statistics and knowledge regarding the actual numbers of asteroids in near–Earth and Martian orbits were not well known. Therefore, the projectile (asteroid) flux was unknown and resultingly there was no accurate ratio for properly transferring the cratering rates. Nevertheless, the earlier approach by Neukum and Wise (1976) based on geological arguments (e. g. the marker horizon idea) could be confirmed by the most up–to–date celestial mechanial consideration (Ivanov, 2001).

Hartmann and Neukum (2001) discussed their Martian cratering chronology model with respect to "dated" surface morphologies and the results of Martian meteorite investigation. The crater counts as indicators of surface ages and the age of the meteorite ALH84001 both emphasize an approximate 4.5 Ga age for the surface and crust formation. Rock ages of meteorites of volcanic origin, one of which mineral assemblages indicating aqueous alteration can be correlated to crater counts of volcanically and fluvially shaped surfaces.

Altogether, there is now solid evidence that the age determination using crater counts leads to reliable ages, which can be used to understand the geological history of Mars.

6. Martian Global Geology

Mars is the fourth planet from the sun and Earth's outer neighbor. Ground–based observations have yielded many albedo features and surface temperatures (mean temperature at solid surfaces ranges between 186 to 268_{o}K) similar to those on Earth. One of the earliest observations of Mars was the strong seasonal variation of the polar caps due to an inclination of 25.19°. Both ice caps are similar to those on Earth, but they are also composed of frozen carbon dioxide (CO_2). In summer the northern hemisphere ice cap loses nearly all of its CO_2 ice, exposing an ice cap of water–ice below. It is thought that large quantities of frozen water conceals within the soil and rocks of Mars at mid–to–high latitudes. This idea is strengthened by permafrost patterns in these regions. Despite the thin atmosphere (about 7 mbar surface pressure), mainly CO_2, long–term wind activity is visible in sand dunes (imaged by orbiter missions), and recently in the form of dust devils and clouds.

After a global dust storm abated in 1971, Mariner 9 revealed a hemispherical dichotomy that separates Mars into old, heavily–cratered southern highlands, and younger northern lowlands. The highlands cover about two–thirds of the southern hemisphere and are dominated by numerous impact basins. Imagery from earlier missions such as Mariner 4, 6 and 7 led to the incorrect conclusion that Mars was geologically "dead", like the Earth's moon. A large number of impact basins suggested that these regions of Mars formed during the "heavy bombardment" period, similar to the Moon and the early Earth, which was believed earlier to be caused by impacts of remnant planetesimals from the earliest formation of the solar system. The northern plains cover much of mid and high–latitudes of the northern hemisphere, and show that Mars has had ongoing geological activity, because almost no large craters are visible. The origin of these plains (relatively flat areas) is not fully known. Some regions appear to be covered by lava flows, while others seem to contain lake sediments and features similar to regions on Earth that experienced massive flooding. The cause of this very distinct difference in surface geology between the northern and southern hemispheres remains unclear.

Enormous Martian volcanoes are located near the equator and in vast areas of the northern mid–latitudes. Volcanism is separated into two distinct regions, the Tharsis Rise (including the record–setting Olympus Mons) and the Elysium volcanoes. Volcanism on Mars has been apparently dominated by smoothly flowing lavas similar to those of Hawaii, forming what are known as "shield" volcanoes (due to their low height/area ratio). The close vicinity of some areas also appears to be covered in volcanic ash. Some of these ash deposits appear to be truncated by previously flowing streams, pointing to a much "wetter" past on Mars.

Other indications for liquid water can be seen in stream valleys eroded by precipitation (run–off channels), valleys eroded by the release of huge amounts of water (outflow channels) and so–called chaotic terrain (collapsed ground). The areas of water activity are correlated in space and probably in time with the volcanic units. Due to the large amount of water having run through the channels and the appearance of the northern lowland units, it was suggested that an early Martian ocean may have existed. Morphologies of impact craters and especially ejecta are largely unique to Mars. With their distinctive lobate ejecta deposits, these craters apparently owe their morphology to fluidization of subsurface material, perhaps by melting of ground ice during impact events. The largest known canyon system in the solar system comprising many small interconnected canyons and collectively named the

Valles Marineris, extends southeast from the Tharsis Rise. The canyon system probably developed as a result of crustal stretching ("tectonic extension") and is the main tectonic feature on Mars. Except these tensional fault valleys (grabens) there are no other surface features that suggest that plate tectonics may ever have operated on Mars. Nevertheless, the formation of the northern lowlands is interpreted to relate to plate tectonics (Sleep, 1994).

6.1. What Do Martian Meteorites Tell Us About Mars

Formerly the group of Martian meteorites were named SNCs for the first three meteorites found: **S**hergotty (1865), **N**akhla (1911), and **C**hassigny (1815). The SNC meteorites are petrologically similar, but highly anomalous compared to other meteoritic samples: The young crystallization age of about 1.3 Ga and their classification as igneous achondrites would require a parent body with prolonged igneous activity. Wood and Ashwal (1982) suggested a Martian origin, which was subsequently proven by comparing the isotope composition of gas inclusions and mass spectrometer measurements of the Martian atmosphere at the Viking landing sites (Bogard and Johnson, 1983). Therefore, they are well distinguishable from other differentiated meteorites.

Currently, 31 Martian meteorites are listed at the *Mars Meteorites* – site at JPL (http://www2.jpl.nasa.gov/snc/) and are widely described in the *Mars Meteorite Compendium* (Meyer, 2003). Here, only a subset of 16 samples will be discussed for which composition, radiometric ages, peak shock pressure, and ejection time from Mars are known (see review by Nyquist *et al.*, 2001). These meteorites are classified by their mineralogical composition into groups of basaltic and Lherzolitic Shergottites, Nakhlites (Clinopyroxenites), Chassignites (Dunites), and Orthopyroxenites. Mineralogically all represent basalts and ultramafic cumulates, and evidently are magmatic in origin. They differ not only in their composition but also in crystallization age.

Basaltic Shergottites are considered analogous to terrestrial basalts (McCoy *et al.*, 1992), and possibly reflect different stages of mixing between Martian crust and mantle material. The texture is consistent with those of surface basaltic lava flows. Together with *Lherzolitic Shergottites*, they represent the youngest group of Martian meteorites. Radiogenic Sr–isotopes indicate that these mafic rocks were formed from different magma sources and under different cooling conditions (Borg *et al.*, 1998). *Chassigny* is the only dunite and seems to have fractionally crystallized from a mafic magma body (Floran *et al.*, 1978). Its crystallization history is similar to that of *Nakhlites.* They are clinopyroxenites containing phyllosilicates and secondary evaporite mineral assemblages of Martian origin, thus confirming the presence of liquid water on Mars (Gooding *et al.*, 1991; Bridges and Grady, 2000; Swindle *et al.*, 2000). When compared to terrestrial augite–rich igneous rocks of the Abitibi greenstone belt (Canada), Treiman (1987) concluded that nakhlites formed in shallow intrusions, which are thought to be common in the Tharsis region of Mars. The oldest Martian meteorite is ALH 84001, a coarse-grained brecciated *Orthopyroxenite*, in which younger carbonates are present. This small amount of carbonates (1%) drew worldwide attention when McKay *et al.* (1996) argued for polycyclic aromatic hydrocarbons (PAH), oxide and sulfide biominerals, and nanofossil-like structures suggesting fossil life on Mars.

Meanwhile, numerous non–biogenic formation mechanisms have been proposed: The PAHs could be due to terrestrial contamination (Becker *et al.*, 1997; Jull *et al.*, 1998), and carbonates and magnetite assemblages might be flood evaporites (McSween and Harvey, 1998; Warren, 1998).

The radiometric crystallization ages of these different Martian meteorite classes indicate the

Martian Meteorite Summary

Meteorite	Age° in Ma	Ejection Age* in Ma	Shock pressure+ in GPa
Shergottites (Basalts):			
Shergotty	165 ± 4	2.73 ± 0.15	29 ± 1
Zagami	177 ± 3	2.92 ± 0.20	31 ± 2
Los Angeles	170 ± 8	3.10 ± 0.20	∼ 35–40
EETA79001A	173 ± 3	0.73 ± 0.15	34 ± 2
EETA79001B	paired (EETA79001A)		
QUE 94201	327 ± 10	2.71 ± 0.20	∼ 30–35
DaG 476	474 ± 11	1.24 ± 0.12	∼ 35–40
Dhofar 019		19.8 ± 2.3	∼ 35–40
SaU 005		1.5 ± 0.3	∼ 35–40
Shergottites (Lherzolites):			
AHLA77005	179 ± 5	3.06 ± 0.20	43 ± 2
LEW88516	178 ± 8	3.94 ± 0.40	∼ 45
Y793605	212 ± 62	4.70 ± 0.50	∼ 45
Clinopyroxenites (Nakhlites):			
Nakhla	1270 ± 10	10.75 ± 0.40	∼20 (±5)
Governador	1330 ± 10	10.0 ± 2.1	∼20 (±5)
Valadares	paired (Governdor)		
Lafayette	1320 ± 20	11.9 ± 2.2	∼20 (±5)
Dunite:			
Chassigny	1340 ± 50	11.3 ± 0.6	∼ 35
Orthopyroxenite:			
ALH 84001		15.0 ± 0.8	∼ 35–40
Silicates	4510 ± 110		
Carbonates	3920 ± 40		

°The preferred crystallization age is given (see Nyquist *et al.*, 2001).
*Mars ejection age calculated as the preferred cosmic–ray exposer age and terrestrial residence time (see Nyquist *et al.*, 2001).
+Estimated peak shock pressure after Stöffler and Weber (1986) Stöffler (2000); Nyquist *et al.* (2001).

Table 6.1.: Martian Metorites: Summary of radiometric crystallization ages, estimates of the peak shock pressure induced during the ejection process, and time since the ejection from Martian surface separated by compositional group.

existence of surface or near–surface rocks (i.e. volcanism) on Mars with ages of about 175 Ma, 300 − 500 Ma, 1.3 Ga and 4.5 Ga, which cover an age spanning the entire history of Mars. Together with their composition, this suggests magmatic activity from planet formation until recent times. The young ages agree with ages derived from crater counts for volcanic provinces in Tharsis, Elysium and Amazonis region (cf. Chapter 15.5). The samples, which contain evaporitic phases, possibly indicate the presence of liquid water at around 3.9 Ga and even 1.3 Ga ago, i.e. the period in which landforms related to fluvial activity are found (cf. Chapter 14.6).

The widely accepted idea of delivering rocks from planet–to–planet is ejection from the planet's surface by large scale impacts. For Mars, the ejection velocity is about 5 km/s. All Martian meteorites are moderately to strongly shock–metamorphosed by peak shock pressures of between 15 and 45 GPa. Rocks which have left the Martian surface have not been molten, but it is likely that the shock metamorphism is related to the ejection event and possibly a function of parent body size (Table 6.1). In this respect, the recent ejection age (less than 20 Ma) and the fact that all samples are of magmatic/volcanic origin is interesting. Ejection and transport mechanism will be discussed later in respect with secondary cratering in a later chapter.

The most reliable crystallization ages of the meteorites span from the formation of the planet nearly to present, while only a single Martian rock is older than 1.3 Ga. This is a rather incomplete set of Martian surface ages and no provenance can be clearly assigned, but they are the only samples from Mars, and of vital importance in understanding its formation and evolution. Nevertheless, radiometric ages provide absolute calibration marks (in terms of setting a time–frame) for relative crater counting records, support absolute ages derived from crater counts through cratering chronology models, and will be discussed in later chapters.

6.2. The Viking–based Stratigraphic System of Mars

A stratigraphic overview of Mars is commonly given by the major physiographic provinces and assemblages as they are shown in a set of 1:15 M–scale maps (Figures 6.1, 6.2, by Scott and Tanaka (1986); Greeley and Guest (1987); Tanaka and Scott (1987)). These maps reflect the overall relation of rock units, their areal distribution, the processes by which they are formed and modified, and the recorded geologic history. The Martian stratigraphic system is based on the identification and delineation of geologic units. They are identified according to their topography, morphology, and spectral properties as recorded from spacecraft images. Relative ages are determined by superposition and intersection of the units and globally by the concentration of impact craters superimposed on the geologic unit, thus providing the local history of regions as well as the geological evolution of the entire planet. This procedure has been applied by Soderblom *et al.* (1974) and is discussed in detail by Condit (1978) for Mars. Historically, the Mariner 9 mission was the first to give a global view of the Martian surface. The dichotomy, dividing Mars into densely cratered southern highlands and smoother northern lowland plains, was confirmed (Scott, 1978). The impression of Mars being moon–like (Mariner 4) rather than Earth–like was revised. Tectonic, volcanic, eolian, and degradational terrains were revealed so that a global geologic time scale could be established: The Amazonian, Hesperian, and Noachian Epochs (Scott and Condit, 1977). Based on high resolution Viking Orbiter imagery, more detailed stratigraphic investigations were undertaken, and more geologic classes as well as a subdivision of the stratigraphy were introduced.

The current time-stratigraphic system of chronologic periods and epochs to subdivide the Martian geologic history was established by Tanaka (1986) and later summarized by Tanaka *et al.* (1992a).

The major geologic division has been mapped and is fundamentally based on the dichotomy: (A) Highland rocks, including the impact basins (Hellas, Argyre, and Isidis) and the southern highland plains; (B) Lowland rocks, the northern plains assemblage, and degraded, ancient rocks along the highland lowland boundary; (C)

Martian Epochs

Epochs	Crater–Frequency Range		
	N(2)*	N(5)*	N(16)*
Upper Amazonian	< 40		
Middle Amazonian	40–150	< 25	
Lower Amazonian	150–400	25–67	
Upper Hesperian	400–750	67–125	
Lower Hesperian	750–1200	125–200	< 25
Upper Noachian		200–400	25–100
Middle Noachian		> 400	100–200
Lower Noachian			> 200

* N(D) = cum. number of craters with diameters $\geq$D, normalized to an area of 10^6 km^2

Table 6.2.: The crater frequencies for crater diameters equal to or larger than 2 km, 5 km, and 16 km, which outline the boundary conditions for the different geological epochs from Tanaka *et al.* (1992a).

Volcanic and tectonic regions, including highland paterae, the Tharsis and Elysium volcanic regions and Valles Marineris; (D) Channel systems, mostly emanating from chaotic terrains close to Valles Marineris; (E) Polar regions, including mantling, polar layered and ice deposits. Geologic type regions have been assigned to the three major time–stratigraphic systems: The oldest Noachian System is named after the ancient cratered and rugged terrain in Noachis Terra (Scott and Carr, 1978). The overlying Hesperian System got its name from ridged plains material represented in Hesperia Planum. The boundary to the most recent Amazonian System has been defined based on the Arcadia Formation in the Amazonis quadrangle, consisting of smooth plains material. This scheme follows developments of terrestrial geology based on the fundamental principle of classifying rocks according to their relative ages (James Hutton and William Smith), long before absolute ages emerged at around 1910. Tanaka's subdivision scheme is based on cumulative crater counts, carried out at different crater diameter ranges in the type areas defining the stratigraphic base of these periods and epochs (e.g. older units are defined by larger craters whereas younger units are defined by smaller craters). The boundaries based on these crater counts are given in Table 6.2. Therefore, he assumed a "minus–two" power–law for the crater diameter distribution. Their cumulative frequencies, base of these periods and epochs, have been recalculated to cumulative frequencies for 1-km craters, and absolute ages were determined from the new unified Martian chronology model by Hartmann and Neukum (2001) (compare Fig. 5.1). All absolute ages given in this thesis are calculated on the basis of equation 11.2, and the Martian crater production function following Neukum (1983) and its updated expression by Ivanov (2001), if not stated otherwise. Any stratigraphic classification is based on the re–measured time–stratigraphic units (Fig. 5.1). Data from the Mars Global Surveyor (MGS) spacecraft has already provided new insights into Martian stratigraphic relationships and the timing of major geological events. Due to the high–resolution imagery, specific stratigraphic issues regarding timing, and extent of resurfacing activity (volcanic and fluvial) have been raised.

Several first–order refinements to improve the Viking-based scheme have been achieved:

1. Tanaka's original crater size–frequency distributions were recalculated to a 1-km cumulative crater frequency using the new Mars production function polynomial by Ivanov (2001).

2. The corresponding cratering model age was calculated for each type area, using equation 11.2.

3. Counts on new images returned from the Mars Global Surveyor Camera redefined the Lower Amazonian base corresponding to a slightly younger cratering model age of 3.14 Ga (Hartmann and Neukum, 2001), revealed by the smaller crater size range not seen in Viking imagery.

Major geological events in Mars history, derived from stratigraphic analysis of geologic units and corresponding crater densities, grouped by geological processes (Head *et al.*, 2001) are in Fig. 6.3.

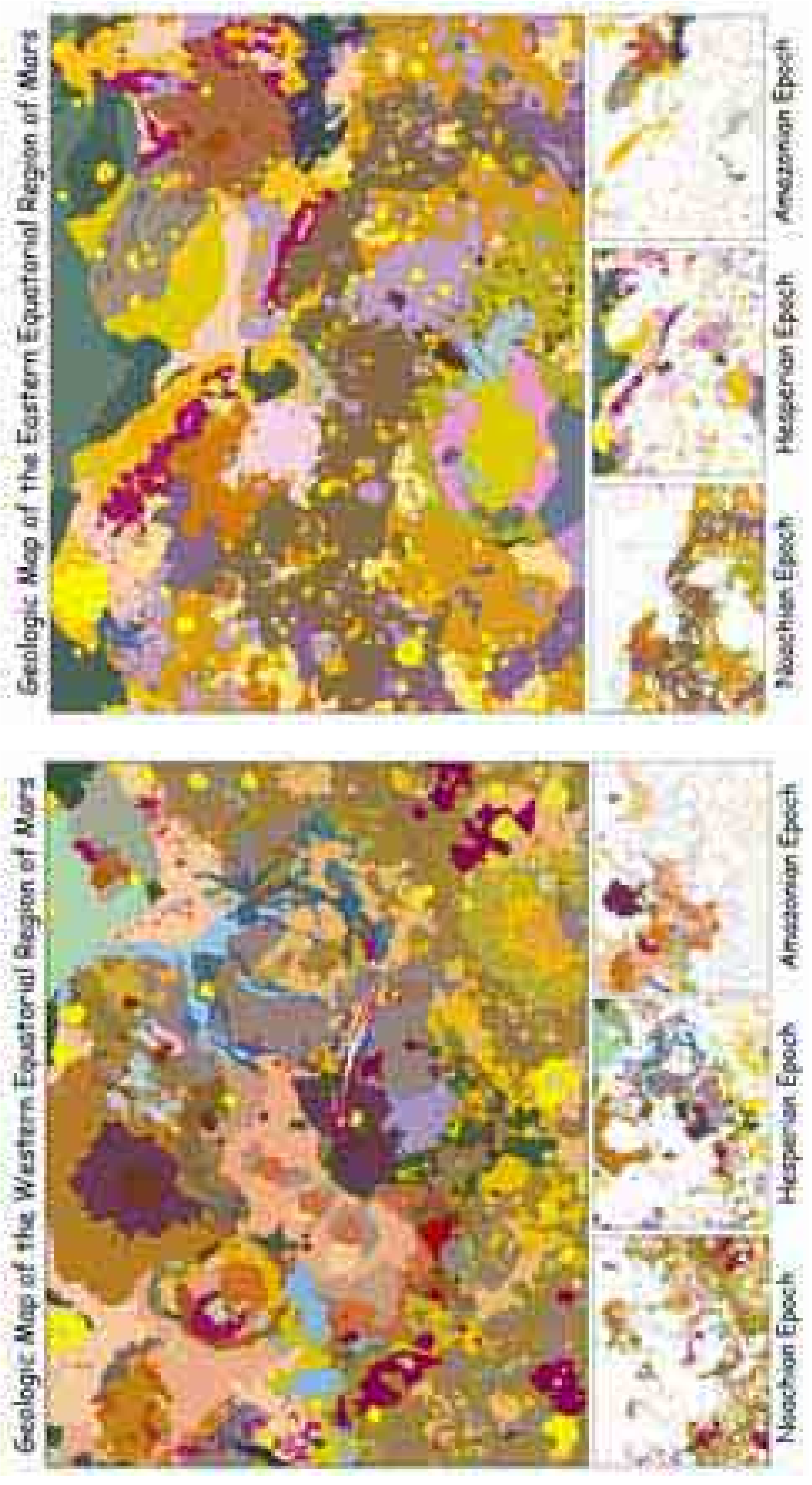

Figure 6.1.: Geologic map of the Western (left) and Eastern (right) region of Mars, from Scott and Tanaka (1986); Greeley and Guest (1987). In the small sketches units are highlighted according to the Noachian, Hesperian and Amazonian time units.

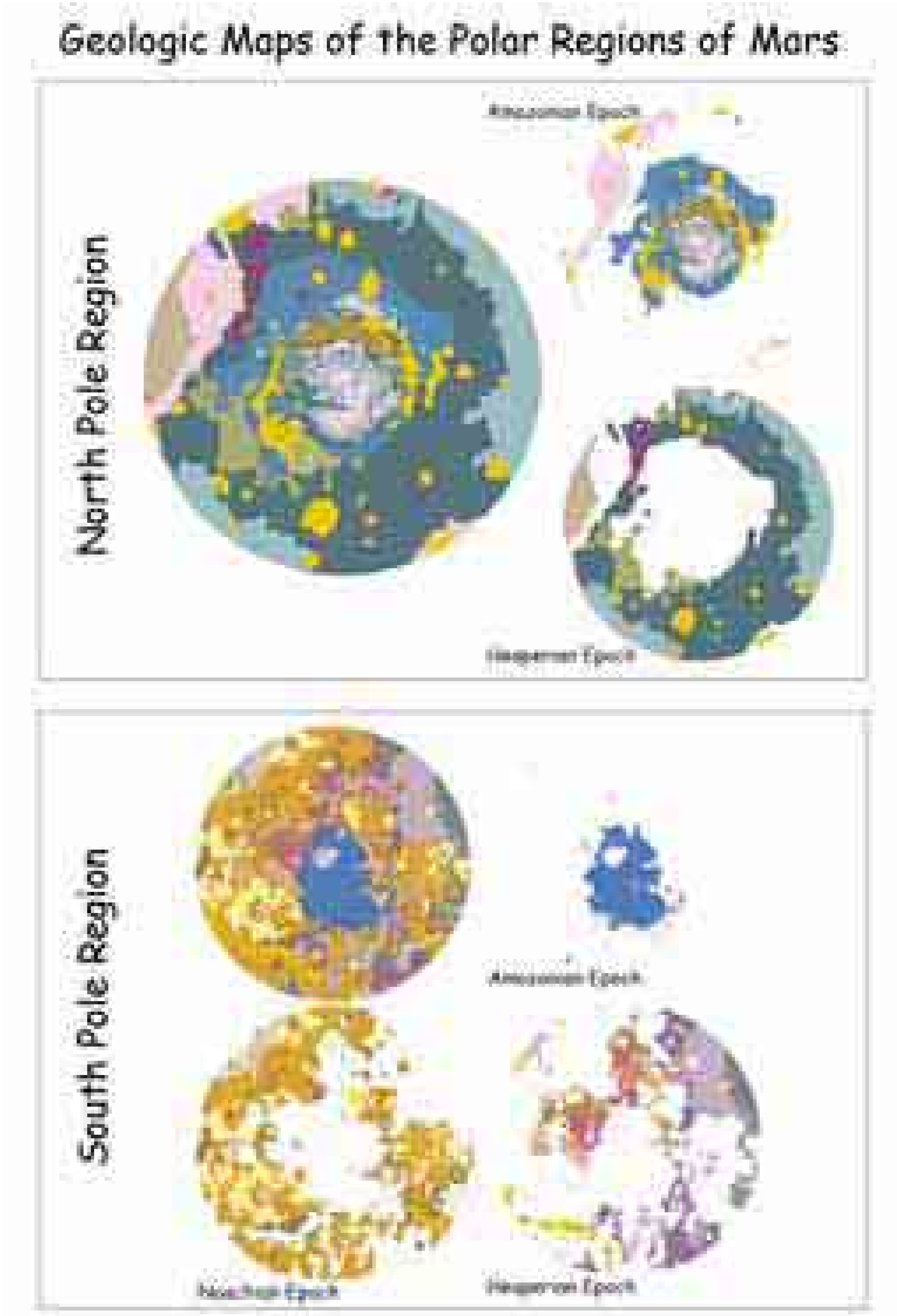

Figure 6.2.: Geologic map of the polar regions of Mars, from Tanaka and Scott (1987). The North–pole region is shown in the upper part (no Noachian units). Below, the South–pole region is shown with sketches highlighting the Noachian, Hesperian and Amazonian time units.

6.3. Towards A New Time–Stratigraphy

As stated already in Chapter 3, various stratigraphic units have been mapped on Mars and their relative ages have been determined from a combination of superposition relations and crater frequencies (Neukum and Hiller, 1981; Tanaka, 1986; Scott and Tanaka, 1986; Greeley and Guest, 1987; Tanaka and Scott, 1987). In principle, absolute ages can be estimated through impact crater frequencies. The absolute chronology and absolute ages of different Martian stratigraphic units had been known only crudely due to uncertainties in the Martian impactor flux. One approach to extract the cratering production function from the geologically distorted record is to transfer the well–known and measured production function of the Moon to Mars by considering impact rate, scaling laws and possible influence of target properties (Neukum and Wise, 1976). The problem with this method is a gap in the image resolution that is demonstrated in Section 12. Older models for understanding the flux in Martian surroundings (Chapter 3) had produced, based on Viking and Mariner 9 data analysis, a wide range of chronologic systems with no clear consensus on the absolute ages (Hartmann, 1973; Soderblom *et al.*, 1974; Neukum and Wise, 1976; Hartmann *et al.*, 1981; Neukum and Hiller, 1981; Neukum, 1983; Strom *et al.*, 1992). A variety of observations initiated debates which processes are responsible. The lack of smaller craters (250 m $<$ D $<$ 16 km) in heavily cratered terrain where the largest craters (D $>$ 64 km) had crater densities similar to those in the lunar highlands (that indicate ages of 3.8 to 4.5 Ga (Leighton *et al.*, 1965)) suggested loss of smaller craters by erosion and deposition (Öpik, 1965, 1966). The variety of observations initiated debates which processes are responsible. As mentioned before (Chapter 3) steady rates of obliteration are not applicable, changes in atmosphere thickness (Sagan *et al.*, 1973; Pollack *et al.*, 1987), increased volcanism (Greeley and Spudis, 1981), the abundance of permafrost associated with creep deformation (Squyres and Carr, 1986) and/or sporadic glacial erosion are plausible explanations. Youngest volcanic units imaged by Mars Global Surveyor at image resolutions of up to 1.5 m/pixel launched further debates. Crater statistics for restricted areas, e.g. Elysium Planitia, indicate ages less than 100 Myr or even 10 Myr (Hartmann and Berman, 2000). Furthermore, massive layering and mobility of dust and fine material is confirmed by Malin (1998) from MGS images.

The current understanding of the geologic history of Mars is mainly based on crater size–frequency measurements carried out on high resolution Viking imagery. Several chronology models were published by different investigators (e.g. Soderblom *et al.*, 1974; Neukum and Wise, 1976; Neukum and Hiller, 1981; Hartmann *et al.*, 1981). The most up–to–date reviews of the Martian impact cratering chronology are found in Hartmann and Neukum (2001) and Ivanov (2001). Until recently, it was not possible to measure the Martian crater size–frequency distribution over the full crater–diameter size range due to a resolution gap in the imagery database. Only with the imagery of the High Resolution Stereo Camera onboard Mars Express, a multiple line scanner instrument, has been acquiring high–resolution color and stereo images of the Martian surface (Neukum *et al.*, 2004), and is it now possible to fill this gap. High resolution up to 10 meters per pixel coupled with a large areal extent (swaths typically 60-100 km wide and thousands of km long) means that small details can be placed in a much broader context than was previously possible. Based on the comparison between crater counts over the entire crater diameter size range, the analytically transfered crater size–frequency distribution can be verified.

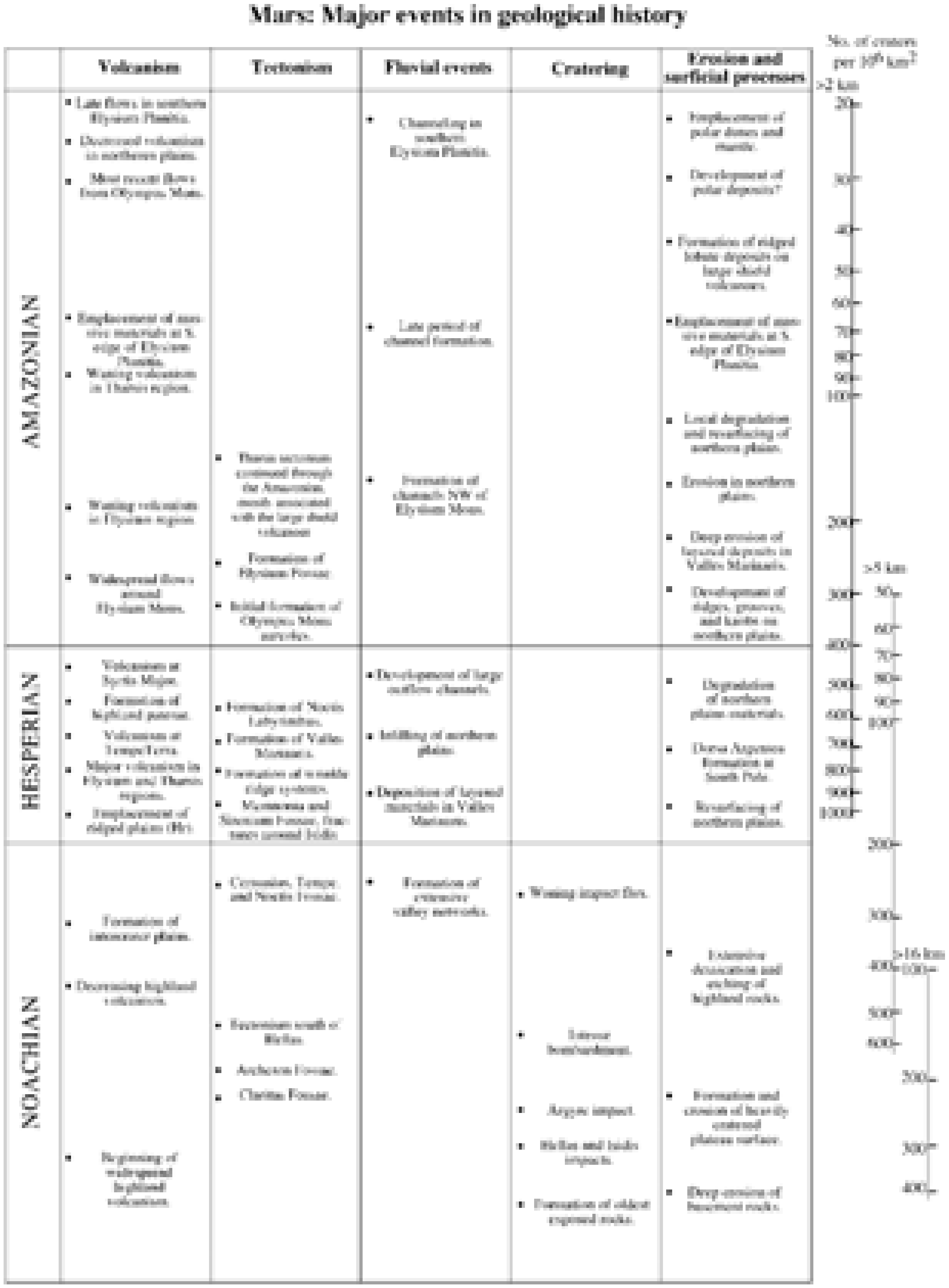

Figure 6.3.: Tabulated description of the major events in the martian geological history, sorted by geological processes including volcanism, tectonism, fluvial action, cratering, as well as erosion and surficial deposition, from Head *et al.* (2001). On the right–hand side, the relative surface ages, expressed as number of craters greater than the indicated diameter per 10^6 km^2 of surface area, are given (cf. Table 6.2 from Tanaka (1986).

6.4. The Geophysical Mars after Mars Global Surveyor

The Mars Global Surveyor (MGS) mission not only allowed access to a detailed topography through the laser measurements, but also mapped the gravity field through two–way Doppler tracking of the spacecraft (Smith *et al.*, 1999a,b). Based on the topography (Fig. 6.4, A) and the gravity fields a map of the of the present crustal distribution was derived (Fig. 6.4, B) (Zuber *et al.*, 2000; Neumann *et al.*, 2004). Both the topography and the crustal thickness confirmed the dichotomy between the smooth northern lowlands and the cratered southern highlands. The latter is defined by higher elevation and thicker crust, but especially in the vicinity of Arabia Terra, the boundary deviates between the morphologically defined and the separation due to crustal thickness. Neumann *et al.* (2004) arrived with average crustal thickness values for beneath the northern lowlands and southern highlands of about 35 and 60 km, respectively. As a result of such a detailed topography, numerous partially buried impact craters and basins have been identified in the lowland regions and led to the idea that the crust of the lowlands and highlands, similarly densely cratered originally, formed both by the Early Noachian (Frey *et al.*, 2002). The crustal dichotomy could be explained by long–wavelength mantle convection (Nimmo and Tanaka, 2005), very early in the Martian history. Subsequently, this crustal distribution was obscured by the formation of the large impact basins, Hellas, Argyre, Isidis and Utopia.

The detection of different compositions of the northern and southern hemisphere by the Thermal Emission Spectrometer suggests two crustal rock types (Bandfield *et al.*, 2000). One of more basaltic composition (like the composition of Martian meteorites) is confined for the older surface, and one more silica rich (andesitic) component in the lowlands. Wänke *et al.* (2001) interpreted the in situ analysis of Martian rocks by the Pathfinder mission to be of two major chemical components, which confirms the remote sensing detection, but also imply a differentiation history and yield constraints for dynamical models (see Spohn *et al.* (2001) or Solomon *et al.* (2005)). Despite the detection of more andesitic composition in the younger northern lowlands, an andesitic composition is assumed for the ancient crust, and a basaltic composition for later volcanic products (Nimmo and Tanaka, 2005).

Doppler and range measurements to the Mars Pathfinder lander gave further insight into the precession rate of the rotational axis (Folkner *et al.*, 1997) and therefore information on the distribution of mass within the planet. The derived moment-of-inertia (e.g. Sohl *et al.*, 2005) implies that Mars possesses a dense metallic core. While plate tectonics cools the mantle and supports driving an early dynamo (Nimmo and Stevenson, 2000), an initially hot core also sufficiently explains an early dynamo without plate tectonics and allows to consistently explain the Martian thermal evolution better (Breuer and Spohn, 2003).

The detection of remnant magnetization dominantly in the southern hemisphere (Fig. 6.4, C), implies an ancient global self–sustained dipole magnetic field (Acuña *et al.*, 1999), which requires a partly fluid metallic core. The global distribution of magnetic anomalies, their presence or lacking correlated to Martian morphology (northern lowlands, volcanic constructs, and large impact basins in the southern highlands), suggests that parts of the crust formed or were erased by different processes (shock, heating, redistribution), after the core dynamo had ceased (Acuña *et al.*, 1999). Models and observations suggest that the cessation of the dynamo, including the loss of core heat, occurred already very early in Martian history (e.g. Stevenson, 2001).

The identification of young lava flows in the Arsia Mons caldera (about 100 Ma), were found by crater counts on Mars Orbiter Camera images (Hartmann, 1999a). It suggests that Mars has been volcanically active until very recently. The age is supported by crystallization ages

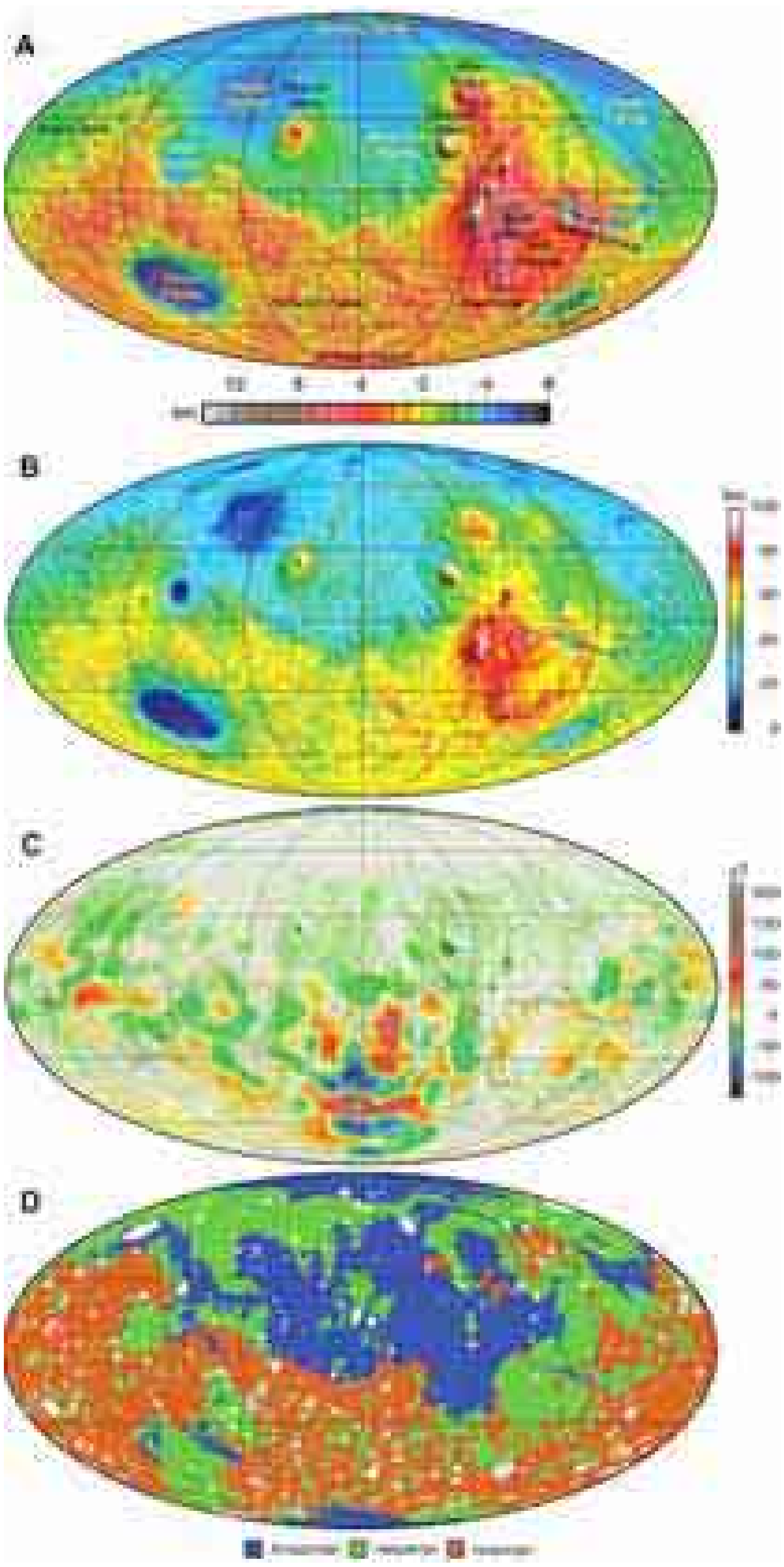

Figure 6.4.: (A) Topographic map of Mars (Smith *et al.*, 1999a; Neumann *et al.*, 2004) with major regions noted. (B) Crustal thickness on Mars (Neumann *et al.*, 2004) for a density contrast at the crust-mantle boundary of 600 kg/m3. (C) Radial component of the magnetic field arising from crustal magnetic anomalies on Mars (Connerney *et al.*, 1999) at an altitude of 400 T 30 km. (D) Map of martian surface units grouped on the basis of age (Scott and Tanaka, 1986; Greeley and Guest, 1987; Tanaka and Scott, 1987). Units transitional between Noachian and Hesperian and between Hesperian and Amazonian have been included in the younger of the two epochs. Areas in white are impact craters and their ejecta deposits. All maps are in Mollweide projection, with 180–longitude at the central meridian (Fig. from Solomon *et al.*, 2005).

of Martian meteorites (see Section 6.1). Considering the formation of Tharsis as one focal point of Martian volcanism that occurred after the global dichotomy had formed, global mantle convection models have to account for long–lived sources in this region (e.g. Stevenson, 2001; Spohn *et al.*, 2001).

7. Cratering on Mars

Impact cratering is one of the fundamental geological processes, and is visible on every solid surface body in the solar system (e.g. Alfred Wegener, 1921). When the disrupted comet Shoemaker–Levi–9 hit Jupiter, it was the only and the most spectacular opportunity to observe an impact event, but it left just short–term turbulences in the Jovian atmosphere. On solid surfaces the impacting projectiles form bowl–shaped depressions, which are named craters after a certain type of ancient Greek vase. Depending on the impacting energy the crater morphology changes with diameter. This progression was already described by Gilbert in 1893.

Mariner 9 images have revealed a diverse range of morphology and ejecta characteristics and potential target differences (Arvidson *et al.*, 1976; McCauley, 1973). Impact crater morphology and especially ejecta are largely unique to Mars (although they are found on the jovian moon Europa and on Earth). They have probably been strongly influenced by subsurface volatiles and are widespread throughout the surface of the planet. The Martian impact record in terms of crater morphology, morphometry, modification and crater frequency has been catalogued by Strom *et al.* (1992), but their study also revealed the difficulties in the fundamental morphologic classification. Keys to explaining the large variety of central crater structures or ejecta blankets include the geological conditions of the surface and subsurface (possibly the atmosphere as well). The dependence of crater diameter on the condition of impacts, defined by the impacting body (radius, mass, density, impact velocity) and the planetary surface (surface gravity, density, strength) is generally estimated by a form of scaling that employs both theory and small scale measurements to extrapolate to the large scales of observed craters and impact basins (Holsapple, 1987; Holsapple and Schmidt, 1987; Schmidt and Housen, 1987; Croft, 1985b,a; O'Keefe and Ahrens, 1981). The cratering process is controlled by the target strength and for larger impacting bodies by the surface gravity (Schmidt and Housen, 1987). The final crater diameter and appearance depends on gravity and material parameters (Croft, 1985b,a). Besides the knowledge of impact mechanism, other obvious differences in the impact environment influences the final crater form, i.e. surface gravity, impact velocity, the presence of atmosphere and the probable abundance of water or ice in the Martian subsurface.

7.1. Cratering Mechanics

Independent of the final crater size, the process of impact cratering always follows a three stage scheme, which has been described in detail by Melosh (1989). The three stages of the impact cratering process are (1) contact and compression, (2) excavation, and (3) modification (Fig. 7.1).

During the first stage, the projectile contacts the target. As it hits, the target is instantaneously compressed and accelerated, while the projectile itself is decelerated by the resistance of the target. A shock wave originates at the point of contact and travels through target and projectile, producing pressures much larger than the yield strength of either the target or the projectile. This stage, lasting a "blink of an eye", ends after the shock wave has passed.

The second stage is divided into the expansion of the shock wave and the excavation flow. While the shock wave expands hemispherically (and subsequently degrades to a stress wave), the target material is set into motion radially away from the impact site (immediately behind the shock wave). Rarefaction waves create an upward–directed pressure gradient behind the shock wave. This additional upward component to the radial velocity initializes the excavation flow and the largest portion of material ejects from the crater. This ejected material follows purely ballistic trajectories, the ejecta curtain. Material ejected first, closest to the impact site, has the highest velocities, and consequently takes the longest to fall. The growth of a crater up to the transient cavity starts as a hemispherical expansion following the shock wave until the final depth is achieved. Due to less resistance at the surface the crater diameter continues to grow further until its final diameter is achieved (Fig. 7.1). This state of the crater is called transient cavity. The final observed rim–to–rim diameter is different from the transient diameter and is reached in the last, so–called modification stage.

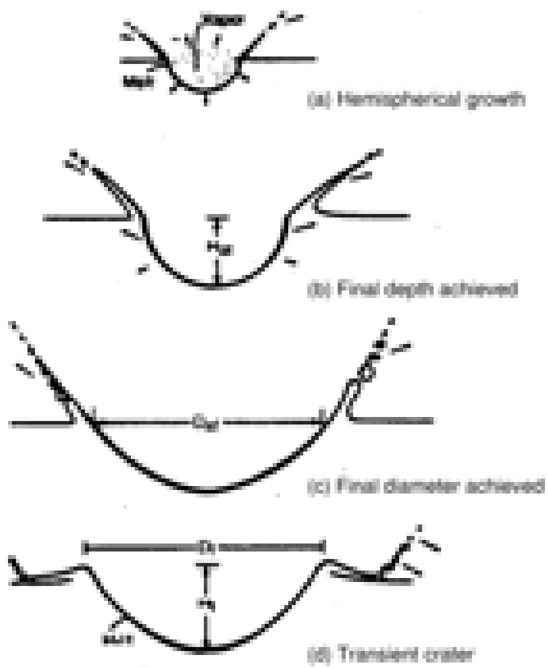

Figure 7.1.: The growth of a crater: The crater first opens following the hemispherical expansion of the shock wave (a). The growth rate is steadily decreasing due to the resistance of the underlying target rocks until its maximum depth is achieved (b). Less resistance at surface let the crater diameter continue to grow (c) and stops when no more material is ejected. The resulting transient crater is broader than a hemisphere (d) (Fig. from Melosh (1989)). Depending of the size of the transient crater, modification in the given gravity field results in different morphologies.

During the final modification stage, the ejected debris is finally deposited and the crater interior becomes modified. The fundamental idea of ejecta emplacement is that the ejected material travels in a near parabolic trajectory as a so–called ejecta curtain (ballistically). Based on observations, one expects very little material to escape the gravitational field of a planet, most falling back to the surface and forming a continuous ejecta blanket surrounding the crater. The innermost ejecta are launched first, travel fastest and can reach long distances. Ejecta originating farther from the center are launched later, moving more slowly and falling sooner and closer to the rim. Only material from the uppermost third to half of the depth of the transient crater is excavated from the crater. Target material deeper than the maximum excavation depth has been displaced beneath the crater floor. The maximum excavation depth (and the strata represented in the ejecta blanket) is considerably shallower than the maximum crater depth. Close to the rim, material is deposited in reversed original stratigraphy (overturned flap, Roddy *et al.* (1975)). The continuous ejecta blanket covers an area of roughly one crater radius from the crater rim, followed by a thin and patchy unit. In the latter unit and beyond, secondary craters can be found, which are formed by large chunks of material during the excavation period. On the Moon, secondary craters can reach a size of about 4% the diameter of the primary impact crater. The secondary crater itself is not necessarily distinguishable on the basis of its morphology (they could appear more elliptical), but ejecta of secondaries have a characteristic V–shaped ridge pointing radially away from the main crater. Cluster or chain formation also help to identify them. Lined up as a chain, the chevron pattern turns into a herringbone pattern (Oberbeck and Morrison, 1973). In general, these crater–field forms are all strongly controlled by the gravity field of the planet.

The change of the crater interior during the modification stage varies, depending upon the size of the transient cavity, and the shape characteristic of simple or progressively complex impact craters. For small craters, forming a final simple bowl–shaped crater, the transient cavity is filled by material falling back from the unstable rim to subsequently fill the center of the crater (wall slumping, Moore (1976)). The larger an impact crater, the further the initial transient departs from gravitational stability and is modified more strongly during this last crater forming stage.

7.2. Crater Modeling

Currently, the applied crater size–frequency distribution is based on the transferred lunar curve. This transfer procedure is outlined in Section 5 and discussed in detail by Neukum and Ivanov (1994); Ivanov (2001). To further refine and verify the modeling and transfer of the Martian crater production function, pre–existing modeling efforts have been continued by refining existing scaling laws, improving models for crater collapse, and estimating the impacting flux of planetesimals, including comets (Ivanov, 2001). Target parameters such as subsurface water, sedimentary and volcanic rocks of different water or ice saturation stages lead to a variety of scenarios that influence the final crater diameter, and therefore deviate from the analytical Martian crater size–frequency distribution. Measurements and analogue modeling of the crater size–frequency distribution on different geological units might be a key to understand the influence of target properties in Martian conditions.

Remote sensing combined with geological and geophysical investigations on Earth provide boundary conditions and "ground–truth" data sets of surface and subsurface morphology for crater modeling. Laboratory experiments and studies of nuclear explosions form the basis for the understanding of the dynamic behavior of the impact cratering event. These experiments are limited in reproducing the effects of high–energy impacts, which involve extreme pressures, temperatures and large crater–diameter range (role of gravity during the formation of large craters). Therefore, computer simulations are the only feasible method to study large–scale impact events. The complexity of the process involved during the crater formation, especially the passage of shock waves and the irreversible behavior of geologic material are translated into computer codes that handle the shock wave propagation (velocities, stresses and strains) as a function of time and position. These are called hydrodynamical computer codes ("hydrocodes"). These codes are based on a discretized particle motion established through the principles of conservation of momentum, mass and energy from a macroscopic point of view (Anderson, 1987), the equation–of–state, relating pressure, density and the specific internal energy (needed to describe compressibility effects and irreversible thermodynamic processes), and a rheology (constitutive) model, which describes the response of a material to deformation (change in shape or strength properties).

One of the most important issues concerning hydrocodes is the description of the discontinuous nature of shock waves, which may introduce instabilities in the discretized representation. The choice of a discretization approach and solving methods depends on the problem to be solved, so a variety of hydrocodes have been developed. An additional difficulty, besides the description of the problem itself, is the equation of state of the geologic material investigated. The crater modeling is an iterative process comparing observations and modelling results.

7.3. Impact Crater Morphologies

A variety of morphology-based classification and description schemes have been proposed to describe the wide range of observed crater and ejecta morphologies. Following Dence (1965), craters are classified as *Simple* and progressively more *Complex* craters:

Simple Craters appear as bowl-shaped circular depressions, with raised rims and approximately parabolic interior cross sections. The inner walls, close to the angle of repose, can be modified due to gravity–driven erosional processes. For lunar craters, Pike (1977) estimated a depth–to–diameter ratio near 1 : 5. Comparison between planets show that the transition diameter between simple and complex craters (see below) is dominantly inversely related to surface gravity, but also to target properties. This transition is on the Moon at diameters around 15 km, on Mars about 7 km, and on Earth depending on the target rock, between 3 to 5 km (for sedimentary or crystalline rocks). Investigations on Earth indicated that the apparent crater is filled roughly to half of its real depth by a lens of broken and shock–melted rocks (Grieve *et al.*, 1977). The mechanical process to generate simple craters is essentially that of the gravitational collapse of the rim of the transient crater cavity.

Complex Craters: Craters reaching the "transition diameter" have a more complex interior. Their rim is more synclined, the craters are surrounded by circular faults and in their interior a central structural uplift is developed. With increasing diameter they show single or multiple central peaks, flat floors and terraced rims. When compared to simple craters, the depth of complex craters increases less with increasing diameter. If the craters grow larger, the central peak evolves to an inner mountain ring. Again, there seems to be a 1/g scaling for the transition diameter.

Multi–Ring Basins: These are the largest, most complex impact craters and show multiple rings. One typical example is the lunar Orientale basin. It possesses at least five circular rings forming inward facing scarps of up to 6 km in height. On icy targets they look slightly different, but they are considered to originate as a tectonic response of the icy and rocky lithosphere to the impact cavity (Melosh and McKinnon, 1978; McKinnon and Melosh, 1980). In the case of Mars, due to strong erosional degradation of the largest basins (Hellas, Argyre, Isidis) and filling, one cannot judge whether or not there have been prominent ring features (Wood and Head, 1976). No gravity scaling could be found and ring separation is most likely dependent on the near-surface rheology.

Martian Special Crater Cases: Ejecta blankets of lunar craters are usually blocky near the rim, grading outward with increasingly more fine–grained particles until the blanket merges with the surrounding area. These features are consistent with the ballistic emplacement of the ejecta. Many Martian craters have ejecta deposits that appear to have flowed over the surrounding surface like mud-flows. These craters are known as rampart, fluidized, or splash craters. Their ejecta consist of several relatively thin sheets with tongue-shaped fronts, while a ridge formed at the front of each ejecta lobe. Numerous characteristics of the Ries Crater (Germany) show similarities to craters on Mars, indicating that Martian fluidized ejecta craters may be closer analogs to this terrestrial crater than lunar craters (Mouginis-Mark, 1981). Geologic evidence indicates that the Martian surface has been substantially modified by the action of water and that much of the water still resides beneath the surface as ground ice. In particular, the fluid appearance of rampart crater ejecta has been cited as evidence for subsurface ice at the time of impact. If this interpretation is correct, then the size–frequency distribution of rampart craters broadly consists with the depth distribution of ice, inferred from stability calculations. Ejecta morphology has proven to be a useful tool for studying the distribution of subsurface ice on Mars (e.g. Kuz'min *et al.*, 1989).

7.4. Crater Morphologies: Indicators of Sub–Surface Water

Morphologies of differently sized craters superimposed on variuos geological units allow us to assess the role of the projectile nature and target properties (e.g. water or ice content) in the crater formation process and thus in the morphological appearance and size parameters of craters (if compared to numerical model results).

Structures/Landforms that may reflect volatile content include craters with fluidized ejecta blankets (FEB, Gault and Greeley, 1978). Schultz and Gault (1979) suggested the atmosphere affected the Martian ejecta emplacement. Barlow and Perez (2003) correlated the occurence of FEBs with the proposed locations of near–surface water/ice as detected by Mars Odyssey (Mitrofanov *et al.*, 2002; Feldman *et al.*, 2002). Craters vary in terms of their interior morphology and some quantitative parameters, including crater depth/diameter, rim height/diameter ratios and diameter ratios of crater cavities to their ejecta blankets. It is widely believed that FEBs indicate the presence of water or ice in the subsurface at the time of impact. Comparing crater morphology and morphometry for various FEB appearances may provide us with a key to understanding both the amount of volatiles in the target as well as crater–scaling laws and, finally, improve the absolute Mars cratering chronology transferred from the Moon (see Chapter 5).

Large–crater morphology: Double–ring craters such as Lyot, Lowell, Kepler, Galle and Flaugergues, all roughly 200 to 250 km in diameter with ages between 3.9 Ga and 3.4 Ga (Chapter 13), were selected. The goal is to find/understand differences in the crater morphometry of large craters in various geologic regions of Mars.

They appear (if not filled by sediments, for example Kepler) as rather deep depressions with distinct inner ring features. Lyot, one of these craters situated in the south of the Northern Plains at the dichotomy boundary, was previously considered by Russell and Head (2002) as a crater whose transient cavity penetrated into the global aquifer suggested in the hydrology model of Mars by Clifford (1993). However, these authors did not find morphological evidence of the cavity penetrating to an aquifer and did not analyze Lyot in relation to the above mentioned morphometric parameters.

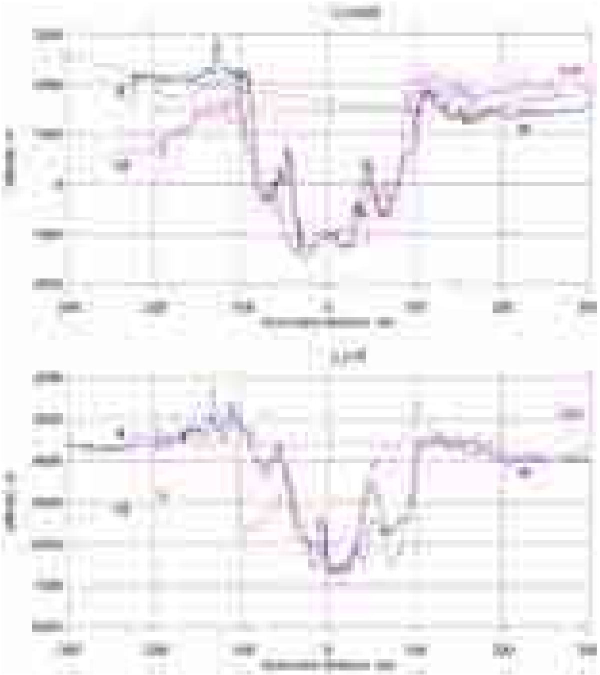

Figure 7.2.: Cross sections based on MOLA topographic data of impact crater Lowell (top) and Lyot (bottom). Lowell is an example for the highland units, while Lyot is the only large crater which could be representative for the lowland units. The main difference is the relative inner rim height when compared to a pre–impact surface level, for absolute values see Table 7.1; (Figure from Werner *et al.*, 2004a).

Morphometric characteristics derived from MOLA topographic data are compared in Table 7.1. Large variations in the maximum apparent depth are observed, yielding different levels of infill. Nevertheless, the apparent depth of the inner rim crest (measured from the pre–impact surface level) is situated about 1.5 km below the local pre–impact level for all craters except Lyot (Werner *et al.*, 2004a, see Fig. 7.2). The inner rim of Lyot reaches the pre–impact level. Considering that only Lyot is situated in the Northern Lowland plains, this indicates that even for large craters some morphometric parameters may vary and reflect differences in the target properties.

Smaller–Crater Morphometry: Considering smaller and more numerous craters, a more representative result might be derived. We started with a set of craters with diameters of about 30 km. From Barlow's catalog we compiled 5 to 6 example craters for various morphologic classes: single, double, and multiple lobated, as well as appearingly "dry" crater ejecta blanket. In addition, several "unclassified" craters are investigated. The profiles for each crater were selected from MOLA topographic data for four cross sections through the crater center.

The more or less prominent central peak is a typical appearance of craters in that size range. Guided by the results of the large craters, we focused on a few of the main morphometric parameters: diameter, inner slope angle, rim height, and central peak position below the pre–impact surface level. The results are represented in Fig. 7.3. Crater depth is not considered, as many craters are partially filled by aeolian or other deposits. It appears that the central peak position below the pre–impact surface level and the average rim height are not in agreement with the expected change in target properties, as reflected in ejecta blanket morphology (Werner *et al.*, 2004a). The main difference found in the limited data test set is a weak tendency for craters with single lobe ejecta to have less steep inner walls (Werner *et al.*, 2004a). We also note the systematic deviation of measured parameters from the generalized relationships published by Garvin *et al.* (2003), Fig. 7.3).

Numerical modeling of impact cratering: Numerical modeling allows us to investigate how the crater size and morphology depends on the projectile impact velocity, target strength, etc. (Ivanov *et al.*, 1997). Modeling of the projectile–type influence (2–km diameter asteroid at 8 km/s vs. 2-km diameter comet at 15.5 km/s) on the crater diameter and depth did not yield any significant difference in the crater diameter (about 30 km), depth (1 km) and inner slope steepness (about 15°). However, the impact melt production and central peak morphology were found to differ (Fig. 7.4).

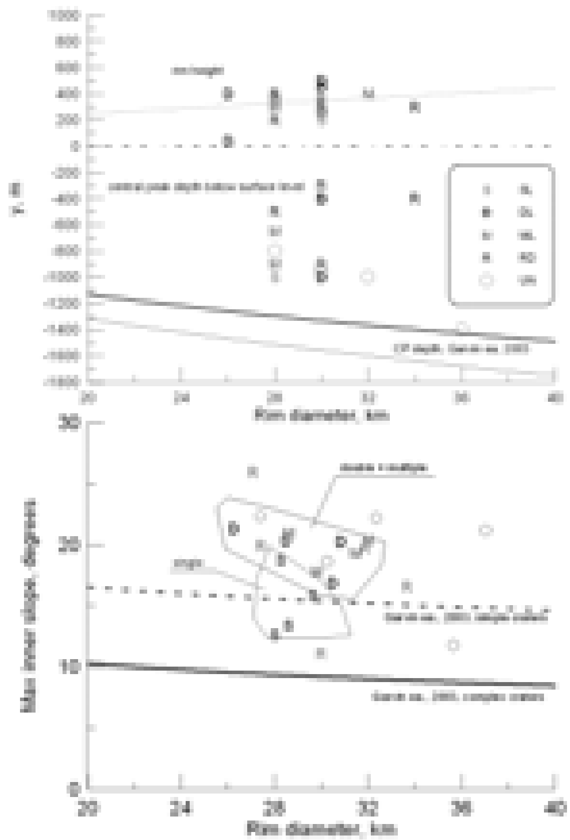

Figure 7.3.: TOP: Rim heights and central peak (CP) depth below the initial target level for craters with various types of ejecta blanket: single (SL), double (DL) and multi-(ML) lobed , radial ("dry") deposites (RD), and unclassified cases (UN). All data for CP depth are well above averaged relationships by Garvin et al. (2003). BOTTOM: Maximum slope for the same craters as in Fig.2. Craters with SL ejecta tend to have less steep maximum slope of inner walls. All data are well above the average relationships from Garvin et al (2003); (Figure assembled and provided by B. A. Ivanov; from Werner *et al.*, 2004a).

We have compared our results with observational data from Garvin *et al.* (2003) and found

Martian Small–Basin Morphology

	Diameter D km	Max. apparent depth h m	Apparent depth of inner rim crest m	Pre–impact altitude (estim.) m	Visible State
Kepler	233	1200	800	+2300	partially filled
Lowell	203	3000	1000	+1500	partially filled
Galle	230	2900	1500	–300	partially filled
Secchi	234	1900	1300	+2200	partially filled
Flaugergues	245	1100	>1100	+150	heavily filled
Lyot	236	3400	200	–3600	lightly filled

Table 7.1.: The dimensions of small Martian basins indicate a difference between highland craters and Lyot, which is situtated at the dichotomy boundary and could be representative for the lowland units. The only difference found is the inner–rim height below the pre–impact surface level (see Fig. 7.2).

a good fit for the crater depth, rim height and central mound width, but a poor fit for the central peak height, i.e. the computed peak was too high.

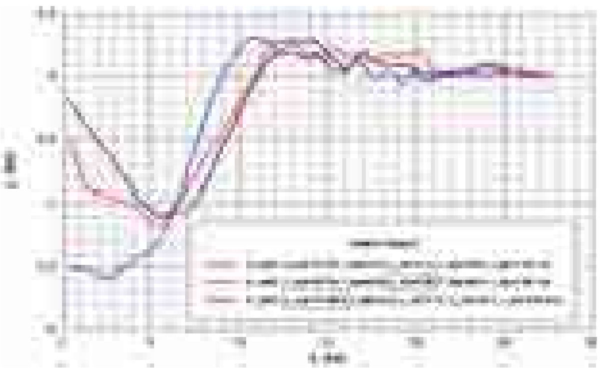

Figure 7.4.: Crater profiles from numerical modeling of a vertical asteroid impact (projectile diameter of 2 km at impact velocity of 8 km s^{-1}). The starting run (black curve) produced a crater with a 28 km rim–crest diameter and central peak uplifted about 200 m below the pre–impact surface. Changes in the model parameters (intensity of the acoustic–fluidization model block oscillations - red curve - or the cohesion of damaged material - blue curve) result in a crater shape with smaller diameter and less developed central peak (Modeling results provided by B. A. Ivanov, 2004)

Nevertheless, modeling the morphologic and morphometric characteristics of these craters gives us sets of model parameters, such as target strength, and a key to understanding the influence of water in the target on the crater morphology and the mobility of ejecta. Comparison with the numerical model of a similarly sized crater shows that the model with the initial set of parameters allows us to reproduce the general crater morphology (central peak crater) and crater depth. The variation of the model parameters can be used to understand the dependence of the crater shape on material properties of a target. Figure 7.4 shows three model runs, where the parameters describing either the intensity of the acoustic–fluidization model block oscillations or the cohesion of damaged material are varied. Decreasing the intensity or increasing the cohesion results in a crater shape with smaller diameter and less developed central peak. Both parameters act on the crater collapse process during crater modification, forcing the movement (central peak rising) to stop earlier for a given initial shear stress.

Slope measurements: We continued our initial attempt to understand target properties, reflected in the resulting crater morphology, by investigating the inner slope angles. We have found a weak tendency (see above) which we try to confirm. Following the findings that inner slope characteristics are dependent on the projectile or target properties, a detailed study of slope angles in different geologic units as well as at different latitudes was undertaken.

In addition to new digital terrain models derived from HRSC imagery, we used THEMIS and HRSC imagery of comparable resolution as well as MOLA topographic information where HRSC data were unavailable.

For the slope measurements, we extracted profiles from track–based MOLA and image–based HRSC topographic data. The slope angles are derived from a linear fit based on a moving–window of about 4 to 5 points, which is equivalent to a baseline of about 1 km. We looked for the maximum slope on each profile and determined the maximum slope angle averaged for all profiles (summarized in Fig. 7.5). The crater diameters of the investigated craters range between 5 km to 70 km. Individual terraces in the inner crater walls were investigated separately. In addition to crater walls, plateau and caldera walls were studied in this way. All measurements are based on imagery from very early on the HRSC mission, and are scattered in the equatorial zone. The comparison of MOLA and HRSC digital terrain models shows no significant differences between the two datasets (within the error bars and not considering systematic shifts or tilts). A slightly underestimated slope angle is observed due to the large footprint of the individual measurement that averages more than the imagery–based HRSC topographic data.

The measured slopes appear to be diameter independent (not as suspected above) and around 28°, indicating a friction coefficient k = 0.53 on a base of 1 km (compare Fig. 7.5, red stars and pink E). A clear difference between highland and lowland material is not observed.

Comparing slope measurements based on MOLA in the equatorial and polar regions of Mars (compare Fig. 7.5, blue P), a different situation appears: the approximate 18° slope angles indicate less steep walls (indicating a friction coefficient k = 0.32 on a base of 1 km). In the polar region, a lower friction is possibly observed. Similar observations have been made by Kreslavsky and Head (2000) and they found a latitudinal change in surface roughness/smoothness (measured in wave length and slope angles) going northward towards smoother regions.

The difference between the polar and mid–latitude to equator crater slopes observed here could signify a difference in the upper crust material between polar and "continental" material, indicating a lower friction. The angle of repose measured for the polar region is less than 20° and between 30° and 40° elsewhere, and could be due to lower cohesion and the presence of water. While we could not correlate slopes to geological units (suggesting different target properties), variations with latitude is seen. In polar regions, observed craters appear to have less steep inner walls than in equatorial regions.

When comparing our slope measurements to a global dataset by Kreslavsky and Head (2000), a similar latitudinal dependency is observed. A general decrease in surface roughness towards the poles does not necessarily reveal a crater formation related effect and must be tested carefully. The presence of water or ice in the subsurface has been heavily discussed. It is unclear whether two competing processes result in larger or smaller craters. The presence of ice could cement and strengthen the target material (resulting in a smaller crater, T. Ahrens, 2004, pers. comm.) or increase the explosive nature of the formation (resulting in a larger crater, B.A. Ivanov, 2004, pers. comm.). Nevertheless, the results both from modeling and geologic target diversity were inconclusively in determining if the difference in inner slope angles is due to the impact cratering process in a target containing ice, or due to subsequent modification processes. In carfully examining the results of Kreslavsky and Head (2000), we found that fresh–looking craters in the polar region have steep slopes similar to those at the equator. Nine craters, with diameter larger than 5 km in the northern latitudes between the polar deposits and 60° N, are highly sampled by MOLA–tracks and show steep walls (more than 35° at 300 m–baseline). Almost everywhere, only the N–facing wall is

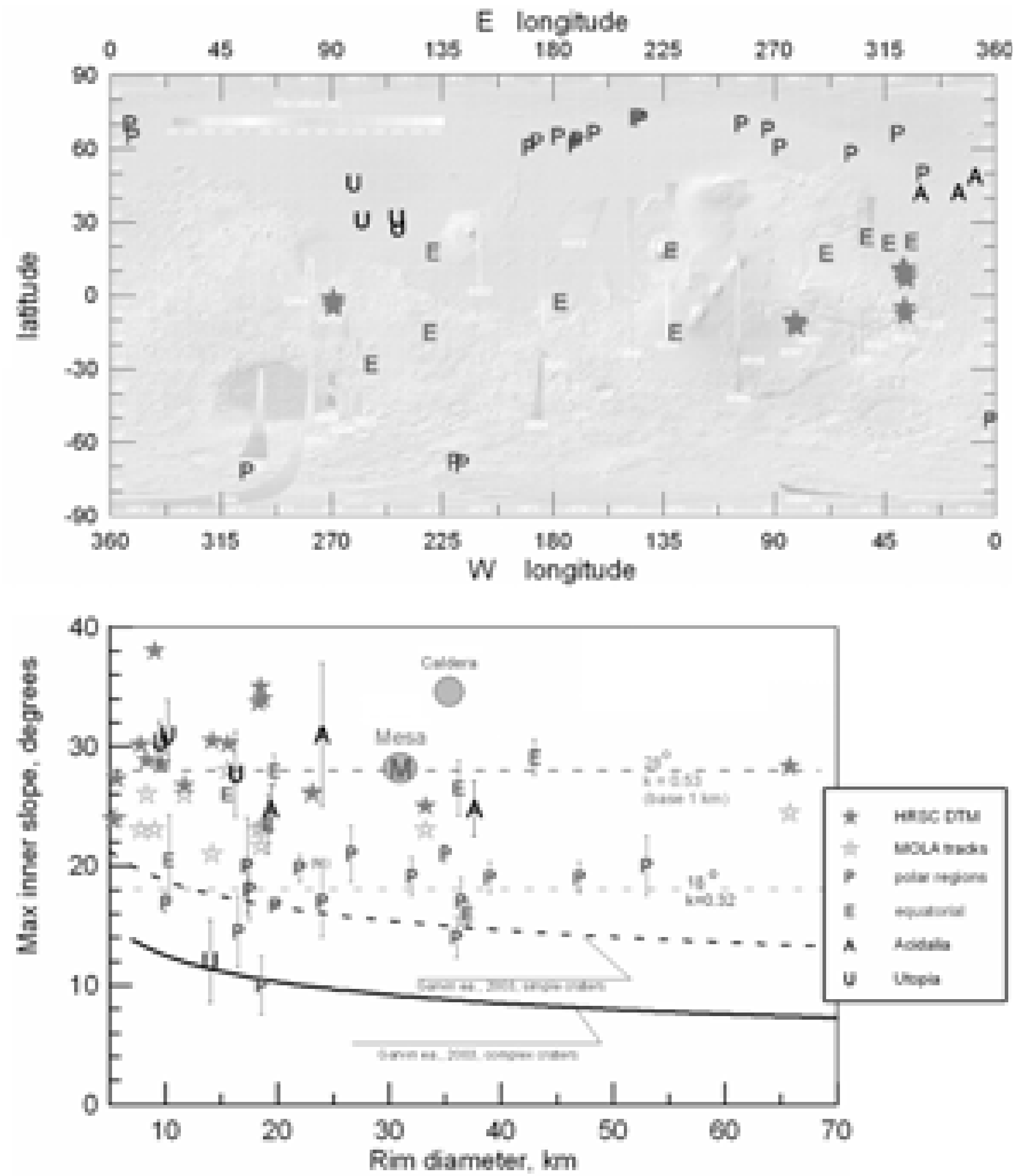

Figure 7.5.: Measurements of the slope of the inner crater rim, for details compare the text. (Figure assembled and provided by B. A. Ivanov, 2004).

steep (M.A. Kreslavsky, 2004, pers. comm.). It is likely that the general and detailed view of slope angles for craters studied here is related to post–formation processes, obscuring any cratering related observations.

Conclusion: Evidently, craters in the gravity–controlled regime do not show target related variations that might obscure the measurable crater size–frequency distribution for different geological units, and therefore, the crater count–based ages.

Part II.

Application and Improvement of the Age Dating Techniques, Secondary Cratering, and the Martian Crater Size–Frequency Distribution

In this Part, **Application and Improvement of the Age Dating Techniques, Secondary Cratering, and the Martian Crater Size–Frequency Distribution**, the method of age determination based on crater–size frequencies is introduced. The characteristics of the statistical distribution is outlined (Chapt. 8). The determination of absolute ages based on crater frequencies is described in Chap. 9. In the case, that resurfacing events have occurred and are present in the crater size–frequency distribution as characteristic kinks, the standard method is not directly applicable. A new method has been developed, its theoretical background outlined in Sec. 9.1.

Crater counts in the Athabasca region have been recently questioned by McEwen *et al.* (2003); McEwen (2003); McEwen *et al.* (2005a) regarding the admixture of secondary craters, implying the vulnerability of this method if only the small–diameter range is measured. The discovery of a secondary–crater strewn field in the Elysium Planitia raised the issue of secondary cratering (craters produced by the ejecta of a primary impact event) (McEwen *et al.*, 2005a), which would influence the steep branch of the crater–production function for craters smaller than 1 km, and making age determinations of this size range unreliable. The relevance of this issue is described in Chap. 10 and discussed comprehensively in Chap. 10.1. Key arguments for the validity of the applied Martian standard crater production function are listed in Sec. 10.1.2 and strongly support the steep branch of the crater size–frequency distributions measured is generated by a primary projectile population. In a "Gedankenexperiment" (Sec. 10.2) hypothetical secondary crater distributions are constructed and their possible contribution to the observed Martian standard crater production function is investigated. In Fig. 10.7 it is demonstrated that all ages measured in this study, are measured in diameter ranges where no or minor (within the statistical error bars) secondary crater contributions are to be expected. As outlined in the above mentioned chapters, it can be concluded, that the discussed special cases of secondary cratering (Zunil's strewn field) is not to be generalized and play a minor role regarding the age determination.

In this work, the crater size–frequency distributions, in many geological units for differntly aged surfaces, and over the entire crater diameter range (given by the available imagery), are measured. Finally, the observed Martian crater production function is given.

Nevertheless, the absolute ages are based on cratering models comprising the actual knowledge regarding the asteroid size and orbital distributions (especially, their impact probability onto Mars and the Moon) as well as crater scaling laws. All inherent uncertainties might cause a change in the applied cratering chronology model, if parameters will be refined in future studies. Therefore, in addition to the absolute ages, the cratering retention age N($\geq$ 1 km) is given. This number reflects the crater frequencies per unit area and is largely model–independent. If the applied cratering model requires revisions, the absolute ages can be recalculated, but relative differences in crater frequencies will stay the same.

8. Age Dating Techniques

In this chapter the age dating techniques, their theoretical concept and mathematical background will be outlined as it has been developed by Neukum (1983). It is the methodical bases for further developments in the context of this thesis (Chapter 9.1) and was utilized for gathering the age data base in the following (Part III).

8.1. Cumulative Crater Size–Frequency Distribution

To derive the relation between crater size–frequency distribution and relative ages on planetary surfaces besides the Moon, a projectile population represented by its mass-velocity distribution is used. Averaging the velocity distribution by means of the projectile mass distribution $n\,(m,t)$ in a mass interval $(m,\ m+dm)$ results in a crater size–frequency distribution $n\,(D,t)$ in the crater diameter interval $(D,\ D+dD)$ for a specific exposer time t.

The *differential cratering rate* $\varphi\,(D,t)$ is the number of craters for a specific diameter D per unit area per time at a given time t. The crater size–frequency distribution of a surface unit exposed to bombardment over a time t has a relative age $(t > 0)$ described by the *differential crater size–frequency distribution* $n\,(D,t)$:

$$n\,(D,t) \;=\; \int\limits_0^t \varphi\,(D,t')\,dt' \qquad (8.1)$$

Crater size–frequency distributions integrated over crater diameters leads to the *cumulative crater size–frequency distribution*, i.e. craters equal to or larger than a given diameter D formed during time t on a planetary surface:

$$N_{cum}\,(D,t) \;=\; \int\limits_D^\infty \int\limits_0^t \varphi\,(D',t')\;dt'\,dD'$$

$$=\; \int\limits_D^\infty n\,(D',t)\;dD', \qquad (8.2)$$

which is the continuous approximation. In reality, differential and cumulative frequencies are derived from discrete numbers.

The Crater Analysis Techniques Working Group, Arvidson *et al.* (1979), suggested some principles to display measured crater size–frequency distributions comparatively: Axes in double logarithmic scale with a base of 10 and equal decade length, consistent units on both axes, crater diameters in kilometer, all frequencies given per square kilometer, and 1σ-standard deviation of each measurement point (given by $\sigma\;\approx\;\pm\,n^{\frac{1}{2}}$, where n is the number of craters of a given crater diameter assuming a Poisson–distribution).

For a better comparison, frequency distributions are standardly–binned by diameter intervals and normalised for the differential distribution. The cumulative distribution is the sum of discrete numbers per bin (Arvidson *et al.*, 1979). Possible bin–sizes are defined by a standard square–root–binning, for each crater bin diameter D_i and $n = (-19,\ -18,\ \ldots,\ 19,\ 20)$:

$$D_i\,(n) \;=\; 2^{n/2} \qquad (8.3)$$

In this work a quasi–logarithmic binning

$$D_i\,(a,n) \;=\; a\,\cdot\,10^n \qquad (8.4)$$

with $n = (-3,\ \ldots,\ 3)$ and $a = 1.0, 1.1, 1.2, 1.3, 1.4, 1.5, 1.7, 2.0, 2.5, 3.0, 3.5, 4.0, 4.5, 5.0, 6.0, 7.0, 8.0, 9.0$ is used. Compared to the standard binning, the resolution along the abscissa (*log* diameter) is higher. All measured diameters D_i of an interval $[D_a,\ D_b)$ are plotted as $D_i\;=\;D_a$.

Crater size frequency distributions measured on geological units of different size (with area A) are scaled for each bin $[D_a,\ D_b)$, here the cumulative crater size–frequency distribution $\log N$:

$$N = \sum_{k=1}^{i} \frac{n_k}{A_k} \qquad (8.5)$$

and plotted versus $log\,(D_a)$. It allows us to compare crater populations measured on different sized surface areas and different image resolutions. The level of uncertainty of the scaled cumulative number N per bin is given by:

$$\pm\sigma_N = \log\left[\frac{\mathrm{N} \pm \mathrm{N}^{1/2}}{\mathrm{A}}\right] \qquad (8.6)$$

for each bin.

8.2. Cumulative Cratering Rate

Following equation 8.2, the *cumulative cratering rate* is given by:

$$\Phi\,(D,\,t) = \frac{\partial\, N_{cum}\,(D,\,t)}{\partial t} \qquad (8.7)$$

Neukum (1983); Neukum and Ivanov (1994); Neukum *et al.* (2001) demonstrated in the lunar case that the crater size–frequency distribution is not directly dependent on time, i. e. the shape $g\,(D)$ or $G\,(D)$ of the differential or cumulative crater size–frequency distribution does not change over the whole exposure time, while the number of impacting projectiles had changed over time $f\,(t)$.

The differential crater size–frequency distribution is given by:

$$\begin{aligned} n\,(D,\,t) &= g\,(D) \int_0^t f\,(t')\,dt' \\ &= g\,(D)\,\cdot\,F\,(t) \qquad (8.8)\end{aligned}$$

and the cumulative crater size–frequency distribution by:

$$\begin{aligned} N\,(D,\,t) &= \int_D^\infty g\,(D')\,dD' \int_0^t f\,(t')\,dt' \\ &= G\,(D) \int_0^t f\,(t')\,dt' \\ &= G\,(D)\,\cdot\,F\,(t) \qquad (8.9)\end{aligned}$$

8.3. Relative and Absolute Ages

If, as for the Moon, the crater size–frequency distribution or the mass–velocity projectile distribution, the so–called production functions, is known, the flux of projectiles onto the surfaces isotropic, and any target influence negligible, then the crater frequencies measured on planetary surfaces exposed for the same time with respect to diameter are the same. Crater frequencies representing different aged surfaces (at t_i and t_j) can be compared by their ratios:

$$\frac{N_{cum}\,(D, t_i)}{N_{cum}\,(D, t_j)} = \frac{F\,(t_i)}{F\,(t_j)} = C \qquad (8.10)$$

Cumulative frequencies differ by a factor c_{ij}, which is related to their age difference (Arvidson *et al.*, 1979; Neukum, 1983; Strom and Neukum, 1988), and represent the relative age. For a better comparison, relative ages based on $N \sim F(t)$ are given for a fixed diameter D (e. g. 1 km, 4 km, 10 km or 20 km), so-called *crater–retention ages* (Hartmann, 1966; Neukum and Wise, 1976; Neukum and Hiller, 1981; Neukum, 1983).

Based on the crater–retention ages and the relation between $N_{cum} = G(D) \cdot F(t)$, absolute surface ages are derived applying *cratering chronology models* which are well known for the Moon and can be transfered to other planetary bodies as shown in Section 5. The *absolute ages* or *cratering model ages* used here are calculated from crater–retention ages for a reference diameter $D = 1\,km$ (Neukum, 1983).

8.3.1. Errors in the Relative and Absolute Ages

Prerequisite for the crater count statistics are (1) careful geologic mapping outlining homogeneous units, and (2) excluding sublimations pits, volcanic and secondary craters. Contamination due to unrecognized global secondary craters unwittingly included in the measurements is less than 10 % (old surfaces), and in most cases less than 5 %. This was concluded in this study, see Chap. 10.

The quality of the crater size–frequency measurements crucially depends on the accuracy of measured crater diameters as well as on the accuracy of geological mapping, which defines the reference area to calculate the crater frequencies per square unit (details in Chap. 9). Resurfacing events are visible in the crater counts and cause characteristic deviations from the crater production function starting at small sizes (e.g. Neukum and Horn, 1976). A improved treatment for such cases is discussed in Chap. 9.1. An possible error source could be the misinterpretation of the reference unit of the resurfaced area within the total counting area which may lead to an underestimation of the age of the resurfacing event.

All these technical error sources can be minimized through the experience and thorough measurements of the operator to a level of a few percent uncertainty in N as has already been shown by Neukum *et al.* (1975) as long as technically good equipment which allows high precision measurements is used (as was the case here).

In this work the crater size–frequency measurements have been presented as cumulative distributions (Sec. 8.1). The measured distribution is used to determine **relative ages** of geological units by comparing crater frequencies. An advantage of a cumulative description is that the statistical error of the measurement "stabilizes" even for small crater numbers (Neukum, 1983). The error estimate for each individual bin is given in equation 8.6. Due to the exponential character of the cumulative crater distribution, any fluctuations of the crater number in the larger–crater diameter range is diminished in the smaller–size range. Similarly the statistical error ($\sqrt{N}$) minimizes towards smaller crater diameters. The basis for the age determination through crater statistics is fitting a standard crater production function (cf. Neukum, 1983) which has been determined for the moon in a diameter range between 10 meters and 300 kilometers. An approximation for the standard crater production function is given by a polynomial expression of 11th order which represents the measurements with less than 50 % deviation, and it has been shown that the shape of the crater production function does not vary with time (Neukum, 1983). This standard crater production function might include an uncertainty in the crater frequency ratio between the upper (300 kilometers) and lower (10 meters) limit of the range of validity which is of the order of a factor of 2. In the range utilized here (usually between 100 meters ands 50 kilometers) this uncertainty is negligible (Neukum, 1983).

For age determinations on Mars, the lunar standard crater production function has been transferred to Martian conditions using crater scaling laws (Ivanov, 2001). In Chap. 11 it is shown, and for the first time for the entire crater–diameter size range, that the theoretically transferred crater production function is a good (less than 1σ) approximation for the measured crater size–frequency distribution of Mars.

For determination of firstly relative and subsequently **absolute ages**, not the N–value for an individual bin is taken, but the standard Martian crater production function (Neukum, 1983; Ivanov, 2001) is fitted to the crater size–frequency measurements of the whole diameter range. The statistical error ($\sqrt{N}$) of the measurement indicates the uncertainties of the relative ages. The fitting procedure for the mean value of N follows the Marquardt–Levenberg algorithm, a weighted non–linear least-squares fit (Levenberg, 1944; Marquardt, 1963). A shift of the crater production function in vertical (y–) direction implies different crater frequencies. The fit quality depends on the number of bins which can be used as fit range. The uncertainty of such a fit for making use of the whole size range for the derivation of a mean N–value at a certain diameter is of the order of the statistical error of 2σ and less than the individual bin error of 1σ (cf. Neukum, 1983).

The fitted crater frequencies given for a reference diameter, in the course of this work $N_{cum} = D(\geq 1km)$, are translated to absolute ages by applying a cratering chronology model.

In the lunar case the cratering chronology model links measured crater frequencies (usually given for $N_{cum} = D(\geq 1km)$) and radiometrically determined ages. In the age range between 4.5 Ga and 3.5 Ga the statistical error implies uncertainties in the measurements of less than 30 %, which reflects an uncertainty of 30 Ma in age; for ages younger than 3 Ga the error estimate of the measurements responds linearly (Neukum, 1983).

For Mars, the applied chronology model is transferred from the moon (Hartmann and Neukum, 2001; Ivanov, 2001). A variety of lunar cratering chronology models existed before (see Neukum, 1983) agreeing within a factor of 2 – 3. These different models have converged in a unified model, while discussing the transfer from Moon to Mars (Hartmann and Neukum, 2001; Ivanov, 2001). Any possible uncertainties inherent in the lunar cratering chronology model might be found in the cratering chronology model for Mars (Hartmann and Neukum, 2001; Ivanov, 2001) because of the transfer from Moon to Mars. However, since the knowledge is limited we cannot be any more specific and the cratering chronology model is assumed to be absolutely correct and the time resolution is based on the characteristic shape of the chronology, and the error estimate of the measurement. The transfer is based on the most up-to-date knowledge of celestial mechanics, crater scaling, and the planetary body flux, which could account for a systematic error and uncertainty of up to a factor of two due to the transfer (Chap. 5).

For absolute ages, this uncertainty of the Martian cratering chronology (factor of 2), causes a possible systematic error. These error estimates are given corresponding to equation 11.2:

$$\begin{aligned} \Delta N &= \Delta(a \cdot e^{b \cdot T} + c \cdot T) \\ &= (a\,b \cdot e^{b \cdot T} \Delta T) + c\Delta T \qquad (8.11) \end{aligned}$$

Therefore, a systematic error could be of about 100 Ma in the age range older than 3.5 Ga, while for the constant flux range the systematic error could be up to a factor of two in N.

The general concept of a similar evolution of the flux in the inner solar system is reflected in the cratering record. This has been tested once again in this study, and has confirmed the approach (Chap. 13) as discussed above. If better knowledge about the projectile flux for Mars will be collected and the chronology model will possibly be changed, the absolute ages have to be recalculated from the measured crater frequency given as $N_{cum} = D(\geq 1km)$. The uncertainty could be a systematic error in every absolute age estimate, while the relative age given here as $N_{cum} = D(\geq 1km)$ is unchanged.

This study has shown that the applied cratering chronology model results in ages for basin formation ages (Chap. 13) and volcanic surfaces (Chap. 15.5) which are in good agreement with Martian meteorite crystallization ages (Chap. 18) with respect to "peak" activity periods which leads us to believe that the chronology model is correct within an uncertainty of less than 20 % .

9. Absolute Ages in Resurfaced Units – Refinement of the Method

The determination of absolute ages on Mars and other solid surface objects is based on the crater production function (Ivanov, 2001, originally in Neukum (1983)) and the applied chronology model (Hartmann and Neukum, 2001). The crater production function describes the expected crater size–frequency distribution recorded in a geological unit at a specific time. This function is scaled from the well established lunar crater production function (Neukum, 1983; Neukum and Ivanov, 1994) to Mars, given the assumption that the inner solar system craters are produced by a single–source population: asteroids, ejected from the asteroid main belt between Mars and Jupiter (e.g. Neukum and Ivanov, 1994; Ivanov, 2001). The lunar crater production function could be determined over the full size range based on multi-resolution image data (which are used here; Neukum, 1983, or Hartmann (1973)). The transfer from the Moon to Mars is based on the calculation of the impacting body flux ratio between the lunar case to Mars under celestial mechanical aspects and the consideration that the condition of the crater formation differ from one planet to another, mainly in gravity and target properties of the impacted body. The validity of this approach has been demonstrated by Neukum and Wise (1976) (and later by Neukum and Ivanov (1994)) by comparing measured crater size–frequency distributions of Mars and the Moon.

To estimate the absolute age of the surface, a chronology model must be applied. This chronology model is based on measurements of the crater size–frequency distribution on areas of the Moon which could be linked to radiometric ages retrieved from sample return missions of lunar rocks (see Chapter 4). This distribution is transferable to other planets and solid surface bodies, assuming that all bodies have suffered from the heavy bombardment period that is generally reflected in the crater frequency, and in the basin population on both bodies (e.g. Neukum and Wise, 1976; Neukum and Hiller, 1981; Hartmann, 1973, 1977, 1978, and unified in Hartmann and Neukum (2001)). The idea of a marker horizon (Wetherill, 1975) specifies that large impact basins on any planet did not form any later than about 3.8–3.9 billion years ago (see Section 13).

Previously, it was almost impossible to determine and verify the predicted crater size–frequency distribution on Mars due to the fact that the image data (in terms of image resolution and covered area) did not reveal craters over the full size–range. During the Viking mission, global coverage was aquired at an average image resolution of about 231m/pxl (Viking MDIM2.1), and allowed confident investigation of the crater distribution larger than about 2 km. For selected areas medium–resolution imagery (about 70 m/pxl) and high-resolution mosaics (about 15m/pxl) exist. During the Mars Global Surveyor mission, the high–resolution Mars Orbiter Camera (MOC, 3-6m/pxl) covered many spots on the Martian surface and revealed very recent geological activity. It is difficult to link the high–resolution MOC imagery to low–resolution Viking imagery (see Chapter 12). Currently, the thermal emission imaging system (THEMIS, 18 m/pxl) onboard Mars Odyssey and the high–resolution stereo camera (HRSC, 12m/pxl) onboard Mars Express are scanning the Martian surface and provide the opportunity to fill the resoluion gap, and to define the full crater size–frequency distribution.

The procedure for determining absolute surface ages by counting craters is illustrated in Fig. 9.1. First, geological units are mapped and their area (in km^2) is determined. Following morphologic or spectral information, different units are delinated, accordingly. Here, the Mars Express–HRSC digital image obtained during orbit 1087 is used as an example. It shows part of the caldera of Meroe Patera, a volcano in the center of the Syrtis Major volcanic province.

Crater counts are carried out by measureing the diameters with high precision. A traditional photogrammetric instrument, a Zeiss PS2K stereocomparater, was used to measure photo coordinates on transparencies. Therefore, the digital and mapped image was exposed to large–size photographic film (20 x 24 cm). The crater rim diameters were measured in microns (μm), and the maximum error in locating the stereocomparator cursor on a crater rim is on the order of 5 microns. Each measured diameter is converted into kilometers using a calibration factor depending on the pixel resolution of the digital image. The measured craters are sorted according to the quasi–logarithmical scheme described in Chapter 8. Graphically, they are represented in a cumulative crater size–frequency distribution diagram (plotted in double–logarithmic scale). The cumulative crater frequency N_{cum} is the number of craters greater than or equal to a crater diameter D_{ref} per normalized unit area (in km^{-2}). Therefore, the crater frequency reflects relative ages between various geological units. Based on fitting the crater production function (Chapter 4) to the measured crater distribution of a given geological unit by a nonlinear regression (least square), a crater retention (or relative) age is calculated directly from the fitted curve.

Two phenomena, saturation or geological resurfacing, cause characteristic deviations from the crater production function. In densely cratered units ($\hat{=}$ old), crater destruction and production eventually reach a steady state, starting at small sizes. Such an equilibrium distribution exhibits a characteristic cumulative slope of "minus–two". Here, a drop in the distribution is observed due to resurfacing of the caldera floor, hence the crater production function fits only part of the measurement and yield two ages (for details see Chapter 9.1).

Relative crater retention ages obtained by applying the cratering chronology model ((Hartmann and Neukum, 2001) and see Chapter 5) can be translated numerically into absolute cratering model ages (given in giga–years [Ga], 1 Ga = 10^9 years).

9.1. How Do Crater Counts Reveal Resurfacing?

Qualitatively, detailed morphologic studies of planetary surfaces yield insights into surface modification processes. Accordingly, geologic unit delineation, following morphologic or spectral characteristics, is based on superposition principles and other stratigraphic relations between different surface units. Quantitatively, the relative abundances and size distributions of impact craters distinguish geologic units chiefly by relative age. A combination of both facets helps to outline homogeneous geologic units. In general, remote–sensing age–dating techniques rely on imaging of planetary surfaces at high enough spatial resolution to allow adequate statistics to be developed on craters over a wide size range. For detailed crater size–frequency distribution studies, any deviation from the crater production function (see Chapter 4) implies a resurfacing event (erosion or deposition). Although a careful separation of the different units might sometimes not be possible due to image resolution, the effect of resurfacing is detectable in the crater size–frequency distribution and resurfacing ages can still be determined. Usually, resurfacing erases the cratering record starting at the smaller size range or resets the cratering record totally when the surface is completely renewed. Thus, it is dependent on the magnitude of the event. When measuring the crater size–frequency distribution of such a unit, any distinct drop in the distribution reveals a resurfacing event. In cases of ongoing resurfacing (e. g. on steep slopes of martian surface structures) or saturation, the crater counts cannot be linked to an age.

For units, where resurfacing has been observed, the determination of ages has to be limited to a certain diameter range (below or above a diameter $d_\star$, where the resurfacing has influenced the crater size–frequency distribution). The oldest age is derived straightforwardly, by fitting the production function to the large–diameter range. For the resurfacing event, if no correction has been applied, the age is slightly overestimated (depending on the magnitude of the resurfacing event) due to the cumulative character of the crater size–frequency distribution. As a first attempt, a cut–off limit (Neukum and Hiller, 1981) applied to the large size range reduces the number of craters in the smaller size range, which is used to estimate the resurfacing event. This approach underestimates the age (depending on the surface age difference). For this work a more precise treatment is developed.

The general description of the cumulative crater size–frequency distribution $N_{cum}(D, t)$ is given by the cumulative number of craters per area for a given diameter D at a certain time t:

$$N_{cum}(D,\, t) = \int\limits_{D}^{\infty} \int\limits_{0}^{t} g(D')\, dD' \cdot f(t')\, dt' \qquad (9.1)$$

for an undisturbed geological unit a simple solution can be found:

$$N_{cum}(D,\, t) = G(D) \cdot F(t), \qquad (9.2)$$

where G represents the cumulative crater size–frequency distribution and F the flux of projectiles. It has been demonstrated that the crater size–frequency distribution is stable over time, but the flux decays (see Chapter 8).

In a unit where subsequent processes (erosion as well as deposition) occurred, the smaller crater population has been modified preferentially. Therefore, the measured crater size–frequency distribution will deviate from the crater–production function for craters smaller than a certain diameter $d_\star$. If the resurfacing event ended at a certain time $t_\star$, the surface accumulates craters as it is a fresh surface. In the cumulative description, the crater size–frequency distribution is represented by the sum of two (or more) populations, where the older one(s) do not cover the entire measurable size range. Such a distribution is represented by:

$$\begin{aligned} N_{eros} \;=\; & \int\limits_{D_{min}}^{D_{max}} g(D')\, dD' \cdot \int\limits_{0}^{t_\star} f(t')\, dt' \\ + & \int\limits_{d_\star}^{D_{max}} g(D')\, dD' \cdot \int\limits_{t_\star}^{t_{max}} f(t')\, dt', \qquad (9.3) \end{aligned}$$

where the measurement is performed with a diameter range between $D_{min} \le d_\star \le D_{max}$ and the original surface has been formed at a time t_{max}, the resurfacing ended at a time $t_\star$, with $0 \le t_\star < t_{max}$. If $t_\star = t_{max}$, no resurfacing occurred and the description follows equation 9.1 and 9.2.

On a planetary surface, a proper remote–sensing method to distinguish both populations is not known. Any attempts to distinguish between erosional state or other parameters are strongly misleading (and subjective). To understand the crater population accumulated on the surface after the resurfacing event, a method is needed to separate both populations. Due to the crater accumulation per time and the cumulative characteristics of the measured crater size–frequency distribution, the contribution of the old crater population has to be calculated with respect to their quantity in the diameter range larger than $d_\star$. The measured crater frequencies in the smaller crater size range, attributed to the resurfacing event, have to be reduced (by the number of craters produced in the period prior to the resurfacing event).

Based on the known crater–production function (see Chapter 4), the cut–off diameter and the age of the old surface can be determined, while the exact resurfacing age remains obscured:

$$\begin{aligned} N_{eros} \;=\; & \int\limits_{d_\star}^{D_{max}} g(D')\, dD' \cdot \int\limits_{0}^{t_{max}} f(t')\, dt' \\ - & \int\limits_{d_\star}^{D_{max}} g(D')\, dD' \cdot \int\limits_{0}^{t_\star} f(t')\, dt' \end{aligned}$$

$$
\begin{aligned}
&+ \int_{D_{min}}^{D_{max}} g\left(D'\right) dD' \cdot \int_{0}^{t_\star} f\left(t'\right) dt' \\
&= \left(\left(G\left(D_{max}\right) - G\left(D_\star\right)\right) \cdot F\left(t_{max}\right)\right) \\
&- \left(\left(G\left(D_{max}\right) - G\left(D_\star\right)\right) \cdot F\left(t_\star\right)\right) \\
&+ \left(\left(G(D_{max}) - G(D_{min})\right) \cdot F\left(t_\star\right)\right) \qquad (9.4)
\end{aligned}
$$

Following the description in equation 9.3 and 9.4, a fit of the crater production function G(D) allows one to predict the shape of the expected distribution in the large–size range of the "resurfacing population", which gives a preliminary but overestimated age $t_{\star_{prelim}}$. Next, the expected number of craters accumulated on the younger surface is predicted. Thus, the contribution (in number) of the old crater population in the large branch can be calculated and the measured number of craters at the cut–off diameter $d_\star$ reduced, accordingly. By fitting the reduced distribution, the younger age is correctly determined.

Equation 9.4 demonstrates that an iterative approach is necessary to determine the age(s) of resurfacing event(s) by fitting the well known crater production function to the crater size range smaller than a certain diameter $d_\star$ and to predict the expected number of craters for diameters larger than diameter $d_\star$. Reducing the measured number to the predicted one allows for the determination of the time when the resurfacing event ended, and therefore, the age of the younger surface. The proper treatment of the cumulative crater numbers, which reduces the influence of the large–crater range on the age determination for the subsequent events, is illustrated in Figure 9.1: First, the crater production function is fitted to the measured crater size–frequency distribution in the appropriate size ranges (below and above $d_\star$). The fit for the large size range is straightforward for the old surface (above $d_\star$). The fit to the crater range (below $d_\star$) representing the subsequent event is used to calculate the expected contribution of craters on a surface of that age. The excess in the large–size range is now easily determined and the measured crater size–frequency distribution can be corrected by the difference of the measured and the expected number of craters at the cut–off diameter. Finally, the corrected cumulative crater size–frequency distribution can be used to derive the resurfacing age. In cases where additional resurfacing processes took place, the correction has to be repeated at the next cut–off diameter.

A typical example of a crater size–frequency distribution is that for the Meroe Patera caldera in the Syrtis Major volcanic province (Fig. 9.1). Resurfacing has occurred and is clearly visible in Figure 9.1, B. The age has been determined at 3.73 Ga and resurfacing at 3.08 Ga. Fig. 9.1 (C) shows the effect on the younger age if a cut–off limit has been used to clear the cumulative crater number in the smaller size range (following Neukum and Hiller, 1981). The calculated age is 1.88 Ga, i.e. much younger. Fig. 9.1 (D) shows the results of treating the crater size–frequency distribution with the previously explained approach. This shows a more accurate 2.33 Ga age for the resurfaced surface. The age differences ($t_{cut-off} \leq t_\star \leq t_{\star_{prelim}}$) between these three approaches of determining the resurfacing event at a time $t_\star$ depend on the magnitude of the event and the time difference between the original surface formation and the modification event. Resurfacing ages described subsequently follow the approach developed here.

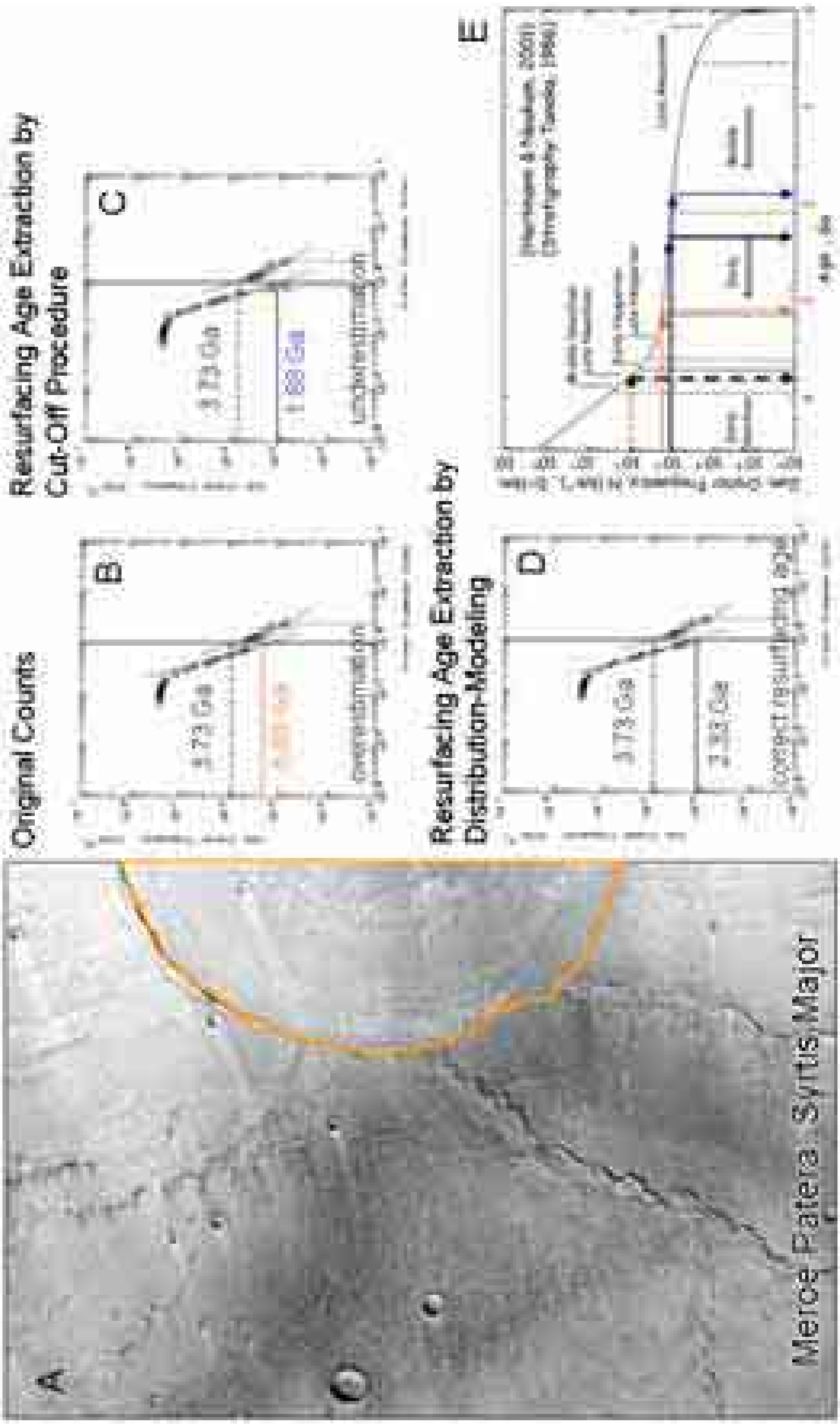

Figure 9.1.: Example of Age Determination of the Meroe Patera Caldera (Syrtis Major volcanic province)

Figure 9.1.: (Cont.) Example of Age Determination of the Meroe Patera Caldera (Syrtis Major volcanic province) and Age Extraction When Resurfacing Occurs: (A) A geological unit is delinated according to the caldera morphology. (B, C, D) Crater counts have been performed, and plotted as cumulative frequency versus diameter (in double–logarithmic scale). The crater–production function was fitted to the measured distribution, yielding at least one resurfacing event. The fitted polynomial is a measure of the relative age of the surface. The area and thus the crater size-frequency distribution observed was affected by resurfacing processes at some time in its geologic history. Therefore, the crater frequency (kink) drops, and deviates from the calibration distribution below a certain crater diameter. To extract the time of the resurfacing event (the age of the resurfaced area) the small and large crater branches can be separated as shown in this diagram. (B) shows the originally measured distribution, (C) the result if all craters larger than a certain diameter (cut-off diameter) are removed, and (D) shows the result if only part of the underlying distribution is removed. The curves are fitted to certain size ranges. The resulting age for the end of the resurfacing period differs according to the approach. (E) The cumulative number of craters for N ($D = 1$ km) is transfered to an absolute surface age by applying the Martian cratering chronology model (Hartmann and Neukum, 2001). The age determined indicated by the black lines (solid and dashed) are the best estimate, because for the resurfacing event the large craters are included in the right proportion (D).

10. Secondary Cratering

It is commonly accepted that impact crater populations on solid–surface planetary bodies predominantly reflect the impacts of a generally known impacting population. As outlined in the previous chapters, this fact is used to estimate relative and absolute surface ages. In the 1960's (e.g. Fielder, 1962; Shoemaker, 1965), the existence of rayed craters and secondary crater clusters in the near–field of craters on the Moon was observed. The shape of the crater size–frequency distribution and therefore the distribution of the projectile population has been topic of discussions. It has been suggested that the observed lunar cratering recored is "contaminated" by an indeterminable number of secondary craters. The discussion to what extent the crater frequencies in the smaller–size range ($D \leq 1$ km) is caused by primary or secondary cratering, includes a discussion of what is the "true" shape of the primary crater or projectile distribution. This also implies whether or not a surface age determination based on crater counts is possible. In the following it will be discussed what secondary–crater contribution is generated by a primary crater population. The shape of the assumed crater production function is given by a power–law description of $N \sim D^{-2}$, N is the cumulative number and D the diameter.

Secondary cratering is observed especially in the closer vicinity of the primary impact crater. These secondary craters are part of the ejecta pattern and characteristically form clusters or chains. The chains are known as herringbone (ejecta) patterns (Wilhelms, 1976; Wilhelms *et al.*, 1978) or, over larger distances, are associated with crater rays which are related to albedo features spanning large amounts of the lunar globe. For age determination based on crater counts, craters belonging to these secondary cratering phenomena, are recognized and eliminated from the counts. For ambiguous situations, where it is not possible to clearly distinguish primaries and secondaries, crater counts naturally are impracticable.

The fact that secondaries can travel far distances and produce craters without any characteristic spatial distribution (clusters or chains), or typical ejecta patterns, challenged age dating technique based on crater count. The unknown contribution unrecognized global secondaries (termed "background secondaries" by Shoemaker (1965)), craters outside identifiable crater clusters and chains, has been discussed to violate the method of surface age determination based on crater counts in the smaller–size range.

Advocators against a steep primary crater size–frequency distribution believe that the observed crater size–frequency distributions is the result of a primary crater distribution reflected by a cumulative -2–sloped power–law (assuming a cumulative distribution of $N \sim D^{-2}$) and a superimposed secondary distribution reflected by a power–law in a slope–index range higher than the primary. For such a piecewise power–law description is argued on observations of the projectile distribution (asteroid belt and near–Earth asteroids), although detailed observations at the smaller size range of the asteroid population are still lacking, and allows speculations about the numbers of smaller bodies (below 1 kilometer in diameter), capable of producing craters below about 10 kilometers in diameter.

The arguments in favour of a steep primary crater size–frequency distribution are summarized in Section 10.1.2.

Nevertheless, due to the newly available image data of the THEMIS instrument, the old debate concerning the influence of secondary cratering (craters produced by the ejecta of a primary impact event) has been raised once again. McEwen *et al.* (2003) and McEwen

(2003) describe a fresh–appearing 10–km diameter crater at 7.7° N and 166° W that should have produced a huge number of very small craters, possibly covering its distant surroundings. The authors conclude that the steep branch of the crater–production function would be highly influenced by secondary cratering for craters smaller than 1 km.

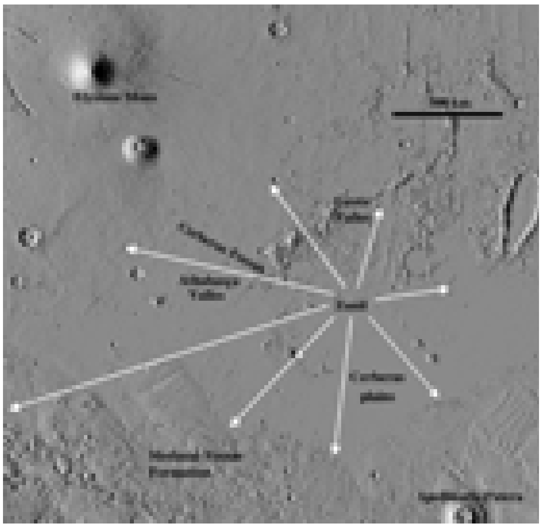

Figure 10.1.: The extent of Zunil's secondary strewn field in the Cerberus plains as described by McEwen *et al.* (2005a).

10.1. Remote Secondary Cratering: The Zunil Case

The effect of secondary cratering on age determination is discussed with respect to the discovery of the 10–km Zunil crater, which is located in the Cerberus plains (Cerberus Planitia/Athabasca Valles region) of Mars and surrounded by a large field of secondary impact pit clusters that can be seen up to radial distance of 1000 km from the main impact crater (McEwen, 2003; McEwen *et al.*, 2003, Fig. 10.1). McEwen *et al.* (2005a) conclude that crater retention ages based on the small–crater range (below about 300 m for young surfaces) could be under– or overestimations of surface ages, thereby making age determinations of this size range unreliable. Especially, if only high–resolution images are available, age determination would be close to impossible, since the issue of distinguishing primaries and secondaries is not fully resolved.

This conclusion ignores the fact that the assumed primary distribution has been measured independently on the Moon, in the asteroid belt (e.g. on Gaspra), which is the source region of the inner solar system projectile (impactor) population, and as here discussed has been measured on Mars.

An argument in favor of a primary small–crater distribution stems from the source region itself, the asteroid belt. Two asteroids, Gaspra and Ida, have been observed during the Galileo flyby. Particularly, Gaspra data fit the lunar standard crater production function and show the steep size–frequency distribution (Neukum and Ivanov, 1994; Chapman *et al.*, 1996; Ivanov *et al.*, 2001). This is direct confirmation that the steepness at small crater sizes (D $\leq$ 1 km) is an effect of the primary impactor size–frequency distribution and not an effect of secondary crater admixture at small sizes.

Additionally, bolide frequencieshitting the Earth atmosphere (fire balls) have been transferred to lunar impact conditions and plotted on the measured lunar crater size–frequency distribution. They fit within a factor of two (Ivanov, 2005). More controversial, but supporting the idea of a "steep" distribution, are predictions of the number of near–Earth asteroids, that is the impactor population for the Earth and the Moon. It fits the measured lunar crater size–frequency distribution. Werner *et al.* (2002) show that the size–frequency distribution of a time–averaged projectile population derived from the lunar crater size–frequency distribution (Neukum and Ivanov, 1994) provides a convincing fit to the size–frequency distribution of the current near-Earth asteroid (NEA) population, as deduced from the results of asteroid search programs. These results suggest that the shape of the size–frequency distribution of the impactor flux has remained in a steady state since the late heavy bombardment and that the steep distribution is primary.

All these measurements are in good agreement. Therefore, the suggestion by McEwen *et al.* (2005a) of an underestimation of surface ages using crater frequencies is untenable. The relevant projectile groups support the steep branch as observed in the crater record.

Bierhaus *et al.* (2005b) and Bierhaus (2004) report their findings of secondaries in a sizable fraction on the jovian moon Europa. Nevertheless, they observe crater size–frequency distributions which show a great variety of slopes, and indices are ranging between -2.5 and -5 for cumulative distributions. These slope ranges are common for crater production function and also secondary crater distributions. It appears that they ignored any geologic unit boundaries, therefore, they were not able to define any reliable production function, but could show that these units are "contaminated" by different amounts of secondaries. Remarkably, the small–crater record show strong clustering, which is their only reasoning to claim that they are dominantly secondaries.

Their observation is made in a dynamically different Solar System regime with respect to the projectile source (possibly dominated by comets) compared to the inner Solar System regime (dominated by asteroids). They agree that in the inner Solar System small craters are also formed by small impact projectiles that are not observed in the Europa case. Nevertheless, they claim that the ratio of primaries to secondaries is unknown.

Hartmann (2005) presented a detailed discussion on whether these findings imply that the steep branch of the small–crater distribution is dominated by primaries (impacts from interplanetary bodies) or by secondaries (impacts of fall-back debris from larger primaries). He concluded that clustered secondaries are generally not included in crater counts and that crater counts made in geological context have more constraints than just the crater frequencies. The steep branch at small crater sizes was recognized on asteroids by Neukum and Ivanov (1994) and Chapman *et al.* (1996) and confirms that small lunar and Martian craters originate from an interplanetary asteroidal primary projectile source, and already having a steep distribution.

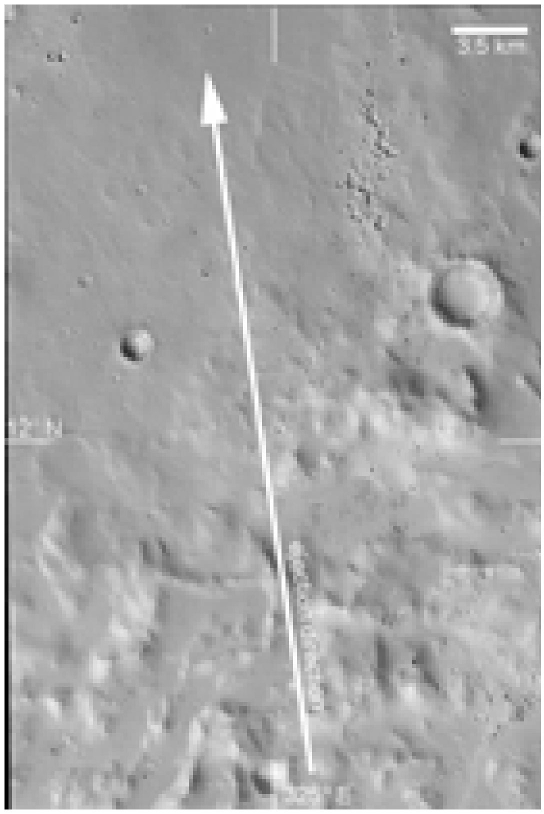

Figure 10.2.: Example of clustered secondary craters around 13° N and 325° E, observed in orbit 2024 by the HRSC experiment. These clusters were produced by crater Mojave which has a diameter of about 57 km and is located in a distance of roughly 500 km south at 7.5° N and 327° E.

The steep small–crater branch on Mars and the Moon might have an admixture of unrecognized secondaries. Hartmann also argues that determining ages, those secondaries are part of the signal. Using the crater counts over the widest possible diameter range, ages can be determined by the fit of the entire distribution and not only at one point or a small range. Ages are reflected in the distribution isochrons and can also be reliably determined from small–crater distributions, even if secondaries are admixed.

10.1.1. Characteristics of the Zunil secondary strewn field

We do not deny the existence of unrecognized global secondaries. There are cases where a separation of primary impact craters and endogenic or secondary craters is impossible and an age determination based on crater frequencies can be carried out. Fig. 10.2 show a prominent example of secondary crater clusters stemming from the 57–km–diameter crater Mojave roughly 500 km south of it. Nonetheless, stratigraphic relations yield insights into the general regional geologic evolution. Exluding the clustered units, studying the geologic evolution not only based on stratigraphic relation, but also on crater counts, is possible. From our experience, admixture is low in most cases, probably on the order of less than 10%. The validity of this statement is examined in detail in Chap. 10.3 (below).

In order to shed further light on this subject, we have performed a detailed examination of the crater populations in the Cerberus plains area, and which has been discussed by McEwen *et al.* (2005a). They used the fact that the secondary population of the Zunil secondary strewn field exhibits a prominent black halo, and the discovery could occur as a result of distinction from the primary population and secondary population. The HRSC experiment has covered the part of this plain (HRSC orbit 1152) where most of the clearly identifiable secondary craters of Zunil have impacted (Fig. 10.3a). In a radial distance of about 300 km from crater Zunil, we have measured on a uniform geologic unit the crater size–frequency distributions for (mostly) primaries and for the proposed secondary craters. Fig. 10.3 shows the resulting crater size-frequency distributions of the primary (Fig. 10.3b) and the secondary (Fig. 10.3c) population. Further contamination by secondary cratering can almost be excluded because of the young age of the unit. The secondary population has a much steeper distribution (red curve) than the Martian crater production function (black curve). This was already observed for near– and far–field secondary crater populations on the Earth's Moon, (e.g. König, 1977; Vickery, 1986) and is in agreement with the observations by Bierhaus *et al.* (2005a,b) for the jovian moon Europa.

If an inexperienced observer measures craters in areas of the Cerberus plains, unwittingly including secondary craters in his measurements, he would achieve the distribution shown in Fig. 10.3d. Investigating the separated primary and secondary crater size–frequency distributions in detail (based on the frequency tables) one observes a crossing diameter at which the number of secondaries exeeds the number of primaries (for detailed discussion see Sec. 10.2.1). At diameters less than 150 m the number of proposed secondaries exceeds the number of primaries by a factor of up to five, while below the number of primaries is double. This observation is in agreement with observations made by König (1977), see below. Based on this observation and utilizing the theoretical approach outlined in Chap. 10.2, one could derive the size of the generating primary crater, which would be around 5 km, smaller than Zunil. If an experienced observer investigates the crater size–frequency distribution of summed secondaries and primaries (Fig. 10.3d), at small sizes (below 150 m), the distribution still appears slightly steeper than the Martian production function. Nevertheless, an experienced observer would recognize the slightly higher steepness and in all likelihood, judge the distribution contaminated by secondaries, thereby carefully inspecting the measurement area for possible further elimination of the secondary craters from the measurement.

This example also illustrates that the proposed factor of at least 20 (McEwen, 2003) is not reached at all, but at most yields a factor of two in age. This is an acceptable error in crater counts for young ages, as pointed out by Hartmann (2005).

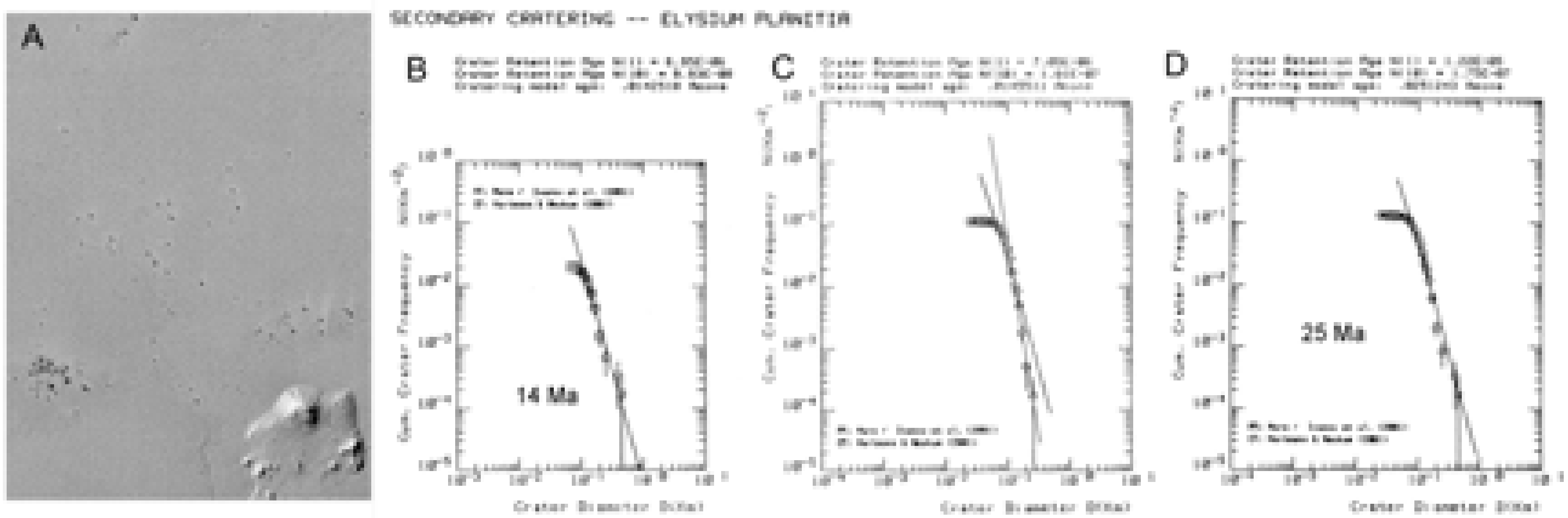

Figure 10.3.: During the MarsExpress orbit 1152 the HRSC experiment has covered part of the Cerberus plains where most of the well identifiable secondary craters of Zunil impacted (A), the image shows a region of 30 km x 35 km. It is easy to separate the primary and secondary population due to the prominent black aureole of the secondaries. (B) shows the resulting crater size-frequency distributions of the primary and (C) the secondary population. The secondary population has a much steeper distribution (red curve; for comparison the Martian crater-production function, black curve) as has been observed already for the Earth's Moon. The crater size–frequency distribution in Fig. (D) demonstrates a situation if both populations (primary and secondary) were measured together. Still the distribution appears slightly steeper at very small sizes than the Martian production function. Fitting the crater production function for Mars it is possible to determine the age of the primary and the mixed population measurement (B and D). The resulting ages differ by a factor of less than two, which shows that crater counts yield absolute ages of tolerable error (of the same order of magnitude) even if secondary craters were included unwittingly.

In our test case areas (Athabasca Valles, Chap. 12), we could rule out the influence of secondary crater admixture. Measured crater size–frequency distribution in areas of different ages show the same the steepness of the size–frequency distribution in the small diameter range (less than 100 m). If secondary crater contamination would influence the distributions, a change in the steepness of the distribution would be observed at differently aged surfaces depending on the relative amount of contributing secondary and primary craters, which depends on age. This has not been observed.

10.1.2. Reasoning for a steep primary crater size distribution branch

The arguments for the steep–slope branch produced by dominantly a primary projectile distribution at the small size range (below about 1 km) can be summarized as follows:

- a steep crater size–frequency distribution is observed on bodies (e.g. Gaspra) in the asteroid belt, the projectile source region
- clusters, chains and even distant secondaries (such as in the Zunil case, which appear clustered too !) can be excluded in measurements
- steep distributions according to the crater production function are observed on Mars and the moon for differntly aged surfaces
- fireball observations (small projectiles hitting the Earth's atmosphere) scaled to cratering the moon show the expected slope steepness (of the crater production function)
- near–Earth asteroids size–frequency distributions (deduced from detection statistics) show the same steep slope. They are the projectile population of the moon and Earth.
- measurements on the moon and Mars in different geologic but homogeneous units always fit the crater production function
- erroneously included secondary craters could lead to an overestimation of surface ages by less than a factor of 2

To finally understand the possible contribution of globally unrecognized background secondaries to the crater production function, here, a crater distribution is constructed based on commonly raised arguments. The resulting distribution is compared with observations.

10.2. Gedankenexperiment: Secondary Cratering

Shoemaker (1965) stated that the primary cumulative distribution follows a power–law of N $\sim$ D^{-2}, and this is used as the basic distribution of this experiment. We assume that a global population of unrecognized secondary craters exists, which is responsible for the change in slope towards smaller crater diameters. They are randomly distributed and not distinguishable from primary craters, and produce the slope of the observed crater size–frequency distribution at crater diameters below about 1 kilometer (with slope indices between -3.5 and -3.0). We ignore how much ejected material volume is deposited near the primary crater. We use measurements of near–field secondaries to characterize the unknown far–field distribution: The largest secondary crater around a primary has a crater diameter of about 5 % of the primary one. Observed near–field secondaries show well–documented distributions (clusters and chains) at the larger size range, given by power–law descriptions with cumulative slopes of $-4\pm$ 1, (e.g. König, 1977; Vickery, 1986). Nevertheless, measurements by Vickery (1986) give an erroneous impression, since they do not cover the smaller–size range of the secondary crater distribution, where a bending to a flatter distribution is firmly observed (König, 1977).

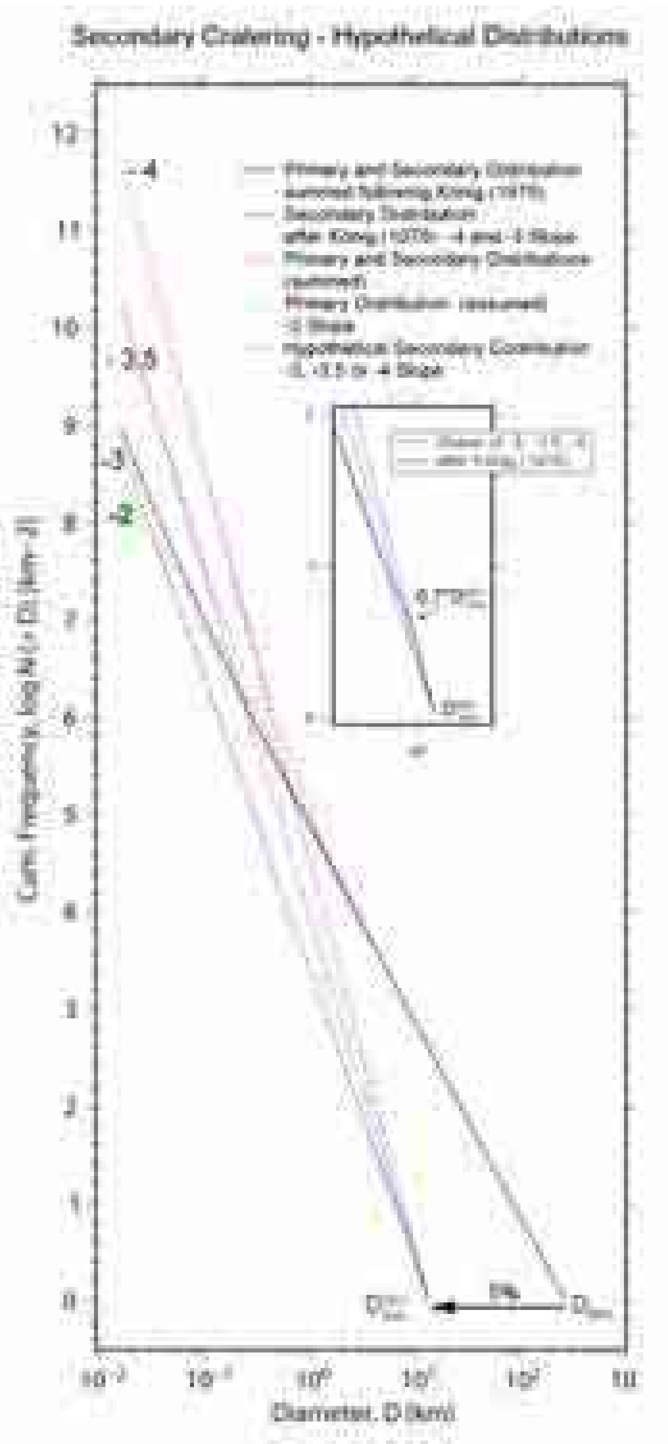

Figure 10.4.: The construction of a hypothetical crater size frequency distribution for Mars, where the global surface is assumed to be 1 Ga old. Different crater distributions are shown: an assumed primary distribution with a slope index of -2 (dashed green), three hypothetical secondary distributions with slope indices of -3, -3.5, and -4 (blue dashed), a secondary crater curve following observations by König (1977) (black dashed). The inset enlarges the important region to display the difference between the latter approach and a pure -3 sloped distribution, for details see text. The summed assumed –2–sloped primary and the individual (slope indices of -3, -3.5, and -4) secondary distributions are given as dashed red and solid black curve, respectively.

The slope steepness with an index around –4 is in contradiction to the observed crater size–frequency distributions, which show cumulative slopes of between -3.5 and -3.0 at crater diameter ranges below 1 kilometer. Such a discrepancy has to be resolved.

The physics of processes such as impact cratering (crushing or grinding) are described by simple conservation constraints for mass, momentum, surface energy and kinetic energy. Naturally, the fragmentation occurring during a single impact event limits the production of secondary projectiles by its available volume and impact energy. It is clear that a very steep power–law distribution cannot continue to arbitrarily small fragments, but there is a cut off at which the number of fragments decrease rapidly. This effect has been observed in grinding or crushing experiments and is known as Rosin–Rammler or Weibull–distributions describing a processes at any scale (see for example Brown and Wohletz, 1995). Weibull–based Grady–Kipp models have been commonly used as models in fracturing–related processes (e.g. cratering (Melosh *et al.*, 1992), volcanic ash production (Wohletz *et al.*, 1989) or asteroidal collisions (Michel *et al.*, 2001)). Generally, a lack of smaller particles has been observed. König (1977) investigated near–field secondaries around lunar rayed craters Aristarchus, Kepler and Copernicus in detail. Measuring crater densities and size–frequency distributions in chains and clusters at different distances from the primary crater, she found distance–independent crater size–frequency distribution curves, which can be described by two straight lines in a double-logarithmic scheme. They are represented by a power law given by $\mathrm{N} \sim \mathrm{D}^{\alpha}$ ($\alpha = -2.5 \pm 0.3$) in the smaller diameter range and for larger craters a power law given by $\mathrm{N} \sim \mathrm{D}^{\beta}$ ($\beta = -4 \pm 1$). The transition diameter D_A at which the steep and flat branch of the distributions merge is related to the largest observed secondary crater D^{sec}_{max}. Summarizing her findings, we can characterize secondary crater distributions having a general form of:

$$N^{sec}_{cum} \sim D^{\alpha}$$

The largest secondary crater controls the transition diameter:

$$0.7 \cdot D^{sec}_{max} \sim D_A$$

The power–law segments are given by

$D^{sec}_{max} > D > D_A$ where $\alpha = -4 \pm 1$

and

$D < D_A$ with $\alpha = -2.5 \pm 0.3$.

Based on the observations and this knowledge, the slope steepness contradiction mentioned above, is solved.

Using the observations of König (1977), the secondary crater distribution characteristics are used to prepare a single master curve.

10.2.1. Construction of a hypothetical total crater distribution

For this exercise, the Martian surface is assumed to be globally 1 Ga old. Applying a cratering chronology model (Hartmann and Neukum, 2001) the largest primary crater derived through a distribution given by $\mathrm{N} \sim \mathrm{D}^{-2}$ is calculated. The largest crater is found to have a diameter of about 265 kilometer. In Fig. 10.4 all distributions which will be discussed here are given in a double–logarithmic scheme, the primary crater distribution is shown as a green dashed line. As a rough estimate the largest secondary crater which can be produced globally has a diameter twenty times smaller than the largest primary. This relation is shown in Fig. 10.4 for a globally 1–Ga-old surface. A largest secondary crater with a crater diameter of 13.25 km following $D^{sec}_{max} = 0.05 \cdot D_{max}$ is produced. At this point three possible secondary crater distributions are shown with slope indices –3.0, –3.5 and –4.0, (blue dashed lines). As discussed above, the –4–slope occurs for secondary craters only over a smaller size range between D^{sec}_{max} and $0.7 \cdot D^{sec}_{max} \sim D_A$ and continues as a cumulative curve with a slope index of at least –3.0, (black dashed line). This approach following König (1977) is shown in greater detail by the inset. While a single impact generates a secondary distribution as observed by König (1977), the global cumulative distribution appears as enveloping curve of secondaries produced by the primary distribution. They must mimic the observed distribution (slope indices range between –3 and -3.5 at the smaller–size range), if the globally produced steep branch is only due to secondary craters. Generally, the frequencies between D_{max}^{sec} and the inflection point D_A are low. Therfore, such a distribution can be considered having a –3–slope in the smaller crater size range, shown in Fig. 10.4, where -3–slope distribution and the two segmented distribution are aligned. For comparison with an observed crater size–frequency distribution, the potential primary (assumed to have a –2–slope over the entire crater size range) and hypothetical secondary distributions are summed. The summed distributions are shown as red dashed curves, having secondary crater contributions given by -4– and -3.5– slope distributions. The sum of primary and secondary craters given through the König approach is depicted as solid black line. This approach is nearly identical with a -3–slope secondary contribution.

It has been discussed that the lunar size–frequency distribution of craters smaller than 3 km is consistent with secondary impact populations predicted for larger craters by Shoemaker (1965) and Brinkman (1966). Craters for which no specific primary craters can be identified were termed "background secondaries" by Shoemaker (1965). This idea was adapted by Soderblom *et al.* (1974) and later resumed by Neukum (1983). Soderblom *et al.* (1974) have shown that the slope for the entire secondary crater population is given by the same slope of the distribution of secondaries generated by a single primary. Furthermore, the secondary population naturally dominates the total crater population at the smaller size ranges (Fig. 10.4) given by the diameter at which the number of secondaries exceeds the number of primaries. This crossing diameter D_c is given by the relation:

$$D_c = D_{max} \left[\frac{\alpha}{(\beta-\alpha)k^{\beta}}\right]^{1/(\alpha-\beta)}$$

where D_{max} is the largest contributing primary crater, α is assumed to be –2 and β is discussed to range between –3 and –4 (see above). Soderblom *et al.* (1974) concluded that this crossing point between primary and secondary crater population curve for a given β = –3.5 is theoretically near 1 km crater diameter (and the largest primaries observed ranged around 50 km in diameters). Their comparison with the most pristine observed Martian crater distribution appeared to be approximated well by such a distribution. It shows that under fixed conditions (a specific time) one could derive such a relation. As will be discussed below, this relation is unstable for differently aged surfaces.

It has already been demonstrated by Neukum (1983) that if the steep branch were due to secondary craters superimposed on a flatter distribution (e.g. N $\sim$ D^{-2}), then the steep branch of the distribution in total abundance of craters per size interval would be dependent on the amount of cratering of the surface by the flatter distribution and the occurrences of primary craters. This would lead to a dependence on exposure time, hence surface age, and would affect the distributions in such a way that the crossover diameter point (i. e. the diameter at which the steep and the flat part of the composed distribution on a log–log diagram cross each other) would move to larger diameters in the distributions measured on older surfaces.

Considering a primary production function given by N $\sim$ D^{-2}, Fig. 10.5, top, show this dependence for the largest primary, and accordingly the largest secondary which would be generated assuming a primary production function with a –2–slope and a projectile flux following Hartmann and Neukum (2001). Naturally, the maximum diameter relation propagates in the crossover diameters given for three discussed slope parameters of possible secondary crater distributions, -3, -3.5 and -4, respectively (Fig. 10.5, bottom). The effect due to different surface ages on the resulting hypothetical total crater distributions are shown in Fig. 10.6 for

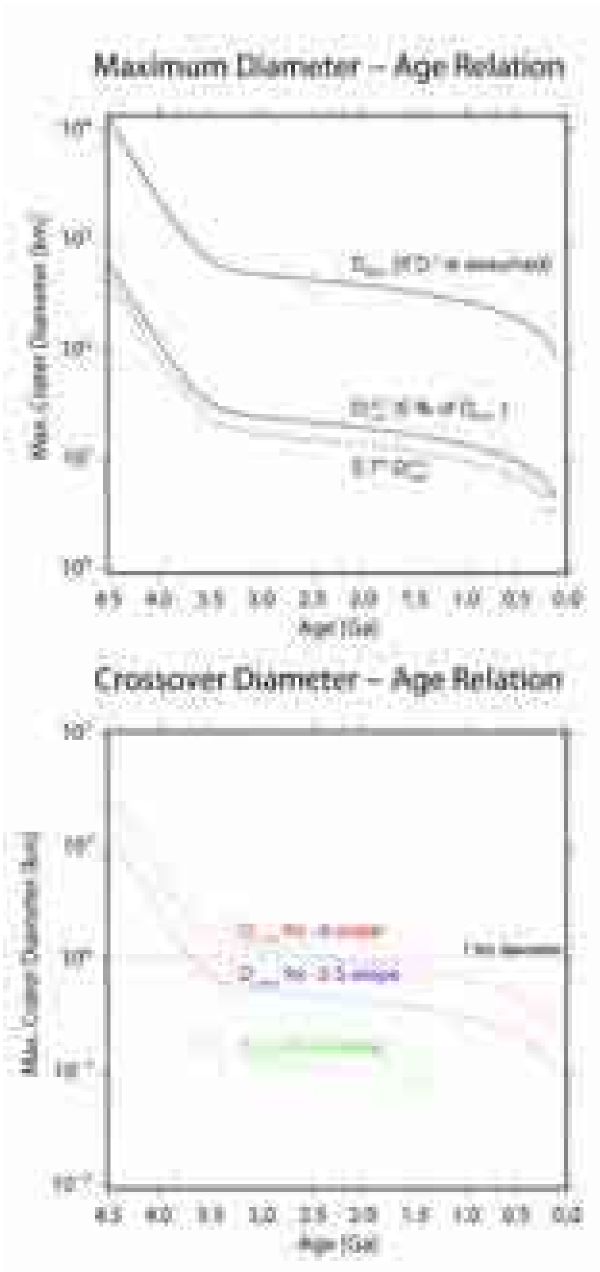

Figure 10.5.: Dependence of surface age and hypothetical maximum diameter, which would be observed on Mars having globally a single surface age (top). This age–dependence is reflected in the largest generated secondary and propagates in the cross–over diameter given (bottom) for three secondary crater distributions considered with slope indices of -3, -3.5, and -4, respectively. For details see text.

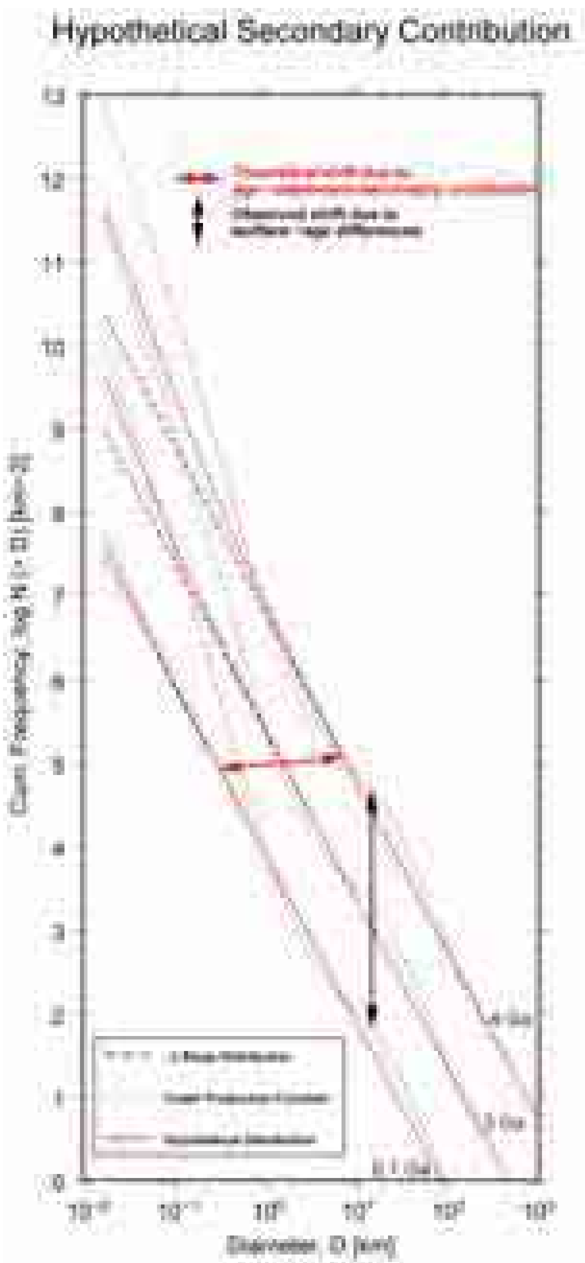

Figure 10.6.: Demonstration of the age–dependence on the hypothetical total crater size–frequency distribution for three different surface ages at global scale (red curves at ages of 4 Ga, 3Ga, 0.1 Ga) in comparison with the Martian standard crater production function for analogous ages. While in reality only a frequency shift is observed, the hypothetical distribution mainly varies in diameter direction.

surfaces of an age of 4 Ga, 3 Ga and 0.1 Ga (red curves).

Obviously, the effective onset of the secondary crater branch is propagating towards larger diameters with growing surface age. What we find in all measurements on the moon or Mars, instead, this point (in observed crater size–frequency distributions) appears at a single diameter value irrespective of the counting area, age and number of large craters. This is a very powerful argument for a primary source for both the flat and steep part of the size–frequency distribution. For comparison, the crater production function for Mars as discussed in Chap. 5 is plotted for analogous ages.

The slope change between a flatter branch (considered as primary) and the steeper branch (considered as secondary–dominated) is the key to the judge, which interpretion reflects reality: Neither on the moon nor on Mars a shift towards larger crater diameters is observed. Numerous measurements gathered and described in the following chapters confirm this for the Martian case, for examples see Chap. 11.

10.3. Hypothetical Secondary–Crater Contribution

The most recent dataset obtained by the HRSC, complemented by Viking, THEMIS and MOC in which crater frequencies over the full crater–size range can be determined, the steep distribution branch is visible and fits the Martian crater production function (and agrees with the lunar one, see Chap.5) over the full size range and for differing surface ages (for further discussion see Chap. 11). Therefore, it is likely that the contribution of theoretically possible background secondaries is minor. To better judge the real amount, predicted secondary crater distributions are compared with the Martian standard distribution. Based on the arguments outlined above the contribution of secondary craters to the total crater number observed and represented by the Martian standard crater production function cannot be the majority at the small size range crater numbers.

Following the theoretical consideration to describe possible secondary crater distributions (after König (1977)), their numbers as a function of surface age are estimated and compared to the observed crater production function. Therefore, the secondary crater curves and Martian crater production functions are calculated in age steps of 0.1 Ga. The secondary crater curves are prepared assuming a –3.0– and a –3.5–slope for the continuation after the inflection point defined by $0.7 \cdot D_{max}^{sec} \sim D_A$. For both distributions, analytical expressions are used. The portion of secondary craters is given through the ratio between the cumulative total crater number determined through the Martian crater production function and the estimated total number of secondaries, respectively. Fig. 10.7 shows the colour-coded ratio for an assumed –3.0–slope index (top) and a –3.5–slope index (bottom). Secondary crater percentages which exceed the number of primaries by 160 % are plotted in dark red and for detailed understanding 1 % to 5 % isolines are plotted in the dark blue areas.

As already discussed in the earlier chapters, the hypothetical contribution of secondaries, assuming a –3.5 slope index, outnumbers the observed Martian crater frequencies for old surfaces (older than 3.6 Ga) which is not observed. Therefore, the probability that this assumption is correct is very low and would contradict detailed investigations made in secondary crater clusters and chains (see e.g. König (1977) or Vickery (1986). Nevertheless, if one want to be cautious: Crater frequencies determined in a diameter range larger than 5 km at any age, almost no secondary contamination are observed. For both slope indices crater counting operates well above the cross–over diameter at which the number of secondaries equals the number of a hypothetical flat primary distribution (given by $N \sim D^{-2}$). Also at young surfaces (less than 2 Ga) saturation is reached before the portion of secondaries would be dangerous (for the –3.5–slope case).

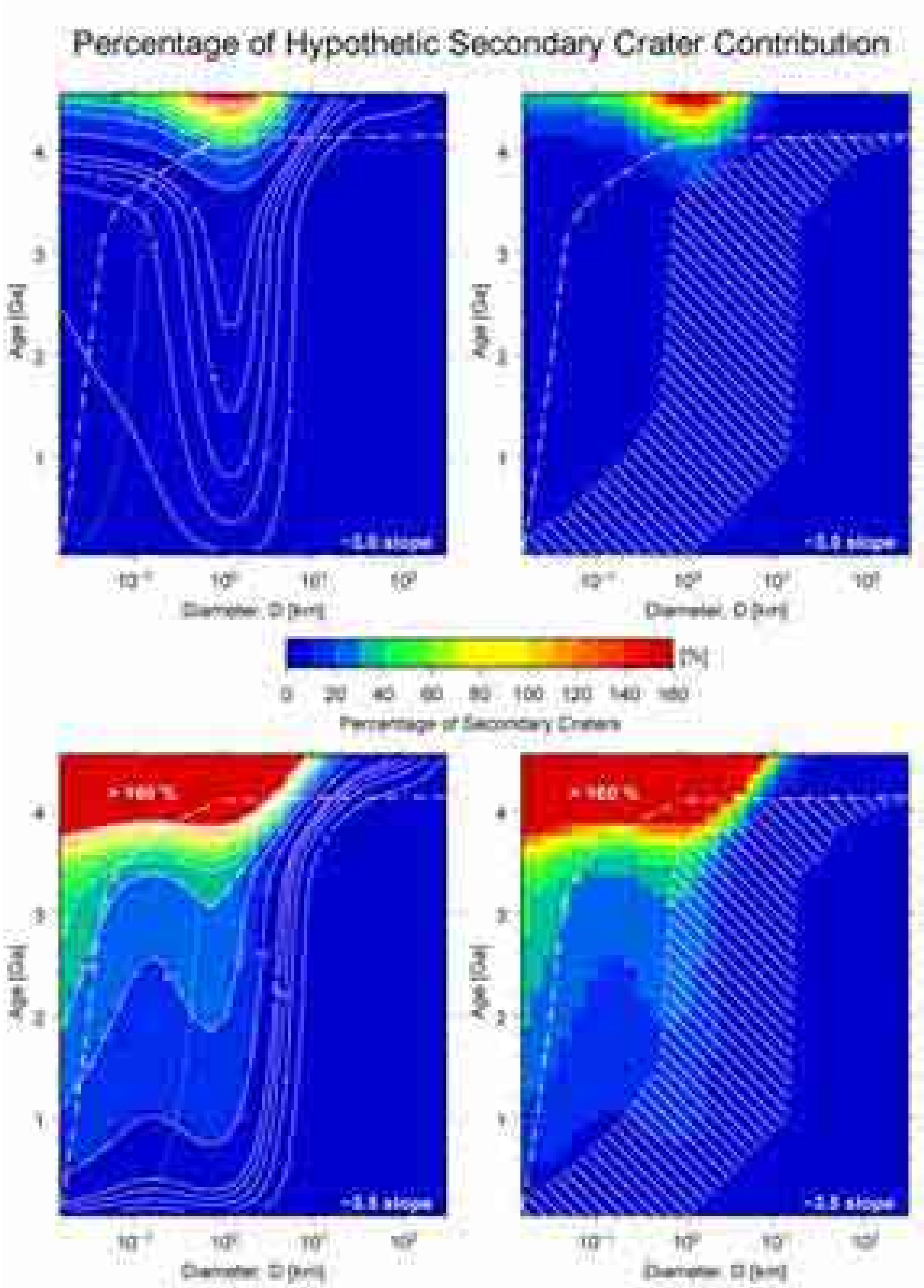

Figure 10.7.: The hypothetical contribution of secondaries assuming a -3–slope (top) and a -3.5–slope (bottom) compared with the Martian standard crater production function for varying surface ages, given as percentage of the primary function (left and right). The dashed curves indicate the saturation limit (left and right), the dotted curve indicates the crossing diameter (left) as shown in Fig. 10.5. The hatched unit (right) indicates the crater diameter range in which all measurements presented in this thesis were performed.

In the –3.0–slope case a "dangerous" region of contamination is never reached. An exception needs to be made for very old surfaces (above 4.0 Ga) if one attempts to determine ages through crater frequencies measured around 1 km. On Mars this is usually impossible, because erosion processes have acted on eliminating the cratering record at this diameter range. It is more likely that one would measure erosional surface ages than any secondary contamination produced by an ancient (older than 4.1 Ga) primary population. For the smaller size range the saturation limit is reached before the contamination exceeds 30 % . Even in these cases measurements at a broad diameter range allows for a reliable age determination.

It is interesting to note, that even in regions of low secondary contribution the diameter range around 1 km is "most" affected. Around 1 km diamter, in the Martian crater production function slope changes occur and the steep "secondary" contribution distribution and the steep primary branch run sub–parallel for a while. Therefore, especially for old surfaces, the "contamination" there is highest.

10.4. Small–crater production on Mars observed by MGS

A recent press release, celebrating 8 years of the Mars Global Surveyor at Mars by the Malin Space Science Systems, describes the possible formation of a small crater at the rim of Ulysses Patera during the 1980s (Fig. 10.8) [1]. By comparing the location of the new crater in a Viking–2 orbiter image taken in 1976 with views taken by the Mars Global Surveyor (MGS) Mars Orbiter Camera (MOC) in 1999 and 2005. The new crater has a diameter of about 25 meters. The images indicate that the distinctly dark rayed ejecta pattern is fading somewhat away between 1999 and 2005.

Commonly, the cratering rate of Mars is determined by scaling from the lunar cratering

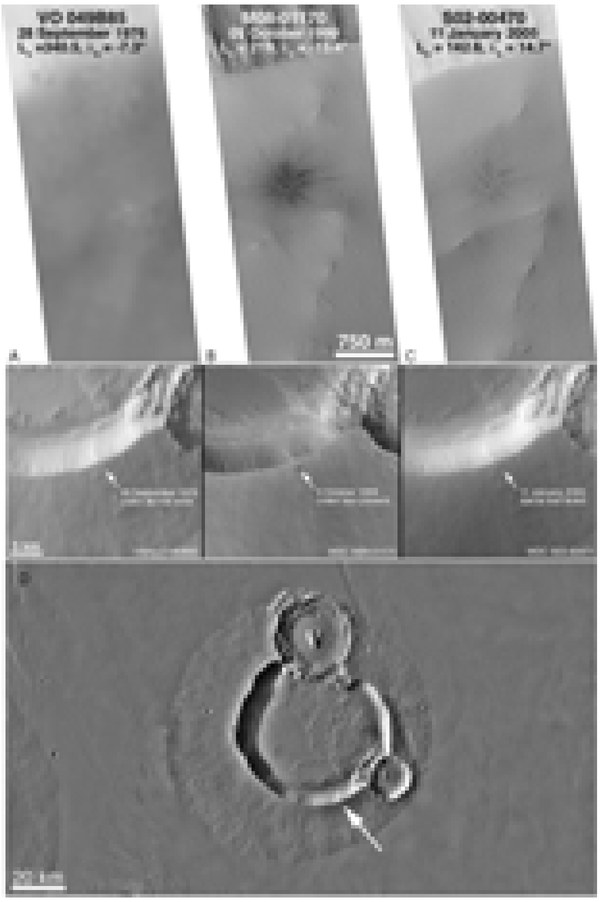

Figure 10.8.: Celebrating 8 years at Mars[1], the Malin Space Science Systems released images showing recent changes on Mars. One of these press releases (MOC2-1221) describes the possible formation of a small crater at the rim of Ulysses Patera (D) during the the 1980s, which is shown here. The upper row (A,B,C) shows the small crater with dark rayed ejecta in Viking imagery of 1976 recalculated to MOC resolution, where most likely no crater is present (A), and two MOC narrow–angle images of 1999 (B) and 2005 (C), indicating a fading in albedo of the ejecta during the last 6 years. The lower row shows the same Viking image in original resolution (A) and the MOC wide–angle context images (B, C).

rate, as discussed before. Long-term observations, e. g. from orbiting spacecraft, now allows the science community to actually locate new craters and possibly to derive cratering rates.

[1]http://www.msss.com/mars_images/moc/2005/09/20/

Based on the discovery of one crater that appears to have formed on Mars in the past 20 years, in addition to possibly several other similar craters, an estimate of the present cratering rate on Mars was given. They claim that the recent cratering rate on Mars is about 3 to 6 x 10^{-8} craters/km^2/year for craters between 25 and 100 m diameters. They argue it is about 5 times lower than previous estimates, although their sample is very small (the MOC narrow angle camera has only imaged just over 4 percent of Mars).

Applying the transferred lunar crater production function by Neukum (1983); Neukum and Ivanov (1994); Ivanov (2001) and the scaled lunar cratering rate (cratering chronology model by Hartmann and Neukum (2001)), about 1.2 x 10^{-7} craters of 25 m in diameter per km^2 and year (0.9 x 10^{-8}, 30 m) and about 1.5 x 10^{-9} craters of 100 m in diameter per km^2 and year would be produced. These results indicate the minima and maxima of the interval of the diameter range (25 to 100 m), and reflect the same frequency.

Considering the uncertainties of the statistically limited extrapolation by Malin, the rate transferred from the moon to Mars and the rate derived by Malin are in good agreement, and indicate that secondary cratering contamination does not invalidate the applied method of surface age determination. Moreover, this calculation given here shows that his argument that the cratering rates determined by Hartmann and Neukum (2001) from small craters are overestimated is wrong.

10.5. Conclusion

In the previous sections, basic assumptions led to the discussion of pros and cons of a secondary– or primary–generated steep distribution branch at the smaller size range. Most assumptions induce artificial crater size–frequency distribution mainly contradicting the measured crater size–frequency distribution. The confirmed measured Martian standard crater production function is given in the next chapter.

Estimates of the fraction of secondaries compared to the Martian standard crater production function, following commonly discussed assumptions, allows only for an entire –3–sloped secondary distribution at most. This is also in agreement with observations (e.g. König, 1977). In this case the percentage of secondary hypothetical global unrecognized craters is usually less than 5 % in any crater size–frequency distribution measurements. Any other hypothetical secondary crater distribution contradicts the observed distribution measurements, e.g. at about 3.7 Ga (compare Fig. 10.7, bottom, for the hypothetical percentage and an example measured at Ceraunius Tholus, Fig. XXXI, Appendix).

Conclusively, the measurements are "contaminated" by secondaries in percentage less than the statistical error assumed.

11. The Observed Martian Crater Production Function

Every interpretation and sequence of events are valid independently of any revision of the applied chronology model, because the crater frequencies are directly related to relative ages. The validity of the cratering chronology model has been discussed above. The applied crater scaling laws are tested as they were utilized to transfer the lunar crater production function to Mars.

In this work, the crater size–frequency distributions, in many geological units for variously aged surfaces, and over the entire crater diameter range (given by the available imagery), are measured. To normalize (following Neukum, 1983) the crater size–frequency distributions to a randomly chosen age t_{norm} using the equation (compare equation 8.10)

$$N_{cum}\left(D, t_x\right) \star \frac{F\left(t_{norm}\right)}{F\left(t_x\right)} = N_{cum}\left(D, t_{norm}\right) \qquad (11.1)$$

the measured crater size–frequency distributions on differently aged surfaces are combined to a representative set of measurements to achieve the unified crater production function. For this purpose, we selected crater size–frequency distributions measured on Viking, HRSC, SRC, THEMIS and MOC imagery to cover the entire diameter range, limited just by the image resolution and/or the image sizes. The very large size range (global basin distribution, diameters ≥ 250 km) is supplemented by a size–frequency distribution derived from basin diameters listed by Barlow (1988a). The given frequency of large basins present in the highland areas yields a global maximum highland surface age of about 4.2 Ga on average.

In Figure 11.1(A), selected crater size–frequency distributions and a set of isochrons are plotted. The isochrons are calculated by applying the cratering chronology model of Hartmann and Neukum (2001) and the crater production function described by Ivanov (2001). The analytical expression for the chronology model is

$$\begin{aligned} N(1\mathrm{km}) &= 2.68 \cdot 10^{-14}[\exp(6.93\mathrm{T}) - 1] \\ &\quad + 4.13 \cdot 10^{-4} T \end{aligned} \qquad (11.2)$$

given by Ivanov (2001). The larger–diameter range of the crater size–frequency distribution is mostly represented by measurements on old surfaces, whereas in the smaller–size range either the image resolution prohibits measurements in that range (< 15 km, Viking) or resurfacing occurred (1–10 km, e.g. THEMIS, HRSC). The smaller size–range is represented mostly by measurements on younger surfaces (< 3.5 Ga). Due to the strong geologic activity over the entire history of Mars, many surface units formed or have been resurfaced by erosion subsequent to the planet's formation. Intentionally, all diameter ranges are represented by several measurements to improve the statistics. Nevertheless, these measurements are based on different image resolution, assuring only a limited range of accuracy. A largest possible overlap of the individual measurements was considered to avoid gaps and minimize statistical uncertainties.

Figure 11.1(B) shows the resulting distribution when all measurements are normalized to a surface age of 3.25 Ga, represented by the measurement "UTOPIA15mA+B". This measurement was performed on a photo mosaic compiled from Viking high–resolution (15 m/pxl) observations taken from the center of Utopia Planitia (see Chap. 14.3). This region was selected because it covers a medium crater–size range and formed at an intermediate time. The assemblage of normalized crater size–frequency distributions is plotted together with an isochron representing a 3.25–Ga age, calculated by applying the Hartmann and Neukum (2001) cratering chronology model and the lunar crater production function transferred

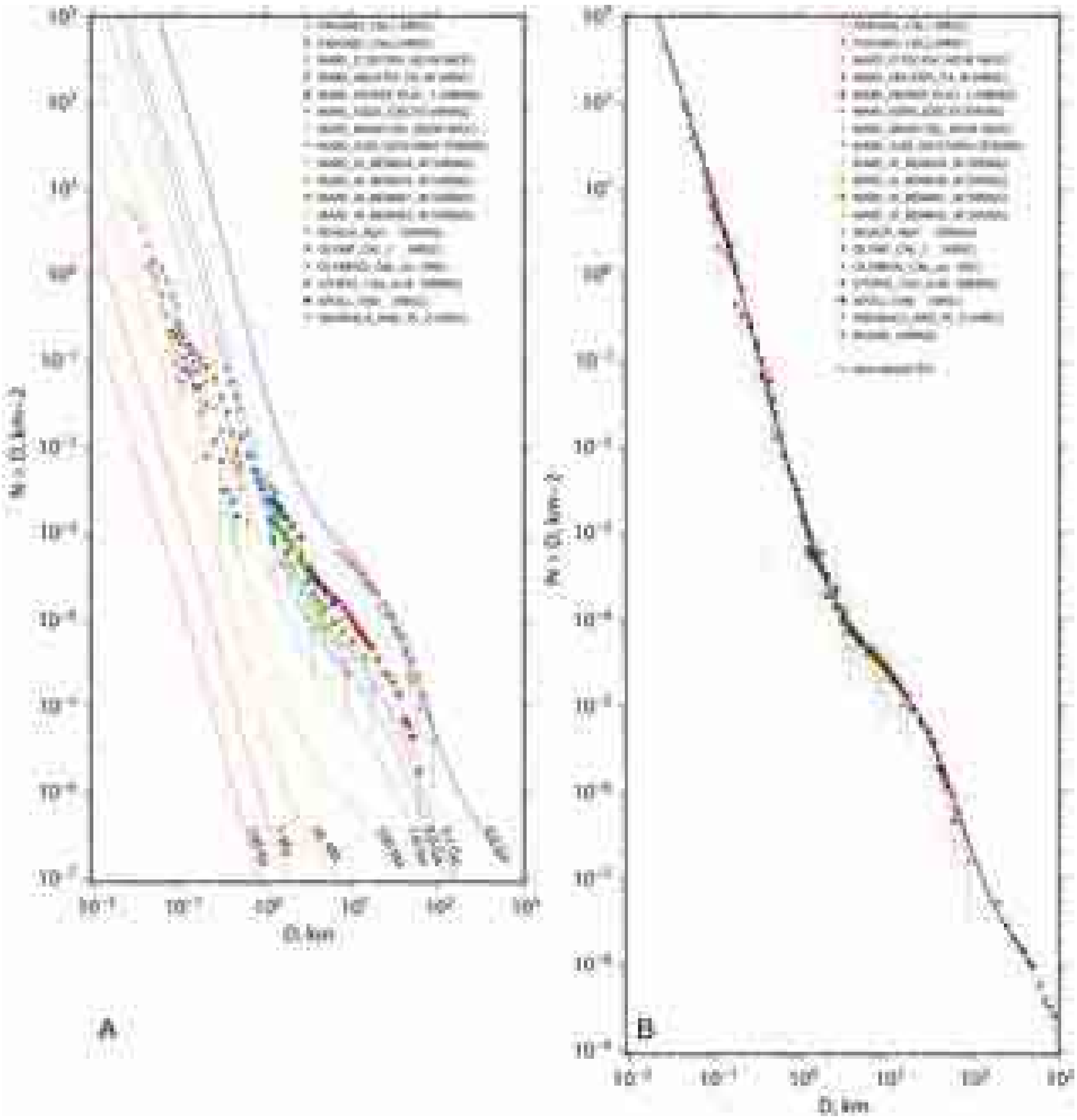

Figure 11.1.: The Martian Size–Frequency Distribution: (A) Assemblage of crater size–frequency measurements obtained for counts performed on HRSC, SRC, VIKING, THEMIS, and MOC imagery. They represent typical crater size–frequency measurements of differently aged surfaces. The set of isochrons indicate the expected distribution applying the Hartmann/Neukum chronology model for different ages, which makes it possible to derive crater retention ages from the measurements by way of visual interpretation of a graph. Usually, we derive ages by fitting the crater production function to the measurements and obtain a numerical value N(1) for a reference crater diameter (usually 1 km). (B) The same assemblage of crater size-frequency measurements normalized to the UTOPIA 15m A+B measurement, which represents a measurement in the medium-sized crater diameter range. The black curve is the lunar crater production function transferred to Martian conditions, representing a surface age of 3.25 Ga. The good fit strongly suggests that the impactor size–frequency distribution is really the same for the Moon and Mars and our previous procedure of transferring the lunar crater size–frequency distribution to Mars was carried out correctly.

to Martian conditions (Ivanov, 2001). The good agreement between the normalized assemblage and the theoretical Martian crater production function strongly suggests that the impactor population is the same for the Moon and Mars and the procedure for transferring the lunar crater size–frequency distribution to Mars has been carried out correctly.

Part III.

Re–Assessment of the Martian Stratigraphy

In **Part III, Re–Assessment of the Martian Stratigraphy**, the crater count results obtained during this investigation will be described, and some key results outlined. A summarizing discussion and interpretation will be given in Part IV, The Evolutionary History of Mars.

The earlier problems of assessing the geologic stratigraphy is introduced by a case–study: the Athabasca Valles. The geologic history of this former candidate landing site of the Mars Exploration Rover landers (MER) will be interpreted. Difficulties and possibilities of data "merging" are shown. This investigation is based on Viking and MOC imagery, and displays the gap in the range between 100 m up to 1 km of determining crater frequencies, due to differently resolved imagery. As outlined in Part II, linking different data sets, we overcame these difficulties due to the newly available imagery received during the Mars Express mission (HRSC experiment) and complementing image data taken by the Mars Odyssey Mission (THEMIS experiment). The latest geologic interpretation (based on MOC and HRSC imagery) for the youngest plains on Mars (Elysium Planitia) is indicating a "frozen sea", and which supports our earlier interpretations for the Athabsaca Valles region (Chap. 12).

The morphologic diversity of Martian impact craters imposes the possiblity to study target influence on the crater size–frequency distribution. A comparative study of the early heavy bombardment as well as the formation of Mars and the Earth's moon is based on the investigation of basin ages and their occurring frequencies. In comparison to the lunar record, it was possible to strengthen the applied chronology model and show the similar planetary evolution of the Moon, and Mars (as recorded by basin ages and their numbers) and most likely the entire inner solar system (Chap. 13). The detailed geologic history of Gusev crater, one of the actual MER landing sites, will also be given. This basin is situated at the highland–lowland dichotomy boundary, and special features such as crater depth will be evaluated (Chap. 13.2). Morphologic differences for large craters were found to be correlated with the dichotomy that splits the Martian surface into the northern lowlands and the southern highlands.

The advantage of additional datasets, e.g. from the Mars Orbiter Laser Altimeter (MOLA), is that they have initiated an enormous mapping effort and new interpretations of the geologic history of the Martian northern hemisphere (Tanaka *et al.*, 2003). Based on these attempts, the ages of all newly mapped geological units will be presented (Chap. 14), including a detailed study of the dichotomy boundary between 330°E and 90° E (Chap. 14.2), as well as a detailed study of major units of the northern plains units, Acidalia and Utopia Planitiae. Their geologic evolution, morphologic characteristics, and giant polygonal patterned troughs will be discussed along with the possible existence of a Martian ocean (Chap. 14.3).

The mophological appearance of the dichotomy boundary has been modified in many places either by volcanic, fluvial or glacial processes. The Medusae Fossae Formation, massive deposits along the boundary, has been studied (Chap. 14.4). Some of the largest outflow channels in the Chryse region have been investigated in greater detail (Chap. 14.5), in order to better understand their individual evolution, and to set a time–frame for the development of the lowland plains. Special type regions such as Amazonis Planitia and Hesperia Planum will be discussed in conclusive interpretations together with the crater size–frequency distribution measurements, in order to understand the geological evolution of the northern lowlands.

Finally, an overview of the volcanic evolution on Mars will be given based on the interpretation of caldera and volcanic surface ages determined from High Resolution Stereo Camera data (received from the Mars Express mission up to now). These results will be compared to earlier measurements based on Viking imagery. The Tharsis, Elysium, and Highland volcanic provinces will be discussed with emphasis on their differing evolution (Chap. 15). Additionally, interrelated glacial and/or fluvial activities are the focus of this study (Chap. 16).

A comprehensive summarizing discussion and interpretation of the global evolutionary history of Mars will be given in Part IV.

12. Athabasca Valles: A Case Study

Athabasca Valles has been studied as one of the candidate landing sites for the Mars Exploration Rover landers (MER) (Werner *et al.*, 2003a,b). The Athabasca Valles system is thought to be an outflow channel system that dissects Cerberus Planitia, a volcanic region of Elysium Planitia (one of the youngest regions on Mars). It is located in an area between 200° and 220° W and extends from the equator to 15° N. The area of interest has been mapped by Greeley and Guest (1987) as primarily younger channel and flood–plain material (unit Achu) of Amazonian age, following Scott and Tanaka (1986). They have interpreted it as fluvial deposits, where distinct albedo patterns probably represent channels with bars and islands. Especially in the west mottled zones represent deposition from ponded terminus of fluvial systems. Contrary to this interpretation, Plescia (1990) describes the Cerberus Formation to be of volcanic origin and points out corresponding surface morphologies, including lobate edges of the unit and the embayment relation of the unit with adjacent older units. Low–viscosity lavas from the Elysium volcano group northwest of the plains have flooded this region and filled the topographic depression. Plescia's (1990) interpretation is supported by Schaber (1980) who describes the radar and thermal characteristics to be similar to those interpreted as flood basalt provinces (e.g. Syrtis Major).

The main valley of the Athabasca Valles system strikes in a NE–SW direction, but also discharges to the Cerberus Plains at an elevation of about –2700 m in a southeast direction following the overall topography. The possible origin of the valley correlates with Cerberus Fossae, a set of sub–parallel grabens or extensive en–echelon fissures striking NW–SE at an elevation of about –2450 m. The fissures may have developed during the rise of the Elysium volcano bulge. Burr *et al.* (2002) identified relatively fresh lava extrusions from Cerberus Fossae associated with the channel origin.

Isolated, irregularly shaped remnants with a maximum elevation above the plain of 1000 m are embayed by plains material and dominate the western and eastern part of the investigated area (see Fig. 12.1). While the southeastern plains slope very gently to a topographic low of –2750 m, the southwestern region is blocked by a sudden rise to an elevation of about –1900 m.

Methodology: For a comprehensive study of the stratigraphic relationships, all available datasets have been combined: MDIM–2 Viking imagery, MOLA based digital elevation models and shaded relief maps, as well as MOC wide– and narrow–angle (MOC–NA up to April 2003, e18–release) imagery of the Mars Global Surveyor spacecraft. The resolution of all the different datasets was set to 231 m/pixel. Longitude and latitude shifts in the Viking and MOC wide–angle imagery were corrected on the basis of the digital elevation model using rubbersheeting methods. For small–scale features and the verification of area boundaries obtained by geological and geomorphological mapping, selected MOC narrow–angle shots were used to achieve higher precision in this highly differentiated terrain. The main mapping procedure was initially performed using Viking and MOC–WA imagery. In order to distinguish different units, various albedo features were analyzed. MOC–WA images were more satisfactory than Viking imagery due to reduced noise. Finally, area boundaries were adjusted using MOLA–derived data and the close views of MOC–NA imagery. For detailed studies, the MOC–NA images M04/02002 and M12/01869 which cover the plains units surrounding the valley and the proposed valley rim at a resolution of 3–5 meters/pixel, were mapped in order to possibly obtain even younger ages, requiring higher image resolution.

Geologic History of Athabasca Valles: In order to determine the stratigraphic relationships and the origin of the valley, ages were measured for different geological units in the region of Athabasca Valles. Details of the mapping results, interpretation of the geological units as well as a detailed age discussion is given in Werner *et al.* (2003a,b). Athabasca Valles was analyzed comprehensively to understand the chronostratigraphic relationships and explore different episodes of resurfacing. The results of the crater statistics investigation contradict the classic assumption that the Athabasca Valles were excavated by one or a few possibly ongoing catastrophic outflow events. As discussed by Berman and Hartmann (2002), various athors cited the age of the Cerberus plains to be Middle or Late Amazonian (around 0.6 Ga), showing signs of even younger resurfacing episodes. Continual volcanic activity accompanied by fluvial activity is a more likely interpretation. In the imagery, we could record the end of several resurfacing events in stratigraphically differing areas and establish the following geological history: The main channel has been incised into the Cerberus volcanic plains with an average plains age of 3.6 Ga. The main fluvial or glacial erosion processes ended 2.6 Ga ago. This result shows that the age of the valley system is itself older than commonly believed. One major, possibly fluvial event occurred 1.6 Ga ago in the topographically lower volcanic plains southwest of the valley. The valley was episodically covered by lavas, until 0.9 Ga, with a few younger episodes 30 Ma ago. The surface texture south of the valley system suggests a younger, possibly fluvial overprinting of the volcanic texture 30 Ma ago. The youngest volcanic activity is dated to about 3 Ma ago. With the latter ages we have not only been able to confirm earlier age estimates by Hartmann and Berman (2000); Berman and Hartmann (2002), but also shown that the valley system itself has undergone a period of two billion years that was dominated by volcanic processes in the most recent times. More erosional episodes might be found if one examines the "terraces" of the streamlined islands. The age determination favors the hypothesis that the streamlined features are erosional remnants. The interpretation of recent fluvial activity could not be verified within the geological units we could identify on the imagery (described in Werner *et al.*, 2003a). However, the ejecta pattern of a few larger craters superimposed on the lava blankets, that cover the valley floor might suggest the presence of water. The results contradict the assumption that the Athabasca Valles were excavated by one or a few possibly ongoing catastrophic outflow events, as claimed by Burr *et al.* (2002).

Cerberus Fossae fissures West of Athabasca Valles: Murray *et al.* (2005) investigated an area west of Athabasca Valles. This plains region has been interpreted earlier by Plescia (1990); Hartmann and Berman (2000); Berman and Hartmann (2002) to be volcanic plains. We could confirm that this plains unit formed about 3.6 Ga ago (Murray *et al.*, 2005), and similar ages were found for plains units in the Athabasca Valles region (Burr *et al.*, 2002; Werner *et al.*, 2003a). It is thought that the Cerberus Fossae fissures on Mars were the source of both lava and water floods two to ten million years ago (Werner *et al.*, 2003a). Nevertheless, based on HRSC and MOC data we were able to observe a strong resurfacing event. The crater size–frequency distribution yields a surface age of about 5 Ma, similar to ages we found in the Athabasca region. Evidence for the resulting lava plains has been identified in eastern Elysium, but seas and lakes from these fissures and previous water flooding events were presumed to have completely evaporated and sublimed. The surface morphology recognized in the HRSC and MOC imagery indicate that such lakes may still exist and resemble terrestrial ice floes. We infer as discussed in detail by (Murray *et al.*, 2005) that the evidence is consistent with a frozen body of water, with surface pack-ice,

Table 12.1.: Summary of all surface ages found for certain units. They correspond to the different isochrones shown in Fig. 12.1 (solid lines). The measured surface age of 0.9 Ga were found in units of all imagery and establish a good connection between high– and low–resolution images.

Unit	Unit Age(s)*				
Viking - Area 1	3.6		0.9		
MOC - WA - Area D		2.6	0.9		
MOC - m1201869 Area 1					0.003
MOC - m1201869 Area 12				0.03	
MOC - m1201869 Area 5			0.9	0.03	
MOC - m0402002 Area 1			0.9		

* in Ga (= billion years)

in southern Elysium around 5°N–latitude and 150°E–longitude. The frozen lake measures about 800 km times 900 km in lateral extent and may be up to 45 metres deep, similar in size and depth to the North Sea (Murray *et al.*, 2005). We also could confirm on the basis of crater counts, that the "ice–plates" are slightly older than the inter–plate areas (for details see Appendix C).

12.1. Implications for the Martian Crater Size–Frequency Distribution and Age Determination

Our interpretation of crater statistics data based on determining absolute surface ages by applying the Martian cratering chronology model presented by Hartmann and Neukum (2001) led to results similar to Hartmann and Berman (2000); Berman and Hartmann (2002) for comparable regions in the Athabasca system. This supports the reliability of the different approaches to determining surface ages using crater statistics.

Additionally, these counts (Fig. 12.1), both on Viking imagery at large crater sizes and MOC imagery at small crater sizes, consistently fit the currently established Martian production crater size-frequency distribution proposed by Neukum *et al.* (2001) and Ivanov (2001). A surface age of 0.9 Ga was measured in units of all high– and low–resolution images (Table 12.1). This constitutes an excellent first order test for the general validity of the Martian size-frequency distribution and cratering chronology model by Neukum *et al.* (2001) and Ivanov (2001). It also demonstrates the difficulty of linking surface units mapped in different image resolution and relating crater frequencies measured from these two datasets. Now, the gap can be filled by the High Resolution Stereo Camera (HRSC) imagery, which covers huge areas at high resolution (up to 11 meters/ pixel), where medium–resolution Viking–mosaics do not existed.

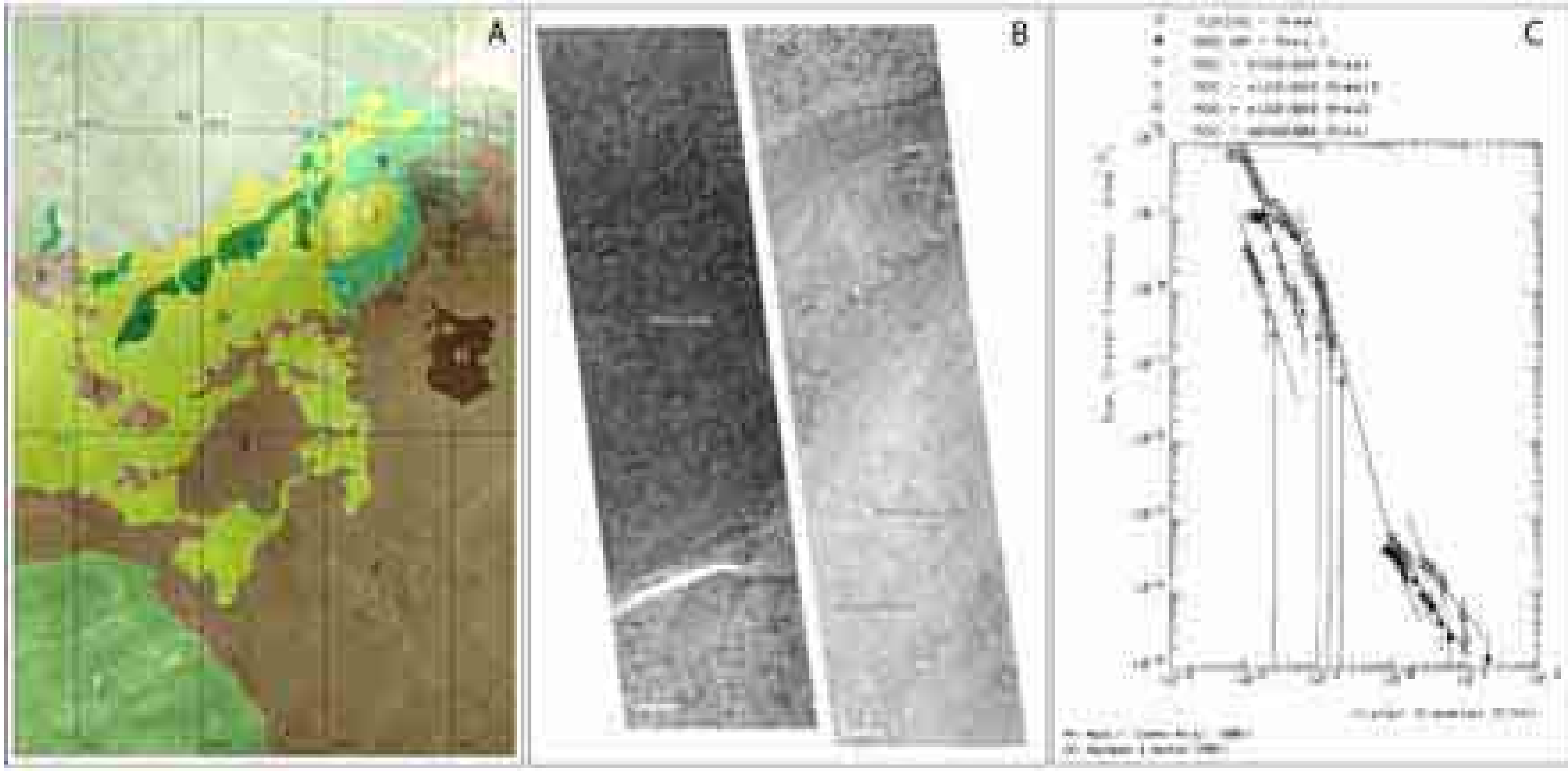

Figure 12.1.: The Athabasca Valles system: (A) Mapped on MOC-WA imagery. (B) MOC-NA image M12/01869 centered at 8.31°N 154.46°E shows a traverse across a mesa remnant near the upper Athabasca Valles system. (left), the northern part, shows the main valley floor. The dark plain (plf) is flooded with volcanic lava. The transition to the mesa remnant is characterized by a steep escarpment that expose of several remnant layers (white arrows). (right) the mesa slopes more gently than the northern slope towards brighter plains. The slope walls (sw) are cut by a set of very narrow subparallel ridges, which resemble small dunes. At the base of the southern slope a streamlined island (si) can be observed, which is clearly defined in the east and rather diffuse at its western margin. Sets of small valleys branch at the front of the island. The channels spread in a southern and western direction onto older lava plains. (C) The crater size frequency distribution of a few prominent ages measured for the Athabasca Valles area. These are selected to give an impression regarding the range of ages. The ages represented by the isochrons are given in table 12.1.

13. Martian Cratering and Implications for the Chronostratigraphy

The record of large impact basins on different planetary bodies allows us to compare the characteristics of the heavy bombardment period and the end of planetary formation. Both the cratering record itself and the age distribution of the impact basins represent the period of highest impactor flux, decaying rapidly within the first half billion years of our solar system. In order to test the plausibility of the Martian chronology model (see Chapter 5), the ages of the large Martian impact basins, using the derived Martian production function, were determined and compared to lunar basin ages. For the Moon, the large basins were produced no later than about 3.8 to 3.9 Ga ago and a similar situation should exist for Mars, following the marker horizon idea (Wetherill, 1975). This idea is based on the assumption that solar system bodies have undergone a similar evolution since planetary formation. In the cratering record on any solid surface body, which has representative large old surface units, this first period of heavy bombardment is present in the general crater size–frequency distribution as well as the large basin record itself. According to our investigation, the oldest surface areas on Mars, roughly the Martian southern highlands, e. g. Noachis Terra, were formed between 4.0 to 4.2 Ga ago during the period of heavy bombardment (Fig. 13.1). On the basis of crater counts of unambiguously defined craters, older surface units have not been found.

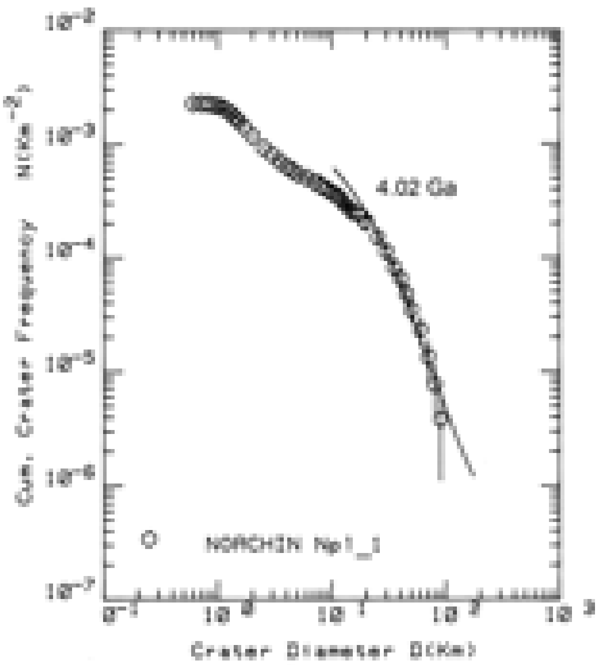

Figure 13.1.: The crater size frequency distribution measured for one of the oldest regions on Mars: Noachis Terra (map nomenclature: unit Npl1).

There have been attempts by Frey *et al.* (2002) to count so–called quasi–circular depressions, many of which are clearly seen in the Mars Orbiter Laser Altimeter (MOLA) elevation data, but generally not visible in available imagery. These depressions are interpreted as remnants of strongly eroded (highlands) or deeply buried (lowlands) craters produced early in Martian history. These measurements indicate that the buried lowland surface is older than the visible highland surface, where crater count ages are based on craters clearly recognized by their morphology.

During the Mars Global Surveyor Mission, vector magnetic field observations of the Martian crust were acquired. The location of observed magnetic field sources of multiple scales, strength, and geometry correlates remarkably well with the ancient cratered terrain of the Martian highlands (Acuña *et al.*, 1999). On the other hand, these (magnetic field) sources are absent in the lowland plains, near large impact basins such as Hellas and Argyre, and in most of the volcanic regions. Formation ages of these features will give a time–frame for the thermodynamical evolution of Mars as will be discussed in Part IV.

13.1. Martian Impact Basin Ages

Large Martian impact basins are randomly distributed in the heavily cratered highlands. The interior of any basin cannot be considered as pristine and crater counts would not indicate the formation age. In this study, we tried to identify units that best represent the formation age for a particular basin. Therefore, we chose a relatively narrow band around the crater rims, considered as a zone of the ejecta blanket. We remapped these blankets individually for the 20 largest impact basins (larger than 250 km) on Viking–MDIM–2 imagery. The image resolution (231 m/pxl) is sufficient to get a representative age, since most of the later geologic activity (mainly erosion) has the least effect in the large–crater size range (crater diameters larger than 3 km). Additional information for the interpretation of important geological units was obtained using Mars Orbiter Laser Altimeter topographic data. For these 20 basins with detectable ejecta blankets, the measured ages are within the expected range of 3.7 - 4.1 Ga (Tab. 13.1).

Name	Cen. Lat. & Lon.		Diameter km	Age Ga
Crater (smaller than 230 km)				
Gusev	14.7S	184.6W	166	4.02
Lowell	52.3S	81.4W	203	3.71
Crater (larger than 230 km)				
Flaugergues	17.0S	340.8W	245	–
Galle	51.2S	30.9W	230	–
Kepler	47.1S	219.1W	233	3.92
Lyot	50.8N	330.7W	236	3.40
Secchi	58.3S	258.1W	234	–
Crater (larger than 250 km)				
Antoniadi	21.5N	299.2W	394	3.79
Cassini	23.8N	328.2W	412	4.03
Copernicus	49.2S	169.2W	294	4.00
de Vaucouleurs	13.5S	189.1W	293	3.95
Herschel	14.9S	230.3W	304	3.95
Huygens	14.3S	304.6W	470	3.98
Koval'sky	30.2S	141.5W	309	3.96
Newcomb	24.4S	359.0W	252	4.00
Newton	40.8S	158.1W	298	4.11
Schiaparelli	2.7S	343.3W	471	3.92
Schroeter	1.9S	304.4W	292	3.92
Tikhonravov	13.5N	324.2W	386	4.10
Planitiae				
Argyre	50.0S	44.0W	800	3.83
Hellas	43.0S	290.0W	2200	3.99
Isidis	13.0N	273.0W	1200	3.96

Table 13.1.: List of the Martian impact basins. Location, diameter and resulting ages are given, see Fig. 13.2.

A few basins, where ejecta could not be identified due to obvious resurfacing processes, are suspected to be even older (possibly up to 4.2 Ga). The spacial distribution of Martian impact basins and their ages are summarized in Fig. 13.2. These basins are clearly situated in the heavily cratered highland unit (with an average age of about 4.0 Ga). Although some authors (e.g. Frey and Schultz, 1989) explain the formation of the northern lowlands as huge impact events (no clear evidence can be found) clearly distinguished basins are not found in the northern lowlands, with the exception of the relatively young and fresh-looking crater Lyot. It resembles a basin, but could also be classified simply as a large crater with a peak-ring. Our crater counts indicate an age of 3.4 Ga, while all other Martian basin ages average around 3.8 to 4.1 Ga.

Lunar Impact Basin Ages: In this study, lunar basin ages have been compiled bymaking use of the crater–frequency measurements obtained by Neukum (1983) and Wilhelms (1987). While 33 of the lunar basins were dated directly from cratering statistics, crater frequency measurements are non–existent for ten of the oldest basins of pre-Nectarian age (Wilhelms, 1987). In these cases, ages are determined by stratigraphic relationship to other basins. It is assumed that the South Pole-Aitkin basin age is roughly the same as the average lunar highland age (assumed to be 4.35 Ga). As a younger limit, Al-Khwarizmi/King is used, which has been dated in terms of superimposed crater frequency (Wilhelms, 1987) and is stratigraphically the youngest in the sequence of old basins (Tab. 13.2). The remaining basins are distributed between these two boundaries and slightly biased towards older ages (Tab. 13.2).

As previously discussed, the lunar basin ages range between 3.85 Ga and about 4.35 Ga,

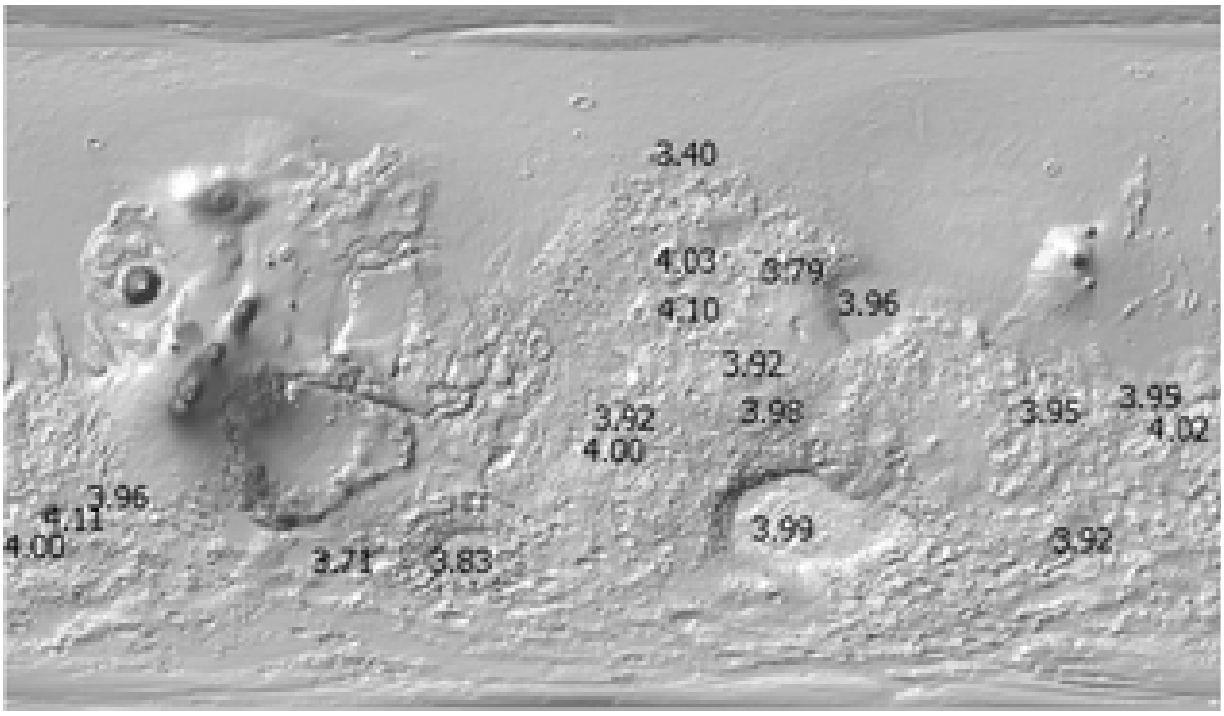

Figure 13.2.: The Martian basin ages are given here. The ages are superimposed on the location of the particular basin. The basemap is a shaded–relief based on MOLA data.

while the ages defined by crater counts range between 3.85 and 4.2 Ga. This upper limit is roughly for ages where saturation even in large crater diameter range still has no major affect.

Mars – Moon Comparison: The Martian surface we observe today appears to be no older than 4.2 Ga. As an important reference, Noachis Terra (the type region for the oldest stratigraphic sequence) shows an age of 4.02 Ga based on our crater counts and in accordance with the oldest basin ages. Almost all Martian basins are approximately 3.8 to 4.0 Ga old or younger, while datable lunar basins give ages between 3.85 and 4.3 Ga (Fig. 13.3). On average, lunar basins appear older, with the majority of occurrences prior to 4 Ga. The oldest surface units on the Moon are considered to be 4.35 Ga old (Wilhelms, 1987). The lunar distribution shows a maximum prior to 4 Ga ago, while the Martian data have a maximum basin occurrence at 4 Ga. This implies that the oldest Martian crustal structures observed today

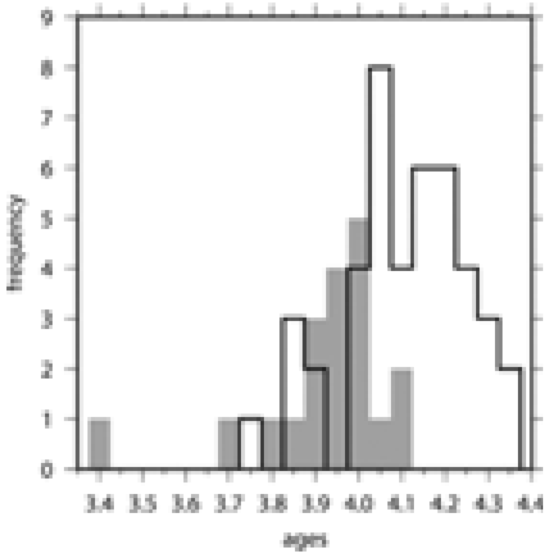

Figure 13.3.: The frequency distribution of the ages of lunar (open) and Martian (filled) impact basins given in this paper.

Name	Diameter km	Density $(10^6 km^2)^{-1}$	Age Ga
Pre–Nectarian Basins (stratigraphically related)			
Procellarum	3200		
South Pole–Aitken	2500		∼4.35
Tsiolkovskiy–Stark	700		
Grissom–White	600		
Insularum	600		
Marginis	580		
Flamsteed–Billy	570		
Balmer–Kapteyn	550		
Werner–Airy	500		
Pingré–Hausen	300		
Al-Khwarizmi/King	590	197	4.17
Pre–Nectarian Basins (ages based on crater frequencies)			
Fecunditatis	990		4.00
Australe	880	212	4.18
Tranquillitatis	800	A 11	3.73
Mutus-Vlacq	700	225	4.19
Nubium	690		4.00
Lomonosov-Fleming	620	177	4.15
Ingenii	650	162	4.14
Poincaré	340	190	4.16
Keeler-Heaviside	780	186	4.16⋆
Coulomb-Sarton	530	145	4.12
Smythii	840	166	4.14⋆
Lorentz	360	166	4.14⋆
Amundsen-Ganswindt	355	156	4.14
Schiller-Zucchius	325	112	4.09
Planck	325	110	4.08
Birkhoff	330	127	4.11⋆
Freundlich-Sharanov	600	129	4.11⋆
Grimaldi	430	97	4.06
Apollo	505	119	4.10⋆
Nectarian Basins (ages based on crater frequencies)			
Nectaris	860	79	4.03⋆
Mendel-Rydberg	630	73	4.02⋆
Moscoviense	445	87	4.05⋆
Korolev	440	79	4.03⋆
Mendeleev	330	63	4.00⋆
Humboldtianum	700	62	4.00⋆
Humorum	820	56	3.98⋆
Crisium	1060	53	3.97⋆
Serenitatis	740	83	4.04
Hertzsprung	570	58	4.04⋆
Sikorsky-Rittenhouse	310	27	3.87
Bailly	300	31	3.89

Table 13.2.: List of lunar impact basins. The crater frequencies are by Wilhelms (1987) and translated to ages, ages marked by ⋆ are ages from Neukum (1983).

(based on crater counts) are no more than 4.2 Ga old, whereas the lunar surface record probably dates back to 4.3 or 4.4 Ga. On Mars, the earlier record has been erased by endogenic and surface erosional processes. The global basin record (diameters and location catalogued by Barlow (1988a)) supports these results, for discussion see Chap. 11.

In order to better compare the lunar and Martian basin population, we analyzed the frequency of basins with respect to the formation age plotted as a histogram (Fig. 13.3). The number of basins per age period is the same for both the Moon and Mars. Mars shows for the time span 3.7 - 4.0 Ga, a total of 16 basins, whereas the moon has 10 basins for the same age period. This is roughly in accordance with the fact that the Martian highland surface that contain basins is almost two times larger than the total surface of the Moon, which is the reference surface for the 43 basins studied here (Werner and Neukum, 2003).

13.2. Gusev Crater – The MER Spirit Landing Site

Among the previously discussed Martian impact basins, there is Gusev crater, the landing site of one of the two robot rovers of the American Mars Exploration Rover (MER) mission, which landed in January 2004. At the same time, the European Mars Express mission arrived at Mars. During its first year, Gusev Crater (about 160 km in diameter) has been imaged several times. The crater is situated at the dichotomy boundary (14.7°S and 175.3°E). directly south of the volcanic construct Apollinaris Patera. To the south, Ma'adim Vallis (valley), which cuts into highland terrain, incises the crater rim and widens into Gusev. The MER mission scientists hoped to find indications of a former lake within Gusev crater, which are allegedly sediments deposited by the Ma'adim Vallis (Squyres *et al.*, 2004b; Kuzmin *et al.*, 2000; Cabrol *et al.*, 2003). Other origins of the deposits that make up the crater floor have also been proposed (Greeley, 2003; Golombek *et al.*, 2003). Most of the Spirit MER lander instruments indicate that the rocks found on the Gusev floor are predominantly basaltic in composition. No evidence for rocks of primary sedimentary origin has been found, although the rocks are altered by weathering involving liquid water (McSween *et al.*, 2004; Gellert *et al.*, 2004; Christensen *et al.*, 2004; Morris *et al.*, 2004). Comparing Gusev crater (imaged by HRSC) and Grimaldi crater on the Moon (imaged by Lunar Orbiter), features inside Gusev crater clearly resemble "mare–type" wrinkle ridges. These are typical of deformation of basaltic lava flows (Greeley *et al.*, 2005), although landforms with a similar morphology can also be the result of compressional defomation of a sedimentray mantle (e.g. the Meckering fault in Australia; Gordon and Lewis, 1980). Based on morphologic data, Greeley *et al.* (2005) suggest that Gusev is flooded by lavas, a finding supported by the chemical and mineralogical findings of the MER lander instruments. The surrounding highland plateau of Gusev to the south and east is characterized by impact craters and inter–crater plains, while the area west of Gusev is dominated by low–lying plains of the impact basin de Vaucouleurs. Northeast of Gusev and east of Apollinaris Patera, the Medusae Fossae Formation is located, which is believed to be pyroclastic material and which is strongly wind–sculpted.

Using the HRSC, THEMIS and MOC imagery, the Gusev crater and its vicinity has been mapped by van Kan (2004). Her results are in approximate agreement with earlier morphological mapping attempts based on Viking imagery by Kuzmin *et al.* (2000) at an image resolution of about 70m/pxl and with a thermophysical characterization of Gusev's interior based mainly on thermal–infrared data from the thermal emission imaging system (THEMIS) at a resolution of 100m/pxl by Milam *et al.* (2003). Selected areas, with simplified unit boundaries representing the mapped units, were used to determine ages. These ages, based on crater frequencies measured on a mosaic of HRSC images obtained during orbits 24,72, 283, 335 with a mosaic resolution of 25 m/pxl, are used to reconstruct the geologic evolution of the Gusev region (Fig. 13.4).

Based on these ages, the following geologic history of the Gusev region can be ascertained: The plain surrounding Gusev, belonging to the heavily cratered highland unit, has a surface age older than 4.0 Ga. At around that time, Gusev itself was most likely formed (see impact basin ages listed in Chapter 13). Later, the plains unit as well as Gusev's interior experienced a resurfacing event, which filled both inter–crater depressions and Gusev, and ended at about 3.65 Ga ago. Subsequent resurfacing of the Gusev interior and its vicinity produced the wrinkled and etched units in the eastern part of Gusev at approximately 3.45 Ga ago. A similar geologic history was reported by Kuzmin *et al.* (2000), but they argued that the main depositional source should have been fluvial sedimentation from the precursor to Ma'adim Vallis and later Ma'adim Vallis itself. The volcanic activity associated

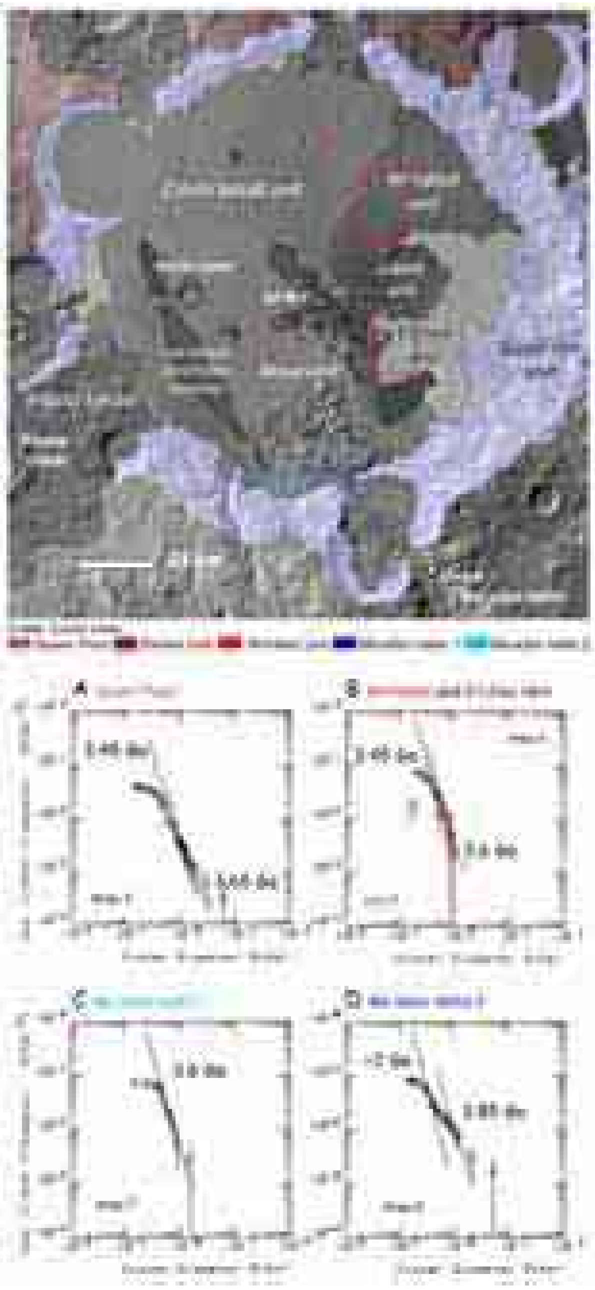

Figure 13.4.: A geologic map of the Gusev crater and its vicinity after van Kan (2004), and the outline of units used for crater counts and age determination. Below, the crater size-frequency distributions for the relevant units are given.

with Apollinaris Patera seems to be morphologically independent and ended already by about 3.75 Ga ago. While pyroclastic deposits of Apollinaris Patera could have contributed to the infill of Gusev, no clear stratigraphic and morphologic evidence is found. Possibly, the fluvial activity of Ma'adim Vallis started very early in Martian geologic history (about 3.85 Ga ago, Fig. 13.4 D) and appears to have ended about 2 Ga ago, at least resurfacing occurred further upstream Ma'adim Vallis. During this period, landforms, whose origin are possibly water related, formed elsewhere on the planet (see e.g. Chap. 14.4). Despite the geochemical evidence from volcanic material found at the Spirit traverse, fluvial deposits should have also contributed to Gusev's infill. Nevertheless, sediment discharge estimates from fluvial activity of Ma'adim Vallis could not solely fill Gusev's interior (Greeley *et al.*, 2005).

To better understand the contribution of volcanic or fluvial sediment infill into the initial impact depression, MOLA topographic profiles of similarly sized craters are investigated and compared with Gusev's morphometry. The size of the Gusev crater (diameter $\sim$ 160 km) suggests a complex internal structure, but the visible floor is very flat. Apparently, these selected craters, located in the Martian highlands, underwent a geological evolution different than Gusev. Nevertheless, most of the comparably sized craters appear partially filled, but some show a distinct central feature above the level of possible sedimentary infill. The two apparently least filled craters (43°S, 343°E and 23°S, 16°E) were used to estimate the Gusev infill (Fig. 13.5). Unlike Gusev, these two craters show a visible rim-to-floor depth of about 2.5 to 3 km, while for Gusev this is in the range of 1 to 1.5 km. Hence, the post–impact infilling of Gusev has a thickness of more than 1 to 1.5 km (Werner *et al.*, 2005a; Ivanov *et al.*, 2005). This is an important constraint for any assumed contribution from the earlier fluvial activity of Ma'adim Vallis and volcanic deposit thickness. The youngest formation in the vicinity of Gusev is the Medusae Fossae Formation ($\sim$ 1.6 Ga), which is a band along the dichotomy boundary between the two large volcanic provinces. Similar ages are found in most locations (compare Chap. 14.4).

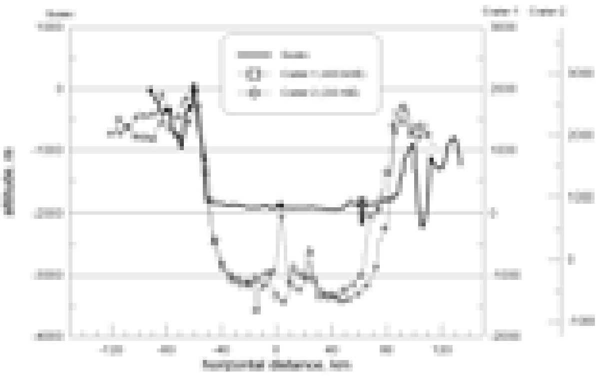

Figure 13.5.: Cross sections of Gusev and two craters of comparable size but less infill, indicating that the post–impact infilling of Gusev has a thickness of more than 1 to 1.5 km (Fig. from Ivanov *et al.* (2005) or Werner *et al.* (2005a)).

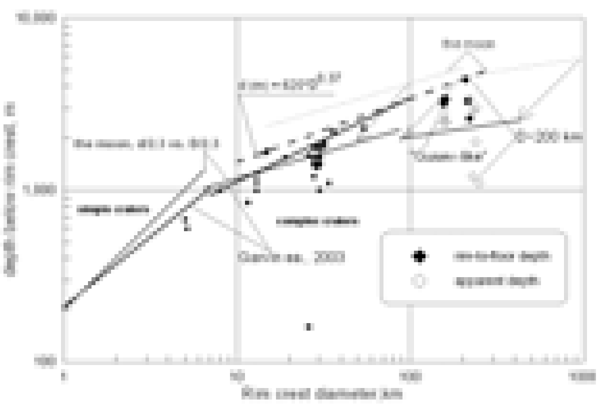

Figure 13.6.: Results of a simple approximate scaling of the depth-diameter relations from planet to planet to evaluate the depth–diameter relation of Gusev–sized craters (Fig. from Ivanov *et al.* (2005)).

Preliminary numerical modeling by Ivanov *et al.* (2005) indicates that the pristine cross section of Gusev–like craters on Mars shows a possible rim-to-floor depth of about 4 km. These model results are affected by the mechanical description of materials, including strength and dry friction for damaged rocks and the Acoustic Fluidization model, which simulates the assumed temporary dry friction reduction around the growing crater. To evaluate the model runs, results were compared with scaled depth/diameter relations for the Moon (Pike, 1977; Williams and Zuber, 1998). The assumption that the final crater shape is controlled by the balance between rock strength/friction and the lithostatic pressure allows us to propose a simple approximate scaling of the depth-diameter relations from planet to planet. In this approximated approach, complex craters with the same value of gD (g is the gravitational acceleration, D is crater diameter) should have a similarly scaled depth gd, where d is the crater depth (Fig. 13.6). The comparison of lunar depth–diameter relationships (Pike, 1977; Williams and Zuber, 1998) scaled to Mars gravity, Garvin et al.'s approximations (Garvin *et al.*, 2003), our previous measurements (Werner *et al.*, 2004a, see next Chapter) and new data for Gusev–like craters, support the maximum depth for a crater of 150 km in diameter and a final depth of the annular trough of about 4 km as stated in Ivanov *et al.* (2005)). Together with the measured results of craters of comparable size to Gusev, the model results constrain the relative thickness of fluvial and volcanic infill to approximately 1 to 1.5 km.

14. Northern Lowlands, Highland–Lowland Dichotomy, and Fluvial Activity

Global Martian geologic mapping and stratigraphic analysis is based mainly on Viking Orbiter image interpretation (Scott and Tanaka, 1986; Greeley and Guest, 1987; Tanaka and Scott, 1987, see Chapter 6.2). One of the dominating features of the Martian surface is the ancient highland-lowland topographic and morphologic dichotomy, superimposed by huge impact basins and volcanic regions. The lowland region, roughly centered on the north pole, covers one third of the planet and is broadly characterized by a smooth, gently sloping surface at the km scale, below the mean planetary radius. Its origin has been attributed to tectonism as well as impact or mantle dynamics (e.g. Wise *et al.*, 1979a; Wilhelms and Squyres, 1984; Frey and Schultz, 1988), but any clear morphologic evidence has been obscured by subsequent resurfacing events. Based on new mission data, the interpretation of the northern lowlands gained new insights due to detailed topographic data of the Mars Orbiter Laser Altimeter (MOLA) and additional imagery of the Mars Orbiter Camera (MOC) (both onboard the Mars Global Surveyor space craft). Based on this new data, Tanaka *et al.* (2003) significantly revised the interpretation of the origin and age for a host of features in the northern lowlands. Their investigation culminated in a remapping of the northern plains of Mars and a preliminary interpretation of the resurfacing history. They relied mostly on a MOLA digital elevation model at a 1/128° resolution (about 500 m/pixel), while the physical interpretation is based on MOC–NA and high–res VIKING imagery (< 100 m/pixel). A summary of the stratigraphy and distribution of the units is given in Tanaka *et al.* (2003). The main definition of the "new" lowland units is based on the topographic outline at an elevation of below –2000 to –5000 m. Major geographic features include the Borealis basin (Vastitas Borealis Formation), Utopia basin (Utopia Planitia), and Isidis basin (Isidis Planitia), implying that they all might have formed by large impacts. To the south, the plains are bounded by densely cratered highland terrain and the broad Tharsis rise, which includes Olympus Mons and the Alba Patera shield volcanoes. East of the huge volcanic Tharsis rise, Chryse and Acidalia Planitiae are located, characterized by old channel mouths as well as likely channel–related flood–plains and chaotic material. The bottom of the western flank of the Tharsis Rise is occupied by Amazonis Planitia and Arcadia Planitia, which extend westwards to the volcanic Elysium rise. The Elysium rise includes the Elysium Mons, Hecates Tholus, and Albor Tholus volcanoes, the largest volcanic constructs in the entire lowlands. To the south, Elysium Planitia surrounds the Elysium rise. Amazonis, Arcadia, and Acidalia Planitiae are merged to the Arcadia Formation, distinguished on the basis of morphology, albedo, and crater frequencies. The dichotomy boundary is intersected by Syrtis Major Planum, a broad shield volcano, and the impact basin Isidis Planitia. The rugged peaks of Lybia Montes surround the southern margin of Isidis Planitia.

The time–stratigraphic classification of the newly mapped northern hemisphere is based on the number of craters for each unit from the crater catalog published by Barlow (1988, revised 2001), which includes craters of +5 km in diameter. Tanaka *et al.* (2003) discuss the relevance of these crater frequencies with respect to their correctness and stated three problems in their approach: (1) the mis-registration of the MOLA–based geologic map and the VIKING–base of the crater catalog, which might attribute craters to a unit to which they do not belong or vice versa, affecting smaller units the most. (2) Taking the cumulative number for a single reference diameter (here 5 km and larger) instead of the entire crater size–frequency distribution, therefore any resurfacing will be obscured and need preselection of the craters to be counted. (3) The crater catalog already excludes highly degraded craters.

To investigate the full cratering record by using the crater size–frequency distribution as described in Chapter 8, it is not necessary to exclude or pre–sort crater populations. Any resurfacing will be visible in the crater counts as described in Chapter 9.1.

14.1. Northern Lowland Stratigraphy

In a joint effort, representative type areas for each geological unit were selected following Tanaka *et al.* (2003). A detailed study using crater size–frequency measurements for each unit to define a time–stratigraphic sequence is given here. Small patches representative of certain geologically mapped units and specific morphologic characteristics are distinguished. The patches are selected to contain a single geological unit and the simple outline is the basis for crater size–frequency distribution measurements. The basis for the surface age determination is the Viking – Mars Digital Image Model (MDIM 2.1) global dataset (a complete orthorectified mosaic) at a pixel resolution of 231 m/pxl. Based on our crater size–frequency measurements, the resulting surface ages and the time–stratigraphic relations of the investigated units are described here. Special focus has been given to four different zones, which represent different characteristics and evolution within the northern plains. The Chryse basin (zone 1), the Utopia basin (zone 2), the Amazonis and Elysium region (zone 3) and zone 4 representing the sequence between the north pole and Alba Patera.

14.1.1. The Geology of the Chryse Region (Zone 1)

The physiographic setting of this region is dominated by Chryse Planitia, a possible impact basin of about 2000 km in diameter. Many of the largest and prominent outflow channels on Mars drain into that nearly circular basin, which opens into the northern lowlands. Clear evidence for the impact origin cannot be found because rim characteristics have eventually been washed away by the fluvial activity (Fig. 14.1).

The extent of Chryse Planitia is outlined by four geological units (*Chryse unit 1 – 4*). The main characteristics of this basin are the scoured features and streamlined islands associated with the outflow channels. A system of deep, wide channels (Kasei, Maja, Shalbatana, Simud, Tiu, Ares, and Mawrth Valles) emanates from chaotic terrains and disappears into the lowlands. Chryse 1 and 2 units delineate plains deposits along the western and eastern margins of Chryse Planitia, characterized by wrinkle ridges, hummocky material, locally lobate scarps and tear–drop shaped islands. While Chryse 1 unit represents deposits from mass–wasting and local fluvial erosion of highland boundary surfaces, Chryse 2 unit was formed by debris flows and fluvial deposits. Further downstream, Chryse 3 and 4 units follow. They appear relatively smooth in the western part of Chryse (unit 3) and are marked locally by irregular grooves, knobs, low shields, and thin circular sheets (unit 4).

There are fluvial deposits in Kasei, Maja and Ares Valles, in the prolongation of Simud and Tiu Valles rapidly emplaced sediments (flood overrun), subsequent compaction, and mud volcanism modified the smooth appearance. A few of units relate directly to the outflow channel morphology (*Ares and Simud unit*). They contain the chaotic source regions and carved floors of the upstream part of Ares Vallis and other valleys. The Simud unit also includes some of the channel floors and large blocks and debris of older material disrupted and possibly transported by high–pressure fluids.

The channels originate from chaotic terrain and dissected highland plateau and boundary plains (*Noachis, Nepenthes, Lunae, and Lybia unit*). Most of the outflow channels do not end in the Chryse basin, but can be traced by the scoured features northward into Acidalia Mensa. The gradual disappearance is interpreted as possibly caused by the development of the Vastitas Borealis Formation.

This formation occupies most of the lowland region and has been mapped as a single unit merging four subunits, defined mainly by texture and albedo differences in earlier map approaches. The *Vastitas interior unit* is characterized by numerous low hillocks, arcuate ridges, dozens of circular depressions (ghost craters), pervasive hummocks, as well as grooved and mottled appearances. The *Vastitas marginal unit* forms plains and low plateaus along much of the outer margin of the interior unit. It has a more pronounced topography compared to the interior unit, showing troughs, knobs, and ridges. Both units are interpreted as sediments delivered over a large area by rapid emplacement due to outflow channel activity.

Many morphologies indicate high subsurface–volatile content and possible glacial, periglacial, lacustrine, or tectonic processes. Units such as the Noachis, Nepenthes and Lybia unit, are widespread throughout the mapped region, represent highland material, and grad from one into the other. The Noachis unit generally outlines rugged highland terrain surrounding most of the northern lowlands and is densely cratered. It resembles a mixture of volcanic and sedimentary material, which is covered by impacts. The Lybia unit has a similar appearance, but is more pronounced in topography, forming massifs and high–standing terrain within the Noachis unit. The Nepenthes unit consists of knobs and mesas of highland rock and interposed slope and plains material, which forms much of the highland/lowland margin. To the northeast, huge parts are covered by perhaps kilometer thick lava plains marked by wrinkle ridges. These belong to Lunae Planum and make up the Lunae unit in this zone.

These geologic–morphologic units are represented by 16 patches on which crater counts were performed. Their distribution and location are given in Fig. 14.1, image clips and resulting crater size–frequency distributions are given in Appendix A, and the ages and dimensions are summarized in Tab 14.1.

14.1.2. The Chrono–Stratigraphy of the Chryse Region

Most of the patches in this zone represent units belonging to the Chryse inner slope region (Fig. 14.1). Ages determined for image clips representing the Chryse 1 – 4 unit range between 3.83 Ga and 3.3 Ga. The ages found for individual units somewhat vary. For example, the Chryse 1 unit, represented by four patches (32, 33, 39, and 41) range between 3.83 Ga and 3.61 Ga. The imagery base and the resulting crater size–frequency distributions are shown in the Appendix A. The variation in age are explained by the visible change in morphology. All crater size–frequency distributions reveal surface ages slightly older than 3.6 Ga. For image clippings, where crater counts also indicate older ages (about 3.8 Ga), the surface morphology is not homogeneous. As for clip 33 and 32, smooth plains with wrinkle ridges and fluvial overprint are visible along with many knobs, which are widespread throughout the units. Particularly, the surface in the southern part of clip 33 resembles degraded highland terrain, which explains a very old surface age of 3.8 Ga.

Clippings representing Chryse 2 and 3 units generally fall into the same age range, but clip 35 appears especially young (3. 45 Ga) compared to the results of the other patches. Regions like Lunae Planum (mapped here as Lunae unit) are the background units for the carved channels of Kasei Valles. Their age indicates an outline for the start of the erosive phase of outflow channel activity. The Lunae unit clip indicates an age of 3.5 Ga and does

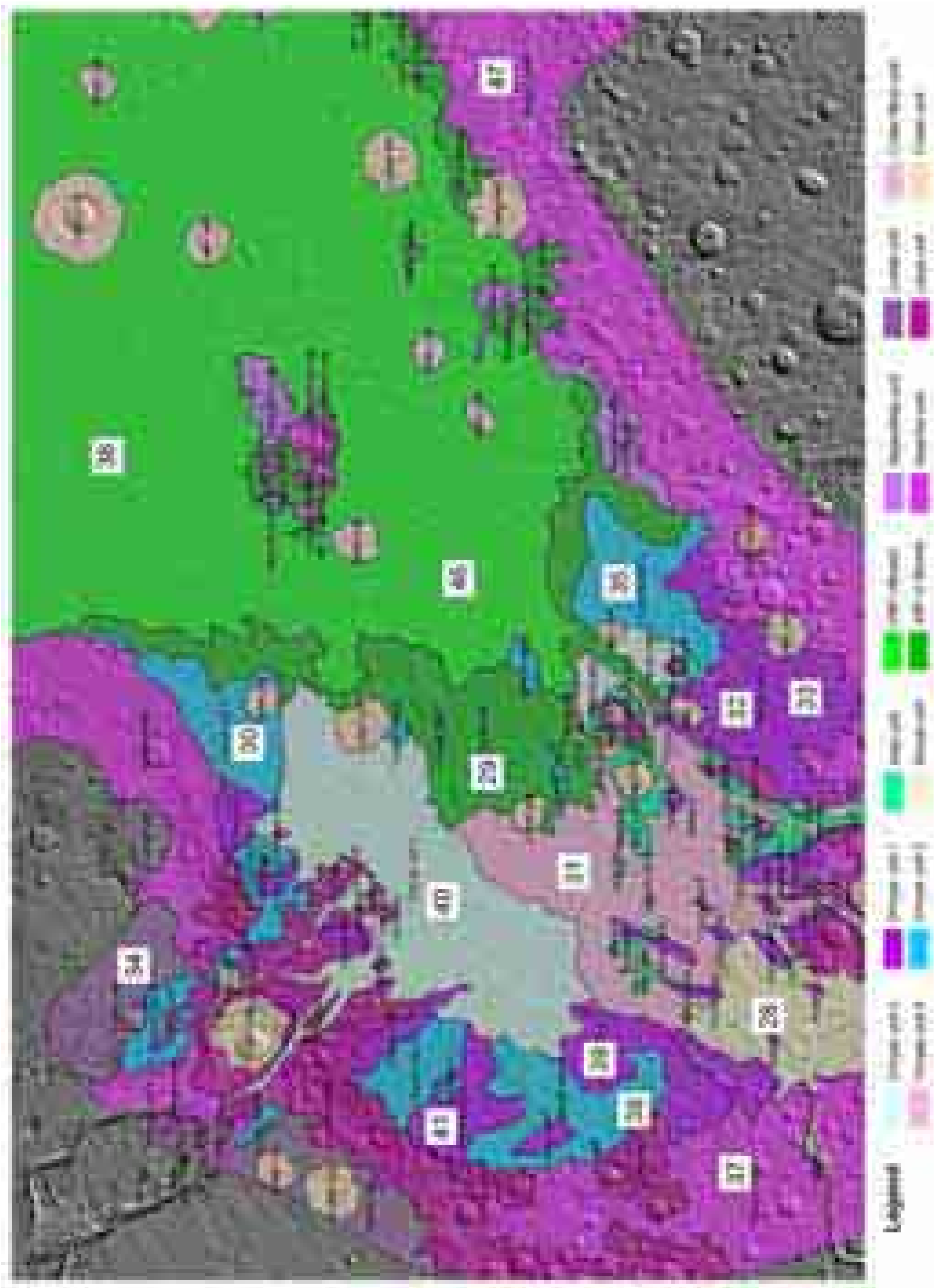

Figure 14.1.: The geologic map of the Chryse region as mapped by Tanaka *et al.* (2005) with numbered patches to indicate their locations. Here, Zone 1 is given. The results of the crater size–frequency distribution measurements are given in Table 14.1.

not support this idea. The volcanic activity that created this lava plain possibly was active over a longer period, ending subsequent to the formation of the Kasei channel system. As expected and already described by Tanaka *et al.* (2003), the oldest ages are found in the highland units (e.g. No. 47 and 37), which are heavily cratered. The geological interpretation of the Noachis unit (assumed to be the oldest by Tanaka *et al.* (2003) and earlier interpretations) indicates a long history of resurfacing and deformation, accounting for secondary erosional, depositional and tectonic features. These are characterized by high crater densities, valley networks, isolated depressions (which are possibly subdued eroded impact structures), as well as ridges, scarps, and troughs. The resurfacing activity is recognized in the crater size–frequency distribution, but not limited to a single episode (gradual deviation from the expected crater production function).

The naming follows the previous type region: Noachis Terra defining the Noachian Epoch. In Chapter 13 we discussed that there is no mapped unit older than about 4.1 Ga, which is close to the age found for Noachis Terra. In the Chryse region as well as in zones that will be discussed later, the oldest units are definitely about 4.0 ± 0.05 Ga old. The patches illustrating the outflow channel activity (Simud and Chryse 4 units) indicate resurfacing slightly younger ages, in the Chryse 4 unit, and which range between 3.6 and 3.4 Ga. It is likely that the erosive processes in Simud Vallis ended at about that time, but possibly later wide spread sedimentary deposition resurfaced the downstream region represented as Chryse 4 unit. The surface age gradually becomes younger towards topographic lows.

In general, all zones in the northern lowland units range between 3.6 Ga and 3.5 Ga, with a few exceptions in zone 2 and zone 3. These exceptions are correlated with morphologic units with a geologic origin that is clearly different than the lowlands characteristics. The gradual change in age correlated with the topographic change is represented by the different Chryse units (1 – 4). The Chryse units 1 and 2, occupying the possible rim region, are about 3.75 Ga old (patches 38, 33, and 32). Even within the Chryse unit 1, the age/elevation relationship is confirmed by the crater counts on patch 32, indicating a resurfacing event about 3.66 Ga ago.

This (3.66 Ga) is roughly the upper limit of the overall lowland age and is related to a constant height everywhere, which has been originally mapped as the Vastitas Borealis Formation grouping four morphologic end members (Scott and Tanaka, 1986; Greeley and Guest, 1987; Tanaka and Scott, 1987). The lower–most region of the Chryse basin appears to be the youngest unit in that zone and is represented by a variety of units all resembling remaining flow features (lower parts of the channel systems) and other channel related units. On the basis of Viking imagery, resurfacing activity has not affected the Chryse region.

14.1.3. The Geology of the Utopia Basin and its Vicinity (Zone 2)

As the Chryse basin, the Utopia basin is also believed to be of impact origin and appears relative circular, about 3200 km wide and about 1 – 3 km deep. In both cases, rim features are not visible. The gravity anomaly maps for these two basins are very different. While the Utopia basin is similar to Isidis, Hellas and Argyre, and reveal typical high amplitudes indicating the general gravity feature of mascons, the anomaly of Chryse is not very distinct (Yuan *et al.*, 2001). The Utopia Basin is bounded by the crustal dichotomy to the south and west. Zone 2 includes, asides from the Utopia basin, the Isidis impact structure to the southwest, interrupting the dichotomy boundary followed westwards by the volcanic province Syrtis Major Planum. From the west, extensive volcanic flow units related to Elysium Mons (mapped here as *Elysium and Tinjar unit 1 and 2*) cover a huge amount of the Utopia basin area (Fig. 14.2). In Chapters 14.2 and 14.3, the highland–lowland

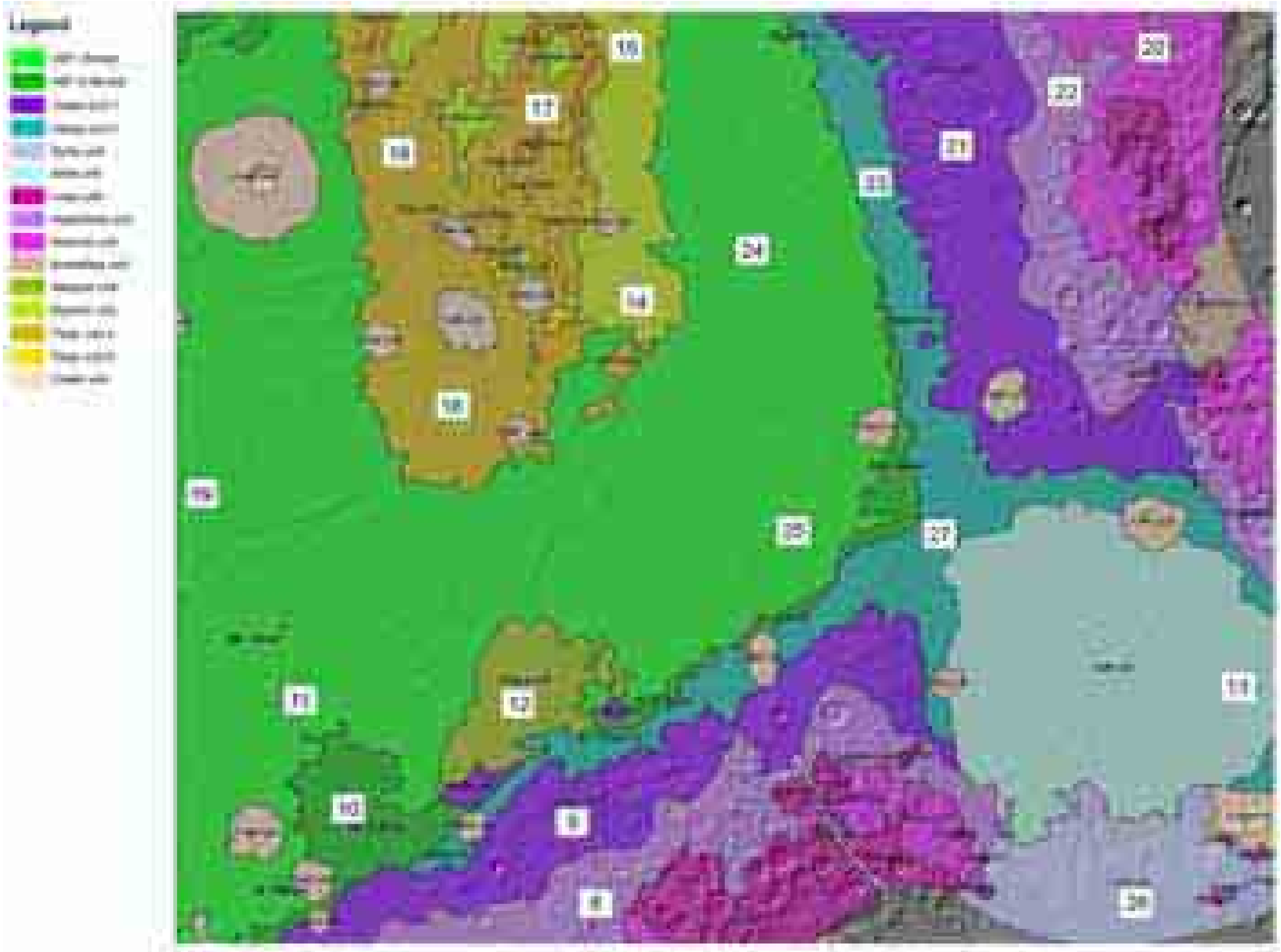

Figure 14.2.: The geologic map of the Utopia basin and its vicinity as mapped by Tanaka *et al.* (2005) and numbered patches to indicate their locations. Here, Zone 2 is given. The results of the crater size–frequency distribution measurements are given in Table 14.1.

boundary as well as aspects of the Utopia Planitia region will be discussed in detail.

The broadest and central area of the Utopia basin is part of the global Borealis province, which includes Vastitas Borealis, Planum Boreum, Utopia and Acidalia Planitiae. The Utopia basin defines two units (*Utopia 1 and 2 unit*) characterizing the southern, western and part of the eastern margin of Utopia Planitia, around most of Isidis Planitia and in parts of southern Elysium Planitia. Both units slope gently away from the highland margin. While Utopia 1 unit (closer to the highland margin) forms lowland plains deposits with irregular depressions, scarps many tens of kilometers long, and pancake domes, the lower parts of the Utopia 2 unit are marked by kilometer-sized knobs and mesas as well as depressions. These morphologies indicate erosion, transport and deposition of clastic material. Alongside, Isidis Planitia and Syrtis Major Planum are situated on the dichotomy boundary. Utopia 2 unit connects the Utopia and Isidis basins.

The *Isidis unit*, making up almost the entire Isidis basin plains, is marked by linear and arcuate ridges as well as chains of pitted cones, hundreds of meters wide, and wrinkle ridges. The basin plain is slightly tilted, with a height difference of about 300 m between the northeastern edge and the lower southwestern margin. The *Syrtis unit* covers the lower margin of Syrtis Major Planum. Flow tongues are visible in the east, including two 200 km long and roughly 30 km wide ridges with a discontinuous narrow depression along the crest. Northwards, the *Astapus unit* is separated from the global northern lowland outlining the Vastitas unit, due to its complex kilometer–scale irregular pits, grooves and ridges.

Besides the Syrtis Major volcanic province, the Elysium rise and flow features delineating units are found in this zone. The *Elysium unit* consists of extensive tongue–shaped flows, the volcanic edifices Elysium Mons, Hecates Tholus, and Albor Tholus, and their surroundings. Flows extending more than 2000 km into Utopia Planitia are separated from the Elysium unit, which is made up of the volcanic shield flows that extend from the vents, as dictated by the morphology of the region. *Tinjar a and b units* are flows typically emanating from mostly northwest–trending fissures and troughs of the Elysium Fossae. Tinjar b unit outlines broad, irregular channel systems of Granicus, Tinjar, Apsus and Hrad Valles, which most likely resulted from magma/volatile interaction and subsequent degradation. Highland units are present in Nepenthes, Noachis, and Lybia units around the Utopia basin. These units comprises heavily cratered highland units (*Noachis unit*), grading into dense knobs, mesas and local depressions (*Nepenthes unit*) to smooth, gently undulating plains (*Utopia 1 and 2 unit*). Mass–wasting is the major contributor to the modification of the circum–Utopia highland-lowland boundary (Skinner *et al.*, 2004).

14.1.4. The Zone–2 Chrono–Stratigraphy

In this zone, 19 patches, representing the geologic units and on which the crater size–frequency distributions were measured, are shown in Fig. 14.2. Imagery and crater size–frequency distributions are shown in Appendix A. The ages and dimensions are given in Tab. 14.1. Crater counts on patch no. 13 representing the Isidis floor unit give an age of about 3.4 Ga, while the basin itself originated at about 4 Ga ago (Table 13.3). Nili and Meroe Patera most likely fed the volcanic province Syrtis Major Planum. Their calderas have an age of 3.73 Ga with a resurfacing event ending 2.5 Ga ago and will be discussed in detail in Chapter 15.3. Here, the crater counts on the patch representing this region (No. 26) indicate an age of about 3.57 Ga, which is close to the latest stage activity of other Paterae volcanic constructs. The oldest surface age in this zone is again found in the Noachis unit (No. 20), that is the heavily cratered highland unit with an age of about 4 Ga.

Following a profile line roughly along the 120°E–meridian (starting with patch no. 20) the surface age gradually decreases with de-

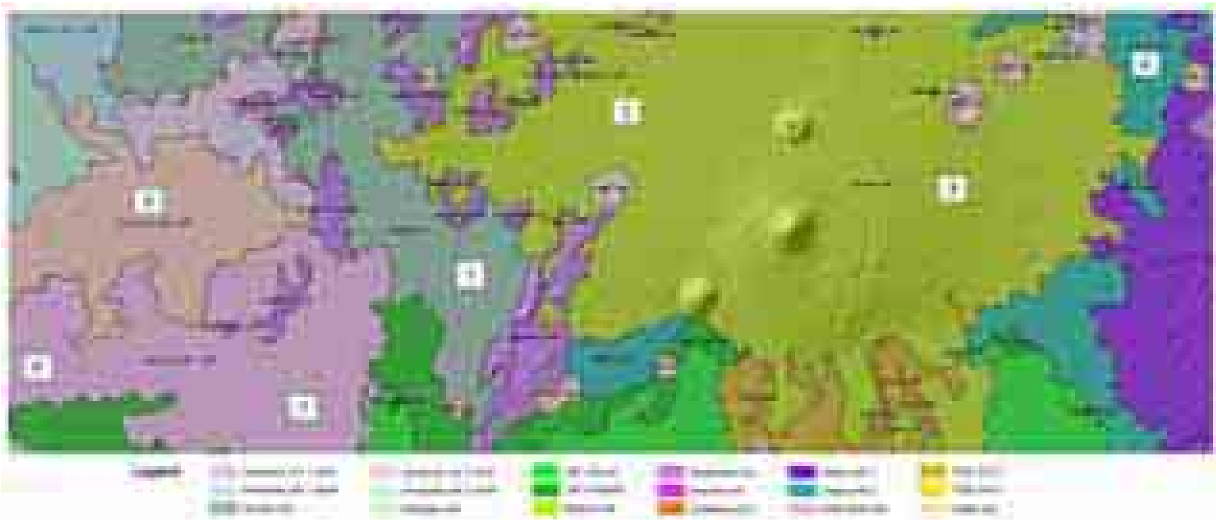

Figure 14.3.: The geologic map of the Elysium volcanic province and Amazonis Planitia as mapped by Tanaka *et al.* (2005) and numbered patches, to indicate their locations. Here, Zone 3 is given. The results of the crater size–frequency distribution measurements are given in table 14.1.

creasing elevation as has been observed in similar morphologic situations in the Chryse region. In Zone 2, the Vastitas Borealis Formation surface ages are the youngest of the investigated patches at about 2.8 Ga. The units related to possible rim parts of the Utopia basin, represented by patches east and west of the Isidis basin (Utopia unit 1, No. 09 and 21), appear to be slightly older at the eastern flank ($\sim$ 3.75 Ga) compared to the 3.65 Ga at the western flank. The outline of Utopia unit 2 is supposed to define a morphologically uniform unit (No. 27 and 23), but the surface ages determined for various patches, representing Utopia unit 1, appear to better fit the surrounding unit ages rather than being homogeneous within this unit. A detailed investigation to understand its evolution as a single surface unit is needed and will be discussed for the western Utopia "rim" unit in Chapter 14.2. All patches (No. 8, 9, (10), 11, 12) resemble units, which also will be discussed in Chapter 14.2, but here they all appear to have an age of 3.65 Ga.

Following the profile line ($\sim$ 120°E), patches representing the Elysium and Tinjar units, which have been interpreted as lava flows, erupted at the flanks of Elysium Mons. Ages of about 3.55 Ga have been measured, but most crater size–frequency distributions indicate that these units suffered a resurfacing episode, which ended about 3.3 Ga ago. During this episode, craters smaller than 3 kilometers in diameter have been erased. Similar ages are found in Zone 3, where similar morphologic units are classified.

In general, when translating the absolute surface ages described here (Tab. 14.1) to geologic epochs (Fig. 5.1), the origin of most of the surfaces represented by the patches in zone 1 and 2 are of Hesperian age except the highland units (Noachian age). Some of the units represented by patches (e.g. no. 19, 23, 24 and maybe even 25) are the youngest in Zone 2, are roughly 2.9 Ga old and considered of Early Amazonian age.

14.1.5. The Elysium Volcanic Province and Amazonis Planitia (Zone 3) – Geology and Chrono–Stratigraphy

The third zone of interest includes the volcanic province Elysium and surrounding plains units (Fig. 14.3). Three volcanoes, Elysium

Mons, Hecates Tholus and Albor Tholus as well as other local sources constituting this region, cover a rather large area of the northern lowlands with volcanic shield flows (see Chapter 15.2). The region lying to the west, between the Tharsis and Elysium rises, consists of Amazonis and Arcadia Planitiae. Amazonis Planitia has been the type region for the youngest of the Martian epochs. These extremely flat regional plains show some subtle, sinuous channels and are sparsely cratered (*Amazonis 2 north unit*). *Amazonis 2 south unit* consists of a sequence of lobate flows that are broad, long, planar, gently sloping and believed to be the result of voluminous lava flows in both units. *Amazonis 1 north and south units* are more rugged, consisting of material that is possibly lava or pyroclastic debris flows. Arcadia Planitia outlined as the *Arcadia unit* is more bumpy in its appearance and shows knobs organized in circular rings, resembling buried crater rims.

The volcanic units represented by patches no. 2 and 3 resemble volcanic flanks of the Elysium rise and give an age of about 3.6 Ga. A similar age is found for patch no. 4 (mapped as Utopia unit 2), which covers part of the plains unit discussed in relation to the Athabasca Valles. In these Athabasca Valles plains units, the same age of 3.66 Ga has been found in our earlier investigations (see Chapter 12, Werner *et al.* (2003b) and Murray *et al.* (2005)) and confirms the crater size–frequency distribution measurements in this study.

Patches representing units in the Amazonis Planitia, the western lowland vicinity of Olympus Mons, indicate ages of Middle to Late Amazonian (No. 5 and 6). While patch no. 7 resembles the same unit as patch no. 6 (Amazonis unit 1 north), it appears to be much older ($\sim$3.35 Ga). In a separate measurement across the entire Amazonis Planitia, the classification of surface morphology correlated to different surface age units is observed (for the crater size–frequency distribution see Chapter 17). Strong resurfacing visible in the eastern part of Amazonis Planitia (close to the Olympus Mons Aureole) might require a remapping of earlier attempts, which described Amazonis Planitia as a wide homogeneous plan. The Arcadia unit represented by patch no. 1 appears to have an overall surface age of about 3.55 Ga.

14.1.6. Between Alba Patera and the North Pole (Zone 4) – Geology and Chrono–Stratigraphy

The northern periphery of the Tharsis region includes the broad volcanic edifice Alba Patera and its foothills, *Alba 1 and 2 units.* Alba 1 unit forms the northern part of the Alba Patera shield and comprises tens of kilometers wide and hundreds of kilometers long well defined sinuous flows. On the other hand, the Alba 2 unit appears more smooth due to flat lying deposits, most likely volcanic and atmospheric deposition (Fig. A.12).

Four patches cover a profile line between Alba Patera and the northern polar ice cap, roughly following the 270°E meridian, and making up the last zone discussed here. Again, the selected units follow the gentle slope down to the northern lowland average elevation. Ages based on the crater size–frequency distributions for patches no. 42, 43, 44, and 45 indicate a surface age of about 3.6 Ga. There is no gradual change in age coinciding with the observed elevation level. A surface age of 3.37 Ga, obtained from crater measurements closest to Alba Patera (patch no. 42) is the youngest. Morphology and ages between the pole and Alba Patera do not follow the typical highland–lowland boundary characteristics. It is most unlikely that similar geologic processes have acted to form this region compared to the dichotomy sector. While units between – 30°E to about 145°E are characterized by the transition between old Noachian heavily cratered highland terrain to Hesperian–aged lowland units, the cliff–like dichotomy boundary characteristics (if ever existed) of the other hemisphere are obscured or fully covered by volcanic (or other resurfacing) activity. The gradual rejuvenation of the observed surface ages is clearly represented by measured patches and will be discussed in de-

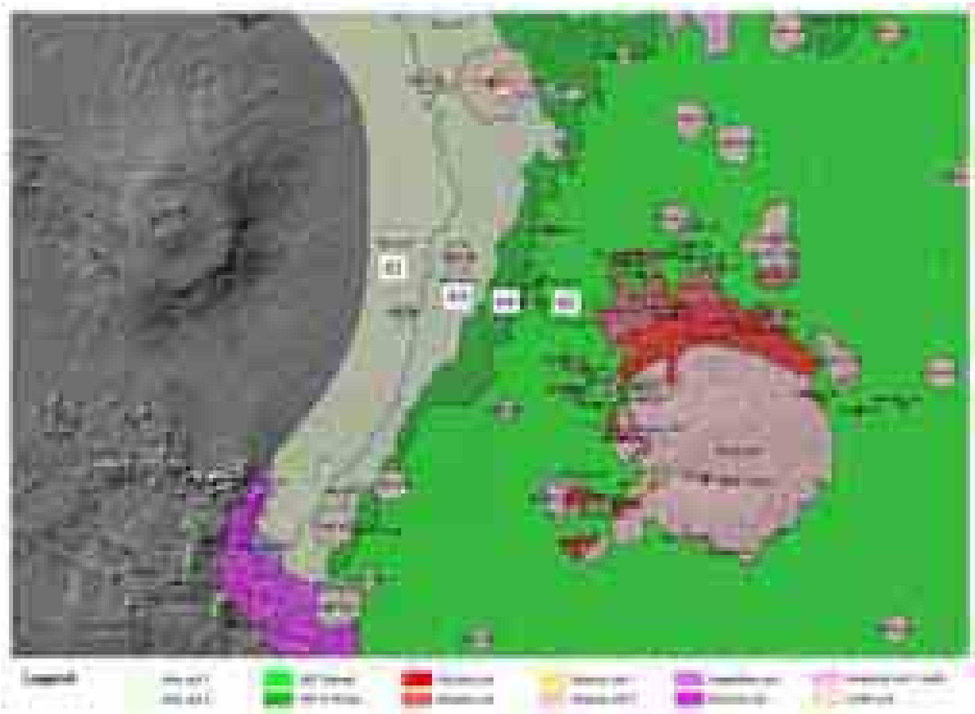

Figure 14.4.: The geologic map between Alba Patera and the North Pole as mapped by Tanaka *et al.* (2005) and numbered patches, to indicate their locations. Here, Zone 4 is given. The results of the crater size–frequency distribution measurements are given in table 14.1.

tail for the sector between – 30°E to about 90°E (Chapter 14.2).

14.1.7. The Viking–Based Chronostratigraphy of the Northern Lowlands, Summary

In the Chryse region, the 4 Ga ages are the oldest found in the highland units, which are heavily cratered with occurrences of small–scale resurfacing. The Chryse inner slope ages range between 3.8 and 3.3 Ga and tend to become gradually younger towards topographic lows. The units belonging to outflow channels have formed before 3.55 Ga ago. The units in continuation of flood plains appear slightly younger. Generally, the Vastitas Borealis Formation (entire plains) is about the same age (3.5 to 3.6 Ga). The lava unit (Lunae Planum) has been formed until 3.5 Ga ago. Nevertheless, many mapped units (mainly outlined topographically) are not homogeneous in age, which is supported by the morphologic diversity of those units.

The Utopia basin and its vicinity indicate similar ages. The bounding highland plains are about 4 Ga old. As in the Chryse region, the Utopia floor age ranges between 3.5 and 3.6 Ga, with older slope units (about 3.75 Ga). Again, a gradual decrease in ages towards topographic lows is observed, with a minimum age of about 3 Ga. Volcanic flows and phreato–magmatic activity (Elysium flank flow units) occurred about 3.5 Ga ago followed by a later phase between 3.4 and 3.1 Ga. The Syrtis Major flank measurements indicate a similar age of 3.55 Ga, while the surface of Isidis Planitia is slightly younger (3.45 Ga; correlating with low topography).

The plains around Elysium are partly type units for the youngest epochs of Martian history. The Elysium flanks and surrounding plains (Arcadia) are about 3.5 to 3.6 Ga old, Results of the Crater Size Frequency Measurements

#	Geologic Unit	Area	Dmin	Dmax	N_{total}	N_{cum}(1km)	Age in Ga*
Results of the Crater Size Frequency Measurements in Zone 1							
28	Simud unit	50726.2	1.0	7	32	3.68e-3	3.58
29	VBF m Boreal	52994.8	1.2	17	35	2.88e-3	3.51
30	Chryse unit 2	36427.9	1.0	17	30	6.05e-3	3.69
31	Chryse unit 4	45069.9	.9	17	55	3.60e-3/1.79e-3+	3.58/3.25+
32	Chryse unit 1	51014.5	.6	50	102	7.93e-3/4.73e-3+	3.75/3.64+
33	Chryse unit 1	48678.8	1.1	20	91	1.29e-2	3.83
34	Lunae unit	27171.1	.8	12	69	2.80e-3	3.50
35	Chryse unit 2	56505.1	.9	17	74	2.46e-3	3.45
36	VBF i Boreal	74655.6	1.0	25	58	3.75e-3	3.59
37	Noachis unit	29945.0	.9	35	121	2.99e-2	3.97
38	Chryse unit 2	15803.8	.9	10	40	8.61e-3	3.76
39	Chryse unit 1	20638.5	1.0	13	39	5.03e-3	3.66
40	Chryse unit 3	56970.1	.9	17	80	3.33e-3	3.55
41	Chryse unit 1	54653.5	1.0	20	69	4.07e-3	3.61
46	VBF i Boreal	121418.3	.6	25	152	2.73e-3	3.49
47	Noachis unit	78954.8	.8	70	168	4.83e-2/1.82e-2+	4.04/3.89+
Results of the Crater Size Frequency Measurements in Zone 2							
08	Nepenthes unit	53657.1	.8	25	67	4.81e-3	3.65
09	Utopia unit 1	48843.0	1.2	25	61	4.93e-3	3.65
11	VBF i Boreal	59549.1	1.7	17	26	4.28e-3	3.62
12	Astapus unit	87457.7	1.3	10	54	4.17e-3	3.61
13	Isidis unit	24149.6	1.1	12	27	2.37e-3	3.43
14	Elysium unit	308995.3	.5	9	84	2.95e-3/1.44e-3+	3.52/2.92+
15	Elysium unit	36978.4	.6	5	51	2.95e-3/1.33e-3+	3.52/2.71+
16	Tinjar unit a	81279.5	1.1	20	34	3.43e-3	3.56
17	Tinjar unit a	55842.5	1.0	12	45	4.24e-3/2.00e-3+	3.62 /3.34+
18	Tinjar unit a	133574.7	1.4	9	24	1.98e-3	3.34
19	VBF i Boreal	229742.8	1.7	17	31	1.38e-3	2.82
20	Noachis unit	21906.1	1.1	25	69	5.07e-2/2.97e-2+	4.05/3.97+
21	Utopia unit 1	30605.7	.8	13	111	8.76e-3	3.76
22	Nepenthes unit	25494.6	1.0	13	45	1.22e-2/3.21e-3+	3.82/3.54+
23	Utopia unit 2	31268.1	.8	17	45	1.47e-3	2.97
24	VBF i Boreal	39105.5	.6	7	74	1.42e-3	2.88
25	VBF i Boreal	25959.0	.7	8	74	4.38e-3/2.02e-3+	3.43/3.35+
26	Syrtis unit	84612.8	.8	10	182	3.51e-3	3.57
27	Utopia unit 2	75724.3	.9	35	57	3.66e-3	3.58
Results of the Crater Size Frequency Measurements in Zone 3							
01	Arcadia unit	129442.5	1.4	20	43	3.28e-3	3.55
02	Elysium unit	133562.1	.6	20	226	4.84e-3	3.65
03	Elysium unit	130913.1	.035	35	126	2.88e-3	3.51
04	Utopia unit 2	61866.9	.9	10	90	5.21e-3	3.66
05	Amazonis unit 2 north	230947.7	.5	20	20	7.09e-4/5.30e-4	1.45 or 1.1
06	Amazonis unit 1 north	110484.1	1.1	13	11	2.09e-4/1.41e-4+	0.95/.29+
07	Amazonis unit 1 north	178776.8	2.0	17	16	1.93e-3	3.32
Results of the Crater Size Frequency Measurements in Zone 4							
42	Alba unit 1	127810.7	1.3	20	62	2.10e-3	3.37
43	Alba unit 2	139594.4	.8	30	57	2.95e-3	3.52
44	VBF m Boreal	44302.2	1.4	13	15	4.73e-3	3.64
45	VBF i Boreal	86840.6	1.5	60	29	3.31e-3	3.55

+ treatment as described in Chapt. 9.1   * billion years

Table 14.1.: This table lists the absolute ages and other statistical parameters for the patches shown in Fig. 14.1 to A.12. All measured crater size–frequency distributions for all patches, including the fit of the crater production function and the resulting age, are shown in Appendix A.

while the youngest plains unit, Amazonis Planitia, cannot be treated homogeneous in age and morphology. We found ages ranging between 3.3 Ga and 400 Ma even if mapped as a single unit.

Between the North Pole and Alba Patera, younger ages in topographic lows (3.64 and 3.55 Ga) are found. While the Alba Patera construct possibly hides the dichotomy boundary, the typical gradual age change towards lows is not observed, but two episodes of volcanism occur (3.37 and 3.52 Ga).

In general, the northern lowland units (in all zones) range between 3.6 Ga and 3.5 Ga, while decreasing age down–slope towards topographic lows are observed. The typical morphology of the dichotomy boundary has been partly covered/erased by volcanic, fluvial, or cratering processes (reflected in ages), while the fluvial activity could not cause resurfacing as effectively as the volcanic process. Usually the morphology and ages correlate well and the new mapping attempt to assign the lowlands as a generally uniform (mapped as Borealis inner unit) unit appears to be valid. Nevertheless, it is unlikely that the lowland surface formation occurred during a single event. Elevation levels and morphology are not necessarily related. Therefore, mapping following the elevation level is misleading, especially in units composed of multiple geological processes.

14.2. The Highland–Lowland Dichotomy Boundary between –30°W and 270°W

The dichotomy boundary is defined as separating the heavily cratered highlands and the northern lowlands observed in Viking imagery. The origin of the Martian dichotomy is unclear, but it has been argued that it was formed by a number of large impacts (e.g. Wilhelms and Squyres, 1984; Frey and Schultz, 1988; McGill, 1989) or internal dynamics (e.g. Wise *et al.*, 1979a; McGill and Dimitriou, 1990; Sleep, 1994; Zhong and Zuber, 2001; Zuber, 2001). MOLA–topography data have revealed a difference in elevation between the northern and southern hemisphere of about five kilometers (e.g. Smith *et al.*, 1998). Especially in the eastern hemisphere (Terrae Sabaea and Cimmeria), the dichotomy boundary is characterized by a prominent scarp and possible extensional and compressional features (Watters, 2003), while other parts in the western hemisphere appear to have gentle slopes (Terra Arabia).

If the dichotomy boundary had once been a global band, in some localities the characteristically steep escarpment is covered by two large volcanic provinces (the Tharsis and Elysium region) and a few impact structures (e.g. Isidis Planitia) or impact basin suspects (e.g. Chryse Planitia). Here the boundary section between Chryse Planitia and Isidis Planitia (30°W to 270°W, and 17.5°N to 60°N) is investigated in detail. An overview is given in Fig. 14.5.

The investigated area is bordered by the large outflow channels in the west. The line of the steep escarpment morphology is interrupted by the Isidis impact basin and the volcanic Syrtis Major complex. The boundary continues almost halfway around Mars in its typical appearance. It is partly covered by the enigmatic Medusae Fossae Formation, which is interpreted as pyroclastic deposits of unknown origin (Greeley and Guest, 1987) or as remnant of ancient polar deposits (Schultz and Lutz, 1988), as discussed later in Chapter 14.4.

Compared to the typically steep escarpments in Terra Cimmeria, the Arabia Terra region appears fairly reliefless. Arabia Terra is associated with a low thermal inertia, which is thought to be due to fine–grained material, centered on 20°N and 330°W (Palluconi and Kieffer, 1981). Spectral information (gathered by the Thermal Emission Spectrometer onboard Mars Global Surveyor) indicated a hematite–rich surface (Christensen *et al.*, 2000). The Neutron spectrometer (onboard 2001 Mars Odyssey) found a hydrogen–enriched (possible water/ice–enriched) region (Feldman *et al.*, 2002; Mitrofanov *et al.*, 2002; Boynton *et al.*, 2002). Basilevsky *et al.* (2003) attributed the decreased epithermal neutrons in the Arabia Terra region (and also in the Medusae Fossae region southwest of Olympus Mons) to chemically bound water, but we found no clear relation to any surface geology (Basilevsky *et al.*, 2004, revealed by MOC–NA imagery). Nevertheless, a region in Arabia Terra close to the equator, Meridiani Planum, has been selected as the MER Opportunity landing site. The finding of so–called blueberry spherules are interpreted as the source of the orbital detection of hematite (Squyres *et al.*, 2004a). Additionally, the formation of jarosite, a hydroxide sulfate mineral found at the landing site (Klingelhöfer *et al.*, 2004) and the deposition scenario requires the presence of liquid water (Squyres *et al.*, 2004a).

Theoretical modeling based on thermal inertia and albedo suggest ground ice might be more stable than elsewhere at the same latitudes, even if obliquity changes are considered (Mellon and Jakosky, 1993, 1995). Compared to other Noachian–aged areas on Mars, Arabia Terra is almost devoid of so–called valley networks. They are believed to be drainage systems, cited as evidence for a formerly wetter and warmer Mars. Two genetic processes for the formation of valley networks are discussed, both involving fluvial activity: surface runoff and water sapping (Mars Channel Working Group, 1983). The lack of networks in Arabia Terra and circumferential Hellas is correlated to the low–lying nature of these areas compared to the generally higher elevation of Noachian units, with a separation elevation of about 1000 meters (summarized by Carr, 1996).

14.2.1. Geology

Our detailed investigation was initiated because of the varying general topography of the dichotomy boundary in Arabia, Sabaea, and Cimmeria Terrae. The transition between both surface morphologies discussed here are separated not causatively but coincidentally by the most prominent impact structure of the northern lowlands, Lyot (roughly centered at the 330°W longitude). A possibly related separation is found in the region of Deuteronilus Mensae. This separation is visible in the derived bouguer anomaly and calculated crustal thickness (Neumann *et al.*, 2004), which was already pointed out by Janle (1983). The heavily cratered highlands are nearly everywhere thicker than 60 km, while the lowland crust has been derived to range between 20 to 40 km. West of 330°W longitude, the crustal–thickness change correlates with the topography, while the crustal thickness of the Arabia Terra region relates to the lowlands, while the surficial appearance is similar to typical highland morphology (heavily cratered).

The existence of outflow channels in the Chryse region demanded a sink region. To find the sink, the search was focused on the smooth northern–lowland plains. Large polygonally–fractured ground (McGill, 1985, for further discussion see Chap. 14.3), mottled plains, patterned ground, terraces and stepped massifs, backflow features, and layered sediments are indicators for a possible, temporary, ancient Martian ocean (Carr, 1996). Shoreline candidates, separating smooth lowland areas from highland units, were traced along the dichotomy boundary (Parker *et al.*, 1989). The key area of this investigation has been Deuteronilus Mensae, exhibiting both gradational (Rossbacher, 1985) and fretted terrain (Sharp, 1973) boundary types. Westward, the boundary is defined by gradational material and to the east by fretted terrain.

Typical of fretted terrain are uplands dissected into a complex pattern with steep escarpments separating upland remnants from low–lying plains. Debris flows (lobate debris aprons) extend about 20 km away from the escarpments. Examples can be found in the northern hemisphere in the Deuteronilus-Proteronilus Mensae region (280 – 360 °W) in the Mareotis Fossae region (50 – 90 °W), Acheron Fossae regions (130 – 140 °W), and in the Phlegra Montes (180 – 200 °W), but also around rim massifs of Hellas and Argyre basin and smaller crater rims. Their creeping appearance is attributed to entrained ice, but this has not been proven (Squyres, 1979; Lucchitta, 1984). These features are thought to be indicators for an earlier wetter Mars (Squyres, 1979).

The goal of this investigation is to attribute ages to the characteristic dichotomy units and to figure out if the different occurrence in topography and crustal structure is supported by measured crater–size frequencies and derived absolute ages. Many interpretations for the evolution of the dichotomy escarpment are focused on the eastern part, such as continental rifting, thrust faulting, or breakup margins (e.g. McGill and Dimitriou, 1990; Sleep, 1994). The western parts are thought to be subduction zones (Sleep, 1994). Therefore, the dichotomy–related units were mapped according to Tanaka *et al.* (2003) and their revised version (Tanaka et al., 2004, pers.comm.). The unit delineation for the age determination is based on Mars Global Surveyor data, which are the MOLA–topography and MOC-WA imagery. Mainly topographic data, but also morphologic and albedo aspects, were considered to outline the geologic units on the global Viking MDIM 2.1 photomosaic. Following the unit description and annotation of Tanaka *et al.* (2003), a brief overview for the unit appearances in the investigation area is given below (Fig. 14.5):

Highland material, undivided (unit HNu): typical ancient highland terrain marked by large craters, isolated depressions, ridges, scarps, and troughs. It can be interpreted as a mixture of volcanic and sedimentary material, showing a long resurfacing history of cratering, erosion, deposition and tectonic deformation. Assigned under *B*, an area around Nili Fossae has been investigated. Morphologically, it repeats knobby–unit characteristics, but is influenced by the Isidis basin and the volcanic construct Syrtis Major.

Knobby unit (unit HNk): consists of knobs and mesas, which are dissected highland remnants with steep escarpments, separating upland remnants from low–lying plains along the highland–lowland boundary. Processes such as fracturing and collapse due to basal sapping of volatiles and mass-wasted debris are likely.

Boundary plains unit 1 and 2 (unit Hb1 and Hb2): Both belong to the northern lowland plains in the map of Tanaka *et al.* (2003). Boundary plains unit 1 is considered to be the oldest exposed northern–plains unit adjacent to older highland and plateau materials. It is closely related to the steep escarpment of the dichotomy boundary itself, gently down–sloping away, and is missing in the northwestern Arabia Terra region. Ridges, scattered knobs up to a few hundreds of meters high, indicate volatile-assisted slope processes. Boundary plains unit 2 is chiefly identified as smooth plains material, marked by wrinkle ridges, coalescing with the base of boundary plains unit 1 if present. Northwest of the Arabia Terra region, the unit embays highland material (unit HNu). The fretted trough floors of Deuteronilus Mensae form a continuous surface with the unit Hb2 surface in northwestern Arabia, where they are not covered by apron material. *Apron material* (unit Aa) includes smooth, sloping deposits along the base of high-standing scarps of Deuteronilus Mensae (lobate debris aprons).

Younger chaos material (unit Act) is represented in a smaller area at the boundary of this investigation area. It usually occupies depressions tens to hundreds of kilometers across and tens to a few hundreds of meters deep in the Acidalia Mensa and includes polygonal fractures, knobs, and irregular scarps.

The majority of the northern lowlands, the Vastitas Borealis Formation, is mapped here as *hummocky member* (unit AHvh). This unit is characterized by numerous low hillocks, arcuate ridges and patches of grooves hundreds of meters wide forming networks of polygons several kilometers (see Chap. 14.3). This unit may be an area where a standing body of water (ocean /mud ocean) has most affected the surface morphology.

We use crater–count results to revisit the earlier age interpretation and to understand if the surface ages yield any clues about different timing of the evolution of the eastern and western part of the dichotomy–boundary units discussed here.

14.2.2. Chronostratigraphy

The crater counts have been performed on Viking–MDIM–2 imagery, which remains the most convenient in terms of image contrast. The mosaic was reprojected in a Lambert–two–parallel projection and divided into eight sheets. Ages were determined for the individual units on different sheets. For some units crater–size frequencies vary from sheet to sheet and yielded slightly varied absolute ages (see Fig. 14.5). These age ranges can be caused by the individual timing of pertinent geological processes. Nevertheless, measuring ages on Viking imagery of relatively low resolution (231 m/pxl) does not permit a discussion of any resurfacing events acting on the removal of craters in the small–size range (less than about 1 kilometer in diameter). Craters smaller than 1 km in diameter will not be reliably detected due to the resolution limit. We do not rule out that resurfacing processes have modified the surfaces after their formation. For a better interpretation, the subresults (individual crater size–frequency distributions) were summed to get the size–frequency distributions and ages for the entire unit, summarized in Table 14.2. The individual results are given in Fig. 14.5 and will be discussed below.

Dichotomy Surface Ages

Unit	Area	N_{total}	N_{cum}(1km)	Age
HNu	1.91 10^6	3356	1.54e-2	3.86 Ga
HNk	1.35 10^6	1480	5.55e-3	3.68 Ga
Hb1	0.78 10^6	455	3.41e-3	3.56 Ga
Hb2	1.34 10^6	676	6.73e-3	3.73 Ga
Hb2			2.72e-3$^+$	3.49$^+$ Ga
AHvh	2.47 10^6	1746	2.07e-3	3.37 Ga
Aa	0.29 10^6	152	1.17e-2	3.82 Ga
			7.16e-3$^+$	3.73$^+$ Ga
Act	0.92 10^6	716	4.80e-3	3.65 Ga
B	0.13 10^6	151	1.01e-2	3.80 Ga
Lyot			2.22e-3	3.40 Ga

$^+$ treatment description see Chapt. 9.1

Table 14.2.: The absolute ages and other statistical parameters summed for all units. In this table the ages are given as an average age for the entire unit. In Fig.14.5, the individual results of the age determination are labeled. Unit boundaries, sheet boundaries and absolute ages measured sheetwise are labeled in Fig.14.5 and are discussed in the text.

Surface Ages at the Dichotomy Boundary: Ages found in this study area range between about 4 Ga and 3.1 Ga. In general, grading in age from old to young is correlated to an elevation change from the highlands, across the dichotomy towards the lowlands (in a south–to–north direction). The second general observation is a reduced age within a single geological unit in the western part compared to the the eastern parts.

The highland units assigned as HNu have been previously considered to consist of rock units that cannot be distinguished morphologically or stratigraphically in order to place them in the Noachian or Hesperian epoch. Our crater counts were performed on four sheets containing the HNu unit. They yield surface ages, which range between 3.98 Ga to 3.89 Ga. These Middle to Early Noachian ages are found elsewhere (see Chapters 14 and 13) and are in good agreement with an almost homogeneously formed highland plateau, where the surface forming processes are dominated by impact cratering. The crater size–frequency distribution measured close to the Isidis basin reveals the oldest surface age, followed by resurfacing reflecting an eventful history, since the impact basin formation. In the eastern part northward from the highland plateau, the escarpment foot is occupied by the knobby unit HNk, which is closely related to the highlands. It originated through dissection of highland plateau units. Here, we observe a broader age range between 3.83 Ga to 3.67 Ga. Areas measured closer to the escarpment appear older than those more distant from the cliff. Larger craters are still visible on the remaining blocks and mesas of the dissected highland plateau, while in the areas further away smooth lowland plains dominate the terrain. After summing all crater counts for this unit, the surface age of about 3.68 Ga is Early Hesperian, with the mesa surfaces

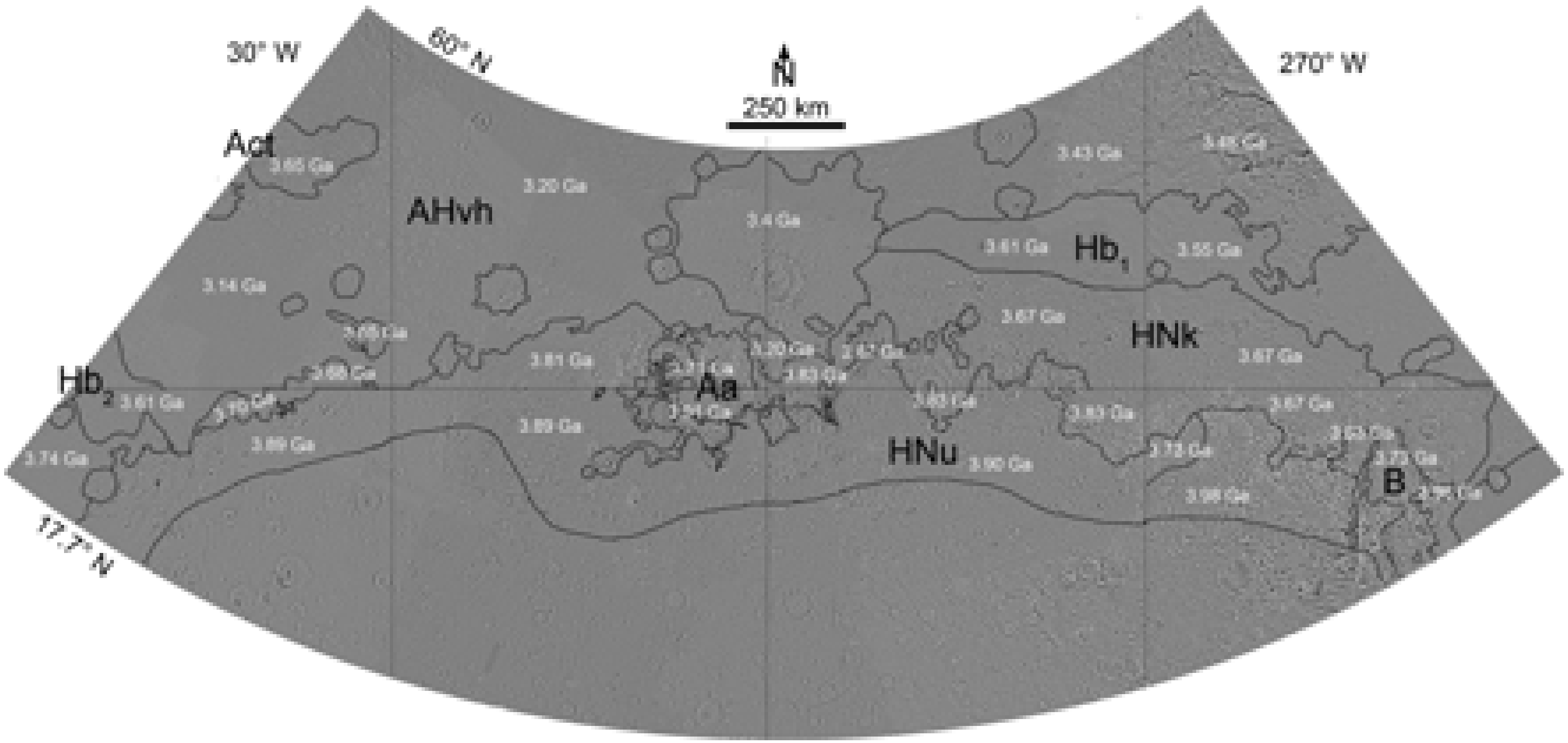

Figure 14.5.: The dichotomy boundary between 30°W to 270°W and 17.5°N to 60°N. Geologic units are delineated following Tanaka *et al.* (2003) on the basis of Viking and MOC–WA imagery and topographic information (MOLA). The huge area was split into eight sheets and ages were determined for each subset separately. The absolute ages (individual results of age determination for each subunit) obtained are labeled in the map for each subunit. Ages resulting for the entire geologic units (by summing the crater counts of the subsets respectively) are listed in Table 14.2.

surfaces Noachian in age. Earlier interpretations considered these units as Hesperian-Noachian, similar to the highland plateau surfaces.

Further north the geological unit considered as boundary unit 1 (Hb1) appears. Both morphologies making up the units Hb1 and HNk are not found in the western part of our investigation area. Here, the trend of younger surface ages towards topographic lows in the lowlands is apparent (as described earlier, Chapter 14). The surface age derived from crater counts is 3.56 Ga, deviating within the individually mapped units between 3.61 Ga and 3.55 Ga (Early to Late Hesperian). A slight absence of large craters is observed, a phenomenon that is known for other units in the Martian lowlands (see Chap. 14.3). The youngest age of 3.48 Ga, measured in the eastern part, is found in the mapped unit AHvh, which has been considered as Amazonian – Hesperian. Here, the largest variation between the western and eastern part of the investigation area is found (west of 330 °–meridian, the crater counts indicate a surface age of 3.2 to 3.14 Ga). Especially in the western part, a deviation from the measured crater size–frequency distribution compared to the crater production function is found in the larger crater–diameter range. This absence of large craters is found in the Acidalia (and Utopia) region and was confirmed by crater counts in units of this area, e. g. in units Hb1, AHvh, Act, which will be discussed in terms of surface and crater formation in the following chapter.

Impact crater or basin Lyot is of comparable age (3.4 Ga), as has been discussed in Chapter 13. The crater counts summed over the entire unit AHvh, representing the northern–lowland unit, yield a surface age of 3.37 Ga. Unit Act, Acidalia Colles (around 20°W and 50°N), is related in morphologic appearance more to the highland remnants, which is reflected in the surface age of 3.65 Ga as well. Earlier, this unit was considered Amazonian, but our age suggests an Early Hesperian age. Compared to the eastern part of the investigation area, only a single boundary unit (Hb2) is present. The ages for this unit range between 3.74 and 3.68 Ga, Late Noachian to Early Hesperian. The summed crater size–frequency distribution of the entire geologic unit gives a surface age of 3.73 Ga and an apparent major resurfacing event occurred before 3.53 Ga ago.

In the Deuteronilus region, assigned here as Aa, one obtains very old ages (see Table 14.2) if measuring all craters on mesas and the lower units together, but if just the lowland parts are considered, the age is as young as the lowland units west of Lyot (about 3.2 Ga).

Summary: The separation between the eastern and western part of the investigated dichotomy boundary area, indicated in morphology, topography and gravity anomalies, has been confirmed by our crater counts. Nevertheless, a convincing interpretation for the origin of these differently evolved boundary parts could not be found.

14.3. Giant Polygonal Trough Units in the Northern Lowlands

Utopia, Elysium, and Acidalia Planitiae (parts of the northern lowlands) are occupied by extensive areas of polygonal patterned terrain, so-called giant polygons. Originally, this polygonal fractured terrain was observed on the Mariner 9 B-frames (Mutch *et al.*, 1976) and revealed, accompanied by other morphologies, that large portions of the Martian surface have been formed by the action of water. Later, high–resolution Viking photographs resolved in greater detail locations and the morphology of the giant polygons. They consist of 200 to 800 meter wide steep–walled and flat–floored troughs, some tens of meters deep, and 5 to 30 km in diameter (Pechmann, 1980). They are distributed around 45°N, 15°W (southeastern Acidalia Planitia); 36°N, 255°W (northwestern Elysium Planitia); 49°N, 233°W (Utopia Planitia). These mid–latitude polygons differ mainly in scale from the permafrost–related polygonal pattern in the polar regions (Rossbacher and Judson, 1981).

Various hypotheses for their origin have been proposed, including thermal cooling and contraction in permafrost (Carr and Schaber, 1977; Carr *et al.*, 1976), desiccation of water–saturated sediments (Morris and Underwood, 1978), cooling of lava (Morris and Underwood, 1978; Masursky and Crabill, 1976; Carr *et al.*, 1976), or tectonic deformation (Mutch *et al.*, 1976; Carr *et al.*, 1976). Pechmann (1980) has shown that none of these terrestrial analogs would lead to a satisfactory description of the mechanisms and scales involved. McGill and Hills (1992) were able to explain the observed large size of the polygons and could account the stresses responsible for the polygon troughs by plate–bending and finite–element models, which indicate the shrinkage of desiccating sediments or cooling volcanics accompanied by differential compaction over buried topography. The giant polygonal pattern is accompanied by ring or double–ring like graben structures, which are assumed to be buried craters and have been used to estimate the thickness of the overburden (McGill, 1986; McGill and Hills, 1992). Another explanation for the origin of undulating surfaces and polygonal crack patterns of this size is based on formation through Rayleigh convection in rapidly emplaced water–rich sediments (Lane and Christensen, 2000). A third force, elastic rebound, which implies the relaxation of the northern Martian lowlands crust after huge water or ice bodies have disappeared, may have accompanied or driven the formation of these large crack patterns (Hiesinger and Head, 2000).

The discussion regarding how giant polygons have formed is linked to the question of did large standing bodies of water and/or catastrophic flood events exist in the past.

14.3.1. Geology

All three sites are located in the northern lowland plains of Mars. This plain assemblage, following the interpretation of Scott and Tanaka (1986) and Greeley and Guest (1987), was deposited in the Late Hesperian. Textural and albedo differences as well as morphologic characteristics have been used to map different members of the so-called Vastitas Borealis Formation. The giant polygon terrain occupies regions mapped as grooved member (Hvg), one of four members that resembles grooves and troughs forming curvilinear and polygonal patterns as much as 20 km wide (Tanaka *et al.*, 1992a, in later attempts modified to a single unit, Vastitas Borealis formation, (Tanaka *et al.*, 2003)). Pechmann (1980) described the geological environment of the three localities in detail and concluded that the polygonal troughs intersect units of all other Vastitas Borealis members, but appear to be similar in morphology at all localities. The age relation of troughs to superimposed craters indicates that the polygon formation occurred immediately after the deposition (McGill, 1986). Lucchitta *et al.* (1986) suggest that the material is of sedimentary origin and was deposited in a standing body of water, emphasizing the areal relation between topographic low regions in the northern plains, polygonal terrain and outflow channels. Carr (1986) describes the capability of the outflow channels to supply immense volumes of wet sediments to the lowland region. Crater counts indicate a coincidence between outflow events and origination of the polygonal terrain (Neukum and Hiller, 1981). The age determination of McGill (1986) indicated, that the channels, which might have fed the lowland region, were cut into a surface that is younger than the polygonal terrain.

Giant–Polygon Terrain Database: The investigation is based on geological mapping of the giant polygon units and measuring their crater size–frequency distribution based on the Viking–MDIM–2 global mosaic and MOLA–topographic information. In the case of the Utopia region, a mosaic made of 28 high-resolution Viking frames (orbit 430Bxx) with a pixel resolution of 15m was prepared. To cover the full range of crater sizes (in this case from 50 km down to 10 m), additional information

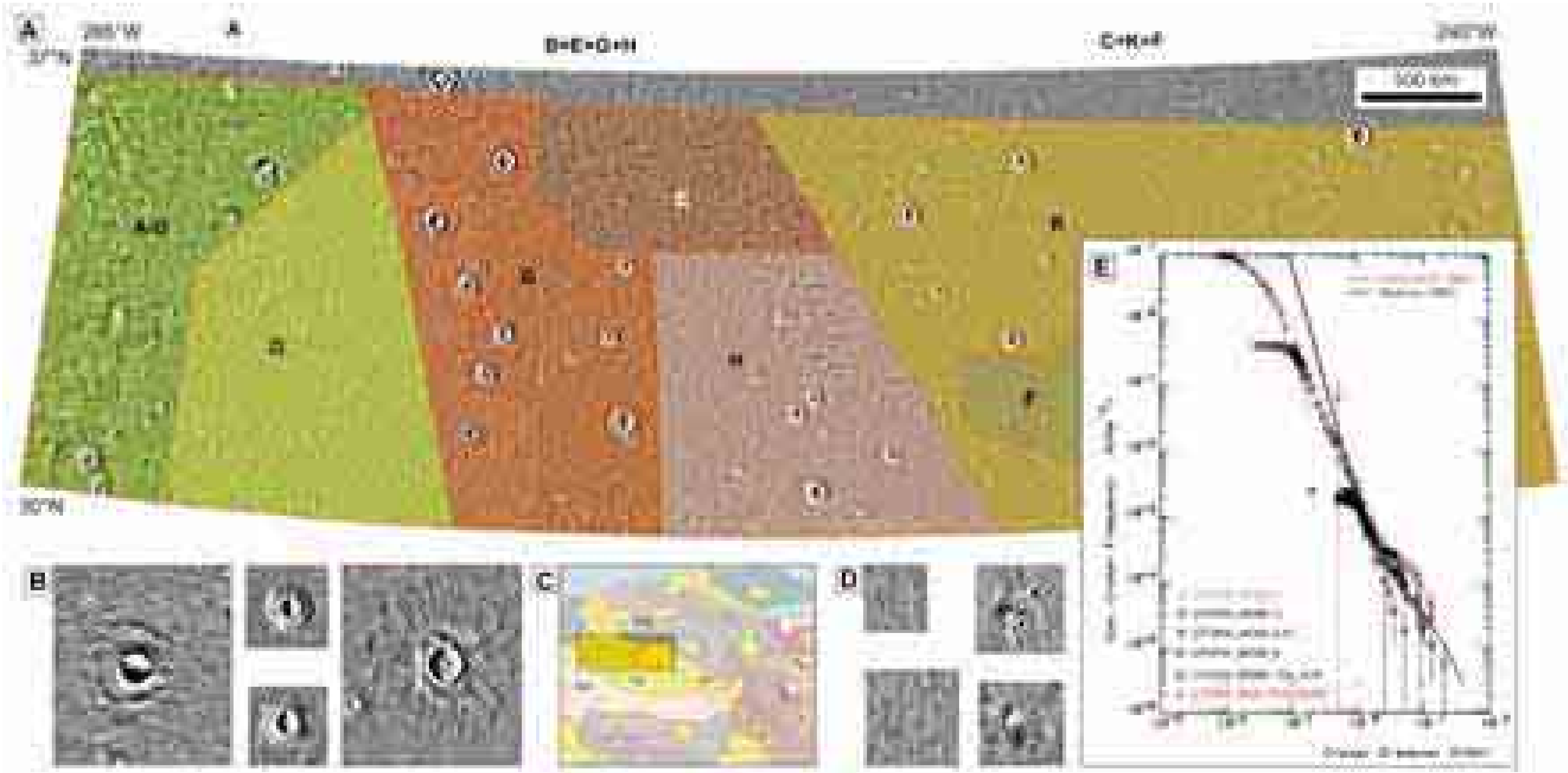

Figure 14.6.: Areas were selected (A) in the central part of the Utopia Planitia (C) according to their diverse crater morphology. Examples are given in (B). Parts of the areas of giant polygons are characterized by ring– or double–ringed graben features, as shown in subset (D). Evaluating the crater size–frequency distributions of these selected areas, a diversity of crater distributions especially in the large–size range is found (E). Few of large craters have been found.

were retrieved from two MOC–NA images M08/03489 (30.90°N, 113.28°E) and E04/02201 (32.66°N, 111.02°E), which superimpose the 15m-VIKING mosaic at a pixel resolution of 3.03m and 6.14m, respectively.

14.3.2. Crater Morphologies

The crater forms on Mars as in Utopia Planitia do largely vary and show a range of complex morphologies. Craters smaller than about 14 km appear bowl–shaped, like simple craters on the Moon or Mercury. A similar size–range for the transition from simple–to–complex interior crater morphology in the Martian lowland plains has been noted by Wood *et al.* (1978). In principle, central peak morphology is expected for craters larger than 5 km (Pike, 1980a), but has been observed for craters as small as 1.5 km in diameter in heavily cratered highland units (Mouginis-Mark, 1979). Craters larger than 15 km are not present in the investigated areas.

The ejecta morphology is slightly dominated by single– or double–lobed ramparts, so–called fluidized ejecta blankets that are believed to indicate the presence of volatiles (see Chapter 7.4, e. g. water ice or water in the subsurface (Carr *et al.*, 1977a)). A number of craters show ballistically emplaced ejecta, spreading outward over distances less than a crater diameter. For both groups, no clear diameter dependence is found. For a few of the larger craters, no ejecta are visible at the given image resolution, meaning they had been formed before the surrounding surface unit was emplaced. They appear "flooded" by later deposits. Examples are shown in Fig. 14.6 B and D.

Among the giant polygonal troughs, circular grabens with diameters between 8 km and 30 km can be found. These are believed to be fracture patterns of counterdrawing buried craters (Carr, 1981; McGill, 1986), yielding a regional cover thickness of about 600 m (McGill and Hills, 1992). These single– and double–ringed grabens are associated with slight topographic depressions seen in the MOLA topography (Buczkowski and McGill, 2002). Based on modeled graben spacing of double-ringed troughs, Buczkowski and Cooke (2004) suggested a cover thickness of 1–2 km. Additionally, the topographic data from MOLA revealed the presence of roughly circular basins in both the Martian highlands and lowlands, which are usually not associated with any structural feature in image data. These so–called Quasi-Circular Depressions are candidates for large, buried or deeply eroded impact structures (e.g. Frey *et al.*, 2002).

Crater Size–Frequency Distributions in the Utopia Region: Based on the Viking–MDIM–2 imagery, we performed new crater size–frequency measurements and determined ages in selected areas of the Utopia region, which cover polygonal terrain and surrounding units (Fig. 14.6 A and E). All crater size–frequency distributions of the selected units converge in the smaller crater diameter size range and give an age of 3.4 Ga. This plains age is observed in many measurements in other lowland regions and is also confirmed by the measurements of the crater size–frequency distribution in the 15m–Viking mosaic. A later resurfacing event is observed in that distribution, which is also supported by the crater counts on the MOC-NA image.

For the larger–crater diameter–size range (larger than 3 km), a variety of shapes for the crater distribution is observed in different units of Utopia, confirming earlier observations by McGill (1986). These all correlate with the presence of giant polygons and other surface structures, indicating resurfacing processes have been acting in a different manner. The diversity or deviation from the expected crater production function (Neukum *et al.*, 2001; Ivanov, 2001) for the larger–crater diameter–size range (larger than 3 km) most likely relies on different target properties or the geologic evolution of the area. A few of these units show an "excess" of larger craters in the crater size–frequency distribution (Fig. 14.6 A and E, Unit G). These units yield an age of 3.8 Ga. The measured small–size converging distri-

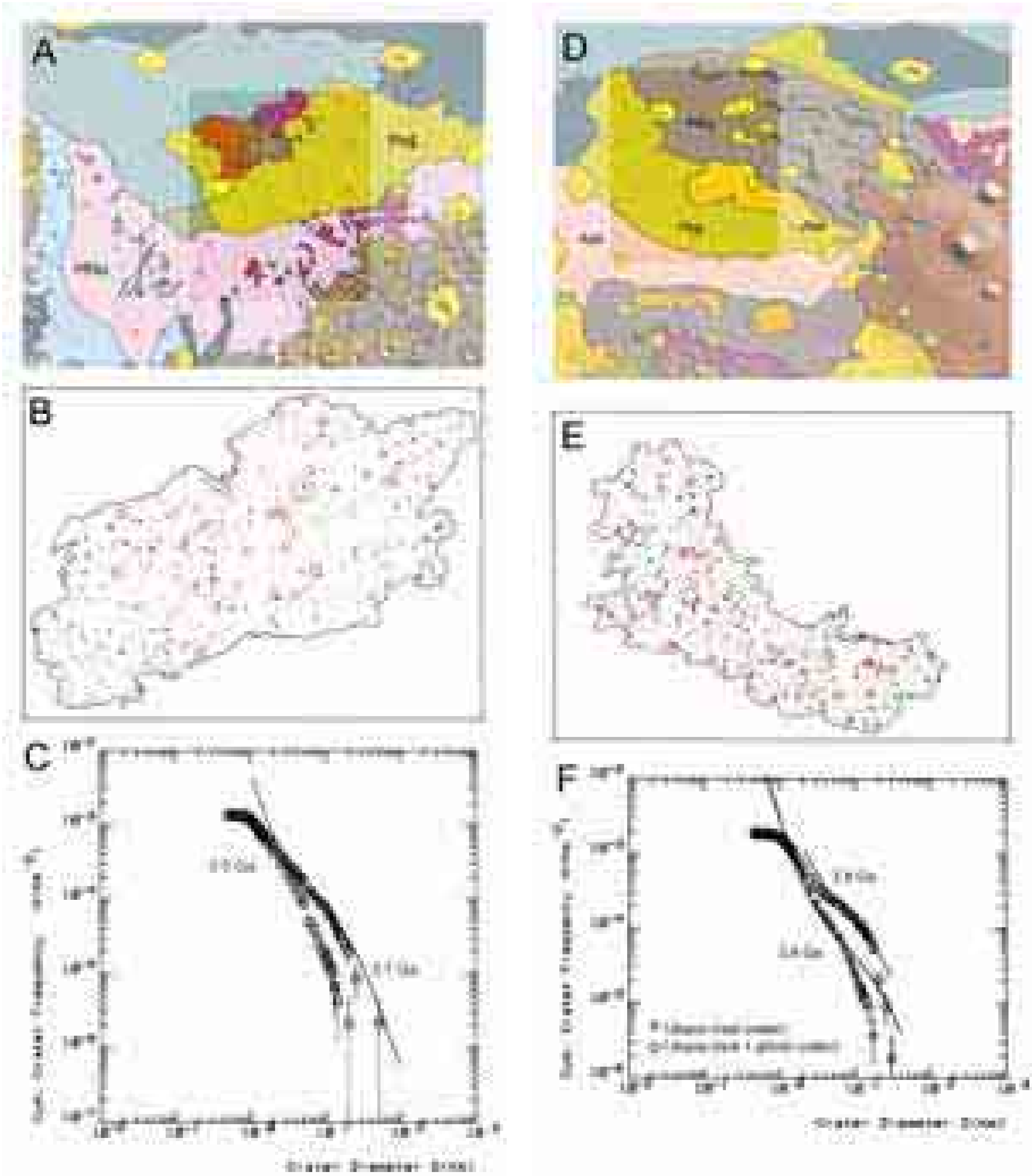

Figure 14.7.: (A,D) The geologic unit Hvg (following Scott and Tanaka (1986) and Greeley and Guest (1987)) in the Acidalia Planitia (left) and in the Utopia Planitia (right) are shown. The detailed outline and the visible (real) craters are indicated in black, the so–called ghost craters in red (subset (B,E), left Acidalia, right Utopia region). In subset (C,F) the resulting crater size–frequency distributions for the visible (real) crater distribution (quadrangular) are given, a clear lack of large craters is observed. Indicated by circles, the summed distribution of visible (real) craters and the most–likely buried crater population (ghost craters) are shown.

butions lead to an age of 3.4 Ga and indicate a resurfacing event that is detectable in all units.

Crater Size–Frequency Distribution in the Polygonal Terrain Measuring the region of polygonal terrain in the Utopia and Acidalia Planitiae, we obtained crater size–frequency distributions that appear to have an unusual deficiency of large craters, as compared to the proposed production function. For the polygonal terrain in Utopia and Acidalia Planitiae, we first measured the crater distribution of clearly visible craters and obtained an age of 3.4 Ga. A lack of large craters is especially observed in the polygonal terrain. Additionally, the distribution of the ringed–graben structures was measured assuming that they are the "counterdrawn" crater population of the underlying surface or basement. The distribution of visible craters was stacked with the population of so-called ghost craters for both regions in Utopia and Acidalia Planitiae. The sum of the visible and ghost crater population yields an age of 3.8 Ga, an age observed in regions where a lack of craters in the larger diameter range is not observed (Figures 14.7). This implys that at the centers of the Utopia basin and Acidalia Planitia large amounts of deposits were emplaced, while in their surrounding most likely the basement of the lowlands is exposed.

Existence of an Ancient Martian Ocean? Irrespective of the cause of the diversity or obscuration of the measured crater size–frequency distribution in the larger–size range compared to the expected crater production function, it occurred between 3.4 and 3.8 Ga in areas where poligonal terrain is observed. These distributions can be explained by extensive resurfacing effects within a period of roughly half a billion years, covering the earlier crater population by a 1–km or even 2–km thick layer. In other regions in Utopia, ring–graben structures and lack of large craters are not observed. These units appear to be at the outer edge of the Utopia basin. This conforms with the existence of a proposed ocean in the northern lowlands and fits the interpretation that the polygons emerged through desiccation and differential compaction of sediment over buried topography. It also implies slow emplacement (period of sedimentation over roughly 400 Ma) of sediments, so that the formation of the giant polygonal pattern is unlikely to be due to Rayleigh convection during the deposit emplacement as suggested by Lane and Christensen (2000). The elastic rebound of the crust as a driving force is possible, but supports the formation of the pattern after the disappearance of a possible ocean. Nevertheless, for elastic rebound to be effective in fracturing the surface, a relatively sudden removal of the surface load is required. Considering the analysis of the northern lowland plains units, a relation between younger ages and topographic lows has been observed. These ages were found to cover an age range between 3.6 and 2.8 Ga, which would imply a very slow water regression. Nevertheless, most younger surfaces appear to have formed through volcanic deposition. An effect directly related to elastic rebound might be unobserved in localized areas such as where the giant polygons are distributed.

14.4. The Medusae Fossae Formation

Along the equator between the Tharsis and Elysium volcanic centers in the Elysium–Amazonis Planitiae region, the highland–lowland boundary is superimposed by massive deposits. These deposits define an extensive unit of somewhat enigmatic origin, named the Medusae Fossae Formation (Scott and Tanaka, 1986). In general, the formation appears as a smooth and gently undulating surface, but is partly wind–sculpted into ridges and grooves. MOLA–based topographic data indicate a thickness of the deposit of up to 3 km. It is commonly agreed that the materials forming Medusae Fossae were deposited by pyroclastic flows or similar volcanic air–fall materials (Greeley and Guest, 1987) and could be a remnant of ancient polar layered deposits of a polar cap which has been once close to the equator (Schultz and Lutz, 1988). Westward of Arsia Mons close to the equator, we find the highland–lowland boundary. An area between 140 °W and 150 °W was imaged by the HRSC during orbit 895 (Fig. 14.8 A) and orbit 917 (Fig. 14.8 B). Both orbits almost completely overlap. The plateau area of the volcanic massif is partly covered by lava flows and partly dissected by valleys, which were most likely carved by fluvial activity (Fig. 14.8 A and B). The remains of water-bearing inner channels are visible in the center of the valleys and at the bottom of the massif (Fig. 14.8 C and D). Superposition of the lobate-fronted pyroclastic flows indicates that the water erosion ended before deposition. A subsequently formed impact crater near the massif shows ejecta blankets that were spread as a flow over parts of the plateau, implying water or ice in the subsurface at the time of impact (see Chapter 7.4).

At the highland-lowland boundary between the old volcanic plateau region and Amazonis Sulci, part of the widespread deposits of the Medusae Fossae Formation (MFF) are shown. At this part of the highland–lowland boundary, the volcanic plateau fed by the southernmost Tharsis Montes volcano Arsia Mons is dissected by several valleys that were most likely carved by running water. Senus Vallis, for example, is shown in detail where the latest–stage inner channel is still visible (Fig. 14.8 C). Abus Vallis resembles a channel of similar type. At its mouth, the steepness of the walls or the narrowness of the valley prevent observation of the channel floor, due to the insolation and shading situation when the image was taken. Nevertheless, the remains of the last stage of water activity can be traced as a small channel at the floor of the lowland plain (Fig. 14.8 D). Additionally, the emplacement of pyroclastic flows is visible in this detail. The action of water erosion ended before the emplacement of the pyroclastic flow. These small channels accompany a larger valley system called Mangala Valles, discussed in Chapter 14.5. Impact craters with pronounced ejecta blankets are the youngest features of the stratigraphic sequence that can be observed in these images. They have well preserved ejecta blankets showing a lobate appearance, which is believed to indicate the presence of water or water ice in the impacted target. As a crater forms on a flat surface, it expands in a circular fashion. Due to the topography of the impact site, the shape of the crater during expansion was disturbed by the walls of the plateau and resulted in a somewhat asymmetric (oval) shape. The distribution of ejecta resembling the wings of a butterfly, is due to a non-vertical impact (less than 45 degrees, e.g. Melosh (1989)).

We performed crater size–frequency distribution measurements for the lava–covered plateau section and parts of the pyroclastic–flow units that formed Medusae Fossae. The resulting ages indicate about 3.1 Ga for the last lava coverage of the plateau and 1.6 Ga for parts of the Medusae Fossae Formation. The latter is also found as a surface age for Medusae Fossae Formation units found in the Gusev vicinity. A single global formation around 1.6 Ga ago of the enigmatic Medusae Fossae Formation is most likely. Both ages provide a time frame for the fluvial activity in that region, using stratigraphic information on superposition and intersection, as discussed above.

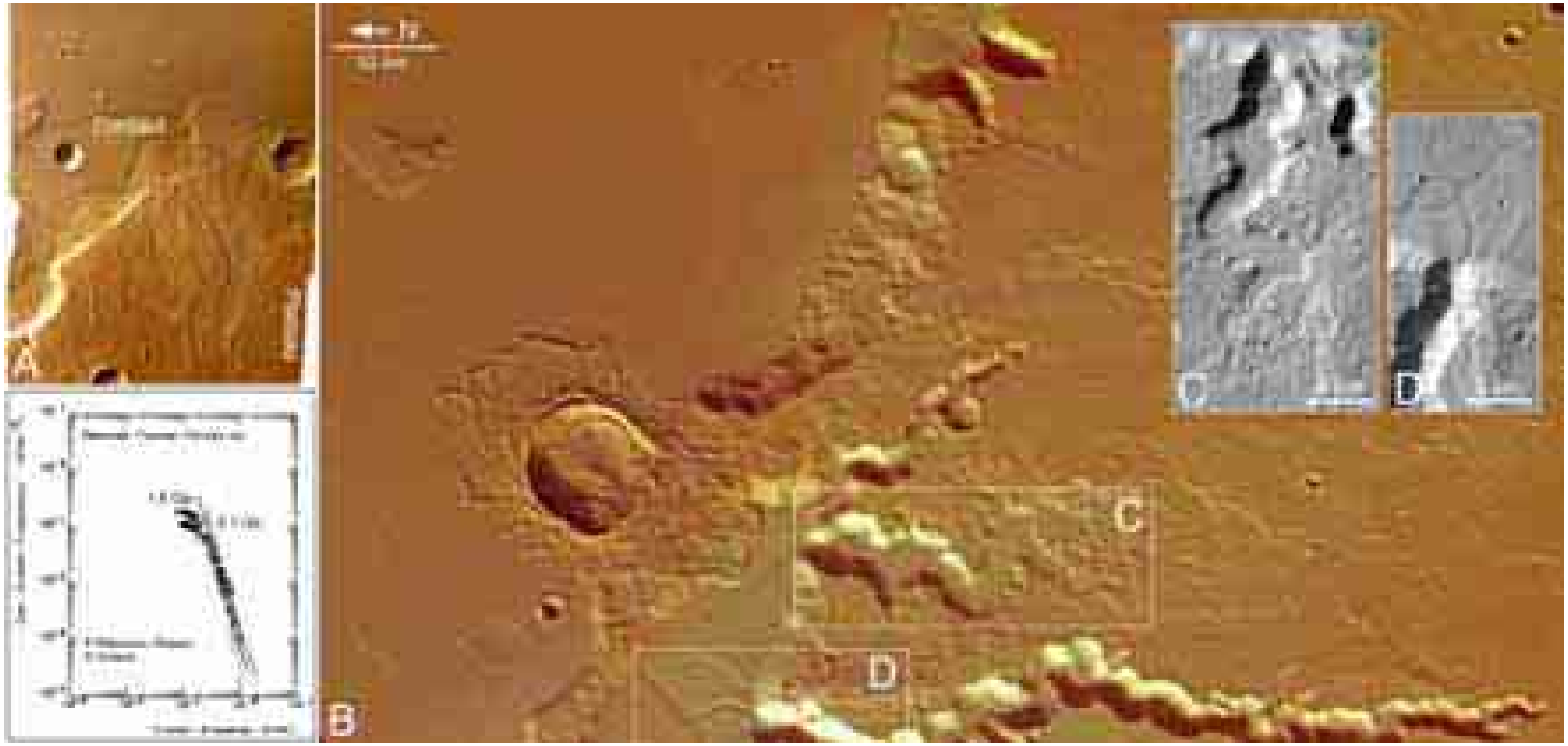

Figure 14.8.: Parts of the Medusae Fossae Formation (MFF) at the dichotomy boundary (between 140 °W and 150 °W close to the equator) west of Arsia Mons: Subset A imaged in orbit 895 shows the volcanic plateau, the dichotomy boundary and possibly volcanic ash flow belonging to the Medusae Fossae Formation. Areas where crater counts have been performed are indicated and their resulting surface age is shown in the diagram below. Image subset B is the continuation westward of subset A. Details C and D show two small channels dissecting the plateau region. So–called inner channels are also present.

14.5. Outflow Channels: Mangala, Kasei, and Ares Valles

One type of channel–system unit is associated with the outflow–channel development occurring from Valles Marineris to Chryse Planitia, while a few occur along the western and southern margin of Amazonis Planitia. It is proposed that the active period of the channels was during the Hesperian and Amazonian (Tanaka *et al.*, 1992b), postdating the development of valley networks. (Baker, 1982) argues that outflow channels are large–scale complexes of fluid–eroded troughs. They appear to have emanated from discrete collapse zones known as chaotic terrain, which sometimes occupy the floor of chasmata. The chaotic terrain generally consists of kilometer–sized knobs and irregular mesas, which gives the impression of tilted blocks of former plateau rocks. Indicators such as channel relics, floodplains along the channel courses, depositional streamlined bars, and erosional islands led to the interpretation that channel system forming floods originated from aquifer outbreaks (Carr, 1979). Many morphologic features hint at diverse erosive forces such as winds, debris or mud flows, glaciers, lavas, however, catastrophic flooding became commonly accepted (for a detailed discussion see e.g. Baker *et al.*, 1992). Some channel systems show no obvious source regions, but possibly emanate at fracture and fissure zones (see discussion in Chap. 12). Most source–region situations are believed to be causatively related to volcanic processes, not only due to the close spacial occurrence especially in the Tharsis vicinity. Observed landforms such as scour marks or chaotic zones can also be considered to be caused by glacial or periglacial processes as well as (sub–)surface mobilization of volatiles.

Here, we studied the predicted causative relationships by age determination, based on HRSC and MOC imagery and digital terrain models. Therefore, three outflow channels (Ares, Kasei, and Mangala Valles) and their individual source regions have been studied in more detail:

Ares Vallis, a typical outflow channel example, is the easternmost channel, originating in the Iani Chaos region. These chaotic terrains are thought to be the characteristic source morphology for outflow channels. **Kasei Valles**, one of the largest valley systems on Mars, shows a more exceptional source region. This system originates in a large chasma–structure, Echus Chasma, where no clear evidence for chaotic terrain can be found. Nevertheless, chaotic terrain is apparent further downstream. Robinson and Tanaka (1990) proposed that the channel formed by catastrophic drainage of a lake in Echus Chasma. HRSC imagery revealed a blanketing by a volcanic layer and possible indications for a previous standing body of water (see Fig. 14.10).

Lastly, the **Mangala Valles** outflow system located southwest of the Tharsis bulge is discussed below. The source region is not characterized by chaotic terrain, but is found further downstream and has been previously related to Memnonia Fossae tectonic features interpreted as en–echelon fissures (compare Chapter 12). This is the only outflow channel extending into the highlands; no continuation is found in Amazonis Planitia, part of the lowland region. Despite the relatively high–resolution of the Viking imagery (Mangala medium-resolution observation, 40 m/pxl), the source region of Mangala is poorly resolved. Nevertheless, Carr (1979) discussed the sudden onset character of water release due to groundwater, which had been released by penetrating a possible permafrost seal. Artesian pressure below the sealed surface amplified the groundwater release after the surface was disrupted by either tectonic activity or melting of the ice seal by dyke emplacement, a volcanic process visible on Earth. HRSC imagery (orbit 286) revealed details of the source region and confirms the onsetless release of water; no surface run–off is observed (Fig. 14.9).

The Mangala Valles outflow channel system is considered, due to a comparable source configuration, to be an analogue to the Athabasca Vallis outflow channel, which has been success-

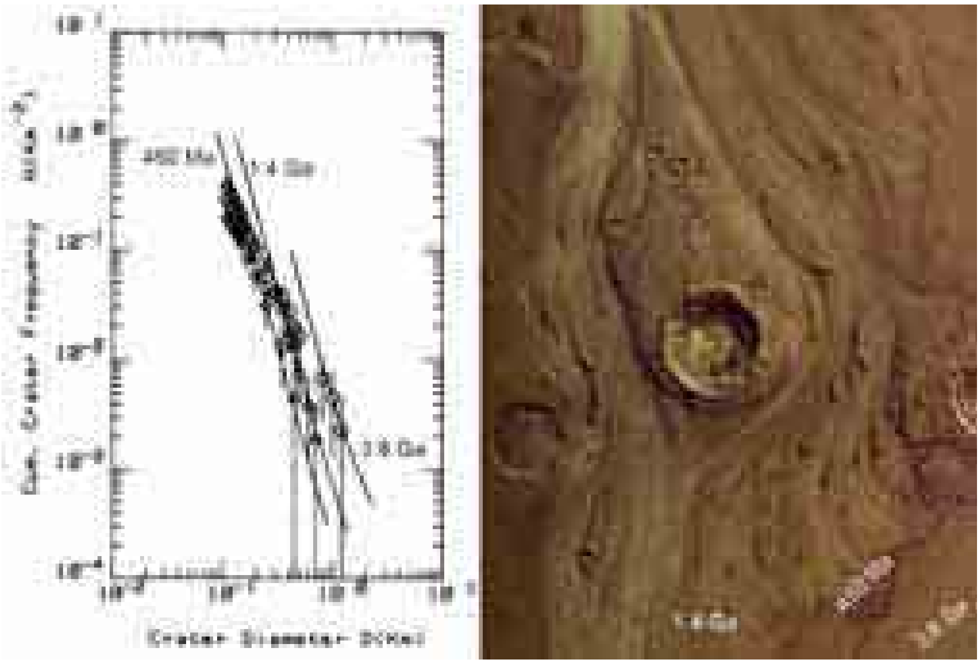

Figure 14.9.: A mid–stream part of Mangala Valles: The HRSC imagery (orbit 286) shows source–region details confirming the onsetless release of water and no surface run–off in the old volcanic plateau region. Crater size–frequency distributions in the channel and secondary source region (lower right corner) indicate episodic erosive activity.

fully investigated in terms of the chronostratigraphy of events and its morphologic inventory (Chap. 12, Werner *et al.*, 2003a). The volcanic plateau, fed by Arsia Mons, generally has an age of about 3.6 Ga. This is similar to Athabasca, where the surrounding plateau fed by Elysium Mons or Albor Tholus formed before 3.6 Ga ago. Crater size–frequency measurements in the source regions of the Mangala Valles system provided ages with major resurfacing periods between about 1.4 Ga for the floor units and as young as about 450 Ma for the secondary source region (Fig. 14.9). Besides the morphologic implications on channel formation, which could be triggered by volcanic activity (e. g. dyke emplacement), age determinations additionally support the correlation between volcanic and fluvial action (see Chap. 16). Temporally, the Athabasca Vallis system itself appears younger in its fluvial and volcanic origin (Chap.12, Werner *et al.*, 2003a), than the Mangala Valles system.

For **Kasei Valles**, we studied the source region Echus Chasma (Fig. 14.10) in terms of morphologic and chronostratigraphic relationships and the main channel region of the Kasei Valles outflow system. The western part of Echus Chasma and its surrounding plains were covered by the HRSC orbit 97, (Fig.14.10). The source region is characterized by a basin-like catchment, in which water from the surrounding plateaus was captured. The plateau is dissected by numerous erosive rilles, which resemble possible valley networks (channels carved by precipitation and surface run–off). Large sapping valleys support the idea of active fluvial processes in that region. From the morphologic observations in HRSC and MOC image data, it seems likely that the Chasma was once filled by a standing body of water, as suggested by Robinson and Tanaka (1990). While Mangold *et al.* (2004) interpreted the regional crater size–frequency distribution to show a Hesperian age, based on a larger portion of

Figure 14.10.: Echus Chasma, the source region of Kasei Valles: The HRSC imagery (orbit 97) show dissected plateaus, sapping valleys, and other morphologic indications for fluvial activity.

the surrounding plateau, we found a resurfacing of the surrounding plateau at about 1.5 Ga, possibly related to fluvial activity. A later resurfacing event, recognizable in crater size–frequency distributions measured on the surrounding plains and on the Chasma floor, is as young as about 90 Ma. The surrounding plateaus could be composed of volcanic ash and lava, as indicated by spectrophotometric investigations of the dark material appearance (T. McCord, 2004, pers. comm.). The distribution of this dark material implies a transport mechanism (either fluvial or aeolian) that moved material downward to the floor or upward to the plateau. Both directions are likely, but a few features at the Chasma walls appear to be related to a downward movement, possibly assisted by fluvial processes. Although the Kasei Valles outflow system and the mechanisms of formation have been studied for decades (summarized by Baker *et al.*, 1992), the formation of this outflow channel system is still debated.

Central parts of the Kasei Valles area (e.g., Sacra Sulci, see Appendix A.1) have shown mesoscale morphologies that strongly support theories of formation by glacial flow or glacial interaction with the ground surface. The morphologic interpretation is reinforced by crater size–frequency measurements in selected areas, which show lava plains in the central Kasei Valles area that are as young as about 1.3 Ga and traces of possible glacial resurfacing with similar ages (between about 1.8 and 1.3 Ga). This suggests a long-lasting period of glacial activity and the co–occurrence of glacial and volcanic processes (see Appendix for details). This work supports theories by e. g. Lucchitta (1982, 2001); Woodworth-Lynas and Guigné (2003) for a glacial origin.

Wagner *et al.* (2004) studied the **Hydraotes Chaos** area, the source region of Simud Vallis and the central circum-Chryse outflow channels. Measurements of the erosion–level, indicated by block and mesa heights, show a correlation between height and ages. Dominated by the episodic activity of significant amounts of flowing water (e.g. Ori and Mosangini, 1998), most of the former mesas and highland units had by then been eroded more or less down to the valley floor level. This process started about 3.7 Ga ago and ended between 400 Ma and 200 Ma ago. On the basis of image data of various instruments with the help of very high–resolution digital terrain models derived from HRSC data, it appears that water may have caused collapse of the surface by the removal of subsurface material, as indicated by variations of surface elevations and tilt angles of individual remnant blocks.

In a joint effort (together with Neukum, Zuschneid, and van Gasselt at Freie Universität Berlin), the **Iani Chaos** region, feeding Ares Vallis, was investigated in a similar manner. It is a chaotic terrain east of Hydraotes Chaos. Crater size–frequency measurements revealed episodic activity at the northern terminus of the Iani Chaos, starting as early as 3.5 Ga ago and ending 50 Ma ago. The upstream areas of the Ares Vallis outflow channel show ages in the range of 650 Ma to 40 Ma. The youngest are most likely aeolian surface modifications. Such an interpretation for Ares and Tiu Valles was outlined already by Marchenko *et al.* (1998).

The higher resolution HRSC imagery allowed us to understand processes resurfacing the circum–Chryse outflow channels subsequent to their formation. They were formed already early in the Martian history, before 3.5 Ga, as discussed in Chapter 14. Possibly, Mangala and Athabasca Valles are exceptional, not only due to their differently appearing source regions, but also in their continual activity.

14.6. Implications of the Evolutionary History of the Highland–Lowland Boundary, and the Northern Lowlands

The evolutionary history of the northern lowlands and the bordering highland–lowland dichotomy will be summarized here.

Following Tanaka *et al.* (2003) and their revision (Tanaka *et al.*, 2005), four zones were studied: the Chryse region, the Utopia basin, plains between the Elysium and the Tharsis volcanic provinces, and a profile between Alba Patera and the north pole. In all regions, the bordering highland units (Noachis and Nephentes units) are the oldest. Additionally, a detailed study of the dichotomy boundary between the Chryse and Isidis Planitiae was undertaken. While the Noachis unit formed during a period between 4.05 and 3.8 Ga ago, the slightly younger Nephentes unit is 3.8 to 3.5 Ga old. Most likely, the Nephentes unit, which belongs to the highland plateau, underwent resurfacing, such as inter–crater plains formation (volcanic), or erosion by surface run–off water (valley networks), and originally formed as early as the Noachis units. All ages discussed in this thesis, gathered for the lowlands and partly modified boundary units, are plotted in Fig. 14.11. Horizontal lines indicate the epoch boundaries as described in Chap. 5. In general, the formation of the most relevant surfaces in the lowlands ended between 3.75 Ga and 3.5 Ga ago. Exceptions are found in Amazonis Planitia, some channel systems (Mangala and Kasei Valles), and other areas that formed through volcanic deposition ($<$ 3.5 Ga).

Following the description in Chap. 14.1, the dominant ages found for surfaces in the Chryse region and Utopia Planitia range between 3.6 Ga and 3.5 Ga, as for the majority of the northern lowland units. Detailed studies of the giant polygonal terrain observed in the Utopia and Acidalia Planitiae indicate that the distribution of visible craters and the ring–graben structures (ghost craters) yield the same basement ages as it is exposed closer to the highland–lowland dichotomy boundary where no thick deposit layer is expected. Most of the lowland units are covered by deposits about 1–2 km or even more thick. Results found in relation to the polygonal terrain conforms with the existence of a proposed ocean (possibly mud ocean etc.) shortly after the crustal formation of the northern lowlands (details in Chapter 14.3). In general, the northern lowland units (in all zones) show gradual changes to younger ages continuing down–slope towards topographic lows. These ages cover an age range between 3.6 and 2.8 Ga. That could imply a gradual water regression. Regardless, most of the younger units in the northern lowlands are considered volcanic in origin, arguing against the ocean theory during the Amazonian Epoch (younger than 3.1 Ga). More arguments for the timing of the possible existence of an ancient Martian ocean is found by investigating the outflow channel activity and related ancient, fluvial processes. The Chryse inner slope ages are found to range between 3.8 and 3.3 Ga and tend to become gradually younger towards topographic lows. The units belonging to outflow channels formed before 3.55 Ga ago. The units in continuation of flood plains appear to be slightly younger, while the Vastitas Borealis Formation is of about the same age. The Utopia basin and its vicinity indicate similar ages. The Utopia floor ages range between 3.5 and 3.6 Ga, with older slope units (about 3.75 Ga) and in a broader unit between 3.8 Ga and 3.4 Ga, as discussed above. Major deposition in the northern lowlands were not driven by emplacement of sediments during the outflow channel formation which ended between 3.5 and 3.6 Ga ago. In such case the difference between basement and visible surface must be smaller (cp. Utopia giant polygonal terrain).

Volcanic flows and phreato–magmatic activity (Elysium flank flow units) occurred about 3.5 Ga ago, followed by later phases between 3.4 and 3.1 Ga ago. The Syrtis Major flank measurements indicate a similar age of 3.55 Ga, while the surface of Isidis Planitia is slightly younger (3.45 Ga).

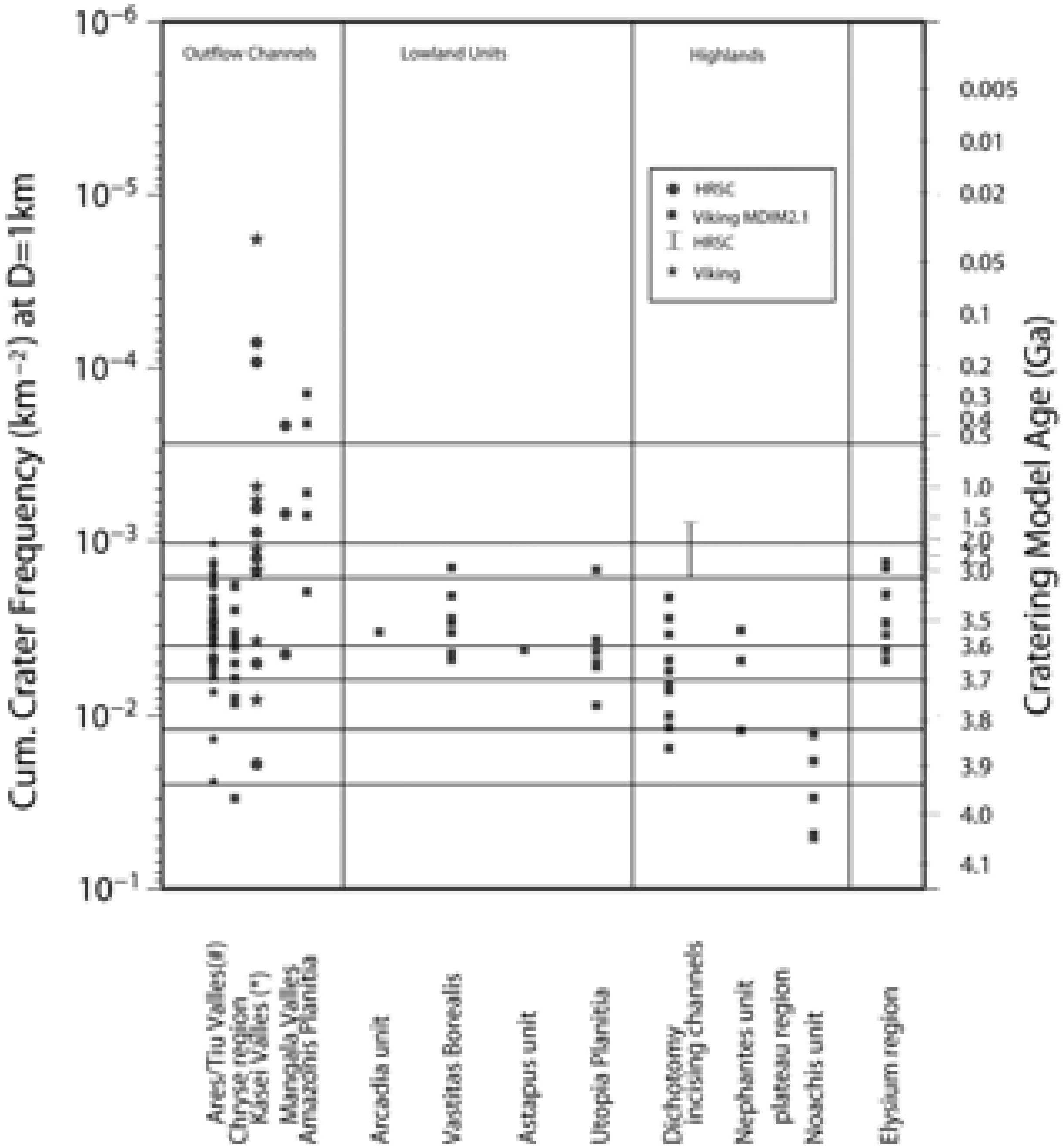

Figure 14.11.: Summary of crater frequencies N_{cum} (1 km) (left scale) and model ages derived applying the cratering chronology model by Hartmann and Neukum (2001) (right scale) for outflow channels, lowland units, and highland areas. These measurements have been performed mainly on Viking MDIM2.1 mosaics (blue squares) and for detailed studies of outflow channels on HRSC imagery (blue circles). This dataset is accomplished by detailed studies in Ares and Tiu Valles (blue stars, # Marchenko *et al.*, 1998), measured on Viking imagery, and Kasei Valles (blue stars, ⋆ Lanz, 2003) measured on Viking and MOC imagery. Horizontal lines show the epoch boundaries, see Chapter 5, Fig. 5.1.

The plains surrounding Elysium are partly type units for the youngest epochs of the Martian history. The Elysium flanks and surrounding plains (Arcadia) are about 3.5 to 3.6 Ga old, while the youngest plains unit, Amazonis Planitia, cannot be treated as homogeneous in age and morphology. The ages range between 3.3 Ga and 400 Ma, even if mapped as a single unit. Their origin is of volcanic nature. Measurements between the North Pole and Alba Patera are generally consistent with age of the entire northern lowlands (Vastitas Borealis Formation). Alba Patera volcanic eruptions might have covered the dichotomy boundary in two episodes (3.37 and 3.52 Ga) indicate that major parts of Alba Patera formed early in the Martian history (cp. Chap. 15).

The bordering highlands are about 4.0 Ga old. The steep escarpment characterizing the highland–lowland dichotomy boundary into segments might have once been present around the globe. Examining the dichotomy between 330° E and 90° E (between Chryse and Isidis Planitiae) a morphologic difference of the regions eastward and westward of the impact basin Lyot is found. This separation is seen in morphology, topography and gravity anomalies (cp. Zuber *et al.* (2000)) and has been confirmed by these crater counts. Nevertheless, a convincing interpretation for the origin of this differently evolved boundary parts can not be given. The typical morphology of the dichotomy boundary has been partly covered/erased by volcanic, fluvial, or cratering processes, which is reflected in ages measured in this work (see Part IV for final discussion). The fluvial activity, e.g. in the Chryse region, was less effective in resurfacing as the volcanic processes, e.g. Tharsis region.

The highland units formed before 4 Ga ago and supposedly the lowland basement formed at about the same time. Generally, surface ages of about 3.6 to 3.5 Ga are observed, which correlates with the major activity period of the outflow channels, dominating the landforms in the Chryse region. Other resurfacing related to water (valley networks) in the highland units acted before 3.7 Ga ago.

The dichotomy boundary formed before major volcanic activity (Olympus Mons aureole formation at about 3.8 Ga ago). Three volcanic provinces superpose either the lowlands (Elysium), possibly the dichotomy itself (Tharsis) or are situated at its closest vicinity (Syrtis Major), and interact with the lowlands (Apollinaris Patera). Volcanic activity and deposition of flood lavas in the lowlands continued after 3.5 Ga ago. Exceptionally strong resurfacing due to volcanic activity occurred in Amazonis Planitia, with ages ranging between 3.0 Ga and less than 400 Ma.

As discussed above, the lowland deposit formation ended between 3.8 Ga and 3.4 Ga ago, but is as young as 2 Ga locally. Additional information for the time frame for the existence of a Martian ocean is indicated in the flank base morphology of the volcanoes located along the highland–lowland boundary. Here, the action of valley networks, possibly formed by precipitation, is visible in the highland areas or at the flanks of older volcanoes (e.g. most likely Hadriaca, Tyrrhena, Apollinaris and possibly Alba Paterae).

Alba Patera and the Elysium rise show smooth slopes, characterized by superposing lava flows or similar volcanic morphologies. On the other hand, the flank base of e.g. Olympus Mons, lowland–sides, are characterized by a prominent so–called aureole. The Apollinaris Patera flank base show similar morphologies, forming a steep escarpment at the flanks towards the lowlands. While the "undisturbed" flank formation of Alba Patera and the Elysium rise occurred before 3.55 Ga ago, the Olympus Mons aureole formed at about 3.8 Ga ago and the lowland-side flanks of Apollonaris Patera at about 3.75 Ga ago, while the last episode manifested in a southward erupted lava fan at about 3.71 Ga ago (details in Chapter 15). Additionally, all ages measured in the closest vicinity of the steep dichotomy escarpment are around 3.7 Ga.

These ages fit the temporal constraint for the possible existence of any kind of Martian ocean that disappeared before 3.75 Ga or more exactly 3.71 Ga ago (Apollinaris flank age). This would imply that the large outflow channels (they have formed until 3.5 Ga ago) did not feed a large ancient ocean at later times anymore, but a general water cycle, including precipitation and surface run–off (valley networks), could still have existed then (further discussion in Part IV).

Any resurfacing ages related to outflow channels younger than about 3.5 Ga could not significantly contribute to most deposits found in the lowlands. Studies of Kasei Valles (Lanz, 2003) and the joint mouth of Tiu and Ares Valles (Marchenko *et al.*, 1998) resulted in similar findings. Major parts of the channels were excavated before 3.5 Ga ago, while any subsequent resurfacing (fluvial and or volcanic) only marginally shaped the inner landforms and surfaces of the channels. Subsequently, volcanic processes dominate the deposition in the northern lowlands, e.g. in Amazonis Planitia, as flows in Utopia Planitia (source Elysium) and, for example, the filling of Gusev crater.

At the dichotomy escarpment, in the Hellas depression, and in the vicinity of Olympus Mons (but also at many other large Tharsis volcanoes), the most recent resurfacing is related to morphologies associated with possible glacial or ice–related landforms or volcanic activity, as discussed in the next chapters.

15. Volcanic Activity on Mars

Martian volcanism, preserved at the surface, is extensive but not uniformly distributed (Fig. 15.1). It includes a diversity of volcanic landforms such as central volcanoes, tholi, paterae, small domes as well as vast volcanic plains. This diversity implies different eruption styles and possible changes in the style of volcanism with time as well as the interaction with the Martian cryosphere and atmosphere during the evolution of Mars. Many volcanic constructs are associated with regional tectonic or local deformational features.

Two topographically dominating and morphologically distinct volcanic provinces on Mars are the Tharsis and Elysium regions. Both are situated close to the equator on the dichotomy boundary between the cratered (older) highlands and the northern lowlands and are approximately 120° apart. They are characterized by volcanoes, whose morphologies are strongly analogous to basaltic volcanic landforms on Earth. The huge volcanoes in the Tharsis region (Olympus Mons, Ascraeus Mons, Pavonis Mons, and Arsia Mons) share many characteristics with Hawaiian basaltic shield volcanoes (Carr, 1973). They are constructed from multiple lobate flows of lava, generally show complex nested coalescing summit calderas of varying age, and gently slope on the order of a few degrees. Their eruption style is effusive and of a relatively non–explosive nature. The main differences between the Martian and terrestrial volcanoes are the greater sizes and lengths of flows of the Martian volcanoes, mainly due to higher eruption rates, the "stationary" character of the source (no plate tectonics) and the lower gravity.

Plescia and Saunders (1979) have summarized the chronology and classification of Martian volcanic activity based on the Viking imagery data. They grouped the volcanic landforms into (1) shield volcanoes (to be of basaltic composition), (2) domes and composite cones, (3) highland paterae, and related (4) volcano-tectonic features. Many plains units like Lunae Planum and Hesperia Planum are thought to be of volcanic origin, fed by clearly defined volcanoes or by huge fissure volcanism. Many small volcanic cone fields in the northern plains are interpreted as cinder cones (Wood, 1979), formed by lava and ice interaction (Allen, 1979), or as the product of phreatic eruptions (Frey *et al.*, 1979).

An overview of the temporal distribution of processes, including the volcanic activity as well as the erosional processes manifested by large outflow channels ending in the northern lowlands and sculpting large units of the volcanic flood plains has been given by Neukum and Hiller (1981). This will be discussed in this work together with new findings. Both Plescia and Saunders (1979) and Neukum and Hiller (1981) gave a chronological classification of the volcanic features on Mars. The difference between these two attempts is the applied reference crater production function. Plescia and Saunders (1979) based their reference crater production function on counts in the Lunae Planum region. As has been demonstrated by Neukum and Wise (1976) and Wise *et al.* (1979a), strong resurfacing obscured the crater size–frequency distribution of this region. Therefore, such an ambiguous calibration curve as used by Plescia and Saunders (1979) might result in wrong stratigraphic relationships, if applied on a more global scale.

Based on Mars Orbiter Laser Altimeter (MOLA) topographic data, Plescia (2004) reexamined the dimensions and volumes of all major volcanic constructs of Mars and could correct the earlier findings of the post–Viking era. During the first two years of the ESA Mars Express mission, the High Resolution Stereo Camera imagery data provides the first opportu–

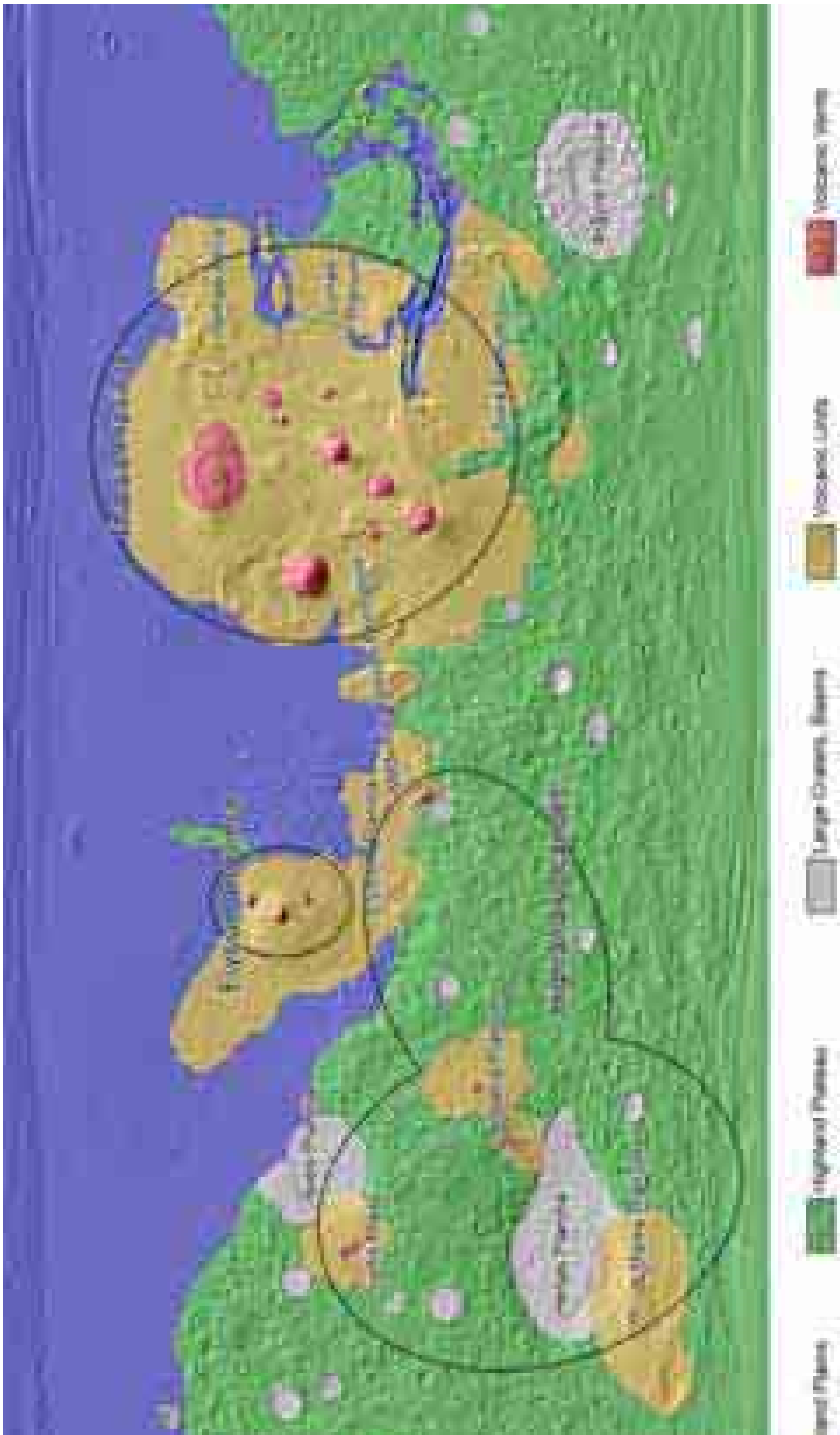

Figure 15.1.: The volcanic provinces of Mars are indicated in yellow. Known central vent constructs are displayed inred. The individual volcanoes are assigned in separate maps. The topographic dichotomy is shown in blue for the lowland parts and green for the highland parts. Large impact structures are shown in white. The background topography is given as a MOLA shaded–relief map.

nity for detailed insights into the morphology and topography of these volcanoes and their chronostratigraphic evolution.

Following the mapping of Spudis and Greeley (1977) and by Scott and Carr (1978), a synthesis of their results indicate that as much as 60% of the surface is covered with volcanic materials. The primary focus outlined in the following sections is on the evolution of the large volcanic provinces Tharsis and Elysium, accompanied by most other volcanic regions on Mars. An additional goal is to understand the interacting processes of erosion and deposition (related to volcanic and fluvial processes) with respect to new and old findings.

Based on the observation of superposition, cross–cutting relations, and, if available, on the number of superposed impact craters, Greeley and Spudis (1981) first described the volcanic history of Mars. To understand the volcanic evolution, caution must be given to the fact that the amount of volcanics represented by the enveloping youngest layer on top of the stratigraphic sequence and sometimes the crater size–frequency distribution reveal an earlier phase(s) by an embayed or flooded crater population.

The oldest unit considered in this investigation are the highland plateau units (e.g. Wilhelms, 1974). We found the oldest highland–plains units to be about 4.1 Ga old (Noachis Terra, see Chapter 17), which is roughly the time of emplacement of the largest Martian basins followed by the emplacement of so–called inter–crater plains 3.9 Ga ago. Most of the highland units range between 4.1 Ga and 3.9 Ga (see e.g. Chapter 17 or 13.2), roughly the decaying end of the heavy bombardment period. At that time, the erosional scarp of the dichotomy boundary between the highlands and lowlands most likely formed as has been suggested already by Zuber *et al.* (2000). Nevertheless, whatever caused the formation of the dichotomy escarpment, subsequent resurfacing acted differently along the boundary (see Chapter 14.2). The temporal overlap of extensive fluvial activity (e. g. valley networks) and volcanic episodes (e.g. highland paterae) is manifested in the observation of phreatomagmatic interaction e.g. at Tyrrhena Patera or at the flank base of western Elysium Mons (Wilson and Mouginis-Mark, 2003). The coincidence of the Hellas basin formation and the accumulation of highland paterae has been noted by Greeley and Spudis (1981), but we find that at least the later–stage patera activities were not triggered by the impact event itself.

Following the interpretation of the volcanic history outlined by Greeley and Spudis (1981) based on the Viking imagery, the plateau plains activity is followed by massive flood volcanism, which resurfaced large areas such as Lunae or Hesperia Plana and huge amounts of the Martian lowland areas. Massive volcanic constructs such as the Tharsis rise, notably Olympus Mons and Alba Patera, cover the dichotomy starting at least 3.8 Ga ago (the age of the aureole has been recalculated from Neukum and Hiller (1981)) and continuing to about 3.5 Ga (Alba Patera, see Section 15.1.1). The presence of the Aureole around Olympus Mons and the absence of such a feature around Alba Patera might indicate a changed environmental situation. The timing and existence of a Martian ocean in the northern lowlands is discussed (Chapter 14.3) and constrained temporally by the surface ages of the two differently appearing flank bases.

Both Martian volcanic centers are dominated by central vent volcanoes and surrounding plains–forming flows. Fracturing (graben formation) is related to the early structural uplift of the volcanic rises, although could be caused by younger volcanic activity (see below). While Greeley and Spudis (1981) found an agreement with a moon–like thermal history, we will show a more diverging evolutionary history of Mars.

All major volcanic constructs including Paterae and Tholi have been imaged in the first period of the ESA Mars Express mission. The ability to image simultaneously in color and stereo gives us the new opportunity to better characterize the geomorphology and chronostratigraphy of most volcanoes in the Tharsis and Elysium region and most highland volcanoes. We have remapped major parts of the volcanic shields and calderas on the basis of the high–resolution HRSC imagery in color and stereo, in combination with nested MOC imagery and the Super Resolution Channel (SRC) (as good as 2.5 m/pixel) of the HRSC.

15.1. The Tharsis Volcanic Province

The Tharsis region is the most dominating feature of the Martian topography and shows numerous volcanic constructs of different age and morphology:

Figure 15.2.: The MOLA shaded–relief map of Albor Tholus.

15.1.1. Alba Patera

The northernmost is the fascinating volcano Alba Patera. It is an enormous volcanic shield with a base diameter of roughly 1100 km, more than the gigantic Olympus Mons. Compared to Olympus Mons, it is a wide but low–relief construct of about 6 km in height, with flank slopes of about 1°, and one of the largest calderas found on Mars (diameter of about 120 km). The surrounding flank grabens (Tantalus and Alba Fossae) extend in a North–South direction. The summit region around the caldera is characterized by extensive lava flows and local dendritic valleys. The construct is divided into two parts indicating at least two formation stages, one broad lower construct (about 4 – 5 km high) cut by the Fossae and marginal lava aprons (Ivanov and Head, 2003) and a much smaller summit shield (of about 1 km in height), which contains a caldera and is situated on top of a broad summit plateau of the lower construct.

Age determinations by Neukum and Hiller (1981) yielded surprisingly young ages based on Viking data. For comparision with the absolute ages derived in this thesis, the relative ages given on the basis of their crater retention ages $N_{cum}(D \geq 1$ km) in Neukum and Hiller (1981) are recalculated applying the most up–to–date chronology model by Hartmann and Neukum (2001). At the western flank of Alba Patera, they found ages indicating at least four episodes of activity: about 3.4 Ga, 2 Ga, 800 Ma ago and as recent as 250 Ma ago. In our measurements based on Viking and HRSC data, we could confirm the maximum age of about 3.5 Ga (see Chapter 14.1). These results were based on Viking imagery measurements taken at the northern flank base of Alba Patera, most likely covering the dichotomy scarp observed elsewhere on the planet. Measurements based on HRSC imagery at the lower flank (north of the summit) support this oldest age found in low–resolution Viking imagery. All other crater counts have been performed in the upper part of the construct and indicate similar ages of about 1.1 Ga to 3 Ga, as reported by Neukum and Hiller (1981). Resurfacing, which is possibly related to the formation of sinuous channels, probably eroded through flowing lava (as observed on other Martian volcanoes). The youngest ages (of comparable range in Neukum and Hiller (1981)) are found in the closest vicinity of the large caldera, yielding two episodes that ended as recent as between 800 Ma and 180 Ma ago. This two–stage activity is supported by the summit caldera morphology, which has been interpreted by e.g. Plescia

(2004) or Ivanov and Head (2003) to represent at least two major episodes of caldera formation and summit volcanic activity.

Alba Patera Flank Regions

Unit	N_{cum}(1km)	Age in Ga
1Ar1	1.23e-3/3.10e-4$^+$/9.09e-5$^+$	2.51/0.636$^+$/0.186$^+$
2Ar1a	6.13e-4/ 2.40e-4$^+$	1.26/0.493$^+$
2Ar2	1.45e-3/3.95e-4$^+$/1.26e-4$^+$	2.93/0.811$^+$/0.259$^+$
3Ar1	5.60e-4	1.15

$^+$ treatment description see Chapt. 9.1
for imagery, area annotation and counts see Appendix B

Both the morphology, the shape and the ages suggest a complex geologic evolution of Alba Patera over most of the Martian history.

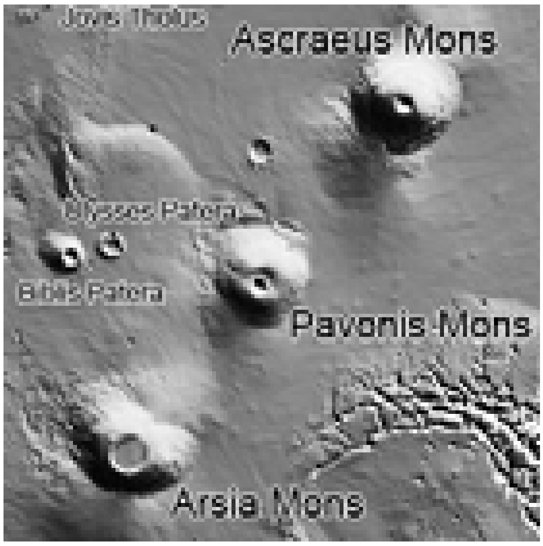

Figure 15.3.: The MOLA shaded–relief map of the Tharsis Montes: Ascraeus Mons, Pavonis Mons, and Arsia Mons.

15.1.2. The Tharsis Montes

Three large volcanoes named Ascraeus Mons, Pavonis Mons, and Arsia Mons constitute the Tharsis Montes. They are centered on top of the volcanic rise as a chain trending from northeast to southwest (where Ascraeus is the northernmost and Arsia the southernmost). Previous age determination by Plescia and Saunders (1981) and Neukum and Hiller (1981) indicated decreasing surface ages towards the northeast. Morphology, slope steepness and caldera complexity were used as arguments to judge Arsia Mons (a broad feature with low slopes and large simple caldera) as the oldest, while the others were considered as subsequently younger, due to their steeper slopes and more complex smaller central calderas.

Comparing the morphometric properties of Viking– and MOLA–derived summit elevations, large differences have been noted by Smith *et al.* (2001). Earlier determinations by the USGS based on Viking imagery (U.S. Geological Survey (USGS), 1989) had to be reduced for all large volcanoes in the Tharsis region (see e.g. Plescia, 2004).

Arsia Mons

The southernmost volcano of the Tharsis triplet is Arsia Mons with a summit height of about 18 km and relief height (compared to the surrounding plains) of about 11 km (second to Olympus Mons). It has a single caldera, the largest on Mars (diameter of about 120 km as first reported by Crumpler and Aubele (1978)). The main edifice has a width of about 430 km and is composed of the central shield and two aprons at the northeastern and the southwestern flank side, roughly following the great circle trend of the Tharsis Montes triplet. These aprons formed by lava flows extending from alcoves on the lower flanks of the main shield. They originated about 5 – 7 km below the summit. Both aprons appear at the tip of some flank depressions, which follow a line of nine low shields (relief of about 150 m) across the caldera floor along the same great circle trend as the Tharsis Montes themselves and roughly the axis of the aprons (Head *et al.*, 1998a,b). While the main edifice has slope angles of about 5°, the flank apron slopes range between 1° and 4°. At the flank base towards the west, a large aureole deposit appears, which is believed to have formed by glacial deposits (Head and Marchant, 2003). Thus far, we have not performed crater counts for these possible glacial deposits.

For the caldera floor, we found a surface age of about 130 Ma (Neukum *et al.*, 2004), which confirms earlier measurements by Neukum and

Caldera and Flank Ages of Arsia Mons

Unit	N_{cum}(1km)	Age in Ga
cal	6.23e-5	0.128
1Ar1	1.00e-4	0.206
1Ar2	3.13e-3/4.10e-4$^+$	3.54/0.841$^+$
2Ar1	9.43e-4/2.11e-4$^+$	1.93/0.432$^+$
2Ar2	1.68e-4	0.345
2Ar3a	9.21e-5	0.189
2Ar4	5.09e-5	0.104
3Ar1	3.02e-5	0.62
4Ar1	5.17e-4/1.37e-4$^+$	1.06/0.280$^+$
5Ar1	9.66e-4/2.79e-4$^+$	1.98/0.572$^+$
5Ar2	4.17e-4/7.13e-5$^+$	0.855/0.146$^+$

$^+$ treatment description see Chapt. 9.1
for imagery, area annotation and counts see Appendix B

Hiller (1981). Construct–wide ages ranging between 100 Ma and 200 Ma have been found and are interpreted by us as the latest stage of the summit and flank eruptions. Earlier episodes stopped at about 500 Ma, 800 Ma, and 2 Ga ago. The oldest age is about 3.54 Ga and indicates the time when the period of major edifice construction ended.

Pavonis Mons

The middle one of the Tharsis Montes triplet is Pavonis Mons, having the lowest summit altitude of about 14 km and a relief compared to the surroundings at the foot of the shield of about 10 km. The two visible caldera depressions occupy an area of about 100 km in diameter and indicate the latest periods of summit activity. Based on crater counts, we determined that the caldera floor formation ended about 370 Ma ago for the larger one and about 80 Ma ago for the well preserved smaller caldera floor. The flanks have a slope angle of roughly 4°, but two lava aprons (similar to those seen at Arsia Mons) originate about 4 km below the summit region (slope of about 1°), aligned to the northeast–southwest fracture trend observed in that region. The southern flank is carved by prominent lava channels and smaller alcoves. The lava aprons and large units at the western flank bottom (towards which most of the lava flowed) are occupied by clusters of small low–shield volcanoes. These regions are associated with the youngest parts of the Pavonis Mons shield, which are reflected in many crater size–frequency distributions obtained on the flanks, aprons and small shields. All ages range between about 100 Ma and about 800 Ma. They appear to be strongly correlated temporally to the latest stage of summit activity. Ages range between 100 Ma and 450 Ma for a series of arcuate concentric grabens cutting across the lower northwestern flank, with lava flows barely covering the graben morphology.

Caldera and Flank Ages of Pavonis Mons

Unit	N_{cum}(1km)	Age in Ga
cal 1	1.79e-4	0.367
cal 2	4.02e-5	0.082
1Ar1	6.32e-4/2.52e-4$^+$/8.91e-5$^+$	1.30/0.516$^+$/0.183$^+$
2Ar1	3.14e-5	0.064
2Ar2	3.72e-4	0.763
2Ar3	3.36e-3/1.93e-4$^+$	3.56/0.395$^+$
2Ar4	6.03e-4	1.25
2Ar5	5.98e-4/1.77e-4$^+$	1.23/0.362$^+$
3Ar1a	4.99e-5	0.102
3Ar2	1.03e-4	0.212
3Ar3	4.64e-5	0.095
3Ar4	1.13e-4/4.33e-5$^+$	0.232/0.089+

$^+$ treatment description see Chapt. 9.1
for imagery, area annotation and counts see Appendix B

In general, the main edifice was erected about 3.56 Ga ago, experiencing a strong resurfacing recorded in the crater size–frequency distribution about 1.2 Ga ago. Similar to Arsia Mons, an aureole–type deposition at the northern flank base is observed, but no ages were determined due to the lack of visible craters in the HRSC dataset.

Ascraeus Mons

With an elevation of about 18 km, Ascraeus Mons is the northernmost of the volcano triplet. Once again, marginal lava aprons are observed extending northeast and southwest at the flanks. Comparatively small aureole deposits are found at the northwestern flank segment as well. The flanks appear to have slope angles of about 7°. The summit caldera is complex compared to the other shield calderas and has at least six coalescing calderas. Strong tectonic features indicate a reworked caldera floor morphology, causing difficulties in a proper interpretation of surface age and the caldera formation time. We obtained ages ranging over the entire history of the volcano, starting about 3.6 Ga ago (when the main edifice was already emplaced) to as recently as about 100 Ma ago (Neukum *et al.*, 2004).

Caldera and Flank Ages of Ascraeus Mons

Unit	N_{cum}(1km)	Age in Ga
cal 1	1.93e-4	0.396
cal 2	1.04e-4	0.213
cal 3	5.07e-5	0.104
cal 4	1.13e-4/3.83e-4	0.233/0.785
cal 5	5.26e-5	0.108
cal 6	4.49e-5/5.03e-3	0.092/3.66
1	4.87e-5	0.100
2Ar1	2.15e-4/7.11e-5^{+}	0.44/0.145^{+}
2Ar2	xx/2.42e-4^{+}/8.99e-5^{+}	xx/0.496^{+}/0.184^{+}
2Ar3	3.01e-4/1.14e-4^{+}	0.617/0.233^{+}
3Ar1	9.24e-4/8.76e-5^{+}	1.90/0.179^{+}
3Ar2	7.62e-4/1.49e-4^{+}/1.06e-4^{+}	1.56/0.306^{+}/0.217^{+}
4	5.07e-4/1.66e-5	1.04/0.034^{+}

$^{+}$ treatment description see Chapt. 9.1
for imagery, area annotation and counts see Appendix B

Most younger ages found for the caldera floors are present in measurements for the caldera surrounding summit unit, ranging between 100 and 800 Ma. Similar ages are found at the flanks. Some large flank units appear even younger, ranging between 50 and 100 Ma in age. A detailed investigation by Plescia (2004) reveals a complex history of flank eruption and apron formation; most units are covered by pronounced flow lobes. Low shield vents, alcoves and other volcanic activity are observed following the overall northeast–southwest trend manifested in the long axis of the triplet as observed at Arsia and Pavonis Mons already.

The Tharsis Montes in general

All three large shield volcanoes have a long complex volcanic history, in which the main shield formation ended about 3.55 Ga ago and was followed by many episodes of surface modification, which covered the edifice by many layers of lava flows. Only the last period of effusive eruption is recorded in terms of surface ages derived from crater counts. The youngest flank eruptions, which still produced an huge volume, and many scattered low shield vents indicate that the volcanoes were active until recently. Most likely, the Martian large shield volcanoes are dormant.

15.1.3. Olympus Mons

The largest and most prominent Martian shield volcano is Olympus Mons, which has a relief of about 22 km and a basal extent of about 800 km by 600 km, measuring the edges of the scarp surrounding the main edifice. The width is almost doubled if the enormous extent of the aureole deposit is considered (despite the unexplained formation process), which is dispersed over many hundreds of kilometers northeastward into the lowland units. The slopes are about 5° and up to 30° at the scarp. Based on HRSC data we performed extensive and detailed structural investigations of the scarp units, flanks and caldera (Neukum *et al.*, 2004; Basilevsky *et al.*, 2005) as well as a chronostratigraphic analysis of the entire edifice, focusing on the caldera, and the western and eastern scarp.

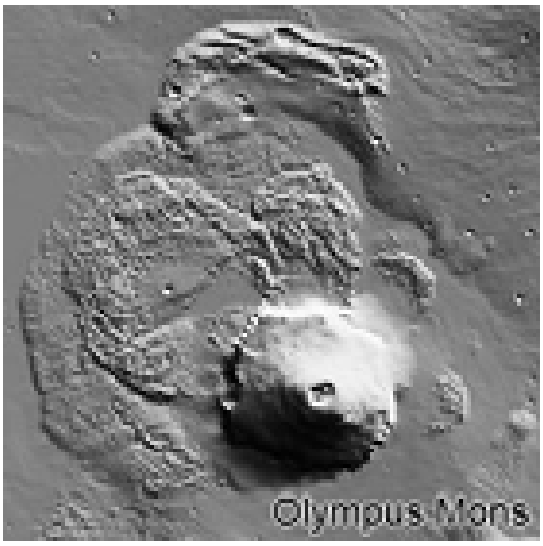

Figure 15.4.: The MOLA shaded–relief map of Olympus Mons.

The caldera of Olympus Mons consists of at least six coalescing depressions, which have been described in morphologic detail by Mouginis-Mark (1981) and suggest a sequence of at least six episodes of caldera collapse. Both of the smallest calderas appear very smooth in their floor morphology and were the last to form

Figure 15.5.: The caldera of Olympus Mons. One of the larger kettles is reworked by tectonics, resulting in a modification of the reference area used to calculate the surface ages. Subset (A) shows the resulting age for the uncorrected area, and (B) for the corrected area used to calculate the age. A difference of 30 Ma is found, for a given age of 140 Ma, (A), and 170 Ma, (B).

in this sequence of collapses. The other sub–caldera floors have experienced strong tectonics, as seen by circular grabens in one of the larger depressions and wrinkle ridges that formed as compressional features spread over the center. Additionally, the floor has been surficially covered by volcanic flows from effusive fissure, resurfacing most of the caldera floors.

All our caldera floor crater counts appear to cluster at about 150 Ma (Neukum *et al.*, 2004), with a slight tendency to invert the expected morphological sequence. As described by Mouginis-Mark (1981), the larger calderas have been reworked by tectonics (graben, wrinkle ridges) and possibly volcanism. Therefore, the crater size–frequency distributions represent a lower limit of the surface formation. For example, in order to reduce the area which is occupied by grabens in the reference area, the crater–size frequencies per area of both large calderas are shifted to be the same, resulting in a slightly older surface age (see Fig. 15.5). A treatment considering the wrinkle–ridged units would have a similar effect, shifting the data for both large calderas towards higher crater–size frequencies per surface area. Nevertheless, to resolve the sequence of events set by the morphology, the crater–count statistics reach its limitations, if we work on statistically non differing crater–size frequencies. Only the morphologic situation could constrain the sequence, while the ages derived from a set of crater size–frequency measurements yield individual fit ages of around 150 Ma, but are statistically indistinguishable within the error limits.

Nevertheless, these results are in strong agreement with earlier measurements (Hartmann, 1999a; Hartmann and Neukum, 2001) based on MOC images in small areas of the calderas of Olympus Mons as well as Arsia Mons. This indicate that the summits of these edifices were essentially active almost in the geological present, the last 2 – 4% of Mars history. The vicinity of the caldera is characterized by superposing lava flows, which represent the latest active phases. Measuring the flank surface ages in four units around the caldera, the average surface age is oldest close to the caldera (resurfacing ended about 210 Ma ago), and shows an age of about 170 Ma further down–slope and elsewhere on the flanks. This appears not only morphologically, but also is reflected in the crater size–frequency distribution, which shows the coverage by lava flows is more effective further down–slope than in the close vicinity of the caldera. Here, besides a few large impact craters that are embayed by younger lava flows (one 10.5 km crater is visible in Fig. 15.5), the flank surface is not completely covered by flows (part of an older 700 Ma–aged surface survived). This observation is in agreement with widely observed flank eruptions on Mars and Earth. Using the observed crater size–frequency distribution, the effect of geological resurfacing is visible in the shape of the distribution Neukum and Horn (1976). The crater diameter (and derived rim height) at which the crater size–frequency distribution is affected, yield a thickness of an uppermost layer a few hundred meters. The summit plateau is truncated by an up to 7 km high scarp, which is present in most places, but is occasionally modified by lava–covering and flattening of the steep flanks. Detailed investigation of the western scarp morphology has been performed based on HRSC and MOC imagery (Neukum *et al.*, 2004; Basilevsky *et al.*, 2005). The western flank exposes at its edge a ridge and several smaller mesas. Ages found for the mesa surface suggest that they could be remnants of the very early and ancient proto–Olympus Mons. Ages of about 3.8 Ga were determined by measurements in the aureole (Hiller *et al.*, 1982), supporting the notion that most of the volcanic construct had been already emplaced very early in Martian history. Prominent and thin layering is visible at the steep slopes of the scarp, indicating the volcanic origin of the plateau. Different slope types have been identified by Basilevsky *et al.* (2005), while one type (S2 slope) is found only at the western flank of Olympus Mons. At the upper part, several chaos–like depression, are found from which channel–like grooves evolve downslope.

This morphology possibly relates to the influence of water (for details see Basilevsky *et al.* (2005) and Chapter 16). The ages derived from crater size–frequency measurements for the volcanic units on the flanks range between 500 Ma until very recently, indicating the flank was blanketed by several episodes about 500 Ma, 200 Ma, and 100 Ma ago. Many of the measured crater size–frequency distributions show, however, relatively flat distributions that indicate the steady (in terms of millions of years) supply of new lava flows (see Neukum *et al.* (2004) and Appendix C).

Flanks of Olympus Mons

Unit	N_{cum}(1km)	Age in Ga
The caldera vicinity		
ar1	3.47e-4/1.04e-4$^+$	0.712/0.213$^+$
ar2	1.13e-4	0.232
ar3	8.30e-5	0.170
ar4	6.51e-5	0.134
The eastern flanks		
plateau1	8.91e-5	0.183
plateau2	2.53e-4/9.44e-5$^+$	0.519/0.194$^+$
floor	8.60e-5/4.12e-5$^+$	0.176/0.085$^+$
The western flanks		
remnants	1.31e-2	3.83
flanks	2.17e-4 – 1.18e-6	0.445 – 0.002

$^+$ treatment description see Chapt. 9.1
for imagery, area annotation and counts see Appendix B

The slope morphologies appear similar for the eastern and western scarp. Only the possibly water–related slope–type 2 does not exist (A. T. Basilevsky, 2005, pers. comm.). In a joint effort (map provided by S. van Gasselt, 2005) at the eastern flank units, crater size–frequency distributions were measured (Fig. B.11). The resulting ages indicate similar peak activities as observed at the western flank, but again the steady depositing of single lava flows is not easily described by these measurements.

In comparing the flank bases of the eastern and western flanks, one major difference appears: While on the western side most of the surface morphology, other than lava, indicates a glacial origin (for details see Neukum *et al.* (2004); Head *et al.* (2005) and Chapter 16), the eastern parts are dominated by fractures and channels that intersect the smooth plains and will be further discussed in Chapter 16.

15.1.4. The Tholi and Paterae on Tharsis

Eight Martian volcanoes are classified as shields: Olympus Mons, Ascraeus Mons, Pavonis Mons, Arsia Mons, Alba Patera, Biblis Patera, Uranius Patera, and Jovis Tholus. Besides these shields, a few dome–type volcanoes are also present in the Tharsis region. Northeast in the prolongation of the Tharsis Montes chain, the Uranius Group is located consisting of Uranius Patera, Uranius Tholus, and Ceraunius Tholus. To the south and east of the Tharsis Montes lies Tharsis Tholus. They all have a basal width of between 100 and 300 km in diameter and a relief of about 3 km (Uranius Patera and Uranius Tholus) and around 6 km (Ceraunius and Tharsis Tholi). Most have an asymmetric shape and a multi–stage caldera, occupying large portions of the entire (visible) construct. Many of their flanks are buried under lava flows of the surrounding plains, generated by the Tharsis Montes, so that the true dimensions remain unknown.

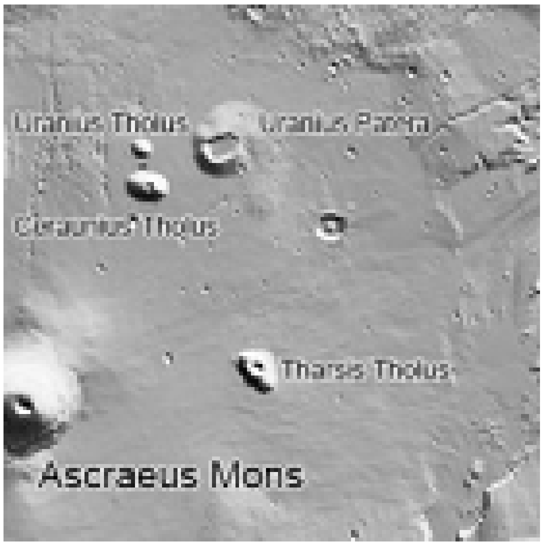

Figure 15.6.: The MOLA shaded–relief map of Tharsis Montes accompanying domes to the northeast: Uranius Patera, Uranius Tholus, Ceraunius Tholus, and Tharsis Tholus.

Uranius Patera appears to have a complex development, indicated by fan–shaped segments emanating from its complex caldera. Our age determination performed on low resolution HRSC limb observation data yield a shield and caldera age of about 3.7 Ga, while a resurfacing event which ended about 3.5 Ga ago affected the caldera and parts of the flanks. Higher resolution imagery by HRSC support the impression that even later resurfacing which is not related to volcanic activity has occurred.

Uranius Tholus is a small cone–like volcano having a two–stage caldera, representing at least two active phases. Our crater counts confirm that the construct had been built up by 4.04 Ga ago, while the caldera floor was emplaced before 3.9 Ga ago. A later event, ending about 3.5 Ga ago, renewed the surface of the cone by either late stage volcanic activity or surface erosion which is not evaluated at the image resolution given.

Ceraunius Tholus is striking to the eye by its prominent sets of radial troughs at its flank, partly leading into the elliptical crater Rahe which through the troughs was filled with lava piles at its bottom. A two–stage caldera indicate more episodic activity which is not revealed by crater counting. The volcanic construct had already been emplaced about 3.75 Ga ago.

Tharsis Tholus has a complex morphology and a uniqueness among Martian volcanoes because of its slumping blocks that segment the flanks. The volcano is an obstacle (embayed by lava flows of Ascraeus Mons) in the surrounding lava plains. The age determined by crater counts indicates that the visible part of the edifice had been emplaced no later than about 3.71 Ga ago.

Domes Northeast of the Tharsis Montes

Unit	N_{cum}(1km)	Age in Ga
Uranius Patera Caldera	6.11e-3/2.44e-3^{+}	3.70/3.45^{+}
Uranius Patera Shield	6.16e-3/3.21e-3^{+}	3.70/3.54^{+}
Uranius Tholus Caldera	1.93e-2	3.9
Uranius Tholus Shield	4.71e-2/2.81e-3^{+}	4.04/3.50^{+}
Ceraunius Tholus	7.50e-3	3.74
Tharsis Tholus	6.63e-3/3.17e-3^{+}	3.71/3.54^{+}

$^{+}$ treatment description see Chapt. 9.1
for imagery, area annotation and counts see Appendix B

West of the Tharsis Montes, another group of volcanoes (Biblis Patera, Ulysses Patera, and Jovis Tholus) is located. All are clearly embayed by younger lavas originating from the Tharsis Montes. The small volcanoes west of the Tharsis Montes became inactive before the latest stage of the Tharsis Montes activity. Only parts of the edifices are exposed to the surface, which is reflected in the low relief of 1 to 3 km above the surrounding plains.

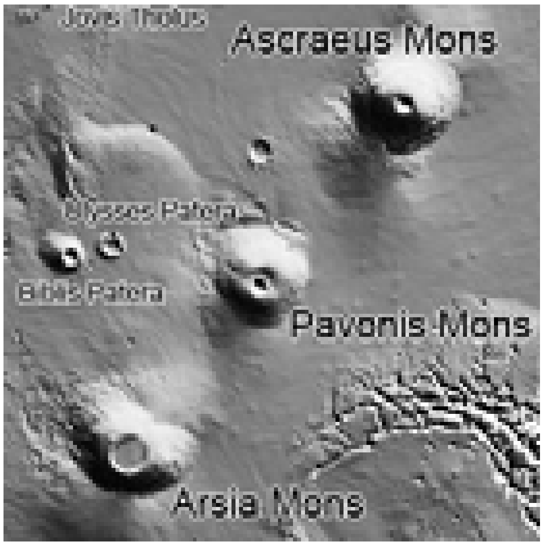

Figure 15.7.: The MOLA shaded–relief map of the Tharsis Montes and the accompanying domes Ulysses Patera, Biblis Patera, and Jovis Tholus to the west.

Biblis Patera 's visible tip extends roughly 130 km by 180 km. Its asymmetrical exposure and caldera floor, lying 1 – 1.5 km below the surface of the surrounding plains might give a clue to the original extent of the edifice. Age determination for the caldera floor indicates that the remaining uppermost region formed before 3.68 Ga ago.

Ulysses Patera 's morphology suggests that most of the edifice has been buried under subsequent lava flows fromed by Arsia Mons. Two large impact craters are visible on the flanks of the relatively small edifice. Crater counts on the flanks and the caldera yield an end of the edifice construction period about 3.73 Ga ago. Nevertheless, the presence of the two large craters implies that the edifice was emplaced even earlier (appr. 3.9 Ga ago).

Jovis Tholus , located further northeast, is an obstacle (embayed by lava flows of Arsia Mons) standing only 1 km above the surrounding plains. The caldera occupies most of the remaining cone, indicating large amounts of lava embaying the edifice. Crater counts were not performed for this volcano, since there is no HRSC coverage.

Domes West of the Tharsis Montes

Unit	N_{cum}(1km)	Age in Ga
Biblis Caldera	5.56e-3	3.68
Ulysses Patera	2.97e-2/7.22e-3^{+}	3.92/3.73^{+}
Jovis Tholus	no measurements	

$^{+}$ treatment description see Chapt. 9.1
for imagery, area annotation and counts see Appendix B

Our results indicate a more homogeneous picture regarding the evolution of the small Tharsis volcanoes than data collected by Neukum and Hiller (1981). Differences are possibly caused by the varying counting strategies, differing operators and variable image quality. Here, only a single operator performed all measurements at uniform image resolution. The overall impression from our measurements, that is the active period of those tholi and paterae stopped early in Martian history (before 3.7 Ga ago).

15.2. The Elysium Volcanic Province

This region is the second–largest volcanic province on Mars, situated in the northern lowlands. The volcanic province consists of three volcanoes: Elysium Mons, Hecates Tholus, and Albor Tholus. Further south, a fourth volcano, Apollinaris Patera, is located at the dichotomy boundary, surrounded by parts of the Medusae Fossae Formation. The Elysium volcanoes and Apollinaris Patera are classified as dome and composite volcanoes respectively, and considered to be constructed from lava that are more viscous than ordinary basalts. The domes are formed by multiple lava flows. Composite volcanoes formed possibly by interbedded lava and pyroclastic material. The enigmatic Medusae Fossae Formation is believed to be (besides other explanations, see Chapter 14.4) made up of possible pyroclastic deposits, spread widely at the dichotomy boundary with no clearly identified source.

The Elysium region has been described in detail by Malin (1977) based on Mariner 9 data. The three Elysium volcanoes are on top of a broad (about 1600 km wide) regional high, similar to the Tharsis rise. However, the structural situation has been compared to Alba Patera (Head *et al.*, 1998a) since the vent volcanoes are superimposed on the risen plateau in an off–center fashion. While Elysium Mons occupies part of the plateau, Hecates Tholus lies at the northeastern base and Albor Tholus at the southeastern margin. The two latter show some embayment contacts at their bases, keeping their complete basal extent hidden.

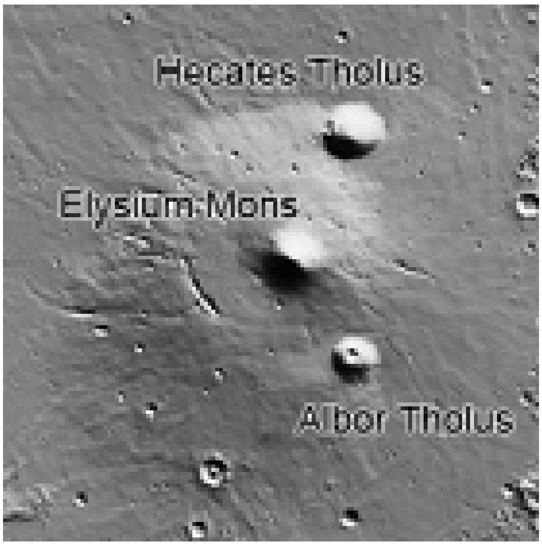

Figure 15.8.: The MOLA shaded–relief map of the Elysium volcanic province. In the north Hecates Tholus is located, in the center Elysium Mons, and towards the south Albor Tholus.

Elysium Mons

The largest of these three volcanoes is Elysium Mons, with a relief of about 14 km and flank slopes ranging between 1° and 10°. The simple summit caldera has a diameter of about 14 km and a shallow appearance. Radial and concentric troughs dominate the western (and partly eastern) flank of the regional high, but are possibly not related to the Elysium Mons. At the western flanks, lava flows extend several hundred kilometers into the northern lowland plains (Utopia Planitia, see Chapter 14.1), which had been associated with Elysium Mons. Fluvial features at the western flank base of the Elysium rise could be interpreted as formed by tectonically–driven release of ground–water or phreatomagmatic interaction. At the southeastern flank base, traces of tectonic grabens extend further in a radial fashion (Cerberus Fossae). They may have originated during the formation of the Elysium rise and are possibly still active, cutting through the youngest region of Mars, Elysium Planitia and the Cerberus plains, as discussed in Chapter 12. This area is discussed to be the youngest volcanic plains unit of Mars. In this very smooth region, large plates have been identified which were interpreted as a frozen sea (Murray *et al.*, 2005). Other nearby similar appearing plates (near the Athabasca Vallis system), though are smaller in dimensions, are interpreted as lava plates, (Werner *et al.*, 2003b,a). The subject remains controversial. The discovery of the impact crater Zunil, and its ejected boulders over an area of about 1600 km in width brought new attention to the secondary cratering issue (for discussion see Chapter 10.1).

Caldera and Flank Ages of Elysium Mons

Unit	N_{cum}(1km)	Age in Ga
Caldera	2.70e-3/7.80e-4	3.49/1.6^{+}
Northern flank	2.68e-3/7.86e-4	3.48/1.61^{+}
Flank (full)	xx/1.71e-3/8.00e-4	xx/3.21/1.64^{+}
Flank (detail)	6.41e-4	1.31

$^{+}$ treatment description see Chapt. 9.1
for imagery, area annotation and counts see Appendix B

The ages based on crater counts from HRSC imagery indicate the final activity of the emplacement of the main edifice at the latest 3.5 Ga ago, while the frequency of a few large craters yields an even older age (3.65 Ga). Both caldera and flank crater size–frequency distributions indicate a resurfacing event ending about 1.6 Ga ago. This is unrelated to the Elysium Mons vent activity, but possibly to an aeolian overprint. Most measurements based on Viking imagery (Chap. 14.1) confirm that the main construction phase had ended about 3.65 Ga ago and only the large flank eruption, flowing northwest and covering Utopia Planitia had formed over a period of 400 Ma and continued to as recently as 3.1 Ga ago.

Albor Tholus

The southernmost dome of these three volcanoes is Albor Tholus. The caldera diameter is about 35 km with a depth of 4 km, which is enormous with respect to its basal extent of about 150 km and relief of about 5.5 km. While the flanks appear convex, with slope angles of about 5°, the caldera–wall slopes range between about 20° and up to 35° (Chap. 7.4).

Caldera Ages of Albor Tholus

Unit	N_{cum}(1km)	Age in Ga
caldera 1	1.05e-3	2.16
caldera 2	2.3e-4	0.471
caldera 3	7.99e-4	1.64

for imagery, area annotation and counts see Appendix C

The caldera morphology indicates a smaller, younger caldera collapse. Ages found for the caldera floors indicate that the summit activity had ended about 500 Ma ago, with an earlier episode ending 2 Ga ago (Werner *et al.*, 2004b; Neukum *et al.*, 2004; Werner *et al.*, 2005b).

Hecates Tholus

The northernmost volcano is Hecates Tholus, located at the edge of the Elysium rise and connected to the lowlands. Numerous radial rills emanate from the top, interpreted as fluvial in origin (Gulick and Baker, 1990), but more recently viewed as eroding through lava flows (Williams *et al.*, 2005). With a relief of about 7 km, the roughly 180 km wide edifice exposes a small (13 km in diameter) and shallow (less than 500 m) multi–staged caldera. Our crater counts indicate a history of summit activity over the last billion years, while the flank age of 3.4 Ga tells us that the construct had been already emplaced at that early stage. Mouginis-Mark *et al.* (1982) studied Hecates Tholus extensively and suggested that the summit is covered with pyroclastic deposits post–dating the flank formation. The flanks appear convex, with slopes varying from 6° at the bottom to 3° at the summit. Detailed age determination for the northern flank of Hecates Tholus was initiated to understand the timing of the summit caldera activity and a possible side–caldera (Hauber *et al.*, 2005), not seen in earlier investigations. Imagery and topographic data from the HRSC revealed previously unknown traces of an explosive eruption at 30.8°N and 14.98°E, on the northwestern flank of Hecates Tholus. The northwestern flank has been mapped by us and studied in detail in terms of morphology and crater size–frequency distributions. Additionally, MOC–NA imagery has been used. We found that both caldera and flanks have similar surface ages. While the caldera indicate an active phase about 1 Ga ago, we find similarly aged deposits on the upper flank segment. Later caldera activities are not reflected in the surface ages of the summit vicinity, which indicates that they were less massive than the one occurring about 1 Ga ago.

Caldera and Flank Ages of Hecates Tholus

Unit	N_{cum}(1km)	Age in Ga
caldera 1	4.97e-4	1.02
caldera 2	1.57e-4	0.322
caldera 3	1.36e-4	0.28
caldera 4	4.4e-5	0.09
caldera 5	5.36e-5	0.11
Side–Caldera and Flanks		
caldera ejecta	1.74e-4	0.357
flank dissected	4.52e-4	0.927
Elysium plains	2.01e-4	0.411
Flank air fall	4.26e-4	0.874
glacier upper	2.39e-5	0.049
glacier lower	6.63e-5	0.136
gl northern	1.19e-4	0.245
gl southern	2.47e-5	0.051

for imagery, area annotation and counts see Appendix C

The eruption at the flank bottom created a large, 10-km-diameter caldera about 350 Ma ago. In the vicinity of the amphitheater–like depression, erupted deposits are found, which show this age. Glacial deposits partly fill the caldera and a younger adjacent depression. Details will be discussed in Chapter 16.

Apollinaris Patera

This volcano is situated at the dichotomy boundary (north of the impact crater Gusev; Chapter 13.2) and surrounded by the Medusae Fossae Formation (Chapter 14.4). It extends over roughly 190 km, and has a two–stage caldera of about 80 km in diameter. The northern rim is characterized by a small scarp facing towards the northern lowlands, resembling a small version of the Olympus Mons scarp. To the south, a lava apron has evolved, making up the youngest unit of the entire construct. Ages derived from our crater counts indicate that the last activity (at the fan and caldera) ended at about 3.71 Ga ago, while the entire volcano had been constructed by 3.74 Ga.

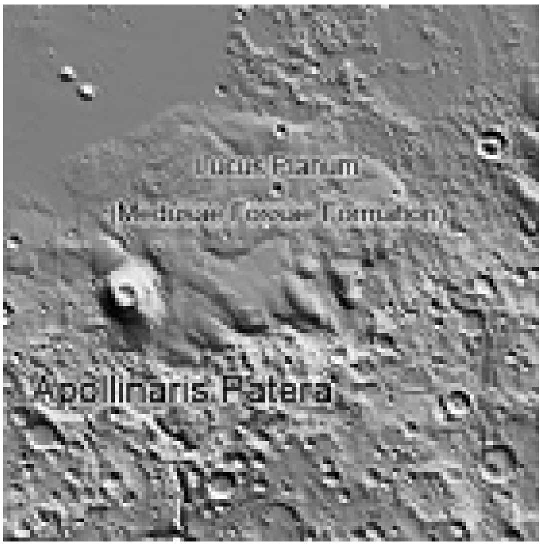

Figure 15.9.: The MOLA shaded–relief map of Apollinaris Patera and part of the Medusae Fossae Formation (Lucus Planum).

Even if the structure of these four volcanoes suggest assignment to one group, their evolutionary history, especially of Apollinaris Patera, is diverse. In the highland vicinity of Apollinaris Patera, a few small Noachian–aged volcanic domes (e.g. Zephyria Tholus) are located

Ages of Apollinaris Patera

Unit	N_{cum}(1km)	Age in Ga
Caldera small	(3.29e-2)/4.08e-3^{+}	(3.98)/3.61^{+}
Caldera big	6.82e-3	3.72
Shield	1.11e-2/7.58e-3^{+}	3.81/3.74^{+}
Fan (south)	6.65e-3	3.71

$^{+}$ treatment description see Chapt. 9.1
for imagery, area annotation and counts see Appendix B

(Stewart and Head, 2001), which are consistent with a stratovolcano origin in which the edifice formed by mixed explosive and effusive eruptions. These observations make Apollinaris Patera different when compared to other highland paterae.

15.3. Highland Paterae

This category of central vent volcanoes has been defined by Plescia and Saunders (1979). Hadriaca and Tyrrhena Patera in addition to others constitute a group of highland paterae. These are low–relief broad features, possessing irregular summit calderas with outward radiating lobate ridges and numerous radial channels on their flanks. Morphology and topographic profiles are attributed to explosive volcanism related to phreatomagmatic processes, comprising ash flow deposits rather than lava flows. Sinuous channels similar to them on Tyrrhena Patera are interpreted as lava channels. Many features in the surroundings of Hadriaca and Tyrrhena Paterae are clearly related to fluvial or phreatomagmatic activity. Subsidence in the vicinity of channels carved by surface water indicates a close correlation between volcanic activity and the removal of surface and sub–surface material.

The Highland Patera group consists of Hadriaca and Tyrrhena Paterae east of the Hellas basin, Amphitrites and Peneus Paterae at the southern margin of the Hellas basin, and Syrtis Major Planum, characterized by two calderas (Meroe and Nili Paterae) and located west of the Isidis basin.

Hadriaca Patera

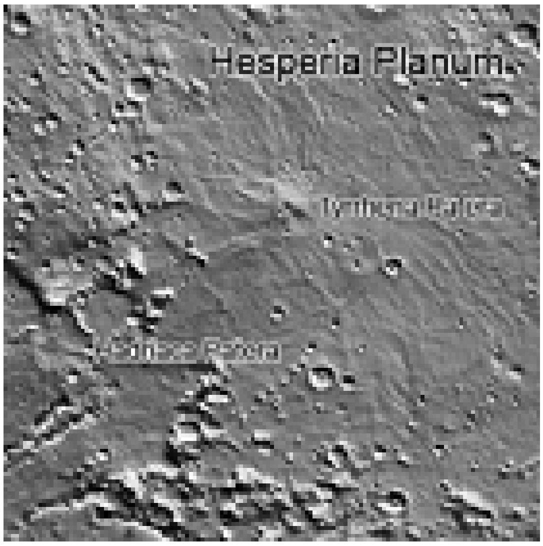

Figure 15.10.: The MOLA shaded–relief map of the Hesperia Planum. In its center Tyrrhena Patera is situated. Hadriaca Patera is situated in between this volcanic plain and the large impact basin Hellas Planitia.

This volcano caught our attention early in the MarsExpress mission. Hadriaca Patera was mapped earlier by Crown and Greeley (1993). Detailed chronostratigraphic investigations were performed on HRSC imagery and a revised map by Williams *et al.* (2005) was published. A very shallow caldera, about 90 km in diameter and surrounded by pyroclastic flows, is strongly modified by possible fluvial erosion. The presence of water is suggested by the existence of a complex trough system named Dao and Niger Valles and phreatomagmatic processes are observed by Zuschneid *et al.* (2005).

Ages of Hadriaca Patera

Unit	N_{cum}(1km)	Age in Ga
Caldera	5.26E-4 – 3.22E-3	1.08 – 3.54
Flank	5.62E-4 – 1.52E-2	1.15 – 3.86

data by Williams *et al.* (2005); Zuschneid (2005)

Crater counts yield episodic activity of mostly explosive (ash) eruptions in the earlier stage and later, more effusive eruptions observed in the caldera. The main edifice was constructed until about 3.9 Ga ago, while stages of activity ending about 3.7 Ga and 3.3 Ga ago are recorded in crater size–frequency distributions for the flank. The caldera floor had been emplaced by about 3.5 Ga ago. Following the formation of a wrinkle ridged surface, the caldera was covered by thin layers created by more effusive eruptions about 1.6 Ga ago. Subsequent resurfacing about 1.1 Ga ago is seen in most areas of the volcano. For a detailed discussion and more advanced geologic analysis see Williams *et al.* (2005) and Zuschneid (2005).

Tyrrhena Patera

This volcano, located at the volcanic ridged plains of Hesperia Planum, was already imaged in high–resolution in Viking–times and studied as a type–locality of highland paterae (Plescia and Saunders, 1979). Its basal extent is about 600 km, while its relief does not exceed 1 km. It has a central caldera, from which a large channel originates, suggesting a formation by lava erosion (Plescia and Saunders, 1979). The summit region is crested by layers of heavily eroded pyroclastic deposits. The flank morphology (radial shallow troughs) is similar to that of Hadriaca Patera.

Ages of Tyrrhena Patera

Unit	N_{cum}(1km)	Age in Ga
Caldera	1.85e-3/7.20e-4$^+$	3.29/1.48$^+$
Flank	2.32e-2/5.24e-3$^+$/1.43e-3$^+$	3.93/3.66$^+$/2.90$^+$
AhrF	1.79e-3/5.38e-4	3.26/1.10
He	6.94e-4	1.42
Nsu1+2	3.33e-2/3.04e-3$^+$/7.68e-4$^+$	3.98/3.53$^+$/1.58$^+$
Ns1	3.98e-3/1.25e-3$^+$	3.60/2.56$^+$
Ns2	1.96e-3/2.84e-3$^+$/9.07e-4$^+$	3.90/3.50$^+$/1.86$^+$
AHcf1	1.59e-3/5.88e-4$^+$	3.11/1.21$^+$
NsL1-4	2.52e-3/7.87e-4$^+$	3.46/1.61$^+$

$^+$ treatment description see Chapt. 9.1;
for imagery, area annotation and counts see Appendix B

The ages determined for the volcanic evolution of Tyrrhena Patera strongly resemble the episodic activity and time frame found for Hadriaca Patera. While the entire construct was emplaced early in Martian history (before 3.9 Ga ago), the flank deposition and erosion happened in periods ending at about 3.7 Ga and 3.3 Ga ago. The large channel was formed through the later stage of the effusive eruption about 1.7 Ga ago. Evidence for a later resurfacing event, about 1.1 Ga ago, can be found in many areas of the volcano.

Amphitrites and Peneus Paterae

The region named Malea Planum, south of the Hellas impact basin has a morphology typical of volcanic plains (e.g. Hesperia Planum) and displays the two well–defined calderas of Amphitrites and Peneus Paterae.

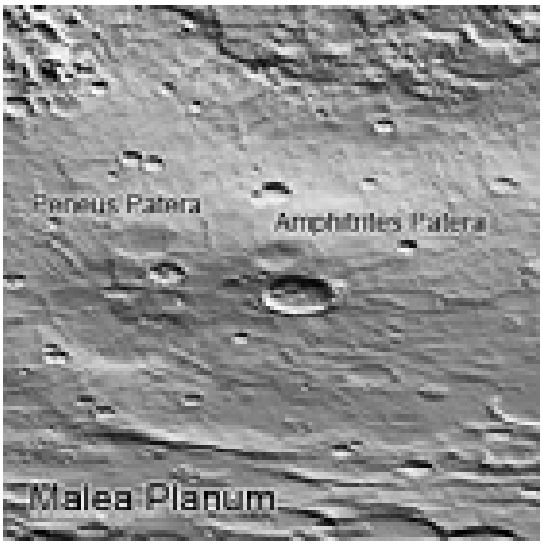

Figure 15.11.: The MOLA shaded–relief map of Malea Planum, a volcanic plain similar to Hesperia Planum. Two calderas of Amphitrites Patera and Peneus Patera are visible.

Ages for Amphitrites and Peneus Paterae

Unit	N_{cum}(1km)	Age in Ga
Amphitrites Caldera	7.69e-3/3.51e-3$^+$	3.74/3.57$^+$
Peneus Patera	no measurements	

$^+$ treatment description see Chapt. 9.1
for imagery, area annotation and counts see Appendix B

They have low reliefs and very shallow flank slopes of about 1°. Other features in the plains unit are caldera suspects (Peterson, 1977). HRSC imagery covers only the Amphitrites caldera, for which crater counts yield an age of about 3.75 Ga and a resurfacing event ending about 3.6 Ga ago. This event probably was not due to volcanic activity.

Syrtis Major Planum

This plains unit was identified as a large volcanic region west of the Isidis impact basin (Greeley and Guest, 1987). Syrtis Major occupies an area of about 1100 km in diameter, and is characterized by two calderas, Meroe and Nili Paterae (Hiesinger and Head, 2002).

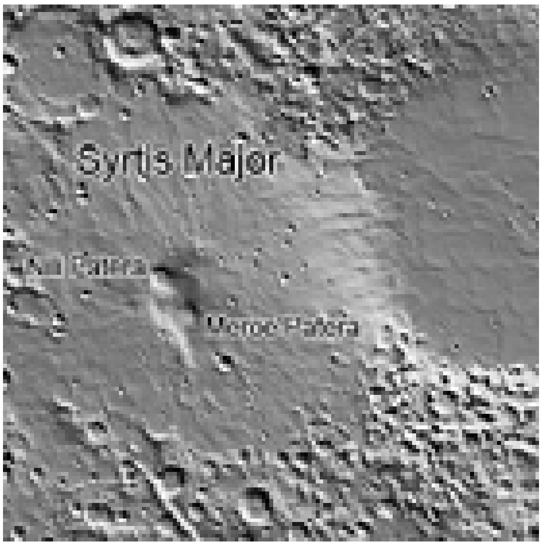

Figure 15.12.: The MOLA shaded–relief map of Syrtis Major Planum and the Meroe Patera and Nili Patera at its center.

They are located almost at the center of the very low shield inside an elliptical depression, which was not interpreted by Hiesinger and Head (2002), but to us appears to resemble an earlier–stage caldera. The plateau is characterized by wrinkle ridges similar to other volcanic plains (e.g. Hesperia Planum). Ages determined for the approximately 70 km diameter caldera of Meroe Patera yield an age of about 3.75 Ga, which probably indicates the end of the main volcanic activity. The crater size–frequency distribution measured for the caldera indicates a later resurfacing ending about 2.3 Ga ago, which we interpret as non–volcanic. Similar ages have been found by Hiesinger and Head (2004).

Caldera Age of Meroe Patera (Syrtis Major)

Unit	N_{cum}(1km)	Age in Ga
Meroe Patera	7.28e-3/1.13e-3^{+}	3.73/2.33^{+}

$^{+}$ treatment description see Chapt. 9.1
for imagery, area annotation and counts see Appendix B

15.4. Volcanic Plains

Four types of Martian volcanoes and their prevailing occurrences in the cratered terrain hemisphere (generally the southern hemisphere) have been described. Paterae, which are large low-profile volcanic structures, appear to be either older shield volcanoes or a unique type of volcano. 'Plains' volcanics represent low-volume eruptions that formed cones, low shields, and other small–scale structures. Flood volcanics are produced by high–volume eruptions, post–dating the older and more degraded plateau plains, and occur mostly as basin–filling materials. Plateau plains, the Martian inter–crater plains, contain many wrinkle ridges and floor–fractured craters. It has been suggested that volcanic processes as well as erosional processes have been important in obliterating small Martian craters (Greeley and Spudis, 1978). Further, volcanic products may constitute a significant fraction (up to 44%) of the surface rocks in the cratered terrain (Greeley and Spudis, 1978).

One of the typical examples of volcanic plains is Hesperia Planum. Typical wrinkle ridges are interpreted as resembling the morphology of lunar maria. Many ridges follow an irregular pattern, but some appear mostly circular and cover what are likely crater rims of a cratered plains unit that has been subsequently covered. Crater size–frequency measurements performed on Viking and THEMIS imagery suggest that the plains were emplaced before 3.7 Ga ago, but experienced a resurfacing event about 3.12 Ga ago (N_{cum}(1km)=1.60e-3, see Fig. 17.1). This emplacement age is valid for the entire Hesperia Planum unit. Another plains unit, a small region of Lunae Planum, yields an age of 3.5 Ga (see Table 14.1).

15.5. The Volcanic Constructs – Discussion of Results

The detailed volcanic evolution of most individual volcanic constructs on the Martian globe is described in Chapter 15. The crater count results and derived relative and absolute ages are given here and listed together with the imagery in Appendix B. In this section, a more general view of the derived geological evolution of Mars based on the volcanic evolutionary history will be discussed. Additionally, the possible correlation of volcanic processes with fluvial (and glacial) activity will be outlined. In Figure 15.13, all resulting crater counts gathered in this work are plotted together with measurements based on Viking imagery by other authors previously (as discussed in Chapter 15). The data used here were assembled by Neukum and Hiller (1981), evaluating measurements published by Blasius (1976); Carr (1976); Carr *et al.* (1977b); Crumpler and Aubele (1978); Masursky *et al.* (1977); Neukum and Wise (1976); Plescia and Saunders (1979); Wise *et al.* (1979b) and their own.

The novelty of the global data set presented and interpreted here is that counts have been performed by a single observer, are based on a single set of high–resolution imagery, and have had a single crater production function and chronolgy model applied. This guarantees a very coherent set of data and allows for a better comparision of the results and subsequent comparison to earlier measurements. Based on the results shown in Fig. 15.13, the following volcanic evolution for Mars is derived.

All volcanic constructs were formed and built up to their present size by very early time in the Martian history (before about 3.6 Ga ago). This implies that most of the volcanism had started about 4 Ga ago or even earlier. In that time period, the highland units had already been emplaced and inter–crater plains were formed. Possibly, even the basement of the lowlands had formed about that time (before 3.8 Ga ago). The **small tholi and paterae in the Tharsis region** are relics of such an early volcanic period. In their case, the vent production of magma stopped about 4 Ga ago and shows only in a few cases subsequent activity until about 3.7 Ga ago. Few of the tholi and paterae show later resurfacing, which is not clearly related to volcanic processes. Global volcanic activity during the early Martian history is manifested in many small shields or domes found e.g in the vicinity of Apollinaris Patera (Chap. 15) or in the Coracis Fossae, where we obtained ages of about 3.9 Ga (Grott *et al.*, 2005). For the other large Tharsis volcanoes, crater size–frequency distributions indicate that they reached their final size about 3.6 Ga ago, with later more or less intensive resurfacing of the flanks. A similar decrease in activity is found for the **highland volcanoes**: Meroe Patera (Syrtis Major), Amphitrites Patera and Apollinaris Patera, with no obvious volcanic activity occurring later than 3.65 Ga ago. Subsequent resurfacing is observed and could be related to a blanketing deposition of unkown origin, which is seen equally inside and outside the calderas. A more varied timing of events is observed for Hadriaca and Tyrrhena Paterae, situated east of Hellas in Hesperia Planum, a volcanic plain that formed about 3.7 Ga ago. The evolutionary history of both volcanoes appears synchronized in processes and timing. After the formation of a cone apparently composed of material from more explosive volcanic activity early in the Martian history (about 3.9 Ga ago, the very shallow broad shields were already constructed). Subsequent activity resurfaced the vicinity by possible ash deposition and by later carving channels into the unstable ash deposits until about 3.7 Ga ago. The eruption style changes later to a more effusive one as observed at their crest regions (about 3.5 to 3.3 Ga ago). Inside the Hadriaca caldera and at Tyrrhena Patera, the latest volcanic activity ended about 1.5 Ga ago, as indicated by the large caldera–flank channel on Tyrrhena Patera. The **Elysium volcanoes** formed before 3.6 Ga ago and reached their final size about 3.6 Ga ago. Extensive volcanic activity is observed at the western flanks of the

Elysium rise during a period between 3.4 and 3.3 Ga ago. Enormous volcanic flows expand into Utopia Planitia, while flank failures support the formation of channels by the release of water. The surrounding plains to the northeast (Arcadia Planitia) indicate subsequent volcanic flooding about 2.6 Ga ago, but the source remains unclear. The caldera and upper flanks of Elysium Mons formed about 3.5 Ga ago, showing a resurfacing about 1.5 Ga that cannot be related to volcanic activity because both ages are found inside and outside the caldera. Especially, measurements at Hecates Tholus, but also at Albor Tholus, indicate that volcanic activity occurred later than previously thought. Caldera and flank ages show subsequent resurfacing over the past 2 Ga, while at Hecates Tholus this happened even over the past 1 Ga until about 100 Ma ago. Elysium Planitia, a region southeast of the Eysium rise, appears as one of the youngest plains on Mars (formed between 10 and 30 Ma ago, see Fig. 10.3). The ages measured in this region are discussed, as a result of the discovery of crater Zunil and its numerous secondary–crater strewn field. As discussed in Chapter 10.1, the misinterpretation in age is less than a factor of two, if secondary craters were included in the measurements unwittingly. As discussed above, the small **Tharsis volcanoes** are classified as very old small tholi and paterae that are relics of the earliest volcanic activity in that region. Major parts of the large shield volcanoes have formed before 3.6 Ga ago. At all shield flanks, episodes of volcanic eruptions (flows) are observed, which have surface ages of between 500 Ma and 100 Ma. The youngest ages determined by the crater size–frequency measurements are about 2 Ma (Olympus Mons escarpment), suggesting that the volcanoes are potentially still active. For Alba Patera, the most recent flank resurfacing occurred about 200 Ma ago, possibly the result of volcanic activity. Caldera floor ages of the Tharsis Montes and Olympus Mons reveal that the latest vent activity happened between 200 Ma and 100 Ma ago. At the foot of Pavonis Mons, small shields are observed that formed about 300 Ma to 100 Ma ago. This latest extensive volcanic activity, observed in both large volcanic provinces (Tharsis and Elysium), correlates well with crystallization ages found for the basaltic Martian meteorites (Shergottites) and shows that the applied chronology model accurately reflect the surface ages.

For the first time, it was possible in this study to determine the age for the formation of the Medusae Fossae: 1.6 Ga. This correlates with late–stage activity of some highland volcanoes (Hadriaca and Tyrrhena Paterae) and at least some ages found at the flank of the Tharsis Montes. The same age is observed for some volcanic surfaces where no clear source can be identified (Elysium Mons, Meroe Patera). If the Medusae Fossae deposits are interpreted as pyroclastic ashes that are wide–spread over the planet and accumulated at the dichotomy boundary, it is possible that they could have been deposited as a thin layer in many places, for example, at the volcanoes. This possible final stage of global volcanic activity is maybe supported by the age of another group of Martian meteorites (Nakhlites).

Crater size–frequency measurements confirm that the most edifices were constructed over billions of years and are characterized by episodically repeating phases of activity that continued in both large volcanic regions almost to the present. A number of caldera floor and flank ages are clustered around 150 Ma, indicating a relatively recent peak activity period and practically coinciding with radiometrically measured crystallization ages of a group of basaltic Martian meteorites (Shergottites). The relation to the second group of Martian meteorites, the Nakhlites, remains more speculative. Most of the smaller volcanoes in the Tharsis region have been active in early Martian geological history, similar to most of the highland volcanoes. The long activity of Martian volcanoes correspondingly implies a long lifetime of the "feeding" source especially in the Tharsis region, that indicates a long and stable dynamic regime in the planet's interior.

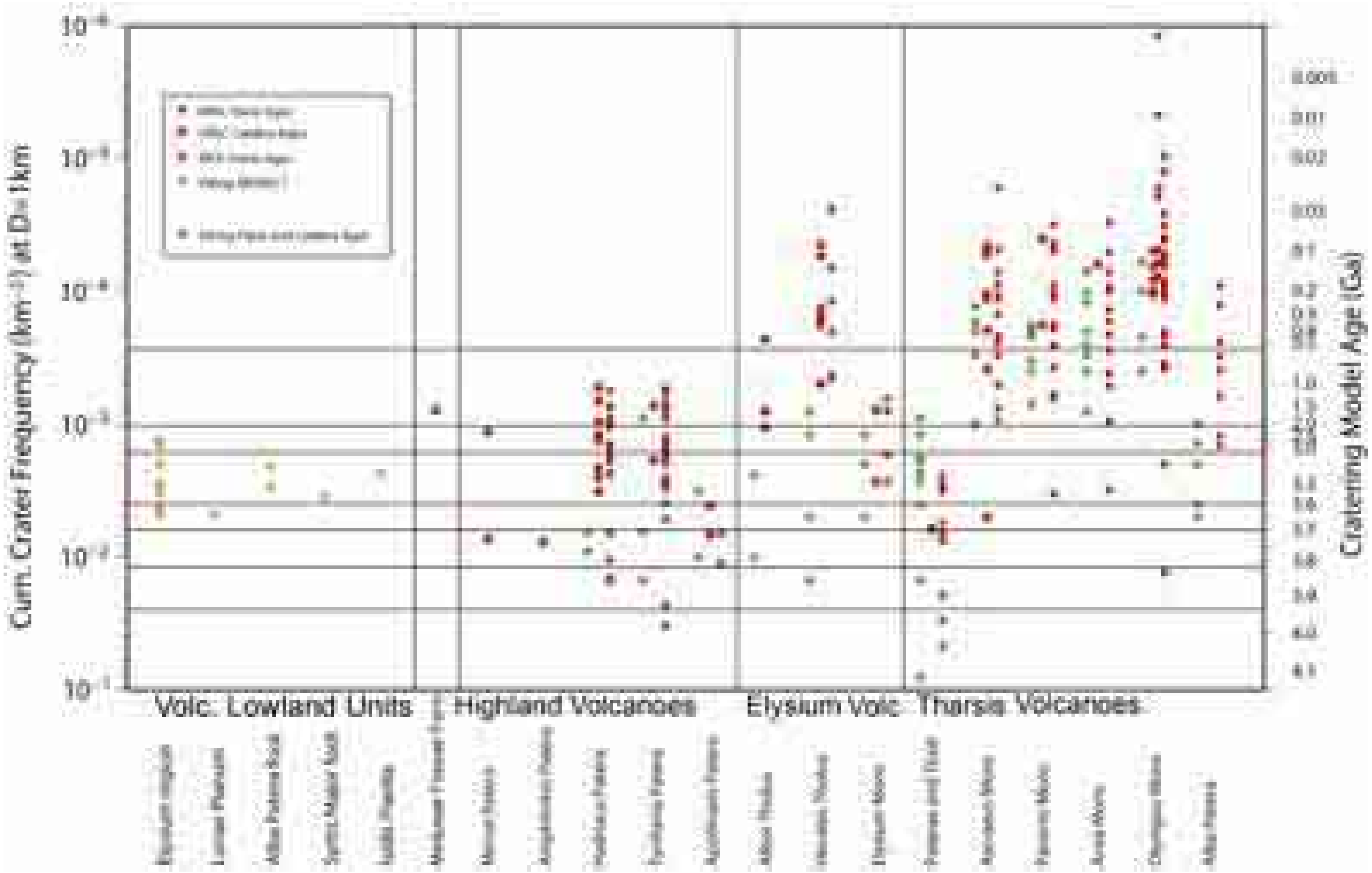

Figure 15.13.: Summary of crater frequencies N$_{cum}$ (1 km) (left scale) and model ages derived applying the cratering chronology model by Hartmann and Neukum (2001) (right scale) for most of the volcanic constructs on Mars (red symbols) and a few volcanic plains units (orange symbols). The results are plotted for each individual volcano and grouped for Highland volcanoes, Elysium and Tharsis volcanoes. Additionally, the results for the Medusae Fossae formation and some volcanic plains are given. Most of the measurements were performed on HRSC imagery (red circles for caldera ages and red squares for flank ages). Measurements on MOC–narrow angle imagery for the flank ages (red triangle) give insight into the small crater size range. For comparison, earlier measurements based on Viking imagery are plotted as green stars. The latter are assembled by Neukum and Hiller (1981) and references therein. Horizontal lines show the epoch boundaries, see Chapter 5, Fig. 5.1.

16. Fluvial, Glacial and Volcanic Interaction

In this chapter, we briefly discuss landforms that are related to fluvial, glacial and possible periglacial processes. The latter are found at the dichotomy boundary, as lobate debris aprons as well as concentric crater and lineated valley fill. These landforms are considered to be composed of substantial amounts of ice and debris (e.g. Squyres, 1979), although this remains unproven. They occur at the highland–lowland boundary of Mars as well as in the vicinity of the large impact basins of the southern hemisphere. Flow– and creep–related landforms, which were observed in the eastern Hellas Planitia area, have already been stratigraphically integrated into a broader context (e.g. Head *et al.*, 2005; van Gasselt *et al.*, 2005).

All age determinations indicate that these landforms in addition to the polar caps (Fishbaugh and Head, 2001) were formed in the latest period of the Late Amazonian epoch (roughly tens to hundreds of million of years ago). These landforms were formed by possible ice–related processes in very recent geological times. Old morphologies, suggesting the involvement of ice in their formation, are not found. Nevertheless, polar–cap surrounding deposits, e.g. at the South Pole, can be substantially older (Head and Pratt, 2001), while the ice just remains as a global cryosphere at a certain depth (Kuz'min, 1983). Speculations of relict polar caps in the Medusae Fossae and Terra Arabia region were initially discussed by Schultz and Lutz (1988), who interpreted the layered and easily deflated (yardangs) deposits in the Medusae Fossae region. Antipodal (Terra Arabia) layering further supported this idea. Neutron spectrometry results have strengthened this interpretation (see Chapters 14.4 and 14.2).

As mentioned earlier, other remnants of glacial or periglacial processes are found, for example, at the western foot of Olympus Mons as well as on the three large volcanoes that make up the Tharsis Montes. Phreatomagmatic processes at the flanks of Elysium Mons and Hadriaca Patera are examples of volcanic–ice interaction, but appear to have occurred much earlier in Martian history. At the eastern flank of Olympus Mons (as well as at many flanks of other Martian volcanoes), fluvial landforms that suggest melting of permafrost or ice–rich surface layers are observed. Landforms related to Athabasca, Mangala and Kasei Valles indicate a close interaction of volcanic and fluvial processes (see earlier Chapters 12, 14.5, and 15). Ages found for related morphologies cover the entire geologic history of Mars (at the latest starting around 3.6 Ga ago, e.g. in Kasei and Mangala Valles, but also appearing as recently as the last 100 Ma, e.g. in Athabasca Valles).

A complex interplay of various processes, such as volcanism, precipitation and accumulation of ice as well as sedimentation and accumulation of atmospheric dust, resulted in the formation of geologic bodies of significant volumes (Neukum *et al.*, 2004; Basilevsky *et al.*, 2005). This interplay occurs in a specific environment of Mars, where voluminous volcanic eruptions alternate with long periods of volcanic dormancy (Neukum *et al.*, 2004; Hartmann and Neukum, 2001; Wilson *et al.*, 2001). This interplay occurred against the background of variations in the obliquity of the rotation axis (Laskar *et al.*, 2004), which would significantly change latitudinal relations of the planet's climate with time and even atmospheric pressure (Kreslavsky and Head, 2005).

The existence of water–ice at the polar caps (Bibring *et al.*, 2004) has been proven spectrally, while it has been proposed for the cryosphere (Kuz'min, 1983; Carr, 1996) and locally on the surface (Lucchitta, 1981) from indirect evidence. Neutron anomalies, (Feldman *et al.*, 2002; Mitrofanov *et al.*, 2002), partly concentrated at the Medusae Fossae Formation and in Arabia Terra, have been discussed, in addition to other explanations such as relics of ancient polar deposits at times of different Martian spin–axis obliquity. Considering strong variations of the axis tilt, the deposition of ice in mid-latitudes or even in equatorial regions is possible (Mellon and Jakosky, 1995).

At the western flanks of Olympus Mons and Tharsis Montes, Viking imagery revealed surficial deposits (mapped by Scott and Tanaka (1986)) that were described as fan–like corrugated sheets (as wide as 600 km) and appear to override topographic obstacles without deflecting the internal structure). Besides a possible volcanic origin, Lucchitta (1981) suggested that they were recessional moraines of former ice–ages. Based on high–resolution imagery of Mars Global Surveyor (Head *et al.*, 2003) and HRSC imagery (Neukum *et al.*, 2004; Head *et al.*, 2005), a glacial origin is supported.

We have studied hydrothermal, fluvial, and glacial activity periods, which were visible in HRSC and MOC imagery. Evidence of very recent and episodic formation of landforms related to these processes is based on our crater counts. Here, we summarize the distribution and time frame of glacial or ice–related morphologic features found in HRSC imagery. Additionally, high–resolution MOC images were used to constrain the crater size–frequency measurements performed on HRSC images. A detailed description of the geologic evidence and ages can be found in Neukum *et al.* (2004); Head *et al.* (2005); Murray *et al.* (2005); Hauber *et al.* (2005), which are attached in Appendix C. In these papers, the arguments for interpreting most of the aforementioned units as glacial, fluvial, or hydrothermal in origin are discussed and not repeated here. Detailed morphological studies and crater counts at the base of Olympus Mons (Neukum *et al.*, 2004) and Hecates Tholus (Hauber *et al.*, 2005), south of Elysium (Murray *et al.*, 2005) and at the southeastern rim of Hellas (Head *et al.*, 2005) have been performed. Fig. 16.1 summerizes the crater frequencies measured at these landforms. Some have been interpreted as landforms that suggest ice on the surface (or under a dust cover) may even be present today. All landforms formed during the last 500 Ma.

A brief summary of the major findings is given below:

Based on crater counts, the different lobate deposits at the Olympus Mons western foot formed in several phases, about 280 Ma ago, 130 Ma ago, acting between 60 and 20 Ma ago, and ending possibly 4 Ma ago. Roughly similar ages (about 450 Ma, 200 Ma, 100 Ma and between 80 and 20 Ma) are obtained volcanic deposition at the Olympus Mons flanks, indicating a possible correlation between these processes (see Chapter 15 and Neukum *et al.*, 2004, for a detailed interpretation).

At the eastern flank of Olympus Mons, glacial landforms have not been observed, but fluvial features are seen at its bases and surrounding plains units. Crater size–frequency distributions at the western and eastern plateau edges reflect similar periods of volcanic eruption. A correlation between these episodes at the lower flanks, upper summit plateau and the caldera is expected and suggested by our measured crater size–frequency distributions (see Chapter 15). Eastwards, eruption episodes which happened about 500 Ma, 200 Ma and 100 Ma ago are recognized. The surrounding plains and lava aprons indicate more recent episodes of volcanic activity (summarized in Chapter 15). The ages of possible fluvial landforms indicate that these processes might have been triggered by the volcanic activity.

Other than the very young glacial deposits found in equatorial regions (e.g. Olympus Mons western scarp (Neukum *et al.*, 2004; Basilevsky *et al.*, 2005; Head *et al.*, 2005) and the approximately 5 Ma old "pack–ice" sea south of Elysium Mons (Murray *et al.*, 2005, for details also see Chapter 12), glacial or ice–related landforms of very young age have been recognized north of Elysium Mons at the northwestern margin of Hecates Tholus (Hauber *et al.*, 2005). An amphitheater–like structure, whose morphology strongly suggests it was the result

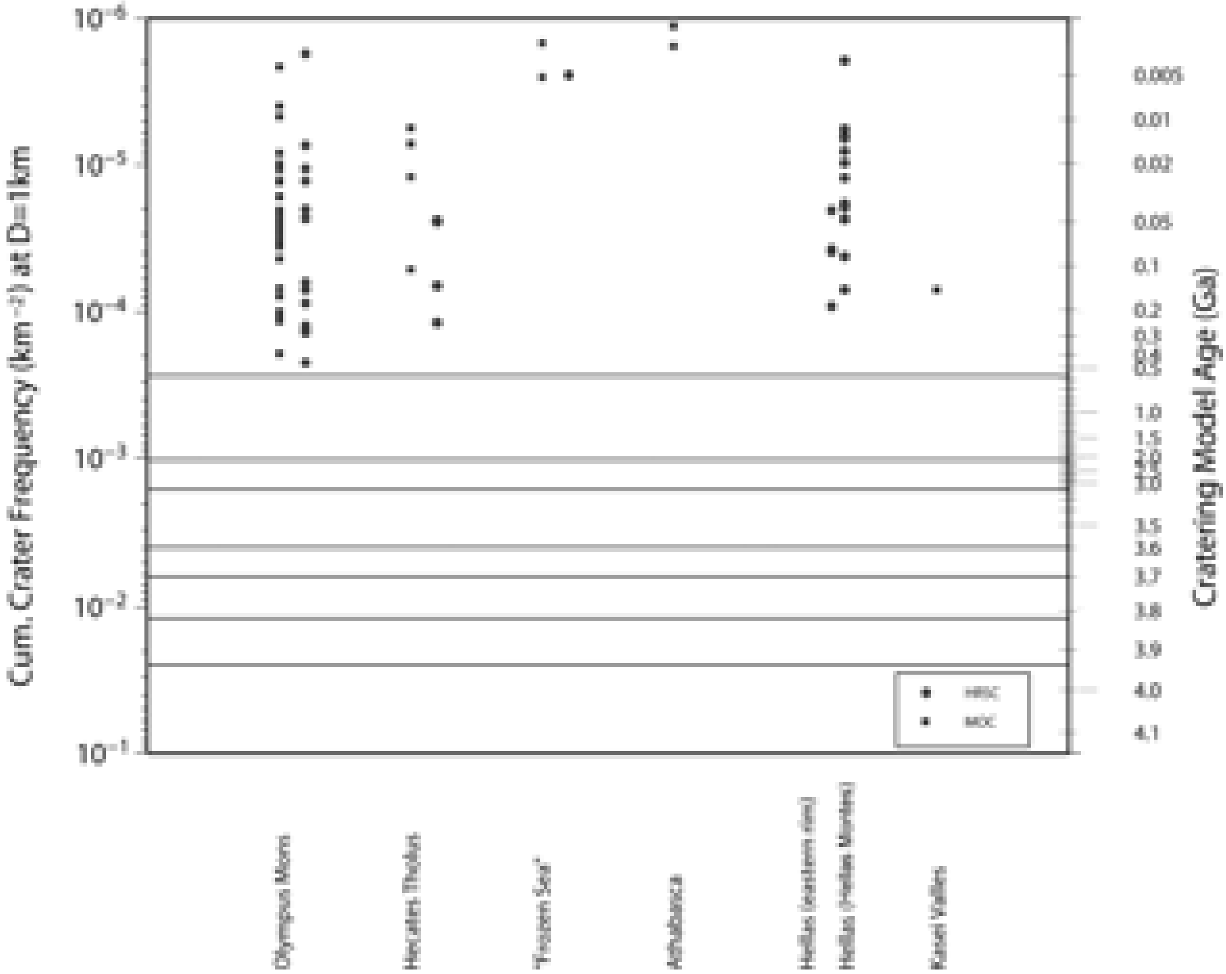

Figure 16.1.: Summary of crater frequencies N_{cum} (1 km) (left scale) and model ages derived by applying the cratering chronology model of Hartmann and Neukum (2001) (right scale) for recent fluvial and glacial activity in close vicinity of Olympus Mons, Hecates Tholus, in Elysium Planitia, and in the Hellas eastern rim region (Neukum *et al.*, 2004; Hauber *et al.*, 2005; Head *et al.*, 2005; Murray *et al.*, 2005; Werner *et al.*, 2003a; van Gasselt *et al.*, 2005). Horizontal lines show the epoch boundaries, see Chapter 5, Fig. 5.1.

of an explosive flank eruption about 350 Ma ago, is probably filled by glacial deposits of very recent ages (between 5 and 24 Ma, Hauber *et al.*, 2005).

The finding of low–latitude glacial landforms or relic–glacial landforms formed in very recent times (tens to hundreds of millions of years), contradicts the present climate situation (cf. e.g. Richardson and Wilson, 2002; Mischna *et al.*, 2003; Haberle *et al.*, 2003). Nevertheless, general climate circulation models (Mellon and Jakosky, 1995), allow for the redistribution of water–ice that was restricted to polar regions to be deposited towards the equator if the Martian spin–axis obliquity changed. Past obliquity changes (Laskar *et al.*, 2004) permit recent "ice ages" in low latitudes, as recorded in the morphology, for example, debris aprons (dichotomy boundary), rock and piedmont glaciers (Olympus Mons, Hecates Tholus and Hellas rim), and suggested by the derived surface ages.

Van Gasselt *et al.* (2005) proved through morphological arguments that mass wasting processes, possibly driven by the presence of ice, occurred episodically. This is supported by crater frequency measurements. Similar episodicity is found at Hecates Tholus and Olympus Mons. In the latter case, the release of water might have been triggered by volcanic activity, and which is indicated by correlating ages found for both processes. A triggering of water release as a result of volcanic activity is observed in the cases of Athabasca and Kasei Valles in most recent times. There, volcanic activity can be linked directly to possible (sub–)surface ice melting. In other places, such a relation is suggested by morphology and surface ages found, e.g. at Olympus Mons during the last 500 Ma.

The general occurrence of fluvial and (peri–) glacial landforms, formed over the latest 500 Ma of the Martian history, might be related to volcanic activity which might induce short–lived atmospheric changes, which support the subsequent deposition of ice and the formation of ice–containing landforms.

These activity phases might also be related to changes in obliqity and/or solar flux, but both relations remains speculative. The results of this thesis strongly support the idea that recent climate changes have occurred and can be explained by an obliquity change of the spin axis or the solar cycle, as seen on Earth. On Earth, ice ages are recorded morphologically in very recent geologic history. For Mars, such a short time scale cannot be resolved on the basis of crater counts. Thus, changes in obliquity or recent climate changes remain speculative.

Part IV.

The Evolutionary History of Mars

Part IV, **The Evolutionary History of Mars**, summarizes the temporal development of the Northern Lowlands and the global volcanic evolution in relation to the decay of the magnetic field, the actual dynamic shape of Mars, as well as their implication to the general evolution of the planet Mars. The interplay of volcanic activity, the northern lowland formation, together with the formation of the dichotomy are put into the context of earlier investigations (see also Part III). New findings with respect to the evolution of Mars are described, and in part, a new view of the most recent evolution will be outlined. An outlook to further investigations and the importance of our findings will also be discussed.

In this thesis, the frequency of craters forming on geological units are used to investigate the sequence of events in various regions of Mars, including

- the lowlands occupying the northern hemisphere, and the outflow channel activity of adjacent regions
- the dichotomy boundary separating the lowlands and highlands
- the global volcanic record, and
- recent fluvial, glacial, hydrothermal, and volcanic processes and their interplay

Except for the chronostratigraphic classification of these regions, this effort has resulted in the determination of the Martian crater size–frequency distribution over the entire measurable diameter range (tens of meters to hundreds of kilometers). Regarding the "contamination" due to secondary cratering in our crater counts, we found, in agreement with Hartmann (2005), that the conclusion by McEwen *et al.* (2005b) that the age determination is impossible, is not valid (Part II).

All absolute ages derived in this thesis are based on the assumption that Mars and the Earth's moon have had a similar bombardment history with respect to the time dependence of impact rate and the source of impactors; therefore, the transfer of the lunar cratering chronology to Mars appears valid. We tested this idea by comparing the early lunar and Martian cratering record, which had a characteristically higher impactor flux than today. The impactor flux for this period between 4.1 Ga (Apollo 16 landing site) and 3.15 Ga (Apollo 12 landing site), has been calibrated for the Moon based on radiometric ages. These have been determined for samples collected on the lunar surface at various landing sites and brought to Earth.

Additional knowledge is gathered by studying large impact basins (larger than 250 km in diameter) that only formed during the so–called heavy bombardment period. On the Moon, these basins did not form any later than about 3.9 Ga ago, and we found a similar situation for Mars. The number of large impact basins per age period appears to be in the correct proportion between the Moon and Mars data. However, on Mars the oldest crustal structures we observe today are no more than 4.2 Ga old, whereas we can probably date the lunar surface back to 4.3 or 4.4 Ga. On Mars the earlier record has been erased by endogenic and surface erosional processes. This implies that the transferred Martian cratering chronology relates the crater frequencies and absolute ages correctly in the exponentially dominated part of the cratering chronology model (before about 3.5 Ga; the higher flux period). For the younger period (younger than about 3.5 Ga) two facts support the validity of the cratering chronology model: (1) the estimates of the asteroidal impactor population has increased in number over the last years (2) their orbital evolution is better known, so that the transfer of the lunar model to Mars now has a good statistical basis. Applying this model we can derive surface ages for volcanic and fluvial landforms of large areal extent. A good agreement with meteorite ages of volcanic origin and aqueously altered minerals is found.

17. Stratigraphic Type Areas Re–Visited

Based on imagery from Mariner and Viking missions, the Martian stratigraphic system has been established (originally by Condit (1978) and later refined by Tanaka, 1986). As no direct measurements of absolute ages of Martian rocks are available (except a few of SNC meteorites), model ages of the stratigraphic system and series are based on estimated projectile flux. Relative ages are measured by means of superimposed crater frequencies and transferred to absolute ages applying the established chronology model (Hartmann and Neukum, 2001). The formal definition of Martian time–stratigraphic units started with a 1:25M-scale map of Mars by Scott and Carr (1978), divided into Noachian, Hesperian and Amazonian units. The exposed base of the Arcadia Formation defines the base of the Amazonian system. Re–measurements in Arcadia Planitia revealed resurfacing processes (as suspected by Tanaka, 1986), which shifted the age boundary of the Lower Amazonian (for comparison see Fig. 17; Hartmann and Neukum, 2001).

For the epoch–boundary definition, cumulative crater frequencies at certain diameters (and larger) for a specific type unit have typically been utilized. In all map approaches, the registration of surface units to an epoch by relative or even absolute ages is based on the predicted cumulative crater frequencies at diameters of 16 km, 5 km, and 2 km (Tanaka, 1986). To classify smaller or younger units, where none of these diameter classes are present, a "minus–two" slope has been formerly suggested in order to extrapolate the crater size–frequency distribution to the smaller–size ranges (e.g. Tanaka *et al.*, 2005). All our measurements show that such a simple approach is invalid; see detailed discussion of the "true" shape of the Martian crater size–frequency distribution in Chapter 11. At least a segmented power–law (Hartmann, see Chapter 4) or a polynomial expression (Neukum, see Chapter 4) is much more adequate for describing the complex structure of the Martian crater size–frequency distribution, as predicted by Hartmann, Neukum, Ivanov and others (see Chapter 4).

We have re–mapped some key geologic units, including Amazonis and Acidalia Planitiae, Hesperia Planum as well as Noachis Terra. In the following, the results of crater size–frequency measurements, which we used to re–examine the age boundaries of the stratigraphic epochs, will be discussed.

17.1. Ages of Martian Basins and the Noachian Epoch

As discussed in Chapter 13, the large lunar basins were produced no later than about 3.8 to 3.9 Ga ago and the situation is similar for Mars. In the case of Mars, most basins formed before 3.9 Ga, based on crater size–frequency distributions and the applied cratering chronology model. When comparing the frequencies of relevant impact basins on Mars and on the Moon for the period prior to 3.9 Ga, roughly similar number of bodies hit the Moon and Mars per surface area. According to our investigation, much of the oldest surface areas on Mars, the Martian southern highlands (e. g. Noachis Terra), were formed at around 4.0 to 4.2 billion years ago during the period of the heavy bombardment. This implies that no surface is found to be older than 4.2 Ga. Radiometrically determined ages for Martian meteorites indicate that some rock ensembles are as old as 4.5 Ga (Chapt. 6.1), i.e. part of the surface material survived from that time until today though no structural relationship is visible any more.

As discussed in Chapter 13, the transferred chronology model supports the idea of a marker horizon, as suggested by Wetherill (1975). An upper limit of surface ages based on crater counting has been introduced by these measurements of the crater size–frequency distribution in Noachis Terra and the number and ages of the large impact basins on Mars. The average age of the Martian highlands, derived from a size–frequency distribution of basin diameters compiled by Barlow (1988a), is about 4.1 Ga.

The boundary between the Middle and Upper Noachian Epoch is defined by the unit assigned as Npl2, which can be found in Noachis Terra as well, adjacent to Npl1 units (Scott and Tanaka, 1986; Greeley and Guest, 1987; Tanaka and Scott, 1987). One of the Noachian type regions is indicated as Npl1, which is the Noachian unit representing the boundary between Lower and Middle Noachian around 4 Ga ago. For the large–crater range (> 2 km) measured in Npl2, we obtained an age of about 3.9 Ga (boundary between the Middle and Upper Noachian). Inspection of the smaller–size range (< 2 km) indicates depletion of craters due to resurfacing, e. g. by erosion as is visible in the valley networks and deposition (inter–crater plains).

17.2. The Hesperian Epoch

Hesperia Planum is the type region for the Early Hesperian period. The crater size–frequency distribution for this region (Hr), based on old Viking data supplemented by high-resolution (17 m/pxl) THEMIS imagery, revealed resurfacing in the smaller crater–size range. The age for this plains unit is 3.71 Ga and the resurfacing event ended 3.18 Ga ago. When comparing our crater frequencies to the corresponding boundary crater density ranges (see Chapt. 6.2), only an approximate agreement is found. Nevertheless, all boundaries were established based on Mariner 9 and Viking imagery. Therefore, crater frequencies below crater diameters of about 800 m were not considered due to the lack of global coverage at high resolution, to effects of erosion and deposition, and the possible but unresolved contribution of secondary craters. Considering only large craters, which are not affected by the above mentioned processes, requires a large sample area to allow for a statistically significant interpretation. On Mars, this is difficult in itself, especially for the younger regions where significant resurfacing occurred and only small patches of homogeneous surface are exposed.

Other regions such as the Northern Lowland units are of Hesperian age. Recent efforts by Tanaka *et al.* (2003) focused on remapping the geologic unit of the northern plain units, considering topographic and stratigraphic aspects rather than morphologic characteristics. They obtained new insights into geological processes and events and proposed four successive stages of lowland resurfacing that are most likely related to the activity of near–surface volatiles.

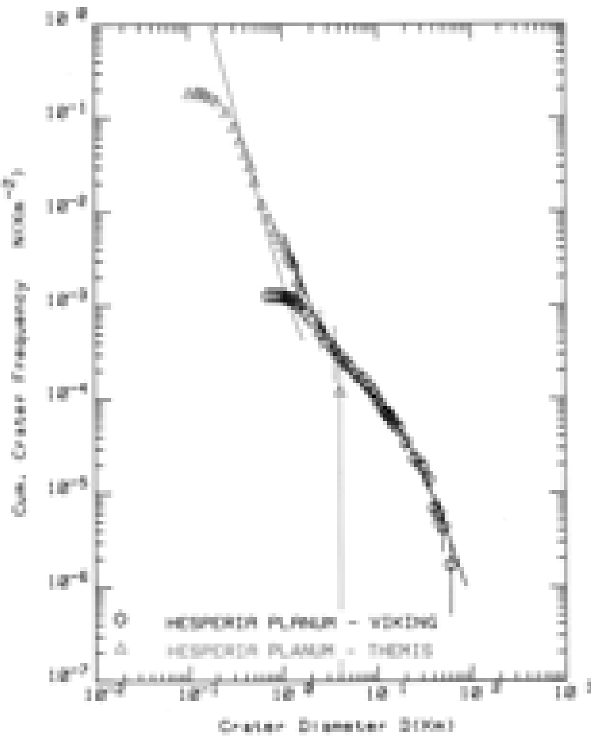

Figure 17.1.: The crater size–frequency distribution measured on Viking (black) and THEMIS (red) imagery. The plains age is about 3.7 Ga (black curve) and experienced a resurfacing event ending about 3.2 Ga ago (red curve).

Measured Crater Size Frequencies for the Type Locations

Series	Type Region	< N(1)	N(1)	N(2)	N(5)	N(16)	> N(16)	abs. Age
Upper Amazonian	Achu	ok	7	–	–	–	–	0.014 Ga
Middle Amazonian	Aa3, Aa2	–	resurf	39	18	–	–	1.15 Ga
Lower Amazonian	Aa1	–	528	292	95	18	older	3.5 Ga
Upper Hesperian	Hv(x)°, here Hvg	–	624	333	87	lack	lack	3.44 Ga
Lower Hesperian	Hr	resurf	4320	705	225	49	ok	3.71 Ga
Upper Noachian	Npl2	resurf	resurf	1040	417	120	older	3.88 Ga
Middle Noachian	Npl1	resurf	resurf	1180	544	245	ok	4.02 Ga
Lower Noachian	Nb	–	–	–	–	–	–	> 4.1 Ga

⋆ N(D) = no. $\geq$ D/10^6 km^2 and Hv(x)° means Hvk, Hvg, Hvr, Hvm

Table 17.1.: The Crater frequencies for crater diameters equal to or larger than 2 km, 5 km, and 16 km as measured for the stratigraphic type areas, which outline the boundary conditions for the different geological epochs, type regions according to Scott and Tanaka (1986); Greeley and Guest (1987); Tanaka and Scott (1987).

As an example for the Northern Lowland units, we selected Acidalia Planitia (similar to Utopia Planitia), which is occupied by extensive areas of polygonal terrain, so-called giant polygons (a general chronostratigraphic interpretation of the new map approach is discussed in Chapter 14.6). Measurements of size-frequency distributions in areas covering polygonal terrain and surrounding units yield (crater retention) ages of 3.4 Ga in the medium-size range. We have obtained size–frequency distributions that appear to have an unusual deficiency of large craters compared to the proposed production function (Chapter 14.3). Such an observed distribution, which roughly follows a single power–law description (with a slope index close to –2), has been discussed for the northern lowlands and other younger Martian units. Barlow (1988b) and most recently Strom *et al.* (2005) argue that the change of the production function is due to a change in the projectile population after the heavy bombardment period. Combining the clearly visible crater population with the population of so–called ghost craters, buried craters causing ring-like grabens, yields an age of 3.8 Ga with resurfacing, which occurred until about 3.4 Ga ago. Similarly shaped distributions (compared with the stacked population distribution in polygonal terrain) are observed in regions with strong "excess" of craters in the larger diameter range (see Chapter 14.3). These distributions can be explained by extensive resurfacing (deposition) effects within a time span of roughly half a billion years. The difference compared with the giant polygon units is that the large craters are blanketed, while in the vicinity the large crater population is preserved mostly unmodified.

Other regions in the northern lowlands, earlier considered as Hv(x) members (Hvk, Hvg, Hvr, Hvm), appear to have formed between 3.8 Ga and 2.8 Ga (see Chap. 14.1). This implies that the causative and temporal formation of the northern lowlands is not completely uniform. Therefore, it is difficult to use any of these unit to define epoch boundaries. The problem is indicated in the inverse age results for the type regions for the Upper Hesperian and Lower Amazonian Epoch. The unit mapped as presumably younger surfaces, actually appears older based on crater counts. The variability of crater size–frequency distributions measured in the northern–lowland regions is mainly due to the deposition of variably thick layers (see Chapt. 14.3 for discussion), which in many places of the lowlands obscure the crater size–frequency distributions. Discussions (e.g. Strom *et al.*, 2005, and earlier by Barlow (1988b)) regarding the change in the projectile population between the period of heavy bombardment and younger times are based on the differing crater size–frequency distributions found in the Martian Lowlands and highland areas. In this thesis, crater counts have been performed to understand and support the stratigraphic relationships between different geologic units and to obtain a coherent view based on the relative crater frequencies. These are based on area sizes that mostly do not reflect the large diameter size range (> 50 km) for surfaces younger than about 3.4 Ga (see Table 14.1). Therefore, a definitive answer as to the shape of the large crater size–frequency distribution cannot be given for the entire northern lowlands.

An ideal crater production function is very rarely found in the lowland areas. Even the surface of geologic units classified as Amazonian, e.g. Aa1, Aa2, Aa3, shows resurfacing events. In the large–scale distribution (> 5km) kilometer–sized craters remain (obviously embayed by later deposits), but smaller–scale resurfacing also occurred, affecting craters below 1 km in diameter (unobservable in Viking imagery).

17.3. The Amazonian Epoch

Amazonis Planitia has been considered the type region for Amazonian ages. This youngest epoch, the Amazonian, includes an absolute time span of 3/4 of the geological record of Mars. Our crater size–frequency distributions reveal strong resurfacing events and a non–uniformity in age. This means that the Amazonian–Hesperian time–stratigraphic boundaries have to undergo careful revision.

In most of our investigations, based on high–resolution imagery (HRSC, THEMIS, and MOC–NA), large areas are occupied by volcanic units, that formed later than 500 Ma ago. Additionally, most surface morphologies associated with ice on the surface or subsurface ice (glacial), such as debris aprons, lineated valley fill, or possible rock glaciers, appear to be relics of the most recent "ice ages" on Mars (see Chap. 16). All landforms related to such processes have formed during the most recent 1/8 of the Martian geologic history.

Based on these results, a revision of the boundary key units is needed to find units that would best represent those youngest Amazonian epochs in high–resolution imagery. A new subdivision of the last three billion years of Martian geologic history (the Amazonian) may have to be considered.

This effort needs an established and unified crater production function, as discussed in Chap. 11. We could not confirm a separation between two different populations before and after the heavy bombardment period. All our measurements have been performed in coherent, uniform geologic units. We have never summarized measurements that ignored geological unit boundaries. Most of the measurements do not cover the large size range of the distribution that would allow us to judge the shape of that part of the distribution, since the areas are both too small and/or too young (< 3.5 Ga) to obtain a statistically significant sample. In areas older and/or larger (e.g. Fig. 17.1), the coverage is extensive enough (statistically significant) to indicate that the shape in the large–size range confirms the shape as described by Neukum (1983); Neukum and Ivanov (1994); Ivanov (2001).

18. Results, Prospects, and Applications

This thesis provides a coherent view on the geological evolution of Mars, focusing on impact cratering, volcanic, fluvial, and glacial processes. In addition to tectonics and aeolian dust distribution, theses processes play a significant role in sculpting the Martian landscape. Notably the volcanic and related tectonic activity sheds lights on the internal dynamics and thermal evolution of planets. By understanding the evolutionary history of Martian volcanic constructs, the formation time of large impact basins, as well as the evolution of the northern lowlands and the dichotomy boundary, essential time–markers are gathered in this work. After having provided a time–frame of surface processes, the timing for the thermodynamical evolution of Mars can now be assessed.

The apparent absence of plate tectonics on Mars and the presence of huge volumes of strongly magnetized crustal materials, requiring the presence of a strong dynamo field in ancient times, makes Mars an interesting planet to compare with Earth or other terrestrial inner Solar System bodies.

One of the most startling planetary scientific discoveries in recent years was the observation of strong Martian crustal magnetism (Acuña *et al.*, 1999). Though an internal dynamo is not currently active, Martian crustal palaeo–sources are orders of magnitude stronger than lunar fields, as strong or stronger than any terrestrial crustal fields. The properties of the current crustal magnetization provide information regarding the geologic processes responsible for its formation, while constraints on the time history of the dynamo will provide information about the thermal history of the interior and in turn will provide vital information concerning Mars's formation and dynamic evolution. Finally, the history of the dynamo may prove relevant to atmospheric loss through time, with implications for climate (and astrobiological considerations). Understanding the age distribution of Martian magnetic anomalies will allow us to determine the history of the Martian dynamo and consider the implications for the formation as well as the geologic and climatic evolution of Mars as will be outlined below.

Many aspects of the scenario of the early and subsequent evolution including internal dynamics of Mars has been discussed earlier (most recently e. g. by Spohn *et al.*, 2001; Solomon *et al.*, 2005; Nimmo and Tanaka, 2005). Usually, the timing is based on educated guesses, while the results of this thesis essentially push the time–frame forward. The evolutionary geologic history of Mars based on ages gathered in this thesis is given in Fig. 18.1.

The visible crustal age in the southern highland unit, carrying the strongest remnant magnetization, appears to have formed before 4.1 to 4.2 Ga (Chapt. 13), while the oldest known Martian meteorites indicate a crustal age of about 4.5 Ga (Chapt. 6.1). Most of the southern highland areas, showing weaker magnetization, are subsequently resurfaced (by fluvial erosion and possibly volcanic deposition). Crater counts yield ages around 4.0 Ga. While the absolute ages for this period do not differ very much, the relative ages from crater frequencies differ up to a factor of two. Crater counting methods, nevertheless, cannot account for any evolution earlier than documented in the crustal formation. Due to the high impact flux, saturation may have been reached and the net accumulation may be indetermined, thereby limiting this method of age determination to about 4.3 Ga. In this investigation no surface is found to be older than 4.2 Ga (Chapt. 13).

The Martian dynamo must have been active before 3.9 Ga. The cessation of the magnetic field seems to be correlated with the formation of the large impact basins, Hellas, Argyre, Isidis

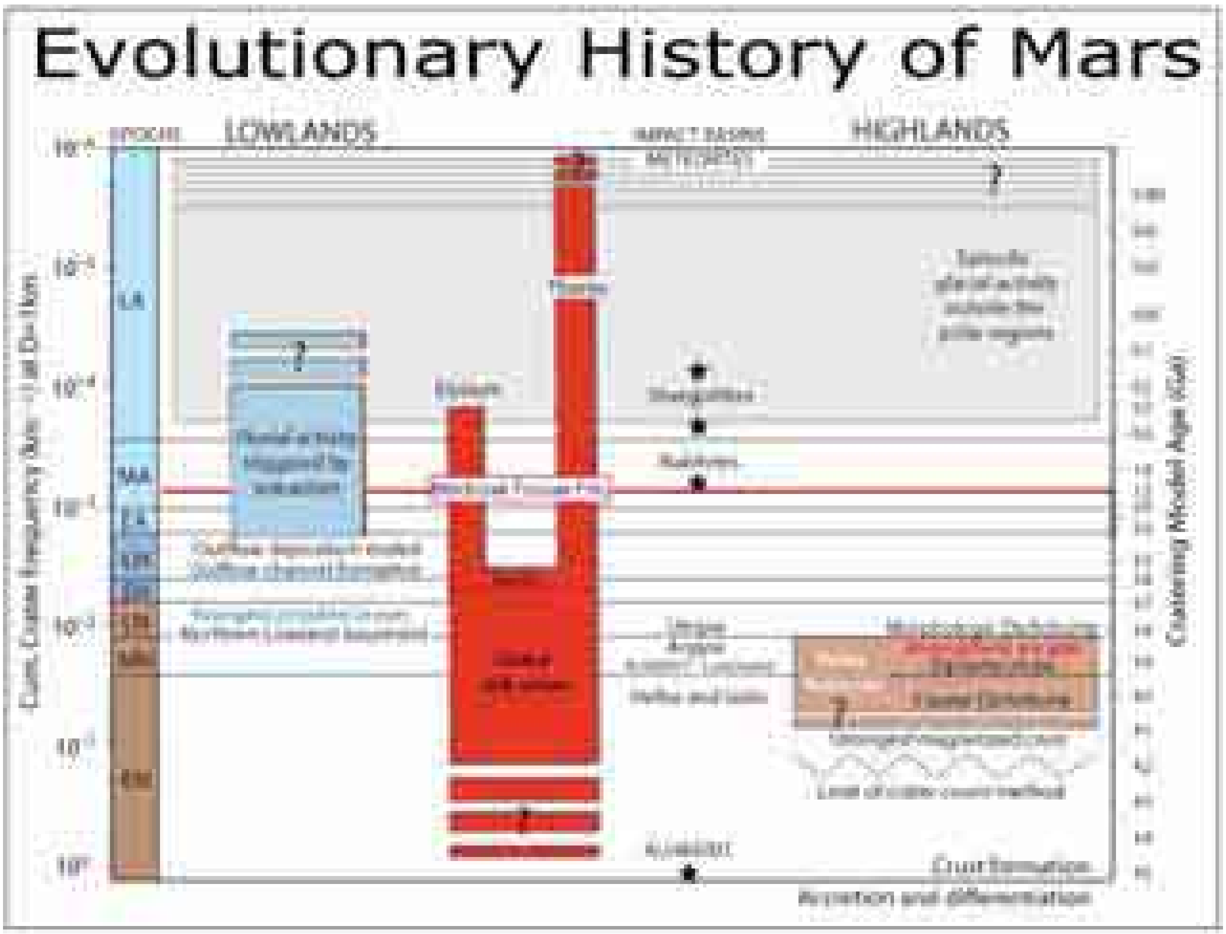

Figure 18.1.: The global geological evolution of Mars derived from ages determined in this work. It is distinguished between the evolution of the lowlands and highlands. Impact basin formation and meteoritic crystallization ages are indicated as time–markers. The volcanic evolution is shown separately because the volcanic history is independent of these two crustal units. Tectonic features are strongly related to the volcanic activity and not specifically discussed in this figure. The *Medusae Fossae formation* and *episodic glacial activity outside the polar regions* are not particularly identified in any of the hemispheres. Similarly, aeolian features appear planet–wide and are not specifically related to any epoch. Generally, a decay of such an activity is observed. Ages are given according to the cumulative crater frequency (left) and in absolute ages (right), additionally, the geologic epoch boundaries are shown (following Tanaka *et al.* (1992a), LA, MA, EA, assign Late, Middle, and Early Amazonian, LH and EH stand for Late and Early Hesperian, and LN, MN, and EN for Late, Middle and Early Noachian. No ages older than about 4.15 Ga are found in this investigation.

and Utopia (Chapt. 13). They are devoid of long–wavelength magnetic anomalies (observed at spacecraft height of about 150 km on average). At least Hellas and Isidis formed about 4.0 Ga ago, while Argyre and most likely Utopia are younger. Nevertheless, the period of cooling of a melt pocket formed by such a large impact event and the temperature drop below the Curie temperature (blocking of a remnant magnetization), could take as much as a few 100 Ma (Reese *et al.*, 2004). The formation time of the crater and the drop below the Curie temperature of the formed melt body is therefore not identical, and hence large basins are not the best time–marker for the cessation of the dynamo (they provide a minimum age). Further confirmation is found at volcanic constructs. Hadriaca Patera shows magnetic signatures, supporting a cessation of the dipole field around 3.9 Ga. Similarly, the basins are used as time–marker for the formation of the crustal dichotomy, reflected in the north–south varying crustal thickness. The observed crustal (thickness) distribution was established early and was modified through these impacts. Nevertheless, this study could not confirm a simultaneous formation of the early lowland and highland crust. The formation of the morphologically defined dichotomy is most likely happened at a different time–scale (Chapt. 14.2). Subsequently, further modification (e.g. crustal thickening) occurred through volcanic activity in the two large volcanic provinces Tharsis and Elysium. No quasi–circular depressions were mapped (Frey *et al.*, 2002), but similar methods were used to define the age differences between visible surface and underlying basement which formed about 3.4 Ga and 3.8 Ga ago, respectively (Chapt. 14.3). The age difference between the highlands and the presumed basement of the lowlands is roughly 200 Ma, based on crater counts. In favour of a crustal formation in the lowlands after the cessation of a dynamo, the results gathered in this thesis fit better.

Plains formation and surface ages of the small tholi and paterae in the Tharsis region indicate that there globally volcanic activity had occurred since 4.1 Ga ago and continued to about 3.7 Ga. All volcanic constructs were emplaced to its now observed size before 3.55 Ga ago (with the exception of Olympus Mons which lost part of its outer shield before 3.7 Ga ago). Most volcanic plains (e.g. Hesperia Planum) were emplaced before this time (Chapt. 15). The end of this period of global volcanic activity is correlated with the outflow channel formation. Generally, the erosive process by fluvial activity and the global volcanic activity decreased after 3.5 Ga. In the northern lowlands the layer of deposits formed during that time and grew to a thickness of possibly a few kilometers in the depressions (Chapt. 14.1). Valley networks are found dominantly in highland regions and are believed to be older than the outflow channels.

In the presence of a self–sustained magnetic field (requiring a partly fluid core) the atmosphere is more stable against solar wind. On Earth (or Venus) the gravitational effect is strong enough to keep an atmosphere even without a dynamo, while on Mars major atmosphere escape probably occurred within 50 – 100 Ma, after the cessation of the dynamo. Any possibly existing water–cycle then vanished due to the atmospheric loss. Escarpments found at Olympus Mons and Apollinaris Patera indicate different environmental conditions during their formation compared to Alba Patera and the Elysium bulge. While the slopes of Alba Patera and the Elysium region formed before 3.6 Ga ago, the aureole of Olympus Mons formed around 3.8 Ga ago. The surface of Apollinaris Patera is older than 3.7 Ga (Chapt. 15). Any ancient ocean in the northern lowlands disappeared before 3.7 Ga ago (Chapt. 14.1), either froze, or a substantial fraction of the water was lost to space as the atmospheric D/H ratio suggests (Owen *et al.*, 1988). The ages of valley networks, believed in general to be older than outflow channels, support this idea of an at least episodically existing water–cycle on early Mars (Chapt. 14.6).

Younger resurfacing is dominated by volcanic activity which triggered subsurface water release and allowed for additional ice deposition, but permanently liquid on the surface of Mars is impossible after the atmosphere was lost (Chapt. 16).

Hand in hand with the understanding of the time frame of the decay of the Martian magnetic field, the thermal evolution and the internal dynamics are more constrained. While large–scale convection in the mantle is responsible for the continuous reshaping of Earth's surface through plate tectonics, plate tectonics is currently not observed on Mars. There are speculations that the dichotomy boundary is a

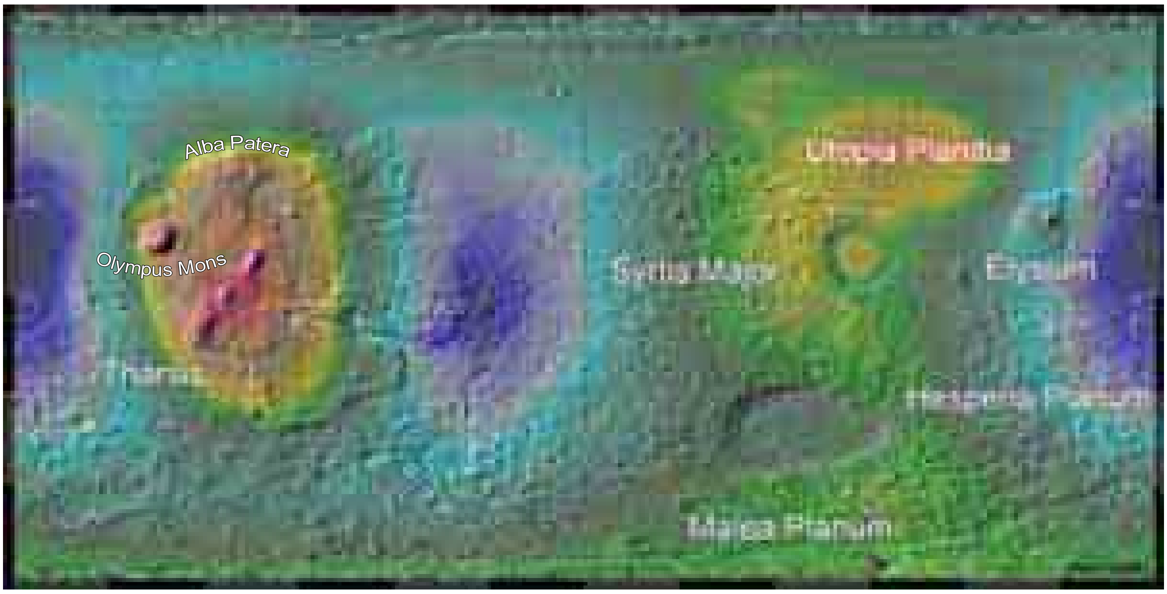

Figure 18.2.: Mars Laser Altimeter Topographic data (shaded relief) with a superimposed areoid (red is high, blue low);(map provided by UNAVCO; http://jules.unavco.org). Volcanic regions are marked. A correlation of possibly still active volcanic provinces and a high areoid is obvious in the Tharsis region, and probably a local high in the Elysium region. Olympus Mons and Alba Patera are situated along the margin of the areoid high as seen from many LIPs from Earth.

Figure 18.3.: Magellan radar maps (gray scale) with a superimposed Venusian geoid (red is high, blue low);(map provided by UNAVCO; http://jules.unavco.org). Prominent features are marked. A correlation of possibly still active volcanic provinces and a high geoid are obvious in e.g. Beta Regio or Atla Regio. These local highs are associated to mantle dynamics as seen from many Large Igneous Provinces on Earth.

relic of ancient plate tectonics, including global–scale resurfacing through Rayleigh–Taylor instabilities or other long–wavelength convections that formed the northern lowlands. The crust (or basement rock) formed earlier than the visible surface implies. Furthermore, ancient plate tectonics was suggested (Sleep, 1994) due to the magnetic anomaly pattern in the highlands (Connerney *et al.*, 1999), despite lacking equivalent surface morphologies. Any visible tectonics, regional tectonics or local deformational features, are usually associated with volcanic constructs, but no landforms are convincingly associated with ancient plate tectonics such as subduction zones, mountain belts or mid–ocean ridges.

On Mars, volcanism is extensive, but not uniformly distributed, and includes a diversity of volcanic landforms. The Tharsis and the Elysium regions are two volcanic provinces that are topographically dominating (Fig. 18.2), situated close to the equator on the dichotomy boundary between the cratered (older) highlands and the northern lowlands (about 120° apart). A possible correlation of young volcanism and aeroid (Mars geoid) highs could suggest upwelling mantle dynamics, contradicting a volcanism driven by a thick insulating crust. The regions, where upwelling might be indicated in the areoid, are characterized by volcanoes whose morphologies are strongly analogous to volcanic landforms on Earth. The huge volcanoes in the Tharsis region (Olympus Mons, Ascraeus Mons, Pavonis Mons and Arsia Mons) have many characteristics that strongly resemble Hawaiian shield volcanoes. The main difference between the Martian and terrestrial volcanoes are the size and length of the flows, mainly due to high eruption rates, the "stationary" character of the source (no plate tectonics), and possibly the lower gravity.

In this thesis, the results for the evolutionary volcanic history provides a time–frame for the general thermal evolution of Mars. In the early Martian history, it is evident that volcanism occurred planet–wide and most volcanic regions were emplaced before about 3.5 Ga ago. It is also demonstrated that the Elysium and Tharsis regions experienced volcanic activity until very recently (i.e. 200 to 100 Ma ago, even in a few places, until 2 to 3 Ma ago), suggesting that the most recent activities (over the last 500 Ma of Martian history) are more wide–spread than previously believed (detailed in Chapt. 15 and 15.5).

In order to explain the internal dynamics of planets, especially that of Mars, the following scenario (Spohn *et al.*, 2001) is required:

After accretion, a planet differentiate into a core, mantle, crust and atmosphere/hydrosphere of unknown conditions. Several accretion and differentiation models are known, usually, time scales of 20 to 50 Ma are involved. Mars's today's mass and moment–of–inertia factor supports the differentiated structure. The subsequent thermal evolution or cooling history is transferring heat by heat conduction and by thermal convection to remove the heat generated by radioactive nuclides and to cool the interior.

Large–scale convection has been considered to form a crustal dichotomy as derived from Mars Global Surveyor gravity and topography data. Numerical models show, simultaneously to a cooling core, the mantle flow is dominated by widely distributed down–welling. Broad local upwelling flows is commonly found in internally heated convection models. In the case of Mars, a hotter (or superheated) core allows for a spinel-perovskite phase transition, even though Mars's temperature and pressure schemes are not well–defined. This boundary might amplify large–scale and localization of upwelling flows as well as might allow for a strong dynamo in the early history of Mars. Later volcanism might no longer be driven by up–welling mantle convection (plumes) but due to crustal thickness growth and buoyancy. Although speculative and not proven for Mars, a similar scenario has been considered for Venus, where global resurfacing occurred due to thickening of the lithosphere until the internal heat excess forces a global lithospheric overturn or continuous volcanic activity covering the surface planet–wide. Both ideas compete but no final proof for one or the other case can be given through gravity. etc., (Fig. 18.3).

In this sense, Earth appears unique among the terrestrial planets in possessing plate tectonics. Possibly, its mantle convection regime produces convective stresses to generate failure in the rigid surface boundary layer. The forces of plate tectonics are not fully understood but the plate tectonics are driven by mantle convection with feedback provided by subduction. The processes requires a rigid lithosphere. Other planets appear to be in a stagnant–lid regime; a regime which is characterized by the formation of a nearly immobile lid on top of a convective mantle, that occurred due to large viscosity of the upper thermal boundary layer. Venus e.g. globally shows young surface (based on crater counts) indicating a crustal subsidence event or planet–wide volcanic eruptions during the most recent 1 billion years. A correlation of the youngest volcanic units and geoid highs is observed. Such local highs are associated to mantle dynamics.

For Mars, the following sequence of events is suggested: Major volcanic (voluminous) activity occurred globally. The cessation of the magnetic dynamo is followed by possible super–plume activity in the Tharsis region (and Elysium region). The last observed global volcanic activity ended around 3.6 Ga ago. Plains–forming activity ended even earlier. Locally, more recent activity is observed in Elysium, Tharsis and possibly at Hadriaca and Tyrrhena Paterae. A more detailed discussion is given in Chapter 15.5. Models suggest that the persistence of mantle convection stopped after the core cooled / the dynamo ceased as a consequence of too–low heat flow across the core–mantle boundary. Volcanism and magmatism continued as on Venus, in places where thick insulating crust formed. As on Earth, thermochemical heterogeneities at the core–mantle boundary could be the reason for localized upwelling. Comparable (localized) volcanic activity on Earth, Large Igneous Provinces (LIPs) result from catastrophically rapid dissipation of great quantities of internal heat, and they are not related to surficial plate tectonic processes. It has been shown (Burke and Torsvik, 2004) that there is a strong spatial correlation between LIP eruption sites for the past 250 Ma (corrected for the effects of plate tectonics) and the low seismic velocity regions (s–waves) at the core–mantle–boundary (Fig. 18.4). Timescales for mantle dynamics (plume formation) and plate tectonics are on the order of a few hundreds million years, which can be derived from ocean floor ages, hot spot ages, and formation and break–up of super–continents.

There are considerable similarities in the geoid patterns and lowermost density heterogeneities (Figure 18.4) on Earth, particularly around Africa, where there is no recent subduction, as well as on Mars. On the other hand, recent work has suggested that areoid anomalies have rather shallow origin (Zhong, 2002). On Earth, a combination of rheological models based on mineral physics and density models based on seismic tomography explains a large part of the geoid shape.

Experiences gathered through investigations on Earth will have an impact on the interpretation of findings on other planets where little detail is known. By comparatively studying Earth and Mars, the source of geoid and areoid undulations will allow a better understanding of a possible relation between lowermost mantle density anomalies and surface volcanism, and constrain crustal thickness for Mars and improve models of its thermal evolution. In most models of Mars's interior, a simple three–layered structure is assumed. Chemical boundaries or boundaries related to pressure or temperature well understood, but must differ from the Earth's structure due to size and gravity differences (see discussion by Spohn *et al.*, 2001).

A comparison of dynamical patterns reflected on the planet's surface, and of its gravity anomalies and geoid patterns allow for a better understanding of the thermal evolution of planets. The results of this thesis strongly support that Mars is a planet which takes its place between the two end–members of planetary evo-

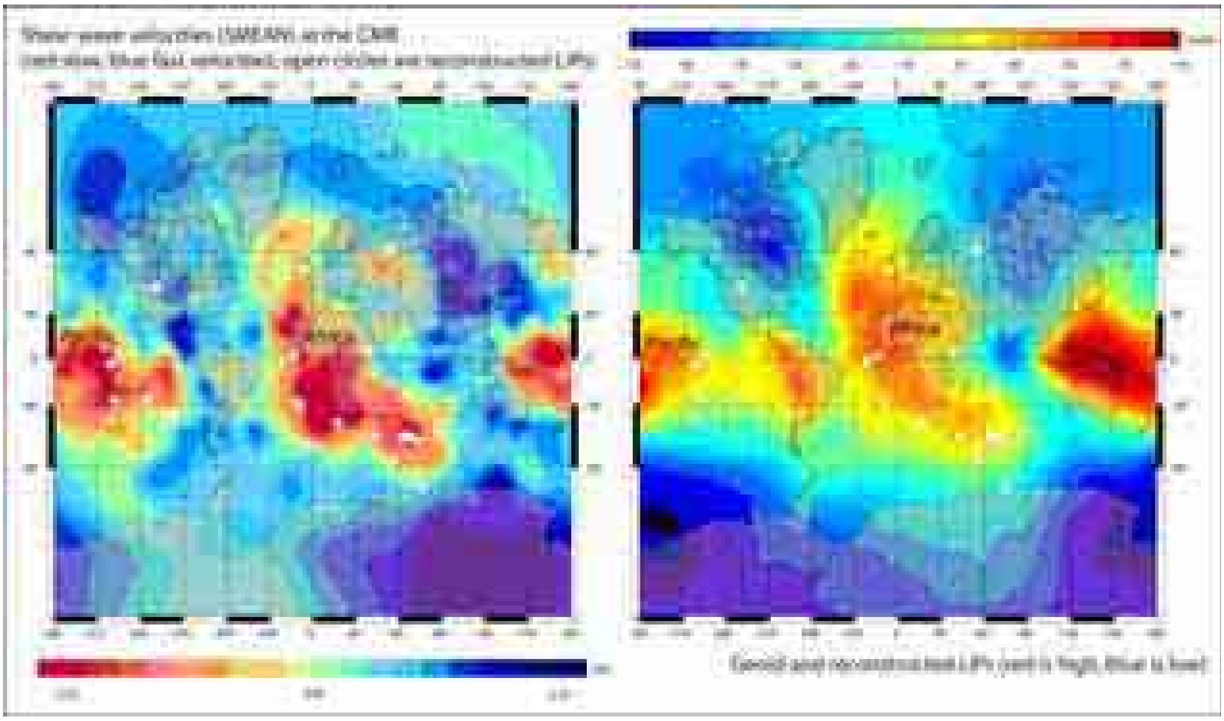

Figure 18.4.: Left: SMEAN shear wave velocity anomaly model for Earth, near the core–mantle boundary, about 2800 km depth (Becker and Boschi, 2002). Right: Earth geoid. Open white symbols are reconstructed Large Igneous Provinces (LIPs) updated from Burke and Torsvik (2004) using a revised palaeomagnetic reference model.

lution: While Mercury and the Moon appear to record the early history of the Solar System, and show no signs of water relevant to their evolution, Mars at least shows a very diverse surface history. It is most likely the only planet whose surface feature show the total record of both internal and external processes from the beginning of its existence 4.5 Ga ago until now. The role of water in its early history is unclear, but evidence for surface action of water is clear. Presently, water and ice is probably hidden in the subsurface and apparent in the polar caps. Episodic volcanic activity allows for water release and ice deposition. Venus and Earth are two end-members which show very young surfaces. The major difference is the presence of water. While Venus is presumably dry, the hydrosphere on Earth might be key to plate tectonics.

The validity of theories concerning (deep) plume activity and plate tectonics versus stagnant–lid and crustal thickening could gain additional support from the comparison between planets. Ultimately, these results will contribute to the knowledge of similarities and differences between two planets, and thus improve our understanding on how each one of them evolves thermally in its interior and geologically on its surface.

A. Northern Lowlands – Crater Size–Frequency Distributions and Images

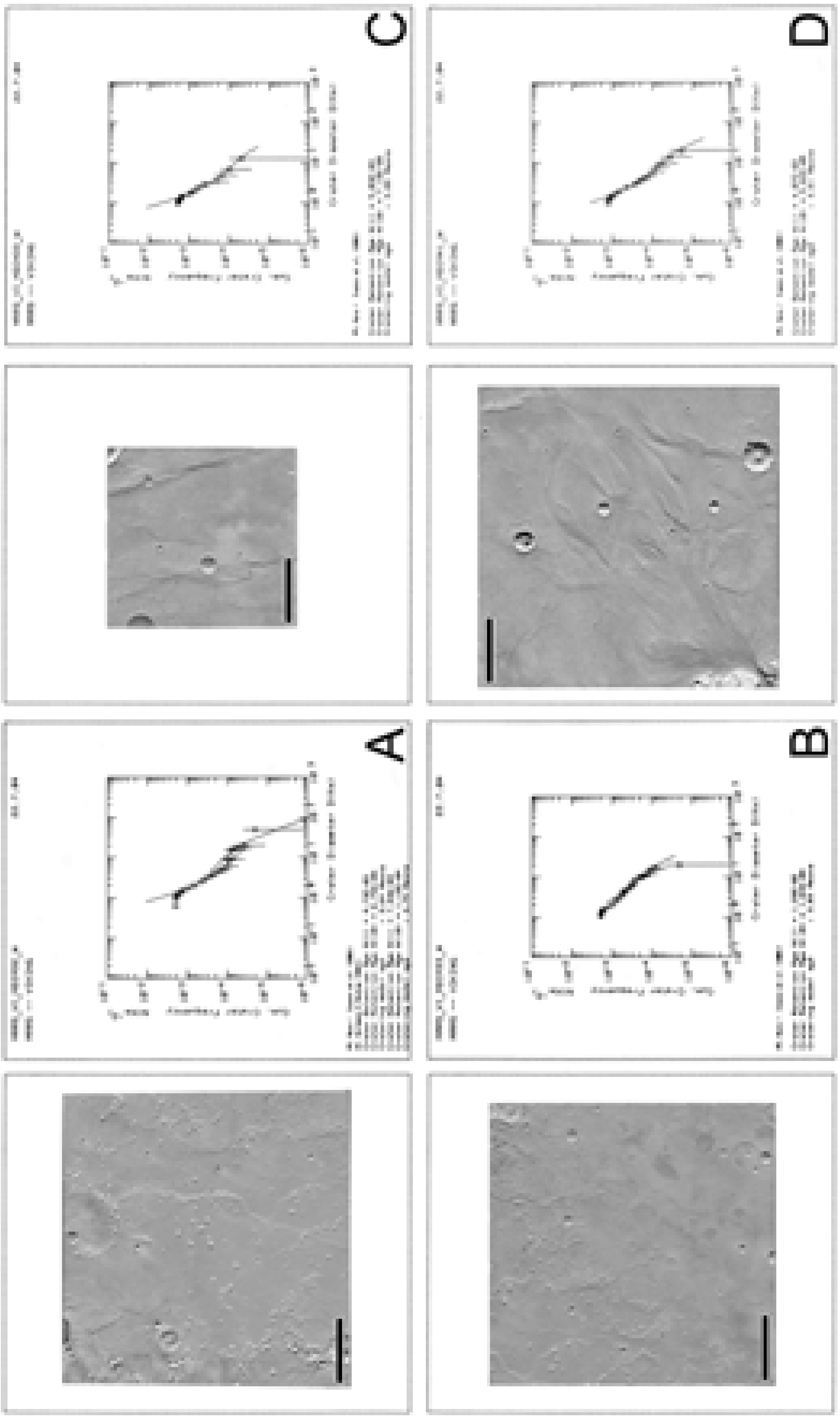

Figure A.1.: Resulting Crater Size–Frequency Distributions for the Chryse region. The entire counting unit is given as image for each measurement as listed by number in List 14.1.

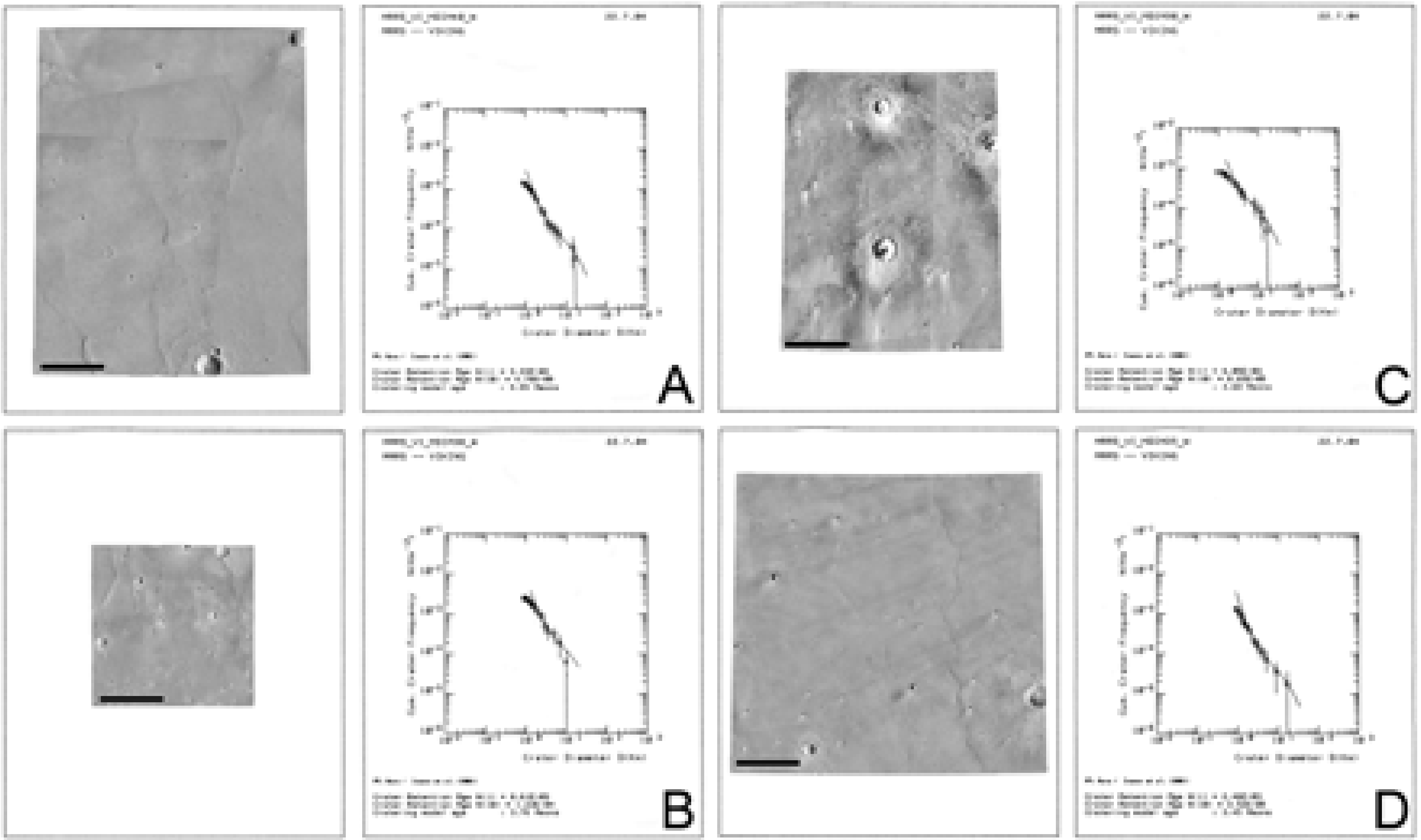

Figure A.2.: Resulting Crater Size–Frequency Distributions for the Chryse region. The entire counting unit is given as image for each measurement as listed by number in List 14.1.

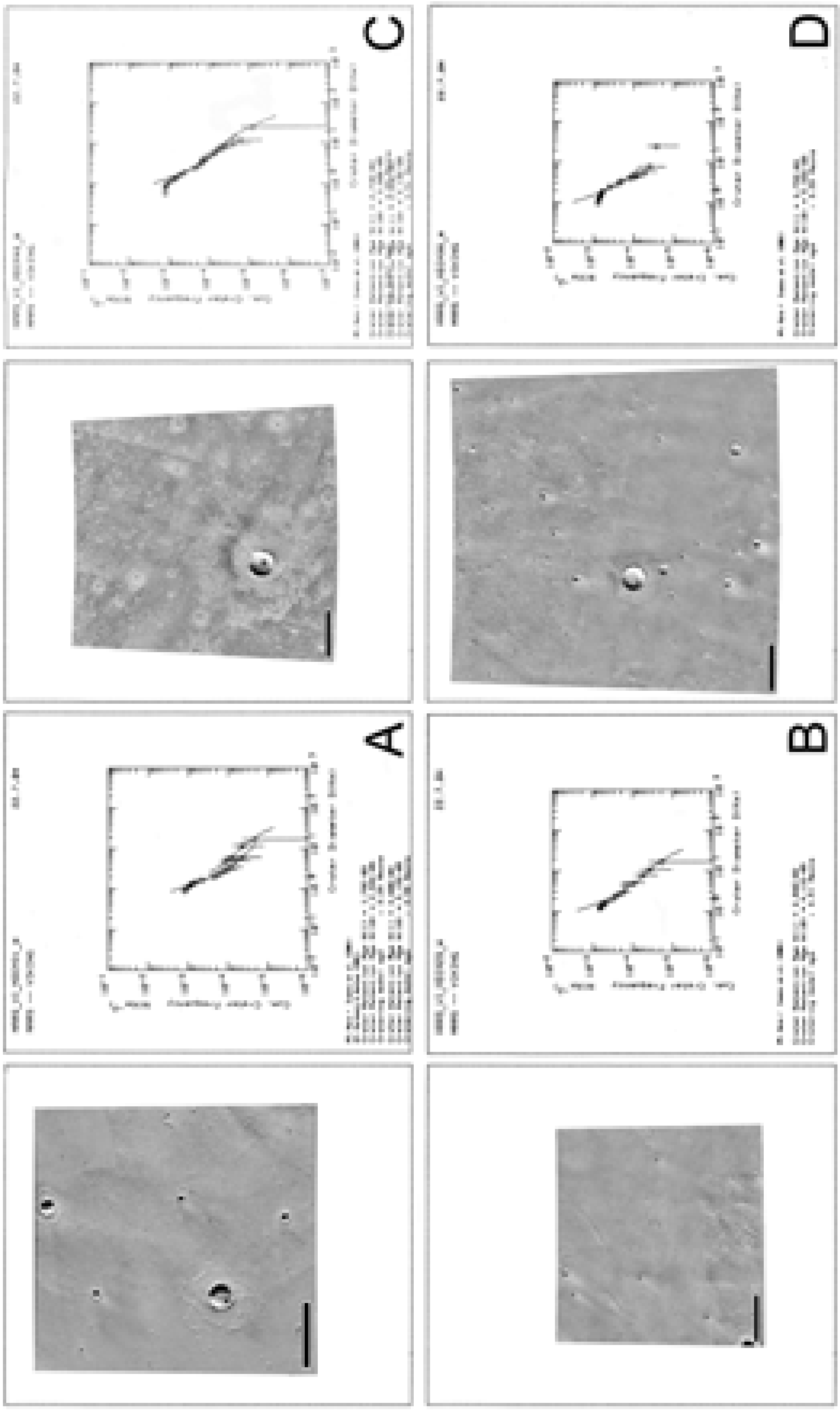

Figure A.3.: Resulting Crater Size–Frequency Distributions for the Chryse region. The entire counting unit is given as image for each measurement as listed by number in List 14.1.

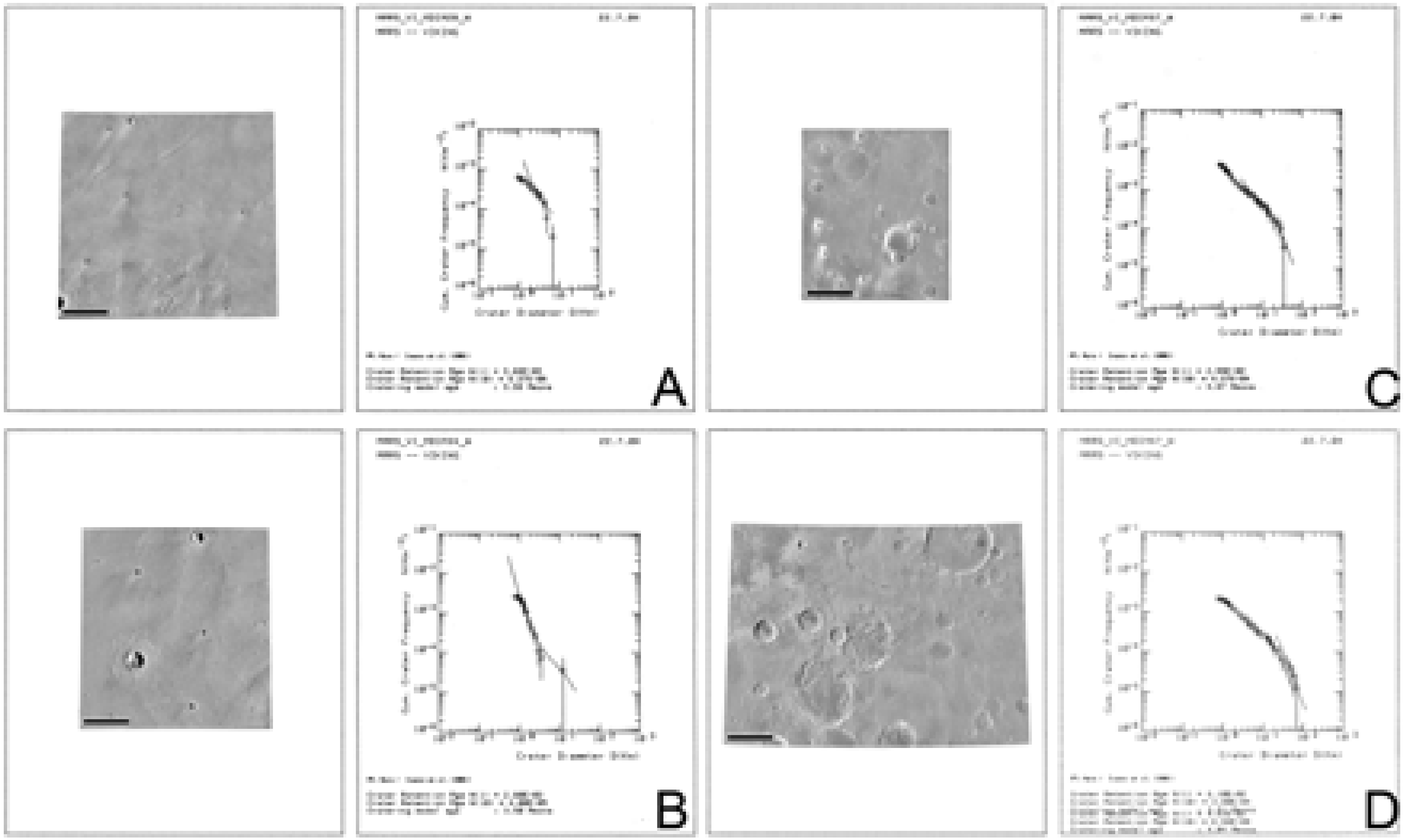

Figure A.4.: Resulting Crater Size–Frequency Distributions for the Chryse region. The entire counting unit is given as image for each measurement as listed by number in List 14.1.

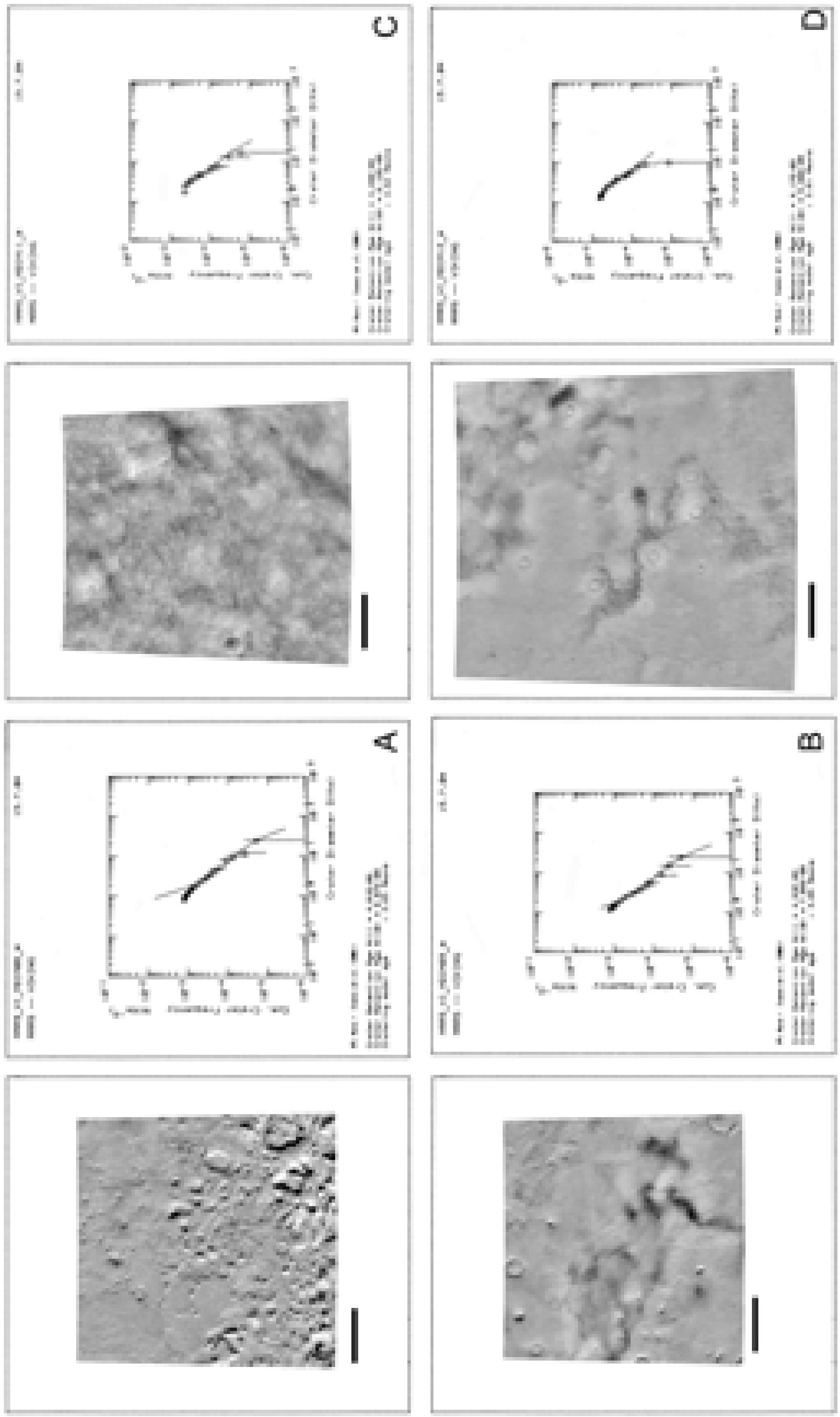

Figure A.5.: Resulting Crater Size–Frequency Distributions for the Utopia region. The entire counting unit is given as image for each measurement as listed by number in List 14.1.

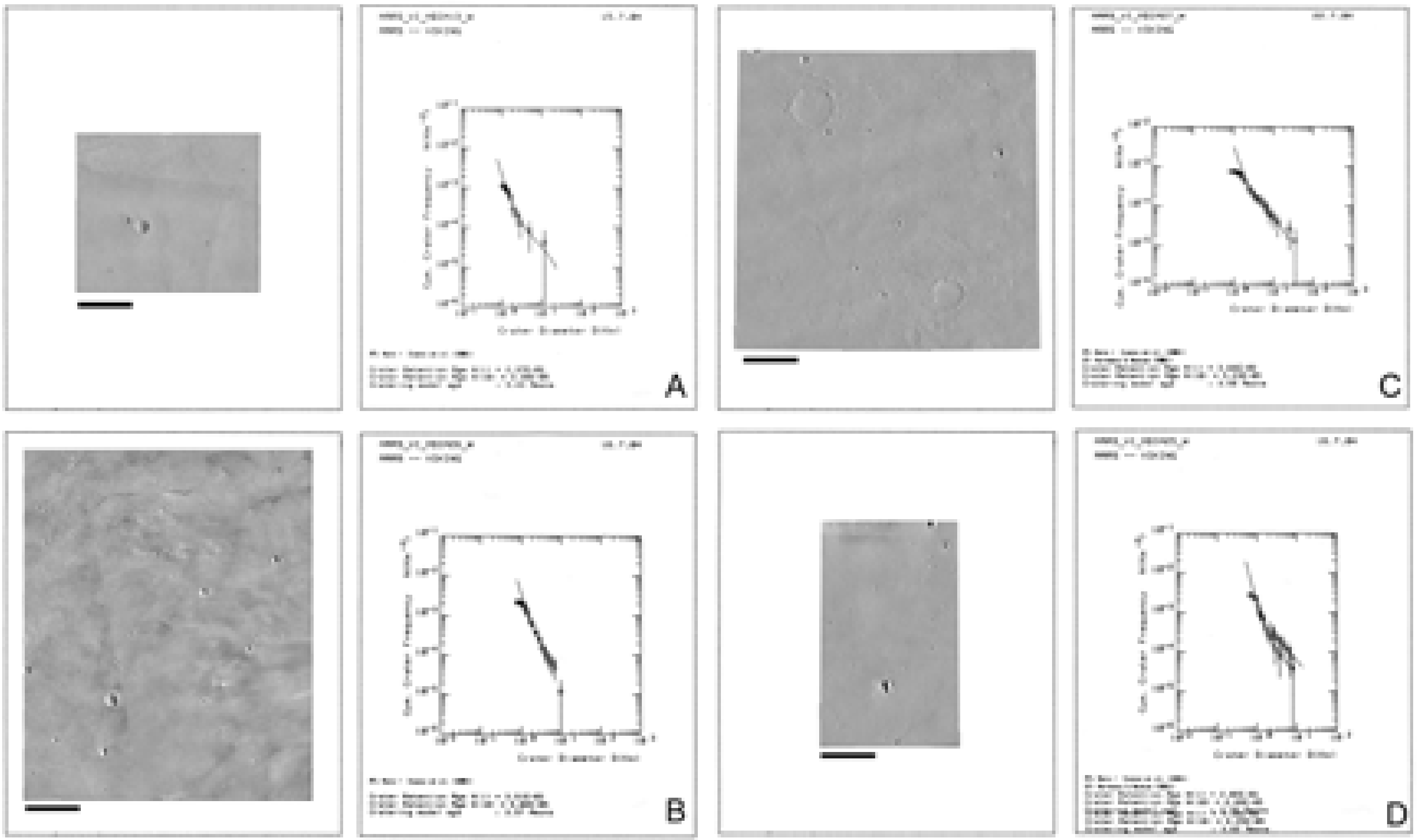

Figure A.6.: Resulting Crater Size–Frequency Distributions for the Utopia region. The entire counting unit is given as image for each measurement as listed by number in List 14.1.

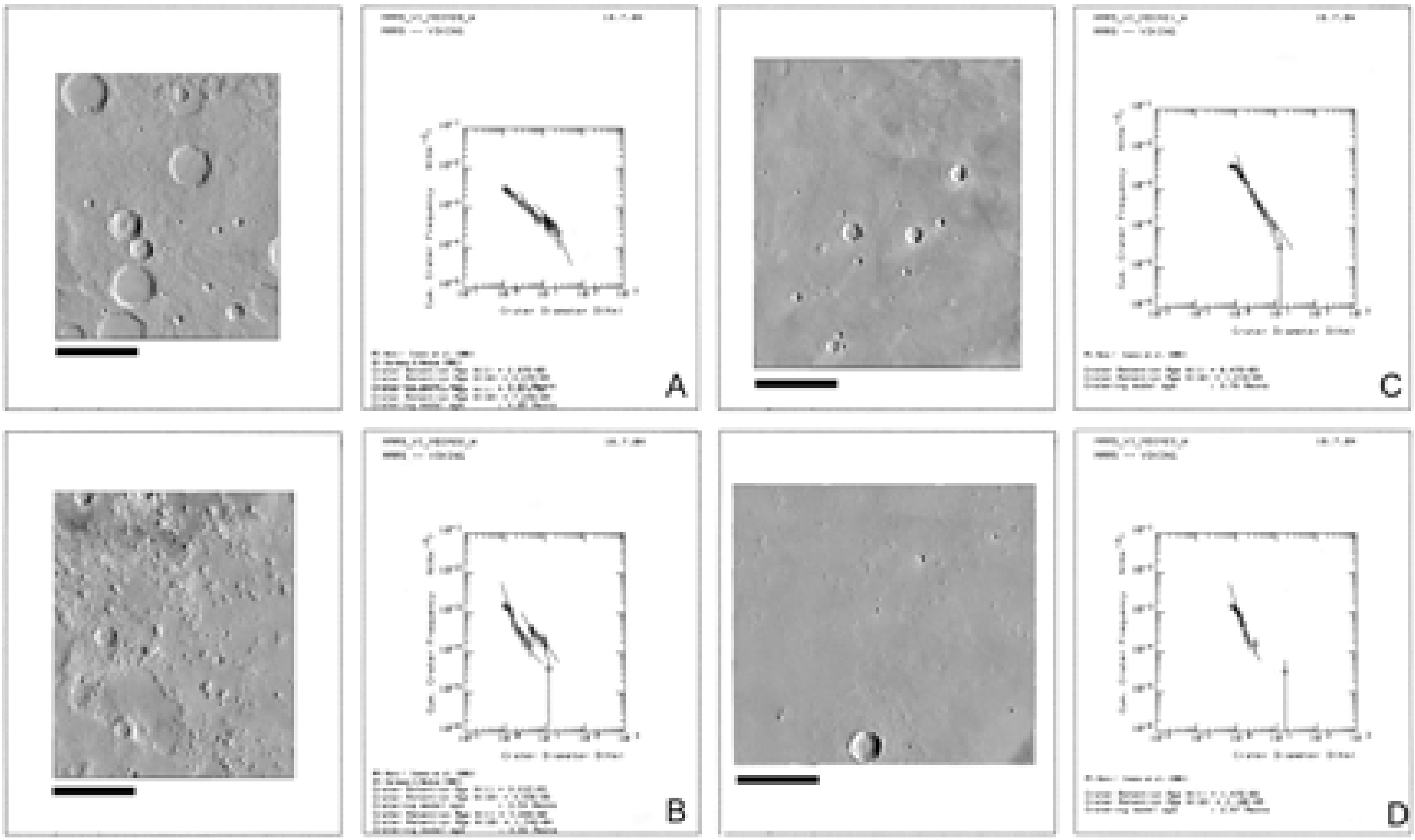

Figure A.7.: Resulting Crater Size–Frequency Distributions for the Utopia region. The entire counting unit is given as image for each measurement as listed by number in List 14.1.

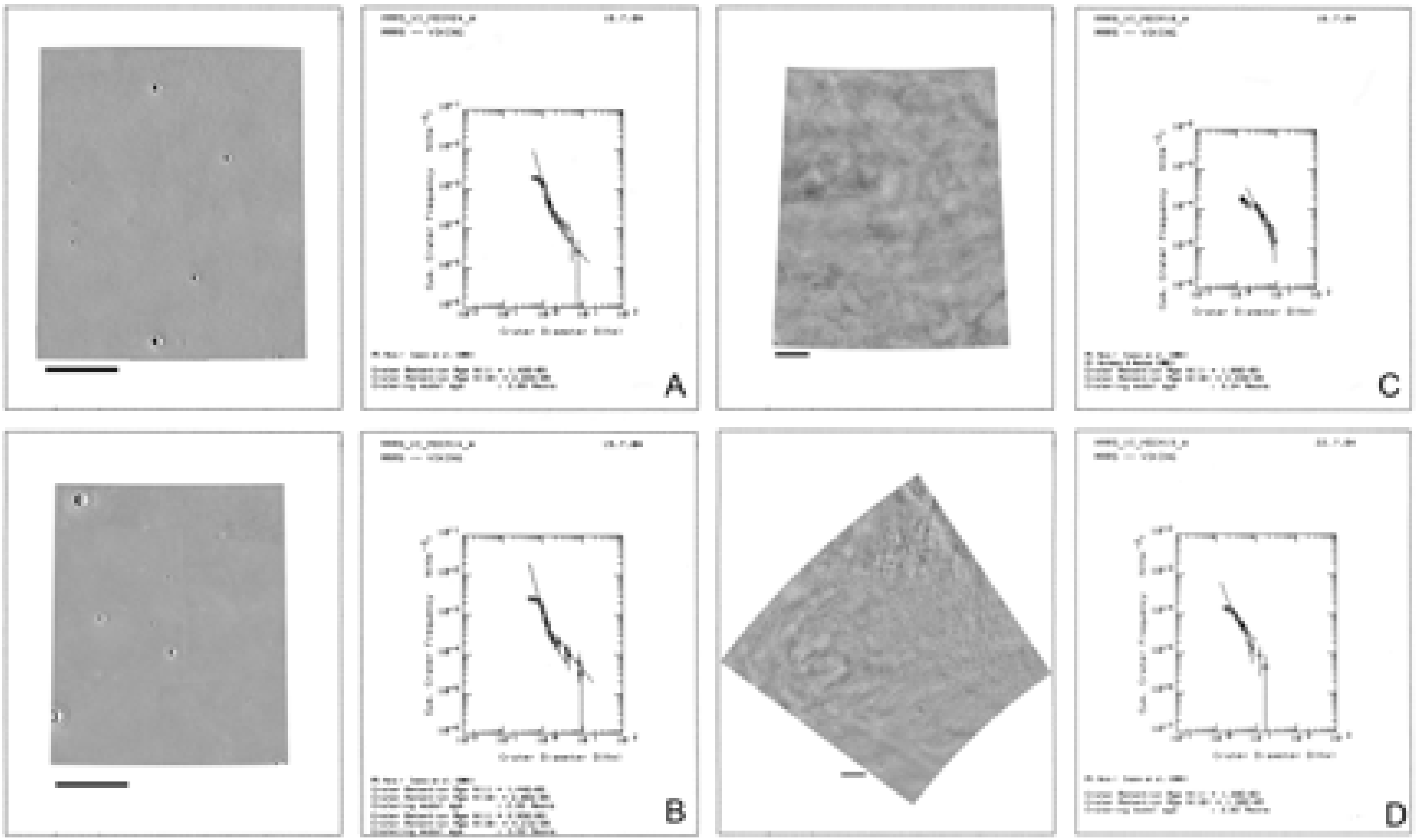

Figure A.8.: Resulting Crater Size–Frequency Distributions for the Utopia region. The entire counting unit is given as image for each measurement as listed by number in List 14.1.

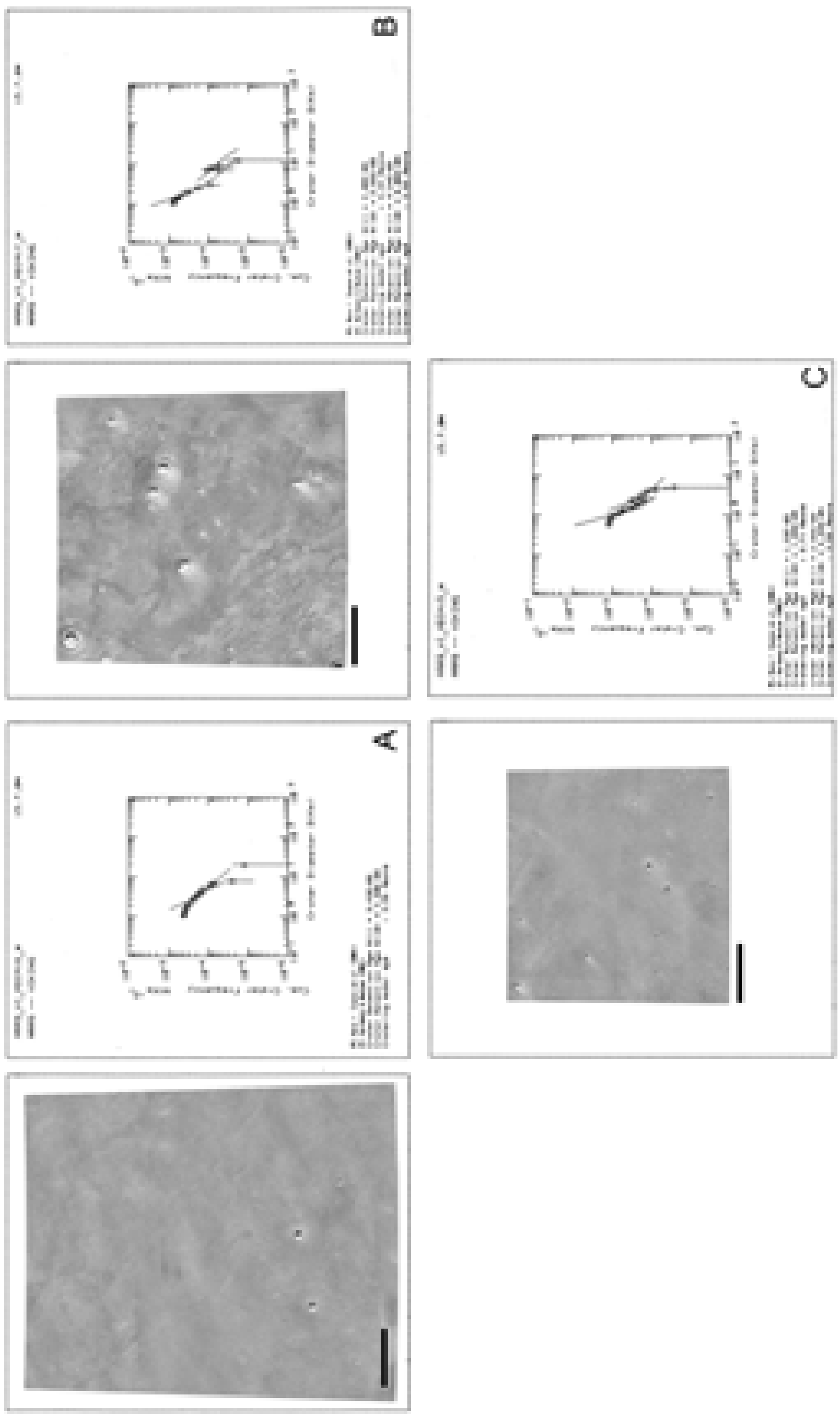

Figure A.9.: Resulting Crater Size–Frequency Distributions for the Utopia region. The entire counting unit is given as image for each measurement as listed by number in List 14.1.

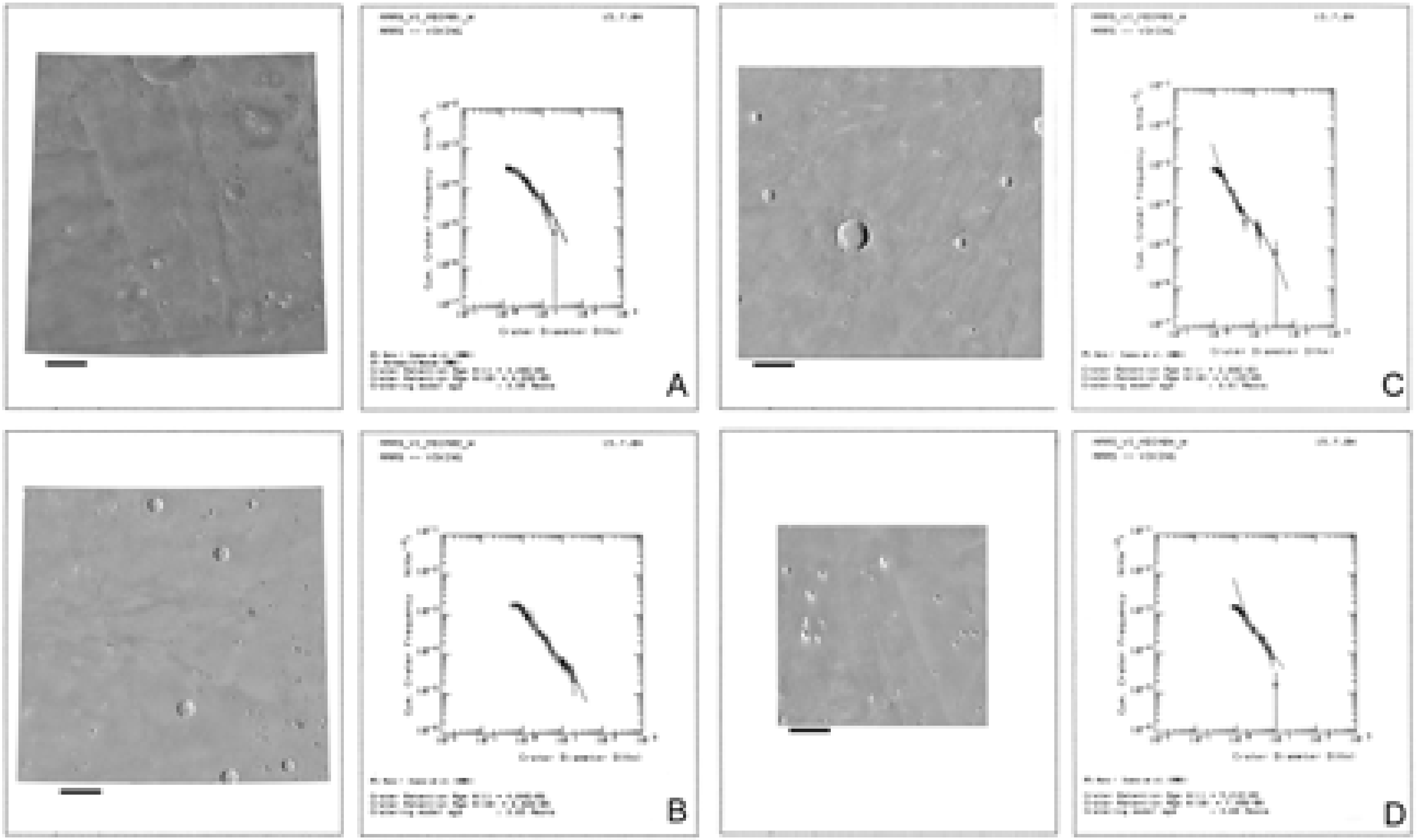

Figure A.10.: Resulting Crater Size–Frequency Distributions for the Elysium Volcanic Province and Amazonis Planitia. The entire counting unit is given as image for each measurement as listed by number in List 14.1.

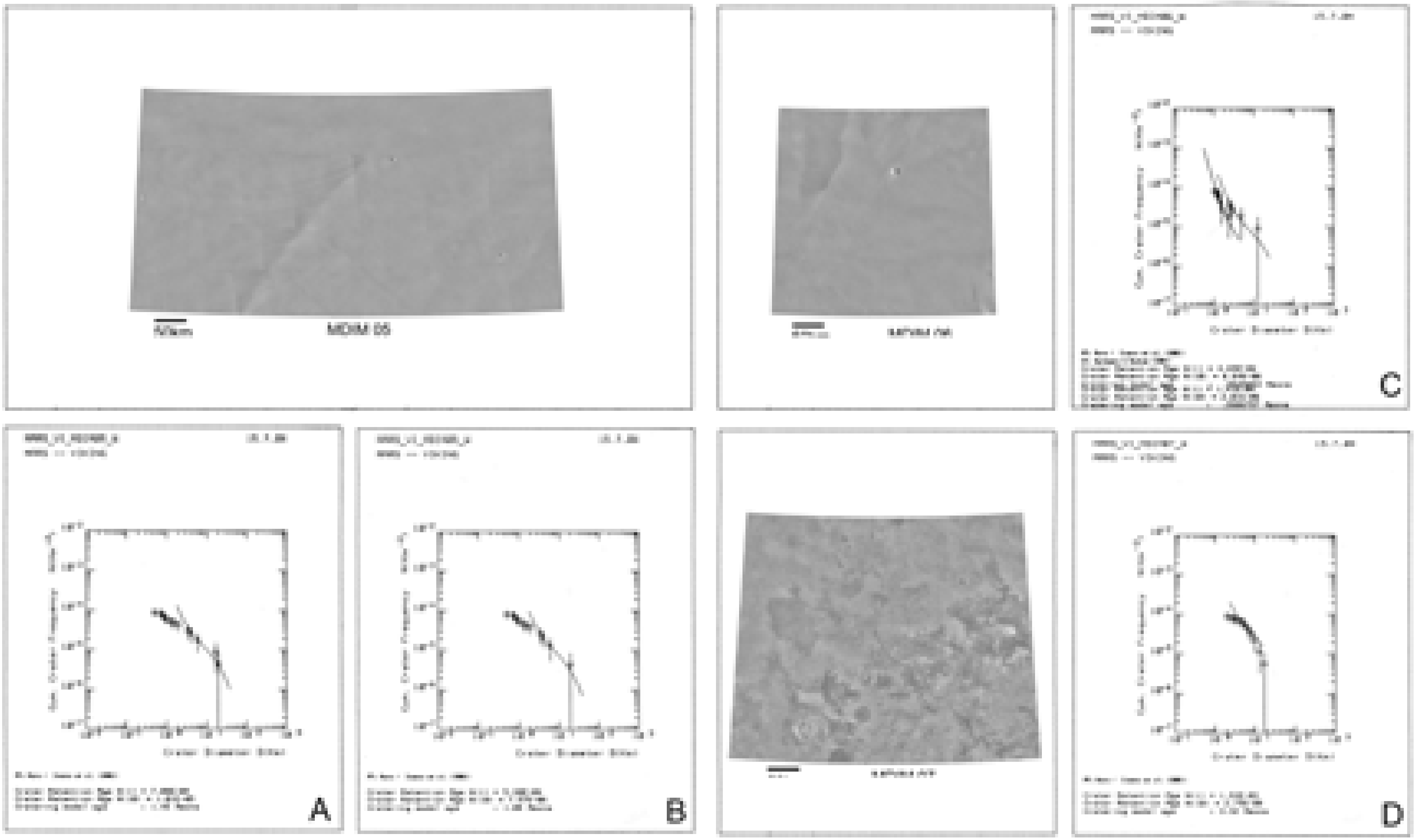

Figure A.11.: Resulting Crater Size–Frequency Distributions for the Elysium Volcanic Province and Amazonis Planitia. The entire counting unit is given as image for each measurement as listed by number in List 14.1.

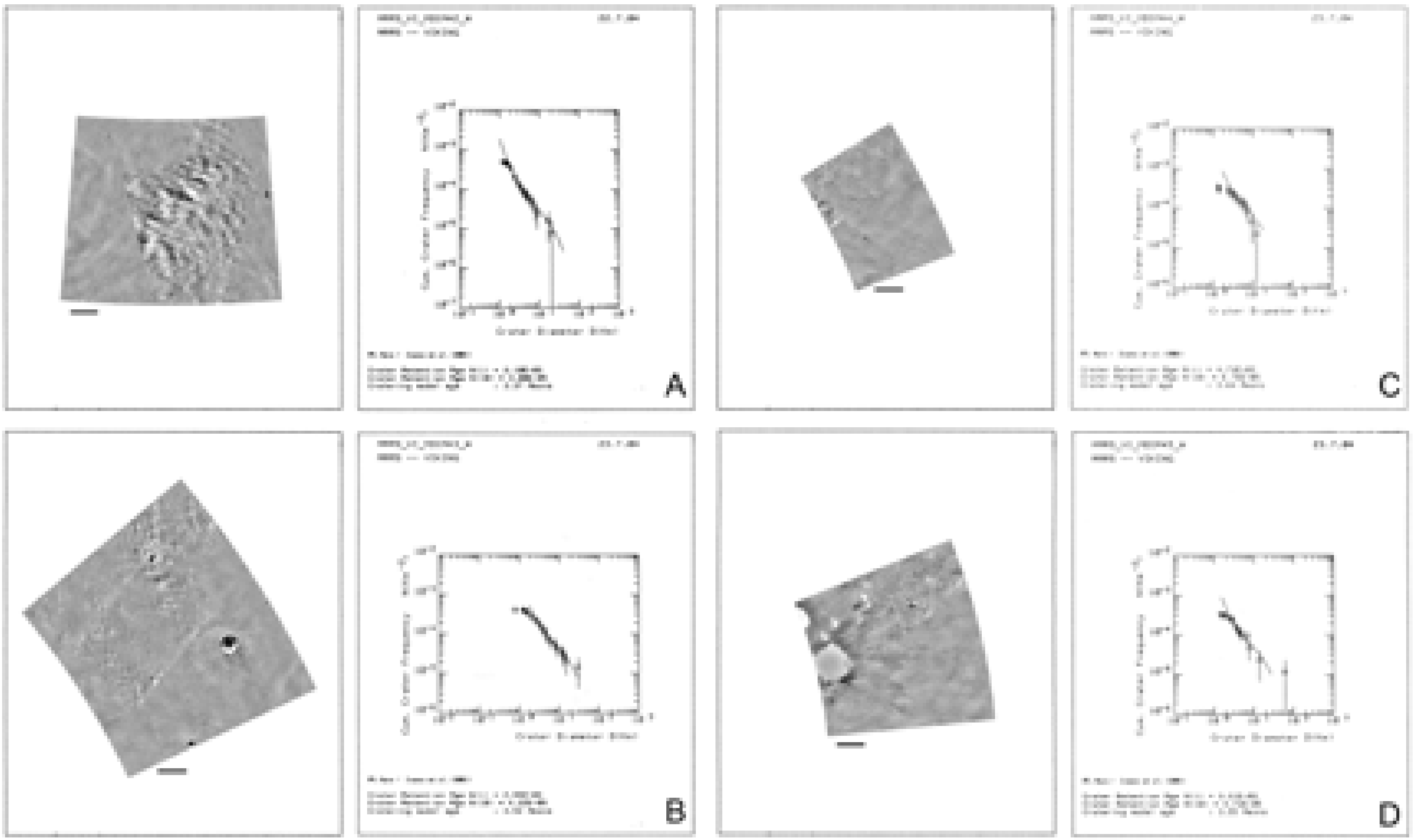

Figure A.12.: Resulting Crater Size–Frequency Distributions for the Profile between Alba Patera and the North Pole. The entire counting unit is given as image for each measurement as listed by number in List 14.1.

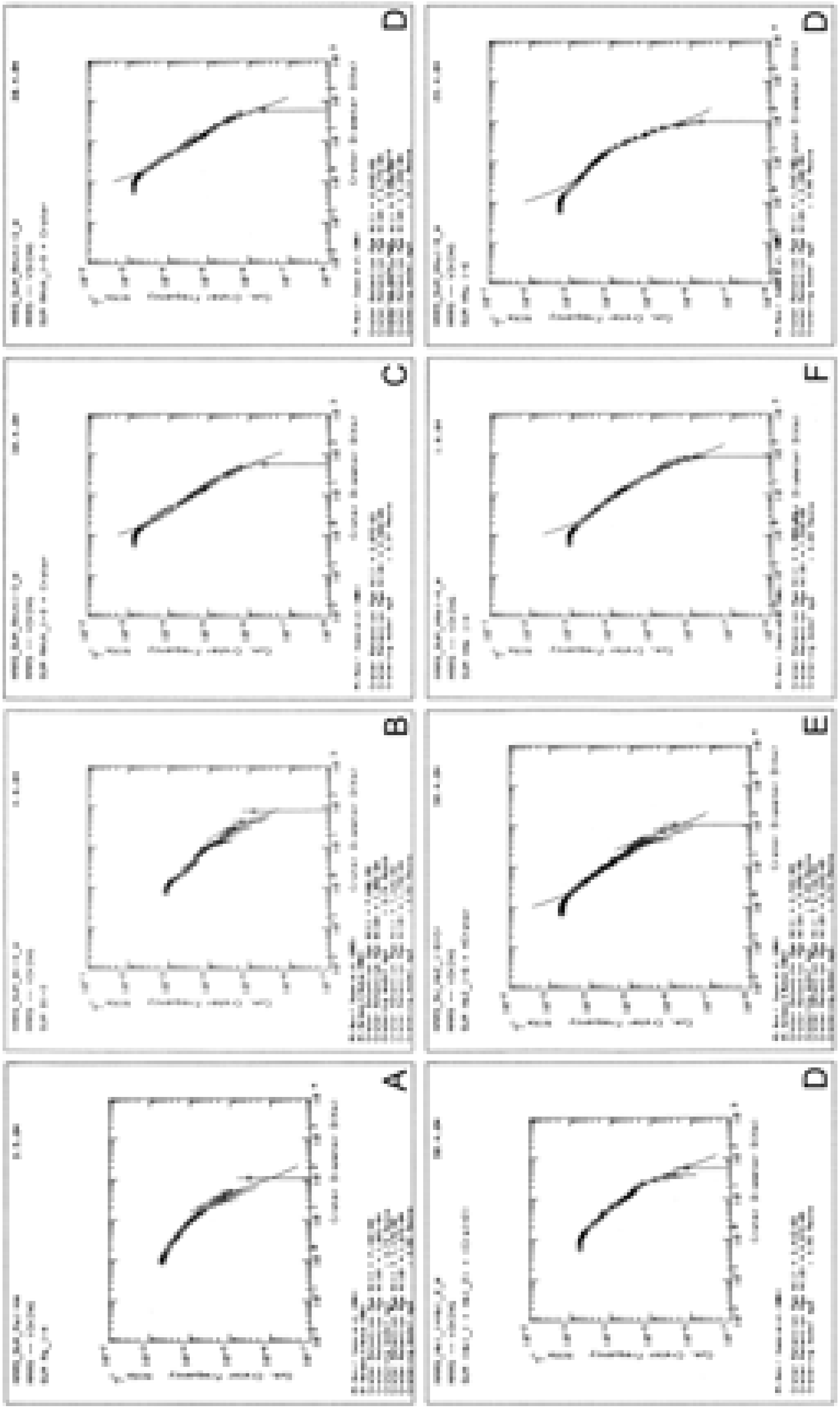

Figure A.13.: Resulting Crater Size–Frequency Distributions summed for the all measurements assigned to one geological unit.

A.1. Kasei Valles – Images and Crater Size–Frequency Distributions

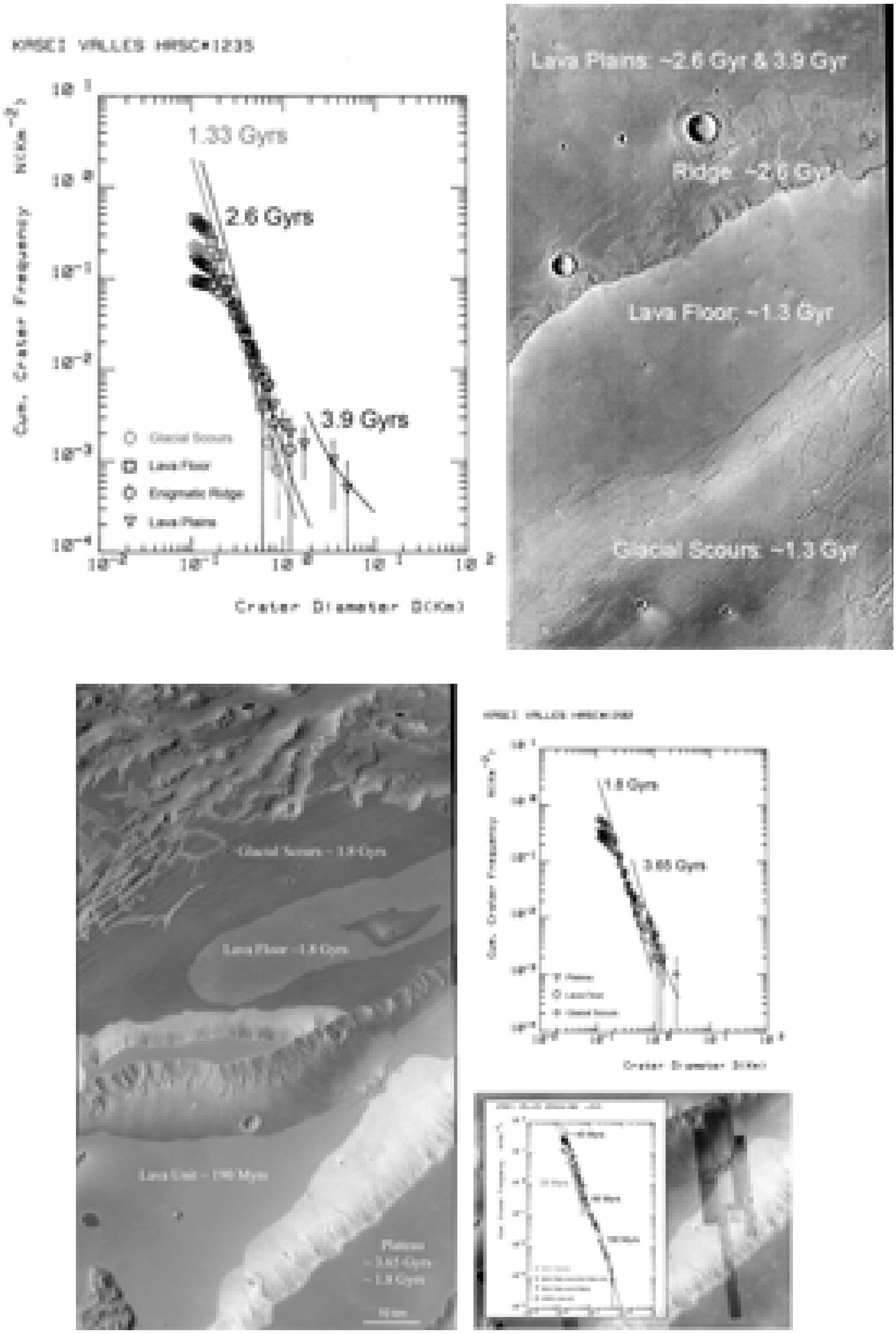

Figure A.14.: Kasei Valles

B. Volcanism on Mars – Crater Size–Frequency Distributions and Images

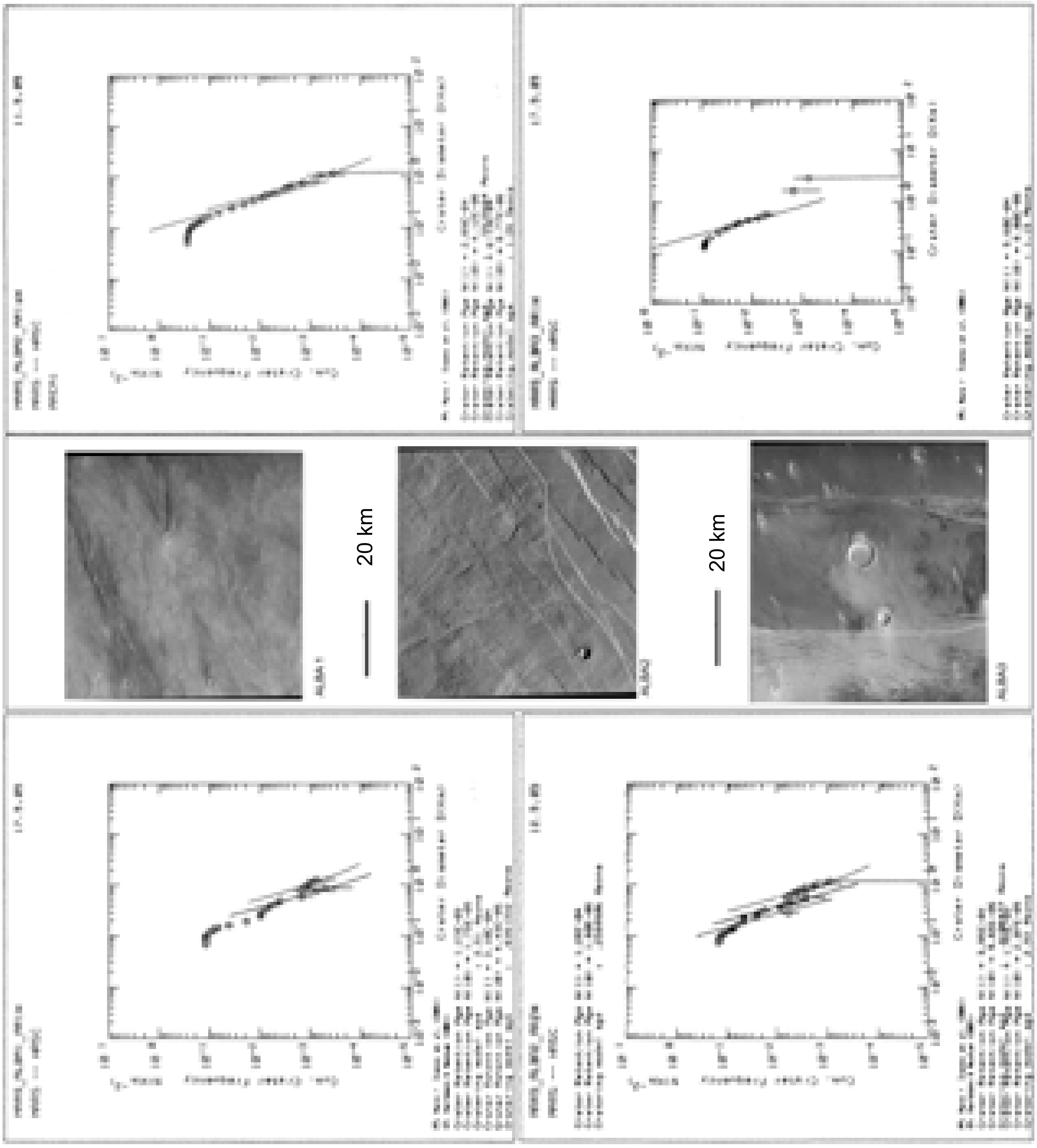

Figure B.1.: Resulting Crater Size–Frequency Distributions for Alba Patera flanks.

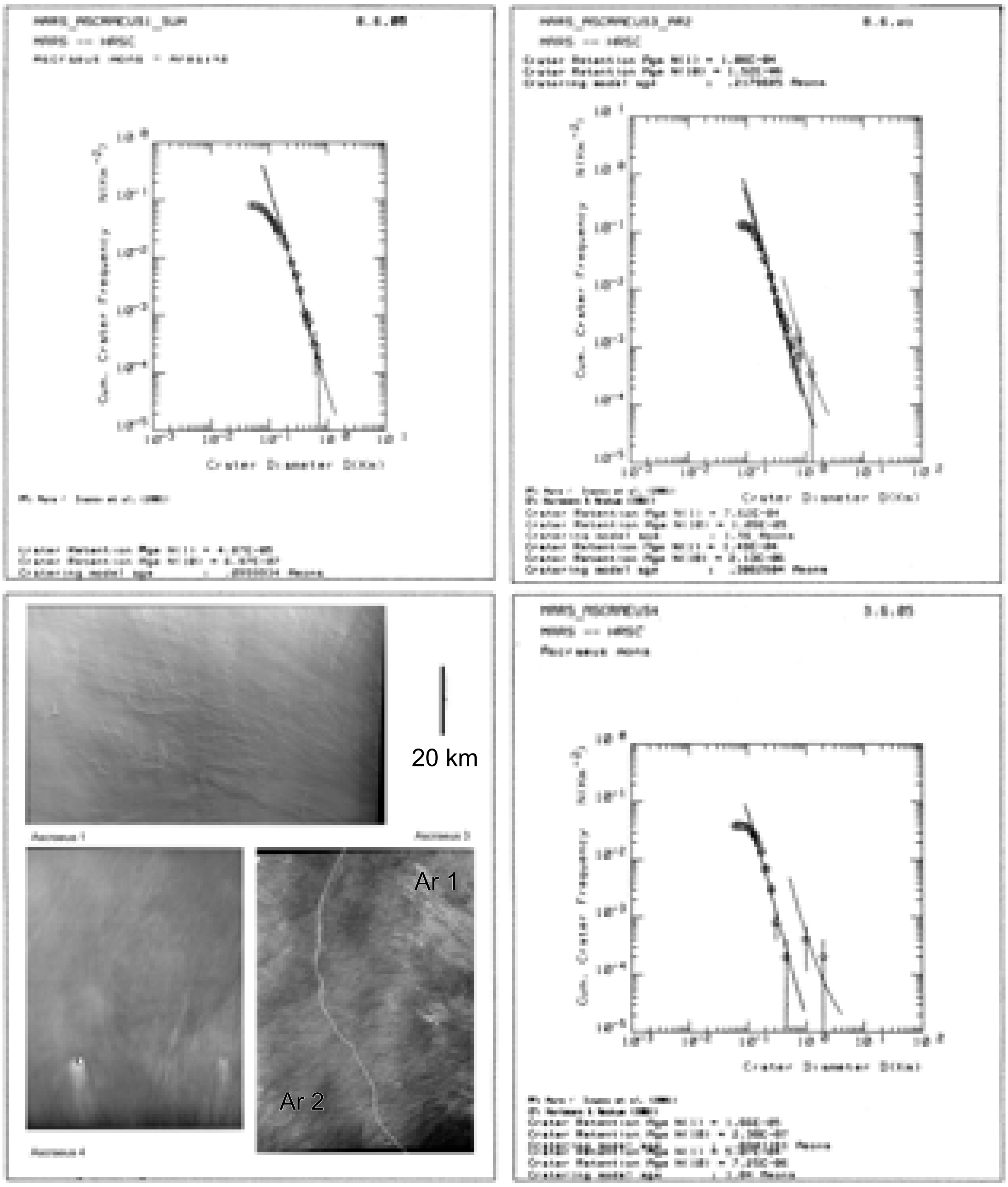

Figure B.2.: Resulting Crater Size–Frequency Distributions for Ascraeus Mons flanks.

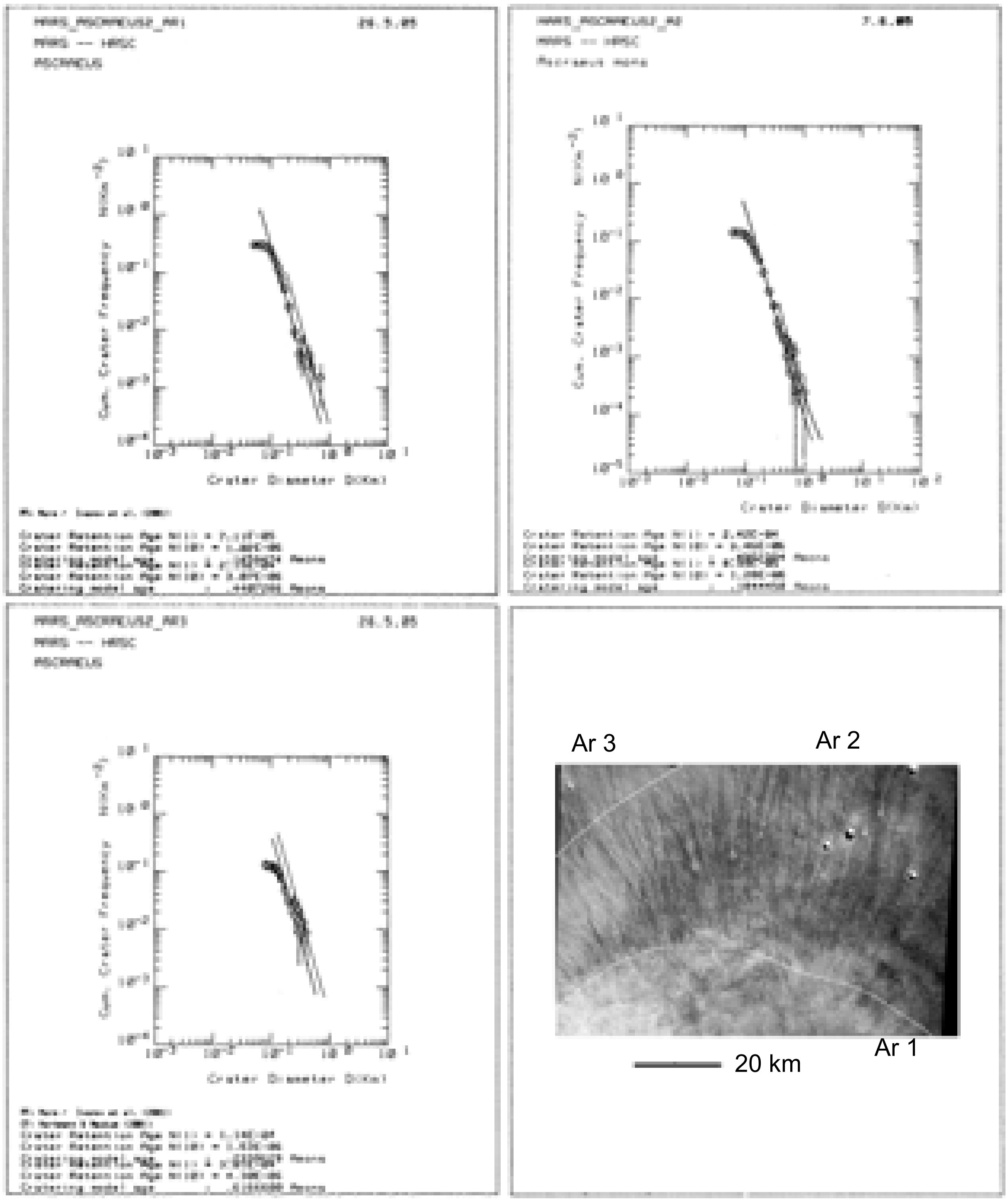

Figure B.3.: Resulting Crater Size–Frequency Distributions for Ascraeus Mons flanks.

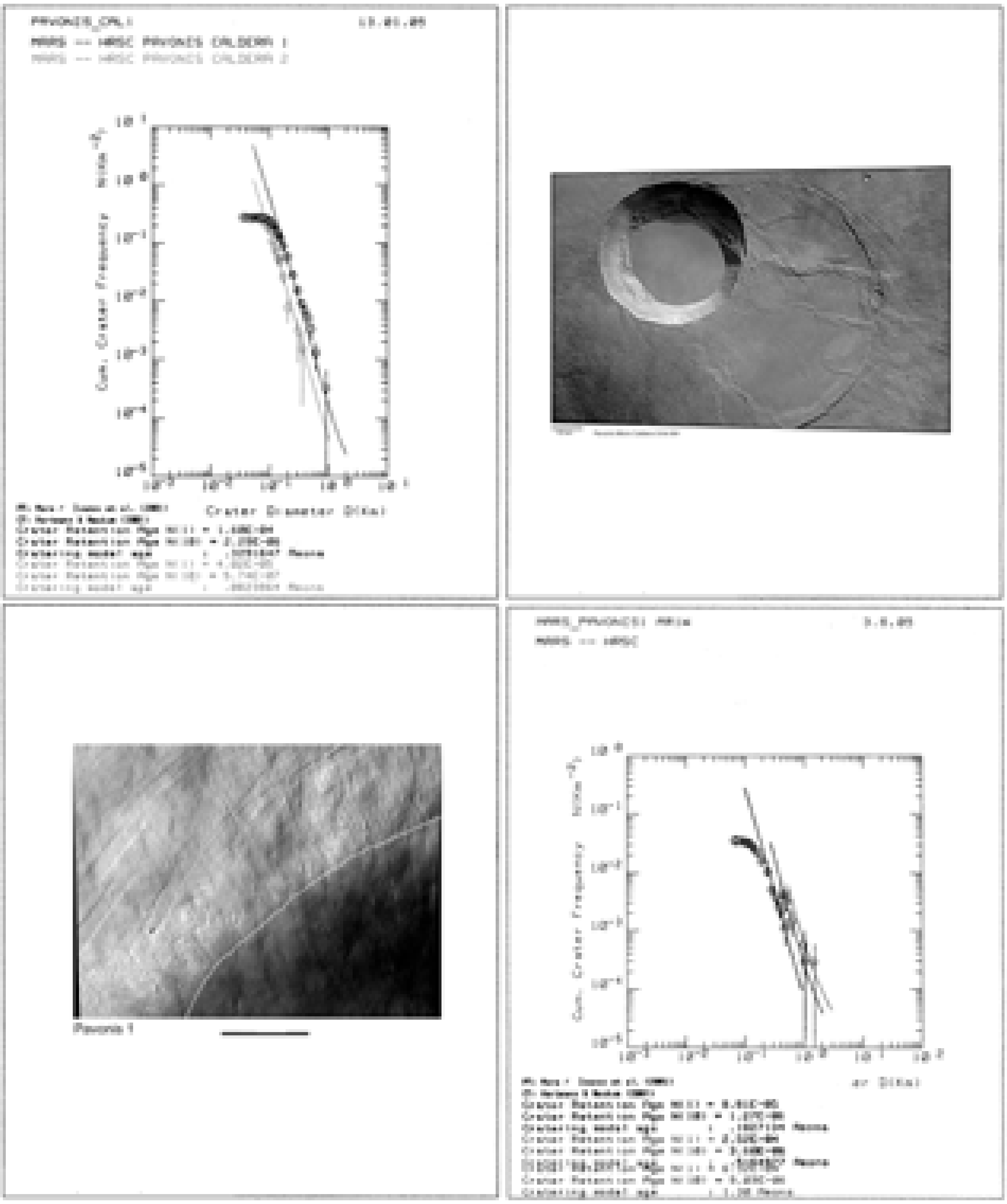

Figure B.4.: Resulting Crater Size–Frequency Distributions for Pavonis Mons flanks.

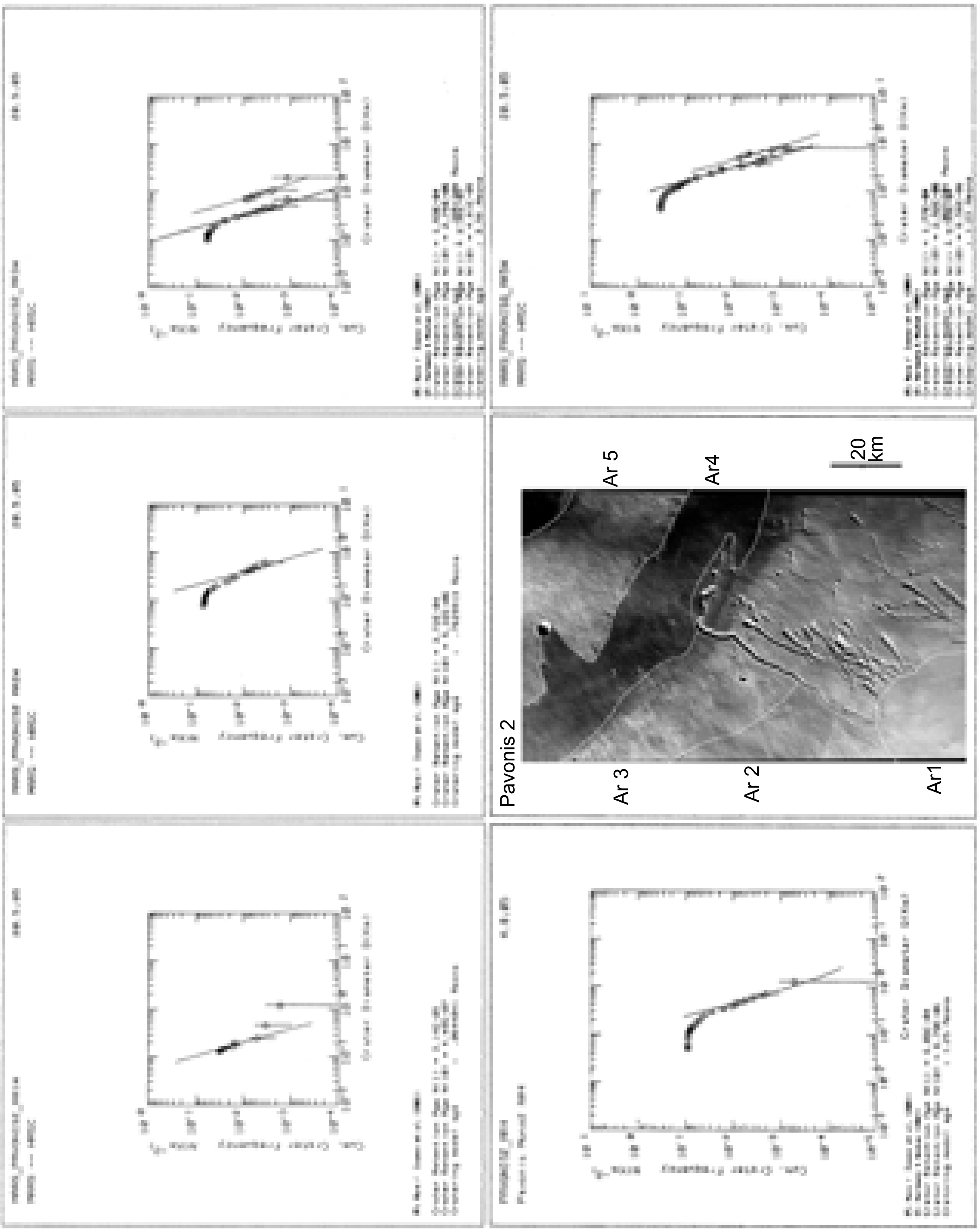

Figure B.5.: Resulting Crater Size–Frequency Distributions for Pavonis Mons flanks.

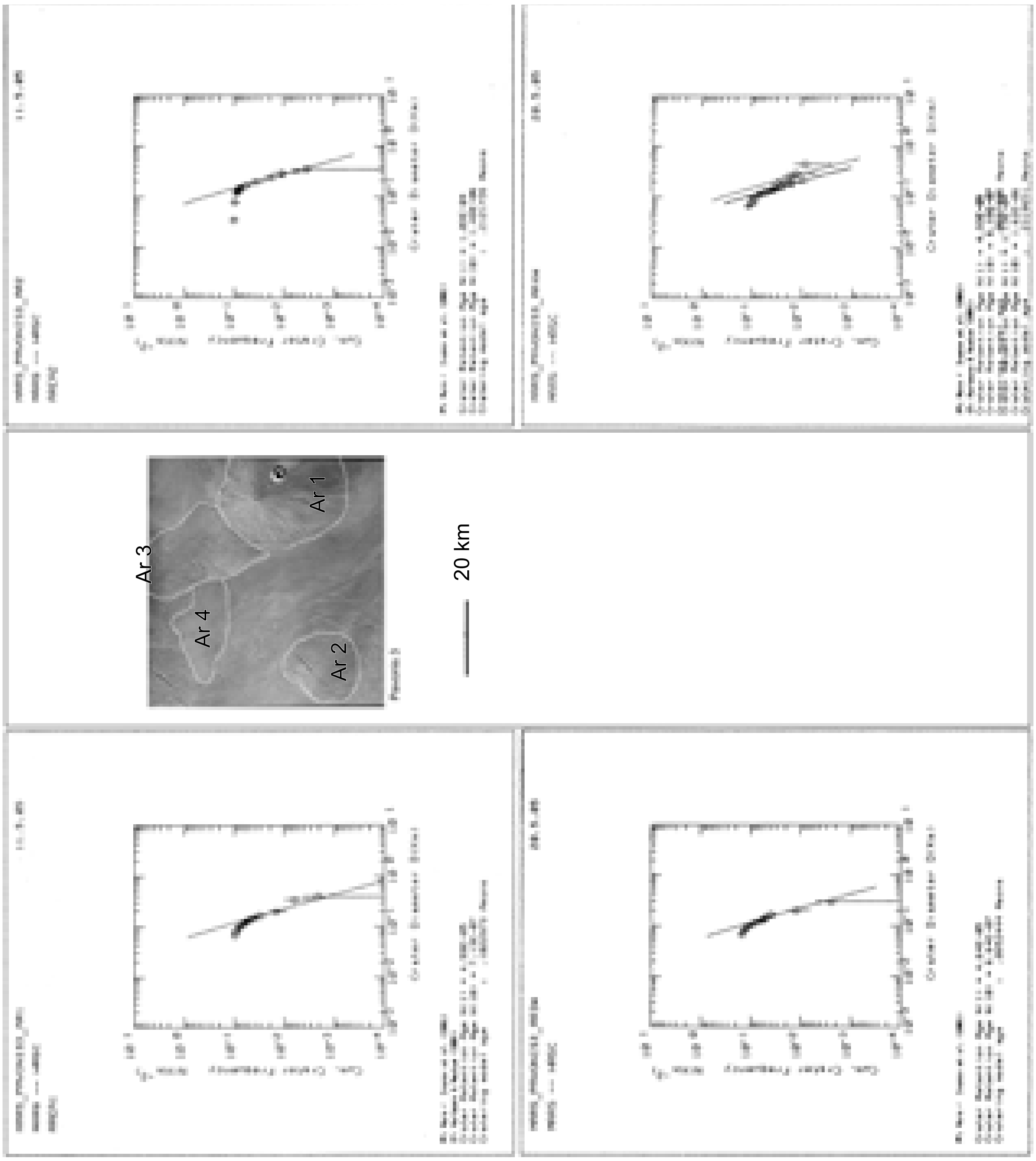

Figure B.6.: Resulting Crater Size–Frequency Distributions for Pavonis Mons flanks.

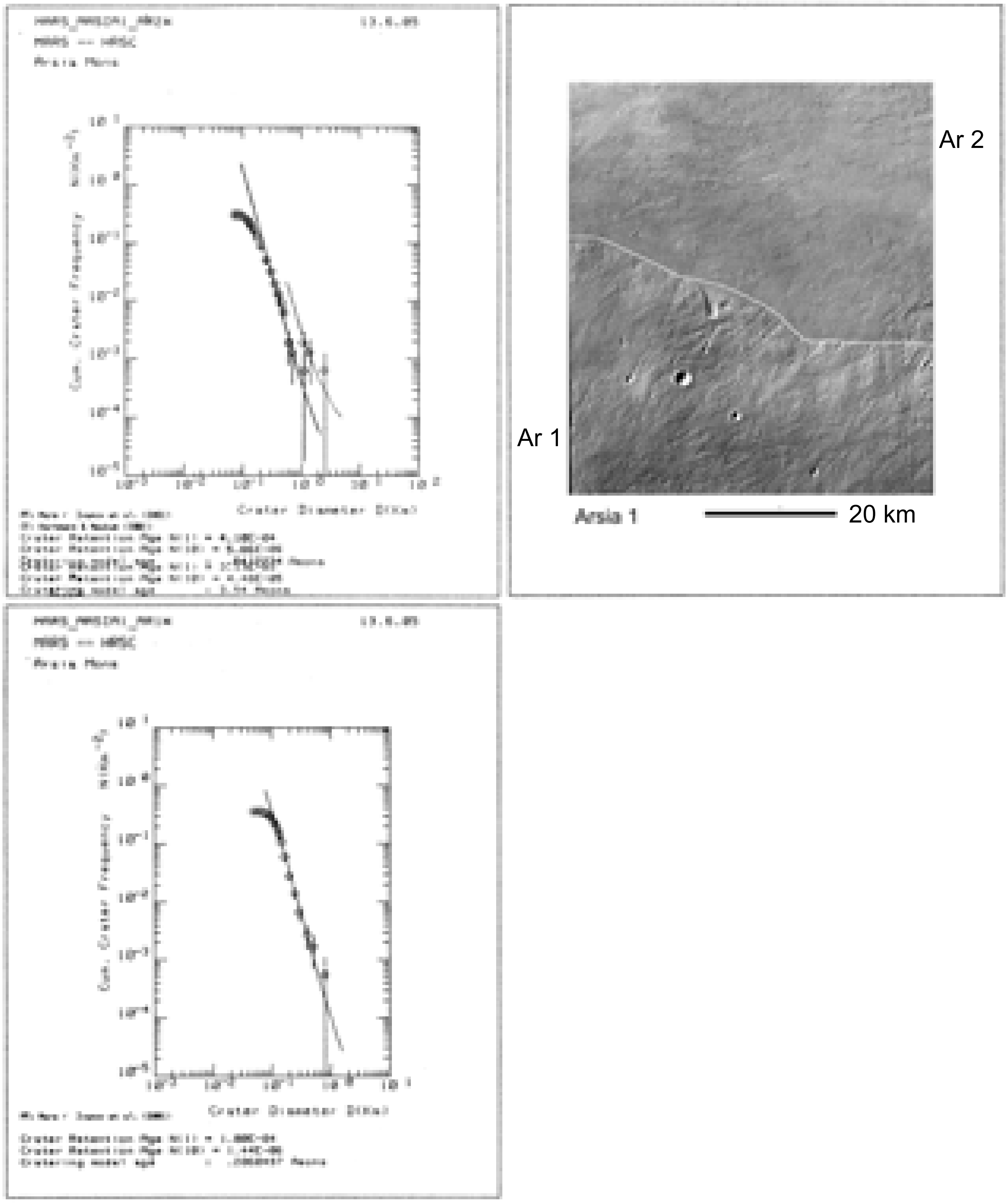

Figure B.7.: Resulting Crater Size–Frequency Distributions for Arsia Mons flanks.

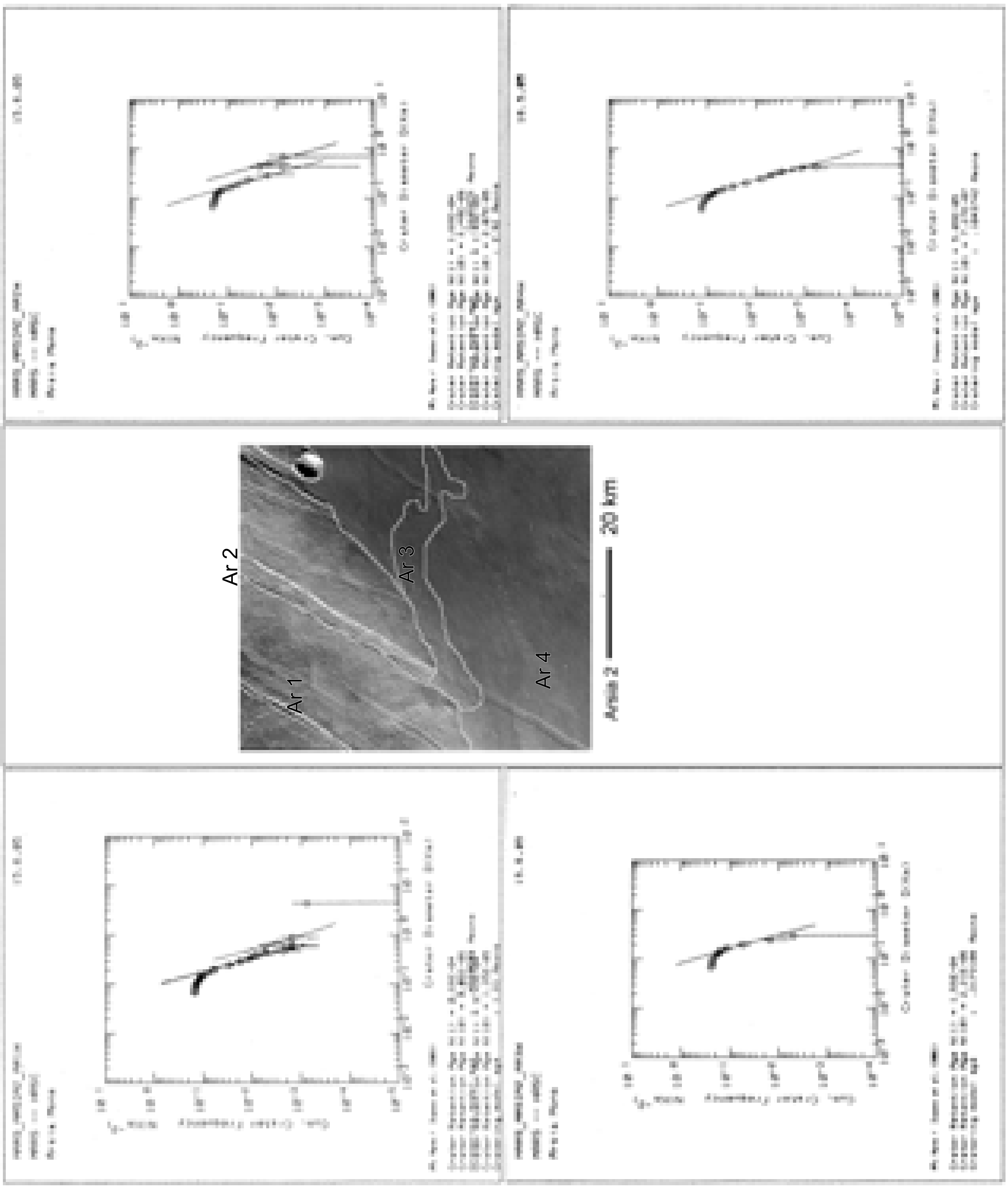

Figure B.8.: Resulting Crater Size–Frequency Distributions for Arsia Mons flanks.

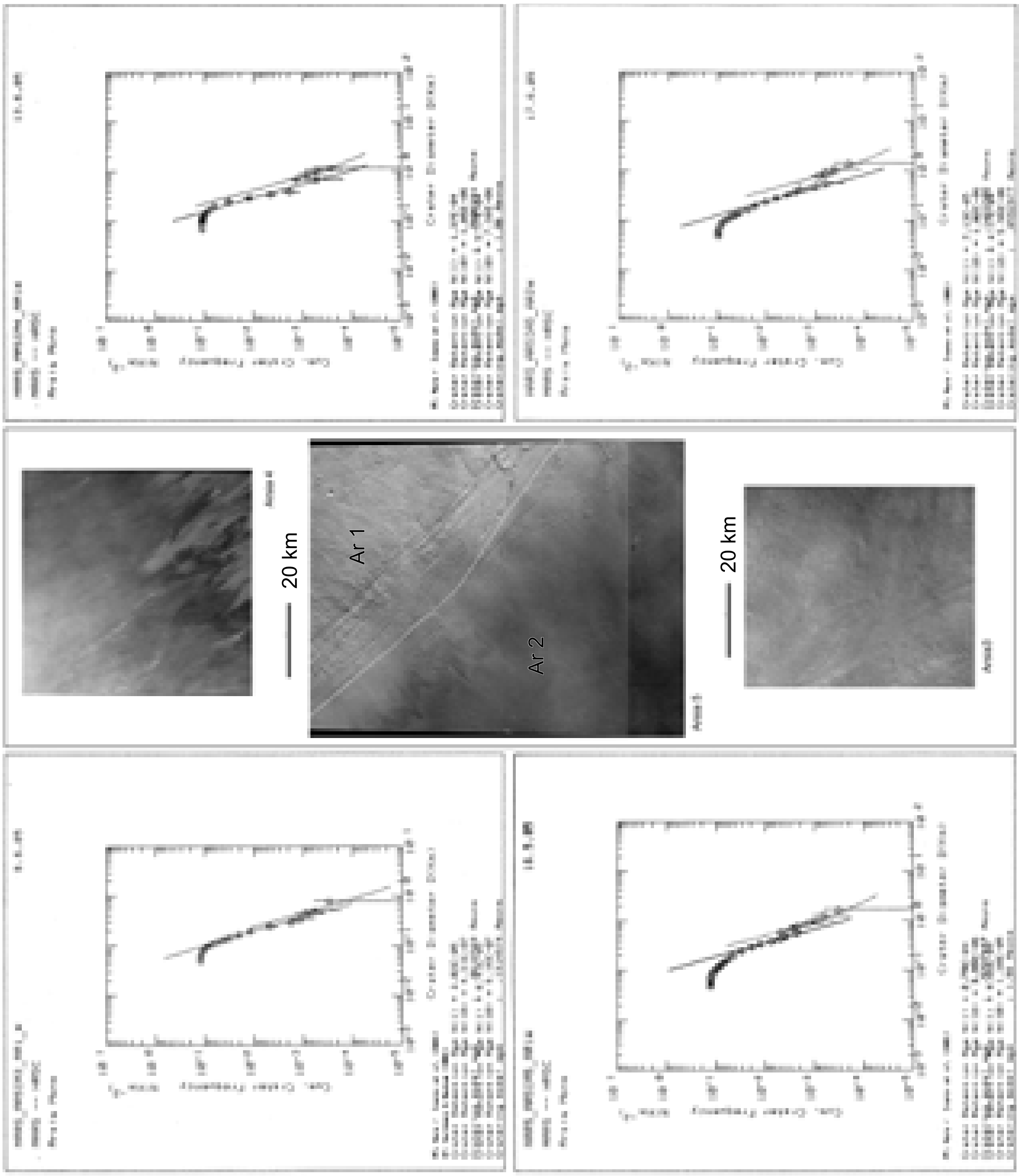

Figure B.9.: Resulting Crater Size–Frequency Distributions for Arsia Mons flanks.

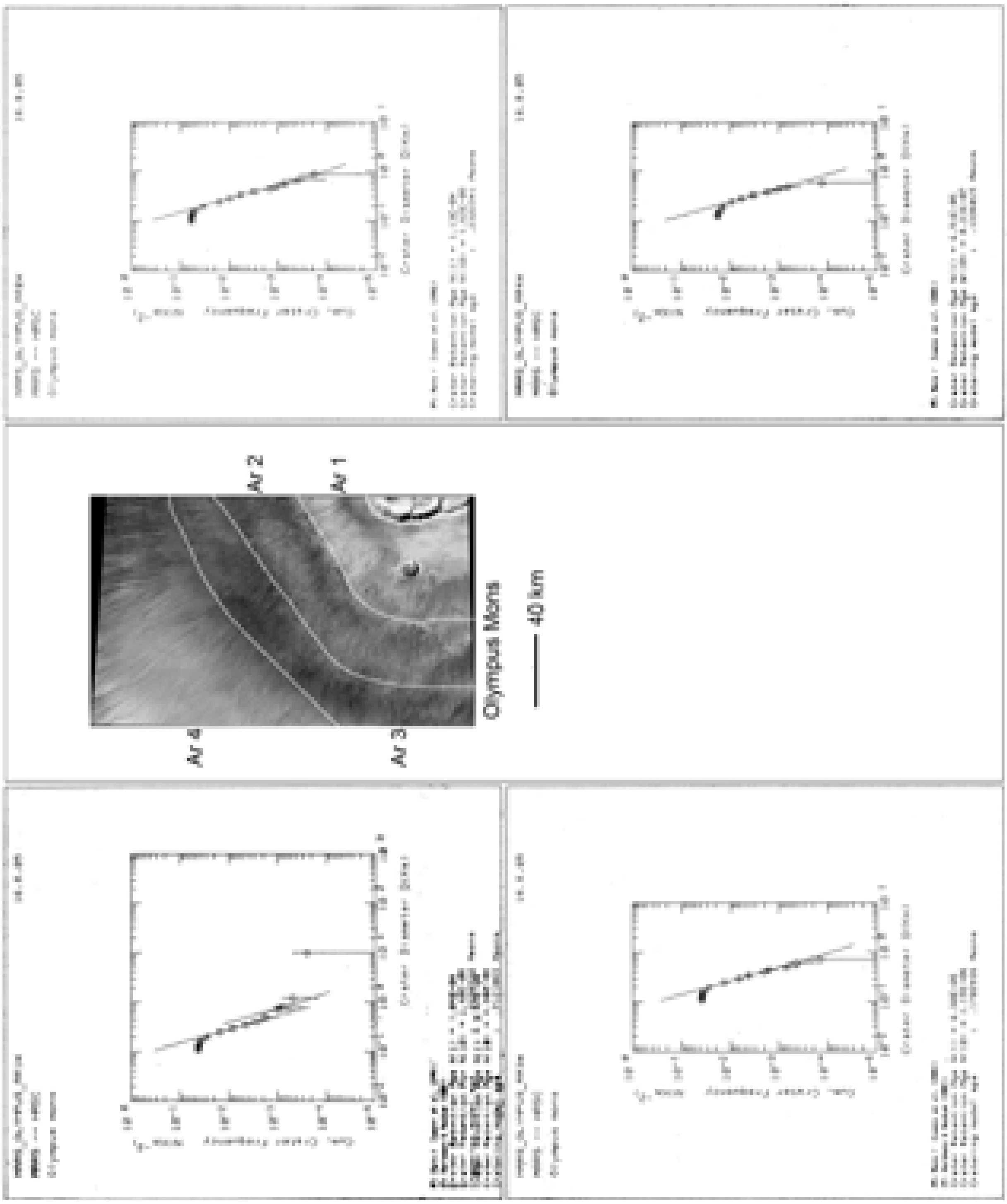

Figure B.10.: Resulting Crater Size–Frequency Distributions for Olympus Mons flanks.

Results of the Crater Size Frequency Measurements of Olympus Mons

Geological Sub–Unit	N_{cum}(1km)	Age in Ga*	Comment
Olympus Mons Caldera Ages			
HRSC_o143_cal1	6.49e-5	0.133	
HRSC_o143_cal2	1.05e-4	0.215	
HRSC_o143_cal3	4.95e-5	0.101	
HRSC_o143_cal4	8.15e-5	0.167	
HRSC_o143_cal5	9.77e-5	0.2	
Flank and Plateau Ages			
HRSC_o143_rem	1.31e-2/3.82e-4	3.83/0.783	
HRSC_o143_kipukas	2.00e-3	3.34	
HRSC_o143_pla1	2.59e-5	0.053	
HRSC_o143_pla2	3.95e-5/9.54e-6	0.081/0.0195	
HRSC_o143_pla1+2	3.21e-5	0.0658	
HRSC_o143_pla3	2.17e-4/9.42e-5	0.445/0.193	
HRSC_o143_pla4	5.24e-5	0.107	
HRSC_o143_pla3+4	2.01e-4/6.37e-5	0.413/0.130	
HRSC_o143_pla5	9.56e-5	0.196	
E04/01135_Ar2	1.92e-5/4.68e-6	0.039/0.009	in rem
E10/03602_Ar2	7.53e-5	0.155	in rem and plat3+4 (resurfacing)
E10/03602_Ar1	4.82e-5	0.1	in pla5
E12/01820_Ar2	5.94e-5	0.122	
HRSC_o143_lava1	1.25e-5	0.025	
HRSC_o143_lava2	5.62e-5	0.115	
E10/00828_Ar1	1.67e-5/1.18e-6	0.034/0.0024	in lava1
Possible Ice Cap Ages			
E11/02748_Ar1	1.10e-4/9.81e-6	0.225/0.020	
_Ar2	3.32e-5	0.068	
_Ar1+2	1.00e-4/1.29e-5	0.205/0.026	
E10/02389_Ar1	1.06e-5	0.022	
_Ar2	1.65e-5	0.034	
_Ar3	1.31e-5	0.027	
_Ar1-3	1.08e-5	0.022	
Surfacial fan-shaped deposits (As); possible rock glacier			
HRSC_o143_As(0)	1.25e-4/6.30e-5	0.257/0.130	around 22N
HRSC_o143_As1(0)south	8.74e-5	0.179	
HRSC_o143_As2(0)north	1.38e-4	0.283	
HRSC_o143_As1(2)	1.29e-5	0.026	around 19N, second measurement
HRSC_o143_As2(2)	1.74e-6	0.004	
HRSC_o143_As3(2)	7.08e-5	0.145	
HRSC_o143_As4(2)	5.45e-4	1.14	!Kipukas
HRSC_o143_As6(2)	2.01e-5	0.041	?Kipukas
HRSC_o143_As4+6	2.22e-4	0.455	
HRSC_o143_As5(3)	1.36e-4/7.36e-6	0.278/0.015	around 17°N
E02/00289_Ar1	3.24e-5/1.63e-5	0.066/0.033	in As(0) and As1(0)
E03/02540_Ar1	2.24e-5	0.046	in As(0) and As2(0)
E04/01135_Ar1	1.93e-4	0.396	in As(0) and As2(0) possibly pits
M12/00197_Ar2	8.34e-6/3.98e-6	0.017/0.008	in As3(2)
_Ar3	2.03e-5/4.69e-6	0.042/0.009	in As2(2)
_Ar4	2.14e-6	0.004	in As2(2)
M04/01782_Ar2	2.58e-5	0.053	in As2(0)
_Ar3	2.72e-5	0.056	
_Ar4	4.36e-5	0.09	
_Ar2-4	2.60e-5	0.053	
_Ar5	1.17e-4	0.240	
E13/01204_Ar1	2.49e-5	0.050	in As1(0)
R01/01050_Ar1	3.66e-5/1.27e-5	0.075/0.026	
_Ar2	2.76e-5	0.057	
E12/01820_Ar1	7.94e-5/1.06e-5	0.163/0.022	

* billion years

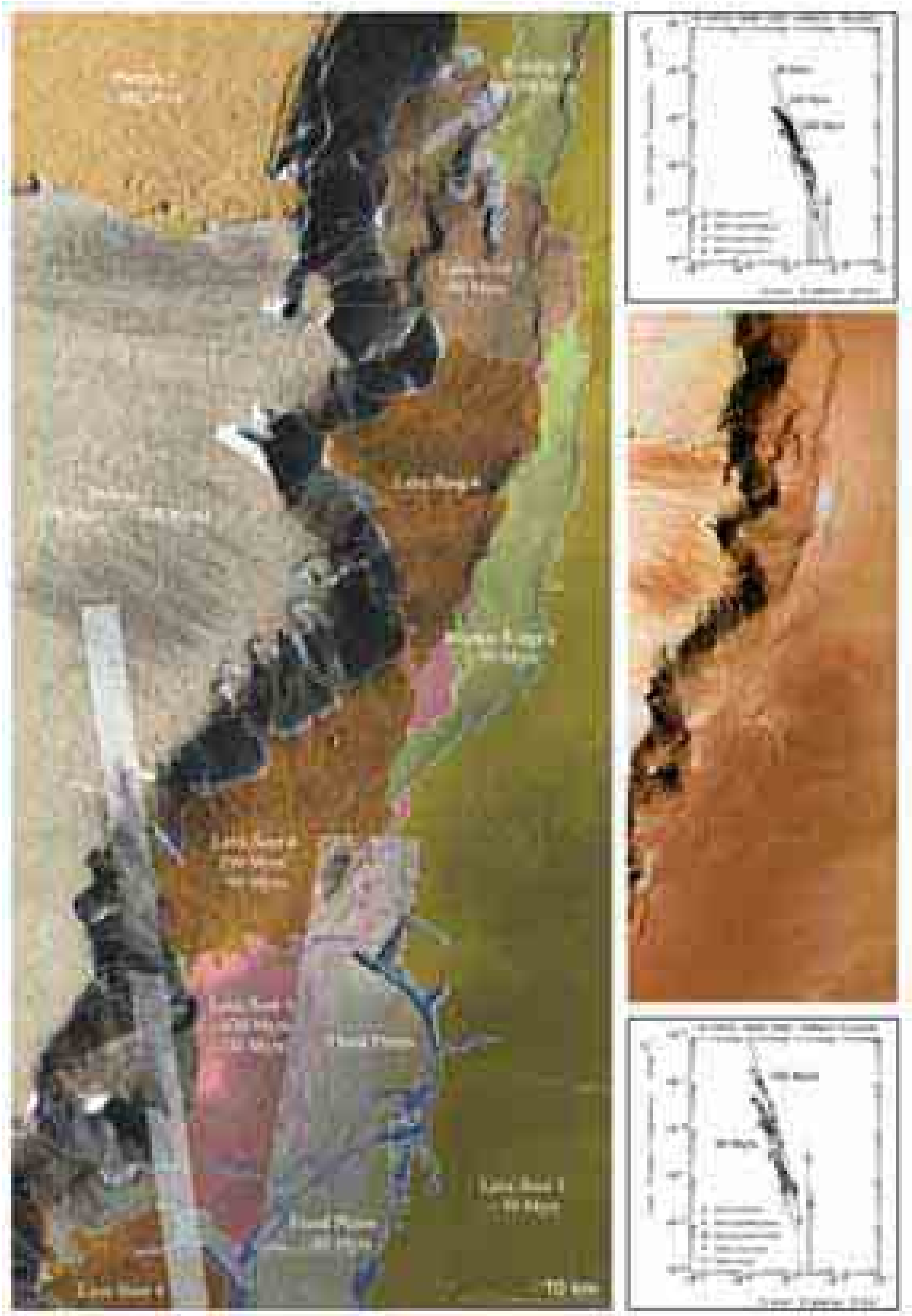

Figure B.11.: The eastern scarp region of Olympus Mons. Left: the mapped regions and the unit ages (map provided by S. van Gasselt, 2005). Right: The measured crater size–frequency distributions for the volcanic units (top) and of possibly fluvial origin (bottom).

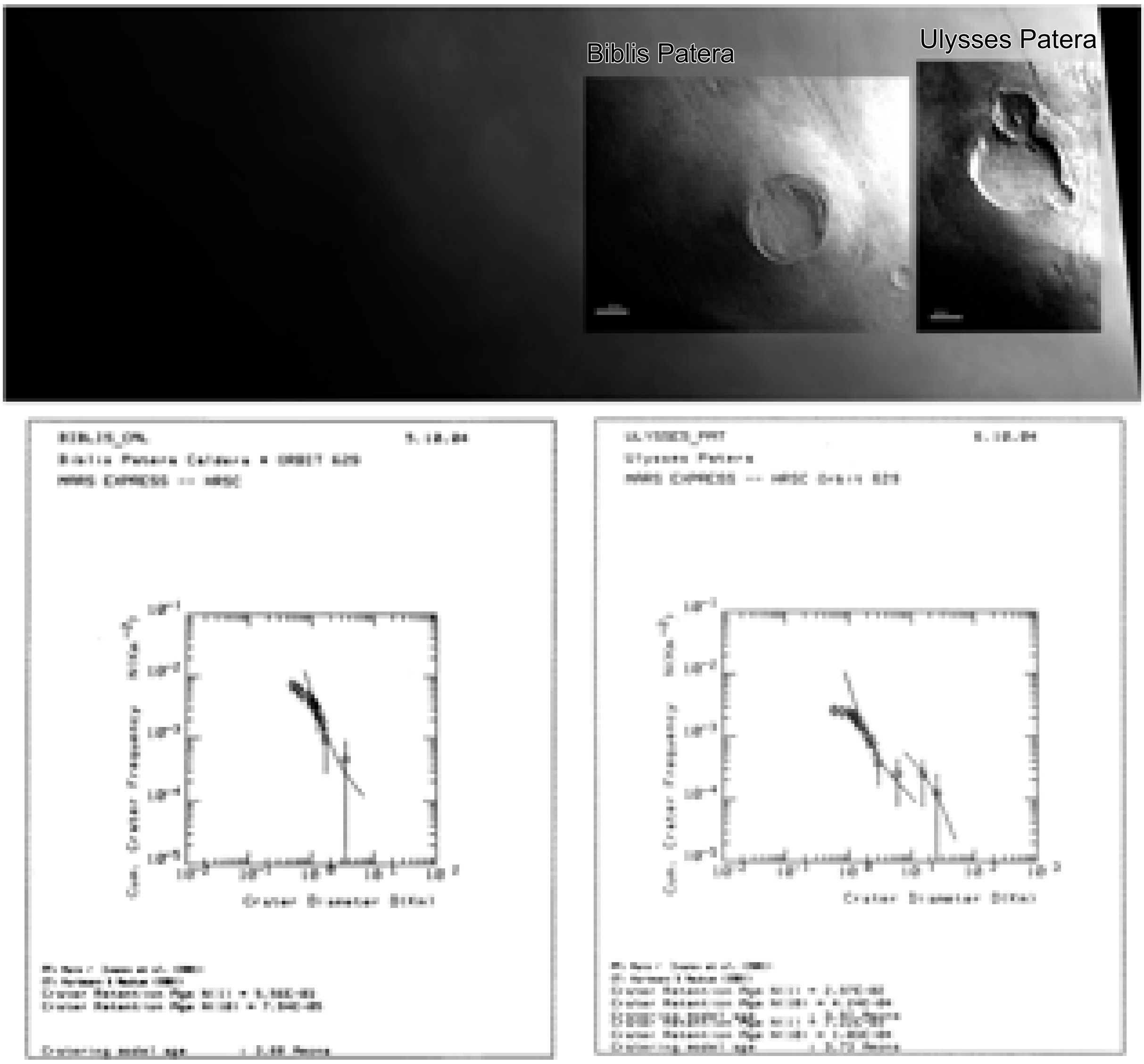

Figure B.12.: Resulting Crater Size–Frequency Distributions for Biblis Patera and Ulysses Patera flanks.

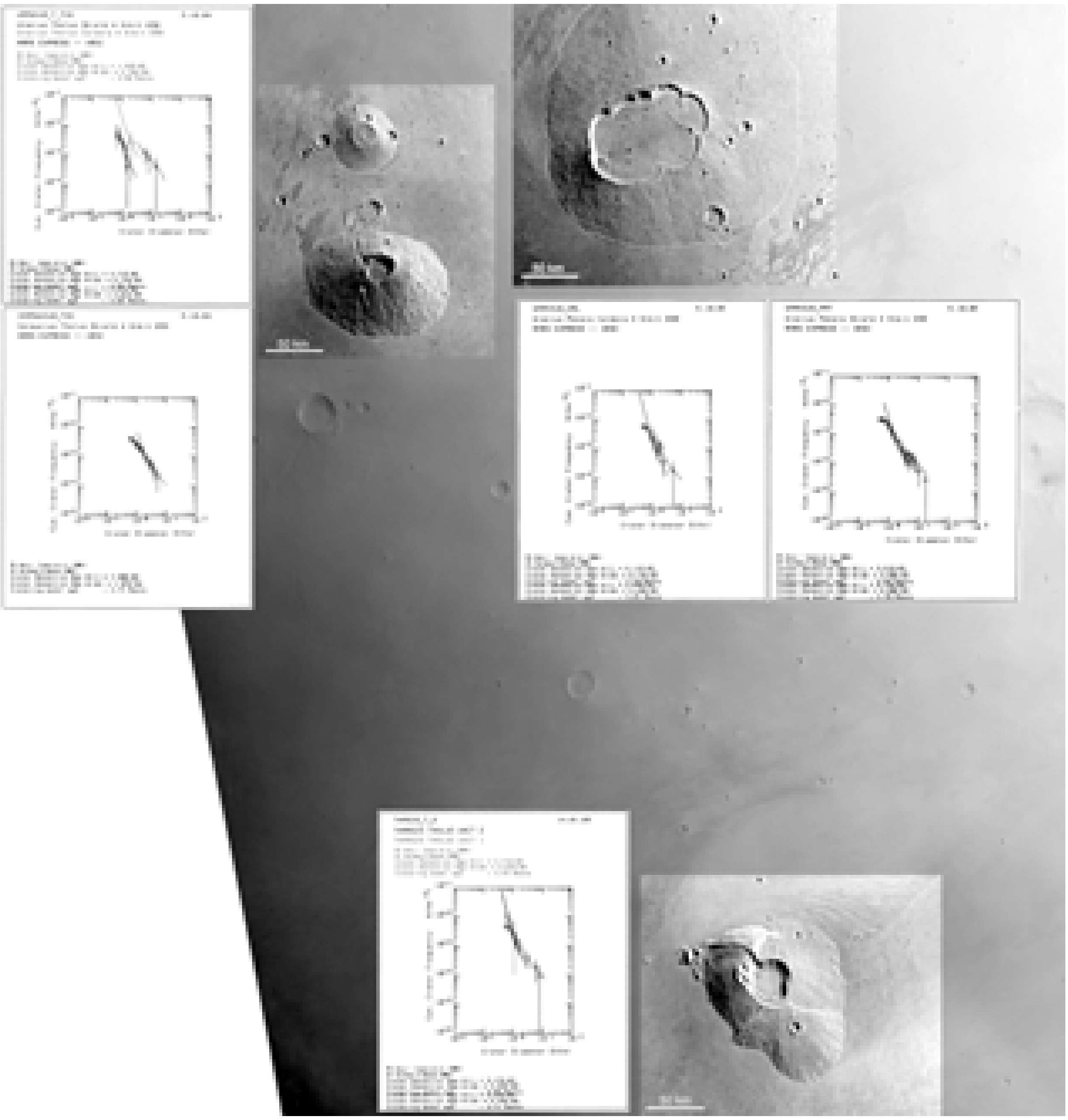

Figure B.13.: Resulting Crater Size–Frequency Distributions for tholi and paterae northeastern of the Tharsis Montes.

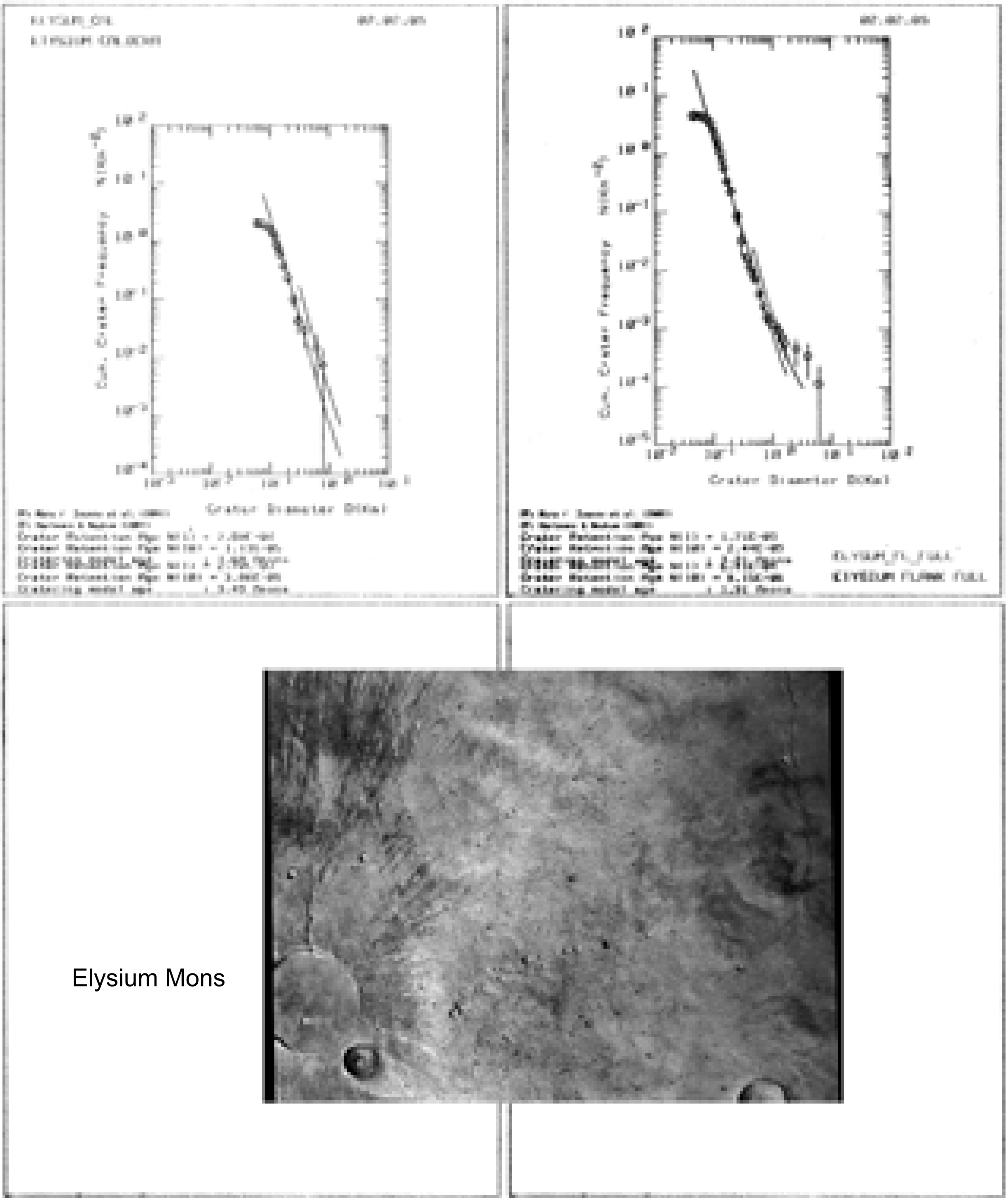

Figure B.14.: Resulting Crater Size–Frequency Distributions for Elysium Mons.

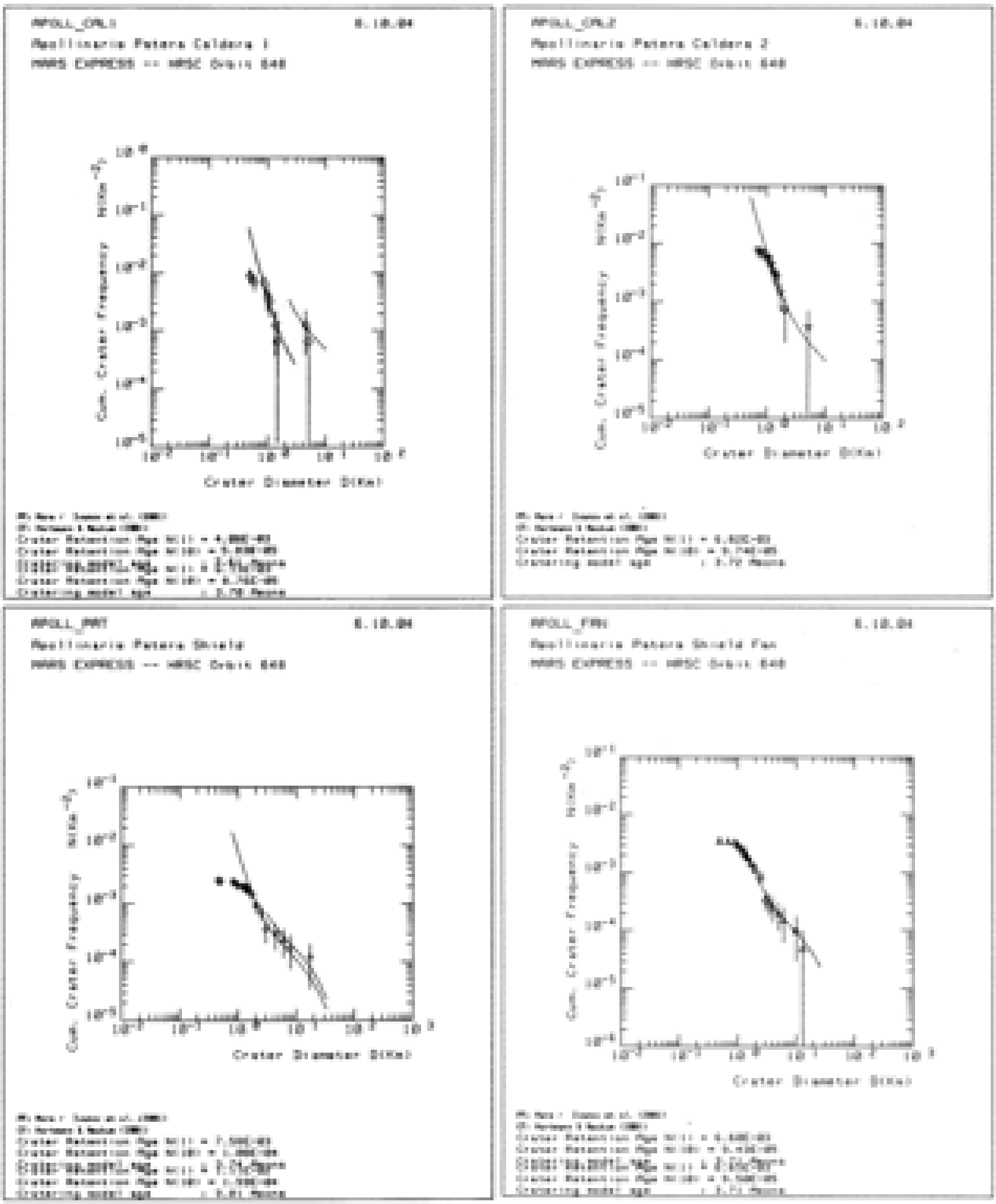

Figure B.15.: Resulting Crater Size–Frequency Distributions for Apollinaris Patera.

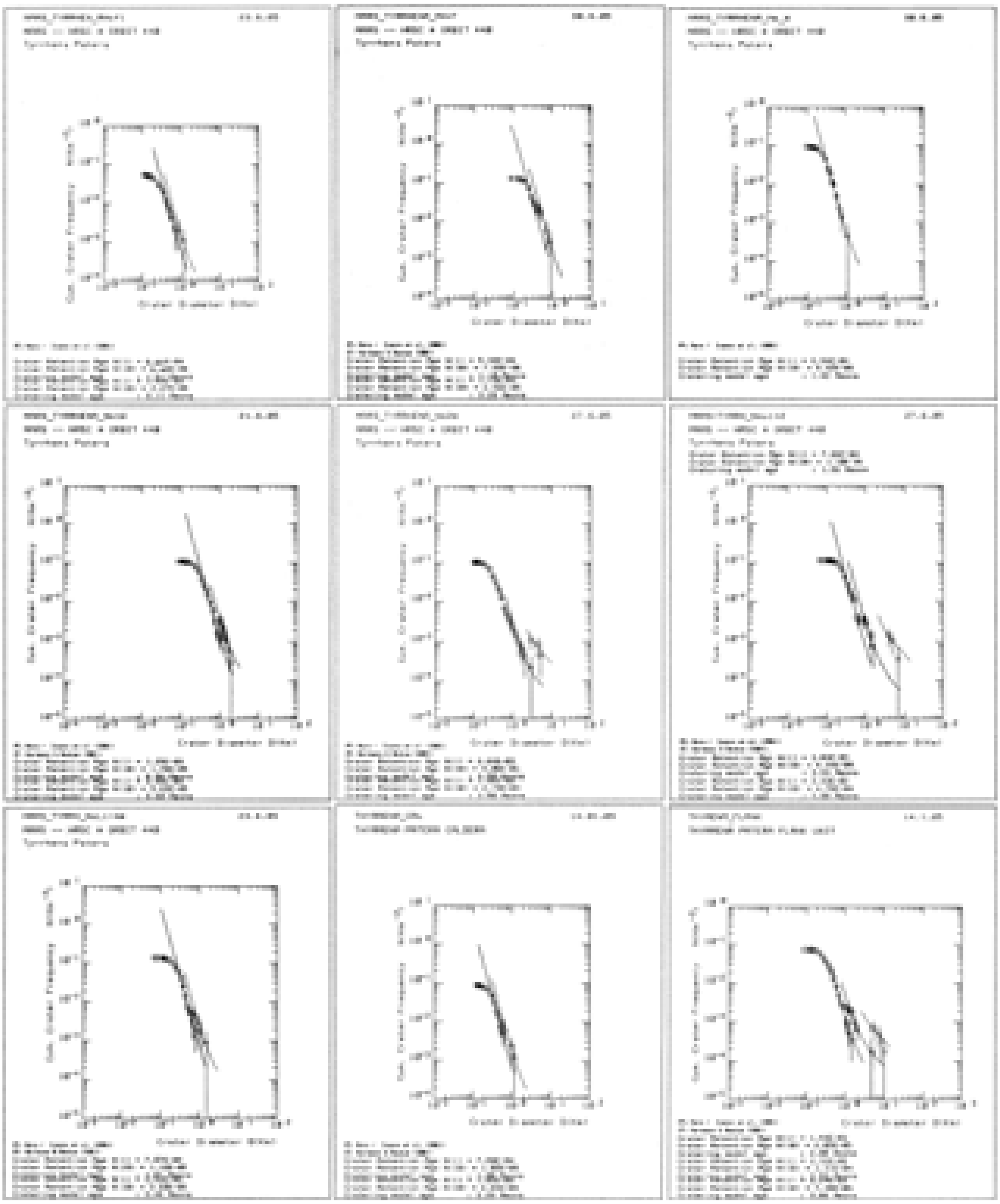

Figure B.16.: Resulting Crater Size–Frequency Distributions for Tyrrhena Patera.

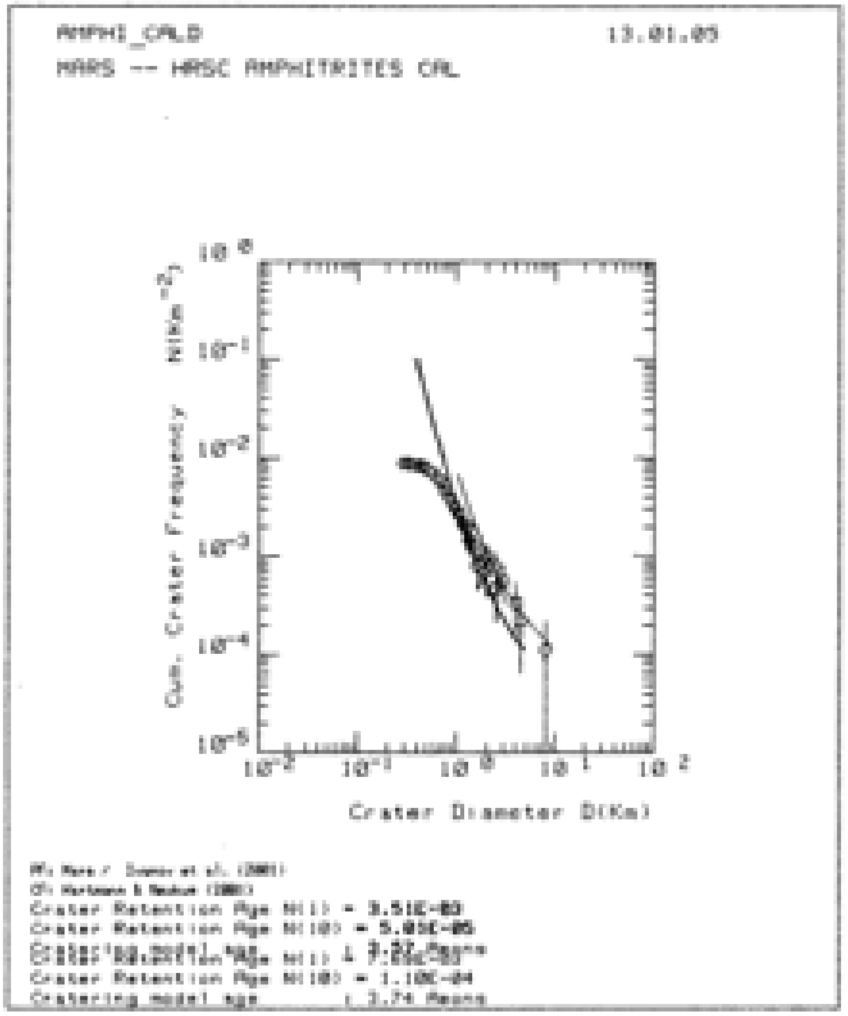

Figure B.17.: Resulting Crater Size–Frequency Distributions for Amphitrites Patera.

C. Fluvial, Glacial, and Volcanic Interaction

Four papers are attached here, whose results have been summarized in Chapter 16. They are most recent publications, which specifically discuss glacial, possible periglacial, and fluvial landforms partly related or triggered by volcanic activity or by proposed climate changes.

These papers are:

1. Neukum, G; Jaumann, R; Hoffmann, H; Hauber, E; Head, JW; Basilevsky, AT; Ivanov, BA; Werner, SC; van Gasselt, S; Murray, JB; McCord, T (2004) Recent and episodic volcanic and glacial activity on Mars revealed by the High Resolution Stereo Camera *NATURE*, 432 (7020): 971-979.

2. Head, JW; Neukum, G; Jaumann, R; Hiesinger, H; Hauber, E; Carr, M; Masson, P; Foing, B; Hoffmann, H; Kreslavsky, M; Werner, S; Milkovich, S; van Gasselt, S (2005) Tropical to mid-latitude snow and ice accumulation, flow and glaciation on Mars *NATURE*, 434 (7031): 346-351.

3. Murray, JB; Muller, JP; Neukum, G; Werner, SC; van Gasselt, S; Hauber, E; Markiewicz, WJ; Head, JW; Foing, BH; Page, D; Mitchell, KL; Portyankina, G (2005) Evidence from the Mars Express High Resolution Stereo Camera for a frozen sea close to Mars' equator *NATURE*, 434 (7031): 352-356.

4. Hauber, E; van Gasselt, S; Ivanov, B; Werner, S; Head, JW; Neukum, G; Jaumann, R; Greeley, R; Mitchell, KL; Muller, P (2005) Discovery of a flank caldera and very young glacial activity at Hecates Tholus, Mars *NATURE*, 434 (7031): 356-361.

Recent and episodic volcanic and glacial activity on Mars revealed by the High Resolution Stereo Camera

G. Neukum[1], R. Jaumann[2], H. Hoffmann[2], E. Hauber[2], J. W. Head[3], A. T. Basilevsky[4,3], B. A. Ivanov[5,3], S. C. Werner[1], S. van Gasselt[1], J. B. Murray[6], T. McCord[7] & The HRSC Co-Investigator Team*

[1]*Institut fuer Geologische Wissenschaften, Freie Universitaet Berlin, Malteserstrasse 74-100, Bldg D, 12249 Berlin, Germany*
[2]*DLR-Institut fuer Planetenforschung, Rutherfordstrasse 2, 12489 Berlin, Germany*
[3]*Department of Geological Sciences, Brown University, Providence, Rhode Island 02912, USA*
[4]*Vernadsky Institute of Geochemistry and Analytical Chemistry, RAS, Kosygin Street 19, 119991 Moscow, Russia*
[5]*Institute of Dynamics of Geospheres, Leninsky Prospect 38, 119334 Moscow, Russia*
[6]*Department of Earth Sciences, Open University, Milton Keynes MK7 6AA, UK*
[7]*Hawaii Institute of Geophysics and Planetology, University of Hawaii, 2525 Correa Road, Honolulu, Hawaii 96822, USA*

*A list of all members of the HRSC Co-Investigator team and their affiliations appears at the end of the paper.

The large-area coverage at a resolution of 10–20 metres per pixel in colour and three dimensions with the High Resolution Stereo Camera Experiment on the European Space Agency Mars Express Mission has made it possible to study the time-stratigraphic relationships of volcanic and glacial structures in unprecedented detail and give insight into the geological evolution of Mars. Here we show that calderas on five major volcanoes on Mars have undergone repeated activation and resurfacing during the last 20 per cent of martian history, with phases of activity as young as two million years, suggesting that the volcanoes are potentially still active today. Glacial deposits at the base of the Olympus Mons escarpment show evidence for repeated phases of activity as recently as about four million years ago. Morphological evidence is found that snow and ice deposition on the Olympus construct at elevations of more than 7,000 metres led to episodes of glacial activity at this height. Even now, water ice protected by an insulating layer of dust may be present at high altitudes on Olympus Mons.

On board the European Space Agency (ESA) Mars Express Orbiter, a multiple line scanner instrument, the High Resolution Stereo Camera (HRSC), is acquiring high-resolution colour and stereo images of the surface of Mars[1]. Resolution down to 10 m per pixel coupled with large areal extent (swaths typically 60–100 km wide and thousands of kilometres long) means that small details can be placed in a much broader context than was previously possible. Among the major objectives of the experiment is an assessment of the level of recent geological activity on Mars, particularly the type of volcanic and climate-related deposits that might indicate areas of hydrothermal activity and recent water exchange conducive to exobiological activity.

We have used the new HRSC images and their particular qualities in mapping out terrain types for the interpretation of morphological features and topographic relationships from the three-dimensional data and high-resolution imagery, including the Super Resolution Channel (SRC) data (resolution down to 2.5 m per pixel)[2]. The high-resolution colour data were very useful for distinguishing different materials. The combined use of the HRSC data and nested Mars Orbiter Camera (MOC) or SRC imagery has proven to be extraordinarily helpful in the interpretation of the morphologies and processes that shaped the landforms now visible. Here we focused on the time-stratigraphic relationships and the sequence of events to understand the geological evolution of the martian areas investigated. Time sequences were obtained by determining the number of superimposed impact craters and deriving absolute ages.

This approach has become a powerful tool of planetary studies since the early 1970s, when frequencies of craters per unit area of lunar basaltic lavas were compared with the absolute ages of these lavas determined through isotopic dating of the returned samples and have thus given us a reference scale for interplanetary comparison[3]. These data, along with theoretical modelling and observational data of fluxes of crater-forming impactors for different parts of the Solar System, have made it possible to apply this method to different planets and satellites[4–6]. For this study we used the recently updated cratering chronology model that combines the efforts of two major research groups in this area[7].

The ages from crater counts are limited in accuracy almost exclusively by the statistical error[8]. Other error sources, such as undetected admixtures of secondary craters, volcanic or sublimation pits, are normally minor (<10% of the frequency of superposed craters)[9,10], provided the geological mapping of the areas and the counts are carried out by experienced observers. The statistical errors of individual data points in our counts are mostly <30% (one standard deviation, 1σ). Because the whole distribution over a wider crater size range is used for fitting the theoretical size-frequency distribution to the measurements, the average statistical error of the data points over the ensemble of measurement is the proper measure for the uncertainty (which, in proportion to the number of data points, is much smaller), resulting in an average uncertainty of 20–30% in frequency. This translates into a 20–30% uncertainty in the absolute ages for ages younger than 3 gigayears (Gyr) and an uncertainty of only 100–200 million years (Myr) for ages older than 3 Gyr. Absolute ages may equally be affected by a possible systematic error of about a factor of two in the crater frequency for an assigned absolute age in the cratering chronology model used. This is due to an uncertainty in the underlying impact flux model used for Mars, relative to the lunar value[6,7].

Time-stratigraphic relationships on martian volcanoes

The Tharsis region of Mars, a huge rise comprising almost 20% of

articles

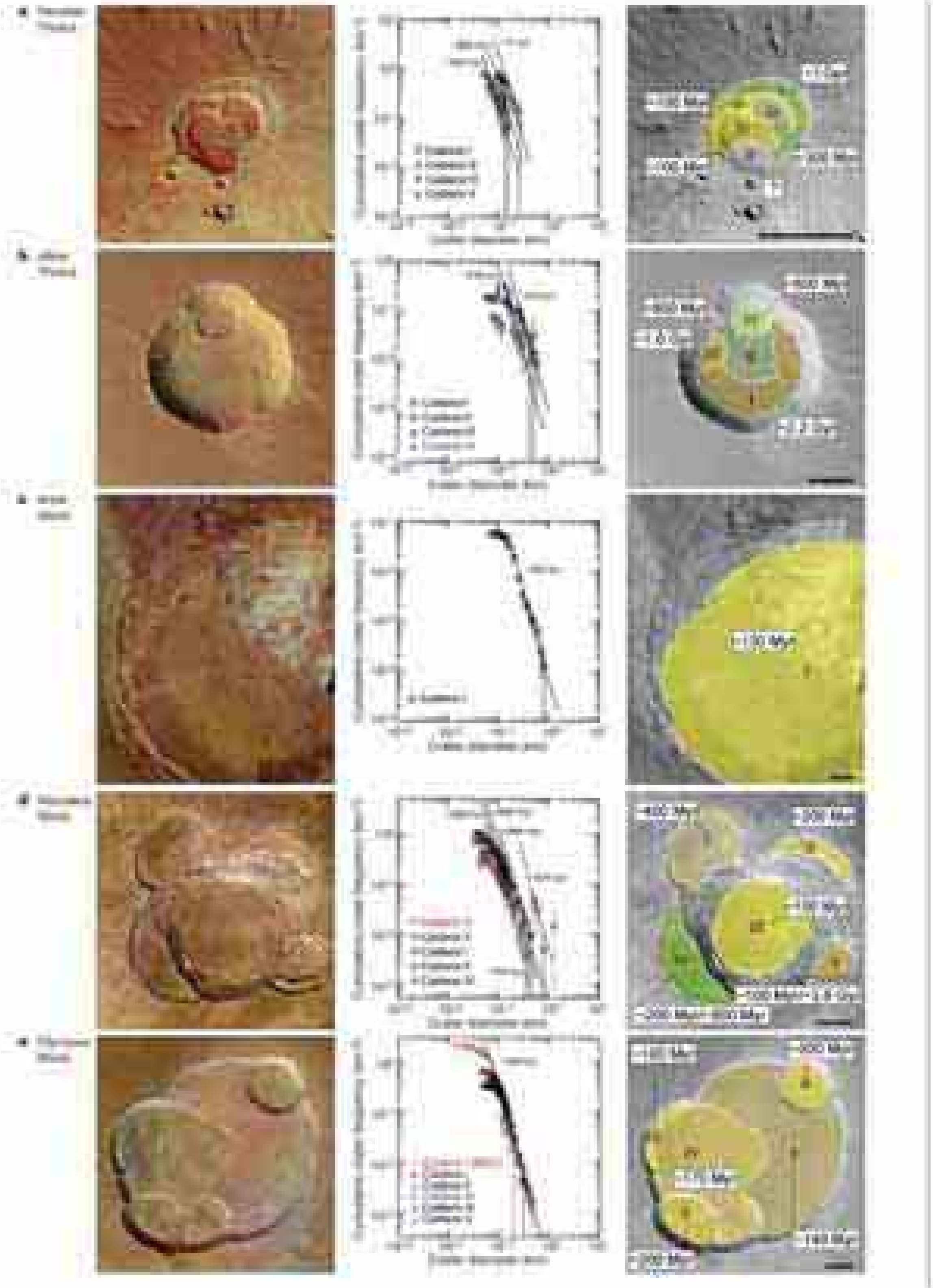

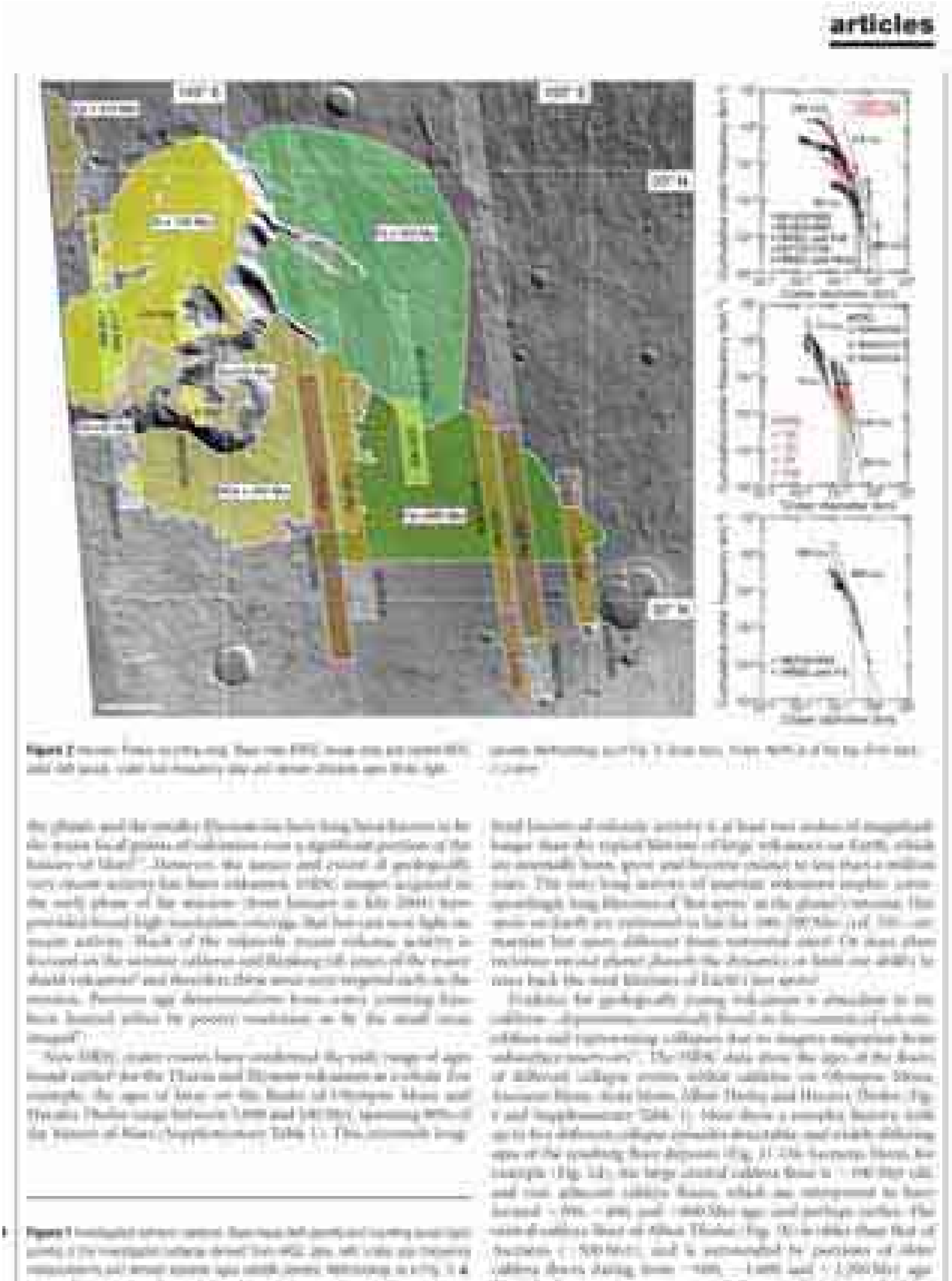
articles

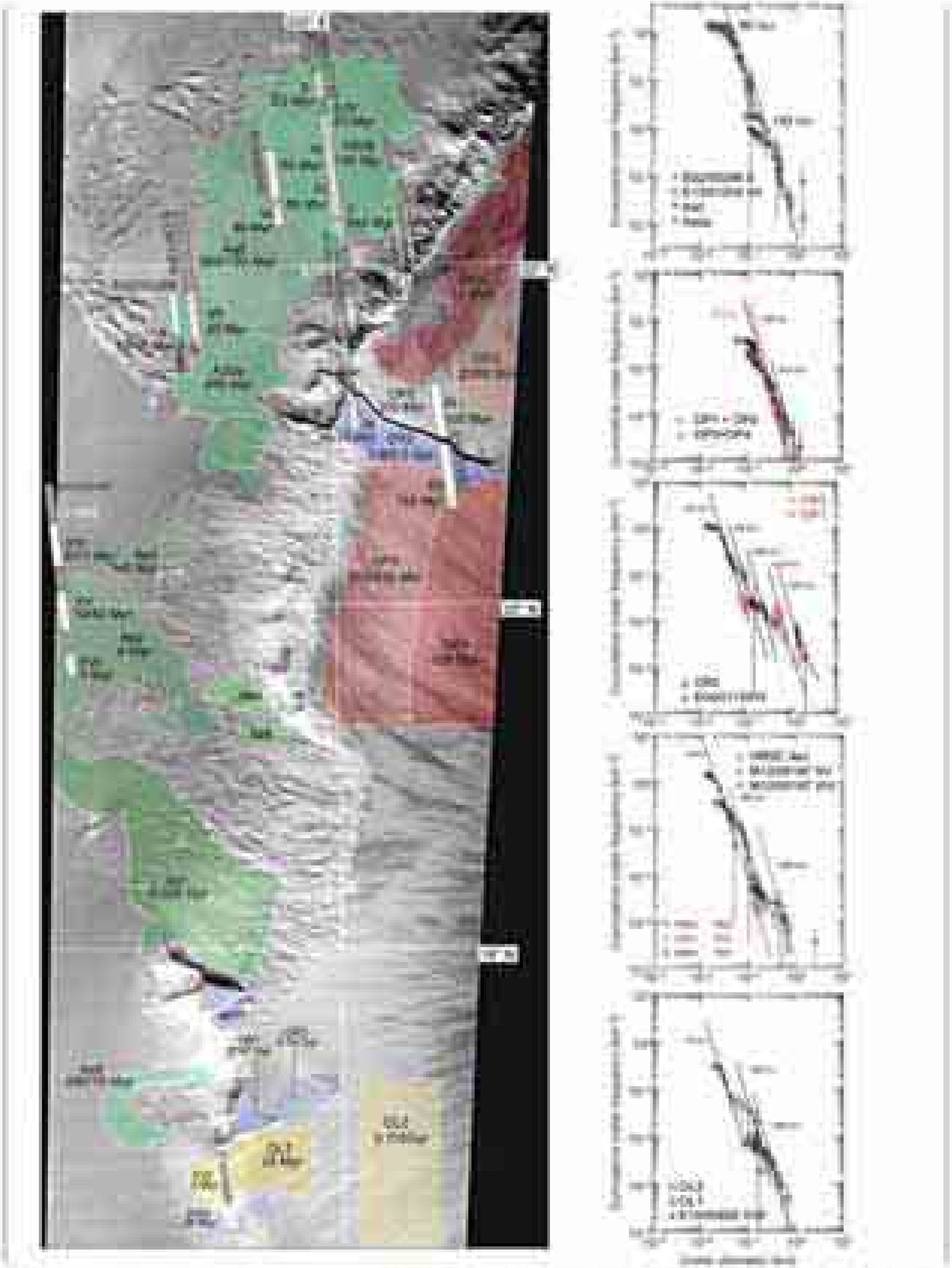

between caldera collapse events, suggesting that magma supply to major shield volcanoes on Mars must have been episodic, rather than continuous[11].

Olympus Mons, however, is unusual by comparison with other calderas. At least five arcuate caldera wall segments can be identified (Fig. 1c), but instead of being spread over hundreds of millions of years in age span, as observed at Ascraeus, Albor and Hecates, the ages of the five Olympus Mons caldera floors cluster in the period 100–200 Myr ago. Theoretically, the ages should be older for high-lying caldera floors and younger for the caldera floors at lower elevation. The different ages are very close to each other within the error limits of ±50 Myr of the age measurements. Thus, the formation of all calderas could have happened in a narrow time span around 150 Myr ago.

It is obvious, however, from the imagery that some of the caldera floors were slightly resurfaced by subsequent thin lava flows or tectonic processes[13] such as horst and graben formation, accompanied by mass wasting processes. Therefore, it is more likely that the calderas formed and were modified subsequently within a period of several tens of millions of years (equivalent to the differences in ages around the average age of 150 Myr). If the theoretical predictions[12] are correct, this implies that separate magma reservoirs were forming, solidifying, and re-forming on timescales averaging perhaps 20 Myr apart. Furthermore, the summit of Arsia Mons is dominated by a single huge caldera whose floor is dated at ~130 Myr ago—falling within the time span represented by the five Olympus Mons ages (~100–200 Myr ago).

These ages confirm some earlier measurements[3,9] on the basis of MOC images in small areas of the calderas of Olympus Mons and Arsia Mons and indicate that the summits of these edifices were very active in essentially the geological present, the last 2–4% of Mars history. These ages provide supporting evidence for the repetitive and episodic nature of caldera formation, and thus magma supply, to the major shield volcanoes on Tharsis and Elysium (compare also with Hecates Tholus in Fig. 2). It is also an interesting coincidence that the summits of four of five of these edifices were very active 100–200 Myr ago, the period in which the crystallization ages of one of two major groups of martian basaltic meteorites fall[14]. This does not necessarily imply a genetic relationship but is a clue suggesting probably widespread volcanic activity on Mars at that time, generating large surface units that the basaltic meteorites may have come from.

It has long been known that the flanking rift zones of the Tharsis Montes and lava flows cascading over the Olympus Mons scarp postdate much of the central edifice-building activity[15]. The new HRSC data permit more precise dating of the duration of activity in these regions. For example, on the lower flanks of Olympus Mons (Fig. 3) are observed flows for which crater size-frequency and age characteristics are interpreted to be representative of activity at ~115 Myr ago, ~25 Myr ago, and with HRSC and MOC data combined, as recently as 2.4 Myr ago.

Figure 3 Olympus Mons western scarp areas. HRSC-image base map with nested MOC data and depiction of the counting areas (left panel) and the resulting ages of the western near-escarpment area of the Olympus Mons volcanic shield, the 7-km-high escarpment and the adjacent plains area to the west with remnants of glacial features (five right panels). The counts show different episodes of resurfacing with erosion of craters and subsequent re-cratering. These episodes and processes are reflected in the different steepnesses of the distributions on the log–log plots, giving a kinked appearance. The flat parts show erosional effects; the steep parts show the re-cratering after the erosional episodes. The martian impact-crater size-frequency distribution[2,3,7,8] has been fitted to the individual segments of the distribution, giving individual crater-frequency values for the different episodes; by application of the Hartmann–Neukum chronology[9] individual absolute ages can be extracted. In this way it is possible to extract the evolutionary history of the area under investigation in detail. Here the fits to the crater frequencies partly have the character of average isochrons for a group of counts yielding similar numbers. Individual ages may be slightly different and are precisely given in Supplementary Table 1. The errors of the ages are usually around 20–30% for ages younger than 3 Gyr (only 100–200 Myr for older ages) owing to the statistical limitations. The error bars given represent a 1-σ error. In the same way, all ages of less than 2 Gyr may be affected by a possible systematic error of about a factor of two in the cratering chronology model[10] used. North is at the top.

Hydrothermal, fluvial, and glacial activity

Further evidence of very recent and episodic geological activity on Mars has been obtained by HRSC in the form of images and ages of several deposits related to recent climate change. We know that water in the form of ice exists at the polar caps and in the cryosphere of Mars[16], and perhaps locally on the surface[17]. Only recently, however, has it become clear that the extreme variability of the obliquity of the spin axis of Mars and orbit eccentricity[18] can cause significant mobilization of polar volatiles and their redeposition equatorward[19,20]. Of particular interest are the types of deposits that are interpreted to represent the accumulation of water ice in non-polar regions, because these are very sensitive environmental indicators and have important implications for possible life and future automated and human exploration.

For these reasons, early targets for the HRSC instrument were parts of the Elysium region, and the western scarp of the Olympus Mons volcano. On the basis of Viking imagery, channels on the flanks of the Hecates shield have already been detected and interpreted as having been produced by running water[21,22]. We have been able to study the Hecates shield at a resolution of 26 m per pixel in great detail and to determine the ages of some areas using crater-statistics methods (Fig. 2). MOC data were also used, as indicated in Fig. 2. The data show a wide age range over which volcanic activity and related mobilization of water (probably released hydrothermally or partly released through melting of snow caps by volcanically induced heating from underground) with subsequent glacial activity occurred. Here, we present only the gross time-stratigraphic relationships of the development in different areas on the volcano, starting more than 3.4 Gyr ago and shaping the volcano through different episodes of activity (for example, ~900, 400 and 50 Myr ago) until very recent times of about 5 Myr ago. Fluvial and glacial activity can be recognized close to or in the depressions at the northwestern base of the volcano. In southern Elysium, to the southwest of Athabasca Valles, surface features have been observed on the HRSC imagery that look similar to pack-ice on Earth. The age of these deposits is only 5 Myr—in the same range as some of the glacial deposits on Olympus Mons and Hecates Tholus. Details of our findings are supplied elsewhere[23,24].

The other outstanding early target, the Olympus Mons volcano (Figs 3 and 4), is a site known to be characterized by lobate deposits thought to be of glacial origin[25] and recently shown on the basis of the NASA Mars Global Surveyor (MGS) and Odyssey mission data to be a series of lobate rock-covered piedmont glaciers[26]. These deposits are well illustrated in the new HRSC data (Fig. 4b). Therefore, it is now possible to determine more specific ages for them (Fig. 3 and Supplementary Table 1): 130 to 280 Myr for the major lobes, with some subunits in the 20–60 Myr range and locally as young as 4 Myr. These data indicate that the lobate deposits represent several phases of formation, most probably representing periods when significant snow and ice accumulation (possibly accompanied by hydrothermal mobilization of water that flowed down over the edge of the shield, entraining large amounts of non-icy surface material and then freezing) at the Olympus Mons scarp caused mobilization and flow of debris-covered piedmont glaciers into the surrounding low-lying regions.

In several places along the scarp, small linear tongue-like deposits can be seen to emerge from within the apparent accumulation zones of the larger lobate deposits (Fig. 4c). These are interpreted to be

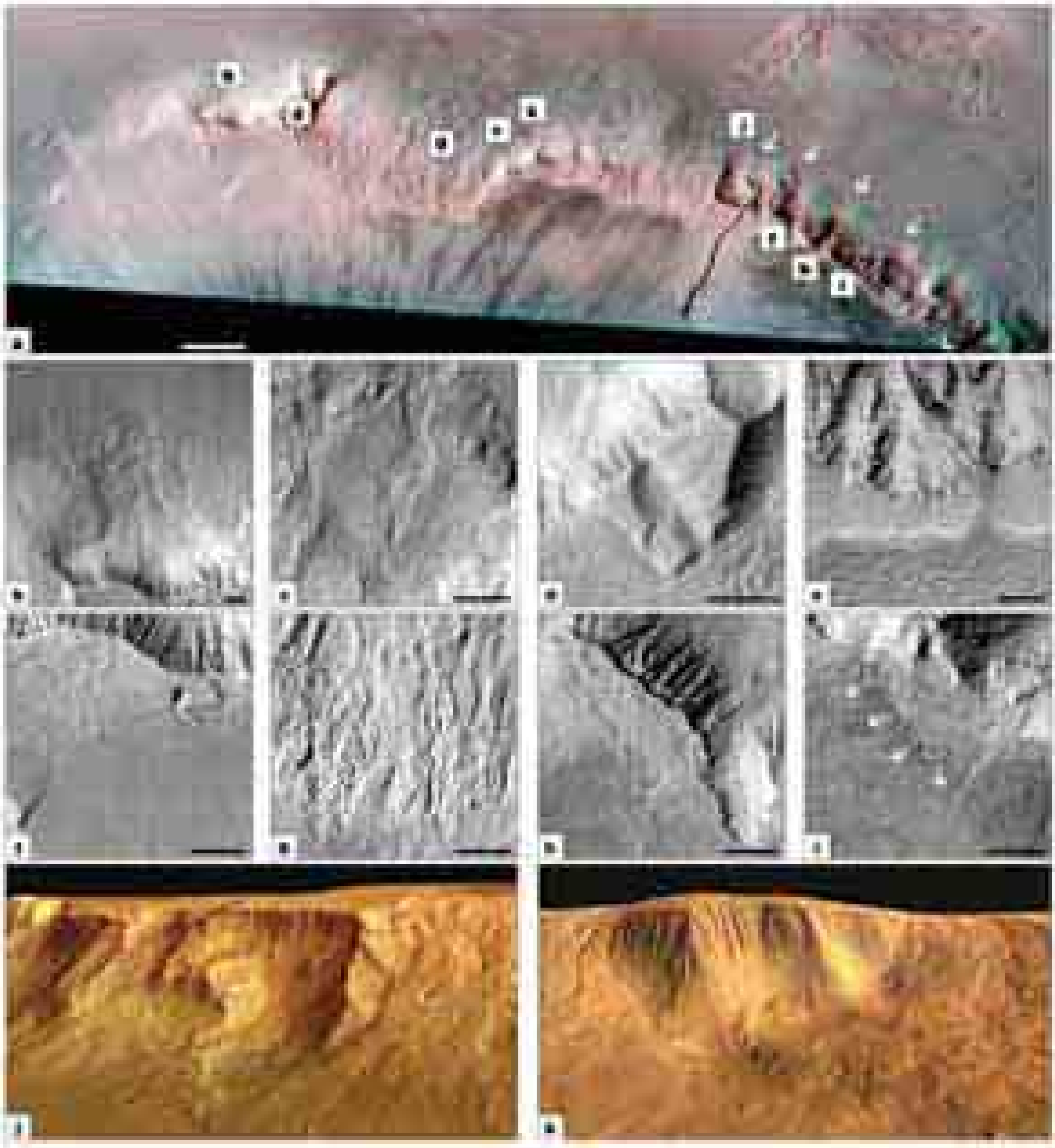

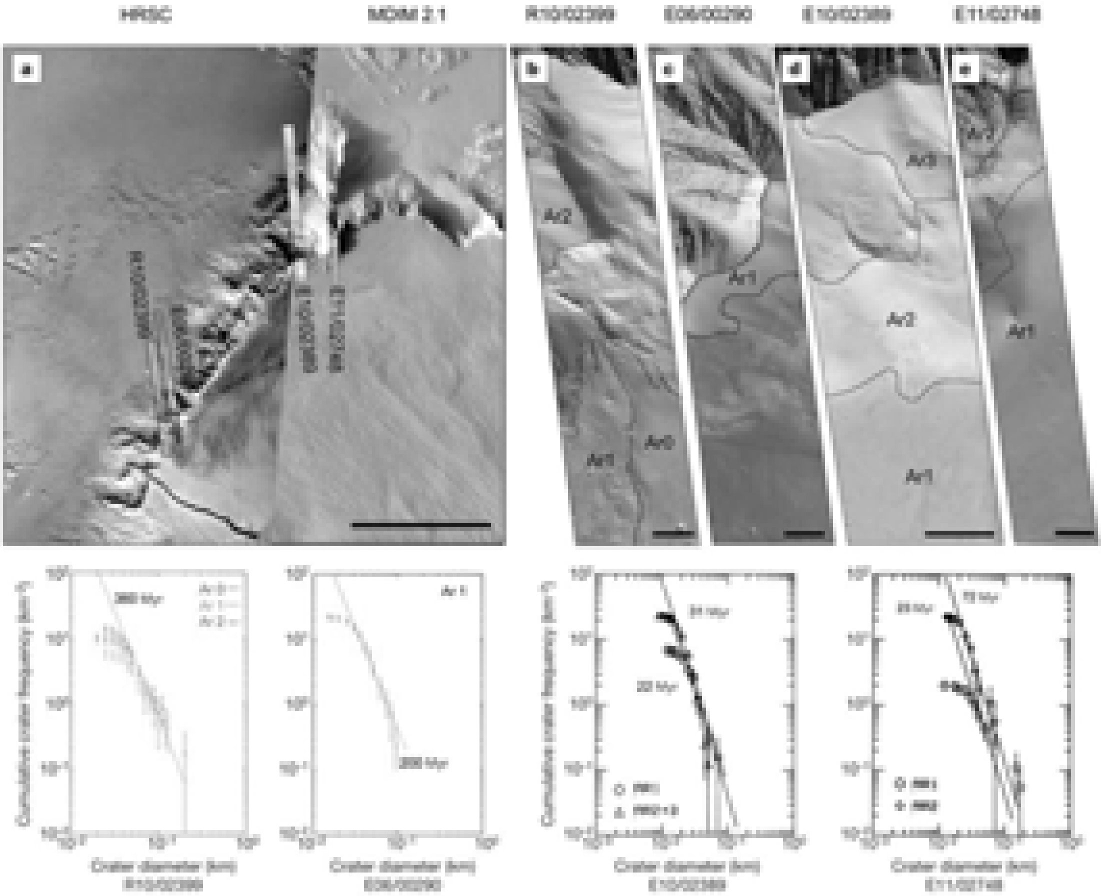

Figure 5 Base map (panels **a**–**e**) and crater statistics (four panels at bottom) of the areas on the northwestern part of Olympus Mons investigated for possible ice–dust coverage and age relationships. **a**, Mosaic of HRSC data (left) and Viking imagery (right) with the location of the MOC images used for morphological study and age determination; scale bar, 50 km. **b**–**e**, MOC images (scale bar, 1 km) with counting areas on flat terrain on the escarpment ridge with its ice–dust cover. **b**, Areas of measurement on MOC image R10/02399 and resulting ages derived from superposed crater frequencies. The ages are roughly the same for all three counting areas on the basis of the fit for intermediate-sized to large craters: 360 Myr with an uncertainty of about 70 Myr. Minor erosion of craters can be recognized in the subtle flattening of the measured distribution in comparison with the fitted theoretical production function. The bending-over characteristics at the small-crater end here and in the other measurements in **c**–**e** stem from loss of craters at the resolution limit of the images. **c**, Areas of measurement on MOC image E06/00290 and resulting age of 200 ± 40 Myr. **d**, Areas of measurement on MOC image E10/02389 and resulting ages of 22 ± 4 Myr and 31 ± 6 Myr. The ages of the individual counting areas AR2 and AR3 have been determined separately with the same results (31 Myr). The AR1 measurements show that some erosion of the ice–dust cover seems to have taken place. **e**, Areas of measurement on MOC image E11/02748 and resulting ages of 23 ± 5 Myr and 72 ± 15 Myr. These ages correlate well with the ages (20 and 80 Myr) measured on adjacent lava flows (OP2 of the base map in Fig. 3). North is at the top. Error bars, 1-σ error.

deposits 50–100 m thick on the rim of the Olympus western scarp, sometimes in the form of mesas (Fig. 4d, e). These optically bright sediments show fine layering obviously different from that which could potentially be formed by accumulation of the lava flows typical of this volcano. We interpret these deposits to represent the remnants of accumulations of dust and ice high on the Olympus construct in previous geological periods. We believe that the presence on some mesas of rimless and deep sinkhole-type depressions (Fig. 4f, upper right) confirms this interpretation. In some places we also see that lava flowing upon these deposits causes their collapse (Fig. 4f, centre left).

Age measurements (Figs 3 and 4) show that the layers formed more than 300 Myr ago, possibly followed by further episodic activity or subsequent major erosional activity until about 65 Myr ago, as seen on the escarpment ridge. Some data for the mesas, from the frequency of some large surviving craters that belong to the underlying substrate, yield age estimates that exceed 3 Gyr. That is close to earlier estimates of the age of the Olympus Aureole, interpreted to have formed by 3.4-Gyr-old gravitation slides of material from the western shield of the Olympus construct[27,28]. This is an indication that the shield of Olympus Mons had already reached heights in excess of 7,000 m very early in its history. The eruption rates must have been very high at the beginning of the growth of the volcano.

Within the broad segments of the upper part of the scarp we observe depressions (Fig. 4g) that are morphologically similar to collapse depressions seen at the source areas of the outflow channels of Mars. The latter are believed to form as a result of release of large amounts of water from below the surface, for example, the melting of ground ice by magma intrusion[21,22]. Water (subsequently freezing to ice) seems to have been mobilized out of the ground hydrothermally. The collapse-type depressions of the Olympus scarp are also often accompanied by fluvial-type channels, although of relatively small size (Fig. 4h). We interpret these as having been formed by melting ice or ice-and-dust deposits via interaction with lavas.

Glaciers on the shield of Olympus Mons

The edge of the northern part of the scarp is rimmed by a ridge also covered with fine-layered deposits (Fig. 4j, k and Fig. 5a–e). The HRSC-based digital terrain model (DTM) model shows that the ridge stands 400–700 m above the surface adjacent to the east. We interpret the deposits on the ridge as a layer of ice and dust now protected from sublimation by a lag of dust. This 'ice cap' on the ridge formed about 400 Myr ago or earlier, as determined by measuring the superposed crater frequencies as given in Fig. 5. We identify different episodes of subsequent resurfacing of the ice cap at times of 200, 70 and 20–30 Myr ago. We have identified several valleys that are transverse to the ridge and cut into it. In a few cases, the valleys cut back into the summit plateau. The valleys have a U-shaped cross profile and end at the scarp foot with hummocky piles (arrows on Fig. 4a) often having lobate outlines. These are interpreted as debris-covered piedmont glaciers. These characteristics of the valleys suggest that glaciers ploughed them and that the source areas of those glaciers were high on the summit plateau. Moreover, in the potential source area of one of these valleys we see a lobate landform whose orientation suggests glacier movement to the east, towards the volcano centre (Fig. 4l). We estimate the age of this landform—now covered by dust, as are almost all other landforms of the region—to be 200–300 Myr (Figs 3 and 4j). We see evidence of sublimational or eolian degradation significantly erasing the cratering record, which implies that the lobate landform has not been active recently.

The colour data have been examined for effects of the presence of water ice, such as brightening of the surface and possibly flattening of the spectral slope. Colour ratio measurements were done for 16 major terrain types. Brightness in the four HRSC colour channels (centre wavelengths 440, 530, 750 and 970 nm) was calculated by applying the scaling factors from the ground calibration and additional factors derived from comparison with telescopic spectral data[30] and cross-calibration to data from the OMEGA experiment[31]. The measurements showed that the brightness values for each colour channel vary only within a factor of 1.5. All the measured ratios are close to those of "bright regions of Mars"[32] indicating that all the studied terrains are dust-covered. If there is ice, then it appears to be covered and protected from sublimation by a sublimation lag of dust on top of the ice or ice–dust deposit.

The accumulation of ice necessary for developing the high-altitude glaciers and the dust–ice deposits on the mesas and the ridge could have happened at times of high inclination of the planet's spin axis[18]. Experimental data[33] and calculations[34] show that under current climate conditions sun-illuminated water ice (snow) sublimates quickly. But even a thin dust cover shifts the vapour pressure in the pore space to close to the saturation pressure and drastically decreases the sublimation rate of the buried ice[35]. The buried ice (more probably an ice and dust mixture) may be practically stable (slowly sublimating) over millions of years, depending on the diffusive resistance of the upper dust cover against the vapour outflow to the dry atmosphere. Therefore, the layered deposits on the mesas and on the escarpment ridge, and the high-altitude lobate landform may still contain ice. This suggestion may be tested in the future by the MARSIS sounding radar[36] and OMEGA[31,37] experiments on board Mars Express.

Conclusions

The new ages from the HRSC data: (1) confirm the very wide age range (billions of years) over which the Tharsis and Elysium regions were volcanically active; (2) reveal that summit caldera activity was periodic and often consistent with theoretical predictions of magma reservoir cooling and regeneration behaviour; (3) show that the most recent summit caldera activity on the Tharsis volcanoes was clustered ~100–200 Myr ago, practically coinciding with radiometric ages of several martian meteorites; (4) reveal that some of the youngest volcanism on the Tharsis edifices appears to be as young as several million years, thus suggesting that these volcanoes could well erupt in the future; (5) yield evidence for former hydrothermal mobilization of water at the western edge of the Olympus Mons volcano shield and probably on the Hecates Tholus volcano with subsequent development of glaciers; (6) reveal evidence for very young glaciations in the tropical regions of Mars; (7) reveal evidence for deposition of dust and ice and episodes of glaciation high on the Olympus Mons construct; and (8) suggest that water ice may now be present at high altitudes on the edge of the Olympus western scarp. □

Received 1 September; accepted 30 November 2004; doi:10.1038/nature03231.

1. Neukum, G., Jaumann, R. & the HRSC Co-Investigator and Experiment Team. HRSC — The High Resolution Stereo Camera of Mars Express 17–35 (European Space Agency Special Publication ESA SP-1240, 2004).
2. Malin, M. C. & Edgett, K. S. Mars Global Surveyor Mars Orbiter Camera: Interplanetary cruise through primary mission. J. Geophys. Res. 106, 23429–23570 (2001).
3. Neukum, G., Ivanov, B. A. & Hartmann, W. K. Cratering record in the inner Solar System in relation to the lunar reference system. Space Sci. Rev. 96, 55–86 (2001).
4. Ivanov, B. A. Mars/Moon cratering rate ratio estimates. Space Sci. Rev. 96, 87–104 (2001).
5. Hartmann, W. K. & Neukum, G. Cratering chronology and the evolution of Mars. Space Sci. Rev. 96, 165–194 (2001).
6. Neukum, G. & Hiller, K. Martian ages. J. Geophys. Res. 86, 3097–3121 (1981).
7. Tanaka, K. The stratigraphy of Mars. J. Geophys. Res. 91, E139–E158 (1986).
8. Greeley, R. & Spudis, P. D. Volcanism on Mars. Rev. Geophys. Space Phys. 19, 13–41 (1981).
9. Hartmann, W. K. et al. Recent volcanism on Mars from crater counts. Nature 397, 586–589 (1999).
10. Steinberger, B. Plumes in a convecting mantle: Models and observations for individual hotspots. J. Geophys. Res. 105, 11127–11152 (2000).
11. Crumpler, L. C., Head, J. W. & Aubele, J. C. Calderas on Mars: Characteristics, structure and associated flank deformation. In Volcano Instability on the Earth and Planets (eds McGuire, W. J., Jones, A. P. & Neuberg, J.) Geol. Soc. Spec. Pub. 110, 307–348 (1996).
12. Wilson, L., Scott, E. D. & Head, J. W. Evidence for episodicity in the magma supply to the large Tharsis volcanoes. J. Geophys. Res. 106, 1423–1433 (2001).
13. Hauber, E. et al. The calderas on Mars—magmatic and tectonic characteristics as revealed through images of the High Resolution Stereo Camera (HRSC) on Mars Express. Eur. Geophys. Union 1st Gen. Assembly (abstr.) EGU04-A-07922 (2004).
14. Nyquist, L. E. et al. Ages and geologic histories of Martian meteorites. Space Sci. Rev. 96, 105–164 (2001).
15. Crumpler, L. S. & Aubele, J. C. Structural evolution of Arsia Mons, Pavonis Mons and Ascraeus Mons: Tharsis region of Mars. Icarus 34, 496–511 (1978).
16. Carr, M. Water on Mars 229 (Oxford Univ. Press, New York, 1996).
17. Lucchitta, B. K. Mars and Earth: Comparison of cold-climate features. Icarus 45, 264–303 (1981).
18. Laskar, J. et al. Long term evolution and chaotic diffusion of the insolation quantities of Mars. Icarus 170, 343–364 (2004).
19. Richardson, M. I. & Wilson, R. J. Investigation of the nature and stability of the Martian seasonal water cycle with a general circulation model. J. Geophys. Res. 107 doi:10.1029/2001JE001536 (2002).
20. Haberle, R. M., Murphy, J. R. & Schaeffer, J. Orbital change experiments with a Mars general circulation model. Icarus 161, 66–89 (2003).
21. Mouginis-Mark, P. J., Wilson, L. & Head, J. W. Explosive volcanism on Hecates Tholus, Mars: Investigation of eruption conditions. J. Geophys. Res. 87, 9890–9904 (1982).
22. Gulick, V. C. & Baker, V. R. Origin and evolution of valleys on Martian volcanoes. J. Geophys. Res. 95, 14325–14344 (1990).
23. Hauber, E. et al. Discovery of a flank caldera and very young and glacial activity at Hecates Tholus, Mars, in Mars Express HRSC images. Nature (submitted).
24. Murray, J. B. Evidence from the Mars Express High Resolution Stereo Camera for a frozen sea close to Mars' equator. Nature (2004) (submitted).
25. Milkovich, S. M. & Head, J. W. Olympus Mons fan-shaped deposit morphology: Evidence for debris glaciers. 6th Int. Mars Conf. (abstr.) 3149 (2003).
26. Head, J. W. et al. Recent ice ages on Mars. Nature 426, 792–802 (2003).
27. Harris, S. A. The aureole of Olympus Mons. J. Geophys. Res. 82, 3099–3107 (1977).
28. Lopes, R., Hiller, K., Neukum, G. & Guest, J. E. Further evidence of the Olympus Mons Aureole. J. Geophys. Res 87, 9917–9928 (1982).
29. Baker, V. R. The Channels of Mars (Austin Univ. of Texas Press, Austin, 1982).
30. McCord, T. et al. The color capabilities of the Mars Express High Resolution Stereo Camera. Eur. Geophys. Union 1st Gen. Assembly (abstr.) EGU04-A-06358 (2004).
31. Bibring, J.-P. et al. OMEGA: Observatoire pour la Minéralogie, l'Eau, les Glaces et l'Activité. 37–49 (European Space Agency Special Publication ESA SP-1240, 2004).
32. Banin, A., Clark, B. C. & Wänke, H. in Mars (eds Kieffer, H. H., Jakosky, B. M., Snyder, C. W. & Matthews, M. S.) 594–625 (Univ. Arizona Press, Tucson, 1992).

33. Head, J. W. et al. Recent mid-latitude glaciation on Mars: Evidence for snow and ice accumulation and flow in Mars Express HRSC data. Nature (in the press).
34. Kossacki, K. J., Kömle, N. I., Leliwa-Kopystyński, J. & Kargel, G. Laboratory investigation of the evolution of cometary analogs: results and interpretation. Icarus 128, 127–144 (1997).
35. Kossacki, K. J., Markiewicz, W. J., Skorov, Y. V. & Kömle, N. I. Sublimation coefficient of water ice under simulated cometary-like conditions. Planet. Space Sci. 47, 1521–1530 (1999).
36. Skorov, Y. V., Markiewicz, W. J., Basilevsky, A. T. & Keller, H. U. Stability of water ice under a porous nonvolatile layer: implications to the south polar layered deposits of Mars. Planet. Space Sci. 49, 59–63 (2001).
37. Picardi, G., et al. MARSIS: Mars Advanced Radar for Subsurface and Ionosphere Sounding. 51–69 (European Space Agency Special Publication ESA SP-1240, 2004).
38. Bibring, J. P. et al. Perennial water ice identified in the south polar cap of Mars. Nature 428, 627–630 (2004).

Supplementary Information accompanies the paper on **www.nature.com/nature**.

Acknowledgements We thank U. Wolf for help with the crater size-frequency distribution measurements and age evaluation, as well as M. Zuschneid and D. Eabel for their technical assistance and T. Denk for support in the colour data reduction effort. We also thank the ESTEC and ESOC staff, and the DLR Experiment and Operations team, especially T. Roatsch, K.-D. Matz, Y. Moreno, J. Flohrer, F. Scholten, and K. Gwinner. J. Kortenieni, M. Aittola, P. Kostama and D. Williams helped with the image planning. This work forms part of the HRSC Experiment of the ESA Mars Express Mission and has been supported by the German Space Agency (DLR) on behalf of the German Federal Ministry of Education and Research (BMBF). Part of the data evaluation is supported by a grant from the German Science Foundation (DFG) within the scope of the priority programme 'Mars and the Terrestrial Planets'.

Competing interests statement The authors declare that they have no competing financial interests.

Correspondence and requests for materials should be addressed to G. N. (gneukum@zedat.fu-berlin.de).

The HRSC Co-Investigator Team (Authors are arranged in alphabetical order) J. Albertz[1], A. T. Basilevsky[2], G. Bellucci[3], J.-P. Bibring[4], M. Buchroithner[5], M. H. Carr[6], E. Dorrer[7], T. C. Duxbury[8], H. Ebner[9], B. H. Foing[10], R. Greeley[11], E. Hauber[12], J. W. Head III[13], C. Heipke[14], H. Hoffmann[12], A. Inada[15,16], W.-H. Ip[16], B. A. Ivanov[17], R. Jaumann[12], H. U. Keller[18], R. Kirk[19], K. Kraus[20], P. Kronberg[21], R. Kuzmin[2], Y. Langevin[4], K. Lumme[22], W. Markiewicz[18], P. Masson[23], H. Mayer[7], T. B. McCord[24], J.-P. Muller[25], J. B. Murray[26], F. M. Neubauer[27], G. Neukum (Principal Investigator)[28], J. Oberst[12], G. G. Ori[29], M. Pätzold[27], P. Pinet[30], R. Pischel[12], F. Poulet[4], J. Raitala[31], G. Schwarz[32], T. Spohn[12] & S. W. Squyres[33]

Affiliations for authors: 1, TU Berlin, D-10623 Germany; 2, Vernadsky Institute-RAS, Moscow 117975, Russia; 3, CNR/IFSI, 00133 Roma, Italy; 4, CNRS/IAS, 91405 Orsay cedex, France; 5, TU Dresden, D-01062 Germany; 6, USGS, MS 975 Menlo Park, California 94025, USA; 7, Universität der Bundeswehr München, D-85577 Neubiberg, Germany; 8, JPL, Pasadena, California 91109, USA; 9, TU München, D-80333 Germany; 10, ESTEC/SCI-SR, Postbus 299, NL-2200 AG Noordwijk, The Netherlands; 11, Arizona State University, Box 871404, Tempe, Arizona 85287-1404, USA; 12, DLR, D-12489 Berlin, Germany; 13, Brown University, Box 1846, Providence, Rhode Island 02912, USA; 14, Universität Hannover, D-30167 Germany; 15, Kobe University, 657-8501 Kobe, Japan; 16, National Central University (NCU), Chung-Li 320, Taiwan; 17, IDG-RAS, Moscow 117979, Russia; 18, MPAE, Postfach 20, D-37191 Katlenburg-Lindau, Germany; 19, USGS, Flagstaff, Arizona 86001, USA; 20, TU Wien, A-1040 Wien, Austria; 21, TU Clausthal, D-38678 Clausthal, Germany; 22, University of Helsinki, PO Box 14, SF-00014 Helsinki, Finland; 23, Orsay-Terre, F-91405 Orsay Cedex, France; 24, PSI-Nw, Winthrop, Washington 98862, USA; 25, University College London WC1E 6BT, UK; 26, The Open University, Milton Keynes MK7 6AA, Buckinghamshire, UK; 27, Universität Köln, D-50923 Germany; 28, FU Berlin, D-12249, Germany; 29, IRSPS, I-65127 Pescara, Italy; 30, Observatoire de Midi-Pyrénées, F-31400 Toulouse, France; 31, University of Oulu, FIN-90401 Finland; 32, DLR, D-82234 Wessling, Germany; 33, Cornell University, Ithaca, New York 14853-1301, USA

articles

Tropical to mid-latitude snow and ice accumulation, flow and glaciation on Mars

J. W. Head[1], G. Neukum[2], R. Jaumann[3], H. Hiesinger[1], E. Hauber[3], M. Carr[4], P. Masson[5], B. Foing[6], H. Hoffmann[3], M. Kreslavsky[1], S. Werner[2], S. Milkovich[1], S. van Gasselt[2] & The HRSC Co-Investigator Team*

[1]*Department of Geological Sciences, Brown University, Providence, Rhode Island 02912, USA*
[2]*Institut fuer Geologische Wissenschaften, Freie Universitaet Berlin, Malteserstrasse 74-100, Bldg D, 12249 Berlin, Germany*
[3]*DLR-Institut fuer Planetenforschung, Rutherfordstrasse 2, 12489, Berlin, Germany*
[4]*US Geological Survey, MS 975, Menlo Park, California 94025, USA*
[5]*Orsay-Terre, F-91405, Orsay Cedex, France*
[6]*ESTEC/SCI-SR, Postbus 299, NL2200AG Noordwijk, The Netherlands*
**A list of all members of The HRSC Co-Investigator Team and their affiliations appears at the end of the paper*

Images from the Mars Express HRSC (High-Resolution Stereo Camera) of debris aprons at the base of massifs in eastern Hellas reveal numerous concentrically ridged lobate and pitted features and related evidence of extremely ice-rich glacier-like viscous flow and sublimation. Together with new evidence for recent ice-rich rock glaciers at the base of the Olympus Mons scarp superposed on larger Late Amazonian debris-covered piedmont glaciers, we interpret these deposits as evidence for geologically recent and recurring glacial activity in tropical and mid-latitude regions of Mars during periods of increased spin-axis obliquity when polar ice was mobilized and redeposited in microenvironments at lower latitudes. The data indicate that abundant residual ice probably remains in these deposits and that these records of geologically recent climate changes are accessible to future automated and human surface exploration.

Among the most sensitive abiotic indicators of climate change are the accumulation, stability and flow of snow and ice. During the Little Ice Age on Earth (late sixteenth to early twentieth centuries), for example, glaciers at high latitude and altitude advanced an average of several kilometres[1] and today many are receding in concert with warming trends[2]. On Mars, shallow subsurface water-ice stability in the current climate is limited to latitudes higher than about 60°, a theoretical prediction[3] borne out by spacecraft observation[4]. At present the spin-axis obliquity of Mars, thought to be among the major factors in climate change, is about 25°, but calculations show that there were several periods of increasingly higher obliquity in the last several millions of years of the history of Mars[5]. General circulation models show that increased obliquity warms ice-rich polar regions and redistributes water-ice deposits equatorward[6–8]. Indeed, geological observations show evidence for a recent ice age in the last several million years in the form of a latitude-dependent dust–ice mantle extending from high latitudes down to about 30° latitude in both hemispheres[9], and evidence for localized tropical mountain glacier deposits that formed during earlier epochs of the Late Amazonian period on Mars tens to hundreds of millions of years ago[10]. Furthermore, there are numerous morphologic features that might involve ice-rich material at low to mid-latitudes throughout the history of Mars (such as landslides, debris aprons, rock glaciers and piedmont glaciers) but the origins, sources, amounts and state of water in these materials has been controversial[11–20].

Here we report on results from the High Resolution Stereo Camera (HRSC)[21] on board Mars Express that show evidence for (1) the presence of significant volumes of ice and glacial-like flow in massif-marginal deposits at low to mid-latitudes (east of Hellas basin), and (2) very young glacier deposits in equatorial regions (Olympus Mons), suggesting recent climate change. Together these deposits are testimony to the importance and scale of equatorward water redistribution during recent climate change, and to the high likelihood of the presence of significant volumes of buried ice currently in low-latitude regions on Mars.

Glacial-like flow in debris aprons

Debris aprons are a class of geomorphic features seen in mid-latitudes of Mars that are hundreds of metres thick, slope gently away from scarps or highland massifs, terminate at lobate margins, and are interpreted to be viscous flow features of material containing some portion of lubricating ice derived from adjacent highlands[11]. New altimetry and high-resolution images have permitted more comprehensive observations and modelling but have not been able to distinguish conclusively among multiple models of apron formation[17] (for example, ice-assisted rock creep, ice-rich landslides, rock glaciers and debris-covered glaciers) because of our inability to determine the proportion of ice in the rock debris (which can range widely, from ice deposited in debris interstices to debris deposited on ice accumulations)[11–17]. Indeed, different aprons may have different modes of formation.

New HRSC data provide wide coverage of high-resolution data with a high signal-to-noise ratio and stereo capability. Analysis of new HRSC data of a massif-marginal lobe in the eastern Hellas region conclusively shows that the proportion of ice in this deposit was substantial enough to signify glacial and debris-covered glacial activity. Specifically, an 18-km-wide lobe extends about 8 km from the base of a 3.75-km-high massif (Fig. 1). The lobe is up to about 250 m thick, has a convex upward topographic profile, and is separated from the base of the massif by an irregular 50–100-m-deep depression (Fig. 1b, c). A broad alcove in the massif (Fig. 1a) adjacent to the lobe could be interpreted as a landslide scar, representing the source region for the lobate deposit. However, we find several inconsistencies with such an interpretation. For example, within the lobe itself (Fig. 1d), a distal 4-km zone is characterized throughout by a fretted and honeycomb-like texture of irregular pits and ridges. Depressions typically 20–40 m deep

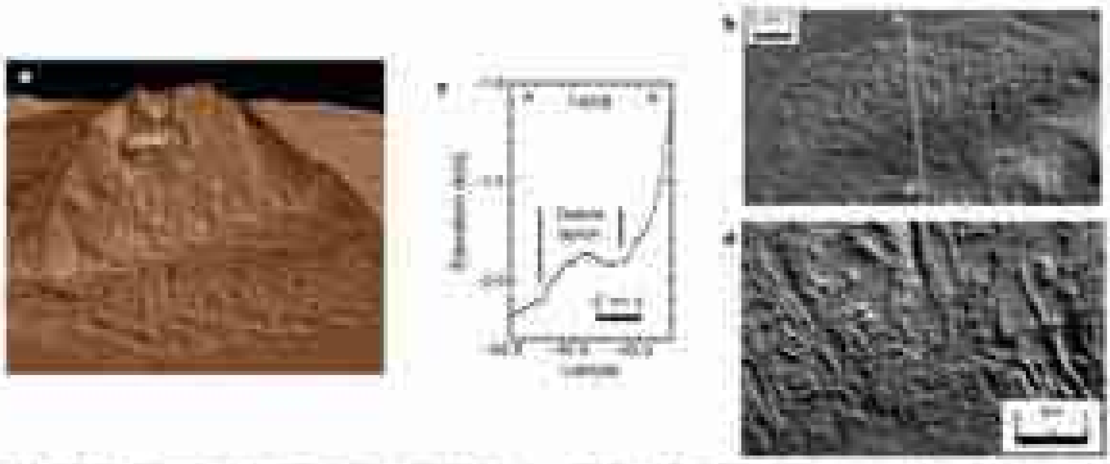

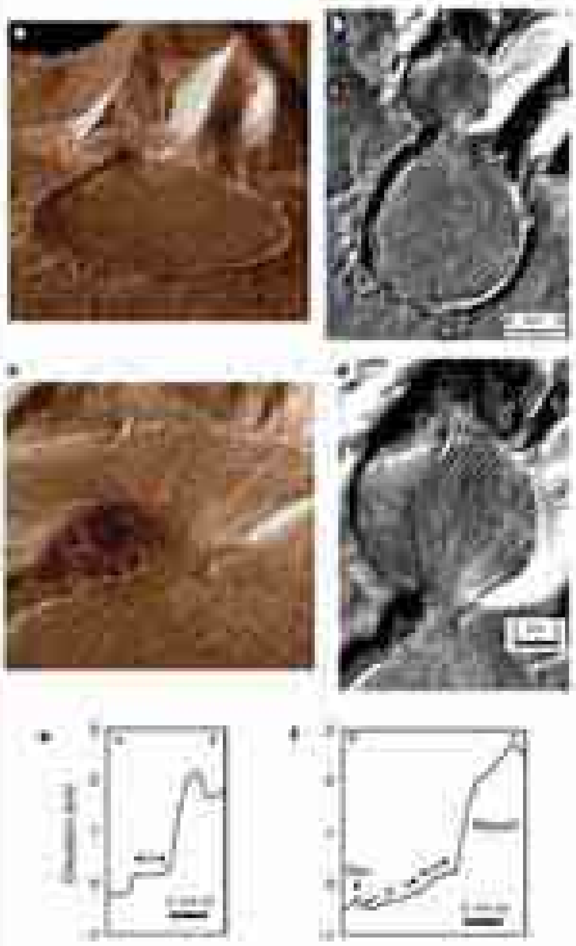

Young rock glaciers at Olympus Mons

Role of glaciation in debris apron origin

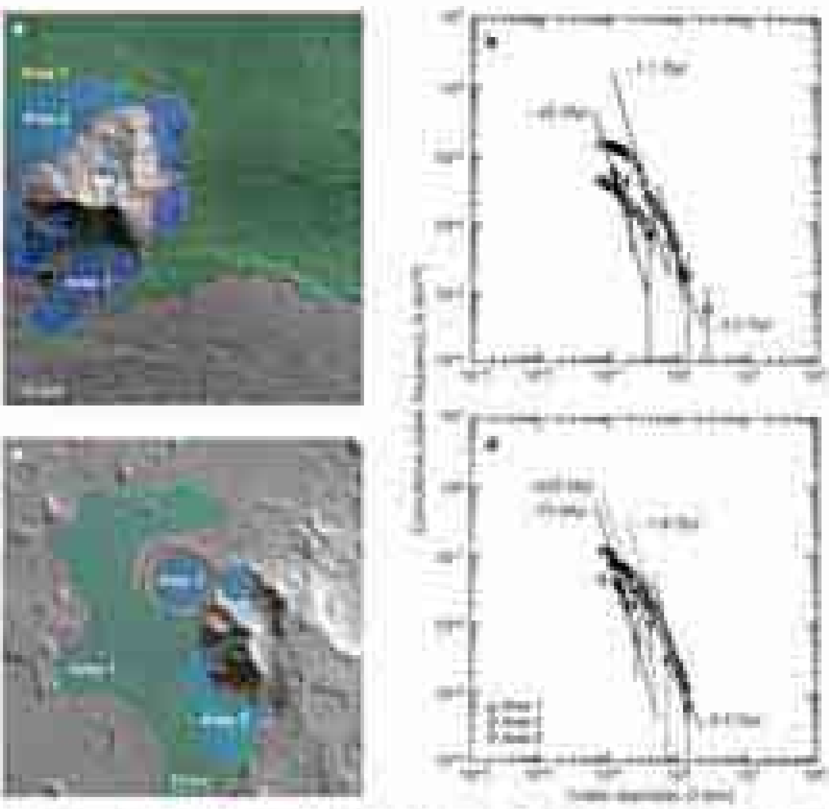

from ice-assisted rock creep, ice-rich landslides, rock glaciers, to debris-covered glaciers)[11–17]. HRSC data provide important new evidence relevant to each of these outstanding questions. First, the HRSC data support a dominant role for ice in the formation of some of these debris aprons and related deposits with evidence from the pitted terrain indicating very high proportions of ice in a debris apron (Fig. 1b, d), and evidence for low-viscosity flow in the hourglass-like feature, indicating high ice–debris ratios (Fig. 2). Second, evidence for the very high abundance of ice in the deposits and hyperarid cold polar-desert-like conditions during formation argues against bottom-up sources such as groundwater, and favours top-down sources, such as atmospheric-related processes of frost, snow or ice accumulation. Third, the proximity of the source regions for these features to steep-sided debris-covered alcoves, and their close analogue to areas on Earth where snow accumulates to form debris-covered, viscously flowing ice deposits (glaciers) (Fig. 3), strongly suggests that many of these features originate as extremely ice-rich, debris-covered glaciers. The geometry of the features discovered along the base of the Olympus Mons scarp, their similar origin in alcoves, their similarities in size and morphology to terrestrial debris-covered ice-rich rock glaciers, and their direct superposition on larger deposits interpreted to be Late Amazonian debris-covered piedmont glaciers[28,29] all strengthen the interpretation of the potential importance of glacial activity in the formation and evolution of debris aprons surrounding massifs on Mars.

Conclusions and implications

The presence of significant volumes of ice and glacial-like flow in massif-marginal deposits at low to mid-latitudes on Mars (east of Hellas basin; −39° to −43° latitude) and in rock glaciers at the base of Olympus Mons (+18°) strongly suggests that conditions in the geological past have favoured the accumulation of snow and ice and its flow in these tropical and mid-latitude regions. Crater size-frequency distribution data collected from the HRSC images (Fig. 4) of the lobate debris aprons east of Hellas (Figs 1, 2) show evidence for multiple eras of ice-related resurfacing, while the Olympus Mons rock glaciers (Fig. 3) are just a few million years old[35]. Thus, these deposits are further testimony to the importance and scale of equatorward water redistribution during climate change[6–8], and its accumulation in specific areas[9,10]. Furthermore, the superposition of the Olympus Mons rock glaciers on older debris-covered piedmont glacier deposits[28–30], dated at 280 to 130 million years (Myr) ago for the major lobes[34], strongly suggests that these conditions fluctuate with time, and that the geologically very young Olympus Mons rock glaciers documented here (Fig. 3a) represent a recent return to these conditions a few million years ago[35] for periods shorter than those that formed the underlying, much more extensive, Late Amazonian deposits. Finally, that none of these features at present seem to be accumulating ice, and thus flowing and advancing, but instead appear to be undergoing sublimation and wasting, strongly suggests that conditions conducive to their formation are not currently in effect. The latter point is consistent with the idea that Mars may now be in an 'interglacial' period due to its relatively low obliquity[5]. Thus, deposits such as those revealed in detail by the HRSC data provide an important geological record of recent climate change that can be used to test and improve both models of recent climate change[6–8] and predictions of the history of orbital parameters[5]. The lower latitudes of these ice-rich deposits also mean that this key climate record is very accessible to automated and human exploration for direct examination and analysis. □

Received 4 October 2004; accepted 13 January 2005; doi:10.1038/nature03359.

1. Grove, J. M. *The Little Ice Age* (Routledge, London, 1988).
2. Warren, C. R. Glaciers in the greenhouse. *Geogr. Rev.* **6**, 1–7 (1995).
3. Mellon, M. T. & Jakosky, B. M. The distribution and behavior of Martian ground ice during past and present epochs. *J. Geophys. Res.* **100**, 11781–11799 (1995).
4. Feldman, W. C. *et al.* Global distribution of neutrons from Mars: Results from Mars Odyssey. *Science* **297**, 75–78 (2002).
5. Laskar, J. *et al.* Long term evolution and chaotic diffusion of the insolation quantities of Mars. *Icarus* **170**, 343–364 (2004).
6. Richardson, M. I. & Wilson, R. J. Investigation of the nature and stability of the Martian seasonal water cycle with a general circulation model. *J. Geophys. Res.* **107**, doi:10.1029/2001JE001536 (2002).
7. Mischna, M. *et al.* On the orbital forcing of Martian water and CO_2 cycles: A general circulation model study with simplified volatile schemes. *J. Geophys. Res.* **108**, doi:10.1029/2003JE002051 (2003).
8. Haberle, R. M. *et al.* Orbital change experiments with a Mars general circulation model. *Icarus* **161**, 66–89 (2003).
9. Head, J. W. *et al.* Recent ice ages on Mars. *Nature* **426**, 797–802 (2003).
10. Head, J. W. & Marchant, D. R. Cold-based mountain glaciers on Mars: Western Arsia Mons. *Geology* **31**, 641–644 (2003).
11. Squyres, S. W. Martian fretted terrain—Flow of erosional debris. *Icarus* **34**, 600–613 (1978).
12. Colaprete, A. & Jakosky, B. M. Ice flow and rock glaciers on Mars. *J. Geophys. Res.* **103**, 5897–5909 (1998).
13. Mangold, N. & Allemand, P. Topographic analysis of features related to ice on Mars. *Geophys. Res. Lett.* **28**, 407–410 (2001).
14. Mangold, N. *et al.* Experimental and theoretical deformation of ice-rock mixtures: Implications on rheology and ice content of Martian permafrost. *Planet. Space Sci.* **50**, 385–401 (2002).
15. Baratoux, D. *et al.* Evidence of liquid water in recent debris avalanche on Mars. *Geophys. Res. Lett.* **29**, doi:10.1029/2001GL014155 (2002).
16. Mangold, N. Geomorphic analysis of lobate debris aprons on Mars at Mars Orbiter Camera scale: Evidence for ice sublimation initiated by fractures. *J. Geophys. Res.* **108**, doi:10.1029/2002JE001885 (2003).
17. Pierce, T. L. & Crown, D. A. Morphologic and topographic analyses of debris aprons in the eastern Hellas region, Mars. *Icarus* **163**, 46–65 (2003).
18. Kargel, J. S. & Strom, R. G. Ancient glaciation on Mars. *Geology* **20**, 3–7 (1992).
19. Baker, V. R. *et al.* Ancient oceans, ice sheets and the hydrological cycle on Mars. *Nature* **352**, 589–594 (1991).
20. Lucchitta, B. K. Mars and Earth—Comparison of cold-climate features. *Icarus* **45**, 264–303 (1981).
21. Neukum, G. *et al.* HRSC: The High Resolution Stereo Camera of Mars Express 17–35 (Report ESA-SP-1240, European Space Agency Publications Division, Noordwijk, The Netherlands, 2004).
22. Benn, D. I. & Evans, D. J. A. *Glaciers and Glaciation* 237–239 (Arnold, London, 1998).
23. Eyles, N. & Rogerson, R. J. A framework for the investigation of medial moraine formation: Austerdalsbreen, Norway, and Berendon Glacier, British Columbia, Canada. *J. Glaciol.* **20**, 99–113 (1978).
24. Boulton, G. S. in *Till: A Symposium* (ed. Goldthwait, R. P.) 41–72 (Ohio State Univ. Press, Columbus, 1971).
25. Skorov, Yu. V. *et al.* Stability of water ice under a porous nonvolatile layer: implications to the south pole layered deposits of Mars. *Planet. Space Sci.* **49**, 59–63 (2001).
26. Marchant, D. *et al.* Formation of patterned ground and sublimation till over Miocene glacier ice in Beacon Valley, southern Victoria Land, Antarctica. *Geol. Soc. Am. Bull.* **114**, 718–730 (2002).
27. Sharp, R. P. Supraglacial and proglacial geology of the Malaspina Glacier, Alaska, and its bearing on glacial features of New England. *Geol. Soc. Am. Bull.* **63**, 1259–1260 (1952).
28. Milkovich, S. M. & Head, J. W. Olympus Mons fan shaped deposit morphology: Evidence for debris glaciers. *6th Int. Mars Conf.* abstr. 3149 (2003).
29. Head, J. W., Shean, D. E., Milkovich, S. M. & Marchant, D. Tropical mountain glaciers on Mars: Evidence for Amazonian climate change. *3rd Mars Polar Conf.* abstr. 8105 (2003).
30. Shean, D. E. *et al.* Tharsis Montes cold-based glaciers: Observations and constraints for modeling and preliminary results. *Lunar Planet. Sci.* **XXXV**, abstr. 1438 (2004).
31. Potter, N. Periglacial geomorphology. *J. Geol. Educ.* **32**, 226–232 (1984).
32. Johnson, P. G. Glacier–rock glacier transition in the southwest Yukon Territory. *Arctic Alpine Res.* **12**, 195–204 (1980).
33. Martin, H. E. & Whalley, W. B. Rock glaciers, part 1. Rock glacier morphology: Classification and distribution. *Prog. Phys. Geogr.* **11**, 260–282 (1987).
34. Morris, E. C. & Tanaka, K. L. *Geologic Maps of the Olympus Mons Region of Mars* (Map I-2327, Misc. Inv. Ser., US Geological Survey, Reston, Virginia, 1994).
35. Neukum, G. *et al.* Recent and episodic volcanic and glacial activity on Mars revealed by the High Resolution Stereo Camera. *Nature* **432**, 971–979 (2004).
36. Hauber, E. *et al.* Discovery of a flank caldera and very young glacial activity at Hecates Tholus, Mars. *Nature* doi:10.1038/nature03423 (this issue).
37. Neukum, G. *et al.* Cratering record in the inner Solar System in relation to the lunar reference system. *Space Sci. Rev.* **96**, 55–86 (2001).
38. Ivanov, B. A. Mars/Moon cratering rate ratio estimates. *Space Sci. Rev.* **96**, 87–104 (2001).
39. Hartmann, W. K. & Neukum, G. Cratering chronology and the evolution of Mars. *Space Sci. Rev.* **96**, 165–194 (2001).

Acknowledgements We thank S. Pratt, A. Cote and J. Dickson for help in data analysis and manuscript preparation, T. Roatsch for data handling, calibration and commanding, F. Scholten and K. Gwinner for photogrammetric processing, and V. Baker for a review. We thank the European Space Agency, DLR (German Aerospace Center), and the Freie Universitaet, Berlin, for their efforts in building and flying the HRSC experiment, and processing the data, and NASA for supporting the participation of J.W.H.

Competing interests statement The authors declare that they have no competing financial interests.

Correspondence and requests for materials should be addressed to J.W.H. (james_head@brown.edu).

The HRSC Co-Investigator Team: J. Albertz[1], A. T. Basilevsky[2], G. Bellucci[3], J.-P. Bibring[4], M. Buchroithner[5], M. H. Carr[6], E. Dorrer[7], T. C. Duxbury[8], H. Ebner[9], B. H. Foing[10], R. Greeley[11], E. Hauber[12], J. W. Head III[13], C. Heipke[14], H. Hoffman[12], A. Inada[15,16], W.-H. Ip[16], B. A. Ivanov[17], R. Jaumann[12], H. U. Keller[18], R. Kirk[19], K. Kraus[20], P. Kronberg[21], R. Kuzmin[2], Y. Langevin[4], K. Lumme[22], W. Markiewicz[18], P. Masson[23], H. Mayer[7], T. B. McCord[24], J.-P. Muller[25], J. B. Murray[26], F. M. Neubauer[27], G. Neukum (Principal Investigator)[28], J. Oberst[12], G. G. Ori[29], M. Pätzold[27], F. Pinet[30], R. Pischel[12], F. Poulet[4], J. Raitala[31], G. Schwarz[32], T. Spohn[12] & S. W. Squyres[33]

Affiliations of authors: 1, TU Berlin, D-10623 Germany; 2, Vernadsky Institute-RAS, Moscow 117975, Russia; 3, CNR/IFSI, 00133 Rome, Italy; 4, CNRS/IAS, 91405 Orsay Cedex, France; 5, TU Dresden, D-01062 Germany; 6, USGS, MS 975 Menlo Park, California 94025, USA; 7, Universität der Bundeswehr München, D-85577 Neubiberg, Germany; 8, JPL, Pasadena, California 91109, USA; 9, TU München, D-80333 Germany; 10, ESTEC/SCI-SR, Postbus 299, NL-2200 AG Noordwijk, The Netherlands; 11, Arizona State University, Box 871404, Tempe, Arizona 85287-1404, USA; 12, DLR, D-12489 Berlin, Germany; 13, Brown University, Box 1846, Providence, Rhode Island 02912, USA; 14, Universität Hannover, D-30167 Germany; 15, Kobe University, 657-8501 Kobe, Japan; 16, National Central University (NCU), Chung-Li 320 Taiwan; 17, IDG-RAS, Moscow 117979, Russia; 18, MPAE, Postfach 20, D-37191 Katlenburg-Lindau, Germany; 19, USGS, Flagstaff, Arizona 86001; 20, TU Wien, A-1040 Wien, Austria; 21, TU Clausthal, D-38678 Clausthal, Germany; 22, University of Helsinki, PO Box 14, SF-00014 Helsinki, Finland; 23, Orsay Terre, F-91405 Orsay Cedex, France; 24, PSI-Nw, Winthrop, Washington 98862, USA; 25, University College London WC1E 6BT, UK; 26, The Open University, Milton Keynes MK7 6AA Buckinghamshire, UK; 27, Universität Köln, D-50923 Germany; 28, FU Berlin, D-12249, Germany; 29, IRSPS, I-65127 Pescara, Italy; 30, Observatoire de Midi-Pyrénées, F-31400 Toulouse, France; 31, University of Oulu, FIN-90401 Finland; 32, DLR, D-82234 Wessling, Germany; 33, Cornell University, Ithaca, New York 14853-1301, USA

Evidence from the Mars Express High Resolution Stereo Camera for a frozen sea close to Mars' equator

John B. Murray[1], Jan-Peter Muller[2], Gerhard Neukum[3], Stephanie C. Werner[3], Stephan van Gasselt[3], Ernst Hauber[4], Wojciech J. Markiewicz[5], James W. Head III[6], Bernard H. Foing[7], David Page[1,8], Karl L. Mitchell[9], Ganna Portyankina[5] & The HRSC Co-Investigator Team*

[1]*Department of Earth Sciences, The Open University, Milton Keynes MK7 6AA, UK*
[2]*Department of Geomatic Engineering, University College London, Gower Street, London WC1E 6BT, UK*
[3]*Geosciences Institute, Freie Universität Berlin, Malteserstrasse 74-100, Building D, 12249 Berlin, Germany*
[4]*DLR-Institut für Planetenforschung, Rutherfordstrasse 2, D-12489 Berlin-Adlershof, Germany*
[5]*Max Planck Institut für Aeronomy, Max-Planck-Strasse 2, 37191 Katlenburg-Lindau, Germany*
[6]*Department of Geological Sciences, Brown University, Box 1846, Providence, Rhode Island 02912, USA*
[7]*ESA Research and Scientific Support Department, ESTEC/SCI-SR postbus 299, 2200 AG Noordwijk, The Netherlands*
[8]*Department of Mineralogy, The Natural History Museum, London SW7 5PB, UK*
[9]*Environmental Science Department, Lancaster University, Bailrigg, Lancaster LA1 4YQ, UK*
**A list of all members of The HRSC Co-Investigator Team and their affiliations appears at the end of the paper*

It is thought that the Cerberus Fossae fissures on Mars were the source of both lava and water floods[1,2–4] two to ten million years ago[1,2,5]. Evidence for the resulting lava plains has been identified in eastern Elysium[1,2,5,6–8], but seas and lakes from these fissures and previous water flooding events were presumed to have evaporated and sublimed away[9–11]. Here we present High Resolution Stereo Camera images from the European Space Agency Mars Express spacecraft that indicate that such lakes may still exist. We infer that the evidence is consistent with a frozen body of water, with surface pack-ice, around 5° north latitude and 150° east longitude in southern Elysium. The frozen lake measures about 800 × 900 km in lateral extent and may be up to 45 metres deep—similar in size and depth to the North Sea. From crater counts, we determined its age to be 5 ± 2 million years old. If our interpretation is confirmed, this is a place that might preserve evidence of primitive life, if it has ever developed on Mars.

Extensive fields of large fractured plate-like features on a horizontal surface are visible near the south end of the High Resolution Stereo Camera (HRSC) imaging strip taken on 19 January 2004 (Fig. 1). This area has previously been covered by NASA high-resolution Mars Orbiter Camera (MOC) imagery at pixel sizes down to 1.5 m (Fig. 2). The latter images show fractured plates at a smaller scale. Individual plates are of all sizes from 30 m up to >30 km, with clear signs of break-up, rotation (Fig. 1c) and horizontal drift for distances of several kilometres. The plates show characteristic differences from plate-like features elsewhere on Mars and in the east of Elysium Planitia. The latter features have been interpreted to be rafts of solidified lava floating on the surface of large flood basalts[6], but several observations indicate that this cannot be the case in this area.

Surface ages were determined[12,13] from the size-frequency distribution of 66 impact craters on HRSC images, which suggest a resurfacing event about 5 million years (Myr) ago. Counts of 268 craters on MOC images show that the plates are older than the brighter inter-plate areas (Fig. 3). The statistical errors of the two data sets (counts on plates and inter-plate areas) indicate that they are almost coincident in age, but the whole inter-plate size-frequency distribution falls consistently below that for the plates. This is an indication that the inter-plate areas are really younger than the plates, but within the error limits the age difference could be from a few hundred thousand years up to 2 Myr, with a most likely value of 1 Myr. This age difference is independent of any systematic error in the cratering chronology model used[12,13]. Basalt lava flows 50 m deep can remain partially molten at the centre for only about 5 yr (ref. 14), so these plates cannot be the result of surges and break-outs of lava carrying previously solidified crust, as occurred over timescales of a week or so during the 1783–84 Laki Fissure eruption, Iceland, which is the closest terrestrial analogue to martian flood lavas[6].

Lava break-outs entail build-up and failure of inflating lava to create the plate-like morphology[6], but there are no signs of the inflation that occurs on terrestrial basalts and in other areas of Mars. The Mars Orbiting Laser Altimeter (MOLA) topographic profiles across the area show a remarkably flat surface with broad topography varying by <5 m over more than 60 km, that is, a slope of <0.005°. This compares to a slope of about 0.2° for terrestrial flood basalts.

Furthermore, a drop in surface level occurred after flooding of 18 to 85 m (equivalent to about 9% to 16% of the depth before flooding) within flooded impact craters (Fig. 4). If this had been lava, such a drop would be impossible in these ponded enclosures, because thermal contraction of ponded lava would amount to less than 1% (ref. 15).

Other features in the HRSC image show unique features that provide a clue to their origin. Where the plates have drifted into obstacles, straight or curved lanes have formed downstream within the plates themselves ('L' and 'I' in Fig. 1c). These are not found within lava rafts. Also, the plates are one to two orders of magnitude larger than the largest-known terrestrial basalt rafts. Both these observations, together with the horizontal surface (<0.005°, corresponding to terrestrial tidal sea surface slopes in some estuarine situations) imply an extremely mobile fluid, with characteristics similar to those of water.

Other observations indicate the strong resemblance of these plates to pack-ice. Where pre-existing small topographic highs protrude through the plates to form islands, plate drift has caused rubble piles with pressure ridges on the upstream side (Figs 1c and 2a). Where the highs are craters, these ridges show a superficial resemblance to fluidized ejecta, but unlike the latter, the ridges are subconcentric to the rim and form on one side of the crater only (always the upstream side), show no lobate overlaps or signs of radial movement, have up to 20 subparallel ridges instead of one to three, and show no broad smoother areas proximal to the crater that indicate ejecta flow. Figure 2a shows pressure ridges (denoted 'R') within the rubble pile on the right with wavelengths between 10 and 70 m, which appear to have extended outward from the crater edge as the liquid level dropped and the frozen surface was grounded progressively further down the outer slopes of the crater. These are strikingly similar to rubble piles of sea ice that form around islands in the Arctic and Antarctic (Fig. 2b). The sagging and consequent surface cracking 'C' within the crater itself as the level dropped are also visible. One plate 'F' has drifted into the crater when the level was higher through the gap in the rim 'G', but then become grounded in its present position as the surface lowered, draping it over the northeast rim.

These craters and islands have acted in a similar manner to ice-breakers as the plates drifted past them, leaving straight or curved leads downstream with uniform width (Fig. 1c). The high-resolution MOC image in Fig. 2a shows that these lanes are still very smooth at the 10-m scale, as are similar features in pack-ice on Earth. In places the plates have moved in channels between zones of more stable ice, and overall the direction of drift is towards the west or southwest.

Combinations of processes are unlikely, and have no terrestrial counterparts. Lava plates rafted on mud are not possible because basalt has a density >70% greater than mud. Lava on ice would create pseudocraters, melting and consequent sagging of the raft centres, none of which is observed in this area, and mud rafts floating on mudflows would sink, solid mud having a density 10% greater than fluid mud.

On the basis of this analysis, we interpret the structures and textures to be due to pack-ice formed as a moving and fracturing thermal boundary layer on top of ponded aqueous floodwater that later froze. An early drop in water level occurred while the ice was still drifting (Fig. 2a), mainly owing to evaporation/sublimation, or perhaps seepage of liquid water into the substratum.

Reasonable estimates of the depth can be made by using the rim height to diameter ratios of submerged impact craters. Mean values for simple martian craters are given by: $H = 0.04D^{0.31}$, where H is exterior rim height and D is crater diameter[14]. The impact crater 'I' (Fig. 1c) is 1.1 km in diameter and has only the highest part of the rim exposed, suggesting an initial water depth of about 42 m at that point. Fourteen other crater rims have been identified from their traces partially above or just below the ice as the surface has lowered, yielding initial water depths of between 31 and 53 m, with an average at 45 m. The true depth may be less than these values, as some suspended sediment transported in the early stages would have settled out before freezing. The MOLA profiles across three flooded craters indicate that low parts of the rim are still 0 to 30 m above the mean ice level, suggesting that the evaporation, sublimation and seepage sagging referred to above may have lowered the ice thickness to a present mean depth of around 30 m.

The area lies at the foot of the Athabasca Valles system, where sinuous ridges within the complex of valleys have been likened to those of pack-ice, and plate-like structures there have been proposed to be casts of sediment-rich ice deposited by an ice-rich debris flow, the ice having later sublimed away[17]. Fluvial bedforms also indicate that the Athabasca Valles contained water channels, perhaps fed by a large over-pressured subsurface aquifer[18] giving rise to high

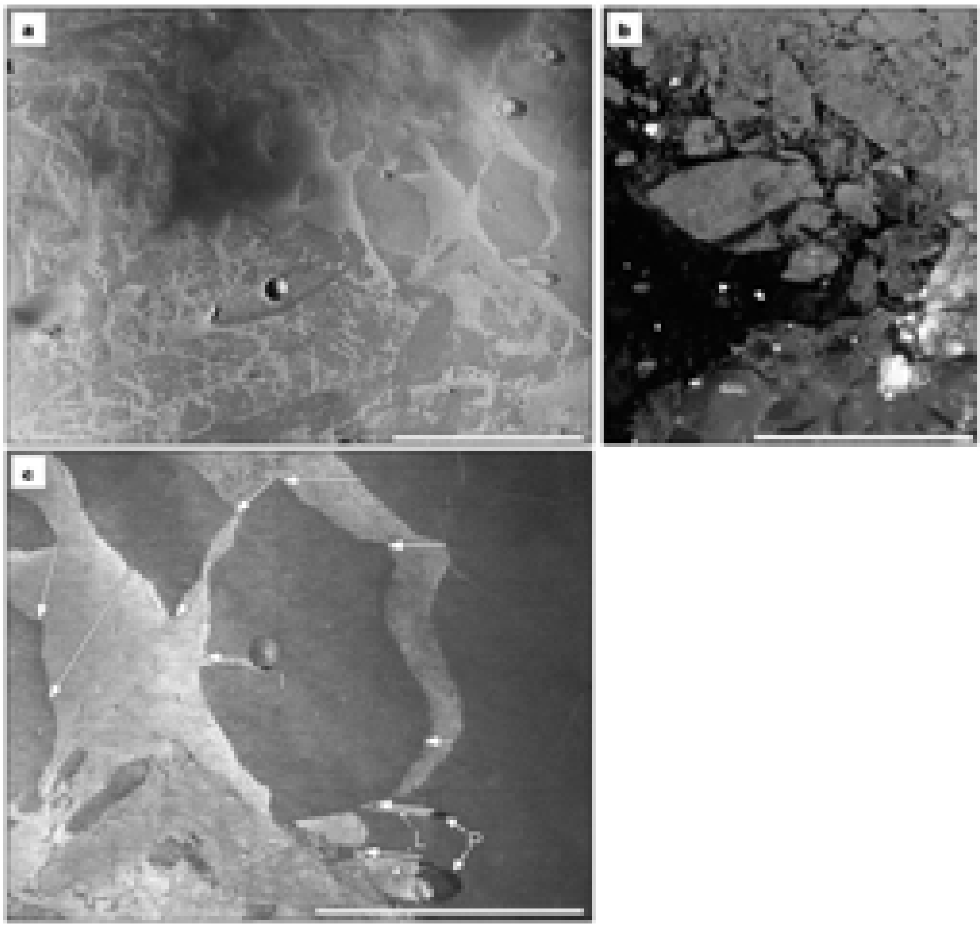

Figure 1 Views of plate-like terrain on Mars, and pack-ice on Earth. **a**, Part of an HRSC image of Mars from orbit 32, with a resolution of 13.7 m per pixel, centred at 5.5° north latitude and 150.4° east longitude, showing plate-like deposits with signs of break-up, rotation and lateral movement to the west-southwest in the lower part of the image. Scale bar is 25 km. **b**, Synthetic Aperture Radar image of pack-ice in the Weddell Sea, Antarctica. Scale bar is 25 km. (ESA image, processed by H. Rott.) **c**, Enlarged view of raft 7 × 12 km showing 8° rotation anticlockwise, causing the clear lane downstream of island 'I' to be curved. Leads 'L' downstream of the crater and small island at lower right are almost straight, indicating unidirectional drift slightly north of westward. Note pressure ridges 'P' upstream of islands. Arrows show relative motion vectors of individual plates. Scale bar is 10 km.

discharge rates[7] of the order of $10^{8}\,m^{3}\,s^{-1}$, causing a flood rich in suspended sediment of all sizes.

Water evaporation would be rapid under present Mars conditions[18], but early work[9] indicated that freezing rates at the surface of martian lakes would be of the order of 10^{-5} to $10^{-4}\,cm\,s^{-1}$, and that surface ice will grow to a thickness of 5–10 m after 1 yr. Freezing will continue until a depth of 30 m is frozen solid in 5–10 yr. Recent work emphasizes that the water should have high concentrations of dissolved salts[20,21], and if it originates from magmatic intrusion, could be several degrees to tens of degrees above freezing on emergence[2]. These factors could produce longer timescales for complete freezing to occur[20], and rapid surface heat loss could cause intense convection that would prevent surface ice formation in the early stages, but allow slush to form.

Ice is unstable at the surface of Mars at present owing to sublimation in the 6-mbar atmosphere, but it is thought that huge volumes of volcanic ash also erupted from Cerberus Fossae[4], which—if contemporaneous with water emission—would have formed a substantial protective layer[22] on the ice. Depending on the porosity and thermal properties of this layer, the subsequent lowering of the floe surfaces could be very slow[23]. Subliming water vapour migrating through the pores will help over time to sinter and chemically bind the particles to form a stronger sublimation lag. To account for the 1-Myr age difference between the plates (pack-ice floes) and the younger lanes in between, we suggest the following sequence of events: first, pack-ice formation with a volcanic ash covering, second, remobilization, break-up and drift of pack-ice, with cessation of volcanic activity, third, freezing of the entire body of water, and finally, the sublimation of the unprotected ice between the ash-covered ice-floes, gradually exposing the suspended sediment at the surface to form a protective layer[22] with a younger age than the floes. Alternatively, the latest Athabasca volcanic activity may be as young as 3 Myr[2], which may have scattered ash that prevented further sublimation of inter-floe areas at this later time. This interpretation is supported by the MOLA profiles, which show them to be up to 3 m lower than the floes.

We do not know whether the frozen body of water is still there, or whether the visible floes are preserved in a sublimation residue draped over the substrate. Two observations suggest that it is still there:

(1) MOLA profiles show that three submerged or partially submerged craters 1.8 to 4.8 km in diameter have depths 2% to 3% of their diameter (Fig. 4), whereas the mean depth of a martian crater of this size range is about 20% of its diameter[24], suggesting that most of the ice is still within the crater, though up to 15% by volume of the crater filling may be suspended sediment. Other submerged craters appear to have similar depths. This point depends on the craters being fresh rather than degraded before

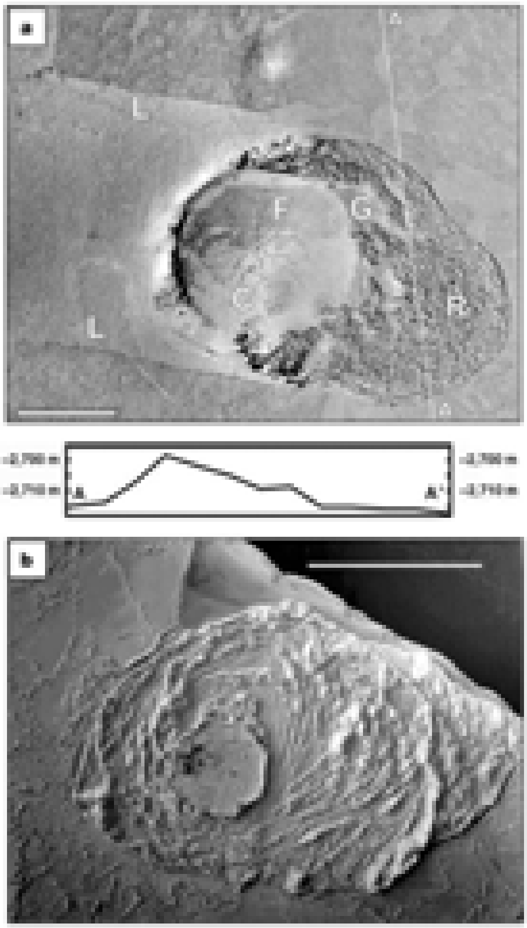

Figure 2 Pressure ridges on Mars, and those caused on Earth by pack-ice drift against obstacles. **a**, High-resolution MOC images E2100112 and R0900475 of an impact crater seen in Fig. 1a. The sides 'L' of the downstream lane are smooth at the 10-m scale, and parallel. The line on the right indicates the MOLA track 19980 crossing the pressure ridges, which are up to 16 m above the surrounding level. The MOLA topographic profile (values in metres) is shown below the image (×60 vertical exaggeration). Scale bar is 1 km. **b**, Air photo of Tarsiut Island, an artificial island in the Beaufort Sea, surrounded by first-year sea ice 1 to 1.5 m thick in the winter of 1983. We note 5-m-high concentric pressure ridging with wavelengths of 2 to 30 m caused by pack-ice rubble becoming grounded on the sloping flanks of the island during winds from different directions. Scale bar is 100 m. (Gulf Canada Resources photo courtesy of T.J.O. Sanderson.) 'C', surface cracking; 'F', a plate that has drifted through a gap 'G' in the rim; 'R', pressure ridges.

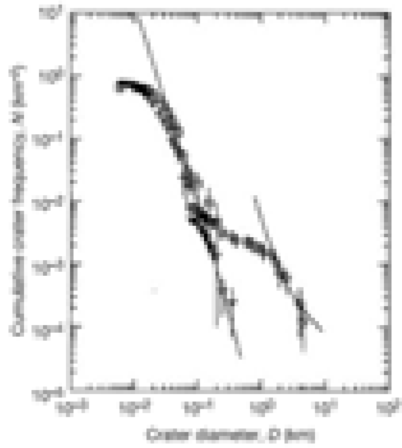

Figure 3 Age dating by crater counting[25–27] on the pack-ice surface using HRSC (triangles) and MOC imagery over a total area of 380 km² (squares and diamonds), including those craters that protrude through the surface from the substratum (circles). Whereas the HRSC data indicate a single re-surfacing event about 5 ± 2 million years ago, counts on MOC images show consistently lower numbers for the brighter inter-plate terrain (diamonds) than the darker plate-like terrain (squares) interpreted as ice floes. The lower frequency occurs at all sizes systematically, indicating an age difference of about 1 Myr. The derived age of the substrate before flooding is 3.66 ± 0.05 billion years.

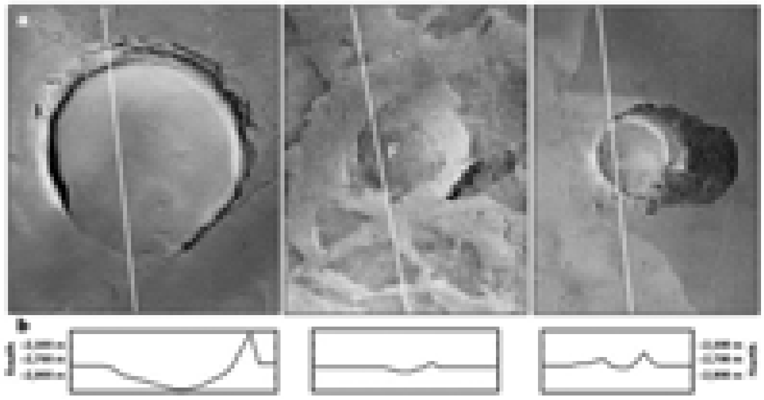

Figure 4 Evidence of ice surface lowering and draping of plate-like features over partly submerged impact craters. MOLA tracks (**a**) and MOLA topographic profiles with 10 × vertical exaggeration (**b**) across three flooded or partially flooded craters 4.8, 2.3 and 1.8 km in diameter from left to right. Values are in metres. Note that the floor sags at least 85, 18 and 25 m respectively, suggesting that 80% to 90% of the proposed ice fill is still within the crater. Note also the raft 'F' draped over the rim and floor of the centre crater. See text for further details.

flooding, but in this area most of the unflooded craters of similar size appear to be fresh with bowl-shaped interiors.

(2) MOLA profiles show a virtually horizontal surface, whereas the ice depth estimates above indicate that the substrate varies in altitude by 55 m. If the ice had been lost, sediment draped over this should have resulted in considerable surface height variation.

Recent work[24,25] has shown that Mars' obliquity, with oscillations of 5° to 10° amplitude and periods of 10^5 yr, was 37° ± 7° between 5 and 10 Myr ago. Global climate model simulations indicate that this would produce a substantially different climate from that of today, with higher dust transport and an atmosphere of higher temperature and pressure[26]. The extremely young age of 5 Myr for the flood suggests that catastrophic flood events from a proposed sub-cryospheric aquifer[20,21] are continuing to happen, as they have done throughout the known history of Mars' surface. The continuous presence of warm water beneath the cryosphere over several billion years might provide more opportunities for life to develop than was once thought. Microorganisms found within deep-sea hydrothermal vent communities[27] are common ancestors to many forms of life on Earth, and the possibility of life developing at similar places elsewhere in the Solar System has been postulated[28]. □

Received 3 September 2004; accepted 18 January 2005; doi:10.1038/nature03379.

1. Berman, D. C. & Hartmann, W. K. Recent fluvial, volcanic and tectonic activity on the Cerberus Plains of Mars. Icarus 159, 1–17 (2002).
2. Burr, D. M., Grier, J. A., McEwen, A. S. & Keszthelyi, L. P. Repeated aqueous flooding from the Cerberus Fossae: Evidence for very recently extant, deep groundwater on Mars. Icarus 159, 53–73 (2002).
3. Head, J. W. III, Wilson, L. & Mitchell, K. L. Generation of recent massive water floods at Cerberus Fossae, Mars by dike emplacement, cryospheric cracking, and confined aquifer groundwater release. Geophys. Res. Lett. 30, 1577, doi:10.1029/2003GL017135 (2003).
4. Plescia, J. B. Cerberus Fossae, Elysium, Mars: a source for lava and water. Icarus 164, 79–95 (2003).
5. Werner, S. C., van Gasselt, S. & Neukum, G. Continual geological activity in Athabasca Valles, Mars. J. Geophys. Res. 108, 8081, doi:10.1029/2002JE002020 (2003).
6. Keszthelyi, L., McEwen, A. S. & Thordarson, T. Terrestrial analogs and thermal models for Martian flood lavas. J. Geophys. Res. 105, 15027–15049 (2000).
7. Fuller, E. R. & Head, J. W. III Amazonis Planitia: the role of geologically recent volcanism and sedimentation in the formation of the smoothest plains on Mars. J. Geophys. Res. 107, 5081, doi:10.1029/2002JE001842 (2002).
8. Lanagan, P. D. & McEwen, A. S. Cerberus Plains volcanism: constraints on temporal emplacement of the youngest flood lavas on Mars. 6th Int. Conf. on Mars abstr. 3215 (2003) (http://www.lpi.usra.edu/meetings/sixthmars2003/pdf/3215.pdf).
9. Carr, M. H. Stability of Martian streams and lakes. Icarus 56, 476–495 (1983).
10. Kreslavsky, M. A. & Head, J. W. III Fate of outflow channel effluents in the northern lowlands of Mars: the Vastitas Borealis Formation as a sublimation residue from frozen ponded bodies of water. J. Geophys. Res. 107, 5121, doi:10.1029/2001JE001831 (2002).
11. Carr, M. H. & Head, J. W. III Oceans on Mars: an assessment of the observational evidence and possible fate. J. Geophys. Res. 108, 5042, doi:10.1029/2002JE001963 (2003).
12. Hartmann, W. K. & Neukum, G. Cratering chronology and the evolution of Mars. Space Sci. Rev. 96, 165–194 (2001).
13. Neukum, G. et al. Recent and episodic volcanic and glacial activity on Mars revealed by the High Resolution Stereo Camera. Nature 432, 971–979 (2004).
14. Patrick, M. R., Dehn, J. & Dean, K. Numerical modelling of lava flow cooling applied to the 1997 Okmok eruption: approach and analysis. J. Geophys. Res. 109, B03202, doi:10.1029/2003JB002537 (2004).
15. Skinner, B. J. Thermal expansion. In Handbook Of Physical Constants (ed. Clark, S. P.) Geol. Soc. Am. Mem. 97, 75–96 (1966).
16. Garvin, J. B., Sakimoto, S. E. H. & Frawley, J. J. Craters on Mars: global geometric properties from gridded MOLA topography. Sixth Int. Conf. on Mars abstr. 3277 (2003) (http://www.lpi.usra.edu/meetings/sixthmars2003/pdf/3277.pdf).
17. Rice, J. W., Parker, T. J., Russel, A. J. & Knudsen, O. Morphology of fresh outflow channel deposits on Mars. Lunar Planet. Sci. XXXIII abstr. 2026 (CD-Rom) (Lunar & Planetary Institute, Houston, Texas, 2002).
18. Baker, V. R. et al. in Mars (eds Kieffer, H. H., Jakosky, B. M., Snyder, C. W. & Matthews, M. S.) 493–522 (Univ. Arizona Press, Tucson, 1992).
19. Wallace, D. & Sagan, C. Evaporation of ice in planetary atmospheres: ice-covered rivers on Mars. Icarus 39, 476–495 (1983).
20. Clifford, S. M. A model for the hydrologic and climatic behavior of water on Mars. J. Geophys. Res. 98, 10973–11016 (1993).
21. Clifford, S. M. & Parker, T. J. The evolution of the Martian hydrosphere: implications for the fate of a primordial ocean and the current state of the northern plains. Icarus 154, 40–79 (2001).
22. Carr, M. H. [illegible] on Mars: effects of floods, volcanism, impacts and polar processes. Icarus 87, 210–227 (1990).
23. Skorov, Y. V., Markiewicz, W. J., Basilevsky, A. T. & Keller, H. U. Stability of water ice under a porous nonvolatile layer: implications for the south polar layered deposits of Mars. Planet. Space Sci. 49, 59–63 (2001).
24. Laskar, J. & Robutel, P. The chaotic obliquity of the planets. Nature 361, 608–612 (1993).
25. Laskar, J., Gastineau, M., Joutel, F., Levrard, B. & Robutel, P. A new astronomical solution for the long term evolution of the insolation quantities of Mars. Lunar Planet. Sci. XXXV abstr. 1600 (2004).
26. Haberle, R. M., Murphy, J. R. & Schaeffer, J. Orbital change experiments with a Mars general circulation model. Icarus 161, 66–89 (2003).
27. Humphris, S. E., Zierenberg, R. A., Mullineaux, L. S. & Thomson, R. E. (eds) Seafloor Hydrothermal Systems 1–466 (AGU Geophys. Monogr. 91, American Geophysical Union, Washington, DC, 1995).
28. Greenberg, R., Geissler, P., Tufts, B. R. & Hoppa, G. V. Habitability of Europa's crust: The role of tidal-tectonic processes. J. Geophys. Res. 105, 17551–17562 (2000).

Supplementary Information accompanies the paper on **www.nature.com/nature**.

Acknowledgements We thank M. Wählisch for assistance in the MOLA processing and S. Clifford and N. A. Cabrol for criticism that greatly improved the paper.

Competing interests statement The authors declare that they have no competing financial interests.

Correspondence and requests for materials should be addressed to J.B.M. (J.B.Murray@open.ac.uk).

The HRSC Co-Investigator Team: J. Albertz[1], A. T. Basilevsky[2], G. Bellucci[3], J.-P. Bibring[4], M. Buchroithner[5], M. H. Carr[6], E. Dorrer[7], T. C. Duxbury[8], H. Ebner[9], B. H. Foing[10], R. Greeley[11], E. Hauber[12], J. W. Head III[13], C. Heipke[14], H. Hoffmann[12], A. Inada[15], W.-H. Ip[16], B. A. Ivanov[17], R. Jaumann[12], H. U. Keller[18], R. Kirk[19], K. Kraus[20], P. Kronberg[21], R. Kuzmin[2], Y. Langevin[4], K. Lumme[22], W. Markiewicz[18], P. Masson[23], H. Mayer[7], T. B. McCord[24], J.-P. Muller[25], J. B. Murray[26], F. M. Neubauer[27], G. Neukum (PI)[28], J. Oberst[12], G. G. Ori[29], M. Pätzold[27], P. Pinet[30], R. Pischel[12], F. Poulet[4], J. Raitala[31], G. Schwarz[32], T. Spohn[12] & S. W. Squyres[33]

Affiliations of authors: 1, TU Berlin, D-10623 Germany; 2, Vernadsky Institute RAS, Moscow 117975, Russia; 3, IFSI/CNR, Rome, Italy; 4, IAS, Orsay Campus 91405, France; 5, TU Dresden D-01062, Germany; 6, USGS, MS 975 Menlo Park, California 94025, USA; 7, Universität der Bundeswehr München D-85577, Germany; 8, JPL, Pasadena, California 91109, USA; 9, TU München, D-80333 Germany; 10, ESTEC/SCI-SR, Postbus 299, NL-2200 AG Noordwijk, The Netherlands; 11, Arizona State University, Box 871404, Tempe, Arizona 85287-1404, USA; 12, DLR, D-12489 Berlin, Germany; 13, Brown University, Box 1846, Providence, Rhode Island 02912, USA; 14, Universität Hannover, D-30167 Germany; 15, Kobe University, Kobe, Japan; 16, National Central University (NCU) Taiwan; 17, IDG-RAS, Moscow 117979, Russia; 18, MPAE, Postfach 20, D-37191 Katlenburg-Lindau, Germany; 19, USGS, Flagstaff, Arizona 86001, USA; 20, TU Wien, A-1040 Wien, Austria; 21, TU Clausthal, D-38678 Germany; 22, University of Helsinki, PO Box 14, SF-00014 Helsinki, Finland; 23, OrsayTerre, F-91405 Orsay Campus, France; 24, PSI-Nw, Winthrop, Washington 98862, USA; 25, University College London, WC1E 6BT, UK; 26, The Open University, Milton Keynes MK7 6AA, UK; 27, Universität Köln, D-50923 Germany; 28, FU Berlin, D-12249 Germany; 29, IRSPS, I-65127 Pescara, Italy; 30, Observatoire de Midi-Pyrénées, F-31400 Toulouse, France; 31, University of Oulu, Fin-90401 Finland; 32, DLR, D-82234 Wessling, Germany; 33, Cornell University, Ithaca, New York 14853-1301, USA

Discovery of a flank caldera and very young glacial activity at Hecates Tholus, Mars

Ernst Hauber[1], Stephan van Gasselt[2], Boris Ivanov[3], Stephanie Werner[2], James W. Head[4], Gerhard Neukum[2], Ralf Jaumann[1], Ronald Greeley[5], Karl L. Mitchell[6], Peter Muller[7] & The HRSC Co-Investigator Team*

[1]*Institute of Planetary Research, German Aerospace Center (DLR), 12489 Berlin, Germany*
[2]*Institute of Geosciences, FU Berlin, 12249 Berlin, Germany*
[3]*Institute for Dynamics of Geospheres, Russian Academy of Sciences, Moscow, 117334, Russia*
[4]*Department of Geological Sciences, Brown University, Providence, Rhode Island 02912, USA*
[5]*Department of Geological Sciences, Arizona State University, Tempe, Arizona 85287-1404, USA*
[6]*Environmental Science Department, Lancaster University, Lancaster LA1 4YQ, UK*
[7]*Department of Geomatic Engineering, University College London, Gower Street, London WC1E 6BT, UK*
**A list of all members of The HRSC Co-Investigator Team and their affiliations appears at the end of the paper*

The majority of volcanic products on Mars are thought to be mafic and effusive[1,2]. Explosive eruptions of basic to ultrabasic chemistry are expected to be common[3,4], but evidence for them is rare and mostly confined to very old surface features[5]. Here we present new image and topographic data from the High Resolution Stereo Camera that reveal previously unknown traces of an explosive eruption at 30° N and 149° E on the northwestern flank of the shield volcano Hecates Tholus. The eruption created a large, 10-km-diameter caldera ~350 million years ago. We interpret these observations to mean that large-scale explosive volcanism on Mars was not confined to the planet's early evolution. We also show that glacial deposits partly fill the caldera and an adjacent depression. Their age, derived from crater counts, is about 5 to 24 million years. Climate models predict that near-surface ice is not stable at mid-latitudes today[6], assuming a thermo-dynamic steady state. Therefore, the discovery of very young glacial features at Hecates Tholus suggests recent climate changes. We show that the absolute ages of these very recent glacial deposits correspond very well to a period of increased obliquity of the planet's rotational axis[7].

The ESA Mars Express mission, an orbiter carrying seven experiments, was inserted into Mars orbit on 25 December 2003. On 19 January 2004, the multiple line scanner instrument, the High Resolution Stereo Camera (HRSC)[8], imaged the volcano Hecates Tholus in the Elysium region. Our study focuses on two overlapping depressions at the northwestern base of Hecates Tholus (Fig. 1) that were mentioned before[9], but without an explanation for their origin. The HRSC image resolution of that area (~20 m per pixel) is better than that of previous images from the Viking Orbiter camera (~40 m per pixel) and from the THEMIS thermal infrared imager (~100 m per pixel). Several very high-resolution images from the Mars Orbiter Camera (MOC) cover small parts of the depressions with 3 to 4 m per pixel. We use digital photogrammetric techniques[10] to derive stereo information with a mean relative point accuracy of ~30 m from the HRSC's multiple line sensors, which observe the surface under different viewing angles.

The smaller of the two depressions (here referred to as 'depression A') has an area of ~12 km × 10 km (Fig. 2a) and a depth between 1,000 and 1,300 m. The northwestern part of its rim is missing where it overlaps with the larger depression (here named 'depression B'). The remaining rim has an elevation between 800 and 1,800 m. The floor is terraced, with an elevation difference of 200–300 m between the two levels. Owing to the incomplete rim, it is difficult to determine its volume. Our best estimate, based on a reconstructed rim, is ~80 km³. On the flanks of the volcano, an unusual hilly and knobby deposit can be distinguished adjacent to depression A. Its surface is rougher than the rest of the flank's surface, and it extends outward from the rim to a maximum distance of about 15 km.

We favour a volcanic over an impact origin of depression A for four reasons. First, the morphology of the depression, including the two different levels of its floor, is remarkably similar to part of the caldera complex at the shield volcano Ascraeus Mons in the Tharsis region (Fig. 2b), and also to the summit caldera of Hecates Tholus itself (Fig. 2c); impact craters on Hecates Tholus have a distinctly different appearance (Fig. 2d). Second, the stereo information indicates that the walls slope at an average angle of about ~30°, which is steeper than the walls of most martian impact craters[11]. Third, there is no elevated crater rim, which would be expected if depression A were an impact crater. Fourth, the remaining parts of the rim are distinctly not circular, owing to a promontory at the topographically highest part of the rim.

Hence, the cumulative evidence of these independent observations suggests that depression A is volcanic rather than impact-related. There is no evidence for effusive eruptions, for example, lava flows, near depression A. Instead, we interpret the rough material near depression A as the proximal part of pyroclastic materials from an explosive eruption. Relative to the other parts of the flanks, an area between depression A and the summit caldera displays a lack of impact craters and a generally smooth surface texture at the scale of the Viking and HRSC image resolution. It has been interpreted to be a mantling deposit from an explosive eruption at the summit[9]. However, it may as easily have been produced by an explosion at depression A. Indeed, the isolines of the crater density on the western flank of Hecates Tholus (figure 7 in ref. 9) are roughly concentric around depression A and would be in better agreement with an explosion there than with one at the summit. We interpret the smooth material as the distal part of the erupted pyroclastic material. The presence of many fluvial channels[1,11] may indicate phreatomagmatic (containing magmatic gases and steam) interactions, which could have enhanced the explosivity of the eruption. Crater counts on HRSC and MOC images on both the proximal and distal pyroclastic material, using a new model of cratering

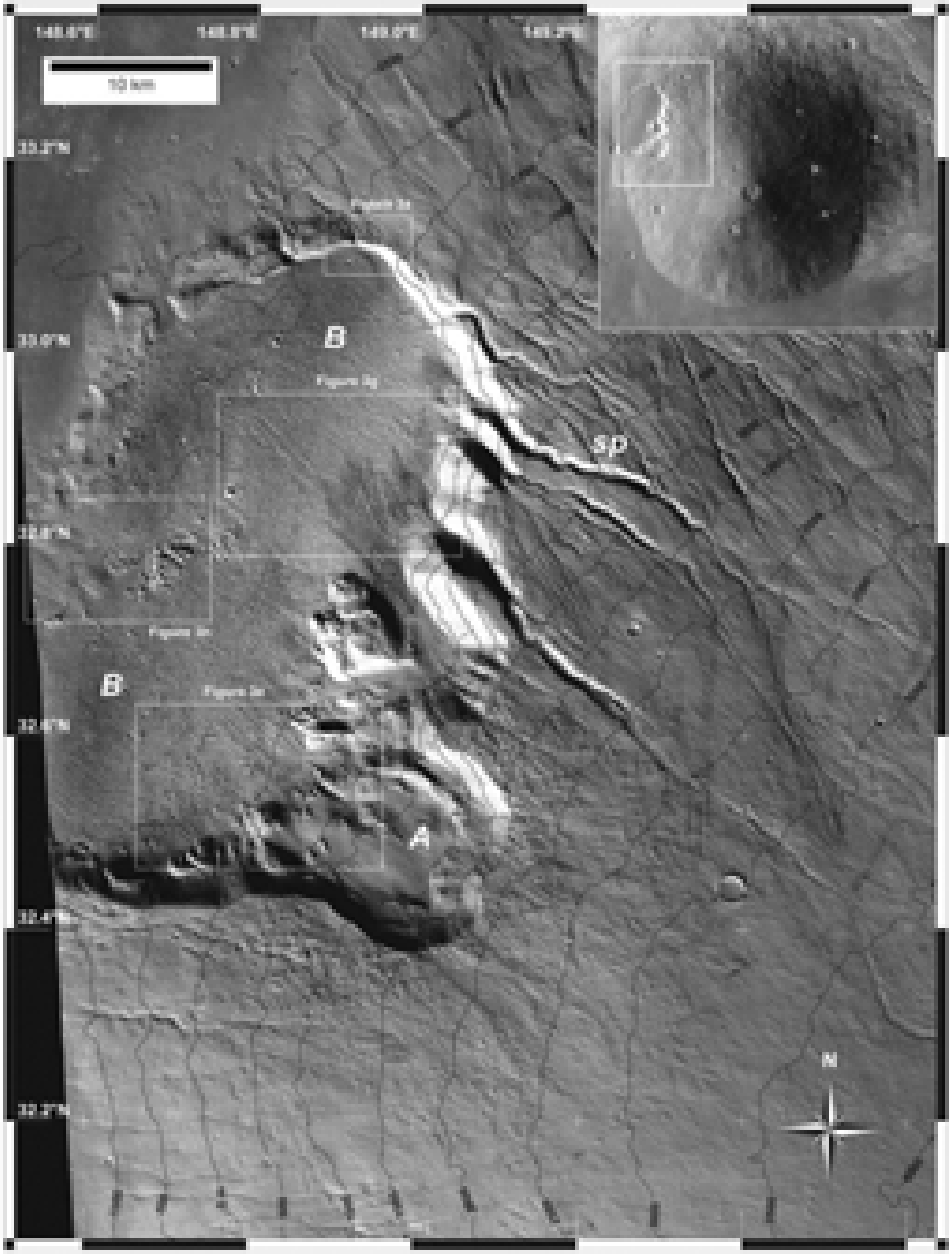

Figure 1 Topographic image map of the study area at the base of the northwestern flank of Hecates Tholus (part of HRSC image h0032_0000.nd). Topographic information (contour line distance 500 m, reference plane is the Mars IAU 2000 ellipsoid) was derived from HRSC stereo imagery. The smaller depression (A) is surrounded by a unique knobby and hilly material. Note the stream piracy pattern (sp) immediately east of a larger depression (B), indicating that an older trend of flow directions was changed as a result of the formation of depression B. The white boxes show the locations of Fig. 3a, e, g and h. The inset on the upper right is a mosaic of Themis infrared daytime images and shows the location of the base map.

chronology[illegible], give an absolute age for the eruption of ~350 Myr. Hence, large-scale explosive volcanism occurred in the last 10% of the planet's history. This is very young when compared to the several-billion-year-old shields in the highlands, which are among the best-documented examples yet of explosive volcanism on Mars.

The shape and distribution of channels near the caldera exhibit several characteristics that shed light on the chronology of volcanic and fluvial processes. East of depression B, we observe two peaks in the azimuthal distribution of the channels. A first set of channels (set A) has an orientation of about N 30° W and is cut off by depression B at several locations. These channels bifurcate and meander where minor surface undulations cause a decrease in flow energy. Several channels that are cut off by depression B can be traced towards the north of the depression, where they seem to continue on its rim. In at least one example (Fig. 3a), the base of a channel starts at a topographically higher level than the floor of depression B, indicating that the channel is older.

A second, younger set of channels (set B) with an azimuthal trend of N 50° W to N 70° W deviates from and partly crosses the older set A, creating a stream piracy pattern. Its channels are deeper and broader than those of set A, and groundwater sapping from a water-rich subsurface might have contributed to their morphology. Set B starts several kilometres away from the eastern rim of depression B, where the topographic gradient becomes higher and is directed towards its rim. The channels follow this topographic trend and deposited large amounts of debris onto the floor. These observations suggest that fluvial activity on Hecates Tholus was continual, not episodic, during the events which formed the depressions, and that the interaction of magma and water or ice may have contributed to the explosive nature of the eruption.

The lower level of depression A and several smaller valleys near the walls of depression B are covered by a smooth deposit, which is lineated in a downslope direction (Fig. 3b). It resembles the lineated valley fill in the fretted terrain near the dichotomy boundary, which has been interpreted as rock glaciers. Where the lineated material flows over a topographic step, its surface is distinctively rougher than on flat ground (Fig. 3c). This pattern resembles the change in surface texture encountered at terrestrial icefalls (Fig. 3d). Beyond the topographic step, it extends outward onto the floor of depression B for a distance of ~6 km. It is bounded by curvilinear ridges that resemble terrestrial end moraines (Fig. 3e). Lobate flow features also extend away from the base of the wall for ~2.5 km (Fig. 3f). Where several valleys debouch into depression B, fan deposits extend for up to 4 km on the surrounding plains (Fig. 3g). We interpret them as debris, transported down the strongly incised channels of set B. Alternatively, these deposits could also be moraines. Long and slightly sinuous features extend downslope (~1° slope) from the end of the fan deposits across the entire floor of depression B towards the northwest. We interpret them as distal meltwater channels extending across a proglacial braided outwash plain, analogous to an Icelandic sandur.

A topographic ridge separates depression B from the topographically lower lava flows from Elysium Mons, which are located further towards the northwest. Where this ridge is breached, some rounded, low and shallow hills are superposed by straight, long and narrow ridges and trenches (Fig. 3h). They resemble terrestrial subglacial erosion features (for example, drumlins or whalebacks), and indicate that the glaciation possibly extended beyond depression B towards the northwest. As elsewhere on Mars, the strongest arguments for a glacial origin are the assemblage of various surface features that are strikingly similar to terrestrial glacial landforms (medial moraines, end moraines, meltwater channels, drumlins) and their consistently glacial proximal-to-distal relationship (Figs 1 and 3). The volatile most likely to have formed the glaciers is water-ice, as the only alternative, CO_2, is particularly unstable at low latitudes under any conceivable atmospheric conditions. The water source could have been precipitation or groundwater that freezes when coming into contact with ice. Precipitation of water on the martian surface is known to take place even under the current thin atmosphere. There are no obvious surficial pathways of water into depression A. Hence, groundwater emerging at the base of scarps bounding the depressions might have fed the glaciers in depression A. However, the local microenvironment at the floors of the depressions, which are partly protected from insolation by steep walls, might act as a cold trap to enhance frost deposition as a water source.

We performed crater counts on HRSC and MOC images of the glacial features shown in Fig. 3, and obtained cratering model ages between ~25 and 5 Myr (Fig. 4). The detection of very young glacial features at a latitude of 30° N in the Elysium region has profound implications for the recent martian climate history. Geologic observations suggest that Mars has experienced recent ice ages, and it is inferred from gamma-ray and neutron spectroscopy that water might indeed be present today near the surface. However,

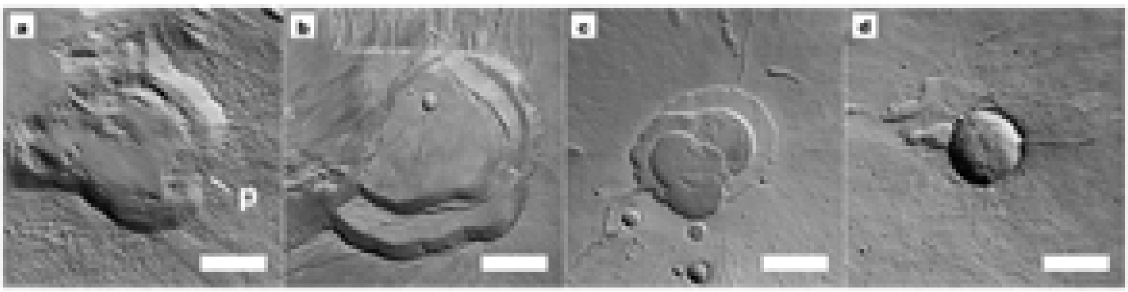

Figure 2 Morphology of calderas. **a**, Feature interpreted to be a caldera on the northwestern flank of Hecates Tholus (depression A of Fig. 1). Owing to a promontory (p), the outline is distinctively non-circular, making an impact origin improbable. Note the two levels of floor elevation, with lineations in the SE–NW direction filling the lower level. **b**, Part of the summit caldera complex of Ascraeus Mons (part of HRSC image h0068_0000.nd, taken on 31 January 2004, centre at 11.13° N, 255.95° E). Note the two levels of floor elevation, similar to what is observed in depression A. **c**, Summit caldera of Hecates Tholus (32.05° N, 150.1° E). Note the morphologic similarity of this caldera and the calderas shown in **a** and **b**. **d**, The largest impact crater on Hecates Tholus (32.29° N, 150.8° E) displays a sharp, elevated crater rim and a continuous floor that is not divided into two elevation levels. Note the overall dissimilarity with **a**, **b** and **c**. In all images, North is up and the white scale bar is 5 km. Figures 2a, c and d are details of HRSC h0032_0000.nd.

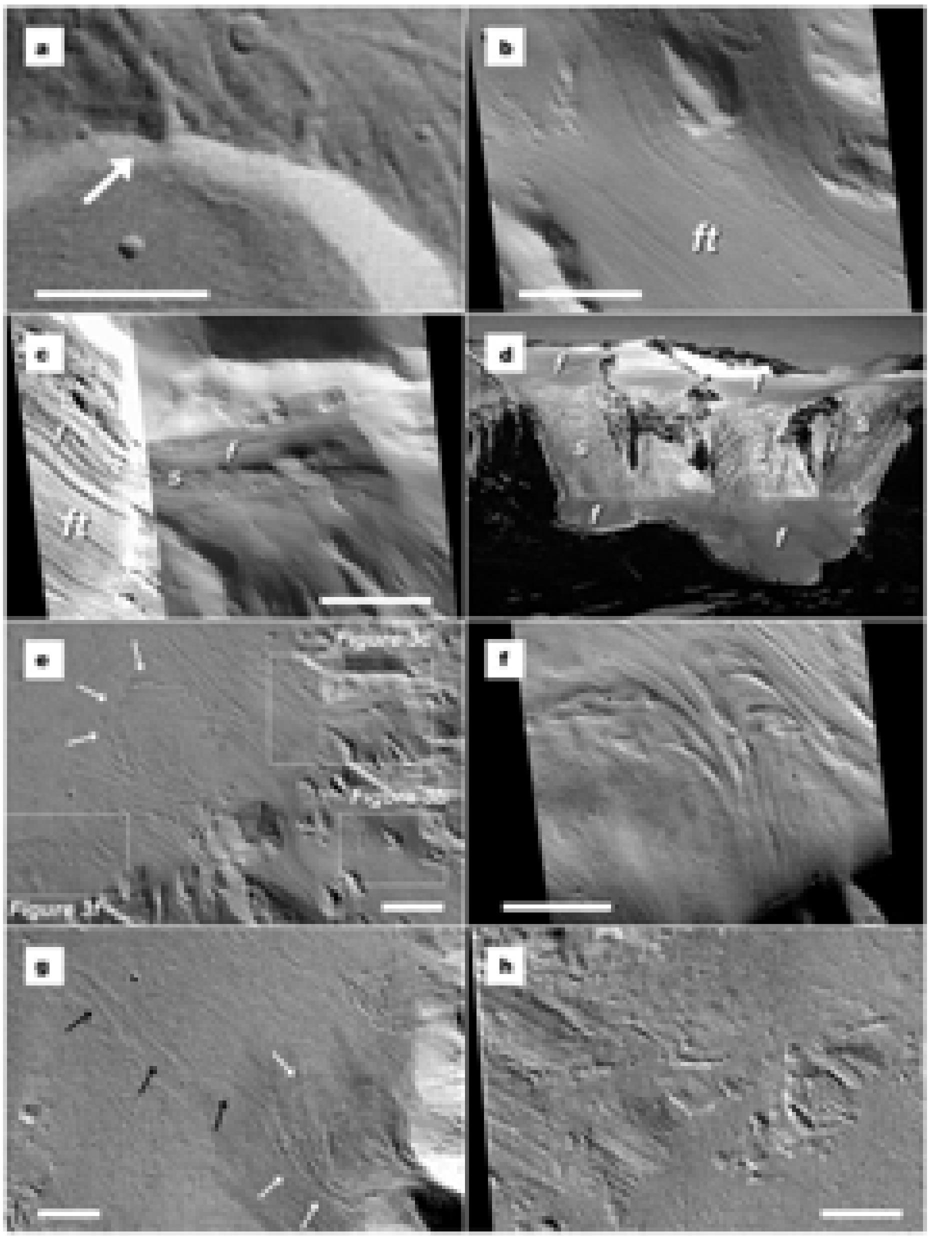

Figure 3 Surface landforms indicative of fluvial and glacial processes at the northwestern flank of Hecates Tholus. **a**, A valley cut upstream by depression B resembles a hanging valley, although true hanging valleys are cut downstream by other valleys. The valley predates the depression (see Fig. 1 for location). **b**, Lineated material (ft), resembling terrestrial medial moraines. A similar surface texture is observed at the fretted terrain[11,28] (MOC image R0802750; see Fig. 3e for location). **c**, Lineated material flowing over the topographic step between depressions A (higher, left) and B (lower, right). Where the topographic gradient is steep (s), the surface texture is rougher than on flat terrain (f), resembling the change in texture observed in terrestrial icefalls (compare with Fig. 3d; MOC images M03-01763 and R06-02750; see Fig. 3e for location). **d**, Icefalls in Taylor Valley, Antarctica (77° 45′ S, 162° 30′ E). Note the change in surface texture between flat (f) and steep (s) terrain, similar to Fig. 3c. Photo courtesy of T. Lowell. **e**, Curvilinear, moraine-like features (white arrows) downslope of the topographic scarp between depressions A and B (see Fig. 1 for location; white boxes show location of Figs 3b, c and f). **f**, Lobate flow features near the base of the wall of depression B, resembling glacial flow features on Earth (MOC image R09-04137; see Fig. 3e for location). **g**, Fan deposits (white arrows) in depression B at the terminations of deeply incised valleys. Faint and slightly sinuous features (black arrows) indicate water runoff from the deposits (see Fig. 1 for location). **h**, Low, rounded hills with superposed long and thin ridges, similar to terrestrial subglacial erosion features (see Fig. 1 for location). Scale bars in Fig. 3a, e, g and h (all part of HRSC image h0032_0000.nd) are 2 km, and in Fig. 3b, c and f are 1 km.

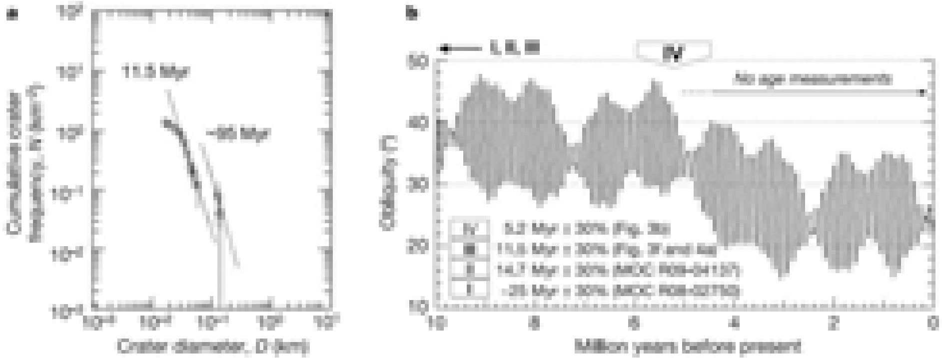

Figure 4 Chronology of glacial surface features and correlation to obliquity changes. **a**, Crater size-frequency distribution for the floor of depression B as observed in MOC R09-04137. Crater model curves according to a new cratering chronology model[13] are fitted to the measurements. The crater model age is 11.5 Myr. An older crater population (right curve) corresponds to an age of ~95 Myr, which might be associated with an older episode of glaciation. Additional ages of 5.2, 14.7 and ~25 Myr were obtained from other MOC images (Fig. 4b). The different ages are in agreement with the locations of the geologic units, with the oldest glacial surfaces at the largest distance from the southeastern part of the depressions, and the youngest surface in the interior of depression A. The error inherent to this technique is ±30% (vertical black lines are error bars). **b**, Changes in the obliquity of Mars' rotational axis over the last 10 Myr (ref. 7). The past ~10 Myr can be reliably modelled despite the chaotic behaviour of the orbits in the Solar System[7,24], so the large increase in obliquity at ~5 Myr is robust. The youngest crater model age derived from our crater counts is plotted as a broad arrow on top of the figure (the other ages fall outside the range shown here). The width of the arrow corresponds to the 30% uncertainty. Note that all our ages are older than the abrupt increase of obliquity at 5 Myr. Our age measurements suggest that the mean obliquity might have been higher than today even before 10 Myr ago, allowing ice to be present globally according to climate models[6].

although there is a hydrogen-rich zone at Elysium[21], the spatial resolution of these measurements is far too low to detect any local enrichment on the scale of the landforms seen at Hecates Tholus. At present, the pressure and temperature conditions of the martian atmosphere prevent near-surface ice from being stable at equatorial latitudes[6]. However, the obliquity of the planet's rotational axis varied significantly over the past 20 Myr (ref. 7). In periods of higher obliquity the climate was different from today's[22].

According to recent climate models, north polar water-ice could be mobilized under such conditions[23] and be deposited at mid- and low latitudes[23,24] where it would have been stable[6]. This study is the first to combine calculations of orbital variations and climate models with the absolute dating of glacial surface features. The ages of glacial deposits on Hecates Tholus range from 25 to 5 Myr before present, with a ±30% error (Fig. 4a). This corresponds very well to a period of increased obliquity, which ended about 5 Myr ago[7] (Fig. 4b). The averaged long-term obliquity between 5 and 20 Myr ago is >35°, a value that is predicted by models to allow ice to be stable globally[6]. Hence, our observations show that the independent results on orbital variations[7] and climate modelling[23,24] are in chronological agreement with geologic surface features.

There are several reasons why ice may still be present at Hecates Tholus. The sublimation of ice results in the accumulation of sediment particles at the surface, and the formation of a lag deposit that is very effective in protecting ice from further sublimation[25]. In addition, Elysium is a long-term sink of atmospheric dust[26], the deposition of which might have further decreased the sublimation rate. There is no evidence for significant degradation or for collapse features like kettle holes in images of the interior of depression A (Fig. 3b). We conclude that there may well have been some unknown amount of sublimation, but that ice is still buried and maintains the 'intact' appearance of the surface. On Earth, Miocene-aged ice (~8 Myr) is still present in the Antarctic dry valleys under a layer of sublimation till[28]. Therefore, the ice at Hecates Tholus may well have been preserved in very shallow depths for geologically long timescales[25,28], and could even be present today and accessible for automated or human exploration. □

Received 3 September 2004; accepted 2 February 2005; doi:10.1038/nature03423.

1. Greeley, R. & Spudis, P. D. Volcanism on Mars. Rev. Geophys. Space Phys. 19, 13–41 (1981).
2. Mouginis-Mark, P. J., Wilson, L. & Zuber, M. T. in Mars (eds Kieffer, H. H., Jakosky, B. M., Snyder, C. W. & Matthews, M. S.) 424–452 (Univ. Arizona Press, Tucson/London, 1992).
3. Francis, P. W. & Wood, C. A. Absence of silicic volcanism on Mars: Implications for crustal composition and volatile abundance. J. Geophys. Res. 87, 9881–9889 (1982).
4. Wilson, L. & Head, J. W. Mars: review and analysis of volcanic eruption theory and relationships to observed landforms. Rev. Geophys. 32, 221–263 (1994).
5. Greeley, R. & Crown, D. A. Volcanic geology of Tyrrhena Patera, Mars. J. Geophys. Res. 95, 7133–7149 (1990).
6. Mellon, M. T. & Jakosky, B. M. The distribution and behaviour of martian ground ice during past and present epochs. J. Geophys. Res. 100, 11781–11799 (1995).
7. Laskar, J. et al. Long term evolution and chaotic diffusion of the insolation quantities of Mars. Icarus 170, 343–364 (2004).
8. Neukum, G. et al. HRSC: The High Resolution Stereo Camera of Mars Express 17–35 (Report ESA SP-1240, European Space Agency Publications Division, Noordwijk, The Netherlands, 2004).
9. Mouginis-Mark, P. J., Wilson, L. & Head, J. W. Explosive Volcanism on Hecates Tholus, Mars: Investigation of Eruption Conditions. J. Geophys. Res. 87, 9890–9904 (1982).
10. Wewel, F., Scholten, F. & Gwinner, K. High Resolution Stereo Camera (HRSC)—Multispectral 3D-data acquisition and photogrammetric data processing. Can. J. Remote Sens. 26, 466–474 (2000).
11. Werner, S. C., Ivanov, B. A. & Neukum, G. Impact cratering on Mars: Search for target influence on morphology. Lunar Planet. Sci. XXXIV, abstr. 1953 [CD-ROM] (Lunar and Planetary Institute, Houston, 2003).
12. Gulick, V. C. & Baker, V. R. Origin and evolution of valleys on martian volcanoes. J. Geophys. Res. 95, 14325–14344 (1990).
13. Hartmann, W. K. & Neukum, G. Cratering chronology and the evolution of Mars. Space Sci. Rev. 96, 165–194 (2001).
14. Neukum, G. et al. Mars: Recent and episodic volcanic and glacial activity on Mars revealed by the High Resolution Stereo Camera. Nature 432, 971–979 (2004).
15. Squyres, S. W. Martian fretted terrain: flow of erosional debris. Icarus 34, 600–613 (1978).
16. Mangold, N. Geomorphic analysis of lobate debris aprons on Mars at Mars Orbiter Camera scale: Evidence for ice sublimation initiated by fractures. J. Geophys. Res. 108, 8021, doi:10.1029/2002JE001885 (2003).
17. Baker, V. R. Water and the martian landscape. Nature 412, 228–236 (2001).
18. Wall, S. W. Analysis of condensates formed at the Viking 2 Lander site: The first winter. Icarus 47, 173–183 (1981).
19. Head, J. W. & Marchant, D. R. Cold-based mountain glaciers on Mars: Western Arsia Mons. Geology 31, 641–644 (2003).
20. Head, J. W., Mustard, J. F., Kreslavsky, A., Milliken, R. E. & Marchant, D. R. Recent ice ages on Mars. Nature 426, 797–802 (2003).

21. Mitrofanov, I. et al. Maps of subsurface hydrogen from the high energy neutron detector, Mars Odyssey. Science 297, 78–81 (2002).
22. Feldman, W. C. et al. Global distribution of near-surface hydrogen on Mars. J. Geophys. Res. 109, E09006, doi:10.1029/2003JE002160 (2004).
23. Jakosky, B. M., Henderson, B. G. & Mellon, M. T. Chaotic obliquity and the nature of the martian climate. J. Geophys. Res. 100, 1579–1584 (1995).
24. Levrard, B., Forget, F., Montmessin, F. & Laskar, J. Recent ice-rich deposits formed at high latitudes on Mars by sublimation of unstable equatorial ice during low obliquity. Nature 431, 1072–1075 (2004).
25. Mischna, M. A., Richardson, M. I., Wilson, R. J. & McCleese, D. J. On the orbital forcing of martian water and CO_2 cycles: A general circulation model study with simplified volatile schemes. J. Geophys. Res. 108, 5062, doi:10.1029/2003JE002051 (2003).
26. Haberle, R. M., Murphy, J. R. & Schaeffer, J. Orbital change experiments with a Mars general circulation model. Icarus 161, 66–89 (2003).
27. Skorov, Y. V. et al. Stability of water ice under a porous nonvolatile layer: implications to the south polar layered deposits of Mars. Planet. Space Sci. 49, 59–63 (2001).
28. Marchant, D. R. et al. Formation of patterned ground and sublimation till over Miocene glacier ice in Beacon Valley, southern Victoria Land, Antarctica. Geol. Soc. Am. Bull. 114, 718–730 (2002).
29. Mellon, M. T., Jakosky, B. M. & Postawko, S. E. The persistence of equatorial ground ice on Mars. J. Geophys. Res. 102, 19357–19369 (1997).
30. Helbert, J. & Benkhoff, J. A new model on the thermal behavior of the near surface layer on Mars and its implications for ground ice deposits in Gusev Crater. 6th Int. Conf. Mars abstr. 3019 [CD-ROM] (Lunar and Planetary Institute, Houston, 2003).

Acknowledgements We thank the entire HRSC experiment and instrument teams at the German Aerospace Center (DLR) and at the Freie Universität Berlin, as well as the Mars Express teams at ESTEC and ESOC. This study would not have been possible without their work. In particular, we appreciate the support of H. Hoffmann, T. Roatsch, K.-D. Matz, V. Mertens, J. Flohrer, R. Pischel, F. Scholten and K. Gwinner. HRSC was developed at DLR and industrial partners. G.N. is the Principal Investigator of this experiment. We are grateful to U. Wolf for her support in crater counting. M. Aittola, J. Korteniemi, P. Kostama and D. Williams supported the HRSC image planning. T. Lowell provided an image of his collection of glacier photographs. Comments by J. Helbert helped to improve the manuscript.

Competing interests statement The authors declare that they have no competing financial interests.

Correspondence and requests for materials should be addressed to E.H. (Ernst.Hauber@dlr.de).

The HRSC Co-Investigator Team: J. Albertz[1], A. T. Basilevsky[2], G. Bellucci[3], J.-P. Bibring[4], M. Buchroithner[5], M. H. Carr[6], E. Dorrer[7], T. C. Duxbury[8], H. Ebner[9], B. H. Foing[10], R. Greeley[11], E. Hauber[12], J. W. Head III[13], C. Heipke[14], H. Hoffmann[12], A. Inada[15,16], W.-H. Ip[16], B. A. Ivanov[17], R. Jaumann[12], H. U. Keller[18], R. Kirk[19], K. Kraus[20], P. Kronberg[21], R. Kuzmin[2], Y. Langevin[4], K. Lumme[22], W. Markiewicz[18], P. Masson[23], H. Mayer[7], T. B. McCord[24], J.-P. Muller[25], J. B. Murray[26], F. M. Neubauer[27], G. Neukum[28], J. Oberst[12], G. G. Ori[29], M. Pätzold[27], P. Pinet[30], R. Pischel[12], F. Poulet[4], J. Raitala[31], G. Schwarz[32], T. Spohn[18] & S. W. Squyres[33]

Affiliations of authors: 1, TU Berlin, D-10623 Germany; 2, Vernadsky Institute-RAS, Moscow 117975, Russia; 3, IFSI/CNR, 00133 Rome, Italy; 4, IAS, 91405 Orsay cedex, France; 5, TU Dresden D-01062, Germany; 6, USGS, MS 975 Menlo Park, California 94025, USA; 7, Universität der Bundeswehr München D-85577, Germany; 8, JPL, Pasadena, California 91109, USA; 9, TU München D-80333, Germany; 10, ESTEC/SCI-SR, Postbus 299, NL-2200 AG Noordwijk, The Netherlands; 11, Arizona State University, Box 871404, Tempe, Arizona 85287-1404, USA; 12, DLR, Berlin D-12489, Germany; 13, Brown University, Box 1846, Providence, Rhode Island 02912, USA; 14, Universität Hannover, D-30167, Germany; 15, Kobe University, 657-8501 Kobe, Japan; 16, National Central University (NCU), Chung-Li 320, Taiwan; 17, IDG-RAS, Moscow 117979, Russia; 18, MPS, Postfach 20, D-37191, Germany; 19, USGS, Flagstaff, Arizona 86001, USA; 20, TU Wien A-1040, Austria; 21, TU Clausthal D-38678, Germany; 22, University of Helsinki, PO Box 14, SF-00014 Finland; 23, OrsayTerre, F-91405 Orsay cedex, France; 24, PSI-Nw, Winthrop, Washington 98862, USA; 25, University College London WC1E 6BT, UK; 26, The Open University, Milton Keynes MK7 6AA, Buckinghamshire, UK; 27, Universität Köln, D-50923, Germany; 28, FU Berlin D-12249, Germany; 29, IRSPS, I-65127 Pescara, Italy; 30, Observatoire de Midi-Pyrénées, F-31400 Toulouse, France; 31, University of Oulu, FIN-90401, Finland; 32, DLR, D-82234 Wessling, Germany; 33, Cornell University, Ithaca, New York 14853-1301, USA

Current measurement by real-time counting of single electrons

Jonas Bylander, Tim Duty & Per Delsing

Department of Microtechnology and Nanoscience (MC2), Chalmers University of Technology, SE-412 96 Göteborg, Sweden

The fact that electrical current is carried by individual charges has been known for over 100 years, yet this discreteness has not been directly observed so far. Almost all current measurements involve measuring the voltage drop across a resistor, using Ohm's law, in which the discrete nature of charge does not come into play. However, by sending a direct current through a microelectronic circuit with a chain of islands connected by small tunnel junctions, the individual electrons can be observed one by one. The quantum mechanical tunnelling of single charges in this one-dimensional array is time correlated[1–3], and consequently the detected signal has the average frequency $f = I/e$, where I is the current and e is the electron charge. Here we report a direct observation of these time-correlated single-electron tunnelling oscillations, and show electron counting in the range 5 fA–1 pA. This represents a fundamentally new way to measure extremely small currents, without offset or drift. Moreover, our current measurement, which is based on electron counting, is self-calibrated, as the measured frequency is related to the current only by a natural constant.

In the mid-1980s, it was suggested[1] that a small current consisting of individual electrons, tunnelling through a small tunnel junction, could at low temperatures result in an oscillating voltage of amplitude e/C, where C is the capacitance of the tunnel junction. The full theory for these so-called single-electron tunnelling oscillations was then developed[2], based on earlier work on Bloch oscillations and the underlying Coulomb blockade[4,5]. This phenomenon of single-electron tunnelling oscillations is similar to the a.c. Josephson effect, as phase and charge are quantum conjugated variables. However, the duality is not complete because the single-electron tunnelling oscillations are lacking coherence. A few years later, these oscillations were detected indirectly by phase locking to an external microwave signal[6]. Shortly thereafter, new devices such as the single-electron turnstile[7] and the single-electron pump[8] were invented in order to create a current given by the fundamental relation $I = ef$. Since then, the single-electron pump has been refined to a very high accuracy[9].

A number of authors have also proposed[10–12] that it should be possible to turn this relation around, and instead measure the current by monitoring the individual electrons as they pass through a circuit. More recently, single-electron tunnelling events have been observed[13–17]. In those experiments, however, there was no time correlation, and thus no relation between frequency and current could be demonstrated.

In order to measure current by electron counting, three main ingredients are necessary: time correlation of the tunnelling events, a fast and sensitive charge detector, and a very stable current bias. To bring about time correlation in a single tunnel junction, in contrast to uncorrelated shot noise[18], care must be taken to make the electromagnetic impedance seen by the junction large[2] compared to the Klitzing resistance, $R_K = h/e^2 \approx 25.8\,\mathrm{k\Omega}$. This can be achieved by placing small-size resistors in close proximity to the junction[17,19] or by using a one-dimensional series array of tunnel junctions[20].

In our experiment, we have used a superconducting array containing $N = 50$ junctions (Fig. 1). The capacitance of each junction is $C_A \approx 0.42$ fF, and the stray capacitance of an electrode inside the array is $C_0 \approx 50$ aF. In such an array, excess charge on one island polarizes the neighbouring islands, so that the charges repel each

Bibliography

Acuña, M. H., Connerney, J. E. P., Ness, N. F., Lin, R. P., Mitchell, D., Carlson, C. W., McFadden, J., Anderson, K. A., Rème, H., Mazelle, C., Vignes, D., Wasilewski, P., and Cloutier, P. (1999). Global Distribution of Crustal Magnetization Discovered by the Mars Global Surveyor MAG/ER Experiment. *Science*, **284**, 790–793.

Allen, C. C. (1979). Volcano-ice interactions on Mars. *J. Geophys. Res.*, **84**(13), 8048–8059.

Anderson, C. E. (1987). An overview of the theory of hydrocodes. *Int. J. Impact Eng.*, **5**, 33–59.

Arvidson, R. E., Coradini, M., Carusi, A., Coradini, A., Fulchignoni, M., Federico, C., Funiciello, R., and Salomone, M. (1976). Latitudinal variation of wind erosion of crater ejecta deposits on Mars. *Icarus*, **27**, 503–516.

Arvidson, R. E., Boyce, J., Chapman, C., Cintala, M., Fulchignoni, M., Moore, H., Neukum, G., Schultz, P., Soderblom, L., Strom, R., Woronow, A., and Young, R. (1979). Standard techniques for presentation and analysis of crater size-frequency data. *Icarus*, **37**, 467–474.

Baker, V. R. (1982). *The channels of Mars.* University of Texas Press.

Baker, V. R., Carr, M. H., Gulick, V. C., Williams, C. R., and Marley, M. S. (1992). *Channels and valley networks*, pages 493–522. University of Arizona Press.

Baldwin, R. B. (1963). *The measure of the moon.* University of Chicago Press, Chicago.

Baldwin, R. B. (1964). Lunar crater counts. *Astronamical Journal*, **69**, 377.

Baldwin, R. B. (1971). On the History of Lunar Impact Cratering: The Absolute Time Scale and the Origin of Planetesimals. *Icarus*, **14**, 36.

Bandfield, J. L., Hamilton, V. E., and Christensen, P. R. (2000). A Global View of Martian Surface Compositions from MGS-TES. *Science*, **287**, 1626–1630.

Barlow, N. G. (1988a). Crater size-frequency distributions and a revised Martian relative chronology. *Icarus*, **75**, 285–305.

Barlow, N. G. (1988b). Crater size-frequency distributions and a revised Martian relative chronology. *Icarus*, **75**, 285–305.

Barlow, N. G. (2001). Status of the "Catalog of Large Martian Impact Craters" Revision. *Bulletin of the American Astronomical Society*, **33**, 1105.

Barlow, N. G. and Perez, C. B. (2003). Martian impact crater ejecta morphologies as indicators of the distribution of subsurface volatiles. *J. Geophys. Res.*, pages 4–1.

Basilevsky, A. T., Litvak, M. L., Mitrofanov, I. G., Boynton, W., Saunders, R. S., and Head, J. W. (2003). Search for Traces of Chemically Bound Water in the Martian Surface Layer Based on HEND Measurements onboard the 2001 Mars Odyssey Spacecraft. *Solar System Research*, **37**, 387–396.

Basilevsky, A. T., Rodin, A. V., Kozyrev, A. S., Mitrofanov, I. G., Neukum, G., Werner, S. C., Head, J. W., Boynton, W., and Saunders, R. S. (2004). Mars: The Terra Arabia Low Epithermal Neutron Flux Anomaly. In *Lunar and Planetary Institute Conference Abstracts*, page 1091.

Basilevsky, A. T., Neukum, G., Ivanov, B. A., Werner, S. K., Gesselt, S., Head, J. W., Denk, T., Jaumann, R., Hoffmann, H., Hauber, E., and McCord, T. (2005). Morphology and geological structure of the western part of the Olympus Mons volcano on Mars from the analysis of the Mars Express HRSC imagery. *Solar System Research*, **39**, 85–101.

Becker, L., Glavin, D. P., and Bada, J. L. (1997). Polycyclic aromatic hydrocarbons (PAHs) in Antarctic Martian meteorites, carbonaceous chondrites, and polar ice. *Geochimica et Cosmochimica Acta*, **61**, 475–481.

Becker, T. W. and Boschi, L. (2002). A comparison of tomographic and geodynamic mantle models. *Geochemistry, Geophysics, Geosystems*, page 3.

Berman, D. C. and Hartmann, W. K. (2002). Recent Fluvial, Volcanic, and Tectonic Activity on the Cerberus Plains of Mars. *Icarus*, **159**, 1–17.

Bibring, J., Langevin, Y., Poulet, F., Gendrin, A., Gondet, B., Berthé, M., Soufflot, A., Drossart, P., Combes, M., Bellucci, G., Moroz, V., Mangold, N., Schmitt, B., and OMEGA team, t. (2004). Perennial water ice identified in the south polar cap of Mars. *Nature*, **428**, 627–630.

Bierhaus, E. B. (2004). Discovery that secondary craters dominate Europa's small crater population. *Ph.D. Thesis.*

Bierhaus, E. B., Chapman, C. R., and Merline, W. J. (2005a). Secondary craters on Europa and implications for cratered surfaces. *Nature*, **437**, 1125–1127.

Bierhaus, E. B., Merline, W. J., and Chapman, C. R. (2005b). Variation in Size-Distributions Between Adjacent and Distant Secondary Craters. In *36th Annual Lunar and Planetary Science Conference*, page 2386.

Blasius, K. R. (1976). The record of impact cratering on the great volcanic shields of the Tharsis region of Mars. *Icarus*, **29**, 343–361.

Bogard, D. D. and Johnson, P. (1983). Martian gases in an Antarctic meteorite? *Science*, **221**, 651–654.

Borg, L. E., Nyquist, L. E., Wiesmann, H., and Reese, Y. (1998). Samarium-Neodymium Isotopic Systematics of the Lherzolitic Shergottite Lewis Cliff 88516. *Meteoritics & Planetary Science*, **33**, 20.

Boynton, W. V., Feldman, W. C., Squyres, S. W., Prettyman, T. H., Brückner, J., Evans, L. G., Reedy, R. C., Starr, R., Arnold, J. R., Drake, D. M., Englert, P. A. J., Metzger, A. E., Mitrofanov, I., Trombka, J. I., d'Uston, C., Wänke, H., Gasnault, O., Hamara, D. K., Janes, D. M., Marcialis, R. L., Maurice, S., Mikheeva, I., Taylor, G. J., Tokar, R., and Shinohara, C. (2002). Distribution of Hydrogen in the Near Surface of Mars: Evidence for Subsurface Ice Deposits. *Science*, **297**, 81–85.

Breuer, D. and Spohn, T. (2003). Early plate tectonics versus single-plate tectonics on Mars: Evidence from magnetic field history and crust evolution. *J. Geophys. Res.*, **108**, 8–1.

Bridges, J. C. and Grady, M. M. (2000). Evaporite mineral assemblages in the nakhlite (martian) meteorites. *Earth and Planetary Science Letters*, **176**, 267–279.

Brinkman, R. T. (1966). Lunar crater distributions from Ranger VI photographs. *J. Geophys. Res.*, **71**, 340–342.

Brown, W. K. and Wohletz, K. H. (1995). Derivation of the Weibull distribution based on physical principles and its connection to the Rosin-Rammler and lognormal distributions. *Journal of Applied Physics*, **78**, 2758–2763.

Buczkowski, D. L. and Cooke, M. L. (2004). Formation of double-ring circular grabens due to volumetric compaction over buried impact craters: Implications for thickness and nature of cover material in Utopia Planitia, Mars. *J. Geophys. Res.*, page 2006.

Buczkowski, D. L. and McGill, G. E. (2002). Topography within circular grabens: Implications for polygon origin, Utopia Planitia, Mars. *Geophysical Research Letters*, **29**, 59–1.

Burke, K. and Torsvik, T. H. (2004). Derivation of Large Igneous Provinces of the past 200 million years from long-term heterogeneities in the deep mantle. *Earth and Planetary Science Letters*, **227**, 531–538.

Burr, D., McEwen, A. S., and Sakimoto, S. E. H. (2002). Recent aqueous floods from the Cerberus Fossae, Mars. *Geophysical Research Letters*, **29**, 13–1–13–4.

Cabrol, N. A., Grin, E. A., Carr, M. H., Sutter, B., Moore, J. M., Farmer, J. D., Greeley, R., Kuzmin, R. O., Des-Marais, D. J., Kramer, M. G., Newsom, H., Barber, C., Thorsos, I., Tanaka, K. L., Barlow, N. G., Fike, D. A., Urquhart, M. L., Grigsby, B., Grant, F. D., and de Goursac, O. (2003). Exploring Gusev Crater with Spirit: Review of science objectives and testable hypotheses. *J. Geophys. Res.*, **108**, 17–1.

Cameron, A. G. W. (1986). The impact theory for origin of the Moon. In *Origin of the Moon*, page 609.

Cameron, A. G. W. and Ward, W. R. (1976). The Origin of the Moon. In *Lunar and Planetary Institute Conference Abstracts*, page 120.

Canup, R. M. and Agnor, C. B. (2000). *Accretion of the Terrestrial Planets and the Earth-Moon System*, pages 113–129. University of Arizona Press, Tucson.

Carr, M. H. (1973). Volcanism on Mars. *J. Geophys. Res.*, **78**(17), 4049–4062.

Carr, M. H. (1976). *Elevation of Martian Volcanoes as a Function of Age*, page 152.

Carr, M. H. (1979). Formation of Martian flood features by release of water from confined aquifers. *J. Geophys. Res.*, **84**(13), 2995–3007.

Carr, M. H. (1981). *The surface of Mars*. Yale University Press.

Carr, M. H. (1986). Mars - A water-rich planet? *Icarus*, **68**, 187–216.

Carr, M. H. (1996). *Water on Mars*. Oxford University Press.

Carr, M. H. and Schaber, G. G. (1977). Martian permafrost features. *J. Geophys. Res.*, **82**(11), 4039–4054.

Carr, M. H., Masursky, H., Baum, W. A., Blasius, K. R., Cutts, J. A., Briggs, G. A., Duxbury, T., Greeley, R., Guest, J. E., and Smith, B. A. (1976). Preliminary results from the Viking orbiter imaging experiment. *Science*, **193**, 766–776.

Carr, M. H., Crumpler, L. S., Cutts, J. A., Greeley, R., Guest, J. E., and Masursky, H. (1977a). Martian impact craters and emplacement of ejecta by surface flow. *J. Geophys. Res.*, **82**(11), 4055–4065.

Carr, M. H., Greeley, R., Blasius, K. R., Guest, J. E., and Murray, J. B. (1977b). Some Martian volcanic features as viewed from the Viking orbiters. *J. Geophys. Res.*, **82**(11), 3985–4015.

Chapman, C. R. and Haefner, R. R. (1967). A Critique of Methods for Analysis of the Diameter-Frequency Relation for Craters with Special Application to the Moon. *J. Geophys. Res.*, **72**(11), 549.

Chapman, C. R.and Veverka, J., Belton, M. J. S.and Neukum, G., and Morrison, D. (1996). Cratering on Gaspra. *Icarus*, **120**, 231–245.

Christensen, P. R., Bandfield, J. L., Clark, R. N., Edgett, K. S., Hamilton, V. E., Hoefen, T., Kieffer, H. H., Kuzmin, R. O., Lane, M. D., Malin, M. C., Morris, R. V., Pearl, J. C., Pearson, R., Roush, T. L., Ruff, S. W., and Smith, M. D. (2000). Detection of crystalline hematite mineralization on Mars by the Thermal Emission Spectrometer: Evidence for near-surface water. *J. Geophys. Res.*, **105**(14), 9623–9642.

Christensen, P. R., Ruff, S. W., Fergason, R. L., Knudson, A. T., Anwar, S., Arvidson, R. E., Bandfield, J. L., Blaney, D. L., Budney, C., Calvin, W. M., Glotch, T. D., Golombek, M. P., Gorelick, N., Graff, T. G., Hamilton, V. E., Hayes, A., Johnson, J. R., McSween, H. Y., Mehall, G. L., Mehall, L. K., Moersch, J. E., Morris, R. V., Rogers, A. D., Smith, M. D., Squyres, S. W., Wolff, M. J., and Wyatt, M. B. (2004). Initial Results from the Mini-TES Experiment in Gusev Crater from the Spirit Rover. *Science*, **305**, 837–842.

Clayton, R. N. and Mayeda, T. K. (1975). Genetic Relations Between the Moon and Meteorites. In *Lunar and Planetary Institute Conference Abstracts*, page 155.

Clifford, S. M. (1993). A model for the hydrologic and climatic behavior of water on Mars. *J. Geophys. Res.*, **98**(17), 10973–11016.

Condit, C. D. (1978). Distribution and relations of 4- to 10-km-diameter craters to global geologic units of Mars. *Icarus*, **34**, 465–478.

Connerney, J. E. P., Acuna, M. H., Wasilewski, P. J., Ness, N. F., Reme, H., Mazelle, C., Vignes, D., Lin, R. P., Mitchell, D. L., and Cloutier, P. A. (1999). Magnetic Lineations in the Ancient Crust of Mars. *Science*, **284**, 794.

Croft, S. K. (1985a). Rim Structures in Lunar Craters and Basins: New Constraints on the Origin of Asymmetric Basin Rings. In *Lunar and Planetary Institute Conference Abstracts*, pages 154–155.

Croft, S. K. (1985b). The scaling of complex craters. *J. Geophys. Res.*, **90**(9), 828–.

Crown, D. A. and Greeley, R. (1993). Volcanic geology of Hadriaca Patera and the eastern Hellas region of Mars. *J. Geophys. Res.*, **98**(17), 3431–3451.

Crumpler, L. S. and Aubele, J. C. (1978). Structural evolution of Arsia Mons, Pavonis Mons, and Ascreus Mons Tharsis region of Mars. *Icarus*, **34**, 496–511.

Dence, M. R. (1965). The extraterrestrial origin of Canadian craters. *Ann. NY Acad. Sci*, **123**, 941–969.

Feldman, W. C., Boynton, W. V., Tokar, R. L., Prettyman, T. H., Gasnault, O., Squyres, S. W., Elphic, R. C., Lawrence, D. J., Lawson, S. L., Maurice, S., McKinney, G. W., Moore, K. R., and Reedy, R. C. (2002). Global Distribution of Neutrons from Mars: Results from Mars Odyssey. *Science*, **297**, 75–78.

Fielder, G. (1962). Ray Elements and Secondary-Impact Craters on the Moon. *Astrophys. J.*, **135**, 632–637.

Fishbaugh, K. E. and Head, J. W. (2001). Comparison of the North and South Polar Caps of Mars: New Observations from MOLA Data and Discussion of Some Outstanding Questions. *Icarus*, **154**, 145–161.

Floran, R. J., Prinz, M., Hlava, P. F., Keil, K., Nehru, C. E., and Hinthorne, J. R. (1978). The Chassigny meteorite - A cumulate dunite with hydrous amphibole-bearing melt inclusions. *Geochimica et Cosmochimica Acta*, **42**, 1213–1219.

Folkner, W. M., Yoder, C. F., Yuan, D. N., Standish, E. M., and Preston, R. A. (1997). Interior Structure and Seasonal Mass Redistribution of Mars from Radio Tracking of Mars Pathfinder. *Science*, **278**, 1749.

Frey, H. and Schultz, R. (1989). Overlapping Large Impacts and the Origin of the Northern Lowlands of Mars. In *Lunar and Planetary Institute Conference Abstracts*, page 315.

Frey, H. and Schultz, R. A. (1988). Large impact basins and the mega-impact origin for the crustal dichotomy on Mars. *Geophysical Research Letters*, **15**, 229–232.

Frey, H., Lowry, B. L., and Chase, S. A. (1979). Pseudocraters on Mars. *J. Geophys. Res.*, **84**(13), 8075–8086.

Frey, H. V., Roark, J. H., Shockey, K. M., Frey, E. L., and Sakimoto, S. E. H. (2002). Ancient lowlands on Mars. *Geophysical Research Letters*, **29**, 22–1.

Garvin, J. B., Sakimoto, S. E. H., and Frawley, J. J. (2003). Craters on Mars: Global Geometric Properties from Gridded MOLA Topography. In *Sixth International Conference on Mars*, page 3277.

van Gasselt, S., Reiss, D., Hauber, E., and Neukum, G. (2005). Mass Wasting in Hellas Montes, Mars. *J. Geophys. Res.*, page submitted.

van Gasselt, S., Hauber, E., Reiss, D., Scholten, F., Neukum, G., and The HRSC Co-Investigator Team (2005). Slope Morphologies of the Hellas Mensae Constructs, Eastern Hellas Planitia, Mars. In *36th Annual Lunar and Planetary Science Conference*, page 2090.

Gault, D. E. and Greeley, R. (1978). Exploratory experiments of impact craters formed in viscous-liquid targets - Analogs for Martian rampart craters. *Icarus*, **34**, 486–495.

Gellert, R., Rieder, R., Anderson, R. C., Brückner, J., Clark, B. C., Dreibus, G., Economou, T., Klingelhöfer, G., Lugmair, G. W., Ming, D. W., Squyres, S. W., d'Uston, C., Wänke, H., Yen, A., and Zipfel, J. (2004). Chemistry of Rocks and Soils in Gusev Crater from the Alpha Particle X-ray Spectrometer. *Science*, **305**, 829–833.

Gersonde, R., Kyte, F. T., Bleil, U., Diekmann, B., Flores, J. A., Gohl, K., Grahl, G., Hagen, R., Kuhn, G., Sierro, F. J., Völker, D., Abdelmann, A., and Bostwick, J. A. (1997). Geological record and reconstruction of the late Pliocene impact of the Eltanin asteroid in the Southern Ocean. *Nature*, **390**, 357–363.

Gilbert, G. (1893). The moon's face. A study of the origin of its features. *Bull. Phil. Soc. Wash.*, **12**, 241–292.

Golombek, M. P., Grant, J. A., Parker, T. J., Kass, D. M., Crisp, J. A., Squyres, S. W., Haldemann, A. F. C., Adler, M., Lee, W. J., Bridges, N. T., Arvidson, R. E., Carr, M. H., Kirk, R. L., Knocke, P. C., Roncoli, R. B., Weitz, C. M., Schofield, J. T., Zurek, R. W., Christensen, P. R., Fergason, R. L., Anderson, F. S., and Rice, J. W. (2003). Selection of the Mars Exploration Rover landing sites. *J. Geophys. Res.*, **108**, 13–1.

Gooding, J. L., Zolensky, M. E., and Wentworth, S. J. (1991). Aqueous alteration of the Nakhla meteorite. *Meteoritics*, **26**, 135–143.

Gordon, F. R. and Lewis, J. D. (1980). The Meckering and Calingiri Earthquakes October 1968 and March 1970. *Geological Survey of Western Australia Bulletin*, **126**, 229pp.

Greeley, R. (2003). Gusev Crater, Mars, as a Landing Site for the Mars Exploration Rover (MER) Project. In *Sixth International Conference on Mars*, page 3286.

Greeley, R. and Guest, J. E. (1987). Geological Map of the Eastern Equatorial Region of Mars (1:15,000,000). *USGS*.

Greeley, R. and Spudis, P. D. (1978). Volcanism in the cratered terrain hemisphere of Mars. *Geophysical Research Letters*, **5**, 453–455.

Greeley, R. and Spudis, P. D. (1981). Volcanism on Mars. *Rev. Geophys. Space. Phys.*, **19**, 13–41.

Greeley, R., Foing, B. H., Neukum, G., Pinet, P., van Kan, M., Werner, S. C., Williams, D., and Zegers, T. E. (2005). Fluid lava flows in Gusev crater, Mars. *J. Geophys. Res.*, page (submitted).

Greenberg, R. and Nolan, M. C. (1989). Delivery of asteroids and meteorites to the inner solar system. In *Asteroids II*, pages 778–801.

Greenberg, R. and Nolan, M. C. (1993). *Dynamical Relationships of Near-Earth Asteroids to Main-Belt Asteroids*, page 473.

Grieve, R. A. F., Dence, M. R., and Robertson, P. B. (1977). Cratering processes - As interpreted from the occurrence of impact melts. In *Impact and Explosion Cratering: Planetary and Terrestrial Implications*, pages 791–814.

Grossman, J. N. (2000). The Meteoritical Bulletin, No. 84. *Meteoritics & Planetary Science, Vol. 35, p.A199-A225*, **35**, 199–.

Grott, M., Hauber, E., Werner, S. C., Kronberg, P., and Neukum, G. (2005). High Heat Flux on Ancient Mars: Evidence from Rift Flank Uplift at Coracis Fossae. *Geophysical Research Letters*, page accepted.

Gulick, V. C. and Baker, V. R. (1990). Origin and evolution of valleys on Martian volcanoes. *J. Geophys. Res.*, **95**, 14325–14344.

Haberle, R. M., Murphy, J. R., and Schaeffer, J. (2003). Orbital change experiments with a Mars general circulation model. *Icarus*, **161**, 66–89.

Halliday, A. N. (2000). Terrestrial accretion rates and the origin of the Moon. *Earth and Planetary Science Letters*, **176**, 17–30.

Hartmann, W., Strom, R., Weidenschilling, S., Blasius, K., Woronow, A., Dence, M., Grieve, R., Diaz, J., Chapman, C., Shoemaker, E., and Jones, K. (1981). *Chronology of Planetary Volcanism by Comparative Studie of Planetary Craters*. Pergamon Press, New York.

Hartmann, W. K. (1965). Terrestrial and Lunar Flux of Large Meteorites in the Last Two Billion Years. *Icarus*, **4**, 157.

Hartmann, W. K. (1966). Early lunar cratering. *Icarus*, **5**, 406–418.

Hartmann, W. K. (1973a). Ancient Lunar Mega-Regolith and Subsurface Structure. *Icarus*, **18**, 634.

Hartmann, W. K. (1973b). Martian Cratering 4. Mariner 9 initial analysis of cratering chronology. *J. Geophys. Res.*, **78**, 4096–4116.

Hartmann, W. K. (1973). Martian Cratering 4. Mariner 9 initial analysis of cratering chronology. *J. Geophys. Res.*, **78**, 4096–4116.

Hartmann, W. K. (1977). Relative crater production rates on planets. *Icarus*, **31**, 260–276.

Hartmann, W. K. (1978). Martian Cratering V: Toward an empirical Martian chronology. *Geophys. Res. Lett*, **5**, 450–452.

Hartmann, W. K. (1999a). Martian cratering VI. Crater count isochrons and evidence for recent volcanism from Mars Global Surveyor. *Meteoritics and Planetary Science*, **34**, 167–177.

Hartmann, W. K. (1999b). Martian cratering VI. Crater count isochrons and evidence for recent volcanism from Mars Global Surveyor. *Meteoritics and Planetary Science*, **34**, 167–177.

Hartmann, W. K. (2004). Martian Cratering 8: Isochron refinement and the chronology of Mars. *Icarus*, page submitted.

Hartmann, W. K. (2005). Martian cratering 8: Isochron refinement and the chronology of Mars. *Icarus*, **174**, 294–320.

Hartmann, W. K. and Berman, D. C. (2000). Elysium Planitia lava flows: Crater count chronology and geological implications. *J. Geophys. Res.*, **105**, 15011–15026.

Hartmann, W. K. and Davis, D. R. (1975). Satillite-sized Planetsimals and Lunar Orign. *Icarus*, **24**, 504.

Hartmann, W. K. and Hartmann, A. C. (1968). Asteroid collisions and evolution of asteroidal mass distribution and meteoritic flux. *Icarus*, **8**, 361–381.

Hartmann, W. K. and Neukum, G. (2001). Cratering Chronology and the Evolution of Mars. *Space Science Reviews*, **96**, 165–194.

Hartmann, W. K. and Wood, C. A. (1971). Moon: Origin and evolution of multiring basins. *Moon*, **3**, 3–78.

Hartmann, W. K., Phillips, R. J., and Taylor, G. J., editors (1986). *Origin of the Moon*. LPI, Houston.

Hauber, E., van Gasselt, S., Ivanov, B., Werner, S., Head, J. W., Neukum, G., Jaumann, R., Greeley, R., Mitchell, K. L., Muller, P., and Co-Investigator Team, T. H. (2005). Discovery of a flank caldera and very young glacial activity at Hecates Tholus, Mars. *Nature*, **434**, 356–361.

Head, J. W. (1975). Lunar Mare Deposits: Areas, Volumes, Sequence, and Implication for Melting in Source Areas. *LPI Contributions*, **234**, 66.

Head, J. W. and Marchant, D. R. (2003). Cold-based Mountain Glaciers on Mars: Western Arsia Mons Fan-shaped Deposits. In *Lunar and Planetary Institute Conference Abstracts*, page 1247.

Head, J. W. and Pratt, S. (2001). Extensive Hesperian-aged south polar ice sheet on Mars: Evidence for massive melting and retreat, and lateral flow and ponding of meltwater. *J. Geophys. Res.*, **106**(15), 12275–12300.

Head, J. W., Seibert, N., Pratt, S., Smith, D., Zuber, M., Solomon, S. C., McGovern, P. J., Garvin, J. B., and MOLA Science Team (1998a). Characterization of Major Volcanic Edifices on Mars Using Mars Orbiter Laser Altimeter Data. In *Lunar and Planetary Institute Conference Abstracts*, page 1322.

Head, J. W., Seibert, N., Pratt, S., Smith, D., Zuber, M., Garvin, J. B., McGovern, P. J., and MOLA Science Team (1998b). Volcanic Calderas on Mars: Initial Views Using Mars Orbiter Laser Altimeter Data. In *Lunar and Planetary Institute Conference Abstracts*, page 1488.

Head, J. W., Greeley, R., Golombek, M. P., Hartmann, W. K., Hauber, E., Jaumann, R., Masson, P., Neukum, G., Nyquist, L. E., and Carr, M. H. (2001). Geological Processes and Evolution. *Space Science Reviews*, **96**, 263–292.

Head, J. W., Mustard, J. F., Kreslavsky, M. A., Milliken, R. E., and Marchant, D. R. (2003). Recent ice ages on Mars. *Nature*, **426**, 797–802.

Head, J. W., Neukum, G., Jaumann, R., Hiesinger, H., Hauber, E., Carr, M., Masson, P., Foing, B., Hoffmann, H., Kreslavsky, M., Werner, S., Milkovich, S., van Gasselt, S., and Co-Investigator Team, T. H. (2005). Tropical to mid-latitude snow and ice accumulation, flow and glaciation on Mars. *Nature*, **434**, 346–351.

Hiesinger, H. and Head, J. W. (2000). Characteristics and origin of polygonal terrain in southern Utopia Planitia, Mars: Results from Mars Orbiter Laser Altimeter and Mars Orbiter Camera data. *J. Geophys. Res.*, **105**, 11999–12022.

Hiesinger, H. and Head, J. W. (2002). Syrtis Major, Mars: Results from Mars Global Surveyor Data. In *Lunar and Planetary Institute Conference Abstracts*, page 1063.

Hiesinger, H. and Head, J. W. (2004). The Syrtis Major volcanic province, Mars: Synthesis from Mars Global Surveyor data. *J. Geophys. Res.*, **109**, 1004.

Hiesinger, H., Head, J. W., Wolf, U., Jaumann, R., and Neukum, G. (2002). Lunar mare basalt flow units: Thicknesses determined from crater size-frequency distributions. *Geophysical Research Letters*, **29**, 89–1.

Hiller, K. H., Neukum, G. P. O., Janle, P., Guest, J. E., and Lopes, R. M. C. (1982). Mars - Stratigraphy and gravimetry of Olympus Mons and its aureole. *J. Geophys. Res.*, **87**, 9905–9915.

Holsapple, K. A. (1987). Impact crater scaling laws. Technical report.

Holsapple, K. A. and Schmidt, R. M. (1987). Point source solutions and coupling parameters in cratering mechanics. *J. Geophys. Res.*, **92**(11), 6350–6376.

Ivanov, B. A. (2001). Mars/Moon Cratering Rate Ratio Estimates. *Space Science Reviews*, **96**, 87–104.

Ivanov, B. A. (2005). Earth/moon impact rate comparison: searching constraints for lunar secondary/primary cratering. *Icarus*, page submitted.

Ivanov, B. A., Nemchinov, I. V., Svetsov, V. A., Provalov, A. A., Khazins, V. M., and Phillips, R. J. (1992). Impact cratering on Venus - Physical and mechanical models. *J. Geophys. Res.*, **97**(16), 16167.

Ivanov, B. A., Deniem, D., and Neukum, G. (1997). Implementation of dynamic strength models into 2D hydrocodes: Applications for atmospheric breakup and impact cratering. *International Journal of Impact Engineering*, **20**, 411–430.

Ivanov, B. A., Neukum, G., and Wagner, R. (1999). Impact Craters, NEA, and Main Belt Asteroids: Size-Frequency Distribution. In *Lunar and Planetary Institute Conference Abstracts*, page 1583.

Ivanov, B. A., Neukum, G., and Wagner, R. (2001). Size-frequency distributions of planetary impact craters and asteroids. *Chemical Physics of Solid Surfaces*, pages 1–34.

Ivanov, B. A., Werner, S. C., and Neukum, G. (2005). Simple estimate for Gusev infilling thickness. In *1st Mars Express Science Conference*, page 151. ESA-ESTEC.

Ivanov, M. A. and Head, J. W. (2003). Syrtis Major and Isidis Basin contact: Morphological and topographic characteristics of Syrtis Major lava flows and material of the Vastitas Borealis Formation. *J. Geophys. Res.*, **108**, 17–1.

James, O. B. (1980). Rocks of the early lunar crust. In *Lunar and Planetary Science Conference*, pages 365–393.

Janle, P. (1983). Bouguer gravity profiles across the highland-lowland escarpment on Mars. *Moon and Planets*, **28**, 55–67.

Jull, A. J. T., Courtney, C., Jeffrey, D. A., and Beck, J. W. (1998). Isotopic Evidence for a Terrestrial Source of Organic Compounds Found in Martian Meteorite Allan Hill 84001 and Elephant Moraine 79001. *Science*, **279**, 366–369.

van Kan, M. (2004). Geologic evolution of the Gusev carter region Mars. *Masterthesis, Utrecht University*, page 149.

Klingelhöfer, G., Morris, R. V., Bernhardt, B., Schröder, C., Rodionov, D. S., de Souza, P. A., Yen, A., Gellert, R., Evlanov, E. N., Zubkov, B., Foh, J., Bonnes, U., Kankeleit, E., Gütlich, P., Ming, D. W., Renz, F., Wdowiak, T., Squyres, S. W., and Arvidson, R. E. (2004). Jarosite and Hematite at Meridiani Planum from Opportunity's Mössbauer Spectrometer. *Science*, **306**, 1740–1745.

König, B. (1977). Investigations of primary and secondary impact structures on the moon and laboratory experiments to study the ejecta of secondary particles. *Ph.D. Thesis*.

Koulouris, J., Janle, P., Milkereit, B., and Werner, S. (1999). Significance of large ocean impact craters. *Reports on Polar Research*, **343**, 48.

Kreslavsky, M. A. and Head, J. W. (2000). Kilometer-scale roughness of Mars: Results from MOLA data analysis. *J. Geophys. Res.*, **105**(14), 26695–26712.

Kreslavsky, M. A. and Head, J. W. (2005). Mars at very low obliquity: Atmospheric collapse and the fate of volatiles. *Geophysical Research Letters*, **32**, 12202.

Kuz'min, R. O. (1983). *Kriolitosfera Marsa.* Moskva : Izd-vo "Nauka", 1983.

Kuz'min, R. O., Bobina, N. N., Zabalueva, E. V., and Shashkina, V. P. (1989). *Structural irregularities of the upper layers of the Martian cryolithosphere*, pages 80–95. Space Chemistry and Comparative Planetology.

Kuzmin, R. O., Greeley, R., Landheim, R., Cabrol, N., and Farmer, J. D. (2000). Geological Map of the MTM–15182 and MTM–15187 Quadrangles, Gusev Crater – Ma'adim Vallis Region, Mars. *U.S. Geol. Surv., Misc. Invest. Map*, pages I–2666.

Lane, M. D. and Christensen, P. R. (2000). Convection in a catastrophic flood deposit as the mechanism for the giant polygons on Mars. *J. Geophys. Res.*, **105**, 17617–17628.

Lanz, J. (2003). Geometrische, morphologische und stratigraphische Untersuchungen ausgewählter Outflow Channel (Ausflusstäler) der Circum–Chryse–region, Mars, mit Methoden der Fernerkundung. *Ph.D. Thesis.*

Laskar, J., Correia, A. C. M., Gastineau, M., Joutel, F., Levrard, B., and Robutel, P. (2004). Long term evolution and chaotic diffusion of the insolation quantities of Mars. *Icarus*, **170**, 343–364.

Leighton, R. B., Murray, B., Sharp, R., Allen, J., and Sloan, R. (1965). Mariner IV Photography of Mars: Initial Results. *Science*, **149**, 627–630.

Levenberg, K. (1944). A Method for the Solution of Certain Problems in Least Squares. *Quart. Appl. Math.*, **2**, 164–168.

Lucchitta, B. K. (1981). Mars and earth - Comparison of cold-climate features. *Icarus*, **45**, 264–303.

Lucchitta, B. K. (1982). Ice sculpture in the Martian outflow channels. *J. Geophys. Res.*, **87**(16), 9951–9973.

Lucchitta, B. K. (1984). Ice and debris in the fretted terrain, Mars. *J. Geophys. Res.*, **89**, 409.

Lucchitta, B. K. (2001). Antarctic ice streams and outflow channels on Mars. *Geophysical Research Letters*, **28**, 403–406.

Lucchitta, B. K., Ferguson, H. M., and Summers, C. (1986). Sedimentary deposits in the northern lowland plains, Mars. *J. Geophys. Res.*, **91**, 166.

Malin, M. C. (1977). Comparison of volcanic features of Elysium /Mars/ and Tibesti /Earth/. *Geological Society of America Bulletin*, **88**, 908–919.

Malin, M. C. . M.-M. i. t. (1998). Early Views of the Martian Surface from the Mars Orbiter Camera of Mars Global Surveyor. *Science*, **279**, 1681–1692.

Mangold, N., Quantin, C., Ansan, V., Delacourt, C., and Allemand, P. (2004). Evidence for Precipitation on Mars from Dendritic Valleys in the Valles Marineris Area. *Science*, **305**, 78–81.

Marchenko, A. G., Basilevsky, A. T., Hoffmann, H., Hauber, E., Cook, A. C., and Neukum, G. (1998). Geology of the Common Mouth of the Ares and Tiu Valles, Mars. *Astronomicheskii Vestnik*, **32**, 425.

Marquardt, D. (1963). An Algorithm for Least-Squares Estimation of Nonlinear Parameters. *SIAM J. Appl. Math.*, **11**, 431–441.

Mars Channel Working Group (1983). Channels and valleys on Mars. *Geological Society of America Bulletin*, **94**, 1035–1054.

Masursky, H. and Crabill, N. L. (1976). The Viking landing sites - Selection and certification. *Science*, **193**, 809–812.

Masursky, H., Boyce, J. M., Dial, A. L., Schaber, G. G., and Strobell, M. E. (1977). Classification and time of formation of Martian channels based on Viking data. *J. Geophys. Res.*, **82**(11), 4016–4038.

McCauley, J. F. (1973). Mariner 9 Evidence for Wind Erosion in the Equatorial and Mid-Latitude Regions of Mars. *J. Geophys. Res.*, **78**(17), 4123–4137.

McCoy, T. J., Taylor, G. J., and Keil, K. (1992). Zagami - Product of a two-stage magmatic history. *Geochimica et Cosmochimica Acta*, **56**, 3571–3582.

McEwen, A., Turtle, E., Burr, D., Milazzo, M., Lanagan, P., Christensen, P., Boyce, J., and The Themis Science Team (2003). Discovery of a Large Rayed Crater on Mars: Implications for Recent Volcanic and Fluvial Activity and the Origin of Martian Meteorites. In *Lunar and Planetary Institute Conference Abstracts*, page 2040.

McEwen, A. S. (2003). Secondary Cratering on Mars: Implications for Age Dating and Surface Properties. In *Sixth International Conference on Mars*, page 3268.

McEwen, A. S., Preblich, B. S., Turtle, E. P., Artemieva, N. A., Golombek, M. P., Hurst, M., Kirk, R. L., Burr, D. M., and Christensen, P. R. (2005a). The rayed crater Zunil and interpretations of small impact craters on Mars. *Icarus*, **176**, 351–381.

McEwen, A. S., Preblich, B. S., Turtle, E. P., Artemieva, N. A., Golombek, M. P., Hurst, M., Kirk, R. L., Burr, D. M., and Christensen, P. R. (2005b). The rayed crater Zunil and interpretations of small impact craters on Mars. *Icarus*, **176**, 351–381.

McGill, G. E. (1977). Craters as "fossils": the remote dating of planetary surface materials. *Geological Society of America Bulletin*, **88**, 1102–1110.

McGill, G. E. (1985). Age and Origin of Large Martian Polygons. In *Lunar and Planetary Institute Conference Abstracts*, pages 534–535.

McGill, G. E. (1986). The giant polygons of Utopia, Northern Martian Plains. *Geophysical Research Letters*, **13**, 705–708.

McGill, G. E. (1989). Buried topography of Utopia, Mars - Persistence of a giant impact depression. *J. Geophys. Res.*, **94**(13), 2753–2759.

McGill, G. E. and Dimitriou, A. M. (1990). Origin of the Martian global dichotomy by crustal thinning in the late Noachian or early Hesperian. *J. Geophys. Res.*, **95**(14), 12595–12605.

McGill, G. E. and Hills, L. S. (1992). Origin of giant Martian polygons. *J. Geophys. Res.*, **97**(16), 2633–2647.

McKay, D. S., Gibson, E. K., Thomas-Keprta, K. L., Vali, H., Romanek, C. S., Clemett, S. J., Chiller, X. D. F., Maechling, C. R., and Zare, R. N. (1996). Search for past life on Mars: Possible relic biogenic activity in martian meteorite ALH84001. *Science*, **273**, 924–930.

McKinnon, W. B. and Melosh, H. J. (1980). Evolution of planetary lithospheres - Evidence from multiringed structures on Ganymede and Callisto. *Icarus*, **44**, 454–471.

McKinnon, W. B., Zahnle, K. J., Ivanov, B. A., and Melosh, H. J. (1997). Cratering on Venus: Models and Observations. In *Venus II: Geology, Geophysics, Atmosphere, and Solar Wind Environment*, page 969.

McSween, H. Y. and Harvey, R. P. (1998). An Evaporation Model for Formation of Carbonates in ALH 84001 Martian Meteorite. *Intern. Geol. Rev.*, **40**, 774–783.

McSween, H. Y., Arvidson, R. E., Bell, J. F., Blaney, D., Cabrol, N. A., Christensen, P. R., Clark, B. C., Crisp, J. A., Crumpler, L. S., Des Marais, D. J., Farmer, J. D., Gellert, R., Ghosh, A., Gorevan, S., Graff, T., Grant, J., Haskin, L. A., Herkenhoff, K. E., Johnson, J. R., Jolliff, B. L., Klingelhoefer, G., Knudson, A. T., McLennan, S., Milam, K. A., Moersch, J. E., Morris, R. V., Rieder, R., Ruff, S. W., de Souza, P. A., Squyres, S. W., Wänke, H., Wang, A., Wyatt, M. B., Yen, A., and Zipfel, J. (2004). Basaltic Rocks Analyzed by the Spirit Rover in Gusev Crater. *Science*, **305**, 842–845.

Mellon, M. T. and Jakosky, B. M. (1993). Geographic variations in the thermal and diffusive stability of ground ice on Mars. *J. Geophys. Res.*, **98**, 3345–3364.

Mellon, M. T. and Jakosky, B. M. (1995). The distribution and behavior of Martian ground ice during past and present epochs. *J. Geophys. Res.*, **100**, 11781–11799.

Melosh, H. (1989). *Impact Cratering*. Oxford University Press.

Melosh, H. J. and McKinnon, W. B. (1978). The mechanics of ringed basin formation. *Geophysical Research Letters*, **5**, 985–988.

Melosh, H. J., Ryan, E. V., and Asphaug, E. (1992). Dynamic fragmentation in impacts - Hydrocode simulation of laboratory impacts. *J. Geophys. Res.*, **97**(16), 14735.

Meyer, C. (2003). *Mars Meteorite Compendium*. NASA – Johnson Space Center, Houston.

Michel, P., Benz, W., Tanga, P., and Richardson, D. C. (2001). Collisions and Gravitational Reaccumulation: Forming Asteroid Families and Satellites. *Science*, **294**, 1696–1700.

Milam, K. A., Stockstill, K. R., Moersch, J. E., McSween, H. Y., Tornabene, L. L., Ghosh, A., Wyatt, M. B., and Christensen, P. R. (2003). THEMIS characterization of the MER Gusev crater landing site. *J. Geophys. Res.*, **108**, 19–1.

Mischna, M. A., Richardson, M. I., Wilson, R. J., and McCleese, D. J. (2003). On the orbital forcing of Martian water and CO_2 cycles: A general circulation model study with simplified volatile schemes. *J. Geophys. Res.*, **108**, 16–1.

Mitrofanov, I., Anfimov, D., Kozyrev, A., Litvak, M., Sanin, A., Tret'yakov, V., Krylov, A., Shvetsov, V., Boynton, W., Shinohara, C., Hamara, D., and Saunders, R. S. (2002). Maps of Subsurface Hydrogen from the High Energy Neutron Detector, Mars Odyssey. *Science*, **297**, 78–81.

Moore, H. J. (1976). *Missile impact craters (White Sands Missile Range, New Mexico) and their applications to lunar research*. Washington : U.S. Govt. Print. O, 1976.

Morbidelli, A. (1999). Origin and Evolution of Near Earth Asteroids. *Celestial Mechanics and Dynamical Astronomy*, **73**, 39–50.

Morris, E. C. and Underwood, J. R. (1978). . Technical report.

Morris, R. V., Klingelhöfer, G., Bernhardt, B., Schröder, C., Rodionov, D. S., de Souza, P. A., Yen, A., Gellert, R., Evlanov, E. N., Foh, J., Kankeleit, E., Gütlich, P., Ming, D. W., Renz, F., Wdowiak, T., Squyres, S. W., and Arvidson, R. E. (2004). Mineralogy at Gusev Crater from the Mössbauer Spectrometer on the Spirit Rover. *Science*, **305**, 833–837.

Mouginis-Mark, P. (1979). Martian fluidized crater morphology - Variations with crater size, latitude, altitude, and target material. *J. Geophys. Res.*, **84**(13), 8011–8022.

Mouginis-Mark, P. J. (1981). Ejecta emplacement and modes of formation of Martian fluidized ejecta craters. *Icarus*, **45**, 60–76.

Mouginis-Mark, P. J., Head, J. W., and Wilson, L. (1982). Explosive volcanism on Hecates Tholus, Mars - Investigation of eruption conditions. *J. Geophys. Res.*, **87**(16), 9890–9904.

Murray, J. B., Muller, J., Neukum, G., Werner, S. C., van Gasselt, S., Hauber, E., Markiewicz, W. J., Head, J. W., Foing, B. H., Page, D., Mitchell, K. L., Portyankina, G., and Co-Investigator Team, T. H. (2005). Evidence from the Mars Express High Resolution Stereo Camera for a frozen sea close to Mars' equator. *Nature*, **434**, 352–356.

Mutch, T. A., Arvidson, R. E., Head, J. W., Jones, K. L., and Saunders, R. S. (1976). *The geology of Mars*. Princeton, N.J., Princeton University Press, 1976. 409 p.

Neukum, G. (1983). Meteoritenbombardement und Datierung planetarer Oberflächen. *Habilitation Dissertation for Faculty Membership, Univ. of Munich*, page 186pp.

Neukum, G. and Hiller, K. (1981). Martian ages. *J. Geophys. Res.*, **86**(15), 3097–3121.

Neukum, G. and Horn, P. (1976). Effects of lava flows on lunar crater populations. *Moon*, **15**, 205–222.

Neukum, G. and Ivanov, B. A. (1994). Crater Size Distributions and Impact Probabilities on Earth from Lunar, Terrestrial-planet, and Asteroid Cratering Data. In *Hazards Due to Comets and Asteroids*, page 359.

Neukum, G. and König, B. (1976). Crater Size-Distribution Studies and Dating of Individual Lunar Craters. In *Lunar and Planetary Institute Conference Abstracts*, page 619.

Neukum, G. and Wise, D. U. (1976). Mars - A standard crater curve and possible new time scale. *Science*, **194**, 1381–1387.

Neukum, G., König, B., and Arkani-Hamed, J. (1975). A study of lunar impact crater size-distributions. *Moon*, **12**, 201–229.

Neukum, G., Ivanov, B. A., and Hartmann, W. K. (2001). Cratering Records in the Inner Solar System in Relation to the Lunar Reference System. *Space Science Reviews*, **96**, 55–86.

Neukum, G., Jaumann, R., Hoffmann, H., Hauber, E., Head, J. W., Basilevsky, A. T., Ivanov, B. A., Werner, S. C., van Gasselt, S., Murray, J. B., McCord, T., and HRSC Co-Investigator (2004). Recent and episodic volcanic and glacial activity on Mars revealed by the High Resolution Stereo Camera. *Nature*, **432**, 346–351.

Neumann, G. A., Zuber, M. T., Wieczorek, M. A., McGovern, P. J., Lemoine, F. G., and Smith, D. E. (2004). Crustal structure of Mars from gravity and topography. *J. Geophys. Res.*, **109**, 8002.

Nimmo, F. and Stevenson, D. J. (2000). Influence of early plate tectonics on the thermal evolution and magnetic field of Mars. *J. Geophys. Res.*, **105**(14), 11969–11980.

Nimmo, F. and Tanaka, K. (2005). Early Crustal Evolution of Mars. *Annual Review of Earth and Planetary Sciences*, **33**, 133–161.

Nyquist, L. E. and Shih, C.-Y. (1992). The isotopic record of lunar volcanism. *Geochimica et Cosmochimica Acta*, **56**, 2213–2234.

Nyquist, L. E., Bogard, D. D., Shih, C.-Y., Greshake, A., Stöffler, D., and Eugster, O. (2001). Ages and Geologic Histories of Martian Meteorites. *Space Science Reviews*, **96**, 105–164.

Oberbeck, V. R. and Morrison, R. H. (1973). The Secondary Crater Herringbone Pattern. In *Lunar and Planetary Institute Conference Abstracts*, page 570.

Öpik, E. J. (1960). The lunar surface as an impact counter. *Monthly Notices of the Royal Astronomical Society*, **120**, 404.

Öpik, E. J. (1965). Mariner IV and Craters on Mars. *Irish Astron. J.*, **7**, 92.

Öpik, E. J. (1966). The Martian Surface. *Science*, **153**, 255.

O'Keefe, J. D. and Ahrens, T. J. (1981). Impact cratering - The effect of crustal strength and planetary gravity. *Reviews of Geophysics and Space Physics*, **19**, 1–12.

Ori, G. G. and Mosangini, C. (1998). Complex depositional systems in Hydraotes Chaos, Mars: An example of sedimentary process interactions in the Martian hydrological cycle. *J. Geophys. Res.*, **103**(12), 22713–22724.

Owen, T., Maillard, J. P., de Bergh, C., and Lutz, B. L. (1988). Deuterium on Mars - The abundance of HDO and the value of D/H. *Science*, **240**, 1767–1770.

Palluconi, F. D. and Kieffer, H. H. (1981). Thermal inertia mapping of Mars from 60 deg S to 60 deg N. *Icarus*, **45**, 415–426.

Parker, T. J., Saunders, R. S., and Schneeberger, D. M. (1989). Transitional morphology in west Deuteronilus Mensae, Mars - Implications for modification of the lowland/upland boundary. *Icarus*, **82**, 111–145.

Pechmann, J. C. (1980). The origin of polygonal troughs on the northern plains of Mars. *Icarus*, **42**, 185–210.

Peterson, J. E. (1977). Geologic map of the noachis quadrangle of mars.

Pike, R. J. (1977). Size-dependence in the shape of fresh impact craters on the moon. In *Impact and Explosion Cratering: Planetary and Terrestrial Implications*, pages 489–509.

Pike, R. J. (1980a). Control of crater morphology by gravity and target type - Mars, earth, moon. In *Lunar and Planetary Science Conference*, pages 2159–2189.

Pike, R. J. (1980b). Formation of complex impact craters - Evidence from Mars and other planets. *Icarus*, **43**, 1–19.

Plescia, J. B. (1990). Recent flood lavas in the Elysium region of Mars. *Icarus*, **88**, 465–490.

Plescia, J. B. (2004). Morphometric properties of Martian volcanoes. *J. Geophys. Res.*, **109**, 3003.

Plescia, J. B. and Saunders, R. S. (1979). The chronology of the martian volcanoes. In *Lunar and Planetary Science Conference*, pages 2841–2859.

Plescia, J. B. and Saunders, R. S. (1981). Tectonics of the Tharsis region, Mars. *LPI Contributions*, **441**, 202.

Pollack, J. B., Kasting, J. F.and Richardson, S. M., and Poliakoff, K. (1987). The case for a wet, warm climate on early Mars. *Icarus*, **71**, 203–224.

Reese, C. C., Solomatov, V. S., Baumgardner, J. R., Stegman, D. R., and Vezolainen, A. V. (2004). Magmatic evolution of impact-induced Martian mantle plumes and the origin of Tharsis. *J. Geophys. Res.*, **109**, 8009.

Richardson, M. I. and Wilson, R. J. (2002). Investigation of the nature and stability of the Martian seasonal water cycle with a general circulation model. *J. Geophys. Res.*, **107**, 7–1.

Robinson, M. S. and Tanaka, K. L. (1990). Magnitude of a catastrophic flood event at Kasei Valles, Mars. *Geology*, **18**, 902–905.

Roddy, D. J., Boyce, J. M., Colton, G. W., and Dial, A. L. (1975). Meteor Crater, Arizona, rim drilling with thickness, structural uplift, diameter, depth, volume, and mass-balance calculations. In *Lunar and Planetary Science Conference*, pages 2621–2644.

Rossbacher, L. A. and Judson, S. (1981). Ground ice on Mars - Inventory, distribution, and resulting landforms. *Icarus*, **45**, 39–59.

Russell, P. S. and Head, J. W. (2002). The martian hydrosphere/cryosphere system: Implications of the absence of hydrologic activity at Lyot crater. *Geophysical Research Letters*, **29**, 8–1.

Sagan, C., Toon, O. B., and Gierasch, P. J. (1973). Climate Change on Mars. *Science*, **181**, 1045–1049.

Sawyer, D. J., McGehee, M. D., Canepa, J., and Moore, C. B. (2000). Water soluble ions in the Nakhla martian metorite. *Meteoritics and Planetary Science*, **35**, 743–747.

Schaber, G. G. (1973). Lava flows in Mare Imbrium: Geologic evaluation from Apollo orbital photography. In *Lunar and Planetary Science Conference*, page 73.

Schaber, G. G. (1980). Radar, visual, and thermal characteristics of Mars: Rough planar surfaces. *Icarus*, **42**, 159–184.

Schmidt, R. M. and Housen, K. R. (1987). Some recent advances in the scaling of impact and explosion cratering. *International Journal of Impact Engineering*, **5**, 543–560.

Schultz, P. and Lutz, A. B. (1988). Polar wandering of Mars. *Icarus*, **73**, 91–141.

Schultz, P. H. and Gault, D. E. (1979). Atmospheric effects on Martian ejecta emplacement. *J. Geophys. Res.*, **84**(13), 7669–7687.

Scott, D. H. (1978). Mars, highlands - lowlands: Viking contributions to Mariner relative age studies. *Icarus*, **34**, 479–485.

Scott, D. H. and Carr, M. H. (1978). The New Geologic Map of Mars (1:25 Million Scale). Technical report.

Scott, D. H. and Condit, C. D. (1977). Correlations: Martian stratigraphy and crater density. Technical report, NASA Technical Memo, X-3511.

Scott, D. H. and Tanaka, K. L. (1986). Geological Map of the Western Equatorial Region of Mars (1:15,000,000). *USGS*.

Sharp, R. P. (1973). Mars: Troughed Terrain. *J. Geophys. Res.*, **78**, 4063–4083.

Shearer, C. K. and Papike, J. (1999). Invited Review: Magmatic Evolution of the Moon. *American Mineralogy*, **84**, 1469–1494.

Shih, C.-Y., Nyquist, L. E., Reese, Y., and Wiesmann, H. (1998). The Chronology of the Nakhlite, Lafayette: Rb-Sr and Sm-Nd Isotopic Ages. In *Lunar and Planetary Institute Conference Abstracts*, page 1145.

Shoemaker, E. (1965). Preliminary analysis of the fine structure of the lunar surface in Mare Cognitum, in Ranger VII, part 2. In *Technical Report*, pages 75–134, California. Jet Propulsion Laboratory–.

Shoemaker, E. M. (1965). *Preliminary analysis of the fine structure of the lunar surface in Mare Cognitum.*, pages 23–78. Johns Hopkins Press.

Shoemaker, E. M. (1977). Astronomically observable crater-forming projectiles. In *Impact and Explosion Cratering: Planetary and Terrestrial Implications*, pages 617–628.

Shoemaker, E. M. and Hackman, R. J. (1962). Stratigraphic Basis for a Lunar Time Scale. In *IAU Symp. 14: The Moon*, pages 289–300.

Shoemaker, E. M., Hackman, R. J., and Eggleton, R. E. (1962). Interplanetary correlation of geologic time. *Advances in the Astronautical Sciences*, **8**, 70–89.

Shuvalov, V. V. (2003). Numerical Modeling of the Eltanin Impact. *Meteoritics & Planetary Science*, **38**, 5150.

Skinner, J. A., Tanaka, K. L., Hare, T. M., Kargel, J., Neukum, G., Werner, S. C., and Rodriguez, J. A. P. (2004). Mass-Wasting of the Circum-Utopia Highland/Lowland Boundary: Processes and Controls. In *Workshop on Hemispheres Apart: The Origin and Modification of the Martian Crustal Dichotomy*, page 58.

Sleep, N. H. (1994). Martian plate tectonics. *J. Geophys. Res.*, **99**(18), 5639.

Smith, D. E., Zuber, M. T., Frey, H. V., Garvin, J. B., Head, J. W., Muhleman, D. O., Pettengill, G. H., Phillips, R. J., Solomon, S. C., Zwally, H. J., Banerdt, W. B., and Duxbury, T. C. (1998). Topography of the Northern Hemisphere of Mars from the Mars Orbiter Laser Altimeter. *Science*, **279**, 1686.

Smith, D. E., Zuber, M. T., Solomon, S. C., Phillips, R. J., Head, J. W., Garvin, J. B., Banerdt, W. B., Muhleman, D. O., Pettengill, G. H., Neumann, G. A., Lemoine, F. G., Abshire, J. B., Aharonson, O., Brown, D. C., Hauck, S. A., Ivanov, A. B., McGovern, P. J., Zwally, H. J., and Duxbury, T. C. (1999a). The Global Topography of Mars and Implications for Surface Evolution. *Science*, **284**, 1495.

Smith, D. E., Sjogren, W. L., Tyler, L., Balmino, G., Lemoine, F. G., and Konopliv, A. S. (1999b). The Gravity Field of Mars: Results from Mars Global Surveyor. *Science*, **286**, 94.

Smith, D. E., Zuber, M. T., Frey, H. V., Garvin, J. B., Head, J. W., Muhleman, D. O., Pettengill, G. H., Phillips, R. J., Solomon, S. C., Zwally, H. J., Banerdt, W. B., Duxbury, T. C., Golombek, M. P., Lemoine, F. G., Neumann, G. A., Rowlands, D. D., Aharonson, O., Ford, P. G., Ivanov, A. B., Johnson, C. L., McGovern, P. J., Abshire, J. B., Afzal, R. S., and Sun, X. (2001). Mars Orbiter Laser

Altimeter: Experiment summary after the first year of global mapping of Mars. *J. Geophys. Res.*, **106**, 23689–23722.

Soderblom, L. A. (1970). A model for small–impact erosion applied to the lunar surface. *J. Geophys. Res.*, **75**, 2655–2661.

Soderblom, L. A., Condit, C. D., West, R. A., Herman, B. M., and Kreidler, T. J. (1974). Martian planetwide crater distributions - Implications for geologic history and surface processes. *Icarus*, **22**, 239–263.

Sohl, F., Schubert, G., and Spohn, T. (2005). Geophysical Constraints on the Composition and Structure of the Martian Interior. *J. Geophys. Res.*, page in press.

Solomon, S. C., Aharonson, O., Aurnou, J. M., Banerdt, W. B., Carr, M. H., Dombard, A. J., Frey, H. V., Golombek, M. P., Hauck, S. A., Head, J. W., Jakosky, B. M., Johnson, C. L., McGovern, P. J., Neumann, G. A., Phillips, R. J., Smith, D. E., and Zuber, M. T. (2005). New Perspectives on Ancient Mars. *Science*, **307**, 1214–1220.

Spohn, T., Acuña, M. H., Breuer, D., Golombek, M., Greeley, R., Halliday, A., Hauber, E., Jaumann, R., and Sohl, F. (2001). Geophysical Constraints on the Evolution of Mars. *Space Science Reviews*, **96**, 231–262.

Spudis, P. D. and Greeley, R. (1977). Volcanism in the cratered uplands of mars –a preliminary viking view. In *EOS Trans. AGU, 58*, page 1182.

Squyres, S. W. (1979). The distribution of lobate debris aprons and similar flows on Mars. *J. Geophys. Res.*, **84**, 8087–8096.

Squyres, S. W. and Carr, M. H. (1986). Geomorphic evidence for the distribution of ground ice on Mars. *Science*, **231**, 249–252.

Squyres, S. W., Grotzinger, J. P., Arvidson, R. E., Bell, J. F., Calvin, W., Christensen, P. R., Clark, B. C., Crisp, J. A., Farrand, W. H., Herkenhoff, K. E., Johnson, J. R., Klingelhöfer, G., Knoll, A. H., McLennan, S. M., McSween, H. Y., Morris, R. V., Rice, J. W., Rieder, R., and Soderblom, L. A. (2004a). In Situ Evidence for an Ancient Aqueous Environment at Meridiani Planum, Mars. *Science*, **306**, 1709–1714.

Squyres, S. W., Arvidson, R. E., Bell, J. F., Brückner, J., Cabrol, N. A., Calvin, W., Carr, M. H., Christensen, P. R., Clark, B. C., Crumpler, L., Des Marais, D. J., d'Uston, C., Economou, T., Farmer, J., Farrand, W., Folkner, W., Golombek, M., Gorevan, S., Grant, J. A., Greeley, R., Grotzinger, J., Haskin, L., Herkenhoff, K. E., Hviid, S., Johnson, J., Klingelhöfer, G., Knoll, A., Landis, G., Lemmon, M., Li, R., Madsen, M. B., Malin, M. C., McLennan, S. M., McSween, H. Y., Ming, D. W., Moersch, J., Morris, R. V., Parker, T., Rice, J. W., Richter, L., Rieder, R., Sims, M., Smith, M., Smith, P., Soderblom, L. A., Sullivan, R., Wänke, H., Wdowiak, T., Wolff, M., and Yen, A. (2004b). The Spirit Rover's Athena Science Investigation at Gusev Crater, Mars. *Science*, **305**, 794–800.

Stöffler, D. (2000). Maskelynite Confirmed as Diaplectic Glass: Indication for Peak Shock Pressures Below 45 GPa in All Martian Meteorites. In *Lunar and Planetary Institute Conference Abstracts*, page 1170.

Stöffler, D. and Ryder, G. (2001). Stratigraphy and Isotope Ages of Lunar Geologic Units: Chronological Standard for the Inner Solar System. *Space Science Reviews*, **96**, 9–54.

Stöffler, W. and Weber, J. (1986). Influence of hydrostatic pressure on the platinum levels in silicon. *Physical Review B*, **33**, 8892–8895.

Stevenson, D. J. (2001). Mars' core and magnetism. *Nature*, **412**, 214.

Stewart, E. M. and Head, J. W. (2001). Ancient Martian volcanoes in the Aeolis region: New evidence from MOLA data. *J. Geophys. Res.*, **106**(15), 17505–17514.

Strom, R. G. and Neukum, G. (1988). *The cratering record on Mercury and the origin of impacting objects*, pages 336–373. Mercury, University of Arizona Press.

Strom, R. G., Croft, S. K., and Barlow, N. G. (1992). *The Martian impact cratering record*, pages 383–423. Mars.

Strom, R. G., Malhotra, R., Ito, T., Yoshida, F., and Kring, D. A. (2005). The Origin of Planetary Impactors in the Inner Solar System. *Science*, **309**, 1847–1850.

Swindle, T. D., Treiman, A. H., Lindstrom, D. J., Burkland, M. K., Cohen, B. A., Grier, J. A., Li, B., and Olson, E. K. (2000). Noble gases in iddingsite from the Lafayette meteorite: Evidence for liquid water on Mars in the last few hundred million years. *Meteoritics and Planetary Science*, **35**, 107–115.

Tanaka, K. L. (1986). The stratigraphy of Mars. *J. Geophys. Res.*, **91**, 139–158.

Tanaka, K. L. and Scott, D. H. (1987). Geological Map of the Polar Regions of Mars (1:15,000,000). *USGS*.

Tanaka, K. L., Scott, D. H., and Greeley, R. (1992a). Global stratigraphy. In *Mars*, pages 345–382.

Tanaka, K. L., Scott, D. H., and Greeley, R. (1992b). *Global stratigraphy*, pages 345–382. Mars.

Tanaka, K. L., Skinner, J. A., Hare, T. M., Joyal, T., and Wenker, A. (2003). Resurfacing history of the northern plains of Mars based on geologic mapping of Mars Global Surveyor data. *J. Geophys. Res.*, **108**, 24.

Tanaka, K. L., Skinner, J. A., and Hare, T. M. (2005). Geological Map of the Northern Plains of Mars (1:15,000,000). *USGS*, page http://pubs.usgs.gov/sim/2005/2888/.

Tanaka, K. L., Skinner, J. A., and Barlow, N. G. (2005). The Crater Production Function for Mars: A -2 Cumulative Power-Law Slope for Pristine Craters >5 km in Diameter Based on Crater Distributions for Northern Plains Materials. In *36th Annual Lunar and Planetary Science Conference*, page 2162.

Taylor, S. R. (1982). *Planetary science: A lunar perspective.* Lunar and Planetary Institute, Houston.

Treiman, A. H. (1987). Geology of the Nakhlite and Chassigny Meteorites. *Meteoritics*, **22**, 517.

U.S. Geological Survey (USGS) (1989). Topographic maps of the western, eastern, equatorial and polar regions of mars.

Vickery, A. M. (1986). Size-velocity distribution of large ejecta fragments. *Icarus*, **67**, 224–236.

Wagner, R., Schreiner, B., van Gasselt, S., Neukum, G., and the HRSC Co-Investigator Team (2004). Chaotic Terrain in the Xanthe Terra and Hydraotes Chaos Areas of Eastern Valles Marineris as seen by the High Resolution Stereo Camera (HRSC): Evolutionary Characteristics, Erosional Processes, and Time-Stratigraphic Relationships. In *40th Vernadsky-Brown Microsymposium*, page 40.

Wänke, H., Brückner, J., Dreibus, G., Rieder, R., and Ryabchikov, I. (2001). Chemical Composition of Rocks and Soils at the Pathfinder Site. *Space Science Reviews*, **96**, 317–330.

Ward, W. R. (1992). *Long-term orbital and spin dynamics of Mars*, pages 298–320. Mars.

Warren, P. H. (1998). Petrologic evidence for low-temperature, possibly flood evaporitic origin of carbonates in the ALH84001 meteorite. *J. Geophys. Res.*, **103**(12), 16759–16774.

Watters, T. R. (2003). Lithospheric fexure and the origin of the dichotomy boundary on Mars. *Geology*, **31**, 271–274.

Werner, S. C. and Neukum, G. (2003). The End of the Heavy Bombardment as Reflected in the Ages of Martian Impact Basins. In *Lunar and Planetary Institute Conference Abstracts*, page 1986.

Werner, S. C., Harris, A. W., Neukum, G., and Ivanov, B. A. (2002). NOTE: The Near-Earth Asteroid Size-Frequency Distribution: A Snapshot of the Lunar Impactor Size-Frequency Distribution. *Icarus*, **156**, 287–290.

Werner, S. C., van Gasselt, S., and Neukum, G. (2003a). Continual geological activity in Athabasca Valles, Mars. *J. Geophys. Res.*, **108**, 22–1.

Werner, S. C., van Gasselt, S., and Neukum, G. (2003b). The Erosional History of Athabasca Valles, Mars. In *Lunar and Planetary Institute Conference Abstracts*, page 1996.

Werner, S. C., Ivanov, B. A., and Neukum, G. (2004a). Impact Cratering on Mars: Search for Target Influence on Morphology. In *Lunar and Planetary Institute Conference Abstracts*, page 1953.

Werner, S. C., Neukum, G., and HRSC Co-Investigator (2004b). New insights into the evolutionary history of the major volcanic constructs from Mars Express HRSC data. In *AAS/Division for Planetary Sciences Meeting Abstracts*, volume 36.

Werner, S. C., Ivanov, B. A., Neukum, G., van Kan, M., Zegers, T. E., Foing, B. H., Greeley, R., Williams, D. A., and The HRSC Co-Investigator Team (2005a). Evolutionary History of Gusev – The MER Landing Site – Seen by MEX-HRSC. In *36th Annual Lunar and Planetary Science Conference*, page 1777.

Werner, S. C., Neukum, G., and The HRSC Co-Investigator Team (2005b). Major Volcanic Constructs Seen from Mars Express HRSC – New Insights into Their Evolutionary History. In *36th Annual Lunar and Planetary Science Conference*, page 1766.

Wetherill, G. W. (1967). Collisions in the asteroid belt. *J. Geophys. Res.*, **72**, 2429–2444.

Wetherill, G. W. (1975). Late heavy bombardment of the moon and terrestrial planets. In *Lunar and Planetary Science Conference*, pages 1539–1561.

Wetherill, G. W. (1979). Steady state populations of Apollo-Amor objects. *Icarus*, **37**, 96–112.

Wilhelms, D. E. (1974). Comparision of Martian and lunar geologicc provinces. *J. Geophys. Res.*, **79**, 3933–3941.

Wilhelms, D. E. (1976). Secondary impact craters of lunar basins. In *Lunar and Planetary Science Conference*, pages 2883–2901.

Wilhelms, D. E. (1987). The Geologic History of the Moon. *U. S. Geol. Surv. Prof. Pap*, **1348**, pp. 302.

Wilhelms, D. E. and Squyres, S. W. (1984). The martian hemispheric dichotomy may be due to a giant impact. *Nature*, **309**, 138–140.

Wilhelms, D. E., Oberbeck, V. R., and Aggarwal, H. R. (1978). Size-frequency distributions of primary and secondary lunar impact craters. In *Lunar and Planetary Science Conference*, pages 3735–3762.

Williams, D. A., Greeley, R., Zuschneid, W., Werner, S. C., Neukum, G., Crown, D. A., Gregg, T. K. P., Gwinner, K., Raitala, J., and The HRSC Co-Investigator Team (2005). Hadriaca Patera: Insights into its volcanic history from Mars Express HRSC. *J. Geophys. Res.*, page in prep.

Williams, K. K. and Zuber, M. T. (1998). Measurement and Analysis of Lunar Basin Depths from Clementine Altimetry. *Icarus*, **131**, 107–122.

Wilson, L. and Mouginis-Mark, P. J. (2003). Phreatomagmatic explosive origin of Hrad Vallis, Mars. *J. Geophys. Res.*, **108**, 1–1.

Wilson, L., Scott, E. D., and Head, J. W. (2001). Evidence for episodicity in the magma supply to the large Tharsis volcanoes. *J. Geophys. Res.*, **106**, 1423–1433.

Wise, D. U., Golombek, M. P., and McGill, G. E. (1979a). Tectonic evolution of Mars. *J. Geophys. Res.*, **84**(13), 7934–7939.

Wise, D. U., Golombek, M. P., and McGill, G. E. (1979b). Tharsis Province of Mars - Geologic sequence, geometry, and a deformation mechanism. *Icarus*, **38**, 456–472.

Wohletz, K. H., Sheridan, M. F., and Brown, W. K. (1989). Particle size distributions and the sequential fragmentation/transport theory applied to volcanic ash. *J. Geophys. Res.*, **94**(13), 15703–15721.

Wood, C. A. (1979). Monogenetic volcanoes of the terrestrial planets. In *Lunar and Planetary Science Conference*, pages 2815–2840.

Wood, C. A. and Ashwal, L. D. (1982). SNC meteorites - Igneous rocks from Mars. In *Lunar and Planetary Science Conference*, pages 1359–1375.

Wood, C. A. and Head, J. W. (1976). Comparison of impact basins on Mercury, Mars and the moon. In *Lunar and Planetary Science Conference*, pages 3629–3651.

Wood, C. A., Head, J. W., and Cintala, M. J. (1978). Interior morphology of fresh Martian craters - The effects of target characteristics. In *Lunar and Planetary Science Conference*, pages 3691–3709.

Woodworth-Lynas, C. and Guigné, J. Y. (2003). Ice Keel Scour Marks on Mars: Evidence for Floating and Grounding Ice Floes in Kasei Valles. *Oceanography*, **16**, 90–97.

Yoder, C. F. (1995). *Astrometric and geodetic properties of the Earth and the solar system*. AGU, Washington.

Yuan, D., Sjogren, W. L., Konopliv, A. S., and Kucinskas, A. B. (2001). Gravity field of Mars: A 75th Degree and Order Model. *J. Geophys. Res.*, **106**(15), 23377–23402.

Zhong, S. (2002). Effects of lithosphere on the long-wavelength gravity anomalies and their implications for the formation of the Tharsis rise on Mars. *J. Geophys. Res.*, **107**, 8–1.

Zhong, S. and Zuber, M. T. (2001). Degree-1 mantle convection and the crustal dichotomy on Mars. *Earth and Planetary Science Letters*, **189**, 75–84.

Zuber, M. T. (2001). The crust and mantle of Mars. *Nature*, **42**, 220–227.

Zuber, M. T., Solomon, S. C., Phillips, R. J., Smith, D. E., Tyler, G. L., Aharonson, O., Balmino, G., Banerdt, W. B., Head, J. W., Johnson, C. L., Lemoine, F. G., McGovern, P. J., Neumann, G. A., Rowlands, D. D., and Zhong, S. (2000). Internal Structure and Early Thermal Evolution of Mars from Mars Global Surveyor Topography and Gravity. *Science*, **287**, 1788–1793.

Zuschneid, W. (2005). Untersuchung der chronostatigraphischen Abfolge im Gebiet der Ausflusstäler Dao und Niger Vallis und des Vulkans Hadriaca Patera, Mars, Diploma Thesis.

Zuschneid, W., Neukum, G., Werner, S. C., Greeley, R., Williams, D., and The HRSC Co-Investigator Team (2005). Development of Fluvial Activity at Dao Vallis, Niger Vallis, and Hadriaca Patera as derived from HRSC Image Data. In *European Geosciences Union*, pages EGU05–A–08664.

D. Curriculum Vitae

08.07.1974	geboren in Würzburg
1980–1984	Grundschule, Hannover
1984–1986	Orientierungsstufe, Hannover und Celle
1986–1994	Gymnasium, Celle
1994	Allgemeine Hochschulreife
1994–1999	Studium der Geophysik, Universität zu Kiel
1996	Vor–Diplom in Geophysik
1997	Studentische Hilfskraft am Flerov Laboratorium für Nucleare Reaktionen des Joint Institute for Nuclear Research, Dubna, Russia
1998	Auslandssemester an der Universität Oulu, Finnland
1999	Diplom in Geophysik
1999–2001	Forschungsstipendium der Münchener Rück–Versicherung am Deutschen Zentrum für Luft– und Raumfahrt (DLR), Berlin
2001	Wissenschaftliche Mitarbeiterin an der Freien Universität Berlin (in Zusammenarbeit mit dem DLR, Berlin)
Seit 2002	Wissenschaftliche Mitarbeiterin an der Freien Universität Berlin

... Stephanie C. Werner

Hiermit versichere ich, dass ich die vorliegende Arbeit selbständig und ohne Benutzung anderer als der angegebenen Hilfsmittel angefertigt habe. Die aus fremden Quellen direkt oder indirekt übernommenen Gedanken sind kenntlich gemacht. Diese Arbeit wurde in gleicher oder ähnlicher Form keiner anderen Prüfungsbehörde vorgelegt.

Berlin, den 01. Dezember 2005 Stephanie C. Werner